Crystallography Reports, Vol. 47, No. 6, 2002, pp. 1003–1006. Translated from Kristallografiya, Vol. 47, No. 6, 2002, pp. 1072–1075.

LATTICE DYNAMICS AND PHASE TRANSITIONS

Characteristics of Irreducible Vectors Rotating in Superstructures with Two One-Component Order Parameters[1]

Yu. D. Zavorotnev and L. I. Medvedeva

Donetsk Physicotechnical Institute, National Academy of Sciences of Ukraine, Donetsk, 83114 Ukraine

Received January 10, 2002

Abstract—It is shown that incommensurate long-period structures formed by two synchronously rotating irreducible magnetic vectors are unstable and split into two interacting superstrucures. The behavior of such states away from and close to the phase-transition line is considered. *© 2002 MAIK "Nauka/Interperiodica".*

The possibility of the formation of modulated magnetic structures (MMS) was indicated for the first time in [1–3]. The first MMS was detected experimentally in $MnAu_2$ [4]. The theory of the formation of MMS proposed in [1–3] was based on the classical analogue of the Heisenberg Hamiltonian.

Some mechanisms of formation of MMS in magnets have become clear after the publication of the paper by Dzyaloshinskiĭ [5], which is devoted to the theory of long-period exchange structures with a spatial period incommensurate with the period of the crystal lattice. The density of nonequilibrium thermodynamic potential (NTDP) was expanded in a power series in the order parameters (OP) and their derivatives with respect to coordinates. The latter appear in the expansion only in the form of antisymmetric combinations (Lifshits invariants). The competition of terms that are linear in the first spatial derivatives with quadratic terms in NTDP leads to the formation of a superstructure. The approximation of constant moduli of irreducible vectors (IRV) [6, 7] simplifies the solution of the problem, leading to a linear system of differential equations for determining the IRV component. It was found that MMS can be formed only in the case of spontaneous continuous phase transitions (PT) (which are close in temperature) in each of the respective IRV involved in the transition under investigation [6, 7]. The corresponding phase diagrams were constructed [6], the magnitude of the vector of propagation of MMS was determined [7], and the behavior of MMS in weak magnetic fields was considered taking weak anisotropy into account [8]. In addition, the possibility of mutual transitions between cycloidal and spiral structures and the existence of structures formed by fragments of a superstructure and separated by domain walls were demonstrated [8].

The MMS obtained in [6–8] are formed by two synchronously rotating vectors. The phase difference φ between these vectors was also assumed to be constant and equal to $\pi/2$ or $3\pi/2$ depending on the sign of the coefficient Δ of the term that is linear in the first spatial derivative of the IRV [7]. The correctness of the approximation of constant moduli of IRVs has not been substantiated so far in connection with MMS. Although this approximation is applied in the absence of anharmonic terms in the NTDP and far away from the PT, the number of such terms is quite large, which can be verified by using the method of rational integer basis of invariants [9]. If anharmonic terms have a much larger weight in the NTDP than the terms containing derivatives, they determine the "rough" structure in accordance with [5]. Consequently, for φ = const, the system of differential equations is linear, and the approximation of constant moduli of IRV "operates" (this approximation becomes incorrect for φ ≠ const and in the presence of small anharmonic terms due to the emerging nonlinearity of the system).

Let us consider the properties of MMS using as an example the rhombic antiferromagnet Cr_2BeO_3 (space group D_{2h}^{16}). In this compound, below 28 K, there exists a long-period double cycloidal structure with the vector of propagation along the *C* axis of the rhombic crystal [10]. The unit crystallochemical cell in Cr_2BeO_3 contains two types of crystallographically inequivalent chromium ions (in the *b* and *c* positions). For each type of ions, we introduce the principal antiferromagnetism vector $\mathbf{G}_1 = \mathbf{S}_1 - \mathbf{S}_2 + \mathbf{S}_3 - \mathbf{S}_4$ and $\mathbf{G}_2 = \mathbf{S}_5 - \mathbf{S}_6 + \mathbf{S}_7 - \mathbf{S}_8$, where $\mathbf{S}_i$ ($i = 1, \ldots, 8$) is the magnetic vector of the *i*th ion. These vectors are single-component Ops, since they are transformed according to one-dimensional irreducible representations of the transposition group. We assume that the coefficient of the invariant $G_1^2 G_2^2$ is small and must be taken into account at the second stage of minimization. The corresponding density of the NTDP in the exchange approximation has the

[1] Presented at the Symposium "Phase Transitions in Solid Solutions and Alloys," Sochi, Russia, 2001.

1063-7745/02/4706-1003$22.00 © 2002 MAIK "Nauka/Interperiodica"

form [10]

$$\Phi = \delta_1 G_1^2 + \delta_2 G_2^2 + \Delta\left(\mathbf{G}_1\frac{d\mathbf{G}_2}{dz} - \mathbf{G}_2\frac{d\mathbf{G}_1}{dz}\right) + \alpha_1\left(\frac{d\mathbf{G}_1}{dz}\right)^2 + \alpha_2\left(\frac{d\mathbf{G}_2}{dz}\right)^2 + \beta G_1^2 G_2^2, \quad (1)$$

where $\delta_1 = \beta_1(T - T_1)$, $\delta_2 = \beta_2(T - T_2)$, and Δ and α_i (i = 1, 2) are the exchange interaction constants; T_1 and T_2 are the characteristic temperatures; and β is the anharmonic interaction coefficient. The Cartesian z axis coincides with the C axis of the crystal. In this system of coordinates, the system of Ostrogradski equations describing the minimum of the NTDP has the form

$$\begin{cases} \alpha_1 G_{1z}'' - \Delta G_{2z}' - \delta_1 G_{1z} - \beta G_{1z}(G_{2z}^2 + G_{2y}^2) = 0 \\ \alpha_1 G_{1y}'' - \Delta G_{2y}' - \delta_1 G_{1y} - \beta G_{1y}(G_{2z}^2 + G_{2y}^2) = 0 \\ \alpha_2 G_{2z}'' + \Delta G_{1z}' - \delta_2 G_{2z} - \beta G_{2z}(G_{1z}^2 + G_{1y}^2) = 0 \\ \alpha_2 G_{2y}'' + \Delta G_{1y}' - \delta_2 G_{2y} - \beta G_{2y}(G_{1z}^2 + G_{1y}^2) = 0. \end{cases} \quad (2)$$

Here and below, all derivatives are calculated with respect to z. The solution of the system of equations (2) can be chosen in the form

$$G_{1z} = |\mathbf{G}_1|\cos(kz), \quad G_{2z} = |\mathbf{G}_2|\cos(kz - \gamma), \quad G_{1y} = |\mathbf{G}_1|\sin(kz), \quad G_{2y} = |\mathbf{G}_2|\sin(kz - \gamma). \quad (3)$$

In the model $|\mathbf{G}_1|$ = const, $|\mathbf{G}_2|$ = const, $\beta = 0$ for γ = const, the system of equations (2) is linear and two equations out of four are independent. The minimization of potential (1) in the parameter γ gives the value $\gamma = \pi/2$ for $\Delta < 0$ and $\gamma = 3\pi/2$ for $\Delta > 0$ [7].

Let us consider the stability of the obtained value of γ. If we remove the requirement of the constancy of γ, the Ostrogradski system in the polar system of coordinates contains five coupled second-order differential equations. One of these equations has the form

$$\alpha_2 G_2^2\gamma'' + 2\alpha_2 G_2 G_2'(\gamma' - k) + \Delta\mathbf{G}_1\mathbf{G}_2 k\cos\gamma - \Delta\mathbf{G}_1'\mathbf{G}_2\sin\gamma + 0.5\beta G_1^2 G_2^2\sin\gamma = 0. \quad (4)$$

For a small variation of the moduli of IRV, i.e., at a large distance from the PT line, the first and third terms in Eq. (4) dominate. In the terminology of the theory of oscillations, the second and fourth terms describe oscillating friction and the last term describes the perturbing force. Obviously, Eq. (4) for $\alpha_2 > 0$, $|2\Delta k| \gg |\beta G_1 G_2|$, and any sign of Δ is analogous to the mathematical pendulum equation with a repulsive force. In the analysis of Eq. (4), it is convenient to pass to a new variable φ through the relations

$$\varphi = \begin{cases} \pi/2 - \gamma, & \Delta < 0 \\ 3\pi/2 - \gamma, & \Delta > 0. \end{cases}$$

For small values of G_1', G_2', and β, the motion is virtually identical to the formal case when $G_1' = 0$, $G_2' = 0$, and $\beta = 0$. It is well known that, for small φ, the phase trajectories of a representative point on the phase plane form a family of equilateral hyperbolas [11]. Only two asymptotes of this family pass through the saddle-type singular point. The representative point is always at an infinitely long distance from the equilibrium position. The only exception is the motion along the asymptote [11], which is the limiting motion in this case, i.e., asymptotic relative to the equilibrium state. For $|2\Delta k| \ll |\beta G_1 G_2|$, the external perturbing force becomes dominant and determines the type of oscillations. For example, for $\beta \neq 0$, stable states are possible for $\gamma = \pm\pi/2$ depending on the sign. The analysis of these cases is beyond the scope of this paper.

Thus, in the approximation of constant moduli of IRV, the incommensurate structure is stable for $\Delta > 0$ and $\Delta < 0$. However, this equilibrium becomes unstable when even small nonlinearities appear (which are always present in real crystals), which leads to the splitting of a single MMS formed by two IRVs into two independent ($\beta = 0$) or interacting ($\beta \neq 0$) superstructures.

Let us consider this problem in greater detail in a model of a NTDP of type (1). In order to find the solution, we will use the Van der Pol method [11]. The solutions of the complete system are sought in the form

$$\begin{aligned} G_{1z} &= G_{11}\cos(kz + \gamma_1) = a(z)\cos kz + b(z)\sin kz, \\ G_{2z} &= -G_{21}\sin(kz + \gamma_2) = -c(z)\sin kz + d(z)\cos kz, \\ G_{1y} &= G_{12}\sin(kz + \gamma_1) = e(z)\sin zk - f(z)\cos kz, \\ G_{2y} &= G_{22}\cos(kz + \gamma_2) = g(z)\cos kz + h(z)\sin kz, \end{aligned} \quad (5)$$

where G_{11}, G_{12}, G_{21}, and G_{22} are the corresponding amplitudes depending on z and the phase shifts γ_1 and γ_2 are functions of z. If we assume that the IRVs in the MMS have circular hodographs, i.e., $G_{11} = G_{12}$ and $G_{21} = G_{22}$, equations of the form $\sin^2 x + \cos^2 x = 0$ emerging in the course of calculations have no solutions. Consequently, the crystal can contain only MMS with an elliptical hodograph, which can be regarded as two waves with mutually perpendicular planes of vibrations.

Substituting relations (5) into the system of equations (2) and discarding all "oscillating" terms, we obtain a system of eight truncated equations. Numerical solution for small values of β and at a large distance from the PT line proved that the quantities a, b, c, d, e, f, g, and h, which are proportional to the amplitudes and to one of the functions ($\sin\gamma$ or $\cos\gamma$), vary according to the sinusoidal law. Such a dependence of these quantities reflects the linear relation between the quantities γ_1 and γ_2 and coordinate z, i.e., the small variation of the amplitudes G_{11}, G_{12}, G_{21}, and G_{22}. Consequently, MMS

has the form of two interacting waves with elliptical hodographs, each of which is formed by only one of the IRVs.

As we approach the PT line, the dependence of the coefficients a, b, c, d, e, f, g, and h on coordinate z becomes more complex than sinusoidal. This indicates the development of a strong coordinate dependence of the amplitudes G_{11}, G_{12}, G_{21}, and G_{22}.

In order to confirm the above conclusions, we carried out a numerical solution of system (2) with the help of the Stifz function in the Mathcad medium. This method of solution makes it possible to confirm indirectly the stability of the solutions obtained. The following results were obtained ($T_2 > T_1$ and the numerical value of Δ is smaller than the numerical values of α_i ($i = 1, 2$)).

1. A stable superstructure is formed for $\delta_1 < 0$ and $\delta_2 < 0$. At a large distance from PT lines and for small values of Δ, the moduli of IRVs are practically constant, and the periods of spatial oscillations of vectors $\mathbf{G}_1$ and $\mathbf{G}_2$ are different. This means that two different interacting superstructures are present in the crystal. As we approach the PT lines, a spatial amplitude modulation (AM) of the components of the "carrier oscillation" appears because of the coordinate dependence of the moduli of each irreducible vector. Since the quantity Δ reflects nonuniformities in the exchange interaction, an increase in $|\Delta|$ leads to an additional complex modulation of IRV components. The carrier oscillation becomes aperiodic at small distances (see Fig. 1a), and different groups of oscillations participate in two different AMs with a phase shift of π. Simultaneously, an AM with a giant period (hyperperiod) appears, which is unnoticeable at small distances (see Fig. 1b). If the value of Δ is comparable with the value of α_i, the AM whose amplitude increases with z is observed, as before, for small values of z, and remodulation takes place for some z values. For large values of z, secondary modulation dominates, and small-amplitude carrier oscillations are observed against the background of this modulation (Fig. 2). In this case, the conventional AM is decomposed into two components which "glide" over the remodulation curve with a large spatial period (hyperperiod) in accordance with a sinusoidal law. The y components of IRV also exhibit a similar behavior, but all processes in this case are shifted in space relative to the z components. As $T \longrightarrow T_1$, remodulation becomes periodic, but not sinusoidal. No remodulation is observed for the $\mathbf{G}_2$ vector, but the AM for $\mathbf{G}_1$ is no longer symmetric relative to the x axis. As $|\Delta|$ increases, the number of periods of remodulation increases.

2. As the value of $|T_2 - T_1|$ decreases, an additional AM with a relatively small amplitude and a period that is an order of magnitude smaller appears below T_1 for large negative values of Δ against the background of the giant modulation (Fig. 3). This AM vanishes as we approach T_1, and the frequency of the giant modulation

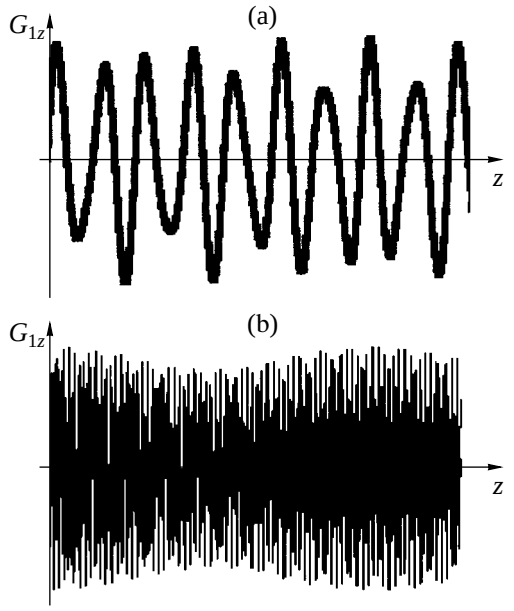

Fig. 1. Coordinate dependence of the component G_{1z} at (a) small and (b) large distances.

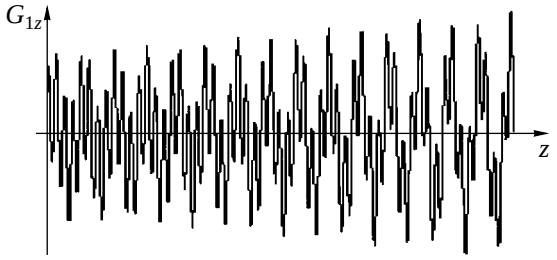

Fig. 2. Coordinate dependence of the component G_{1z} for large values of Δ.

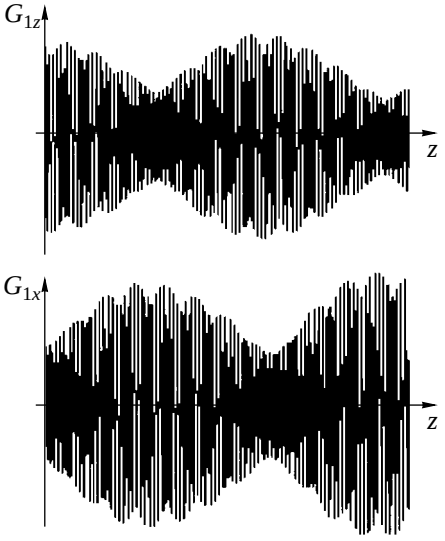

Fig. 3. Coordinate dependence of irreducible vectors for large negative values of Δ and for small values of $|T_2 - T_1|$ below T_1.

increases significantly. As before, hypermodulation is accompanied by conventional remodulation, which also splits into two components. Four components appear for the same values of the parameters, except for $T_1 > T_2$.

In an eight-sublattice magnet, there are eight irreducible magnetic vectors whose sum is a constant quantity. Only two of these vectors ($\mathbf{G}_1$ and $\mathbf{G}_2$) form a superstructure, and a change in their moduli leads to a change in the remaining vectors. Only the sum of the squares of six vectors exhibits a synchronous behavior, but each of these vectors is not fixed in sign and, hence, is not ordered.

Thus, in the approximation of constant moduli of IRV, the long-period structure is found to be unstable. The variability of the IRV moduli for small values of β leads to the emergence of two weakly interacting superstructures each of which is stable. These superstructures have different spatial periods; consequently, there is no need to synchronize the phases of rotation of IRV. The superposition of several temperature-dependent AMs with different periods is responsible for the complex nature of variation of IRV moduli.

REFERENCES

1. J. Villain, J. Phys. Chem. Solids **11**, 303 (1959).
2. T. A. Kaplan, Phys. Rev. **116**, 888 (1959).
3. A. Yoshimori, J. Phys. Soc. Jpn. **14**, 807 (1959).
4. A. Herpin and P. Meriel, J. Phys. (Paris) **22**, 337 (1961).
5. I. E. Dzyaloshinskiĭ, Zh. Éksp. Teor. Fiz. **46**, 1420 (1964) [Sov. Phys. JETP **19**, 960 (1964)].
6. V. G. Bar'yakhtar and E. P. Stefanovskiĭ, Fiz. Nizk. Temp. **22**, 904 (1996) [Low Temp. Phys. **22**, 693 (1996)].
7. V. G. Bar'yakhtar, E. P. Stefanovskiĭ, and D. A. Yablonskiĭ, Fiz. Tverd. Tela (Leningrad) **28**, 504 (1986) [Sov. Phys. Solid State **28**, 281 (1986)].
8. Yu. D. Zaviritnev and L. I. Medvedeva, Fiz. Nizk. Temp. **25**, 567 (1999) [Low Temp. Phys. **25**, 420 (1999)].
9. Yu. M. Gufan, *Structural Phase Transitions* (Nauka, Moscow, 1982).
10. V. G. Bar'yakhtar, E. P. Stefanovskiĭ, and D. A. Yablonskiĭ, Pis'ma Zh. Éksp. Teor. Fiz. **42**, 258 (1985) [JETP Lett. **42**, 317 (1985)].
11. A. A. Andriniv, A. A. Vitt, and S. É. Khaĭkin, *Theory of Oscillations* (Fizmatgiz, Moscow, 1959).

Translated by N. Wadhwa

Crystallography Reports, Vol. 47, No. 6, 2002, pp. 1007–1011. Translated from Kristallografiya, Vol. 47, No. 6, 2002, pp. 1076–1080.

LATTICE DYNAMICS AND PHASE TRANSITIONS

Growth and Study of $PbFe_{1/2}Ta_{1/2}O_3$ Single Crystals[1]

I. P. Raevskiĭ, V. V. Eremkin, V. G. Smotrakov, M. A. Malitskaya, S. A. Bogatina, and L. A. Shilkina

Research Institute of Physics, Rostov State University, pr. Stachki 194, Rostov-on-Don, 344090 Russia

e-mail: rip@ip.rsu.ru

Received January 10, 2002

Abstract—Single crystals of the composition $PbFe_{1/2}Ta_{1/2}O_3$ are grown by the method of mass crystallization from flux. It is established that, unlike the $PbFe_{1/2}Ta_{1/2}O_3$ ceramic, the synthesized single crystals possess pronounced relaxor properties: the maximum of the dielectric constant is diffuse and its temperature, T_m, increases by more than 70 K with an increase in the frequency from 10^2 to 10^6 Hz. It is assumed that the unusual properties of the $PbFe_{1/2}Ta_{1/2}O_3$ crystals are caused by mesoscopically inhomogeneous compositional ordering and comparatively high conductivity providing favorable conditions for the appearance of the volume-charge and thermal electron polarization. © *2002 MAIK "Nauka/Interperiodica".*

INTRODUCTION

Ternary perovskites of the 1 : 1 type described by the general formula $Pb(B^{3+}_{1/2}B^{5+}_{1/2})O_3$, where B^{3+} = Sc, In, and Yb and B^{5+} = Nb and Ta, are the classical model objects for studying ferroelectric–relaxors, because their properties can vary over a wide range without changes in their chemical composition only because of the variation in the degree of order, S, of B^{3+} and B^{5+} ions distributed over the equivalent sites of the crystal lattice (the compositional order) [1–4]. In a state with a high degree of order, these oxides undergo a nondiffuse antiferroelectric (B^{3+} = In, Yb) or a ferroelectric (B^{3+} = Sc) phase transition, whereas in a disordered state, they possess the properties typical of relaxors [1–5], namely, both the dielectric constant ε_m and the temperature of the maximum $\varepsilon(T)$ of T_m are essentially dependent on the frequency f of the measuring field.

Oxides with B^{3+} = Fe have a special place among $Pb(B^{3+}_{1/2}B^{5+}_{1/2})O_3$ perovskites. Unlike the situation with other oxides of this series, all the numerous attempts to synthesize ordered PFT ceramics with the aid of prolonged high-temperature annealing [1, 11] gave no rise to the formation of the superstructure associated with the ordering of Fe^{3+} and Nb^{5+} (Ta^{5+}) ions: the X-ray diffraction method revealed no superstructure either in $PbFe_{1/2}Nb_{1/2}O_3$ (PFN) or in $PbFe_{1/2}Ta_{1/2}O_3$ (PFT) [1, 5–11]. At the same time, the experimental values of the Néel temperature T_N for PFN and PFT (~150 K) lie approximately in the middle between the calculated values for $S \approx 1$ and 0, which is usually interpreted as evidence of the partial ordering of ions (T_N is essentially dependent on S because, during ordering, the number of magnetically active ions in the neighboring cells changes [5, 6]). Most probably, the ordering of ions in PFN and PFT occurs locally; i.e., the crystal has mesoscopic regions several nanometers in size that have different S values. The small dimensions of the ordered regions explain the difficulty in observation of superstructure reflections by X-ray diffraction methods. A similar situation is also characteristic of the model relaxor of the composition $PbMg_{1/3}Nb_{2/3}O_3$ [2]. The role of compositionally ordered nanoregions in the formation of the relaxor properties in perovskites is still not quite clear, although it is well known that these regions play an important part as sources of random local electric and mechanical fields [12].

According to the existing models [13, 14], the degree of diffusion of the phase transition and the stability of the relaxor state in ternary perovskites of the 1 : 1 type increase with an increase in the difference between the ionic radii of B^{3+} and B^{5+}. These concepts are consistent with the behavior of PFN, where the ionic radii of Fe^{3+} and Nb^{5+} ions (0.064 and 0.0645 nm, respectively) differ only insignificantly. Unlike other disordered $Pb(B^{3+}_{1/2}B^{5+}_{1/2})O_3$ oxides, both PFN ceramics and single crystals show a comparatively narrow maximum of $\varepsilon(T)$, whose temperature T_m is practically independent of frequency [5, 6, 10]. Since a Ta^{5+} ion (0.065 nm) is only slightly larger than Nb^{5+}, one can expect that the relaxor properties of PFT would be more pronounced than those of PFN. Indeed, according to data [7, 10, 11], the temperature T_m of both PFT single crystals and ceramics increases with an increase in f, but much less than in the model $PbMg_{1/3}Nb_{2/3}O_3$ relaxor.

[1] This work was presented to the Symposium "Order, Disorder and Properties of Oxides" (ODPO), Sochi, Russia, 2001.

1063-7745/02/4706-1007$22.00 © 2002 MAIK "Nauka/Interperiodica"

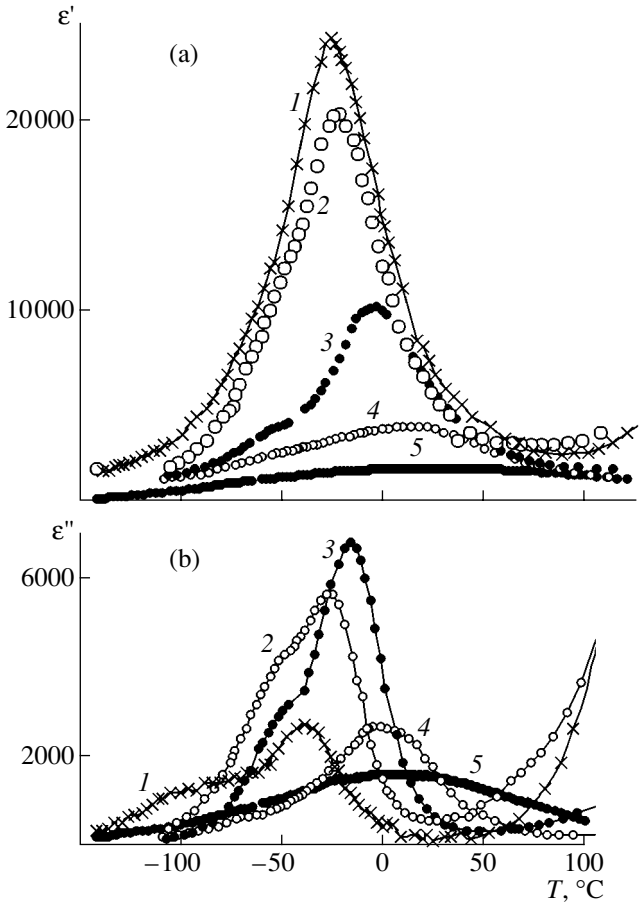

Fig. 1. Temperature dependences of (a) ε' and (b) ε'' for a PFT crystal obtained at the frequencies (*1*) 0.1, (*2*) 1.0, (*3*) 10, (*4*) 100, and (*5*) 1000 kHz.

The failure of numerous attempts to synthesize ordered PFT ceramics with the aid of prolonged high-temperature annealing [1, 11] led one to the conclusion that the presence of a small amount of the pyrochloric phase as an impurity in all the ceramic samples hinders ordering [11]. In this connection, the growth of ordered PFT crystals seems to be more promising, because it is much easier to change the *S* value of $Pb(B'^{3+}_{1/2}B''^{5+}_{1/2})O_3$ crystals by varying the growth conditions than to change *S* of the ceramic using high-temperature annealing [15].

Our aim was to synthesize PFT single crystals and study their dielectric properties over wide temperature and frequency ranges. It should be noted that we found only one publication in which the ε(*T*) dependence was studied for PFT [7], which is explained by the high conductivity of these crystals (revealed later in [8, 9]).

EXPERIMENTAL

Single crystals of the composition $PbFe_{1/2}Ta_{1/2}O_3$ were grown by mass crystallization from flux with the use of the PbO solvent. The PFT preliminarily synthesized for four hours from the corresponding oxides at 850°C, along with Fe_2O_3 and PbO, were loaded into a platinum crucible in the ratio 37.8 : 2.2 : 60. The crucible was kept for 3 to 6 h at 1200–1220°C, then was cooled, first, down to 1150–1160°C at a rate of 2–2.5 K/h, then, down to 1080°C at a rate of 3.5 K/h, and finally down to 900–950°C at a rate of 6 K/h. Then, the mother solution was poured out, and we obtained black cubic crystals with 1.5-mm-long edges faceted along the (001) planes of the perovskite basis. The X-ray diffraction studies were made on powders (obtained by crystal grinding) on a DRON-3 diffractometer (FeK_α radiation).

The dielectric measurements were made in the frequency range 10^2 to 10^6 Hz with the aid of P5083 and E7-12 ac bridges. The Aquadag electrodes were applied to the natural faces of the crystals.

RESULTS AND DISCUSSION

The X-ray diffraction analysis showed that, at room temperature, the crystals have a perovskite cubic unit cell with the lattice parameter 0.4008 nm, which is consistent with the known data for PFT crystals [7–9]. The diffraction patterns of some series of crystals also showed weak superstructural lines corresponding to the doubled lattice parameter which, we believe, is associated with the ordering of Fe^{3+} and Ta^{5+} cations. The degree of order, *S*, evaluated with respect to the intensities of the basis (100) and superstructural (1/2, 1/2, 1/2) lines [1] did not exceed 0.2.

At room temperature, the conductivity γ of the grown crystals at dc current was about 10^{-9} Ω^{-1} cm^{-1}, i.e., was lower by an order of magnitude than the conductivity of the crystals studied in [8, 9]. The activation energy of conductivity was 0.17–0.18 eV at $T < 70$°C (which agreed quite well with data [8]) and 0.8–0.85 eV obtained at higher temperatures.

The temperature dependences of the real, ε', and imaginary, ε'', parts of the dielectric constant of the PFT crystals measured at the frequencies 10^2–10^6 Hz are shown in Fig. 1. In addition to the minimum corresponding to the diffuse transition from the tetragonal to the cubic phase, the dependences ε'(*T*) and ε''(*T*) also had bends at temperatures of 40–50 K less than T_m. These anomalies seem to correspond to the transition between the monoclinic and tetragonal ferroelectric phases revealed earlier in the optical and X-ray diffraction studies of PFT crystals [8, 9]. At $T > T_m$, with an increase in the temperature, the decrease in ε' and ε'' changed to an increase. The higher the measurement frequency, the higher was the temperature at which ε began to increase. This character of the ε'(*T*) and ε''(*T*) dependences seems to be associated with the volume-charge or thermal electron polarization and was observed in numerous perovskites, especially in those characterized by an oxygen deficit [16, 17].

The maximum ε'_m value (about 20000 at f = 1 kHz) is approximately twice as high as the value for the crystals studied in [7] and decreases with an increase in f especially pronouncedly in the range 10^3–10^5 Hz. The temperature dependence of ε in the vicinity of the maximum for many crystals characterized by a diffuse ferroelectric phase transition is described by the expression [5]

$$\frac{1}{\varepsilon} = \frac{1}{\varepsilon_m} + \frac{(T - T_m)^2}{2\varepsilon_m \sigma^2}, \quad (1)$$

where T_m is the temperature at which ε' attains its maximum value ε'_m and σ is the parameter of the diffusion of the transition. As is seen from Fig. 2a, this equation is valid for PFT over a wide temperature range above T_m. The value of the parameter of the diffusion of the transition σ, estimated from the data presented in Fig. 2a, is almost independent of frequency at f < 10 kHz and equals 20 ± 2 K. At higher frequencies, σ drastically increases with f, attaining the value of 90 K at f = 1 MHz. Similar dependence of σ on f was also observed in numerous relaxors [18].

At temperatures exceeding T_m by more than 100 K, the Curie–Weiss law is valid: $1/\varepsilon' = (T - T_{CW})/C$ (C is a constant) (Fig. 2b). Because of the increase in ε' with the temperature at $T > T_m$ indicated above, the fulfillment of this law is clearly seen only at the highest frequencies used in the measurements. The Curie–Weiss temperature T_{CW} obtained by the extrapolation of the dependence $1/\varepsilon'(T)$ is 145°C, i.e., is much higher than T_m. Such a proportion between T_m and T_{CW} and the transition from the square-law dependence $1/\varepsilon'(T)$ to the linear one observed in the experiments are characteristic of the ferroelectrics with diffuse phase transitions [2, 5].

As is seen from Fig. 1a, the PFT crystals studied show considerable frequency dispersion in ε and an increase in T_m at higher frequencies f of the measuring field. In the Arrhenius coordinates, the dependence of T_m on f considerably deviates from the linear one (Fig. 3a), which indicates the non-Debye character of the relaxation characteristic of ferroelectric–relaxors [2, 5, 19]. At the same time, it is seen from Fig. 3b that the dependence of T_m on f is well described by the Vogel–Fulcher law [2, 13, 19]

$$f = f_0 \exp[-E/k(T_m - T_0)], \quad (2)$$

where f_0 is the frequency of the attempts to overcome the potential barrier E, k is the Boltzmann constant, and T_0 is the Vogel–Fulcher temperature interpreted as the temperature of static freezing of the electric dipoles or of the transition to the dipole-glass state [2, 13, 19]. For PFT crystals, $f_0 = (0.5–1) \times 10^{11}$ Hz, which is close to the values obtained for other ferroelectric–relaxors [13, 19]. The value $T_0 \approx 170$ K, which is lower than the

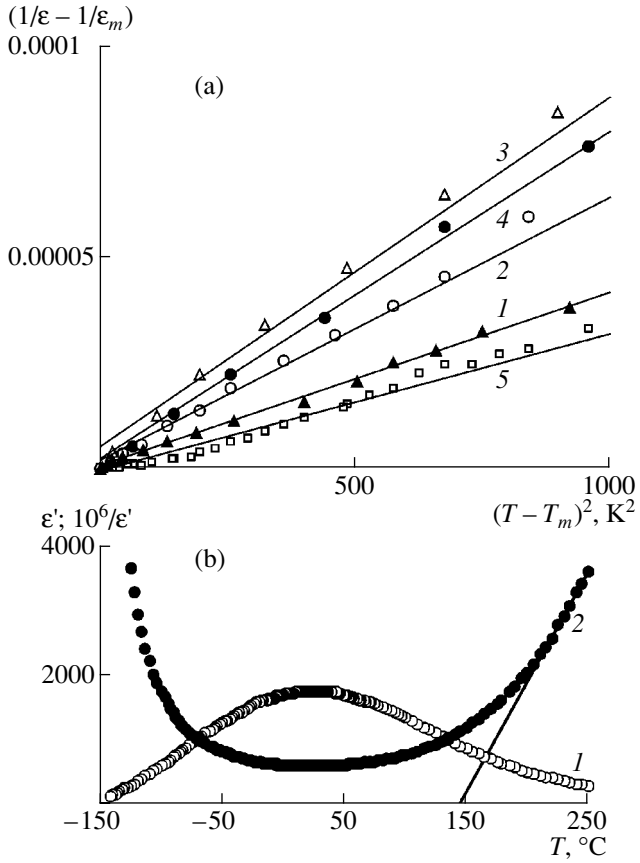

Fig. 2. Dependences of (a) $1/\varepsilon$ on $(T - T_m)^2$ for PFT crystals at the frequencies of (*1*) 0.1, (*2*) 1.0, (*3*) 10, (*4*) 100, and (*5*) 1000 kHz and (b) temperature dependences of (*1*) ε' and (*2*) $1/\varepsilon'$ for PFT crystals at a frequency of 1 MHz.

temperature of the transition from the ferroelectric monoclinic and tetragonal phases. The activation energy E in the Vogel–Fulcher law (~0.12 eV) and the difference ΔT between T_m (at the frequency 1 kHz) and T_0 (~80 K) have higher values than the corresponding values for the crystals of the model $PbMg_{1/3}Nb_{2/3}O_3$ relaxor [2, 13]. The ΔT and E values similar to those for PFT were also observed in disordered $PbIn_{1/2}Nb_{1/2}O_3$ crystals [19].

It should be indicated that, although the temperature of the maximum of $\varepsilon''(T)$ for PFT increases with an increase of f monotonically, the value of this maximum first increases and then, at $f > 10^4$ Hz, dramatically decreases (Fig. 1b). In the same frequency and temperature ranges, a dramatic increase in the frequency dependence of ε' is observed (Fig. 1a). These data indicate that, in addition to the relaxation processes characteristic of relaxors and provided by the presence of ferroelectric nanoregions in the paraelectric matrix [2, 19], some other relaxation processes also play an important part in the crystals under study. In particular, the comparatively high values of conductivity, in combination with mesoscopically inhomogeneous composition

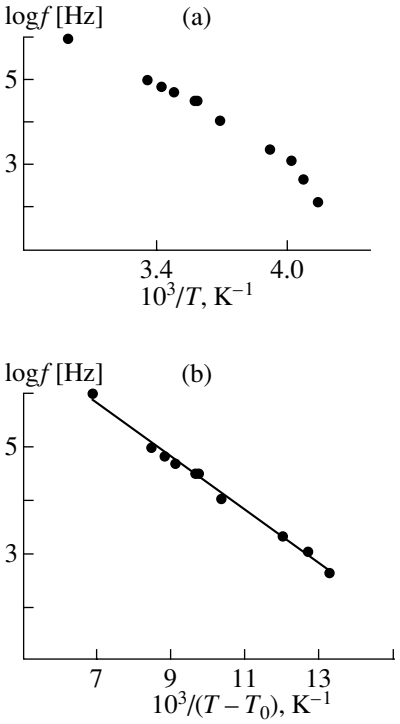

Fig. 3. Dependences of (a) the temperature T_m of the maximum in ε'(*T*) and (b) the difference $T_m - T_0$ (illustrating the fulfillment of the Vogel-Fulcher law) on frequency in the Arrhenius coordinates for PFT crystals.

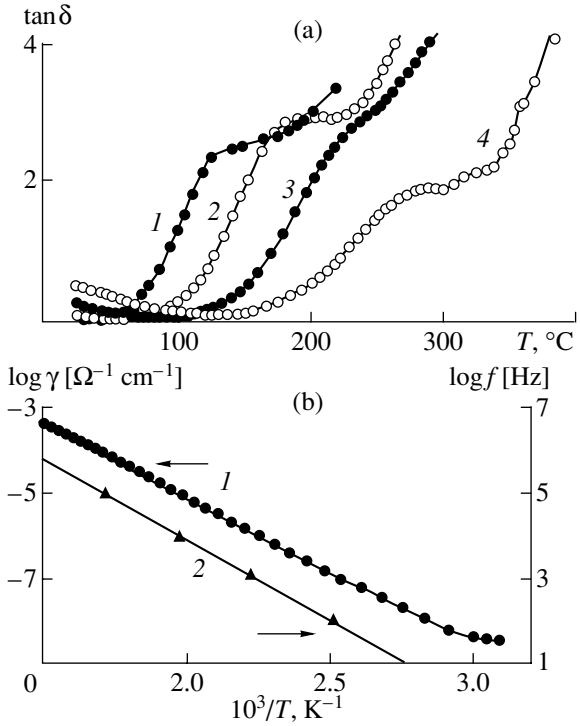

Fig. 4. Temperature dependences of (a) tanδ at frequencies (*1*) 0.1, (*2*) 1.0, (*3*) 10, (*4*) 100 kHz and (b) conductivity γ (*1*) and the dependence of the temperature *T* of the maximum of tanδ on frequency *f* at $T > T_m$ (*2*) for PFT crystals.

ordering, promote the appearance of the volume-charge and thermal electron polarizations [16, 17]. This interpretation is confirmed by the considerable enhancement of the dependence $T_m(f)$ in the $PbW_{1/3}Fe_{2/3}O_3$ ceramic with elevated conductivity observed in [20].

One more maximum of dielectric losses is observed in PFT above T_m (Fig. 4a), whose temperature increases with frequency according to the Arrhenius law (Fig. 4b). The activation energy of the relaxation process corresponds to this maximum and equals 0.9 ± 0.05 eV, which is close to the activation energy of conductivity at constant current in this temperature range (Fig. 4b). The close values of the activation energies of conductivity and relaxation are considered to be confirmation of the fact that the given relaxation process is provided by the electron polarization associated with various lattice defects [16, 21].

At the same time, it should be emphasized that, within the framework of the theory of random fields, the existence of several groups of the maxima of dielectric constant and dielectric losses in relaxors of the 1 : 1 type was predicted in [22]. The frequency dependence of the lowest temperature maximum should be described by the Vogel–Fulcher law; the frequency dependences of the remaining maxima, by the Arrhenius law. In accordance with the calculations made in [22] for the 1 : 1 relaxors whose degree of compositional order is such that they are in the vicinity of the boundary of the states of ferroelectric and dipole glasses, the temperature T_m of the maximum described by the Vogel–Fulcher law is 140–200 K, and the difference $T_m - T_0$ = 90 K, whereas the temperature of the closest maximum is described by the Arrhenius law and equals T_m = 360–500 K and the activation energy of the relaxation process ~0.85 eV. These values are very close to the experimentally determined values for PFT crystals in our study. On the other hand, recent studies [17] showed that, in $SrTiO_3$ with different additions, there exists a system of relaxation maxima provided by thermal electron polarization associated with oxygen vacancies and associates formed by these vacancies with other lattice defects. In particular, a group of such maxima is observed in the temperature range 350–650 K and is characterized by the activation energy of the relaxation process 0.74–0.86 eV, which is close to the activation energy of conductivity (0.59–0.78 eV). The establishment of the details of the relaxor behavior of a PFT crystal and their description based on various theoretical models require some additional experimental studies.

CONCLUSION

The pronounced relaxor properties of partly ordered PFT crystals seem to be provided by the mesoscopi-

cally inhomogeneous ordering and comparatively high conductivity of these crystals, which creates favorable conditions for the development of the volume-charge and thermal electron polarizations.

ACKNOWLEDGMENTS

This study was supported by the Russian Foundation for Basic Research, project no. 01-03-33119, and the Ministry of Education of the Russian Federation, project no. E00-3.4-287.

REFERENCES

1. C. G. F. Stenger and A. J. Burggraaf, Phys. Status Solidi A **61**, 653 (1980).
2. L. E. Cross, Ferroelectrics **76**, 241 (1987).
3. A. A. Bokov and I. P. Rayevsky, Ferroelectrics **90**, 125 (1989).
4. A. A. Bokov and I. P. Rayevsky, Ferroelectrics **144**, 147 (1993).
5. G. A. Smolenskiĭ, V. A. Bokov, V. A. Isupov, *et al.*, *Physics of Ferroelectric Phenomena* (Nauka, Leningrad, 1985).
6. Yu. N. Venevtsev, V. V. Gagulin, and V. N. Lyubimov, *Ferromagnetics* (Nauka, Moscow, 1982).
7. S. Nomura, H. Takabayashi, and T. Nakagawa, Jpn. J. Appl. Phys. **7**, 600 (1968).
8. W. Brixel, J. P. Rivera, and H. Schmid, Ferroelectrics **55**, 181 (1984).
9. L. A. Geddo and P. Sciau, J. Phys.: Condens. Matter **11**, 1235 (1999).
10. B.-H. Lee, N.-K. Kim, J.-J. Kim, and S.-H. Cho, J. Korean Phys. Soc. **32**, S978 (1998).
11. W. Z. Zhu, A. Kholkin, P. Q. Mantas, and J. L. Baptista, J. Eur. Ceram. Soc. **20**, 2029 (2000).
12. H. Qian and A. Bursill, Int. J. Mod. Phys. B **10**, 2007 (1996).
13. F. Chu, I. M. Reaney, and N. Setter, Ferroelectrics **151**, 343 (1994).
14. A. A. Bokov, Zh. Éksp. Teor. Fiz. **111**, 1817 (1997) [JETP **84**, 994 (1997)].
15. A. A. Bokov, I. P. Raevskiĭ, V. G. Smotrakov, and S. M. Zaĭtsev, Kristallografiya **32**, 1301 (1987) [Sov. Phys. Crystallogr. **32**, 769 (1987)].
16. O. I. Prokopalo and I. P. Raevskiĭ, *Electrophysical Properties of Oxides of the Perovskite Family* (Rostovs. Gos. Univ., Rostov-on-Don, 1985).
17. C. Ang, Z. Yu, and L. E. Cross, Phys. Rev. B **62**, 228 (2000).
18. A. A. Bokov and Z.-G. Ye, Solid State Commun. **116**, 105 (2000).
19. A. A. Bokov, M. A. Leshchenko, M. A. Malitskaya, and I. P. Raevski, J. Phys.: Condens. Matter **11**, 4899 (1999).
20. L. Zhu, P. M. Vilarinho, and J. L. Baptista, J. Appl. Phys. **85**, 2312 (1999).
21. V. Eremkin, V. Smotrakov, E. Gagarina, and I. Raevski, J. Korean Phys. Soc. **32**, S1597 (1998).
22. M. D. Glinchuk, V. A. Stephanovich, B. Hilczer, *et al.*, J. Phys.: Condens. Matter **11**, 6263 (1999).

Translated by L. Man

Crystallography Reports, Vol. 47, No. 6, 2002, pp. 1012–1015. Translated from Kristallografiya, Vol. 47, No. 6, 2002, pp. 1081–1084.

LATTICE DYNAMICS AND PHASE TRANSITIONS

Study of Cation Ordering and Magnetic Phase Transitions in Ternary Fe-Containing Perovskite Oxides by Mössbauer Spectroscopy[1]

I. P. Raevskiĭ*, D. A. Sarychev*, S. A. Bryugeman*, L. A. Reznichenko*, L. A. Shilkina*, O. N. Razumovskaya*, V. S. Nikolaev*, N. P. Vyshatko, and A. N. Salak****

** Research Institute of Physics, Rostov State University, Rostov-on-Don, 344090 Russia*

e-mail: rip@ip.rsu.ru

*** Institute of Solid-State and Semiconductor Physics, National Academy of Sciences, Minsk, 220072 Belarus*

Received March 28, 2002

Abstract—Nuclear gamma-resonance (NGR) spectra were studied in ceramics of ternary perovskite-type oxides $Pb(Fe_{2/3}W_{1/3})O_3$, $Pb(Fe_{1/2}Ta_{1/2})O_3$, and $Pb(Fe_{1/2}Nb_{1/2})O_3$ and in the $Pb(Fe_{1/2}Sb_{1/2})O_3$ oxide synthesized under pressure. A singlet corresponding to compositional-ordering regions was observed in the NGR spectra for $Pb(Fe_{1/2}Sb_{1/2})O_3$. Weak doublets associated with paramagnetic regions (in which the degree of cation ordering is higher than the volume average) were observed in the spectra for $Pb(Fe_{2/3}W_{1/3})O_3$ and $Pb(Fe_{1/2}Nb_{1/2})O_3$ at temperatures 30–70 K below the antiferromagnetic phase transition point. © *2002 MAIK "Nauka/Interperiodica".*

INTRODUCTION

Complex ferroelectric and antiferroelectric perovskite-family oxides $Pb(B'_{1-m}B''_m)O_3$ ($m = 1/2, 1/3$) have been studied intensively in recent years [1–6]. Of special interest, is the possibility of varying the degree of ordering of B' and B'' ions over equivalent crystallographic positions. Such ordering is usually called compositional to differentiate it from the ferroelectric and antiferroelectric order. For the characterization of such ordering, a long-range order parameter S is usually introduced, which is equal to unity for a fully ordered state, and to zero, for a disordered state [2].

The perovskite oxides with B^{3+} = Fe are of particular interest. The superstructural reflections on X-ray patterns associated with the ordering of B cations have been observed only in $Pb(Fe_{2/3}W_{1/3})O_3$ (PFW) [7]; numerous attempts to fabricate ordered ceramics $PbFe_{1/2}Ta_{1/2}O_3$ (PFT) and $PbFe_{1/2}Nb_{1/2}O_3$ (PFN) by long annealing at high temperatures have not met with success [1–6]. At the same time, the experimental values of the antiferromagnetic Néel temperature T_N for PFW, PFN, and PFT are located approximately halfway between calculated values of this temperature for $S \approx 1$ and $S \approx 0$, which is usually interpreted as an evidence of a partial ordering of B cations (T_N depends strongly on S, because the ordering changes the number of magnetic ions in neighboring unit cells [3, 4]). The ordering of cations in these oxides seems to occur locally; i.e., mesoscopic regions of the size of several nanometers with different values of S arise in a crystal. Small sizes of ordered regions are responsible for the difficulties in observing superstuctural reflections on X-ray diffraction patterns. The urgent problem is the development of new methods for detecting local ordering in complex oxides. One of these methods is nuclear gamma-resonance (NGR) spectroscopy. For example, information about the presence of ordered regions and the distribution of T_N (and, hence, of S) can be obtained by studying the temperature dependence of the relative intensity of a paramagnetic NGR spectrum near T_N. However, the temperature dependence of NGR spectra has been studied in detail only near ferroelectric phase transition points [4].

The aim of this work was to produce ceramics of ternary Fe- containing complex perovskite-type oxides with a variable degree of B cations ordering, and to study the influence of compositional ordering on NGR spectra and their temperature dependence.

SAMPLE PREPARATION AND THE EXPERIMENTAL PROCEDURE

The PFW and PFT ceramics were obtained by solid-phase synthesis of high-purity PbO, Fe_2O_3, Ta_2O_5, and WO_3 oxides. The PFN and $Pb(Fe_{1/2}Sb_{1/2})O_3$ (PFS) ceramics were fabricated using solid-phase synthesis under pressure [8]. Details of the sample preparation are described in [9]. An X-ray phase analysis did not reveal the presence of phases other than perovskite in any ceramics.

[1] This work was presented at the Symposium "Order, Disorder, and Properties of Oxides" (ODPO), Sochi, Russia, 2001.

1063-7745/02/4706-1012$22.00 © 2002 MAIK "Nauka/Interperiodica"

NGR spectra were measured with the aid of an MS-1104E rapid Mössbauer spectrometer of the latest design with improved velocity and technological characteristics, using Co^{57} in a Cr matrix as a source of resonance radiation (activity 20 mCi). Calibration was carried out with a standard α-Fe absorber. The Mössbauer spectra were analyzed by using the UNIVEM computer programs.

The dielectric constant ε was measured for samples with fired-in silver electrodes using R5082 and E7-12 bridges at frequencies 10^2–10^6 Hz.

EXPERIMENTAL RESULTS AND THEIR DISCUSSION

X-ray diffraction patterns from PFW contained weak superstructural lines corresponding to a doubled perovskite unit cell; these lines were likely associated with the ordering of Fe and W ions. Despite their low intensity, these lines are comparatively weakly spread; the average size of the regions of coherent scattering, estimated by Schering's formula, is about 30–80 nm. Such a large size of ordered regions in PFW suggests that the ordering of Fe and W ions is of the "random-site" type [1] (with allowance for the formula $Pb[(Fe_{1/2}W_{2/3})_{1/2}Fe_{1/2}]O_3$ ensuring the electrical neutrality of the ordered clusters).

An NGR spectrum of PFW at 300 K is shown in Fig. 1. This spectrum is a superposition of two sextets. Previously, a similar spectrum consisting of two sextets has been observed only after the firing of PFW ceramics in oxygen, while the spectrum from a sample fired in air contained a single sextet [7]. The existence of two sextets in an NGR spectrum for PFW was associated in [7] with a partial ordering of Fe^{3+} and W^{6+} ions and the formation of two magnetic subsystems due to nonequivalent surrounding of iron ions in ordered and disordered regions. According to calculations by the Guillaud method, the values of T_N at $S \approx 1$ and $S \approx 0$ for PFW are 310 and 460 K, respectively [3, 4]. Experimentally, the values of $T_{N1} \approx 355$ K and $T_{N2} \approx 425$ K were obtained for PFW ceramics synthesized and sintered in oxygen, while the sintering in air usually gives $T_N \approx 363$ K [4, 7]. Despite the fact that our measurements were made at a temperature approximately 50 K below T_{N1}, the NGR spectrum for PFW contained a paramagnetic component (doublet). This doublet may be associated with clusters in which the degree of ordering is higher than the volume average and, hence, the values of T_N are lower.

NGR spectra of the PFN and PFT ceramics measured at 300 K (Figs. 1, 2) are doublets, which is in accordance with the published data. The NGR spectrum for PFN in a cubic paraelectric phase is also a doublet [4]. The cause of quadrupole splitting in spectra of PFN and PFT for the cubic phase appears to be the incompletely ordered distribution of Fe^{3+} and Nb^{5+}

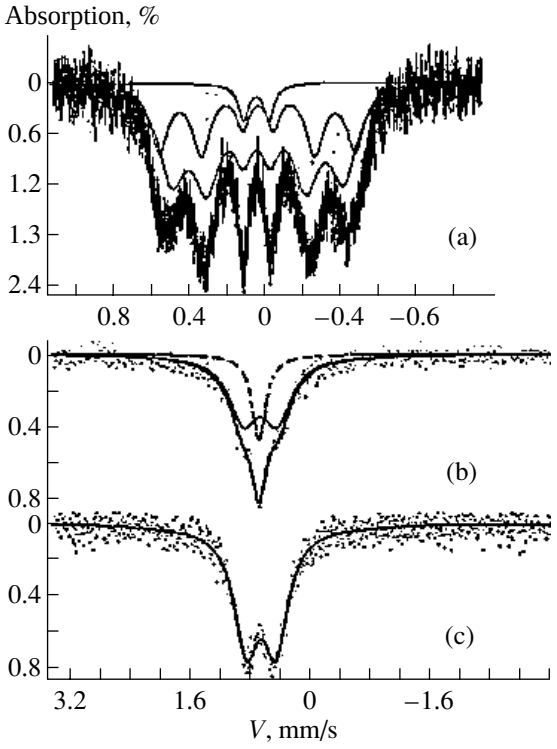

Fig. 1. NGR spectra of (a) the $PbFe_{2/3}W_{1/3}O_3$ enriched by Fe^{57}, (b) $PbFe_{1/2}Sb_{1/2}O_3$, and (c) $PbFe_{1/2}Ta_{1/2}O_3$ ceramics measured at 300 K. The decomposition of the experimental spectra into antiferromagnetic sextets and paramegnetic doublets and singlets is shown by lines.

(Ta^{5+}) over octahedral lattice sites [4, 7]. In this case, the symmetry of the environment of F^{3+} cations is not cubic. To verify of this assumption, we synthesized the perovskite PFS. At atmospheric pressure, PFS crystallizes into the pyrochlore structure; therefore, to obtain a perovskite modification, we performed synthesis under pressure of 6 GPa following the procedure described in [8]. X-ray diffraction patterns for PFS exhibited superstructural lines corresponding to a doubled perovskite unit cell and were caused by the ordering of Fe^{3+} and Sb^{5+} ions. The value of S estimated from the ratio of the intensities of the fundamental and superstructural lines was 0.7–0.9. Dielectric measurements showed the existence of a maximum in the $\varepsilon(T)$ dependence near 200 K, whose position was independent of frequency. These data allow one to conclude that PFS, similarly to other complex perovskite oxides of the $Pb(B^{3+}_{1/2}Sb_{1/2})O_3$ family [10], is antiferroelectric.

As distinct from PFN and PFT, the NGR spectrum of PFS contains a singlet, in addition to a doublet (Fig. 1b). The singlet likely corresponds to compositionally ordered regions (fairly large in size), whereas the doublet is associated with regions where the long-range order in the arrangement of Fe^{3+} and Sb^{5+} ions is disturbed. The values of quadrupole splitting and iso-

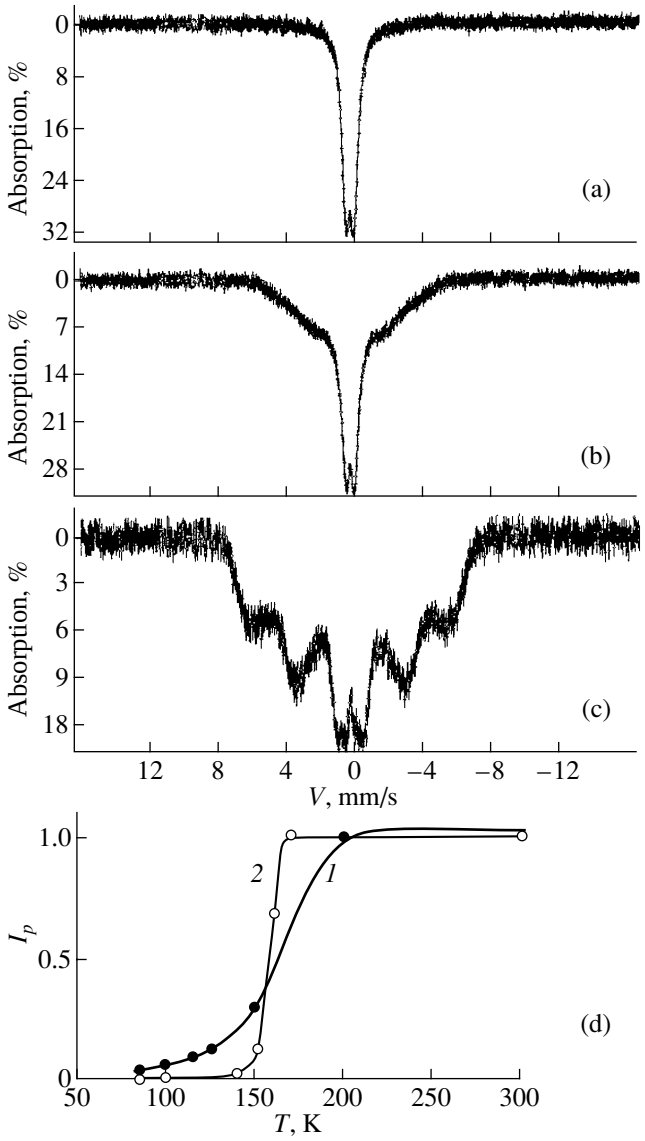

Fig. 2. NGR spectra of $Pb(Fe_{0.475}\ Nb_{0.515})O_3$ at (a) 200, (b) 150, and (c) 100 K; and (d) the temperature dependence of the relative intensity I_p of a paramagnetic NGR spectrum for $Pb(Fe_{0.475}\ Nb_{0.515})O_3$ enriched by Fe^{57} and prepared using solid-phase synthesis at 1420 K under a pressure of 4 GPa. The measurements were made (*1*) immediately after synthesis and (*2*) after annealing at 1320 K for 2 h.

mer shift of the sextets, doublets, and the singlet in NGR spectra of all the ceramics studied by us correspond to trivalent iron in an octahedral environment. Note that the NGR spectrum in the form of a singlet was obtained in Fe-containing perovskite oxides. These results support the assumption that the environment of the octahedral ions in compositionally ordered perovskite oxides possesses cubic symmetry.

A study of dielectric properties showed that the temperature T_m corresponding to the maximum in the $\varepsilon(T)$ dependence for the PEN ceramic prepared under pressure is 10–20 K higher than that of the samples prepared without application of a pressure. The temperature T_m increases with increasing temperature of ceramic synthesis [9]. The increased temperature T_m for the ceramic obtained under pressure can be hardly explained by the effect of residual mechanical stresses, because isotropic mechanical stresses reduce T_m in ferroelectric ceramics pressed at high temperatures [11]. It appears that the PFN ceramic obtained under pressure is more disordered than the one prepared using simple sintering. Indeed, compositional disordering in the majority of ferroelectrics causes T_m to increase [5, 6]. If the above assumption is correct, the value of T_N in PFN prepared under pressure at a high temperature should be higher than in PFN sintered not under pressure at a lower temperature.

A study of NGR spectra of PEN enriched by the Fe^{57} isotope, prepared at 1420 K under a pressure of 4 GPa revealed the presence of a small amount of α-Fe_2O_3. This impurity seems to exist in the form of nanoclusters, because an X-ray phase analysis showed the absence of any phases other than the perovskite ones. The further analysis consisted of the subtraction of the α-Fe_2O_3 spectrum from the total NGR spectra. Figure 2 illustrates the evolution of the NGR spectra of PFN with temperature. It can be seen that, in accordance with the data on PFN available in the literature, the paramagnetic NGR spectrum (doublet) gradually transforms into an antiferromagnetic spectrum (the superposition of several sextets) on cooling below 200 K. The temperature dependence of the relative intensity I_p of the paramagnetic component of the NGR spectra is shown in Fig. 2d. Assuming (following [4]) that the average temperature of the magnetic phase transition corresponds to the middle of the transition region where the reduction of I_p occurs, we obtain $T_N \approx 165$ K. This value of T_N is 20–40 K higher than the T_N obtained for PFN from the temperature dependence of the inverse magnetic susceptibility [3, 4]. To verify the assumption about the relation of the observed effects to the ion ordering, the sample obtained under pressure was ground into powder and annealed at 1320 K for 2 h. After this procedure, T_m reduced by 10 K and the $I_p(T)$ dependence became more pronounced and shifted toward lower temperatures (Fig. 2d, curve *2*). These results are in good agreement with the data presented above on the difference in T_m between the PFN ceramics prepared under pressure and using conventional sintering. In addition, we note that the paramagnetic component of the NGR spectra remains observable below T_N over a considerably wide temperature range. This is indicative (as for PFW) of the existence of clusters in this material in which the degree of compositional ordering of Fe^{3+} and Nb^{5+} ions is higher than the volume average.

ACKNOWLEDGMENTS

This study was supported in part by the Russian Foundation for Basic Research (project nos. 01-03-33119 and 02-02-17785) and by the Ministry of Education of the Russian Federation (project no. E00-3.4-287).

REFERENCES

1. I. W. Chen, J. Phys. Chem. Solids **61**, 197 (2000).
2. C. G. F. Stenger and A. J. Burggraaf, Phys. Status Solidi A **61**, 653 (1980).
3. G. A. Smolenskiĭ, V. A. Bokov, V. A. Isupov, N. N. Krainik, R. E. Pasynkov, A. I. Sokolov, and N. K. Yushin, *The Physics of Ferroelectric Phenomena* (Nauka, Leningrad, 1985).
4. Yu. N. Venevtsev, V. V. Gagulin, and V. N. Lyubimov, *Magnetoelectrics* (Nauka, Moscow, 1982).
5. A. A. Bokov and I. P. Rayevsky, Ferroelectrics **90** (1–4), 125 (1989).
6. A. A. Bokov and I. P. Rayevsky, Ferroelectrics **144** (1–4), 147 (1993).
7. Yu. N. Venevtsev, V. V. Sklyarevskiĭ, I. I. Lukashevich, *et al.*, Kristallografiya **21** (5), 971 (1976) [Sov. Phys. Crystallogr. **21**, 556 (1976)].
8. N. P. Vyshatko, N. M. Olekhnovich, and A. N. Salak, Dokl. Akad. Nauk Belarusi **42** (4), 63 (1998).
9. I. P. Raevskiĭ, D. A. Sarychev, N. Yu. Polushkin, *et al.*, in *Proceedings of the International Symposium "Order, Disorder and Properties of Oxides,"* Sochi, 2001, p. 253.
10. I. N. Danilenko, E. D. Politova, A. N. Abramova, *et al.*, Izv. Akad. Nauk SSSR, Neorg. Mater. **21** (8), 1407 (1985).
11. I. P. Raevskiĭ, L. A. Reznichenko, and A. N. Kalitvanskiĭ, Zh. Tekh. Fiz. **50** (9), 1983 (1980) [Sov. Phys. Tech. Phys. **25**, 1154 (1980)].

Translated by A. Zalesskiĭ

Crystallography Reports, Vol. 47, No. 6, 2002, pp. 1016–1022. Translated from Kristallografiya, Vol. 47, No. 6, 2002, pp. 1085–1091.

LATTICE DYNAMICS AND PHASE TRANSITIONS

Improper Superconductivity in Uniaxial Crystals with Weak Anisotropy in the Basal Plane[1]

Yu. M. Gufan*, I. A. Sergienko*, S. Urazhdin, and M. B. Stryukov***

** Research Institute of Physics, Rostov State University, pr. Stachki 194, Rostov-on-Don, 344090 Russia*
e-mail: iserg@uic.rsu.ru
*** Department of Physics and Astronomy, Michigan State University, East Lansing, MI 48824 USA*
Received April 23, 2002

Abstract—In the context of the Landau theory, we refined the structure and analyzed the phase diagram for *d* states of the uniaxial superconductor with weak anisotropy in the basal plane. It was shown that taking into account improper order parameters makes it possible to reduce to four the degree of polynomial corresponding to the Landau potential. The gap functions for all phases were found taking into account the improper order parameters. © *2002 MAIK "Nauka/Interperiodica"*.

1. IMPROPER SUPERCONDUCTIVITY

Currently, it is generally accepted that most experiments with high-T_c superconductors such as $YBa_2Cu_3O_{7-y}$ can be interpreted under the assumption that the order parameter is characterized by the symmetry $d_{x^2-y^2}$. The observed deviations of the superconductor from its ideal behavior lead to the conclusion that there exist additional states of the Cooper pairs with *s* and/or d_{xy} symmetry; these states play an important role for the surface and bulk properties of high-T_c superconductors [1, 2].

It has been shown [3] that superconducting states with *s* symmetry can naturally arise in the case of the $d_{x^2-y^2}$ order parameter under the assumption that the "strong" symmetry of the crystal field $YBa_2Cu_3O_{7-y}$ is cubic. Such an assumption is justified by the fact that the structure of $YBa_2Cu_3O_{7-y}$ can be derived from the perovskite-type cubic structure [4]. The $d_{x^2-y^2}$ component of the wave function is a component of the two-dimensional E_g representation of group O_h. The second component of this order parameter has the symmetry $d_{2z^2-x^2-y^2}$. The multidimensionality of the order parameter plays a key role because the symmetric powers of a multidimensional representation of any group always contain nonidentity representations of this group. In its turn, this leads to the existence of improper additional orderings in the phases admissible by the symmetry of the proper order parameter responsible for the loss of stability in the normal state.

Let us discuss the following example. We assume that the *n*th symmetric power of the two-dimensional irreducible representation related to the (η_1, η_2) order parameter contains a certain nonunitary one-dimensional representation related to the ξ order parameter. Then, there exists at least one invariant of the group transformation that has the following form:

$$P_n(\eta_1, \eta_2)\xi^* + P_n^*(\eta_1, \eta_2)\xi, \tag{1}$$

where $P_n(\eta_1, \eta_2)$ is the homogeneous polynomial of degree *n*. Since $|\xi|^2$ is an invariant, the equation of state in the Ginzburg–Landau theory for ξ can be written as

$$\begin{aligned}\partial F/\partial\xi^* &= \alpha P_n(\eta_1, \eta_2) + \beta\xi \\ &+ \text{higher order terms} = 0.\end{aligned} \tag{2}$$

This means that ξ must be nonzero if $P_n(\eta_1, \eta_2) \neq 0$. From Eq. (2), it is clear that the value of improper order parameter ξ is proportional (to the first approximation) to the *n*th ($n > 1$) power of the proper order parameter. That is why one usually neglects the improper order parameters. However, in high-T_c superconductors the contribution of the *s* component to the wave function is small. This can imply that such a contribution can be described by the improper order parameter.

In this paper, we discuss the role of improper superconducting order parameters in a hypothetical uniaxial crystal that is isotropic in the basal plane (point group ∞m). Here, the main channel for pairing is related to the singlet *d* states. Some experiments with $YBa_2Cu_3O_{7-y}$ suggest that the Bose condensate is insensitive to anisotropy in the basal plane, whereas the others lead to the opposite conclusion. The analysis of the isotropic case should help to clarify the extent to which the crystal field affects the Bose condensate. An additional stimulus for this study was the argument that the $d_{x^2-y^2}$ and d_{xy} components of spherical harmonics Y_2 taken together form a two-dimensional irreducible represen-

[1] This work was presented at the Symposium "Order, Disorder, and Properties of Oxides" (ODPO), Sochi, Russia, 2001.

Matrices corresponding to the generators of group G_0 in the representation formed by the order parameter (η_+, η_-, η_-^*, η_+^*) and in the representations appearing in its symmetric square. The notation in column *a* is explained in the text; column *b* presents the basis functions formed by components of the proper order parameter. The diagonal matrices are shown as the columns consisting of their diagonal elements

a	*b*	g_α	C_ϕ	σ^x	*T*
η_+	η_+	$e^{i\alpha}$	$e^{2i\phi}$		
η_-	η_-	$e^{i\alpha}$	$e^{-2i\phi}$	0 1 0 0	0 0 1 0
η_-^*	η_-^*	$e^{-i\alpha}$	$e^{2i\phi}$	1 0 0 0 0 0 0 1	0 0 0 1 1 0 0 0
η_+^*	η_+^*	$e^{-i\alpha}$	$e^{-2i\phi}$	0 0 1 0	0 1 0 0
φ	$\eta_+\eta_-$	$e^{2i\alpha}$	1	1	0 1
φ^*	η_-^* η_+^*	$e^{-2i\alpha}$	1	1	1 0
ψ_+	η_+^2	$e^{2i\alpha}$	$e^{4i\phi}$		
ψ_-	η_-^2	$e^{2i\alpha}$	$e^{-4i\phi}$	0 1 0 0 1 0 0 0	0 0 1 0 0 0 0 1
ψ_-^*	η_-^{*2}	$e^{-2i\alpha}$	$e^{4i\phi}$	0 0 0 1	1 0 0 0
ψ_+^*	η_+^{*2}	$e^{-2i\alpha}$	$e^{-4i\phi}$	0 0 1 0	0 1 0 0
	$(\eta_-)^2$	1	1	0 1	0 1
	$(\eta_-)^2$	1	1	1 0	1 0
	$\eta_+\eta_-^*$	1	$e^{4i\phi}$	0 1	0 1
	$\eta_-\eta_+^*$	1	$e^{-4i\phi}$	1 0	1 0
k_+	$k_x + ik_y$	1	$e^{i\phi}$	0 −1	−1
k_-	$k_x - ik_y$	1	$e^{-i\phi}$	−1 0	−1

tation of the point group ∞m. In the context of such an approach, the expected contribution of the d_{xy} components does not seem to be accidental.

2. SYMMETRY AND THE FINE STRUCTURE OF THE $ad_{x^2-y^2} + bd_{xy}$ STATES IN A SUPERCONDUCTOR

The analysis of the symmetry and physical properties of the ordered *d* states in a uniaxial superconductor with zero anisotropy in the basal plane was initiated in [5]. In this section, we supplement these results with the description of possible additional improper orderings.

The normal-state symmetry of the superconductor under study corresponds to the group

$$G_0 = O_2 \times SO_2 \times U_1 \times T,$$

where O_2 is the two-dimensional complete orthogonal group in the real space, SO_2 is the group of two-dimensional rotations in the spin space, U_1 is the group of the gauge transformations g_α, and *T* is the time reversal. We consider here the four-dimensional irreducible representation of G_0 related to the order parameters $\eta_\pm \propto (k_x^2 - k_y^2) \pm 2ik_xk_y$ and $\eta_\pm^*$.

The spin rotations do not affect the singlet states, and group O_2 is formed by the two-dimensional rotations C_ϕ and reflection planes σ_v normal to the basal plane; therefore, all matrices of this representation of group G_0 can be represented as products of matrices corresponding to four generators, g_α, C_ϕ, σ^x, and *T*. In the table, we present the matrices of the generators of the leading (proper) representation, as well as the matrices of the generators of representations involved in its symmetric square. The symmetric square of the representation according to which $\eta_\pm$ is transformed splits into five irreducible representations, two of which correspond to the superconducting order parameters (ψ_+, ψ_-, ψ_-^*, ψ_+^*, and φ, φ^*), while the others correspond to the nonsuperconducting order parameters. Later, we discuss only the superconducting order parameters, since they directly affect the Bose condensate states.

It is easy to show that we can construct only two independent invariants using components of the proper order parameter; i.e.,

$$J_1 = |\eta_+|^2 + |\eta_-|^2, \quad J_2 = |\eta_+|^2|\eta_-|^2. \tag{3}$$

The superconducting states admissible by the symmetry of the proper order parameter (η_+, η_-, η_-^*, η_+^*) were listed in [5]. According to the Curie principle, if some structural distortion is admissible by the symmetry, it must exist. We consider possible phases taking into account the improper distortions. Sometimes we use polar coordinates to denote complex parameters $\eta_\pm = \xi_\pm \exp(i\Omega_\pm)$, $\psi_\pm = \rho_\pm \exp(i\omega_\pm)$, and $\varphi = \lambda\exp(i\Theta)$.

(I) $\eta_- = 0$ and $\eta_+ \neq 0$. The symmetry of this state corresponds to the $d_{x^2-y^2} + 2id_{xy}$ component of the wave function. Its symmetry group H_1 can be formed by the following operations:

$$H_1 = \{g_{-2\phi}C_\phi, T\sigma^x C_{-\Omega_+}\}.$$

Improper order parameters do not affect the symmetry of the state but refine its structure. The table demonstrates that the additional orderings described by relationships $\varphi = \psi_- = 0$, $\psi_+ \neq 0$, and $\omega_+ = 2\Omega_+ + 0(\pi)$ are compatible with the H_1 symmetry; hence, they exist in this phase. These relationships can be also obtained from the equations similar to Eqs. (2). Here, we should note that ambiguity in the choice of relations between the phases of the condensates actually means that the symmetry allows both possibilities, which correspond to different anti-isostructural phases [6]. Which of them actually takes place depends on the sign of the constant of interaction between the proper and improper order parameters (see Section 4).

(II) $|\eta_+| = |\eta_-| \neq 0$ ($\cos\gamma d_{x^2-y^2} + \sin\gamma d_{xy}$, $\gamma = (\Omega_+ - \Omega_-)/2$). The symmetry of this superconducting state is described by the group

$$H_2 = \{g_\pi C_{\phi/2}, Tg_{(-\Omega_+-\Omega_-)}, \sigma^x C_{(\Omega_--\Omega_+)/2}\}.$$

Symmetry H_2 demands the following additional orderings:

$$\varphi \neq 0,$$
$$\Theta = \Omega_+ + \Omega_- + 0(\pi),$$
$$|\psi_+| = |\psi_-| \neq 0,$$
$$\omega_\pm = 2\Omega_\pm + 0(\pi).$$

The physical meaning of improper order parameters φ and $\psi_\pm$ is clear from the table. The phases of these order parameters change by 2α under the effect of the gauge transformation g_α. This means that φ and $\psi_\pm$ describe interactions involving complexes of two Cooper pairs [7]. Transformational properties of improper order parameters under the effect of rotations C_ϕ demonstrate that φ and $\psi_\pm$ correspond to the interactions of pairs with opposite (*s* states, $L = 0$) and unidirectional (*g* states, $L = 4$) orbital moments, respectively.

(III) Phase of the generic type corresponding to the arbitrary values of η_+ and η_- ($ad_{x^2-y^2} + bd_{xy}$). The symmetry of this state is determined by the kernel of homomorphism for the representation according to which the components of the order parameter (η_+, η_-, η_-^*, η_+^*) are transformed

$$H_3 = \{g_\pi C_{\phi/2}, T\sigma^x g_{(-\Omega_+-\Omega_-)} C_{(\Omega_--\Omega_+)/2}\}.$$

In this state, any positive values of φ and $\psi_\pm$ are possible but their phases are strictly correlated with the phases of the components of the proper order parameter: $\omega_\pm = 2\Omega_\pm + 0(\pi)$, $\Theta = \Omega_+ + \Omega_- + 0(\pi)$.

3. THE PHASE DIAGRAM FOR *d* STATES OF THE UNIAXIAL SUPERCONDUCTOR WITHOUT TAKING INTO ACCOUNT IMPROPER ORDER PARAMETERS

We discuss the possible mutual arrangement of the normal state and three superconducting states in the phase diagram in the context of Landau's phenomenological theory. Here, we restrict ourselves to the analysis of homogeneous states and do not take into account the gradient terms in the Landau potential. In this section, we temporarily forget about the existence of improper order parameters and deal with them in Section 4 in order to compare the results.

Further on, we discuss the equations of state and the stability conditions for their solutions corresponding to three superconducting phases. Let $\Phi(J_1, J_2)$ be the Landau potential describing the phase transitions between possible phases including the normal one. We introduce notation Φ_k and Φ_{il} for the first and the second derivatives, respectively, of Φ with respect to invariants J_k. The enumeration of phases coincides with that introduced in Section 2; i.e.,

(I)

$$\Phi_1 = 0, \quad \Phi_2 > 0, \quad \Phi_{11} > 0. \tag{4}$$

(II)

$$\Phi_1 + |\eta_+|^2\Phi_2 = 0,$$
$$\Phi_2 < 0, \quad \Phi_2 + 2(\Phi_{11} + 2|\eta_+|^2\Phi_{12} + |\eta_+|^4\Phi_{22}) > 0. \tag{5}$$

(III)

$$\Phi_1 = \Phi_2 = 0,$$
$$\Phi_{22} > 0, \quad \Phi_{11}\Phi_{22} - \Phi_{12}^2 > 0. \tag{6}$$

From the last inequality in (6), we can see that the expansion of Φ in power series of J_1 and J_2 should contain the terms with J_1^2 and J_2^2 to ensure the existence of stable solutions to the equations of state corresponding

to phase (III). This means that the minimal model of the Landau potential should contain the eighth-power terms in η_+ and η_-.

$$\Phi = a_1 J_1 + a_2 J_1^2 + b_1 J_2 + a_3 J_1^3 + cJ_1 J_2 + a_4 J_1^4 + b_2 J_2^2 + dJ_1^2 J_2. \quad (7)$$

Model (7) involves all possible invariant terms up to the eighth power in components of the proper order parameter. To ensure the stability with respect to infinitely large fluctuations, function $\Phi(\eta_+, \eta_-)$ should not have minima at infinity. This implies a positive value of coefficient a_4, and the representative point in the (b_2, d) plane must lie in the shaded region in Fig. 1.

We assume that coefficients a_1 and b_1 depend on external effects and the other coefficients are constant. In Fig. 2, we present the phase diagram corresponding to potential (7), when the following conditions are met:

$$d > 0, \quad c > 0, \quad b_2 > 0, \quad a_3 > 0, \quad 4a_2 b_2 - c^2 > 0. \quad (8)$$

Under these restrictions imposed on the coefficients of the Landau potential, the phase diagram contains the maximum number of lines corresponding to the second order phase transitions. However, as is clear from Fig. 2, the transition from the normal state to state (II) is also possible as the first-order phase transition to the left of point *B*. The equation determining line *BC* of the first-order phase transition can be written as

$$BC: 27(16a_4 + 4d + b_2)^2 a_1^2 + 2(4a_3 + c)[8(4a_3 + c)^2 - 9(16a_4 + 4d + b_2)(4a_2 + b)]a_1 - (4a_3 + c)^2(4a_2 + b)^2 + (16a_4 + 4d + b_2)(4a_2 + b)^3 = 0. \quad (9)$$

Above the *BC* line, phase (II) exists as a metastable phase up to the line *BA* given by the equation

$$BA: 108(16a_4 + 4d + b_2)^2 a_1^2 + 108(4a_3 + c)[(4a_3 + c)^2 - (16a_4 + 4d + b_2)(4a_2 + b)]a_1 - 9(4a_3 + c)^2(4a_2 + b)^2 + 8(16a_4 + 4d + b_2)(4a_2 + b)^3 = 0. \quad (10)$$

The phase transitions from states (II), $\cos\gamma d_{x^2-y^2} + \sin\gamma d_{xy}$, and (I), $d_{x^2-y^2} + 2id_{xy}$, to state (III) with an arbitrary relationship between the $d_{x^2-y^2}$ and d_{xy} condensates are possible as the second-order phase transitions. It is most convenient to represent the equations for the corresponding lines in the form of the parametrically defined functions $a_1(b_1)$,

$$OD: \begin{cases} a_1 = -4a_2 t - (12a_3 + c)t^2 - 4(8a_4 + d)t^3 \\ b_1 = -2ct - 2(b_2 + 2d)t^2, \end{cases}$$
$$OE: \begin{cases} a_1 = -2a_2 t - 3a_3 t^2 - 4a_4 t^3 \\ b_1 = -ct - dt^2, \end{cases} \quad (11)$$

where *t* is a nonnegative parameter.

Curves *OD* and *OE* have a common tangent at the origin of coordinates

$$\frac{da_1}{db_1} = \frac{2a_2}{c},$$

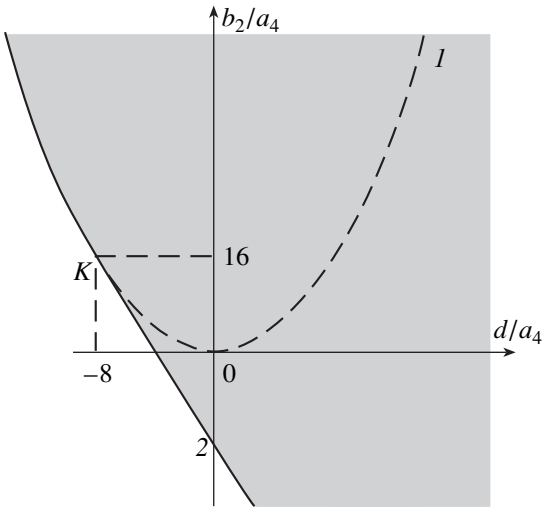

Fig. 1. The region of stability (shaded in gray) for the Landau potential (7) with respect to infinitely large fluctuations of the order parameter. Parabola *1* described by the equation $4a_4b_2 = d^2$ and straight line *2* ($16a_4 + 4d + b_2 = 0$) are tangent at point *K*.

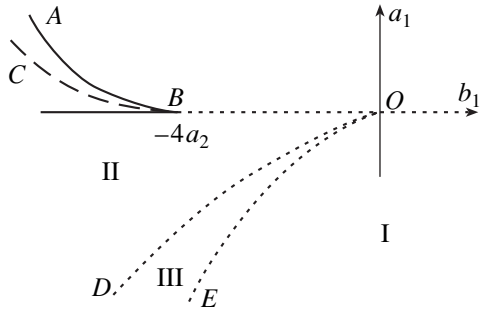

Fig. 2. The phase diagram for the Landau potential (7) in the space of phenomenological coefficients (a_1, b_1) when conditions (8) are met. Solid lines indicate the boundaries of the coexistence between the normal state and phase (II). Dashed and dotted lines correspond to the first- and second-order phase transitions, respectively.

i.e., the existence domain for phase (III) near the four-phase point *O* is much narrower than that for the other phases.

4. THE PHASE DIAGRAM FOR THE FOURTH POWER MODEL TAKING INTO ACCOUNT IMPROPER ORDER PARAMETERS

As mentioned above, only taking account of the proper order parameter whose components are involved in invariants (3) results in the need to use the Landau potential containing the terms up to the eighth power. For the full phase diagram, this requirement stems from the need to have all phases that are admissible by the symmetry of the order parameter. The use of the Landau potential containing only the terms of lower order should result in contradictions between the symmetry analysis based on the group theory and the results of calculations based on the relevant models.

However, it is necessary to keep in mind that the phenomenological theory of phase transitions in unconventional superconductors originated from the generalized microscopic Bardeen–Cooper–Schrieffer theory as a result of using the method of self-consistent field to average the Hamiltonian that describes the interactions among quasiparticles [7]. Thus, the applicability of the Landau theory requires certain validation, which can be accomplished only by returning to the microscopic mechanisms of the interactions.

As a rule, the microscopic calculations used in the modern physics of condensed matter are based on the methods of quantum field theory. As is well known, the condition that quantum field theories must be renormalizable leads to the exclusion of the Feynman diagrams containing more than four vertices. Therefore, the degree of polynomials used in the Lagrangians does not exceed four [8]. When we pass from the microscopic models to phenomenological ones, the integration of the Gibbs partition function can give rise to the terms of arbitrary order in the series expansion in powers of the components of the order parameter. However, the coefficients of these terms are not independent and are determined by a small number of coupling constants. In other words, the phenomenological theory will be equivalent, in fact, to the fourth-power Landau potential.

The improper order parameters help to remove the contradiction between the group-theory approach and the requirement imposed on the Landau potential that only terms of the order no higher than four should be taken into account. In this section, we demonstrate that taking the invariants involving improper order parameters into account allows us to include in the phase diagram all phases required by the symmetry of the proper order parameter.

Using the table, we can find that, in addition to invariants (3), there also exist the following invariant polynomials:

$$\begin{aligned} J_3 &= \eta_+^2\psi_+^* + \eta_-^2\psi_-^* + \eta_+^{*2}\psi_+ + \eta_-^{*2}\psi_- \\ &= 2[\xi_+^2\rho_+\cos(2\Omega_+ - \omega_+) + \xi_-^2\rho_-\cos(2\Omega_- - \omega_-)], \\ J_4 &= \eta_+\eta_-\varphi^* + \eta_+^*\eta_-^*\varphi \\ &= 2\xi_+\xi_-\lambda\cos(\Omega_+ + \Omega_- - \Theta), \\ J_5 &= |\psi_+|^2 + |\psi_-|^2 = \rho_+^2 + \rho_-^2, \\ J_6 &= |\varphi|^2 = \lambda^2. \end{aligned} \tag{12}$$

Let us choose the Landau potential in the form

$$\begin{aligned} \Phi_I = {} & a_1J_1 + a_2J_1^2 + b_1J_2 + fJ_6 \\ & + g_3J_3 + g_4J_4 + g_5J_5 + hJ_6^2. \end{aligned} \tag{13}$$

Here, we take into account the terms involving components of proper and improper order parameters with powers no higher than four. The condition for the global minimum imposes the following restrictions on the coefficients in (13):

$$a_2 > 0, \quad 4a_2 + b > 0, \quad g_5 > 0, \quad h > 0. \tag{14}$$

The ambiguity in the choice of relations between the phases of the order parameters mentioned in Section 2 is removed by specifying the signs of coefficients g_3 and g_4 according to the following scheme:

$$\begin{aligned} g_3 > 0 \Rightarrow \omega_\pm &= 2\Omega_\pm + \pi; \quad g_3 < 0 \Rightarrow \omega_\pm = 2\Omega_\pm; \\ g_4 > 0 &\Rightarrow \Theta = \Omega_+ + \Omega_- + \pi; \\ g_4 < 0 &\Rightarrow \Theta = \Omega_+ + \Omega_-. \end{aligned} \tag{15}$$

Nevertheless, the choice among these possibilities does not affect the phase diagram since only g_3 and g_4 squared appear in the final expressions.

Here, we discuss only the superconducting states listed in the previous Section 3; i.e., we assume that the interactions with the symmetry of order parameters φ and $\psi_\pm$ are not strong enough to form an independent pairing channel without coupling to the proper order parameter. Such a requirement allows us to restrict ourselves to the region of the phase diagram where $f > 0$, since at $f < 0$, the phase determined by conditions $\varphi \neq 0$ and $\eta_\pm = \psi_\pm = 0$ can exist.

The phase diagram of model (13) is shown in Fig. 3 for the space of coefficients a_1 and f. This diagram is topologically equivalent to the phase diagram of model (7) (see Fig. 2). We retained the same notation for lines and points and marked them by primes. The coordinates of these points and the equations of lines are written below.

$$O': a_1 = 0, \quad f = \frac{g_4^2 g_5}{b_1 g_5 + 2g_3^2};$$

$$B': a_1 = 0, \quad f = \frac{g_4^2 g_5}{(4a_2 + b_1)g_5 - 2g_3^2};$$
$$B'A': \frac{1}{27h}\left(f - \frac{g_4^2 g_5}{(4a_2 + b_1)g_5 - 2g_3^2}\right)^3 + \left(\frac{g_4 g_5 a_1}{(4a_2 + b_1)g_5 - 2g_3^2}\right)^2 = 0. \quad (16)$$

Straight line $O'E'$ is parallel to the a_1 axis and is tangent to parabola $O'D'$ at point O'.

$$O'D': f = -\frac{2h}{g_4^2}a_1^2. \quad (17)$$

Thus, taking account of improper order parameters allowed us to avoid involving the high-power terms in the Landau potential, which are prohibited by the renormalizability requirement imposed on the theory.

5. CALCULATIONS OF THE GAP IN THE ELEMENTARY EXCITATION SPECTRUM OF THE BOSE CONDENSATES TAKING INTO ACCOUNT IMPROPER ORDER PARAMETERS

It is well known that the gap function in the linear approximation in the components of the order parameter is constructed as the following sum [7]:

$$\Delta(\mathbf{k}) = \sum_{\mu=1}^{n} \eta_\mu^* \Psi_\mu(\mathbf{k}), \quad (18)$$

where n and $\Psi_\mu(\mathbf{k})$ are, respectively, the dimension and the basis function of the representation according to which the components of the order parameter are transformed.

As was first noted by Yip and Garg [9], we must supplement Eq. (18) with all the terms that are transformed like Eq. (18) under the effect of elements of group G_0. This is necessary to ensure the full correspondence of the gap function to the symmetry of the problem and to avoid, in particular, spurious zeroes prohibited by the symmetry. To find such terms, we can use the following theorem.

Let $\Phi(J_\nu)$, $\nu = 1, \ldots, m$, be an arbitrary function of invariants $J_\nu = J_\nu(\eta_\mu)$. Then $\frac{\partial \Phi}{\partial \eta_\mu} = \sum_{\nu=1}^{m} \frac{\partial \Phi}{\partial J_\nu}\frac{\partial J_\nu}{\partial \eta_\mu}$ transforms as η_μ^*.

For the uniaxial crystal with zero anisotropy in the basal plane under consideration, the relationship governing the transformation of the gap function is determined by the following linear approximation (see table for the notation):

$$\Delta(\mathbf{k}) = \eta_+^* k_+^2 + \eta_-^* k_-^2. \quad (19)$$

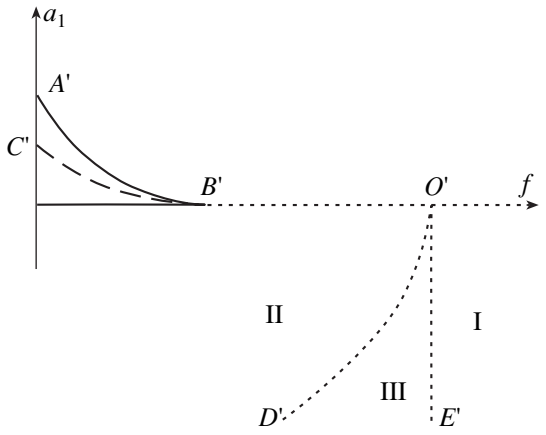

Fig. 3. The phase diagram for the Landau potential (13) in the space of phenomenological coefficients (a_1, f). The notation is the same as in Fig. 2.

To construct the gap function, for simplicity we take into account only the improper s condensate corresponding to φ.

In addition to invariants (3) and (12), we construct invariants containing the k_+ and k_- components of the wavevector; i.e.,

$$J_7 = k_+ k_-,$$
$$J_8 = k_+^4 \eta_- \eta_+^* + k_-^4 \eta_+ \eta_-^*, \quad (20)$$
$$J_9 = (k_+^4 \eta_+^{*2} + k_-^4 \eta_-^{*2})\varphi + (k_+^4 \eta_-^2 + k_-^4 \eta_+^2)\varphi^*.$$

Then, following the procedure described above, we find the expression for the gap function in the following form:

$$\Delta(\mathbf{k}) = A_1(\eta_+^* k_+^2 + \eta_-^* k_-^2) + A_2 \eta_+^* \eta_-^* (\eta_+ k_-^2 + \eta_- k_+^2) + A_3 \varphi^* (\eta_+ k_-^2 + \eta_- k_+^2) + A_4 \eta_+ \eta_- \varphi^* (\eta_+^* k_+^2 + \eta_-^* k_-^2). \quad (21)$$

Here, coefficients A_i are arbitrary functions of all invariants $J_1, \ldots, J_9$. It has been mentioned previously [5] that $\Delta(\mathbf{k})$ has no zeroes in phases (I) and (III), whereas there exists lines of zeroes in phase (II). Let us express the gap function for phase (II) in polar coordinates as

$$\Delta(\mathbf{k}) = \xi_+ k^2 (\exp(-i(2\alpha + \Omega_-)) + \exp(i(2\alpha - \Omega_+))) \times (A_1 + A_2 \xi_+^2 \pm A_3 \lambda \pm A_4 \lambda \xi_+^2), \quad (22)$$

where $k_\pm = k\exp(\pm i\alpha)$.

It can be seen from (22) that the lines of zeroes in the direction $\alpha = (\Omega_+ - \Omega_-) + (2l + 1)\pi/4$ do not disappear despite the existence of the additional terms. This is a direct consequence of the symmetry of phase (II), while the improper order parameter does not change the symmetry of the phases. Nevertheless, modern experimental techniques provide an opportunity not only to deter-

mine the type of zeroes in the elementary excitation spectrum of the Bose condensates but also to gain more detailed information on the form of the gap function. The existence of the distortions in the state of the Bose condensate caused by improper order parameters can be significant for the interpretation of such experiments.

REFERENCES

1. D. Pines and P. Monthoux, J. Phys. Chem. Solids **56**, 1651 (1995).
2. M. B. Walker, Phys. Rev. B **62**, 11 854 (2000).
3. G. M. Vereshkov, Yu. M. Gufan, I. G. Levchenko, and I. T. Okroashvili, Kristallografiya **42** (1), 18 (1997) [Crystallogr. Rep. **42**, 13 (1997)].
4. Yu. M. Gufan, Pis'ma Zh. Éksp. Teor. Fiz. **61**, 646 (1995) [JETP Lett. **61**, 665 (1995)].
5. Yu. M. Gufan, G. M. Vereshkov, P. Toledano, *et al.*, Phys. Rev. B **51**, 9219 (1995).
6. Yu. M. Gufan, *Structural Phase Transitions* (Nauka, Moscow, 1982).
7. M. Sigrist and K. Ueda, Rev. Mod. Phys. **63**, 239 (1991).
8. N. N. Bogoliubov and D. V. Shirkov, *Introduction to the Theory of Quantized Fields* (Nauka, Moscow, 1976; Wiley, New York, 1980).
9. S. Yip and A. Garg, Phys. Rev. B **48**, 3304 (1993).

Translated by K. Kugel

Crystallography Reports, Vol. 47, No. 6, 2002, pp. 1023–1030. Translated from Kristallografiya, Vol. 47, No. 6, 2002, pp. 1092–1099.

LATTICE DYNAMICS AND PHASE TRANSITIONS

Ferroelectric Domain Structure in SBN Crystals (Its Statics and Dynamics)

N. R. Ivanov*, T. R. Volk*, L. I. Ivleva, S. P. Chumakova*, and A. V. Ginzberg***

** Shubnikov Institute of Crystallography, Russian Academy of Sciences, Leninskiĭ pr. 59, Moscow, 119333 Russia*

e-mail: nrivanov@ns.crys.ras.ru

*** Institute of General Physics, Russian Academy of Sciences, ul. Vavilova 38, Moscow, 117942 Russia*

Received April 12, 2002

Abstract—The domain structure and its switching mechanism are studied on various cleaved facets of single crystals of SBN solid solutions. © *2002 MAIK "Nauka/Interperiodica".*

INTRODUCTION

Single crystals of $Sr_xBa_{1-x}Nb_2O_6$ (SBN-*x*) solid solutions have the structure of partially disordered tungsten bronze and are characterized by structural disordering of Ba and Sr atoms along two structural channels, in which only five sixths of atomic positions are occupied [1]. Such disordering results in the spreading of phase transitions and in considerable nonlinearities of physical properties. Owing to the ferroelectric nature of these phase transitions and the comparatively low values of the transition temperatures, SBN crystals at room temperature display high values of some parameters, such as electrooptical and nonlinear-optical coefficients, and, thus, are candidates for applications in optics. Despite the fact that SBN crystals posses a tetragonal atomic structure and some highly anisotropic physical properties, there is a temperature (sensitive to the composition and lying slightly above the transition temperature) at which these crystals are optically isotropic. In the vicinity of this temperature, SBN crystals have low birefringence ($\Delta n \approx 0.01$–0.05 at room temperature), which makes it impossible to use them for frequency multiplication of optical radiation under conditions of true phase synchronism in a spectral band of up to 2–3 μm [1]. However, SBN crystals could be potentially used for frequency conversion in a quasi-phase-matching mode in the presence of regular domain structures ensuring the spatial modulation of the sign of nonlinear susceptibility [2, 3]. We note that due to comparatively low coercive fields, $E_c \approx 1$–4 kV/cm [1], SBN crystals are more attractive for the formation of regular domain structures than $LiNbO_3$ [2] (commonly used for this purpose), in which $E_c \approx 200$ kV/cm.

Several studies were devoted to second-harmonic generation on regular domain structures in SBN-0.75 and SBN-0.61 [4–6]. During propagation of intense laser radiation through an SBN-0.6 crystal, diffuse visible radiation was observed in the bulk of the samples which was interpreted as a frequency conversion on incidental domains [3, 7, 8].

In order to estimate the above-mentioned capabilities of the domain structure in SBN, one has to possess information about the shapes and sizes of domains, the switching and polarization processes, etc. Only a few publications on this subject have been devoted to SBN crystals. Static domain structures in SBN crystals have been studied using scanning electron microscopy [9], X-ray diffraction [10], and chemical etching [3]. These studies revealed in SBN crystals the existence of thin (spike-shaped) domains about several micrometers in width and up to 0.5 mm in length. Similar estimates are yielded from measurements of the intensity of diffuse frequency-converted radiation [7] and integral scattering [11]. These data are insufficient for understanding the mechanisms of organization and switching of domain ensembles.

The aim of this work is to study the domain structure of SBN-0.61 and SBN-0.75 crystals by optical methods at room temperature. The choice of the compositions was dictated by strong differences in their ferroelectric phase transition temperatures (approximately 80 and 40°C for SBN-0.61 and SBN-0.75, respectively) which could not but affect the shape and sizes of domains and their density.

To avoid a possible misunderstanding in terminology, we should note that in relaxor ferroelectrics (to which the SBN crystals belong [12]) so-called nanodomains usually form near a diffuse phase transition, which were found, for example, for SBN-0.75 [13]. However, the present study deals only with conventional ferroelectric domains, which exist in a much lower temperature range than T_c and grow in the presence of an electric field. Of course, one cannot exclude that the presence of nanodomains affects the nucleation of conventional domains.

1063-7745/02/4706-1023$22.00

GROWTH OF SINGLE CRYSTALS OF SBN SOLID SOLUTIONS

Single crystals of SBN solid solutions were grown from a melt in the form of volume profiling boules by using a capillary shaping [14]. The distinctive features of this method that ensured that crystals of high optical quality were obtained are (i) the absence of rotation of a crystal during the growth, (ii) the controlled thermal conditions of crystallization (the constancy of temperature gradients in the growth zone due to a precisely fixed position of the crystallization front), and (iii) the stability of the cross section of a single-crystal boule.

The typical values of the pulling rate and axial temperature gradient were equal to 6–8 mm/h and 80°C/cm, respectively. The seeds were oriented along the tetragonal (*z*) axis. The grown crystals had compositions SBN-0.61 and SBN-0.75 and dimensions $12 \times 24 \times 110$ mm.

STATIC DOMAIN STRUCTURE OF SBN-0.61 AND SBN-0.75 CRYSTALS

Ferroelectric domains in SBN were observed with the help of an optical polarizing microscope on glass-like cleaved facets of two orientations: parallel and perpendicular to the polar *z* axis (nonpolar and polar facets, respectively).

The preliminarily oriented bars were cleaved by a direct impact for obtaining nonpolar cleaved facets. During the impact, a propagating crack is refracted at a domain wall through a small angle of several degrees. As a result, the cleaved surface acquires a microrelief, which can be observed in the reflected light under conditions of normal incidence. This microrelief corresponds to the domain structure at the moment of cleaving and can be well distinguished from the steps and other cleavage defects.

The domain structure of an SBN-0.61 crystal on a nonpolar cleaved facet is shown in Fig. 1. The domains are spike-shaped (with apex angles of about 0.5° or less) and propagate from the surface deep into the sample, into a depth range of 0.2–1 mm. Several spike-shaped domains grow through the whole thickness of the sample (through domains see the left part of Fig. 1).

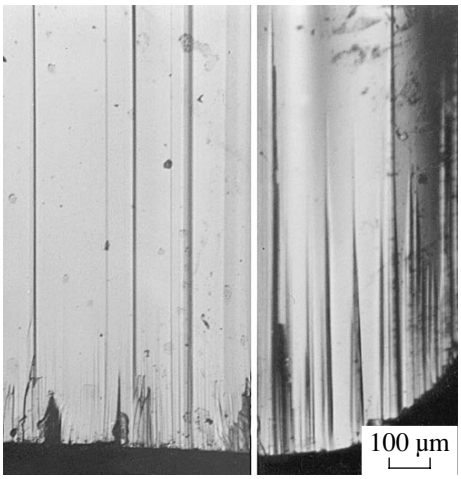

Fig. 1. Domains on the (110) plane in the SBN-0.61 crystal.

For obtaining polar cleavage planes, samples were subjected to the action of a decreasing sign-alternating electric field, creating mechanical stresses in crystals and sometimes resulting in the fracture of a crystal. Such experiments are described below. The domains of the polar (001) facet were visualized by decorating with nematic liquid crystals (NLC) with positive dielectric anisotropy. This method proved to be very efficient for studying many ferroelectrics [15–19]. Unfortunately, the orientational contrast of NLC for domains in SBN was too weak. Nevertheless, the domain walls were visible due to the reflection and refraction of light propagating along the walls. This phenomenon is similar to the Becke effect [20] in crystallooptics, where the role of the immersion medium is played not by the NLC, but rather by the solid matrix surrounding the domains, and the difference in refractive indices is due to the local electrooptical and piezooptical effects. By focusing the objective slightly above or below the sample surface, the Becke strip (which has the form of a domain wall near the surface) can be positioned such that it enhances the natural contrast of the NLC (if it exists) or produces an illusion of three-dimensional relief. The resolution for this method is 1 μm.

Domain patterns on the (001) plane are shown in Figs. 2 and 3. The idealized pattern consists of squares whose sides are parallel to the [110] and $[\bar{1}10]$ directions. Taking into account the shape of domains seen on the nonpolar cleavage surface (Fig. 1), we can conclude that the idealized spike-shaped domain has the shape of a sharp tetragonal pyramid (at least at the moment of its active growth, not during its degradation). One can distinctly see a periodicity (with a period of 24 μm) in domain positions along both orthogonal symmetry-equivalent directions, which results in a chessboard-type cellular pattern (with a surface domain density of about 0.5) with a characteristic length of the side of squares of about 12 μm. In reality, depending on the method of preparation of the domain structure, the idealized forms become distorted, the angles are rounded, the periodicity is broken, and the basal planes of pyramids are merged together into multicomponent groups (Figs. 2 and 3).

Now, we give some details of the preparation of domain structures observed on the (001) cleavage surfaces. A sample (whose structure is shown in Fig. 2) was prepared by the application of an intense pulse of a high-ac-voltage discharge to a polished cube with electrodes on the polar faces resulting in the fracture of the crystal with the formation of the (001) cleaved facet. This fresh cleavage surface was coated with an NLC. At the beginning of observation (in the transmitted light) a regular orthogonal network that looked like a system of

microcracks was seen. After a time, the cells of this network began to be covered with growing domains with a cross section of several μm, while the microcracks were being healed. A part of the surface had a chessboard like arrangement of quasi-square domains. Some of the domains had tails coinciding with the residual microcracks (Fig. 2). The cellular positional long-range order of domains and the size of cells can be explained by taking into account growth lamination, the character of the piezoeffect, and the distribution of elastic strains. Below (when considering the domain dynamics), it will again be shown that the domain and growth periods (but not their directions) are identical.

The domain structure shown in Fig. 3 was obtained under softer conditions: the sample (cut from the same crystal) was switched in gradually decreasing (in amplitude) sign-alternating pulsed electric field and then was split mechanically and decorated with an NLC (the orientations in Figs. 2 and 3 differ by 45°, the frame sides of Fig. 3 are parallel to the [100] and [010] directions). The resulting domain structure had the same configuration and average dimensions of quasi-squared elements as in Fig. 2 (with a surface domain density of 0.5) but showed no signs of breaking into microcracks. Besides, the character of the division of elements into groups was more chaotic, and the long-range chessboard like order was less pronounced.

A domain structure similar to that shown in Fig. 3. but with finer details and with a lower surface density of domains was observed in the SBN-0.75 crystal (Fig. 4). In all cases, the cellular positional long-range order of domains observed and the cell size (but not the domain size) seem to be attributable to the growth lamination of the crystal and the corresponding distribution of elastic strains.

We also studied the effect of high-temperature annealing (at ≅1000°C) on the domain structure of the SBN crystals; such treatment, as a rule, is used to improve the optical homogeneity of these crystals. This annealing was found to be highly critical for the SBN-0.75 crystals: the annealing not only removed fine surface domains (monodomenization) but also resulted in the formation (in the bulk) of phase precipitate crystallites (Fig. 5a) which scattered light and had more or less isometric and chaotically oriented forms when observed from the outer side of the polar (001) surfaces. In [1], such phase precipitates in SBN solid solutions was associated with a centrosymmetrical monoclinic phase (we do not consider here the symmetry of phase precipitates). Crystallites by themselves do not take part in switching. In cross sections parallel to the polar axis, the crystallites looked elongated along the [001] direction (Fig. 5b) and consisted of a nucleus (the phase precipitate proper) and two coatings grown on them along and opposite to the polarization vector. These coatings may be considered as domains formed due to the charged interphase boundaries. These domains are internal and actually cannot be visualized on outer polar surfaces without cutting or deep etching a sample. An alternative explanation of the pattern shown in Fig. 5b may be the existence of precipitates of a centrosymmetrical phase, which are rolled out by a purely elastic interaction [21] in the paraelectric phase during the cooling of the sample after annealing.

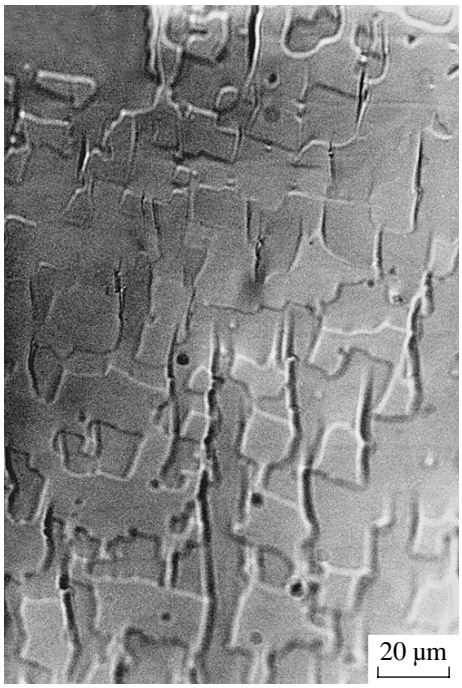

Fig. 2. Domains on the (001) plane in the SBN-0.61 crystal after chock treatment in a strong electric-field pulse.

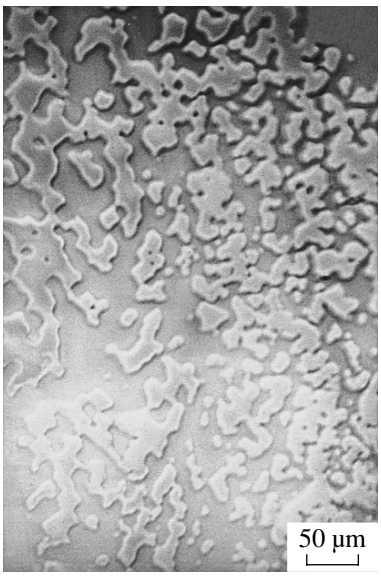

Fig. 3. Domains on the (001) plane in the SBN-0.61 crystal without preliminary treatment in a strong electric field.

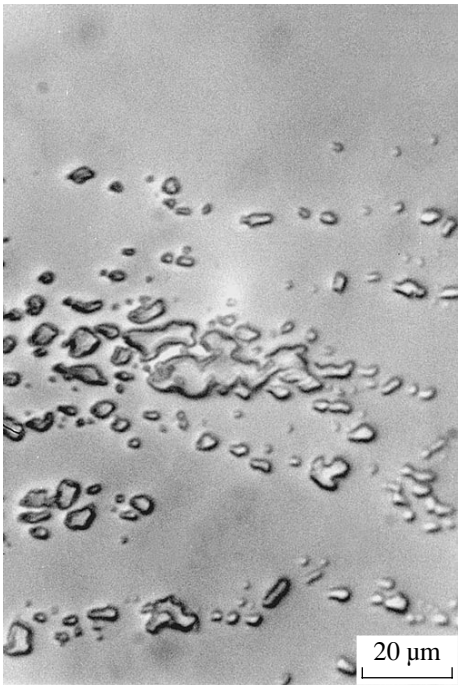

Fig. 4. Domains on the (001) plane in the SBN-0.75 crystal.

DOMAIN DYNAMICS IN SBN-0.61 CRYSTALS

Video Recording of the Switching Process

Video recording of the switching process allows one to see this process in real time and to verify the validity of the above conclusions. The switching was performed in a field that was increased by small steps in the vicinity of the coercive field. Such a mode ensured the almost optimal sharpness and contrast of a dynamic image at the appropriate magnification. It was difficult to obtain a satisfactory result by this method, because the image was not located on the surface but was formed within a relatively thick layer (in transmitted polarized light). The optimal visualization in this case was possible only when the domain density was approximately equal to 0.5. Figure 6 presents some snapshots (Fig. 6h gives the scale, with the value of small scale division being 10 μm). Figures 6a–6d correspond to the dynamic domain structure on the polar (001) surface under observation along the ferroroelectric *z* axis through the transparent electrodes with NLC immersion. In this case, a dynamic NLC method was used to visualize the domain structure [15–17]. As a rule, the switching front of many domains is visible. In an inhomogeneous crystal, this front makes border around more or less large areas with similar dynamic characteristics (e.g., a threshold switching field). The topography of the front usually corresponds to the distribution of growth defects [19]. Figures 6a and 6b correspond to a more homogeneous crystal. In Fig. 6a, the switching front is long and fragmentated. It separates growing polydomain (at the top left of the snapshot) and decreasing monodomain (on the lower right) regions. Figure 6b shows the continuation of this process (the rapid-switching stage). The next pair of snapshots (Figs. 6c, 6d) corresponds to an inhomogeneous crystal. The inhomogeneous area in the center of Fig. 6c was initially fringed with the distributed NLC (as the field reached a certain threshold value), then

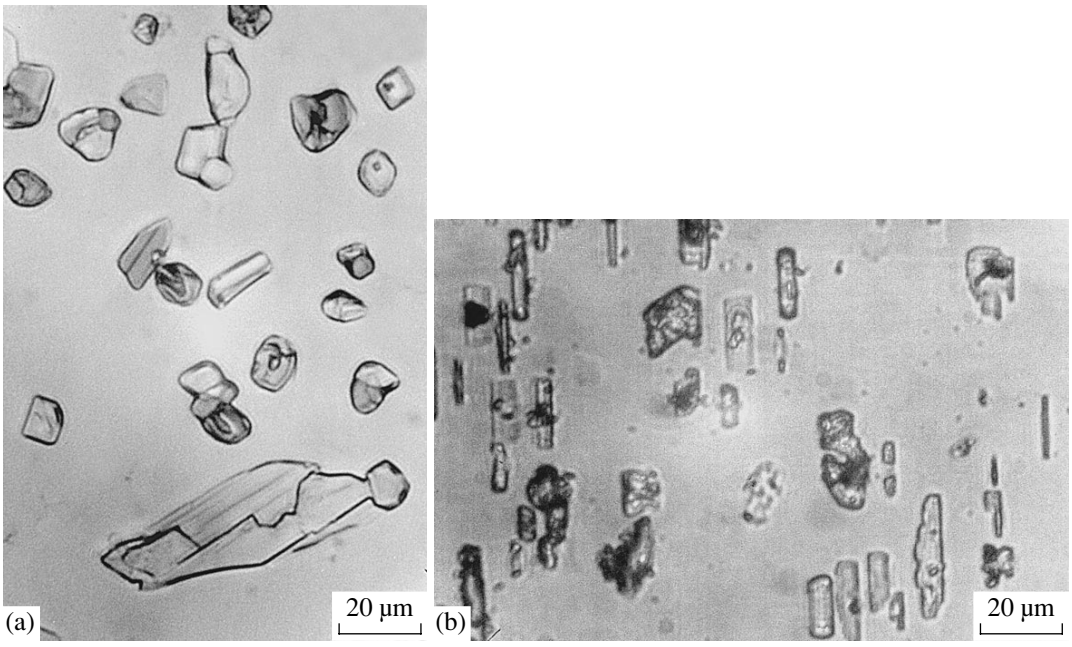

Fig. 5. Phase precipitate crystallites on the outer (001) plane of an SBN-075 crystal plate: (a) after annealing and (b) the section of the same plate by a plane parallel to the [001] polar axis.

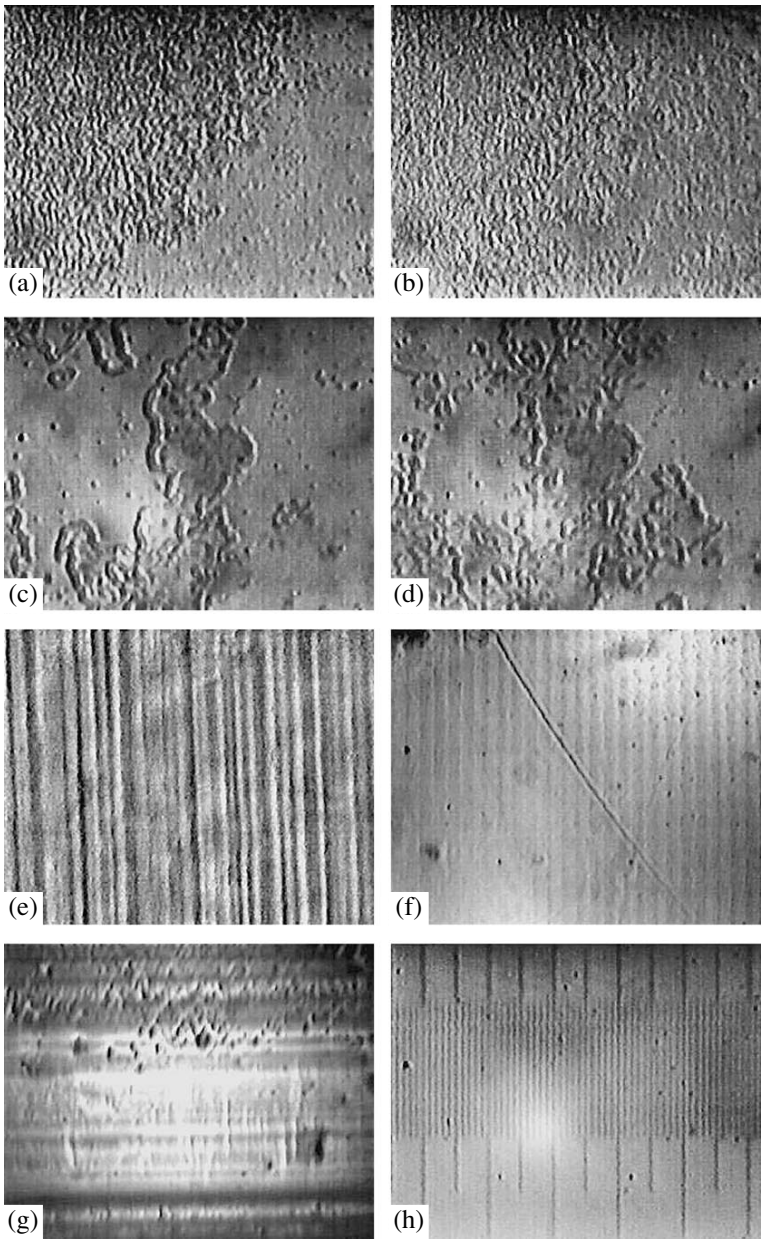

Fig. 6. (a–g) Snapshots and (h) the scale of video recording of the switching process in the SBN-0.61 crystal.

(Fig. 6d) the process went on the same way as in Fig. 6b, through the formation of new domains. The threshold field was 2–2.5 kV/cm, which is equal to the static coercive field of the crystal.

The snapshots shown in Fig. 6e and 6f are most interesting. Figure 6f presents growth stripes (the striations are typical for this crystal) with a period of about 24 μm. The growth stripes are directed normally to the polar *z* axis (the [001] axis in Fig. 6f lies horizontally). Such growth stripe structure is generally typical for Czochralski-grown SBN crystals [1]. Figure 6e gives the visualization on the front (110) plane of the switching process in a laminated homogeneous sample under the application of a field along the [001] axis (almost vertical in Fig. 6e). The visualization is caused by a local transverse electrooptical effect; variations in brightness in this case are due to surface domains. The vertical stripes in Fig. 6e are the growing domains. The process is in a rapid switching stage at a domain density of about 0.5; therefore, the width and thickness of a domain stripe are equal (on average) to the width and thickness of the matrix stripe, and this ensures an optimal contrast. Even a simple calculation of the number of stripes shows that the periodicity of both systems (growth and domain stripes) is actually the same, although these stripe structures are orthogonal to each other in the crystal. The domains grown through are not

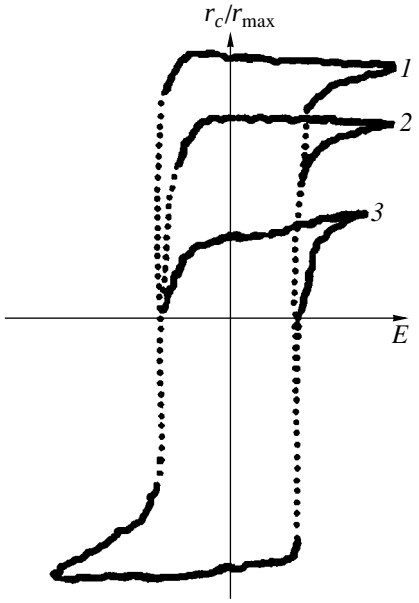

Fig. 7. Example of a local elecrooptocal hysteresis loop in the SBN-0.61 crystal and (*1–3*) its behavior under the successive cycles of training. The ordinate is proportional to the electrooptical coefficient r_c/r_{max}.

pyramidal (unlike the static surface domains shown in Fig. 1), but prismatic ones.

Finally, Fig. 6g illustrates the case of switching an inhomogeneously layered crystal in the same geometry as in Fig. 6e. Visualization was performed in the same way but with the additional use of decoration with NLC. The use of NLC did not increase the contrast but additionally brightened the area of switching between the growth layers due to the perturbation of the NLC by forward-moving charged domain walls (a kind of dynamic NLC method). It can be seen that the growth layers can accumulate charges and screen the switching process.

Hysteresis Loops

It is expedient to relate the domain dynamics to the shape of ferroelectric hysteresis loops. For inhomogeneous system, it is desirable to know data on local processes. A suitable quasi-local method for recording hystereis loops is the electrooptical method [19]. We present the results of measurements of the transverse linear electrooptical effect in the SBN-0,61 crystals by using an He–Ne laser (λ = 6328 Å) for the case where an electric field was applied along the *z* axis and the wave vector was directed normal to *z*. The crystal bars had the dimensions ratio l/t = 0.366 (l = 1.38 mm is the crystal width along the wave vector direction, t = 3.77 mm is the length along the *z* axis). The diameter of a light beam was 0.1 mm. The $r_c(E)$ dependence was measured, where $r_c = r_{33} - (n_o/n_e)^3 r_{13} \cong r_{33}$ for SBN (the point symmetry group is 4*mm*). The sample was subjected to a saw-tooth voltage with an amplitude 2.5 times higher than the coercive field. The time of recording of the complete cycle of an $r_c(E)$ loop was 27 min. By scanning the front surface at room temperature, a set of $r_c(E)$ loops was obtained at various points of the crystal. Figure 7 shows the results of measurements for a representative point, for which a hysteresis loop exhibits the main characteristics typical of other observed loops. The labels *1*, *2*, and *3* indicate the successive cycles of switching. The static coercive field was equal to 2 kV/cm, the bias field in the case under consideration was equal to zero (the latter field can reach 0.5 kV/cm for other points). The saturated value of the electrooptical coefficient r_c (for a mechanically free crystal) corresponded to the half-wave voltage $V_{\lambda/2}$ = 250 V (normalized to the ratio l/t = 1). The values of E_c and $V_{\lambda/2}$ obtained are in good agreement with the published data for SBN-0.61 [1]. The observed variation in the form and amplitude of $r_c(E)$ loops during cyclic switching is in accordance with earlier observations of loops differing in shape in several initial cycles of dielectric hysteresis in the case of switching in quasi-static fields [22]. This difference can be explained by processes that are typical for inhomogeneous systems: "the freezing" or "pinning" of domains (in conventional ferroelectrics) or that of polarized areas and clusters (in relaxor ferroelectrics). Being macroscopic and volume-sensitive, the electrooptical method cannot distinguish domains and clusters; however, this method allows one to estimate the volume fraction of the frozen part of a crystal (within the region illuminated by the laser beam) and to construct two-dimensional distribution maps. Preliminary results of electrooptical scanning are in qualitative agreement with the layered nature of the crystal and with the results of the video recording of the front surfaces (*x*, *z*).

We can point out the following common features of the switching process, independent of the specific form of a quasi-local $r_c(E, x, z)$ loop:

(i) The beginning of switching has a threshold nature and goes fast until a polydomain state with a domain density of about 0.5 or somewhat higher is reached.

(ii) The final stage of switching proceeds with difficulty and slowly when the domain density varies from 0.9 to 1.

In other words, even independently of training, the crystal easily breaks into domains but tends to a monodomain state with a great difficulty. Taking into account the results of the study of static domains, the fast stage of switching above the threshold can be associated with a free forward growth of spikes, until the walls become pinned on defects. The slow stage is connected with the process of depinning spikes. It should also be noted that the domain nuclei are small (micron- and submicron-sized) and, therefore, virtually do not contribute to the volume effects but increase light scattering by nonuniformities in a field below the threshold.

DISCUSSION OF RESULTS

Summing up the results of our research into static domain structure and domain dynamics in the SBN crystals, we can single out the following regularities.

These crystals tend to form lengthy domain structures with domains that have the form of sharp tetragonal pyramids (with apex angles of about 0.5°) extending from the surface into the depth of the sample. The domains grown through the whole thickness of the crystal have the form of tetragonal prisms. The cross-sectional dimension and the length of the domains are several micrometers and 0.2–1 mm, respectively. The domains in aged and nontrained samples are mainly located near the surface, and the inner volume is almost monodomain.

The study of the domain dynamics and elecrooptical hysteresis loops (in longitudinal and transverse geometry and also after training) testifies to two stages of the switching process (we do not consider nucleation here, because it does not contribute to the volume-sensitive properties): a comparatively easy stage in which the beginning of the process of getting the polydomain state up to a domain density of about 0.5 has a pronounced threshold character, and a hindered stage of getting single-domain state (an order of magnitude slower and without a threshold) of the residual part (about 10% of the volume). Thus, the switching process can be described as a mainly forward growth of spike-shaped domains. The sideways motion of domain walls (at least a part of them) is hindered and requires the application of higher fields.

There is a well-defined positional long-range order in the domain arrangement. Direct observation and the video recording of the switching process confirm the relationship between the one-dimensional periodicity of the layered growth structure along the tetragonal axis and the two-dimensional periodicity of the dynamic domain structure in the perpendicular plane. The correlation in the periodicity of the mutually orthogonal systems representing growth layers (according to the terminology used in [21], they can be elastic concentration domains) and that of the growing ferroelectric domains can be qualitatively explained as follows.

Let us suppose that a plate with a layered structure exhibiting a highly anisotropic piezoeffect ($|d_{33}| > |d_{31}|$) is placed into a uniform electric field directed along the polar axis perpendicular to the layer plane. Suppose also that a thin cylindrical domain exists in an "active" growth layer (containing a sufficient amount of pinned charged defects). Owing to the large value of the piezoelectric modulus d_{33}, there is a misfit between the domain and matrix lattices along the z axis, which results in mechanical stresses, for example, compression along the z axis, localized at the ends of the domain. The stresses create a sign-alternating deformation wave in the layer along the x' axis (decaying with distance from the source); the spatial Fourier component of this wave is equal to the layer thickness. If the sign of the transverse piezoelectric modulus d_{31} is opposite to that of d_{33} (as is the case in SBN crystals [1]), the deformation wave in the layer is equivalent to a sign-alternating shear (compression and tension in the mutually perpendicular principal directions) in the zx' plane. The distribution of piezoelectric charges (and their signs) over the layer surface will also become periodic, determining the localized nucleation of new domains in the regions of the increased field and conserving the matrix in the neighboring regions of the lowered field. The tetragonal symmetry and the need to preserve continuity require phase matching, i.e., the fulfillment of the same conditions in the zy' plane. This can be achieved only in a chessboardlike distribution. The domains localized in such a cellular way in the active layer grow towards the surface (because this is the dominant switching mechanism) and reproduce their distribution on the surface. The occurrence of microcracks can be described in the same way.

The choice of the x' direction in a habit plane is dictated not only by the symmetry, but also by the possibility of minimizing longitudinal elastic deformation [21]; therefore, the [110] direction (both for domains and for microcracks) is more preferable than [100].

The above discussion refers to comparatively large domains in an electric field or just after a shock effect (Fig. 2). In the case of fine domains (Fig. 4) or after the complete relaxation of local elastic stresses on microcracks and other surfaces and defects (Fig. 3), the surface energy begins to play a dominant role. Unlike the elastic energy, the surface energy in a tetragonal crystal is isotropic in a habit plane; therefore, the forms of cross sections become rounded. Within a macroscopic approach, one might expect the form of spike-shaped domains to becomes conical near the apex.

CONCLUSION

The analysis of static and dynamic domain structures in SBS crystals shows that the crystals of this family, in principle, are attractive for the fabrication of surface and deeply penetrated regular domain structures. At the same time, because of the formation of spike-like domains, the surface and volume domain densities differ considerably; The monodomain state in the bulk of a uniform crystal is more stable than surface configurations. The switching process has two stages: a slow stage and a fast one. The fast stage has a threshold and corresponds to the forward growth of spike-shaped domains. The formation of domain walls is accompanied by the piezoelectric effect (clamping) and elastic interaction. The inhomogeneity of the layers assists the pinning of domains on defects and hampers getting single-domain state. These mechanisms of the interaction of domains with a real growth structure, as well as the features of their piezoelectric interaction, should be taken into account when considering relaxor behavior.

ACKNOWLEDGMENTS

This study was supported by the INTAS (grant no. 01-0173) and Russian Foundation For Basic Research (project no. 00-02-16624).

REFERENCES

1. Yu. S. Kuz'minov, *Ferroelectric Crystals for Laser Emission Control* (Nauka, Moscow, 1982), p. 400.
2. P. Houe and D. Townsend, J. Phys. D **28**, 1747 (1995).
3. J. Romero, D. Jaque, J. García-Sole, and A. A. Kaminskii, Appl. Phys. Lett. **78** (14), 1961 (2001).
4. B. Fischer and M. Horowitz, Appl. Phys. Lett. **64** (14), 1756 (1994).
5. A. S. Kewitsch, M. Segev, A. Yariv, *et al.*, Appl. Phys. Lett. **64** (23), 3068 (1994).
6. Y. Y. Zhu, J. S. Fu, R. F. Xiao, and G. K. L. Wong, Appl. Phys. Lett. **70** (14), 1793 (1997).
7. S. Kawai, T. Ogawa, H. S. Lee, *et al.*, Appl. Phys. Lett. **73** (6), 768 (1998).
8. A. A. Kaminskiĭ, J. García-Sole, S. N. Bagaev, *et al.*, Kvantovaya Élektron. (Moscow) **25** (12), 1059 (1998).
9. L. A. Bursill and P. J. Lin, Philos. Mag. B **54**, 157 (1986).
10. G. Fogarty, B. Steiner, M. Cronin-Golomb, *et al.*, J. Opt. Soc. Am. B **13**, 2636 (1996).
11. A. A. Bezhanova, V. G. Silvestrov, G. A. Zeinalova, and T. R. Volk, Ferroelectrics **111**, 299 (1990).
12. L. E. Cross, Ferroelectrics **76**, 241 (1987).
13. W. H. Huang, D. Viehland, and R. R. Neurgaonkar, J. Appl. Phys. **76** (1), 490 (1994).
14. L. I. Ivleva, N. V. Bogodaev, N. M. Polozkov, and V. V. Osiko, Opt. Mater. **4**, 168 (1995).
15. N. A. Tikhomirova, L. I. Dontsova, S. A. Pikin, and L. A. Shuvalov, Pis'ma Zh. Éksp. Teor. Fiz. **29**, 37 (1979) [JETP Lett. **29**, 34 (1979)].
16. N. A. Tikhomirova, A. V. Ginzberg, L. I. Dontsova, *et al.*, Fiz. Tverd. Tela (Leningrad) **28** (10), 3055 (1986) [Sov. Phys. Solid State **28**, 1718 (1986)].
17. N. A. Tikhomirova, S. P. Chumakova, A. V. Ginzberg, *et al.*, Kristallografiya **32** (1), 143 (1987) [Sov. Phys. Crystallogr. **32**, 80 (1987)].
18. N. R. Ivanov, N. A. Tikhomirova, A. V. Ginzberg, *et al.*, Kristallografiya **39** (4), 659 (1994) [Crystallogr. Rep. **39**, 593 (1994)].
19. N. R. Ivanov, S. P. Chumakova, A. V. Ginzberg, and V. V. Dolbinina, Kristallografiya **45** (6), 1061 (2000) [Crystallogr. Rep. **45**, 979 (2000)].
20. R. E. Stoiber and S. A. Morse, *Microscopic Indentification of Crystals* (Ronald, New York, 1972; Mir, Moscow, 1974).
21. A. G. Khachaturyan, *Theory of Phase Transformations and Structure of Solid Solutions* (Nauka, Moscow, 1974), p. 384.
22. V. V. Gladkiĭ, V. A. Kirikov, S. V. Nekhlyudov, *et al.*, Fiz. Tverd. Tela (St. Petersburg) **42** (7), 1296 (2000) [Phys. Solid State **42**, 1334 (2000)].

Translated by A. Zalesskiĭ

Crystallography Reports, Vol. 47, No. 6, 2002, pp. 1031–1035. Translated from Kristallografiya, Vol. 47, No. 6, 2002, pp. 1100–1104.

LATTICE DYNAMICS AND PHASE TRANSITIONS

High-Temperature Phase Transition in Ferroelastic $K_2Ba(NO_2)_4$

L. F. Kirpichnikova*, V. S. Shakhmatov, and A. Pietraszko*****

** Shubnikov Institute of Crystallography, Russian Academy of Sciences, Leninskiĭ pr. 59, Moscow, 119333 Russia*

e-mail: luba@ns.crys.ras.ru

*** Joint Institute for Nuclear Research, Dubna, Moscow oblast, 141980 Russia*

**** W. Trzebiatowski Institute of Low-Temperature and Structure Research, Polish Academy of Sciences, P.O. Box 1410, Wroclaw 2, 50-950 Poland*

Received April 17, 2002

Abstract—X-ray diffraction studies of $K_2Ba(NO_2)_4$ crystals were performed in the vicinity of the paraelastic–ferroelastic phase transition. The structural parameters and the behavior of the spontaneous deformation near the phase transition were determined. The experimental data were analyzed based on a phenomenological theory. It was shown that the high-temperature phase transition is of the first order. *© 2002 MAIK "Nauka/Interperiodica".*

INTRODUCTION

Ferroelastic $K_2Ba(NO_2)_4$ (KBN) crystals undergo two ferroelastic phase transitions, at T_c = 420 K (from 6/*mmm* to *mmm*) and at 200 K [1]. These phase transitions can be characterized as improper second-order phase transitions of the order–disorder type and are related to the ordering of three different, crystallographically inequivalent NO_2 groups [1–6]. According to [7], the transition occurring at a higher temperature is accompanied by significant changes in the lattice vibration spectrum, whereas at the lower temperature transition, the internal-vibration modes of nitrite ions are changed. At room temperature, KBN crystals belong to the *Pbam* space group (Z = 2) and have the following unit-cell parameters: a = 11.427 Å, b = 6.604 Å, and c = 6.161 Å [4]. The symmetry of the low-temperature phase is $C2/m$ (Z = 8), and its unit-cell parameters are a_m = 13.062 Å, b_m = 12.310 Å, c_m = 13.06 Å, and β = 120.00° [8]. Measurements of the elastic moduli of KBN crystals were performed using the ultrasonic and Brillouin light scattering techniques [3, 9]. A phenomenological theory of the low-temperature phase transition was developed in [10], and a description of the phase transitions in terms of the frustration theory was given in [11]. Studies of the domain structure [1, 12] have shown that KBN crystals exhibit three types of domains and, therefore, six types of domain walls that meet the compatibility conditions for spontaneous deformations. All domain walls in KBN crystals belong to the *W* type, according to the classification of Sapriel [13]. However, the space symmetry of the paraelastic phase has not yet been determined, and a phenomenological description of the high-temperature phase transition has not yet been given. Therefore, the present work was aimed at creating an X-ray diffraction study of the KBN crystal structure in the vicinity of the paraelastic–ferroelastic phase transition and a group-theoretical analysis of this transition in terms of phenomenological theory of phase transitions, as well as an analysis and comparison of the experimental data with theoretical predictions.

EXPERIMENTAL RESULTS

The structural studies were performed using a KUMA KM4 automated diffractometer (CuK_α radiation, graphite monochromator). In our calculations, we used computer program HELXTL93, R = 0.0155.

At 432 K, KBN crystals correspond to the $P6/mmm$ space group (Z = 1) and have the following unit-cell parameters: $a_h = b_h$ = 6.6677 Å, c_h = 6.1370 Å, V = 236.24(6) Å^3, and d_{calcd} = 2801 kg/m^3. Figures 1a and 1b show projections of the crystal structure onto the *XOY* and *YOZ* planes, respectively. The atomic positional and thermal parameters of the atoms are listed in the

Positional ($\times 10^{-4}$) and thermal parameters ($U_{equiv} \times 10^{-3}$) of atoms for KBN crystals

Atom	x	y	z	U_{equiv}
K(1)	3333	6667	0	40(1)
Ba(1)	0	0	5000	32(1)
N(1)	0	5000	5000	84(6)
O(1)	0	4297(16)	3320(18)	53(3)
N(2)	0	0	0	102(11)
O(2)	0	1468(45)	0	113(14)

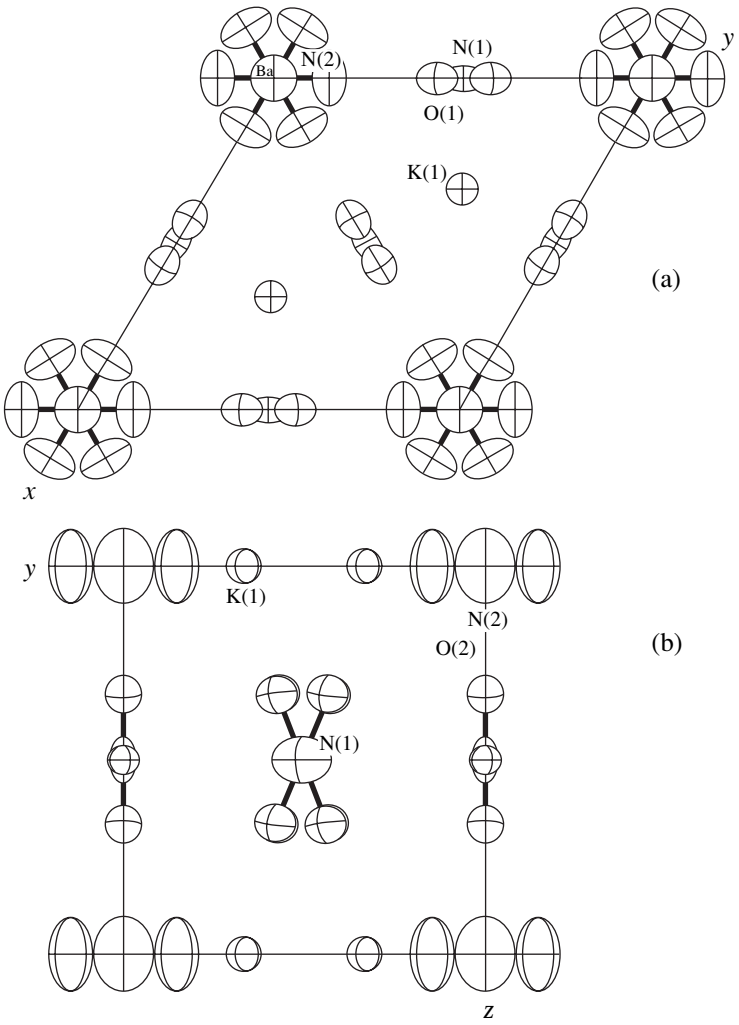

Fig. 1. Projections of the KBN crystal structure in the paraelastic phase onto planes (a) *XOY* and (b) *YOZ*.

table. Difference Fourier diagrams for the electron density distribution in the vicinity of different nitrogen atoms are shown in Fig. 2. The temperature dependences of the lattice constants for the ferroelastic orthorhombic phase below the Curie point are presented in Fig. 3. It can be seen from Fig. 3, that lattice constants *a* and *b* increase and *c* decreases with increasing temperature. At $T = T_c$, the lattice constants undergo a small jump. Calculations give the following values for these jumps: $\Delta e_1 = (a - \sqrt{3}\,a_h)/\sqrt{3}\,a_h = -15 \times 10^{-4}$, $\Delta e_2 = (b - a_h)/a_h = 8 \times 10^{-4}$, and $\Delta e_3 = (c - c_h)/c_h = 0.8 \times 10^{-4}$. Here, *a*, *b*, and *c* and a_h, b_h, and c_h are the lattice constants for the orthorhombic and hexagonal phases, respectively. The temperature dependence of the spontaneous strain deformations in KBN crystals ($\varepsilon = \varepsilon_1 = -\varepsilon_2$), determined from experimental temperature dependences of the lattice constants by using the relationship $\varepsilon(T) = 1/2\sqrt{3}\,[a(T)/b(T) - 1]$ [12], is shown in Fig. 4. It is clearly seen that the spontaneous deformation is a linear function of temperature over a range roughly 20 K wide. At $T = T_c$, we see a small jump in the spontaneous deformation, which is a signature of a first-order phase transition.

The phase transition from *P*6/*mmm* (D_{6h}^1) ⟶ *Pbam* (D_{2h}^9) in $K_2Ba(NO_2)_4$ crystals results in the hexagonal primitive cell doubling in volume. From the experimental data on the lattice parameters in the *P*6/*mmm* and *Pbam* phases, it follows that this phase transition is related to one of wavevectors $\mathbf{b}_1/2$, $\mathbf{b}_2/2$, or $\mathbf{b}_3/2$ (Fig. 5). The phase transition is characterized by a three-component order parameter (φ_1, φ_2, φ_3). The φ_1, φ_2, and φ_3 components are characterized by wavevectors $\mathbf{b}_1/2$, $\mathbf{b}_2/2$, and $\mathbf{b}_3/2$, respectively. The free-energy expansion for the phase transition from *P*6/*mmm* to *Pbam* has the form

$$F = F_\varphi + F_e + F_{\varphi e}, \qquad (1)$$

$$F_\varphi = \frac{1}{2}r(\varphi_1^2 + \varphi_2^2 + \varphi_3^2) + u\varphi_1\varphi_2\varphi_3$$
$$+ \frac{1}{4}u_1(\varphi_1^4 + \varphi_2^4 + \varphi_3^4) + \frac{1}{6}u_2(\varphi_1^6 + \varphi_2^6 + \varphi_3^6)$$
$$F_e = \frac{1}{2}C_{11}(e_1^2 + e_2^2) + \frac{1}{2}C_{33}e_3^2 + \frac{1}{2}C_{44}(e_4^2 + e_5^2)$$
$$+ C_{12}e_1e_2 + C_{13}e_3(e_1 + e_2) + \frac{C_{11} - C_{12}}{4}e_6^2, \quad (2)$$
$$F_{\varphi e} = (\varphi_1^2 + \varphi_2^2 + \varphi_3^2)[\alpha_1(e_1 + e_2) + \alpha_3e_3]$$
$$+ \frac{\alpha_2}{2}[2\sqrt{3}(\varphi_2^2 - \varphi_3^2)e_6 + (2\varphi_1^2 - \varphi_2^2 - \varphi_3^2)(e_1 - e_2)].$$

Here, $r = \alpha(T - T_c)$, T_c is the phase transition point, C_{ij} are the elastic moduli, and u_i and α_i are the phenomenological coefficients.

Condensation of the order parameter of the types ($\varphi_1 \neq 0$, $\varphi_2 = 0$, and $\varphi_3 = 0$), ($\varphi_1 = 0$, $\varphi_2 \neq 0$, and $\varphi_3 = 0$), or ($\varphi_1 = 0$, $\varphi_2 = 0$, $\varphi_3 \neq 0$) is accompanied by the formation of domains of three different types, shown in Figs. 5b–5d, respectively. The order parameter is related to the orientational ordering of NO_2 groups. The possible types of the orientational ordering of these groups at the *P6/mmm* ⟶ *Pbam* phase transition will be discussed in another paper.

The effective free energy describing the phase transition in domain $\varphi \equiv \varphi_1 \neq 0$, $\varphi_2 = 0$, and $\varphi_3 = 0$ (Fig. 5b) has the form

$$F_{\text{eff}} = \frac{1}{2}r\varphi^2 + \frac{1}{4}u_1\varphi^4 + \frac{1}{6}u_2\varphi^6 + \frac{1}{2}C_{11}(e_1^2 + e_2^2)$$
$$+ \frac{1}{2}C_{33}e_3^2 + \frac{1}{2}C_{44}(e_4^2 + e_5^2) + C_{12}e_1e_2$$
$$+ C_{13}e_3(e_1 + e_2) + \frac{C_{11} - C_{12}}{4}e_6^2 \quad (3)$$
$$+ [\alpha_1(e_1 + e_2) + \alpha_3e_3]\varphi^2 + \alpha_2(e_1 - e_2)\varphi^2.$$

The temperature dependences of the order parameter and of the spontaneous-deformation tensor is determined by the set of equations

$$\frac{\partial F_{\text{eff}}}{\partial \varphi} = 0,$$
$$\frac{\partial F_{\text{eff}}}{\partial e_i} = 0, \quad i = 1, \ldots, 6. \quad (4)$$

From these equations, we find

$$e_1 = \varphi^2\frac{-C_{33}\alpha_1 + C_{13}\alpha_3}{C_{33}(C_{11} + C_{12}) - 2C_{13}^2} - \varphi^2\frac{\alpha_2}{C_{11} - C_{12}},$$

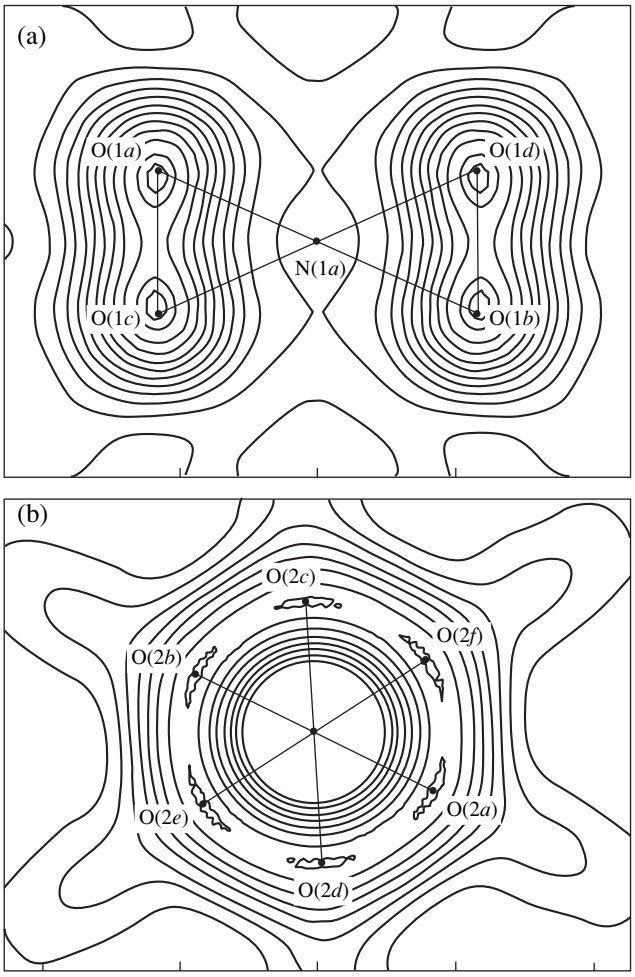

Fig. 2. Difference Fourier diagrams for the electron density distributions in the vicinity of nitrogen atoms (a) N_1 and (b) N_2 for the paraelastic phase of the KBN crystal.

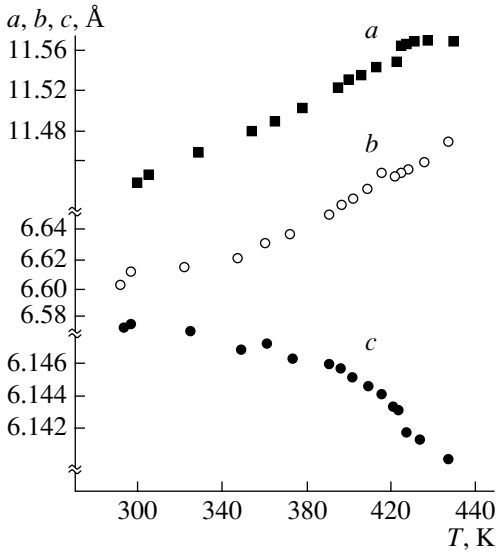

Fig. 3. Temperature dependences of the KBN lattice constants for the ferroelastic *Pbam* phase.

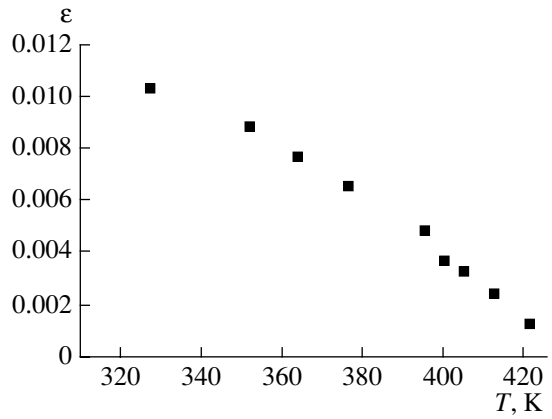

Fig. 4. Temperature dependence of spontaneous strain $\varepsilon = \varepsilon_1 = -\varepsilon_2$ in the KBN crystal.

$$e_2 = \varphi^2 \frac{-C_{33}\alpha_1 + C_{13}\alpha_3}{C_{33}(C_{11}+C_{12}) - 2C_{13}^2} + \varphi^2 \frac{\alpha_2}{C_{11}-C_{12}}, \quad (5)$$

$$e_3 = \varphi^2 \frac{2C_{13}\alpha_1 - (C_{11}+C_{12})\alpha_3}{C_{33}(C_{11}+C_{12}) - 2C_{13}^2}.$$

It is clear from Eqs. (5), that the temperature dependence of the spontaneous deformation tensor is completely determined by the temperature dependence of the order parameter squared:

$$\alpha(T - T_c) + u_1\varphi^2 + u_2\varphi^4 + 2\alpha_1(e_1 + e_2) + 2\alpha_2(e_1 - e_2) + 2\alpha_3 e_3 = 0. \quad (6)$$

Substituting Eq. (5) into Eq. (6), we find the temperature dependence of the order parameter. In the case where $u_2 = 0$, we get

$$\varphi^2 = \frac{\alpha(T_c - T)}{\tilde{u}_1}, \quad (7)$$

where $\tilde{u}_1 = u_1 + 2\alpha_1 \frac{-2C_{33}\alpha_1 + 2C_{13}\alpha_3}{C_{33}(C_{11}+C_{12}) - 2C_{13}^2} - 2\alpha_2 \frac{2\alpha_2}{C_{11}-C_{12}} + 2\alpha_3 \frac{2C_{13}\alpha_1 - (C_{11}+C_{12})\alpha_3}{C_{33}(C_{11}+C_{12}) - 2C_{13}^2}$.

For an adequate description of the phase transition, it is necessary to take into account the sixth power of the order parameter in the free-energy expansion (in this case, we have $u_2 \neq 0$, and the stability condition yields $u_2 > 0$). From Eq. (7), we find

$$\varphi^2 = -\frac{\tilde{u}_1}{2u_2} - \frac{\tilde{u}_1}{2u_2}\sqrt{1 + \frac{4u_2\alpha(T_c - T)}{\tilde{u}_1^2}}. \quad (8)$$

Near the phase transition point ($T \leq T_c$), we have

$$\varphi^2 \approx -\frac{\tilde{u}_1}{u_2} - \frac{\alpha(T_c - T)}{\tilde{u}_1}. \quad (9)$$

From Eqs. (8) and (9), it follows that $\tilde{u}_1 < 0$ and a stepwise change in the order parameter occurs at $T = T_c$, with the value of the corresponding jump being $\Delta\varphi^2 = \frac{|\tilde{u}_1|}{u_2}$. It is this jump of the order parameter at the phase transition that leads to jumps in the components of the spontaneous deformation tensor. The temperature dependences of the elastic moduli are given by the expressions

$$\Delta C_{11} \equiv C_{11}\big|_{T<T_c} - C_{11}\big|_{T>T_c} = -\frac{2(\alpha_1 + \alpha_2)^2}{\tilde{u}},$$

$$\Delta C_{22} \equiv C_{22}\big|_{T<T_c} - C_{11}\big|_{T>T_c} = -\frac{2(\alpha_1 - \alpha_2)^2}{\tilde{u}},$$

$$\Delta C_{12} = -\frac{2(\alpha_1^2 - \alpha_2^2)}{\tilde{u}}, \quad \Delta C_{33} = -\frac{2\alpha_3^2}{\tilde{u}},$$

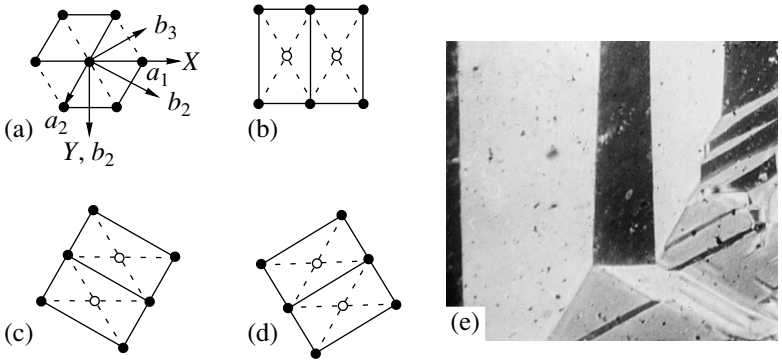

Fig. 5. (a) Projection of the KBN crystal habit onto (001) planes, orientation of different crystal axes, and the directions of wavevectors at 300 K. (b–d) Model of domains of different types related to the order parameter condensation of the types ($\varphi_1 \neq 0$, $\varphi_2 = 0$, $\varphi_3 = 0$), ($\varphi_1 = 0$, $\varphi_2 \neq 0$, $\varphi_3 = 0$), and ($\varphi_1 = 0$, $\varphi_2 = 0$, $\varphi_3 \neq 0$), respectively. (e) A photograph of the domain structure in the KBN crystal at 300 K.

$$\Delta C_{13} = -\frac{2\alpha_3(\alpha_1 + \alpha_2)}{\tilde{u}}, \quad \tilde{u} = u + 2u_1\varphi^2.$$

Using the experimental values of the elastic moduli $C_{11} = 3.06 \times 10^{10}$ N/m^2, $C_{12} = 1.47 \times 10^{10}$ N/m^2, $C_{33} = 5.75 \times 10^{10}$ N/m^2, $C_{13} = 2.72 \times 10^{10}$ N/m^2, and $C_{44} = 0.805 \times 10^{10}$ N/m^2 and $2C_{66} = C_{11} - C_{12}$, we find the following values for the phenomenological constants: $\alpha_2/\alpha_1 = 1.37$, $\alpha_3/\alpha_1 = 1.05$, and $\tilde{u} = 5.54 \times 10^{-10}$ N/m^2.

CONCLUSIONS

We have describe the improper ferroelastic *P*6/*mmm*–*Pbam* phase transition in $K_2Ba(NO_2)_4$ crystals by using a free-energy expansion. It was demonstrated that three types of domains corresponding to different types of condensation of the order parameter arise in the ferroelastic phase.

The X-ray diffraction studies showed the existence of small jumps in the lattice constants observed at T_c. The calculations demonstrated that the value of the jump in the order parameter at the phase transition point is given by the relationship $\Delta\varphi = \sqrt{\frac{|\tilde{u}_1|}{u_2}}$. This jump results in the corresponding jumps in the components of the spontaneous deformation tensor. Thus, the analysis of the temperature dependences of the lattice parameters and of the components of the spontaneous deformation tensor leads to the conclusion that the *P*6/*mmm*–*Pbam* phase transition is a first-order, close to a continuous second-order, phase transition. The jump in the order parameter can be measured using the neutron diffraction technique by determining the occupation probabilities and the type of orientational bases for different NO_2 groups, as well as the character of the ordering.

ACKNOWLEDGMENTS

The work was supported by the Russian Foundation for Basic Research, project no. 02-02-16864.

REFERENCES

1. N. R. Ivanov, L. F. Kirpichnikova, V. P. Konstantinova, *et al.*, Kristallografiya **23** (4), 788 (1978) [Sov. Phys. Crystallogr. **23**, 443 (1978)].
2. M. Chabin, F. Gilletta, Y. Luspin, *et al.*, J. Phys. (Paris) **43**, 337 (1982).
3. G. Sorge, U. Straube, B. Thamke, and L. A. Shuvalov, Phys. Status Solidi A **59**, K183 (1980).
4. M. Harada, J. Phys. Soc. Jpn. **52**, 3448 (1983).
5. H. Unruh, J. Raman Spectrosc. **17**, 113 (1986).
6. H. Unruh, Phys. Status Solidi B **126**, 115 (1984).
7. V. P. Dmitriev, L. M. Rabkin, L. V. Soboleva, *et al.*, Kristallografiya **23** (4), 774 (1978) [Sov. Phys. Crystallogr. **23**, 435 (1978)].
8. Y. Iwata, I. Shibuya, and Y. Ishibashi, J. Phys. Soc. Jpn. **60**, 2139 (1991).
9. Y. Luspin and G. Haure, Solid State Commun. **46**, 397 (1983).
10. Y. Ishibashi, S. Tanaka, and V. Dvorak, J. Phys. Soc. Jpn. **59**, 2995 (1990).
11. Y. Yamada and M. Harada, J. Phys. Soc. Jpn. **55**, 4315 (1986).
12. A. Yu. Belov and L. F. Kirpichnikova, Kristallografiya **42** (6), 1101 (1997) [Crystallogr. Rep. **42**, 1025 (1997)].
13. J. Sapriel, Phys. Rev. B **12**, 5128 (1975).

Translated by K. Kugel

Crystallography Reports, Vol. 47, No. 6, 2002, pp. 1036–1040. Translated from Kristallografiya, Vol. 47, No. 6, 2002, pp. 1105–1109.

PHYSICAL PROPERTIES OF CRYSTALS

Growth and Some Properties of TeO_2 Single Crystals with a Large Diameter

A. V. Vinogradov, V. A. Lomonov, Yu. A. Pershin, and N. L. Sizova

Shubnikov Institute of Crystallography, Russian Academy of Sciences, Leninskiĭ pr. 59, Moscow, 119333 Russia

e-mail: aopt@ns.crys.ras.ru

Received March 21, 2002

Abstract—Large-diameter single crystals of TeO_2 are grown by the Czochralski method in specially designed setups with automatic monitoring of the crystal growth. The degree of perfection of the grown crystals is examined using selective etching and X-ray topography (the Shultz method). The temperature dependence of the microhardness of TeO_2 single crystals is investigated for different crystallographic planes, namely, (001), (100), and (110). © *2002 MAIK "Nauka/Interperiodica".*

INTRODUCTION

Among the crystals currently used as acoustooptic materials, paratellurite α-TeO_2 stands out because of its unique properties. This material is widely used in various devices, especially in wide-aperture deflectors, spectrum analyzers, and noncollinear filters. The considerable interest expressed by many researchers in α-TeO_2 paratellurite is associated with the fact that this compound belongs to the rare crystal class 422 and has no close analogues among solids in terms of the combination of its physical and chemical properties. This crystal is characterized by an extremely strong elastic anisotropy. The ratio between the maximum and minimum elastic moduli of α-TeO_2 is estimated as $E_{max}/E_{min} \sim 11$, which substantially exceeds the corresponding ratio for other crystals.

GROWTH OF PARATELLURITE SINGLE CRYSTALS

Single crystals of the TeO_2 paratellurite were grown in CROT-M setups [1], which were specially designed for crystal growth from melt. Setups of this type are characterized by small dimensions of the growth chamber and automatic monitoring of the Czochralski growth of the crystals. In this setup, the rotational speed of the growing crystal can vary from 0.5 to 100 rpm and the pulling speed ranges from 0.1 to 10 mm/h. The balance used in the setup makes it possible to measure crystals weighing as much as 5 kg with an accuracy of ±0.1 g. The growth of crystals to the required diameter and the subsequent maintenance of a constant diameter are controlled automatically. The controlling algorithm developed at the laboratory is based on the calculation of the diameter of the growing single crystal from the measured rate of weight increase. All information on the growth process is stored and then is processed with the aim of refining the coefficients of the growth controller. The statistical processing and digital filtering of input data lead to a considerable increase in the signal-to-noise ratio and ensure reliable control of the crystal growth at the threshold of sensitivity of the measuring elements.

Paratellurite single crystals with a diameter ranging from 42 to 75 mm and a length of the cylindrical part in the range from 50 to 70 mm were grown using the above setup. For the most part, the crystals were grown on a seed oriented along the (110) plane. Moreover, the crystals oriented along the [100] axis were grown on a seed oriented along the (100) plane. The crystallization was performed at atmospheric pressure in air. According to the spectral chemical analysis, iron ions are the majority impurities in the initial material and the grown crystal. The iron content remains unchanged and is approximately equal to 2×10^{-4} wt %. In the initial batch, the contents of Ca, Si, Mn, Cu, Pb, V, Ni, and Cr ions are each approximately equal to $2–3 \times 10^{-5}$ wt %. Their content in the grown crystals decreases by one order of magnitude compared to that in the initial material.

INVESTIGATION OF THE DEGREE OF PERFECTION OF TeO_2 SINGLE CRYSTALS

The dislocation density was studied by selective etching. For this purpose, a TeO_2 single crystal ~60 mm in diameter was cut perpendicularly to the growth direction ⟨110⟩ into plates ~3 mm thick. The plates were chemically polished in a 12 M KOH solution and then were selectively etched in a 50% HCl solution. The dislocation density was examined using optical microscopy when scanning the sample with a step of 1 mm through the sample center along the ⟨001⟩ direction and in the perpendicular direction. It is found that, in the crystal, the central region 30 mm in diameter

1063-7745/02/4706-1036$22.00 © 2002 MAIK "Nauka/Interperiodica"

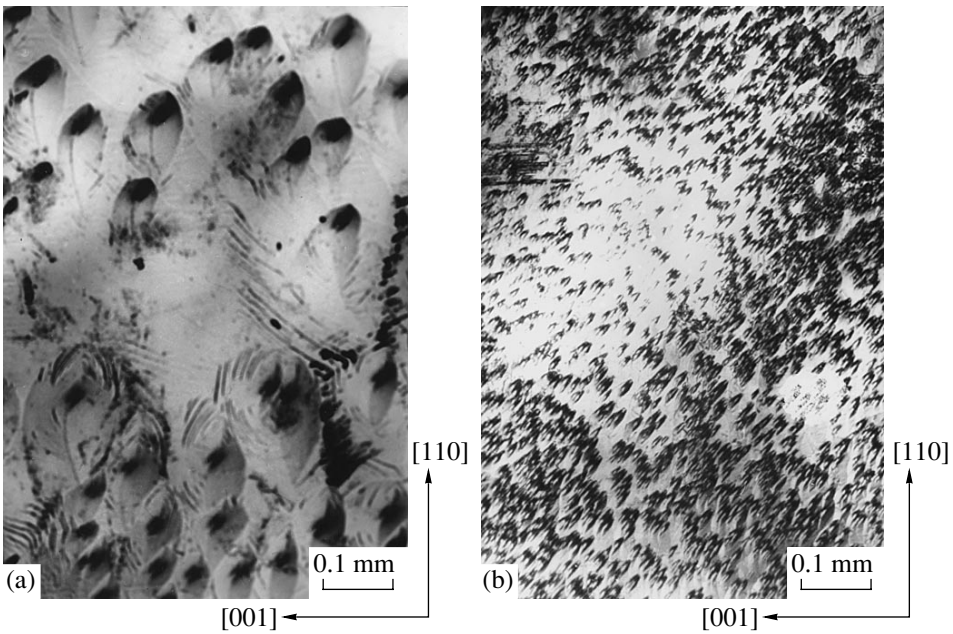

Fig. 1. Patterns of selective etching of the (110) surface of the TeO_2 single crystal: (a) the density of dislocations in the central region of the crystal and (b) the density of dislocations in the transition region of the crystal.

exhibits a relatively low dislocation density of ~10^6 m^{-2} and has no grain boundaries (Fig. 1a). Along the periphery of this central region (on both its sides), there exist two grain boundaries extended throughout the crystal along the ⟨001⟩ direction. In the crystal, the peripheral regions ~10 mm thick are characterized by a high dislocation density of ~10^9–10^{10} m^{-2}. Moreover, the peripheral regions contain inclusions that are frequently extended along the ⟨001⟩ direction. These inclusions are surrounded by regions with an increased dislocation density, most likely, due to relaxation of elastic stresses around the inclusions. The transition region ~5 mm thick with a dislocation density of ~10^7–10^8 m^{-2} is located between the central and peripheral region of the crystal (Fig. 1b). The high dislocation density in the peripheral region of the TeO_2 single crystal can be associated with the presence of thermoelastic stresses. The degree of strain of the crystal can be represented by the relationship $\varepsilon \sim \rho bl$, where ρ is the dislocation density, b is the Burgers vector magnitude, and l is the distance between the obstacles. By assuming that $\varepsilon \sim \partial a/a \sim 10^{-4}$, $b \sim 10^{-9}$ m, and $l \sim 10^{-5}$ m, we obtain $\rho \sim 10^6$ m^{-2}. This result coincides with the dislocation density observed in the central region of the TeO_2 single crystal in the experiment.

The paratellurite single crystals were studied by X-ray topography (the Shultz method) with the use of radiation of a Cu anode. The diffraction spots formed by a continuous spectrum exhibit a uniform darkening. The characteristic lines are represented by straight lines with a well-resolved doublet without noticeable discontinuities and shifts. This suggests that the TeO_2 single crystals have a sufficiently high degree of perfection and contain no grains with grain-boundary angles larger than 10″.

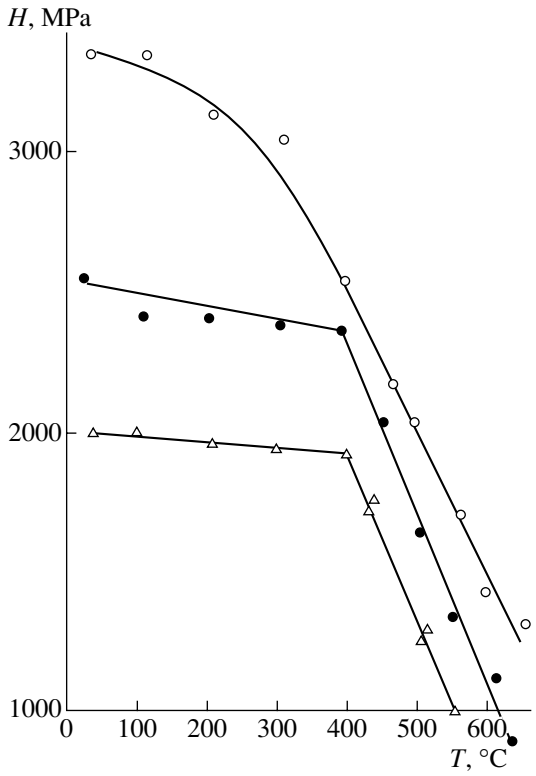

Fig. 2. Temperature dependences of the microhardness of the TeO_2 single crystal for different crystallographic planes: (001) (open circles), (100) (closed circles), and (110) (triangles).

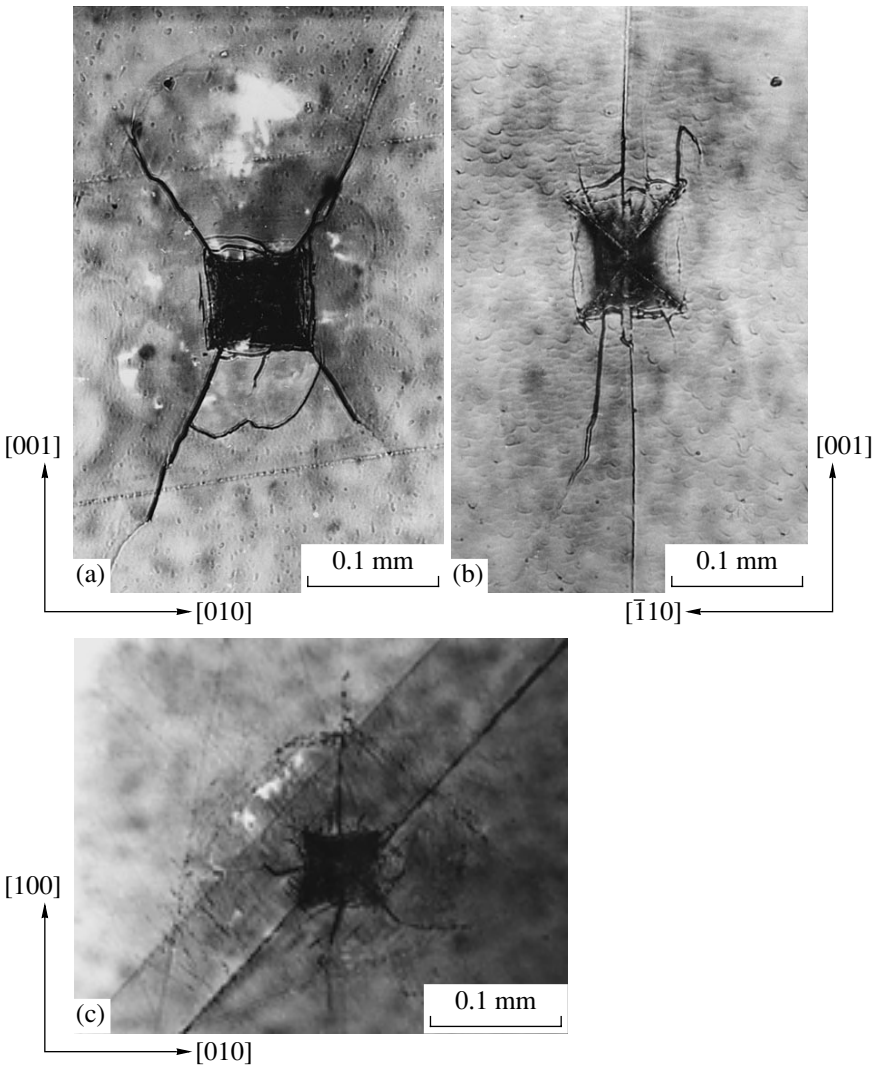

Fig. 3. Indentation patterns on the (a) (100), (b) (110), and (c) (001) planes of the TeO_2 single crystal at 650°C.

MICROHARDNESS MEASUREMENTS OF PARATELLURITE SINGLE CRYSTALS

Experimental Technique

Plates 10 × 10 × 2 mm in size were cut along the (100), (010), (001), and (110) planes from the central part of a TeO_2 single crystal 50 mm in diameter. To accomplish this, the samples were oriented in accordance with the conoscopic interference patterns to an accuracy of ~0.5°. The plates were subjected to mechanical and chemical polishing. The indentation was carried out with a high-temperature microhardness tester [2] at the load P = 1.5 N in the range from room temperature to 650°C. The Vickers indenter was oriented in such a way that indentations had well-defined edges and the edge cracks thus formed did not cause any cleavage of the surface [3, 4]. The indentation sides were parallel to the Z[001] and X[100] crystallographic axes for the (010) plane, the Z[001] and Y[010] axes for the (100) plane, the X[100] and Y[010] axes for the (001) plane, and the Z[001] axis and the [110] direction

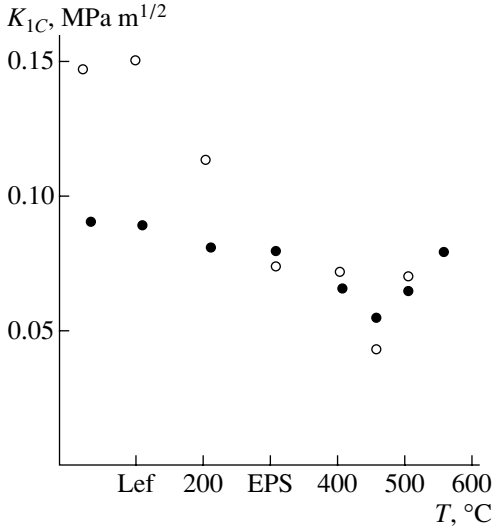

Fig. 4. Temperature dependences of the fracture toughness coefficient K_{1C} of the TeO_2 single crystal for different crystallographic planes: (001) (open circles) and (100) (closed circles).

for the (110) plane. The crack directions in the indentation patterns were analyzed using the stereographic projections constructed for all the planes under investigation.

Experimental Results

The microhardness H was calculated from the formula $H = 1854P/d^2$ [5], where P is the indenter load and d is the indentation diagonal. Figure 2 depicts the temperature dependences of the Vickers microhardness H_V of the TeO_2 single crystal for the (001), (100), (010), and (110) planes in the range from room temperature to 650°C. As can be seen from Fig. 2, the (001) plane is the "hardest" plane of the crystal over the entire temperature range. It is worth noting that this pattern is most pronounced in the range from room temperature to 300°C. The microhardness H_V of the paratellurite single crystal slightly decreases with an increase in the temperature to 300°C and drastically decreases from ~3000 to ~1300 MPa with a further increase in the temperature to 650°C. For the crystallographic planes (100), (010), and (110), the temperature dependences of the microhardness H_V exhibit a kink at $T \sim 450$°C. This indicates a sharp crossover of the deformation mechanism. As follows from structural considerations, the crystallographic planes (100) and (010) are characterized by an identical microhardness. The highest plasticity is observed in the (110) plane of the studied crystal. This is in good agreement with the data obtained by Peter *et al.* [6], according to which the slip elements calculated theoretically for TeO_2 on the basis of the elastic energy at the minimum correlate well with the results of macromechanical measurements. As a rule, the slip planes in covalent crystals can be more properly chosen from the consideration of chemical bonds, i.e., from the nuclear energies rather than from the elastic energy at the minimum. However, the anisotropy of TeO_2 single crystals is so strong that the elastic approach gives the true contribution of the dislocation activity. For a paratellurite single crystal, the {110}[110], {010}⟨100⟩, and (001)⟨100⟩ slip systems are the most probable in terms of the elastic energy. Judging from the indentation patterns obtained at high temperatures and the temperature dependences of the microhardness H_V for all the studied planes of the TeO_2 single crystal, the crystal remains brittle at temperatures $T < 0.7T_{melt}$, which is a common feature of all covalent crystals [7]. It is interesting to note that the cracks in the vicinity of the indentation on the (100), (001), and (110) planes persist up to a temperature of 650°C (Figs. 3a, 3b). The slip bands in the [110] direction on the (001) plane appear at a temperature of 500°C and cover the whole crystal at temperatures of 600–650°C; as a consequence, the radial cracks virtually disappear (Fig. 3c). Apparently, this stems from the fact that the deformation of the paratellurite single crystal in the (001) plane is characterized by the {101}⟨101⟩ slip system, which most clearly manifests itself in a rutile lattice [8]. According to [6], the above Burgers vector corresponds to perfect dislocations with a high energy.

The use of the indentation technique provides information not only on the microhardness—a characteristic correlating with the deformation parameters—but also on the fracture strength of the studied materials. In particular, this method makes it possible to estimate the fracture toughness coefficient K_{1C} along the length C of the radial cracks formed upon indentation. This coefficient can be determined from the formula $K_{1C} = 0.016(E/H)^{1/2}P/C^{3/2}$ [9], where P is the indenter load and E is the Young modulus. The Young moduli in the range from room temperature to 100°C were calculated from the measured elastic moduli C_{ik}^E. For this purpose, the velocities of longitudinal and transverse ultrasonic waves were measured by the ultrasonic pulse-phase method in the crystallographic directions that were necessary for calculating all the independent components of the C_{ik} tensor describing the elastic properties [10]. Figure 4 shows the temperature dependences of the fracture toughness coefficient K_{1C} for the (001) and (100) planes of the TeO_2 single crystal. It follows from analyzing these dependences that the fracture mechanism of the paratellurite crystal changes at $T \sim 450$°C. Most probably, the formation of cracks in the vicinity of the indentation in the temperature range up to 450°C is caused by residual elastic stresses and the cracks grow upon unloading the indenter. At temperatures above 450°C, the mechanisms of formation and growth of radial cracks can be associated with plastic deformation (i.e., with the mobility of dislocations at a crack tip) and, therefore, can be described by the Arrhenius kinetic equation $dC/dt \sim \exp(-U/kT)$, where U is the activation energy of plastic deformation.

CONCLUSIONS

The laboratory automated setup, which included monitoring of the diameter of the crystal during growth, was designed for the purpose of growing large-diameter paratellurite single crystals by the Czochralski method.

Paratellurite single crystals with a diameter up to 60 mm and a length of the cylindrical part from 50 to 60 mm were grown.

The crystals grown were examined using selective etching and X-ray topography (the Shultz method). It was demonstrated that the TeO_2 single crystals have a high degree of perfection (i.e., they are characterized by a low dislocation density and have no grain boundaries in the central region).

The temperature dependences of the microhardness H_V and the fracture toughness K_{1C} were investigated for the (001), (100), (010), and (110) planes of the paratellurite single crystal. It was demonstrated that, at $T \sim 450$°C, the mechanisms of deformation and fracture of the

TeO_2 single crystal change and plastic deformation becomes the dominant mechanism of elimination of the material from under the indenter.

REFERENCES

1. A. V. Vinogradov, V. A. Lomonov, Yu. A. Pershin, *et al.*, in *Proceedings of the IX National Conference on Crystal Growth, Moscow, 2000*, p. 203.
2. N. L. Sizova and V. R. Regel', Fiz. Tverd. Tela (Leningrad) **27**, 3693 (1985) [Sov. Phys. Solid State **27**, 2226 (1985)].
3. V. A. Lomonov, Yu. V. Pisarevski, N. L. Sizova, *et al.*, Cryst. Res. Technol. **27**, 981 (1992).
4. V. A. Lomonov, A. V. Vinogradov, Yu. A. Pershin, *et al.*, in *Proceedings of the IX National Conference on Crystal Growth, Moscow, 2000*, p. 270.
5. Yu. S. Boyarskaya, *Deformation of Crystals in the Course of Microhardness Testing* (Shtiintsa, Kishinev, 1977).
6. A. Peter, E. Frils, J. Janszky, *et al.*, Rev. Phys. Appl. **21**, 289 (1986).
7. T. Bretheau, J. Castaing, J. Rabier, *et al.*, Adv. Phys. **28**, 829 (1979).
8. M. G. Blanchin, G. Fontaine, and L. P. Kubin, Philos. Mag. A **41**, 261 (1980).
9. G. R. Anstis, P. Chantikul, B. R. Lawn, *et al.*, J. Am. Ceram. Soc. **64**, 533 (1981).
10. I. M. Silvestrova, Yu. V. Pisarevski, P. A. Senyushenkov, *et al.*, Phys. Status Solidi A **101**, 437 (1987).

Translated by O. Borovik-Romanova

Crystallography Reports, Vol. 47, No. 6, 2002, pp. 1041–1048. Translated from Kristallografiya, Vol. 47, No. 6, 2002, pp. 1110–1118.

LIQUID CRYSTALS

Phenomenological Theory of Phase Transition from Isotropic to Uniaxial, Biaxial, and Reentrant Nematic Phases in Achiral Liquid Crystals[1]

A. E. Prostakov*, E. S. Larin, and M. B. Stryukov*****

** Rostov State University, Rostov-on-Don, Russia*
*** Research Institute of Physics, Rostov State University, pr. Stachki 194, Rostov-on-Don, 344104 Russia*
e-mail: eslarin@rsu.ru
**** College of Communications, Rostov-on-Don, Russia*

Received March 28, 2002

Abstract—The topological properties of phase diagrams of liquid crystals with achiral molecules (mesogens) were studied for transitions from the isotropic to uniaxial and biaxial phases by using the phenomenological Landau–de Gennes theory. An isostructural phase transition between two uniaxial nematic phases was investigated. *© 2002 MAIK "Nauka/Interperiodica".*

INTRODUCTION

Typical liquid-crystalline compounds consist of organic molecules with an anisotropic, e.g., rodlike or disklike, shape [1]. The rodlike molecules form a calamitic structure, while the disklike molecules form discotic or calamitic structures. According to Friedel, the liquid crystals (LCs) composed of achiral molecules are divided into two types: the nematics (*N*) and the smectics (*Sm*) [2]. The phase transition from the isotropic (*I*) to the nematic (*N*) phase has been the objective of many theoretical and experimental studies (see, for example [1, 3–18] and references therein). The basic property that distinguishes the *N* phase from an ordinary liquid is a predominant orientation of the long molecular axes along a certain direction specified by a vector **n** called the Frank director, with the disordered molecullar centers of gravity like an ordinary isotropic liquid.

An isotropic liquid has a full orientational and translational symmetry of the group $G = T(3) \times O(3)$. At a transition to the nematic phase, the translational symmetry $T(3)$ is preserved, while the rotational symmetry $O(3)$ is violated. The symmetry of the calamitic or discotic *N* phase corresponds, for achiral molecules, to one of the following subgroups of the $D_{\infty h}$ group: $D_{\infty h}$, $C_{\infty h}$, $C_{\infty v}$, D_{nh}, D_{nd}, C_{nh}, C_{nv}, and S_{2n}. Hence, it follows that nematics can be both uniaxial (N_a) and biaxial (N_b). The N_b phase was first observed in lyotropic [5] and then, in thermotropic [6, 9] LCs. In thermotropic LCs, the mesophases are formed as the temperature is changed, while in the lyotropic LCs, these phases are formed during the dissolution of the rodlike or disklike molecules in a liquid. Experimental studies [1, 3–8] have shown that the *I–N* transition is always of the first order but is weakly marked thermodynamically (the latent heat of the transition is about 1 kJ/mol). There are several approaches to the theoretical description of this transition. In the molecular-field theory [10–18], one starts with choosing a model for the intermolecular-interaction energy. Then, the anisotropic field acting on one particle is calculated. Such calculations call for a knowledge of the pair correlation function. The original version of the mean-field theory is the model proposed by Onsager [10], who introduced the repulsive forces related to the shape anisotropy of solid rods (whose thickness is much smaller than their length). An orientational order is attained at a certain density of rods: the free energy minimum corresponds to the *I* phase at low density and to the *N* phase at high density. In the Meier–Saupe theory, the formation of the ordered *N* phase is related to the anisotropic part of an intermolecular interaction (the shape anisotropy is neglected) [11]. In [12, 13], both the short-range repulsive forces due to the solid cores of molecules and the angle-dependent long-range attractive forces are taken into account. In recent years, computer modeling methods have become very popular [14, 15]. However, due to the lack of an exact expression for the intermolecular interaction, the results are approximate.

In order to interpret experimental results and predict new phases, the phenomenological Landau–de Gennes theory [1] is generally employed. In this theory, the thermodynamic potential is expressed in terms of an order parameter and its derivatives. The Landau–de Gennes theory is most attractive from the physical

[1] This work was presented at the Symposium "Phase Transitions in Solid Solutions and Alloys" (OMA-II), Sochi, Russia, 2001.

standpoint and is mathematically convenient. This theory also offers many advantages in describing phase diagrams. Despite the widespread application of the Landau–de Gennes theory to the description of phase transitions in LCs (in particular, the *I–N* transition) [1, 3–8, 16], no complete study of the specific features of the isotropic–nematic phase diagrams has been performed, as yet. For example, the qualitative phase diagram presented in [16] contains a number of topological errors. In this paper, we study all of the specific features of the complete phase diagram for the transition from the *I* to the *N* phase (including N_a, N_b, and reentrant N_r phases) by using the phenomenological Landau theory of phase transitions.

MODEL THERMODYNAMIC POTENTIAL

In order to describe the behavior of physical quantities and the specific features of a phase diagram in terms of the Landau theory of phase transitions, an order parameter and a model thermodynamic potential should be chosen. At the *I–N* transition in a system with achiral molecules, the order parameter describing the orientational order transforms according to an irreducible representation of the group $G_0 = O(3)$. The orientation distribution function of anisotropic molecules depends on the coordinate **r** and the director **n** and can generally be written as

$$\rho(\mathbf{r}, \mathbf{n}) = \Sigma\rho_{lm}(\mathbf{r})Y_{lm}(\mathbf{n}), \quad (1)$$

where $Y_{lm}(\mathbf{n})$ are spherical functions and $\rho_{lm}(\mathbf{r})$ are tensors which transform according to an irreducible representation of G_0. For a transition to the nematic phase, we have $l = 2$. Following [1], we assume the order parameter to be a symmetric traceless tensor Q_{nm}. The eigenvalues are taken in the form $(-1/2(\eta_1 + \sqrt{3}\eta_2); -1/2(\eta_1 - \sqrt{3}\eta_2); \eta_1)$. In this case, the integral rational basis of invariants is

$$I_1 = 2/3\,\mathrm{Sp}(\mathbf{Q}^2) = (\eta_1^2 + \eta_2^2);$$
$$I_2 = 4/3\,\mathrm{Sp}(\mathbf{Q}^3) = (\eta_1^3 - 3\eta_1\eta_2^2). \quad (2)$$

Generally, the order parameter depends on **r** and the free energy must contain derivative-dependent invariants describing the Frank elastic energy

$$F_{el} = 1/2(K_1(\mathrm{div}\,\mathbf{n})^2 + K_2(\mathbf{n}\,\mathrm{rot}\,\mathbf{n})^2 + K_3(\mathbf{n}\times\mathrm{rot}\,\mathbf{n})^2). \quad (3)$$

Here, K_1, K_2, and K_3 are the splay, twist, and bend elastic constants, respectively. For calamitic achiral LCs, the inequalities $K_3 > K_1 > K_2 > 0$ usually hold, while for discotic LCs, we have $K_2 > K_1 > K_3 > 0$ [8]. In this case, an equilibrium state corresponds to the solution $n = \mathrm{const}$. Then, the thermodynamic potential for the *I–N* transition has the form

$$\Phi(\eta_1, \eta_2) = F(I_1, I_2). \quad (4)$$

From the set of equations of state

$$\begin{cases} \partial\Phi/\partial\eta_1 = 2F_1\eta_1 + 3F_2(\eta_1^2 - \eta_2^2) = 0 \\ \partial\Phi/\partial\eta_2 = 2F_1\eta_2 - 6F_2\eta_1\eta_2 = 0, \end{cases} \quad (5)$$

where $F_i = \partial F/\partial I_i$ ($i = 1, 2$), we find solutions corresponding to four different phases:

$$I: \eta_1 = 0, \quad \eta_2 = 0; \; N_a^{\pm}: \eta_1 \neq 0, \quad \eta_2 = 0; \; N_b: \eta_1 \neq 0, \quad \eta_2 \neq 0. \quad (6)$$

Here, the solution N_a^+ ($\eta_1 > 0$) corresponds to the uniaxial calamitic phase, N_a^- ($\eta_1 < 0$), to the discotic phase, and N_b, to the biaxial phase. The stability of the phases is determined by the condition that the matrices of the second derivatives $H_{ik} = \partial^2 F/\partial\eta_i\partial\eta_k$ be positively definite. The set of equations (5) for the N_b phase can then be written as

$$F_1 = 0, \quad F_2 = 0, \quad (7)$$

while the stability condition is $F_{11}F_{22} - F_{12}^2 > 0$, where $F_{ik} = \partial^2 F/\partial I_i\partial I_k$. Hence, it follows that, when analysing the stability of the N_b phase, we have to take into account the terms of the $2n$th order, where n is the highest degree of the basis invariants (in our case, $n = 3$). As shown below, in order to describe the transition to the reentrant uniaxial phase, we have to take into account the terms of the eighth order in η_1 and η_2:

$$F = a_1I_1 + a_2I_1^2 + a_3I_1^3 + a_4I_1^4 + b_1I_2 + b_2I_2^2 + c_{12}I_1I_2 + c_{112}I_1^2I_2 + c_{122}I_1I_2^2. \quad (8)$$

Model thermodynamic potential (8) involves nine phenomenological parameters: a_1, a_2, a_3, a_4, b_1, b_2, c_{12}, c_{112}, and c_{122}. Let us first consider a simplified (to the sixth order) model to study the specific features of the phase diagram that are retained in model (8):

$$F = a_1I_1 + a_2I_1^2 + a_3I_1^3 + b_1I_2 + b_2I_2^2 + c_{12}I_1I_2. \quad (9)$$

The model with an account for the sixth-power terms was discussed previously under the assumption that $c_{12} = 0$ [8]. Below, we show that the inclusion of the $c_{12}I_1I_2$ term allows one to describe two interesting, experimentally observed phenomena: an isostructural transition in the uniaxial N_a^- phase at $c_{12} > 0$ (in the N_a^+ phase at $c_{12} < 0$) and a first-order transition between uniaxial phases. Within the model of thermodynamic potential (9), the global minimum of the solutions to the set of equations of states (the case where all the phases are stable for finite values of the order parameter) requires that $a_3 + b_2 > 0$ and $a_3 > 0$. In the Landau theory

of phase transitions, the temperature dependence of only one phenomenological parameter, $a_1 = a_1^0(T - T^*)$, is assumed (see, for example, review [8]). In this work, we study the phase diagram while under the assumption that three variable parameters, namely, a_1, b_1, and a_2, depend on external conditions in a thermostat. The nonvariable parameters of the potential are determined from experimental data. Experimental data on the following quantities are most frequently used to study LCs: (1) the transition temperatures, determined by optical and calorimetric methods; (2) the change in the density on the transition, $\Delta\rho$, determined by dilatometric methods; (3) the entropy and enthalpy of the transition, measured with the aid of classical adiabatic calorimetry; (4) the jump in the order parameter at the transition; and (5) the value dT_P/dP, determined from the dependence of the transition temperature T_P on an external pressure, and the jumps ΔC_P, $\Delta\alpha$, and ΔK, where $C_P(T)$, $\alpha(T)$, and $K(T)$ are the specific heat at constant pressure, the coefficient of thermal expansion, and isothermal compressibility, respectively. The singular points on a phase diagram, whose coordinates are determined by the parameters of the model potential, are also of interest. In this work, we determine the coordinates of the triple points, the critical point of an isostructural transition of the liquid–vapor type, and the tricritical points.

PHASE DIAGRAM

Uniaxial Phases

Let us consider the regions of stability for the $N_a^{\pm}$ uniaxial nematic phases. The state equation for these phases has the form

$$\eta_1[2a_1 + 3b_1\eta_1 + 4a_2\eta_1^2 + 5c_{12}\eta_1^3 + 6(a_3 + b_2)\eta_1^4] = 0. \quad (10)$$

For the sake of precision, we assume that $c_{12} > 0$ (the phase diagram for $c_{12} < 0$ can be obtained through the replacements $\eta_1 \longrightarrow -\eta_1$, $b_1 \longrightarrow -b_1$). The degeneracy conditions for the matrices of second derivatives break into two equations:

$$3b_1 + 8a_2\eta_1^2 + 15c_{12}\eta_1^3 + 24(a_3 + b_2)\eta_1^4 = 0, \quad (11)$$

$$b_1 + c_{12}\eta_1^2 + 2b_2\eta_1^3 = 0. \quad (12)$$

Equations (10)–(12) determine the bifurcation values of variable parameters in the space $R^3 = \{a_1, b_1, a_2\}$. For convenience, we shall study the phase diagrams in planar cross sections $R^2 = \{a_1, b_1\}$ for different values of a_2. From Eqs. (10) and (11), we obtain a curve in the parametric form (Fig. 1)

$$a_1 = 2a_2\eta_1^2 + 5c_{12}\eta_1^3 + 9(a_3 + b_2)\eta_1^4,$$
$$b_1 = \frac{-8}{3}a_3\eta_1 - 5c_{12}\eta_1^2 - 5(a_3 + b_2)\eta_1^3. \quad (13)$$

Curve (13) specifies the regions of stability of the solutions to the equation of state (10); the equilibrium values of the solutions correspond to the $N_a^{\pm}$ phases. At $0 \le a_2 < \frac{(5c_{12})^2}{64(a_3 + b_2)}$, there are two cuspidal points, Q and Q_1 (Fig. 1b), in curve (13); their coordinates can be found by substituting into Eq. (13) the quantity

$$\eta_1 = \frac{-5c_{12} \pm \sqrt{25c_{12}^2 - 64a_2(a_3 + b_2)}}{24(a_3 + b_2)}. \quad (14)$$

It follows from Eq. (11) that the existence of the Q and Q_1 points is possible at $c_{12} > 0$ and $c_{12} < 0$ for the N_a^- and N_a^+ phases, respectively (compare with [16]). In the region bounded by the TQQ_1 curve, the state equations have four solutions (two minima and two maxima) corresponding to two N_a^- ($c_{12} > 0$) phases of the same symmetry but differing in the η_1 values. An isomorphous $N_a^-(\mathrm{I}) \longrightarrow N_a^-(\mathrm{II})$ phase transition occurs along the TQ line, terminating at point Q (a critical point of the liquid–vapor type). There is a jump in the order parameter at this transition.

The second condition of the degeneracy of H_{ik} [Eq. (12)] corresponds to the stability of the $N_a^{\pm}$ phases against biaxial heterogeneous fluctuations. The topology of curves (12) on the $R^2 = \{a_1, b_1\}$ plane varies in the following way for changes in the parameter a_2: at $a_2 > a_2(Q)$, the curves with $\eta_1 > 0$ and $\eta_1 < 0$, which have a common tangent $a_1 = \frac{2a_2}{c_{12}}b_1$, converge at a quadruple point $O(0, 0)$ (Fig. 1a); at $a_2 < \frac{c_{12}^2}{4b_2}$ these curves intersect (Fig. 1c) at point P:

$$b_1(P) = \frac{-c_{12}(2\Delta b_2 + 3a_3c_{12}^2)}{12a_3b_2^2}\left(1 \pm \sqrt{\frac{2b_2\Delta + 3a_3c_{12}^2}{3a_3c_{12}^2}}\right),$$
$$a_1(P) = \frac{c_{12}}{2b_2}b_1\left[1 + \frac{18a_3^2b_2}{c_{12}(2b_2\Delta + 3a_3c_{12}^2)}\right], \quad (15)$$

where $\Delta = 4a_2b_2 - c_{12}^2$. In the region bounded by portions OP ($\eta_1 > 0$) and OP ($\eta_1 < 0$), the N_a^+ and N_a^-

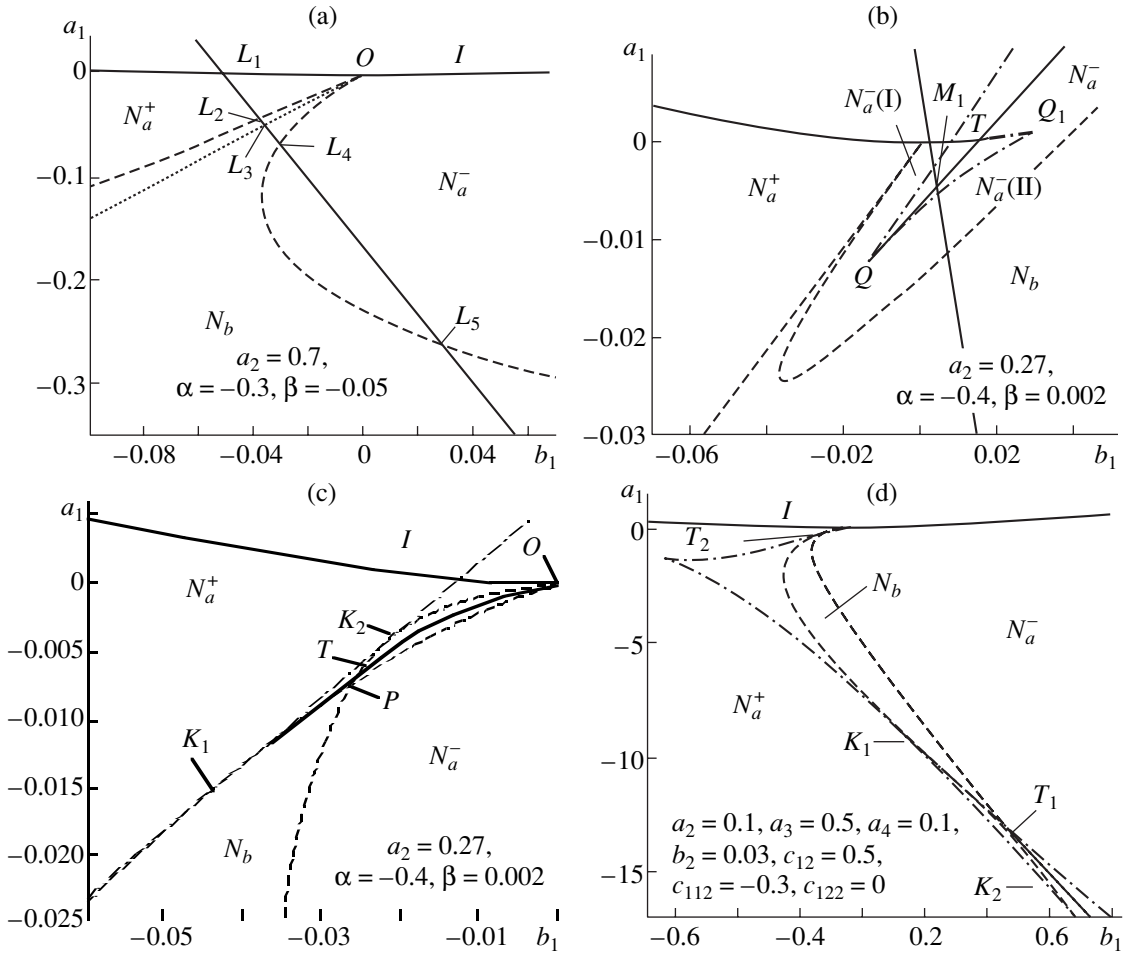

Fig. 1. Phase diagrams in the space $R^2 = (a_1, b_1)$ for the potential $F(\eta_1, \eta_2)$ (a–c) in the form of Eq. (9) (at $a_3 = 0.03$, $c_{12} = 1$, $b_2 = 1$) and (d) different a_2 values and in the form of Eq. (8). Solid curves represent the first-order transitions; dashed curves, the second-order transitions; dotted curves correspond to the maximum bistability of the N_b phase [Eq. (20)]; the dot-and-dash curves are the curves along which the phases become unstable; and the straight lines are thermodynamic paths for different α and β values.

uniaxial phases coexist and a first-order phase transition $N_a^+ - N_a^-$ occurs between them.

Biaxial Nematic Phase

The existence of the biaxial phase N_b was first predicted in [3], in the framework of the Landau–de Gennes theory. A transition to the N_b phase was shown [3] to be possible in a system consisting of a mixture of cylindrical and disklike molecules. For this system, the stability region of the N_b phase lies between the stability regions of the N_a^+ (cylinders) and N_a^- (disks) phases and is separated by curves of second-order transitions, which converge at one point to the curve of the first-order I–$N_a^\pm$ phase transitions. Experimental studies of lyotropic [5], thermotropic [6, 7], and polymer LCs confirmed the possibility of the existence of the N_b phase. It was assumed in [4, 7] that the thermotropic N_b phase can be obtained by synthezing molecules (mesogens) which exhibit the combined properties of disks and cylinders. In principle, the N_b phase can form in a single-component system for the following reasons: (1) a change in the effective molecular symmetry, (2) strong intermolecular interaction resulting in the formation of molecular aggregates with biaxial symmetry, (3) the mixing of rodlike and disklike molecules close in size and shape, and (4) the application of an external field which affects the effective molecular symmetry.

In the present work, we consider phase diagrams for the first two cases. The variable parameters a_1, b_1, and a_2 are functions of external parameters, namely, the temperature T and the parameter λ, which specifies the shape of a molecule. In the first case, the effective molecular symmetry is changed, due to transitions of the molecules from the rodlike type to the disklike type. The second case is realized in lyotropic systems with amphiphilic (soaplike) molecules dissolved in water. In such solutions, the molecules form clusters (micelles), in which the hydrophilic groups are located at the sur-

face, thus improving contact with water [3, 6]. The micelles behave like large-sized molecules which change their shape (depending on the temperature, concentration, and, sometimes, an additional solvent) to form the N_a^+, N_a^-, and N_b nematic phases.

Within model (9), the set of equations of state for the N_b phase has the form

$$\begin{aligned} F_1 &= a_1 + 2a_2 I_1 + 3a_3 I_1^2 + c_{12} I_1 I_2 = 0, \\ F_2 &= b_1 + 2b_2 I_2 + c_{12} I_1 = 0. \end{aligned} \tag{16}$$

The determinant of the matrix of second derivatives $H_{ik} = \dfrac{\partial^2 \Phi}{\partial \eta_i \partial \eta_k}$ (i = 1, 2) equals

$$D = \begin{vmatrix} \dfrac{\partial I_1}{\partial \eta_1} & \dfrac{\partial I_1}{\partial \eta_2} \\ \dfrac{\partial I_2}{\partial \eta_1} & \dfrac{\partial I_2}{\partial \eta_2} \end{vmatrix} \begin{vmatrix} \dfrac{\partial^2 F}{\partial I_1^2} & \dfrac{\partial^2 F}{\partial I_1 \partial I_2} \\ \dfrac{\partial^2 F}{\partial I_1 \partial I_2} & \dfrac{\partial^2 F}{\partial I_2^2} \end{vmatrix} \tag{17}$$

$$= 6\eta_2(3\eta_1^2 - \eta_2^2)(4a_2 b_2 - c_{12}^2 + 12a_3 I_1) = 0.$$

From Eq. (17), it follows that, if one of the two conditions, $\eta_2 = 0$ or $\eta_2^2 = 3\eta_1^2$, is met, the degeneracy conditions for the $\|H_{ik}\|$ matrix coincide with Eq. (12). The second condition at $4a_2 b_2 - c_{12}^2 \le 0$ defines a straight line, which is tangent to curve (12) at points K_1 and K_2 (Fig. 1c).

Figure 1a shows the phase diagram for $a_2 > a_2(Q)$. The curves of the N_a^+–N_b and N_a^-–N_b second-order phase transitions, as well as the curves of the I–N_a^+ and I–N_a^- first-order phase transitions, converge at the quadruple point O.

At $\dfrac{c_{12}^2}{4b_2} < a_2 < \dfrac{25c_{12}^2}{64(a_3 + b_2)}$, there is a region of coexistence of the N_a^-(I) and N_a^-(II) phases on the phase diagram (Fig. 1b). An isostructural transition between these phases occurs along the line TQ, terminating at the critical point Q. At the triple point T, the curve of the isostructural phase transition is approached by the curve of the I–N_a^-(II) first-order phase transition (these curves have a tangent in common at this point) and, at an angle, by the curve of the I–N_a^-(I) first-order phase transition.

At $0 < a < \dfrac{c_{12}^2}{4b_2}$ ($\Delta \le 0$) (Fig. 1c), there is a point P (15) on the phase diagram at which the two curves of the N_a^+–N_a^- and N_a^+–N_b first-order phase transitions and the curve of the N_a^-–N_b second-order phase transition converge.

DISCUSSION

In order to study the behavior of the order parameter and other physical quantities during the change of one external parameter (e.g., the temperature), one has to choose a thermodynamic path on the phase diagram:

$$b_1 = \alpha + \beta a_1. \tag{18}$$

The position of this line (which specifies the sequence of phase transitions induced by a change in temperature) is determined by the α and β values.

The following phase-transition sequence is realized along the thermodynamic path shown in Fig. 1a: I–N_a^+–N_b–N_a^-–N_{br}. At point L_1, the I–N_a^+ first-order phase transition takes place. In the $N_a^\pm$ phases, the state equation (10) admits of the solutions of three types:

$$\begin{aligned} &N_a^+\text{: } \eta_1 \ge 0, \quad \eta_2 = 0; \quad \eta_1 \le 0, \quad \eta_2 = \pm\eta_1\sqrt{3}; \\ &N_a^-\text{: } \eta_1 \le 0, \quad \eta_2 = 0; \quad \eta_1 \ge 0, \quad \eta_2 = \pm\eta_1\sqrt{3}. \end{aligned} \tag{19}$$

Figures 2a and 2e show equipotential lines of the thermodynamic potential in the N_a^+ and N_a^- phases, respectively. Solutions (19) describe three types of domains in the N_a^+ phase ($D_{\infty h}^x$, $D_{\infty h}^y$, and $D_{\infty h}^z$). For the $D_{\infty h}^z$ domain, we choose the laboratory system of coordinates with the z axis parallel to the director, which specifies the orientation of long molecular axes in the calamitic phase. In this coordinate system ($\eta_1 > 0$, $\eta_2 = 0$), the eigenvalues of the order parameter tensor Q_{ik} have the form: $-\eta_1/2$, $-\eta_1/2$, and η_1. The largest eigenvalue, $Q_{zz} = \eta_1$, corresponds to the eigenvector $\eta_1(0, 0, 1)$, which specifies the director. The second eigenvalue $Q_{xx} = Q_{yy} = -\eta_1/2$ is doubly degenerate and corresponds to an arbitrary vector $(\lambda_1, \lambda_2, 0)$, which lies in the xy plane normal to the z axis. The projection of the director onto this plane rotates in an arbitrary way, having no definite direction (uniaxial symmetry). At point L_2 of the thermodynamic path, the transition to the N_b phase occurs, in which all the three eigenvalues are different: $1/2(\eta_1 - \sqrt{3}\,\eta_2)$, $-1/2(\eta_1 + \sqrt{3}\,\eta_2)$, and η_1. In the N_b phase, the solutions to the system of equations admit six types of domains (Figs. 2b–2d). The eigenvalues Q_{xx}, Q_{yy}, and Q_{zz} correspond to three eigenvectors, and the phase symmetry is biaxial. The determination of the N_b phase biaxiality becomes a nontrivial problem and depends on the director orientation. We define the biaxiality as the minimum of the three possible values $b_{ik} = Q_{ii} - Q_{kk}$, where $i, k = x, y, z$; the director is parallel

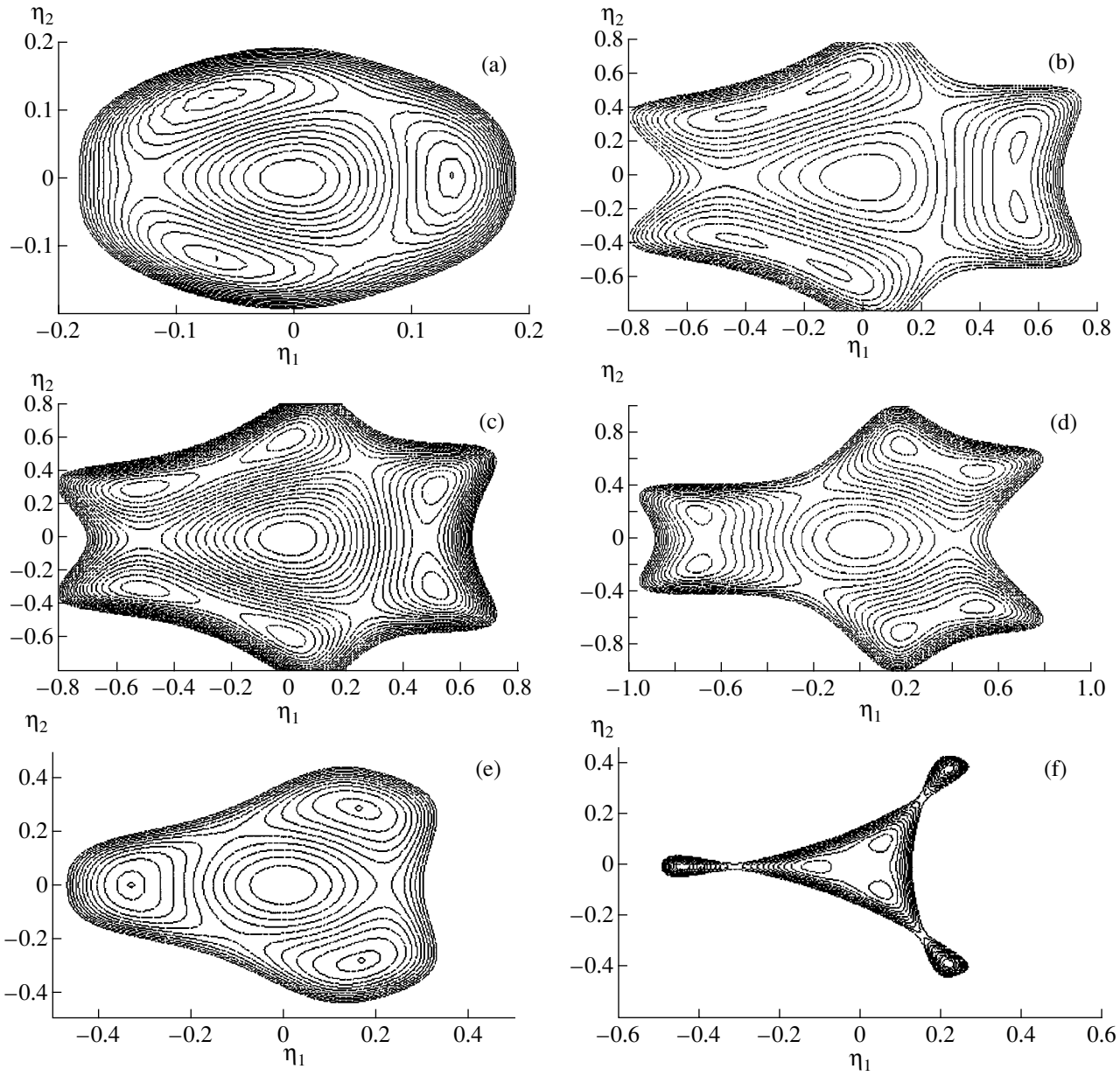

Fig. 2. Equipotential lines for the free energy $F(\eta_1, \eta_2)$ in the form of Eq. (9) (at $a_3 = 0.03$, $c_{12} = 1$, $b_2 = 1$) in the space $R^2 = (\eta_1, \eta_2)$ for different parameters a_1 and b_1: (a) $a_1 = -0.025$ and $b_1 = -0.04$, (b) $a_1 = -0.125$ and $b_1 = -0.1$, (c) $a_1 = -0.13$ and $b_1 = -0.1$, (d) $a_1 = -0.2$ and $b_1 = -0.06$, (e) $a_1 = -0.2$ and $b_1 = 0.02$, and (f) $a_1 = -0.0025$ and $b_1 = 0.015$.

to the axis normal to the biaxiality plane. In our case, near to the N_a^+–N_b transition the biaxiality is $b_{xy} = Q_{xx} - Q_{yy}$ (domain with $\eta_1 > 0, \eta_2 = 0$), the director being parallel to the z axis. As the external conditions change along the thermodynamic path (Fig. 1a), the values of biaxiality become equal at point L_3. From the conditions $b_{xy} = b_{zy} = \sqrt{3}\,\eta_2$ and $b_{zy} = 1/2(3\eta_1 + \sqrt{3}\,\eta_2)$, it follows that $\eta_2 = -(1/\sqrt{3})\eta_1$ (at $\eta_2 = (1/\sqrt{3})\eta_1$, we have $b_{xy} = b_{zx}$). On the phase diagram, this condition determines a curve (Fig. 1a)

$$a_1 = -2a_2I_1 - 3a_3I_1^2, \quad b_1 = -c_{12}I_1, \qquad (20)$$

in which two equivalent director orientations exist and the biaxiality reaches a maximum. As the N_a^- phase is more closely approached, the biaxiality $b_{xy} > b_{zy}$ (or $b_{xy} > b_{zx}$). In this case, the director is parallel to the eigenvector corresponding to the minimum eigenvalue Q_{xx} (or Q_{yy}). At point L_4, the transition to the N_a^- phase occurs. In this phase, the eigenvalues become degenerate, $Q_{yy} = Q_{zz}$ (or $Q_{xx} = Q_{zz}$), and the director of the discotic phase (normal to the disk plane) is parallel to the x axis (or y axis); that is, the director rotates through an angle of $\pi/2$ during the transition from the N_a^+ to the N_a^- phase via the N_b phase.

Figure 1b shows the thermodynamic path that intersects the curve of the isostructural phase transition in the uniaxial N_a^- ($c_{12} > 0$) or N_a^+ ($c_{12} < 0$) phases at point M_1. At this transition, the symmetry of the uniaxial phase, $D_{\infty h}$, persists, but the order parameter exhibits a jump ($\eta_1(\mathrm{I}) < \eta_1(\mathrm{II})$, $\eta_2(\mathrm{I}) = \eta_2(\mathrm{II}) = 0$). Within the region bounded by the coexistence curve of two phases, $N_a^-(\mathrm{I})$ and $N_a^-(\mathrm{II})$, the solutions to the state equation correspond to two minima of the potential $F(\eta_1, \eta_2)$ (Fig. 2f), which become equal under the external conditions specified by the point M_1 on the phase diagram (Fig. 1b). The jump in the order parameter at the $N_a^-(\mathrm{I}) \longrightarrow N_a^-(\mathrm{II})$ transition results in an increase in the degree of molecular orientational order. If, for example, the concentration of molecules in a mixture is varied, a thermodynamic path can share no common points with the curve of the isostructural phase transition that terminates at the critical point Q. In this case, there will be a smooth anomaly in the temperature dependence of the order parameter. In [18], such an isostructural (N_1–N_d) transition was observed in the vicinity of the transition to the smectic-A phase. The transition predicted by us occurs in the vicinity of the I–N_a transition and terminates at the triple point T (Fig. 1b), transforming into the I–$N_a^-(\mathrm{II})$ first-order transition. Point T is approached, at an angle, by the curve of the I–$N_a^-(\mathrm{I})$ first order phase transition. We emphasize that this transition is only realized in small ranges of the model parameters and, by analogy with the blue phase *BP*III, can be observed in narrow temperature and concentration ranges.

The $c_{12}I_1I_2$ invariant is also important for the description of the transition to the reentrant N_{br} phase (Fig. 1a).

The invariant $c_{112}I_1^2I_2$ is important when describing a transition to the reentrant uniaxial phase (Fig. 1d). Experimentally, such a sequence was observed in a potassium laurate–1-decanol–D_2O mixture at $25.95 < C_K < 26.1\%$ [5]. In the phase diagram for this case (Fig. 1d), there are two triple points, T_1 and T_2, at which the curves of the $N_a^+ \longrightarrow N_a^-$, $N_a^+ \longrightarrow N_b$, and $N_a^- \longrightarrow N_b$ transitions converge. Here, the $N_a^\pm \longrightarrow N_b$ first-order phase transitions are possible, which transform into second-order transitions at the tricritical points K_1 and K_2 (Fig. 1d).

It is worth noting, that at $a_2 < 0$ a direct first-order phase transition from the isotropic I to the biaxial N_b phase is possible [19].

CONCLUSIONS

We have performed a complete analysis of the specific features of the phase diagram for the model thermodynamic potential involving an order parameter Q_{ik} which characterizes the transitions from the isotropic I to the nematic $N_a^\pm$ and N_b phases. This order parameter characterizes the long-range orientational order of the molecules (mesogens). The hierarchy of the levels of the structural organization in LCs (due to the absence of translational symmetry, anisotropic shape of molecules, and the possibility of their aggregation) can be separated into the following three levels of order: the molecular (short-range), the supermolecular (medium-range), and the macroscopic (long-range). Each level is characterized by a set of parameters relevant to the symmetry and structure of the structural order. For the segregation of molecules, e.g., in solutions of amphiphilic molecules and gels, the local order is specified by the shape of mesogens and gels. It is well known that the local symmetry of mesogens and gels can change with the temperature (in thermotropic LCs) and the solvent concentration (in the lyotropic LCs) [8]. According to the Landau theory, a change in symmetry must be characterized by an order parameter and can be considered as a phase transition between different forms, which are the stable states (phases). The relevant order parameter $\xi = (\xi_1, \xi_2, \ldots, \xi_n)$ (being, generally, n-component) transforms according to a representation of the group G_0, characterizing the symmetry of the starting mesogen (gel). A change in the form is dictated, by analogy with crystals, by instability of the relatively small homogeneous deformations and is described by a system of inequalities for the elastic moduli of the second and higher orders; that is, a change in the form is determined by the components of the strain tensor u_{ik} ($i, k = x, y, z$), which transform according to the symmetric square of the vector representation of the G_0 symmetry group. Generally, this representation is reducible and should be decomposed into irreducible representations. For instance, the representation for a mesogen with cubic ($G_0 = O_h$) or spherical $G_0 = O(3)$ shape decomposes into three representations: one-dimensional (A), two-dimensional (E), and three-dimensional (T) [19]. The one-dimensional, fully symmetric representation characterizes transformations of the order parameter

$$\xi_1 = u_{xx} + u_{yy} + u_{zz}, \tag{21}$$

which specifies a change in the mesogen volume. The two-dimensional representation characterizes transformations of the linear combination of the u_{ik} components

$$\xi_2 = (1/\sqrt{6})(2u_{zz} - u_{xx} - u_{yy}),$$
$$\xi_3 = (1/\sqrt{2})(u_{xx} - u_{yy}). \tag{22}$$

The integral rational basis of invariants consists of two functions

$$I_1 = \xi_2^2 + \xi_3^2, \quad I_2 = \xi_2^3 - 3\xi_2\xi_3^2. \tag{23}$$

A comparison of Eqs. (2) and (23) shows that the invariants specifying the homogeneous elastic deformations of the mesogen and the macroscopic orientation are identical. This implies that the phase diagrams for Q_{ik} in the space $R^3(a_1, b_1, a_2)$ and in the space of elastic moduli are topologically equivalent [20]:

$$\begin{aligned} a_1 &= (1/2)(C_{11} - C_{12}), \\ b_1 &= (1/6\sqrt{6})(2C_{111} + 2C_{123} - 3C_{112}), \\ a_2 &= (1/\sqrt{6})(2C_{1111} - 4C_{1112} + C_{1122}), \end{aligned} \tag{24}$$

where C_{lm}, C_{lmk}, and C_{lmkn} are the elastic constants of the second, third, and fourth order, respectively. The I phase corresponds to the cubic (spherical) shape of the mesogen; the N_a^+ phase, to the tetragonal shape (uniaxial ellipsoid); and the N_b phase, to the orthorhombic shape (biaxial ellipsoid). The three-dimensional representation characterizes transformations of the shear components of the u_{ik} tensor

$$\xi_4 = u_{xy}, \quad \xi_5 = u_{xz}, \quad \xi_6 = u_{yz}. \tag{25}$$

The description of an effect of the shape of mesogens and gels on the LC structure involves the study of a thermodynamic potential which includes interaction between the order parameters $\xi = (\xi_1, \xi_2, \ldots, \xi_n)$ and Q_{ik}. For a two-component order parameter $\xi = (\xi_2, \xi_3)$ and for highly symmetric structures, the interaction has the form

$$I = \xi_1\eta_1 + \xi_2\eta_2. \tag{26}$$

The study of this thermodynamic potential is in progress.

The above approach enables one to explain the behavior of acrylamide gels dissolved in an acetone–water mixture [21], where the size varies jumpwise with temperature and concentration, with the form being preserved. In this case, ξ_1 can be chosen as the order parameter. Within the model

$$F(\xi_1) = A\xi_1 + B\xi_1^2 + C\xi_1^3 + D\xi_1^4 \tag{27}$$

the isostructural phase transition involving a change in ξ_1 (volume) is possible [22]. This transition terminates at a critical point of the liquid–vapor type, which was actually observed in [21]. The parameters A, B, C, and D in Eq. (27) are expressed in terms of the elastic constants C_{lm}, C_{lmk}, … [20]. During the preparation of the manuscript, the authors became acquainted with the results of the publication [23], in which the properties of thermotropic liquid-crystalline polymers composed of hard mesogens linked by "spacers" with different flexibilities were studied. Two nematic phases (highly nematic phase and weakly nematic phase) were observed depending on the temperature and spacing length; these phases differ in the decree of the order. The phase transition between these phases occurs in a region close to the isotropic phase, and the phase diagram obtained in the framework of the Flory theory and the Meier–Saupe model [23] is topologically equivalent to that shown in Fig. 1b.

ACKNOWLEDGMENTS

The authors are grateful to one of the authors of [23] (Akhiko Mutsuyama) for sending a reprint of the paper.

REFERENCES

1. P. de Gennes, *The Physics of Liquid Crystals* (Clarendon, Oxford, 1974; Mir, Moscow, 1977).
2. G. Friedel, Ann. Phys. **18**, 273 (1922).
3. M. I. Freiser, Phys. Rev. Lett. **24**, 1041 (1970).
4. R. Alben, Phys. Rev. Lett. **30**, 778 (1973).
5. L. I. Yu and A. Saupe, Phys. Rev. Lett. **45**, 1000 (1980).
6. S. Chanderasekhar, Mol. Cryst. Liq. Cryst. **124**, 1 (1985).
7. P. Sheng and E. B. Priestley, *The Landau–de Gennes Theory of Liquid Crystal Phase Transition* (New York, 1974), p. 143.
8. S. Singh, Phys. Rep. **324**, 107 (2000).
9. J. Malthete, L. Liebert, and A. M. Levelut, C. R. Seances Acad. Sci. **303**, 1073 (1986).
10. L. Onsager, Ann. N. Y. Acad. Sci. **51**, 627 (1949).
11. W. Meier and A. Saupe, Z. Naturforsch. **14a**, 882 (1959).
12. N. V. Madhusudana, *Liquid Crystals: Applications and Uses* (World Scientific, Singapore, 1990), Vol. 1, p. 370.
13. M. A. Cotter, J. Chem. Phys. **66**, 1098 (1977).
14. G. R. Luckhurst and S. Romano, Mol. Phys. **40**, 129 (1980).
15. R. Berardi and C. Zannoni, J. Chem. Phys. **113**, 5971 (2000).
16. P. Toledano, A. M. F. Neto, V. Lorman, *et al.*, Phys. Rev. E **52**, 5040 (1995).
17. Yu. M. Gufan, E. S. Larin, and M. B. Stryukov, Izv. Akad. Nauk, Ser. Fiz. **65**, 1102 (2001).
18. G. Nounesis, S. Kumar, S. Pfeiffer, *et al.*, Phys. Rev. Lett. **73**, 565 (1994).
19. V. P. Sakhnenko and V. M. Talanov, Fiz. Tverd. Tela (Leningrad) **21**, 2435 (1979) [Sov. Phys. Solid State **21**, 1401 (1979)].
20. Yu. M. Gufan, E. S. Larin, M. J. Novgorodova, *et al.*, Ferroelectrics **40**, 820 (2002).
21. T. Tanaka, Phys. Rev. Lett. **40**, 820 (1978).
22. Yu. M. Gufan and E. S. Larin, Dokl. Akad. Nauk SSSR **242**, 1311 (1978) [Sov. Phys. Dokl. **23**, 754 (1978)].
23. A. Mutsuyama and T. Kato, Phys. Rev. E **58**, 585 (1998).

Translated by A. Zolot'ko

Crystallography Reports, Vol. 47, No. 6, 2002, pp. 1049–1050. Translated from Kristallografiya, Vol. 47, No. 6, 2002, pp. 1119–1121.

SURFACE, THIN FILMS, AND NANOMATERIALS

Formation of Zinc Oxide Quasibicrystal Structures[1]

B. M. Ataev, A. M. Bagamadova, V. V. Mamedov, S. Sh. Makhmudov, and A. K. Omaev

Institute of Physics, Dagestan Scientific Center, Russian Academy of Sciences, ul. Yaragskogo 94, Makhachkala, 367003 Russia

e-mail: crystal@dinet.ru

Received January 10, 2002

Abstract—Quasibicrystal structures with interblock boundaries of epitaxial zinc oxide layers on a sapphire substrate along a given direction have been obtained for producing submicron electronic devices. It is shown that the use of the buffer technique allows one to grow on one $(10\bar{1}2)$ α-Al_2O_3 substrate ZnO layers oriented in the $(11\bar{2}0)$ and (0001) planes with clearly pronounced interlayer boundaries. The morphology and structural characteristics of these layers are studied. © *2002 MAIK "Nauka/Interperiodica".*

It is well known that bicrystal substrates are widely used for the formation of grain boundaries in epitaxial layers in submicron electronic devices. The Y–Ba–Cu–O Josephson HTSQ-transitions and their chains [1, 2], devices with extremely high magnetoresistance based on rare-earth manganites [3], etc., are, as a rule, much more efficient (from several times to several orders of magnitude) than analogous devices manufactured according to the conventional planar technology. These devices require searching for special bicrystals and substrates which would provide a clearly pronounced structural transition along a certain direction.

Below, we propose a method for preparing quasibicrystal structures—the formation of grain boundaries in epitaxial layers along a fixed specified orientation of the substrate. Such a boundary, or a set of such boundaries, can be formed at any part of the substrate depending on the character of the problem to be solved. We selected the α-sapphire substrate, which is very popular in practice, and zinc oxide as an object to form grain boundaries. It is evident that the choice of both substrate and object is rather arbitrary, and, in fact, any high-temperature oxide can be used as an object. At the same time, we believe that zinc oxide is especially interesting, because the nonlinear conduction of grain boundaries of special ZnO-based ceramics is successfully used in varistors [4]. It seems that the proposed method can be used as a variant for obtaining planar varistor devices.

In our experiments, we used $(10\bar{1}2)$-oriented Al_2O_3 substrates 2×2 cm^2 in size. Preliminarily, a part of the substrate was screened, whereas the other part was coated (magnetron sputtering) with a 20 to 100-nm-thick zinc oxide film. This method allows one to obtain layers of basal orientation (at least, at substrate temperatures of up to 600 K) irrespective of the material and substrate orientation [4, 5]. Then, the substrate was placed into a flow-type reactor under a low pressure, and zinc oxide [6] layers were grown by chemical transport in a hydrogen atmosphere on the whole substrate surface up to a thickness of 3–5 μm.

The morphology and crystal structure of films thus grown showed that, on the part of the $(10\bar{1}2)$ oriented α-Al_2O_3 substrate with the preliminarily deposited ZnO film, (0001)-oriented layers grow, whereas on a clean sapphire surface, $(11\bar{2}0)$-oriented epitaxial ZnO layers are formed [5, 6].

The morphology of both parts of the surface with the zinc oxide layers is shown in Fig. 1 at a magnification of ×350 (MII-4 microscope) (a) on a clean sapphire surface and (b) with the use of an intermediate magnetron deposited layer. One can see the growth figures characteristic of the above orientations—(a) a more pro-

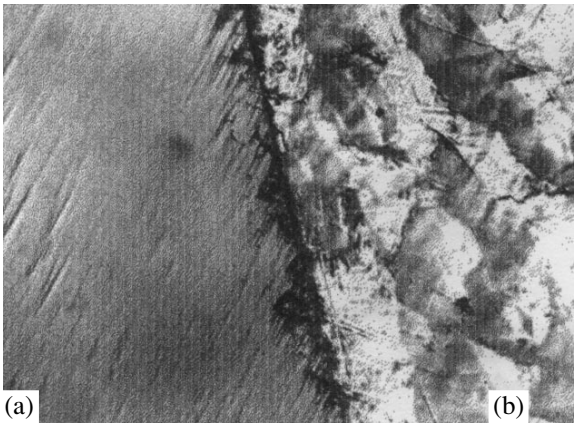

Fig. 1. Morphology of the epitaxial ZnO layers (a) with the $(11\bar{2}0)$ plane and (b) with the (0001) plane parallel to the $(10\bar{1}2)$ plane of the Al_2O_3 substrate (magnification ×350).

[1] This study was submitted to the Symposium "Phase Transitions in Solid Solutions and Alloys" (OMA), Sochi, Russia, 2001.

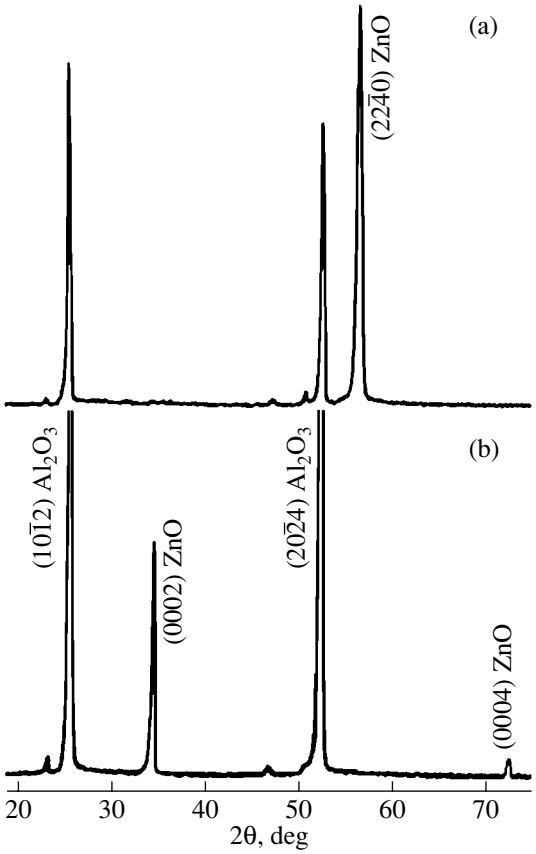

Fig. 2. Diffraction patterns of ZnO epitaxial layers obtained by chemical transport (a) on a clean sapphire surface and (b) with the aid of an intermediate deposited layer.

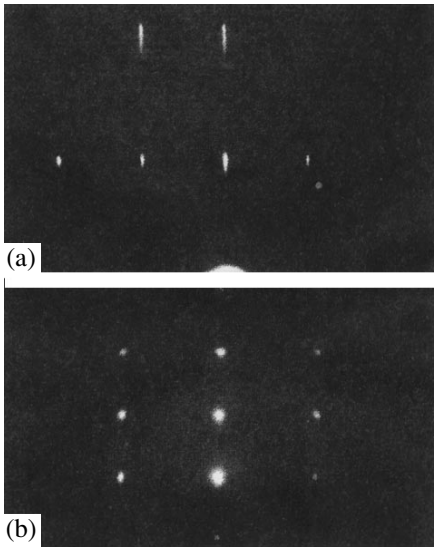

Fig. 3. The electron diffraction patterns of ZnO epitaxial layers grown by chemical transport (a) on a clean sapphire surface and (b) with the intermediate deposited layer and correspond to (a) and (b) in Fig. 2.

nounced growth figure for the $(11\bar{2}0)$-oriented ZnO layer and (b) a less distinct one for the (0001) orientation. It should be noted that the clearly seen shadow at the boundary of the two orientations is explained by the different thickness of the epitaxial layers because of the much higher growth rate of the layers in the basal orientation with respect to the $(11\bar{2}0)$-oriented ZnO layers.

An X-ray diffraction study on a DRON-2 diffractometer (monochromatized CuK_α-radiation) was performed using a pyrographite crystal. The diffraction patterns of zinc oxide layers obtained (a) on a clean $(10\bar{1}2)$ α-Al_2O_3 surface without an intermediate layer and (b) on the surface part with a preliminarily deposited film are shown in Fig. 2. The diffraction pattern in Fig. 2a is characteristic of the $(11\bar{2}0)$ ZnO epitaxial layer, whereas the pattern in Fig. 2b corresponds to the layers of the basal orientation. The ZnO layers on both parts of the substrate were also studied on an EMP-100 electron diffraction camera. The electron diffraction patterns of the ZnO layers are shown in Fig. 3. The results obtained by both methods on both parts of the substrate allowed us to determine the degree of perfection of the structure on both parts of the substrate.

Thus, using the two-stage method, we obtained epitaxial ZnO layers with two orientations—$(11\bar{2}0)$ and (0001)—on the surface of only one $(10\bar{1}2)$-oriented α-Al_2O_3 substrate. The thickness of the boundary dividing the differently oriented layers depends on the accuracy of screening made at the first stage, which should prevent material deposition onto the screened part of the substrate. It is also evident that, in order to obtain a sequence of chains of such transitions, one has to use the appropriate masks for screening at the first stage of formation of the structures by the method of magnetron sputtering.

ACKNOWLEDGMENTS

This study was supported by the Russian Foundation for Basic Research, project nos. 01-02-16200 and 02-02-17627.

REFERENCES

1. A. A. Verevkin, V. A. Il'in, A. P. Lipatov, *et al.*, Pis'ma Zh. Tekh. Fiz. **24** (24), 83 (1999) [Tech. Phys. Lett. **24**, 983 (1999)].
2. A. D. Mashtakov, K. I. Konstantinyan, G. A. Ovsyannikov, *et al.*, Pis'ma Zh. Tekh. Fiz. **25** (7), 1 (1999) [Tech. Phys. Lett. **25**, 249 (1999)].
3. N. D. Mathur, G. Burnell, S. P. Isaac, *et al.*, Nature **387**, 266 (1997).
4. T. Shiosaki, S. Ohnishi, and A. J. Kawabata, J. Appl. Phys. **50** (5), 3113 (1979).
5. B. M. Ataev, I. K. Kamilov, A. M. Bagamadova, *et al.*, Zh. Tekh. Fiz. **69** (11), 138 (1999) [Tech. Phys. **44**, 1391 (1999)].
6. A. Kh. Abduev, B. M. Ataev, and A. M. Bagamadova, Izv. Akad. Nauk SSSR, Neorg. Mater. **23** (11), 1928 (1987).

Translated by T. Dmitrieva

Crystallography Reports, Vol. 47, No. 6, 2002, pp. 1051–1057. Translated from Kristallografiya, Vol. 47, No. 6, 2002, pp. 1122–1129.

SURFACE, THIN FILMS, AND NANOMATERIALS

Structure of Porous Surface Layers of Single-Crystal GaAs(001) Wafers from Data of X-ray Diffractometry and Reflectometry

A. A. Lomov*, V. A. Karavanskiĭ, R. M. Imamov*, A. G. Sutyrin*, and V. A. Dravin*****

** Shubnikov Institute of Crystallography, Russian Academy of Sciences, Leninskiĭ pr. 59, Moscow, 119333 Russia*

*** Institute of General Physics, Russian Academy of Sciences, ul. Vavilova 38, Moscow, 117942 Russia*

**** Lebedev Physical Institute, Russian Academy of Sciences, Leninskiĭ pr. 53, Moscow, 119991 Russia*

e-mail: imamov@ns.crys.ras.ru

Received December 18, 2001

Abstract—The surface morphology and structure parameters of the surface layers of the single-crystal GaAs(001) wafers subjected to He^+ ion implantation (E = 300 keV, $D = 10^{16}$ atoms/cm^2) and subsequent electrochemical etching in a 0.5 M H_2SO_4 aqueous solution are investigated by X-ray reflectometry and double-crystal X-ray diffractometry. The strain and amorphization profiles over the layer thickness are determined from X-ray diffraction data. The density of surface layers, their thickness, and the changes of the surface relief upon etching are evaluated from the reflectometric data. The experimental parameters of the studied layers are compared with the theoretical distributions of implanted impurities and intrinsic point defects, which are calculated by the Monte Carlo method. A correlation is revealed between the layer thickness and the depth of the maximum defect concentration. It is found that the electrochemical etching predominantly occurs in strongly amorphized regions of the surface layer and does not lead to a change in the total layer thickness. The results of X-ray diffraction investigations are confirmed by scanning electron microscopy. © *2002 MAIK "Nauka/Interperiodica".*

INTRODUCTION

High-resolution X-ray diffraction techniques in different diffraction geometries have been widely used both for characterizing structural distortions in thin subsurface layers of single crystals after different treatments and for investigating multilayer heterostructures and thin films [1, 2]. The advent of new materials used in electronics, for example, porous Si films, has given impetus to improvements in these techniques with the aim of determining the strain, density, and pore size in the samples under investigation [3–7]. In our earlier work [8], we proposed a technique for characterizing porous layers on a single-crystal substrate. This technique is based on analyzing a certain part of small-angle scattering that experiences subsequent Bragg reflection. In $A^{III}B^{V}$ crystal layers, unlike porous silicon, the anodizing does not result in a change in the lattice parameter of the layers and they do not manifest themselves in the diffraction curve. The X-ray reflectometric technique is characterized by a high sensitivity to any changes in the surface layers [9, 10] and makes it possible to evaluate independently the density of surface layers, and, hence, to obtain information complementary to the results of diffraction investigations. Moreover, X-ray scattering by porous surface layers involves a diffuse scattering component [11], which also provides important information on the structure of pores, their sizes, and correlation parameters. However, it should be noted that the Born approximation, which is traditionally used for the description of scattering, is invalid for thick porous films, because the contribution from the diffuse scattering by pores can be several orders of magnitude larger than that from the specular scattering. At present, there has been no general theory of X-ray scattering by porous materials. In this respect, the aforementioned X-ray techniques should be applied in combination to characterize porous layers and to determine their parameters.

Structural defects play a decisive role in many electrophysical and electrochemical processes in surface layers of crystals and, in particular, affect the formation of pore structures. In order to elucidate the influence of defects on the etching, they can be additionally produced in a sample through the ion implantation, which is extensively used to modify the semiconductor composition, specifically for fabricating doped surface layers with a conductivity of the specified type and magnitude [12]. Over a few last years, this method has also been applied to synthesize nanometer-sized semiconductor structures [13]. In this case, one of the main

Parameters of the surface layers of the studied samples according to X-ray reflectometry and scanning electron microscopy

Sample no.	Treatment conditions	Parameters of the layers											
		σ, nm	l_i, nm			$\nu = \rho/\rho_{theor}$				ϑ, arcmin			
			l_1	l_2	l_{SEM}	ν_0	ν_1	ν_2	ν_{SEM}	ϑ_{c0}	ϑ_{c1}	ϑ_{c2}	ϑ_{theor}
381	Chemical–mechanical polishing	1.45(5)				1.005(5)				18.5(1)			18.45(2)
382	Implantation (He^+, E = 300 keV, $D = 10^{16}$ atoms/cm^2)	0.4(1)	3.5(5)			1.02(2)	0.29(3)			18.8(3)	9.9(1)		18.45(2)
383*A*	Implantation (He^+, E = 300 keV, $D = 10^{16}$ atoms/cm^2 and anodizing (current I = 2 mA/cm^2; etching time, 5 min)		>1000		>1300		0.85(5)		~0.8		17.0(2)		18.45(2)
383*B*	Implantation (He^+, E = 300 keV, $D = 10^{16}$ atoms/cm^2) and anodizing (current I = 2 mA/cm^2; etching time, 30 min)		<200	>1000	~1500		0.21(1)	0.87(2)	~0.7		8.5(3)	17.3(4)	18.45(2)

advantages of ion implantation over other techniques is the possibility of forming nanoparticles of virtually any composition. Pavesi *et al.* [14] and Schmuki *et al.* [15] demonstrated that the density of pores, their distribution, and pore structure can be controlled during the formation of a required defect profile. For the purpose of obtaining reliable structural information on porous layers, it is necessary not only to investigate thoroughly the structure of implanted layers but also to reveal and analyze the interrelation between electrochemical etching and the evolution of defects in the crystal lattice of modified layers.

In this work, we applied X-ray diffractometry and X-ray reflectometry to investigate the morphology and structure of surface GaAs(001) layers subjected to He^+ ion implantation (E = 300 keV, $D = 10^{16}$ cm^{-2}) and subsequent electrochemical etching.

SAMPLE PREPARATION AND EXPERIMENTAL TECHNIQUE

Samples 10 × 10 × 0.35 mm in size were prepared from standard single-crystal *n*-GaAs(001) wafers doped with sulfur to the charge carrier concentration $n \sim 3 \times 10^{16}$ cm^{-3}. Then, the samples were subjected to implantation by He^+ ions with the energy E = 300 keV at the dose $D = 10^{16}$ cm^{-2} on a Heavy Ion Accelerator (High Voltage Engineering Europa B. V.). The choice of inert gas ions was motivated by the fact that the implanted He^+ ions only generate defects and should not substantially affect the electrical and chemical properties of the studied layers. The electrochemical etching (anodizing) was performed in a two-compartment electrochemical cell with platinum electrodes in a 0.5 M H_2SO_4 aqueous electrolytic solution. The etching conditions used for the samples and the reflectometric parameters of the surface layers are presented in the table.

The experiments on X-ray reflectometry and double-crystal X-ray diffractometry were carried out on a TRS-1 triple-crystal X-ray diffractometer controlled using a PC AT through a Matex programmable controller. An X-ray tube with a copper anode (λ = 0.154 nm) at a power of 1.1 kW was used as a radiation source. A grooved Ge single crystal with the triple reflection (004) was used as a crystal monochromator. An X-ray beam on a collimator exit was formed by a system of slits with a horizontal size of 0.3 mm and a vertical size of 2 mm in recording the diffraction reflection curves and with a horizontal size of 0.02 mm and a vertical size of 2 mm in recording the reflectometric curves. In order to decrease the intensity of the diffuse and background components and to measure only the specular component of radiation reflected from the crystal sample, the narrow horizontal slits were located ahead of the scintillation detector. The angular sizes of these slits in measurements of the diffraction reflection and reflectometric curves were equal to 3′ and 8′, respectively. The diffraction reflection curves in the vicinity of the 004 point of the reciprocal lattice and the reflectometric curves were recorded using an ω/2ϑ scan mode. With the aim of estimating the intensity of diffuse scattering and accounting for its effect on the X-ray data, additional investigations were performed using both techniques in the ϑ and ω scan modes at fixed positions of the sample and detector, respectively.

RESULTS AND DISCUSSION

Figure 1a shows the experimental (curve *1*) and theoretical (curve *2*) diffraction reflection curves for sample no. 382. It is seen that, apart from the principal maximum at the exact Bragg angle ($\Delta\vartheta = 0$), three additional intense maxima are observed in the low-angle range. This diffraction reflection curve indicates that the layer with an increased lattice parameter and a thickness comparable to the extinction length L_{ex} is formed in the vicinity of the surface. In the case of GaAs, the extinction length for the 004 reflection and the Cu$K_{\alpha 1}$ radiation is equal to 1.57 μm for the σ polarization and 3.88 μm for the π polarization [1]. The considerably intense additional maxima suggest that, despite a high dose of implanted He^+ ions, no noticeable amorphization occurs in the surface layer, which can be treated as a quasi-single-crystal layer. (The amorphization is considered to mean a decrease in the scattering power of a crystal due to the presence of lattice defects.) The diffraction reflection curves for sample nos. 383*A* and 383*B* (Fig. 1b) almost completely coincide with those for sample no. 382. Consequently, the etching in the sulfuric acid solution virtually does not affect crystal regions of the resulting implanted layer. The sole difference observed in the diffraction curves for the studied samples is concerned with the maximum at the angle $\Delta\vartheta = -340''$ (Fig. 1c). An increase in the etching time leads to a decrease in the intensity of this maximum, its shift toward the low-angle range, and splitting (Fig. 1c, curve *3*).

In order to determine the profiles of the strain $\Delta d/d$ and the amorphization f over the layer thickness, it is necessary to fit the theoretical diffraction reflection curves to the experimental data [16]. At present, there exist a number of mathematical techniques for performing this procedure. We used the fitting procedure based on the χ^2 method proposed in [17]. In the fitting, the layer with constant parameters over the depth was used as a starting approximation. The strain was calculated from the relationship $\Delta d/d = \cot\vartheta_B \Delta\vartheta = 3.36 \times 10^{-3}$. Here, ϑ_B is the Bragg angle and $\Delta\vartheta = \vartheta - \vartheta_B = -450''$ is the angular position of the diffraction reflection from the surface layer. The mean value $f = 0.5$ was chosen for the amorphization parameter. Then, the surface layer was separated into individual sublayers. In the course of the fitting of the theoretical and experimental curves, we introduced the corrections for the diffuse scattering intensity, which was measured by triple-crystal X-ray diffraction [1, 18]. An additional Ge analyzing crystal (004 reflection) was placed ahead of the detector. The diffraction reflection curves were measured at a constant angular position of the crystal sample. Then, we analyzed the intensity ratio between the Bragg and diffuse components of the total scattering intensity in an angular range of 8′, which is equivalent to the entrance slit of the detector in the recording of the diffraction reflection curves.

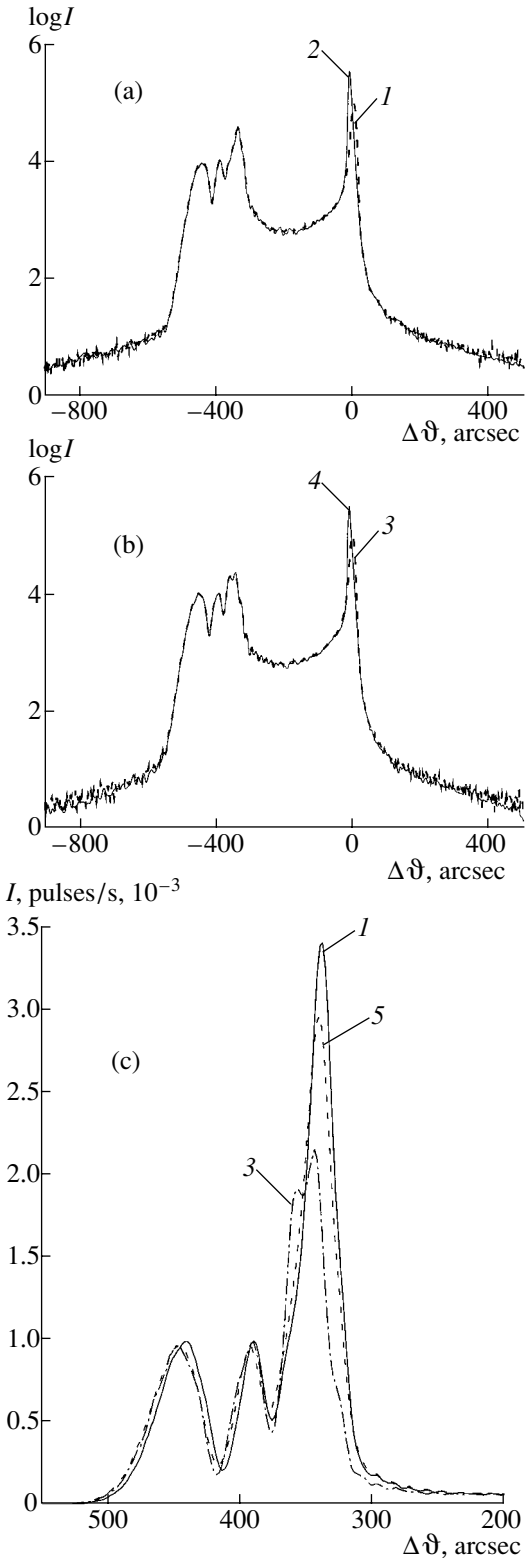

Fig. 1. (a) (*1*) Experimental and (*2*) theoretical diffraction reflection curves for sample no. 382 ($\chi^2 = 2.9$), (b) (*3*) experimental and (*4*) theoretical diffraction reflection curves for sample no. 383*B* ($\chi^2 = 2.6$), and (c) diffraction reflection curve portions corresponding to the reflection from the crystal surface layer in sample nos. (*1*) 382, (*3*) 383*B*, and (*5*) 383*A* (400 reflection, CuK_α radiation).

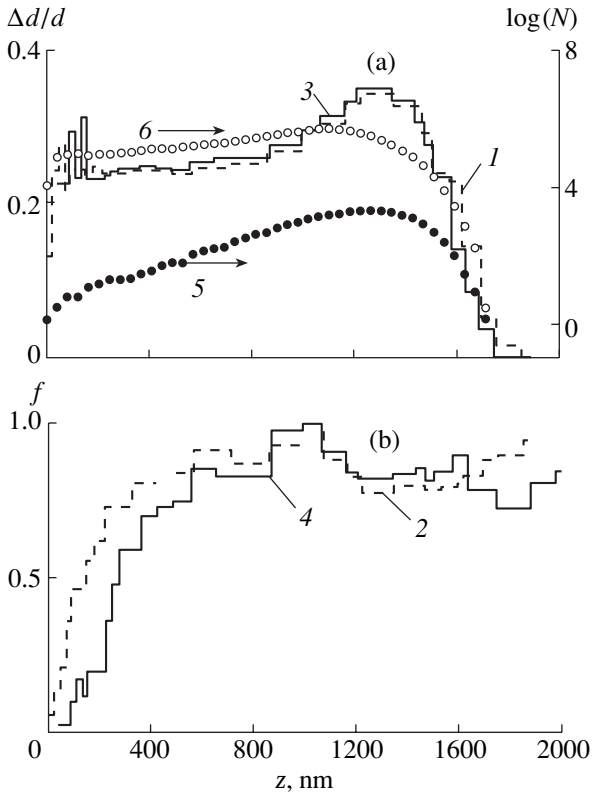

Fig. 2. Distributions of (a) the strain $\Delta d/d$ and (b) the amorphization f in surface layers of sample nos. (*1*, *3*) 382 and (*2*, *4*) 383*B* (determined from X-ray diffraction data) and distributions (right scale, arb. units) of (*5*) implanted He^+ ions and (*6*) vacancies over the thickness of the surface GaAs layer (calculated by the Monte Carlo method).

The gradual change in the structure parameters of the adjacent sublayers served as a criterion for the choice of a reliable model of the distorted surface layer. The calculations were terminated when the introduction of additional layers resulted either in a jumpwise change in the parameters of adjacent layers or in errors exceeding the corresponding parameters. Figures 2a and 2b depict the fitted distributions of the strain $\Delta d/d$ and the amorphization f for implanted sample no. 382 (curves *1*, *2*) and sample no. 383*B* etched for 30 min (curves *3*, *4*). It can be seen that the strain distribution (curve *1*) exhibits a nonmonotonic behavior. The maximum strain is observed at a depth of ~1200 nm. With a decrease in the depth to 1700 nm, the strain gradually decreases virtually to zero. The depth distribution of the amorphization coefficient (curve *2*) is also characterized by specific features. The coefficient f is small in the vicinity of the sample surface, which indicates a strong amorphization of the surface layer due to the implantation. On the whole, an increase in the depth leads to a monotonic increase in the coefficient f, except for the region corresponding to the maximum strain in which $f = 0.8$. It is reasonable to assume that the number of generated secondary defects is maximum at this depth. Unfortunately, the strain and amorphization of layers subjected to the ion implantation are difficult to estimate numerically, because data on the subsequent migration of implanted ions and generated point defects, their annihilation and aggregation into clusters with an excess number of defects of a particular type, and other processes are unavailable in the literature. The depth distributions of He^+ ions (curve *5*) and also vacancies and interstitial atoms of the matrix (curve *6*) are depicted in arbitrary units in Fig. 2a. The calculations were carried out using the Monte Carlo method [19]. Both distributions of intrinsic point defects are virtually identical. As can be seen, the depth of the maximum strain agrees well with the depth of the maximum concentration of defects. Therefore, the surface layer ~1.6 μm thick with an increased content of defects was produced in the GaAs(001) sample by high-dose implantation.

Analysis of the model of the layer in sample no. 383*B* (Figs. 2a, 2b, curves *2*, *4*) demonstrates that the strain $\Delta d/d$ and the static factor f upon anodizing remain almost unchanged. The observed difference consists in relieving stresses at the crystal film–substrate interface and decreasing the amorphization factor f owing to the etching of a scattering crystal material in the layer 100–200 nm thick at the boundary between vacuum and the surface region of the crystal. The total layer thickness after anodizing remains nearly the same, and a weak variation in the profiles of $\Delta d/d$ and f is associated with insignificant changes in the diffraction reflection curves (Fig. 1c). However, according to the estimates made by Gerischer [20], the amount of the material etched in sample no. 383*B* should be equivalent to a single-crystal layer 1.17 μm thick. The fact that the anodizing does not result in a decrease in the thickness of the implanted surface layer indicates a porous structure of this layer. Since the modification of the layer is not accompanied by a noticeable change in the profiles of $\Delta d/d$ and f, it can be assumed that the electrochemical etching of GaAs(001) in the 0.5 M H_2SO_4 aqueous solution affects only strongly amorphized sample regions, which do not participate in the diffraction scattering.

It is known that, in the surface layer of semiconductors, the high-energy He^+ ion implantation leads to the formation of clusters composed of radiation-induced defects, about which the matrix structure is strongly distorted [12]. These regions do not contribute to the Bragg scattering and give rise only to the diffuse scattering component. However, a diffracted wave traveling through these regions should undergo a phase increment. At the same time, the wave amplitude should remain almost unchanged, because the regions have a small thickness. When the local density (the real and imaginary parts of the polarizability) of the material in these regions is changed, for example, by etching, the phase factors of scattered waves change to a greater extent than the wave amplitudes. This should result in a variation in the intensity of interference maxima. It

seems likely that this physical phenomenon is observed in our case. The constancy of both the shape and intensity of the diffraction reflection curves shows that the anodizing virtually does not affect the crystal regions of the surface layer (Figs. 1a, 1b) and leads to the etching of the strongly amorphized regions. Actually, the parameters of the surface layers in sample no. 383*A* do not differ from those in the unetched sample. Upon anodizing for 30 min (sample no. 383*B*), the etching begins to affect the crystal regions in the layer (as judged from the decrease in the Debye–Waller static factor in a layer 0–200 nm thick). It can be assumed that, with an increase in the etching time, this process will proceed in deeper regions in the sample.

However, the X-ray diffraction data in the case under consideration cannot uniquely confirm the decrease in the density of the surface layer. In order to verify this assumption, we measured the reflectometric curves and the scattering indicatrices (Fig. 3) [10]. Figure 3a displays the theoretical specular-reflection curves for the initial (no. 381) and implanted (no. 382) samples. The critical angles of total external reflection ϑ_{ci} and the relative densities of the surface layers $\nu_i = \rho/\rho_0$ for the studied samples are listed in the table, where i is the layer number counting from the surface and $\vartheta_{c0} = 18.4'$ and ρ_0 are the critical angle and the density of bulk GaAs. The theoretical and experimental reflectometric curves were fitted according to the technique described in [7, 21]. The surface and surface sublayer parameters were theoretically calculated within the model of rough surface for sample no. 381 and the model of thin rough film on the surface for sample no. 382. The parameters of the surface layer were estimated in the presence of one and two sublayers with different densities for sample nos. 383*A* and 383*B*, respectively. The following designations are used in the table: $\sigma_\perp$ is the root-mean-square height of surface roughnesses, $\nu_i = \rho_i/\rho_{theor}$, $i = 1$ and 2 is the sublayer number, ρ is the density, ϑ_{ci} is the critical angle of total external reflection, and l_i the sublayer thickness.

Analysis of the results obtained demonstrates that layers with densities differing from the substrate density are absent on the surface of sample no. 381 (experimental curve *1* and theoretical curve *2* in Fig. 3a), which is characterized only by a roughness with the characteristic size $\sigma_\perp = 1.4$ nm. In contrast, the curves for implanted sample no. 382 (Fig. 3a, curves *3*, *4*) exhibit a clear-cut thickness oscillation. According to calculations, this oscillation corresponds to the layer 3.5 ± 0.5 nm thick with the decreased density $\nu = 0.29$. These results were obtained without regard for the diffuse scattering. Note that the preliminary measurements of the scattering indicatrices for these samples in the ϑ scan mode showed that the scattering predominantly consists of the specular component.

The scattering curves for the samples after electrochemical etching considerably differ in shape from the above curves and from each other. In the angle range

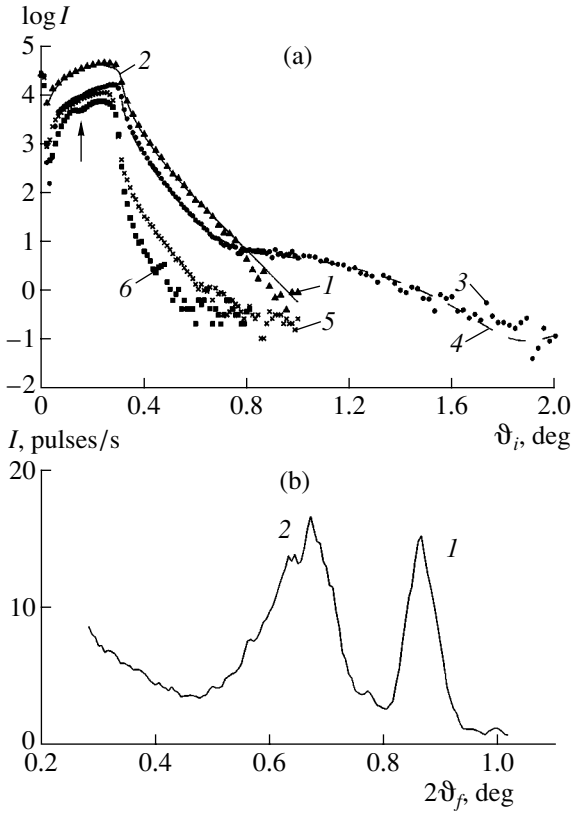

Fig. 3. (a) Experimental (symbols) and theoretical (lines) curves of specular reflection from sample nos. (*1*, *2*) 381, (*3*, *4*) 382, (*5*) 383*A*, and (*6*) 383*B*. (b) Scattering indicatrix with (*1*) specular and (*2*) diffuse peaks for sample no. 383*B* at the angle of incidence $\vartheta_i = 0.43°$ (CuK_α radiation).

$\vartheta \le \vartheta_{c0}$, one critical angle is observed for sample no. 383*A* and two critical angles ϑ_{ci} occur for sample no. 383*B* (Fig. 3a, curves *5*, *6*). It is seen that each etching leads to the formation of layers with a lower density in the vicinity of the surface. The critical angles of total external reflection are equal to 17.0′ for sample no. 383*A* and 8.5′ (marked by the vertical arrow) and 17.3′ for sample no. 383*B*. In spite of the layer porosity and the related decrease in the photoelectric absorption coefficient, X-rays do not reach the bulk of the sample matrix. No jumps in the reflection at $\vartheta_{c0} = 18.45'$ are observed in curves *5* and *6* (Fig. 3a). This indicates that layers of thickness larger than 1 μm are etched across the whole depth. According to the estimates obtained from analysis of the X-ray absorption, the thickness of the upper sublayer in sample no. 383*B* appears to be equal to ~0.2(1) nm. This supports the inference made from the X-ray diffraction data that the thickness of the surface layer after anodizing remains unchanged. However, at angles larger than the critical angle ϑ_c, the intensity of specular reflection from the samples subjected to the anodizing is substantially lower than that from the samples prior to the etching. In this angular range, the techniques [21, 22] become inapplicable. Figure 3b dis-

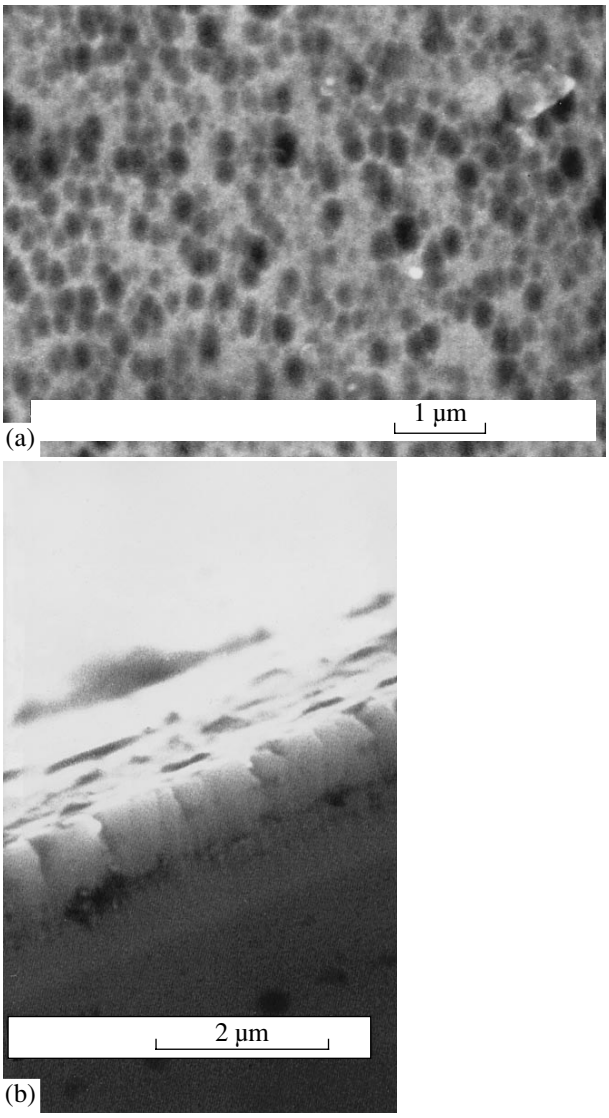

Fig. 4. SEM images of (a) the surface and (b) the cleavage of sample no. 383*B* (FEI Company XL30 scanning electron microscope; accelerating voltage, 15 kV).

plays the intensity distribution of reflected X-rays (scattering indicatrix), which was measured by scanning in exit angle ϑ_f with the detector at the fixed angle of incidence $\vartheta_i = 0.43°$. It can be seen that the distribution exhibits a specular peak at the angle $2\vartheta_f = 0.87°$ and an additional maximum at $2\vartheta_f = 0.65°$ with a higher intensity. This intense diffuse scattering corresponds to the so-called Yoneda peak [23] at the angles $2\vartheta_f \approx \vartheta_i + \vartheta_c$. A critical angle of 16.3′ determined from the location of the Yoneda peak does not agree with the critical angles obtained from the positions of the jumps of the reflection coefficient in the reflectometric curve for sample 383*B* (see table). This confirms the theoretical conclusions drawn in [9, 10] that the critical angles ϑ_c can be determined from the angular location of the jumps in the reflection coefficient only for ideal surfaces. First, this is associated with a change in the shape of the total external reflection curve due to the influence of the roughness. Second, owing to the diffuse scattering, an intense X-ray beam arrives at the entrance slit of the detector, which leads to the smearing of the angular position of the reflection jump (Fig. 3a, curves *5*, *6*). It should be noted that a decrease in the intensity of the specular-scattering component and its subsequent complete disappearance (Fig. 3a, curves *5*, *6*) are caused by the scattering of the X-ray beam from numerous boundaries inside the porous layer. The arising diffuse scattering provides information on the layer structure.

The results of the investigation performed indicate that, upon electrochemical etching, the thickness of the surface crystal layers produced by the ion implantation in sample nos. 383*A* and 383*B* remains unchanged. These layers are not continuous and contain a large number of pores etched upon anodizing.

Therefore, the data on the conditions of the sample preparation and the results of the X-ray investigation allow us to make the inference that the porous layer formed has a colonnar structure in which the cross section of pores decreases deep into the layer. An increase in the etching time leads to the separation of the porous layer into the sublayers with different densities. The lower the density of the layer, the shorter the distance between the layer and the surface.

The X-ray diffraction data on the sample structure were compared with the results of investigations into the morphology of the surface and cross-sectional cleavages of the same samples by scanning electron microscopy (SEM). The SEM images were obtained using an FEI Company XL30 microscope at an accelerating voltage of 15 kV. Figure 4a shows the image of the surface of sample no. 383*B* with bright and dark regions of mean size 200–300 nm. These are the etched macropores on the sample surface. According to the estimates, their area is 20–30% of the surface area. The image of the cross-sectional cleavage of the surface layer of sample 383*B* is depicted in Fig. 4b. The channels in the direction normal to the surface are observed in this image. It is seen that they have different depths and cross sections. The etched holes located predominantly along the sample surface can be observed at a depth of approximately 0.8–1.1 μm. The origin of these holes is not completely clear. Most likely, large-sized microdefects disappearing as a result of anodizing were located in these regions. However, the formation of these holes is undeniably associated with the lower mechanical strength of the porous layers and their partial fracture upon cleavage. The question of whether they are formed upon cleavage or are etched in the course of anodizing calls for further investigation. As can be seen from the image, the total layer thickness is equal to 1.5–1.8 μm, which is in agreement with the X-ray data.

CONCLUSIONS

Thus, it was demonstrated that the combined use of X-ray diffractometry and X-ray reflectometry holds considerable promise for the reliable characterization of porous layers. This approach made it possible to investigate thoroughly the crystal layers in the surface region of the GaAs(001) semiconductor wafers subjected to He^+ ion implantation and subsequent electrochemical etching. The densities, thicknesses, and profiles of the strain and amorphization of the crystal framework were determined for porous layers. The structural model of porous layers was proposed on the basis of the X-ray data. This model was confirmed by the SEM data. Intense diffuse scattering from the porous structures studied was revealed. The specific pore parameters obtained in the study of this scattering will be published in a separate paper.

ACKNOWLEDGMENTS

We would like to thank V.A. Bushuev for his careful reading of the manuscript and helpful remarks and A.L. Vasil'ev for providing the electron microscope images of the samples studied in this work.

This study was supported by the Russian Foundation for Basic Research (project nos. 00-02-17716 and 00-02-17521), the Program "Integration of the Higher School and Basic Science" (project no. A0103), and the International Scientific and Technical Program "Physics of Solid-State Nanostructures" (project no. 97-1073).

REFERENCES

1. A. M. Afanas'ev, A. P. Aleksandrov, and R. M. Imamov, *X-ray Diffraction Diagnostics of Submicron Layers* (Nauka, Moscow, 1989).
2. V. Holy, U. Pietsch, and T. Baumbach, *High-Resolution X-ray Scattering from Thin Films and Multilayers* (Springer-Verlag, Berlin, 1999), p. 257.
3. D. Bellet, G. Dolino, M. Ligeon, *et al.*, J. Appl. Phys. **71** (1), 145 (1992).
4. A. A. Lomov, D. Bellet, and G. Dolino, Phys. Status Solidi B **190** (1), 219 (1995).
5. M. Binder, T. Edelmann, T. N. Metzger, *et al.*, Solid State Commun. **100** (1), 13 (1996).
6. T. R. Guilinger, E. Chasson, and M. J. Kelly, J. Electrochem. Soc. **142** (5358), 1634 (1995).
7. V. A. Bushuev, A. A. Lomov, A. G. Sutyrin, and V. A. Karavanskiĭ, Perspekt. Mater., No. 4, 25 (2000).
8. A. A. Lomov, V. A. Bushuev, and V. A. Karavanskiĭ, Kristallografiya **45** (5), 918 (2000) [Crystallogr. Rep. **45**, 842 (2000)].
9. A. V. Andreev, Usp. Fiz. Nauk **145** (1), 113 (1985) [Sov. Phys. Usp. **28**, 70 (1985)].
10. B. M. Alaudinov, I. A. Artyukov, V. E. Asadchikov, *et al.*, Kristallografiya **39** (4), 605 (1994) [Crystallogr. Rep. **39**, 540 (1994)].
11. V. Chamard, G. Dolino, and J. Stettner, Physica B (Amsterdam) **283**, 135 (2000).
12. J. W. Mayer, L. Eriksson, and J. A. Davies, *Ion Implantation in Semiconductors: Silicon and Germanium* (Academic, New York, 1970; Mir, Moscow, 1973).
13. A. Meldrum, L. A. Boatner, C. W. White, *et al.*, Mater. Res. Innovations **3**, 190 (2000).
14. L. Pavesi, L. Dal Negro, C. Mazzoleni, *et al.*, Nature **408**, 440 (2000).
15. P. Schmuki, L. E. Erickson, and D. J. Lockwood, Porous Mater. **7**, 233 (2000).
16. J. Burgeat and D. Taupin, Acta Crystallogr., Sect. A: Cryst. Phys., Diffr., Theor. Gen. Crystallogr. **24**, 99 (1968).
17. A. M. Afanas'ev, M. A. Chuev, R. M. Imamov, *et al.*, Kristallografiya **42** (3), 514 (1997) [Crystallogr. Rep. **42**, 467 (1997)].
18. A. A. Lomov, P. Zaumseil, and U. Winter, Acta Crystallogr., Sect. A: Found. Crystallogr. **41** (2), 223 (1985).
19. A. M. Mazzone, Phys. Status Solidi A **95**, 149 (1986).
20. H. Gerischer, Ber. Bunsenges. Phys. Chem. **69**, 578 (1965).
21. V. A. Bushuev, A. A. Lomov, and A. G. Sutyrin, Kristallografiya **47** (4), 741 (2002) [Crystallogr. Rep. **47**, 683 (2002)].
22. M. Tolan and W. Press, Z. Kristallogr. **213**, 319 (1998).
23. Y. Yoneda, Phys. Rev. **131**, 2010 (1963).

Translated by O. Borovik-Romanova

Crystallography Reports, Vol. 47, No. 6, 2002, pp. 1058–1062. Translated from Kristallografiya, Vol. 47, No. 6, 2002, pp. 1130–1134.

SURFACE, THIN FILMS, AND NANOMATERIALS

Structural Characterization of $Si_{1-x}Ge_x$ Ultrathin Quantum Wells in a Si Matrix by High-Resolution X-ray Diffraction

A. M. Afanas'ev*, M. A. Chuev*, R. M. Imamov, É. Kh. Mukhamedzhanov**, M. M. Rzaev***, F. Schäffler****, and M. Müehlberger******

** Institute of Physics and Technology, Russian Academy of Sciences, Nakhimovskiĭ pr. 36, Moscow, 117218 Russia*

*** Shubnikov Institute of Crystallography, Russian Academy of Sciences, Leninskiĭ pr. 59, Moscow, 119333 Russia*

e-mail: imamov@ns.crys.ras.ru

**** Lebedev Institute of Physics, Russian Academy of Sciences, Leninskiĭ pr. 53, Moscow, 117024 Russia*

***** Institut für Halbleiter- und Festkörperphysik, Johannes-Kepler-Universität, A-4040 Linz, Austria*

Received February 15, 2002

Abstract—The structural characteristics of silicon samples containing one and two $Si_{1-x}Ge_x$/Si quantum wells 1.8 to 15 nm thick were determined by high-resolution X-ray diffraction. A detailed analysis of X-ray rocking curves made it possible to reproduce the Ge-concentration profiles in the quantum wells. The diffusion of germanium (up to 20%) into interface layers was observed, with a consequent broadening of the quantum well interfaces. *© 2002 MAIK "Nauka/Interperiodica".*

INTRODUCTION

In modern silicon technology, complementary metal–oxide–semiconductor structures prevail in the market of integral microschemes. These materials are gaining in popularity due to the rather simple technology of their production and their high input resistance. However, *p*-channel devices are inferior to *n*-channel devices in current and frequency characteristics. Strained $Si_{1-x}Ge_x$/Si heterostructures are very attractive systems for use in high-speed *p*-channel devices due to higher mobility of holes, as compared with a three-dimensional material [1–3]. The theoretical μ_p values are substantially higher than the corresponding values achieved in experiments because of a decrease in the effective weight of the holes in the SiGe layers of the structures. Several mechanisms of carrier scattering in quantum wells (by ions of both specially introduced and noncontrolled impurities; fusion scattering and scattering by roughnesses of the buffer layer–quantum well–barrier interfaces) constrain the hole mobility. Earlier, it was demonstrated that the major mechanism of hole mobility constraint in a quantum well involves scattering by interface inhomogenieties [4–6]. Hence, the quality of the interfaces and of the layer of the quantum well by itself (component segregation, diffuse broadening, etc.) is a very important parameter, which has a strong effect on the electrophysical properties of strained heterostructures. For this reason, an independent analysis of the quality of the main layers and interfaces is of topical importance.

High-resolution X-ray diffraction is a powerful tool for the analysis of multilayer structures [7–9]. In the case of rather abrupt interfaces, the X-ray diffraction curve shows a pronounced interference pattern containing a large number of minima and maxima, which allows one to extract abundant quantitative information on both the main layers of the structure and the interfaces.

In this study, we determined the structural parameters of the $Si_{1-x}Ge_x$ ultrathin quantum wells and their interfaces in a silicon crystal through high-resolution X-ray diffraction.

SAMPLE PREPARATION. EXPERIMENTAL

Samples of multilayer $Si_{1-x}Ge_x$/Si heterostructures with quantum wells were grown by molecular beam epitaxy on a RIBER SIVA 45 apparatus at the Institute for Semiconductor and Solid State Physics of the Johannes Kepler University of Linz (Austria). The preepitaxial cleaning was carried out according to a procedure developed by the Radio Corporation of America (RCA). The procedure involved alkaline (with a 1 : 1 : 5 $NH_4OH : H_2O_2 : H_2O$ mixture) and acid (with a 1 : 1 : 5 $HCl : H_2O_2 : H_2O$ mixture) etching of silicon substrates. The treatment with each etchant was performed in a Teflon bath at 80°C for 15 min, followed by a 15 min wash with deionized water with a resistance of no lower than 15 MΩ cm. The thin oxide layer pro-

duced in the acid etchant was removed by heating in a growth chamber at 1000°C for 5 min. A buffer Si layer was grown at 750°C. Then the temperature of the substrate was decreased to 500°C, and all subsequent layers were grown. The $Si_{1-x}Ge_x$/Si structures containing one (sample *A*) and two (sample *B*) quantum wells were thus obtained. The structural parameters specified by the growth technology are given in Table 1.

The high-resolution X-ray diffraction experiment was carried out using a double-crystal scheme with a quasidispersion (*m*, –*n*) arrangement of the crystals (Fig. 1). The X-ray radiation of a copper-anode X-ray tube (2 kW) was collimated with a planar Ge(004) crystal monochromator. A slit block S_1 of the monochromator was used for the separation of the Cu$K_{\alpha 1}$ line (the slit width in the horizontal plane was 0.2 mm) and the restriction of the vertical size of the emergent beam (the slit height was 2 mm). To decrease the contribution of the diffuse scattering component to the signal, the angular aperture of the detector was optimized by mounting a 0.4-mm horizontal S_2 slit in front of the detector. The distance between the sample and the detector was 310 mm. The optimum geometry of the experiment allowed us to substantially improve the ratio of the coherent signal to the diffuse-scattering background, thus extending the dynamic range of the measured intensities of the diffraction reflections up to seven orders of magnitude. The X-ray diffraction curves were recorded in the θ/2θ scanning mode in a broad range of incidence angles, namely, $-7500'' < \Delta\theta < 7000''$ ($\Delta\theta$ is the deviation from the exact Bragg angle θ_B).

RESULTS AND DISCUSSION

Figure 2 shows experimental diffraction curves, which are represented by vertical bars, that take into account statistical errors. The curves have numerous oscillations, which is typical of multilayer systems characterized by a high quality of the layers and rather abrupt interfaces.

The diffraction curves were analyzed according to a known procedure [7, 8]. The parameters of the structure corresponding to the growth conditions (Table 1) were used as the initial approximation. The theoretical data for the structures under examination, which were calculated within the framework of the dynamical theory of X-ray diffraction, are shown as solid curves in Fig. 2. A comparison of the calculated and experimental diffraction curves demonstrated that the parameters of the structures grown in this study only approximately correspond to the technological characteristics. In regard to the number of oscillations in the diffraction curves and their shapes, the theoretical curves adequately describe the experimental data for the samples *A* and *B*. However, the theoretical curves are evidently inconsistent with the experimental data with regard to, primarily, the positions of the peaks and their amplitudes. This inconsistency is quantitatively characterized by

Table 1. Parameters of the samples *A* and *B* (Å) specified by the growth conditions

Sample *A*	Sample *B*
Si , $l = 500$	Si, $l = 500$
Si : B^+ (10^{19} cm^{-3}), $l = 16$	Si : B^+ (8×10^{18} cm^{-3}), $l = 30$
Si, $l = 100$	Si , $l = 100$
$Si_{0.7}Ge_{0.3}$ quantum well, $l = 150$	$Si_{0.8}Ge_{0.2}$ quantum well, $l = 25$
Si buffer, $l = 3000$	Si barrier, $l = 35$
Si (001) substrate	$Si_{0.8}Ge_{0.2}$ quantum well, $l = 18$
	Si , $l = 100$
	Si : B^+ (8×10^{18} cm^{-3}), $l = 30$
	Si buffer, $l = 1000$
	Si (001) substrate

large values of the χ^2 parameter (200 and 138 for the samples *A* and *B*, respectively), which must be close to unity for the correct model. This pronounced inconsistency indicates that the real structure differs from the specified one.

In subsequent analysis, we varied the thickness of the layers l_j (*j* is the ordinal number of the layer); the perpendicular components of the relative change in the lattice parameter $\Delta a_j^{\perp}/a$, which characterize, in particular, the germanium concentration in quantum wells, and the Debye–Waller factors f_j characterizing the layer imperfection. It should be noted that the experimental data were processed taking into account diffuse scattering. Unlike diffraction scattering, diffuse scattering is incoherent, and its angular dependence is not oscillating. The latter fact makes it possible to approximate the intensity of diffuse scattering by the piecewise smooth function

$$I_i^{(D)} = B_k + (B_{k+1} - B_k)\frac{\theta_i - \theta_k}{\theta_{k+1} - \theta_k} \qquad (1)$$

for $\theta_i \in (\theta_k, \theta_{k+1})$, where *i* is the ordinal number of the point in the diffraction curve, and *k* is the ordinal number of the angle range. The angle ranges (θ_k, θ_{k+1}), in

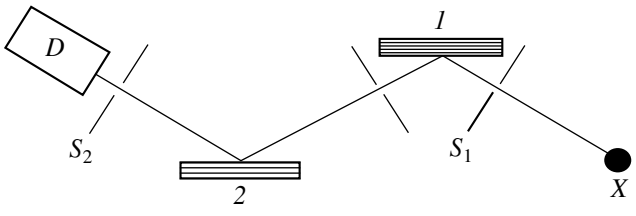

Fig. 1. Experimental scheme: *X*, X-ray source; *1*, monochromator; S_1, slit block of the monochromator; *2*, sample; S_2, slit in front of the detector for lowering of the diffuse-scattering background; *D*, detector.

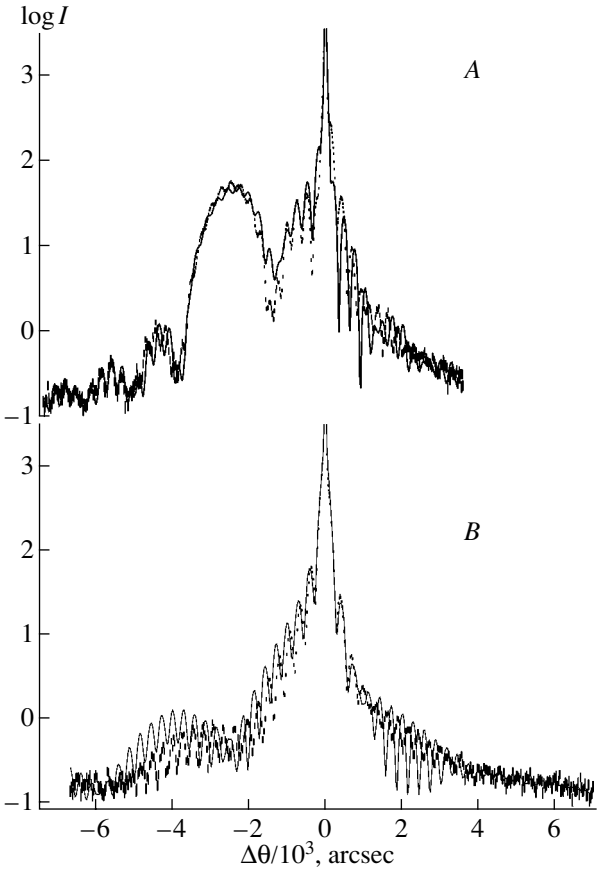

Fig. 2. Experimental X-ray diffraction curves from the samples *A* and *B* (statistical errors are represented by vertical bars) and theoretical curves (solid) calculated for the structure models with the parameters specified by the growth conditions (χ^2 = 200 and 138, respectively).

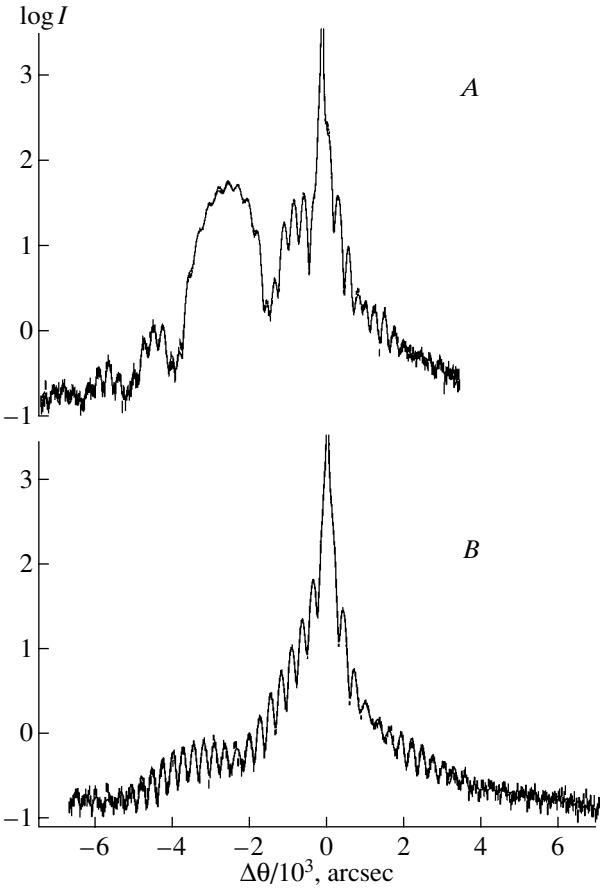

Fig. 3. Experimental X-ray diffraction curves from the samples *A* and *B* (vertical bars) and calculated curves (solid) for the resulting models (χ^2 = 2.58 and 1.96, respectively).

which the function $I_i^{(D)}$ has a continuous derivative, must be much larger than the oscillation periods observed in diffraction curves. The coefficients B_k are variable parameters.

The calculated diffraction curves for the models are shown in Fig. 3 (solid curves). As can be seen from Fig. 3, the calculated curves adequately describe the experimental diffraction data throughout the Δθ angle

Table 2. Parameters of the layers in the resulting models for the samples *A* and *B*

Sample *A*				Sample *B*			
Layer	l_j, Å	$\Delta a_j^{\perp}/a$, %	f_j	Layer	l_j, Å	$\Delta a_j^{\perp}/a$, %	f_j
1	41(3)	0	0.08(1)	1	544.3(2)	0.001(1)	0.95(1)
2	369(2)	0.009(1)	0.96(1)	2	30	−0.03(1)	0.95(1)
3	249(2)	−0.006(1)	1.00(1)	3	100	0.037(3)	0.95(2)
4	33(1)	0.32(2)	1.00(2)	4	25	0.94(2)	0.85(2)
5	150	1.829(2)	0.96(2)	5	35	0.12(1)	0.75(3)
6	16(1)	0.49(9)	0.98(2)	6	18	0.95(4)	0.70(3)
7	403(3)	−0.013(1)	0.97(1)	7	100	0.036(5)	0.71(2)
8	1047(7)	−0.001(1)	0.91(1)	8	30	−0.04(1)	0.71(2)
9	1329(8)	−0.002(1)	0.88(1)	9	1000	0.002(1)	0.71(2)
substrate				substrate			

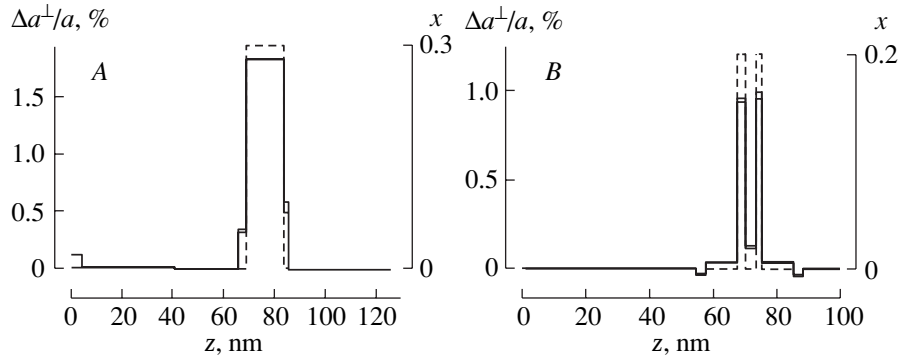

Fig. 4. Histograms of the distributions with depth of the lattice parameter and germanium concentration for the samples *A* and *B* (the errors in the determination of *x* is shown by parallel lines). The profile of the germanium concentration specified by the growth conditions is indicated by dashed lines.

range, which is also confirmed by the χ^2 parameter (2.58 and 1.96 for the samples *A* and *B*, respectively). The parameters of the layers determined by curve fitting are given in Table 2.

For all the oscillations observed in the experimental diffraction curve for the sample *A* to be described, we were led to introduce a larger number of layers (or sublayers) into the sought-for model. Thus, we used nine layers instead of five layers, in accordance with the growth technology. For the sample *B* containing the initially deposited ultrathin nanometer layers, no additional sublayers were introduced. Moreover, the thickness of the quantum wells in sample *B* was kept fixed in the course of fitting, and only the germanium concentration in these wells was varied (or $\Delta a_j^\perp/a$ was determined merely for the layers containing no germanium). This situation is associated with the fact that the direct contribution of these nanometer layers to the diffraction scattering is very small, and the shape of the diffraction curve is determined primarily by the coherent shift of the atomic planes of the upper rather thick Si layer with respect to the substrate, which is caused by thin quantum wells. This shift gives rise to an additional phase in the amplitude of X-ray scattering from the upper layer relative to the amplitude of scattering by the substrate, which is the main reason for the appearance of a large number of oscillations in diffraction curves [10]. The resulting diffraction pattern is determined by the shift $\Delta_u \approx (\Delta a_j^\perp/a) l_j$, i.e., two parameters of quantum wells are interrelated, and their independent variation provides no additional information.

The parameters of the crystal lattice $\Delta a_j/(x)/a$, which are associated with the replacement of the Si atoms by the Ge atoms in the quantum wells, are related to the determined $\Delta a_j^\perp/a$ values according to the known equation

$$\frac{\Delta a_j^\perp(x)/a}{a} = \frac{\Delta a_j(x)/a}{a}\frac{1+\nu}{1-\nu}, \qquad (2)$$

where ν is the Poisson ratio, which depends only slightly on the concentration *x* and was taken equal to 0.277. The values *x* were determined from $\Delta a_j(x)/a$ according to the Vegard law. Then the corrections proposed in the study [11] were applied.

The histograms of the distributions with depth of the lattice parameter and germanium concentration for the samples under study are shown in Fig. 4; the profiles of the germanium concentration specified by the growth conditions are indicated by dashed lines. To summarize briefly, the following facts should be noted. For the sample *A*, the interface layers of the quantum well were detected. The thicknesses of the upper (with respect to the quantum well) and lower layers are 3.3 and 1.6 nm, respectively. A portion of the germanium atoms (about 6%) diffuse into these layers, the germanium concentration in the quantum well being decreased by approximately the same value. As mentioned above, the sample *B* contained a large number of thin layers. In the study of the sample *B*, the thickness of these layers was kept fixed, and only the lattice parameters were varied. The analysis demonstrated that the germanium concentration in the quantum wells decreased by approximately 20%, and this portion of the germanium diffused into both the layer separating the quantum wells and the interface layers (Fig. 4). On the whole, the total amount of germanium in the samples corresponds to the germanium concentration introduced according to the technology used.

CONCLUSIONS

To summarize, the multilayer $Si_{1-x}Ge_x/Si$ heterostructures with quantum wells were studied through high-resolution X-ray diffraction. Optimization of the geometry of the X-ray diffraction experiment made it possible to measure the diffraction curves in the dynamic range of intensities up to seven orders of magnitude (which corresponds to the broad range of incidence angles $-7500'' < \Delta\theta < 7000''$) with the use of a standard X-ray tube as the X-ray source. The detailed

diffraction pattern thus obtained and the consideration of the diffuse scattering background allowed us to determine the structural parameters of the $Si_{1-x}Ge_x$ ultrathin quantum wells and their interfaces with high accuracy. Diffusion of germanium (up to 20%) from the quantum wells into the interface layers was observed, with a consequent broadening of the quantum well interfaces.

ACKNOWLEDGMENTS

This study was supported by the Russian Foundation for Basic Research (project nos. 00-02-17716, 00-02-17542, and 01-02-02007-BNTS-a), the Ministry of Industry, Science, and Technology of the Russian Federation (Programs "Prospective Technologies and Devices for Micro- and Nanoelectronics" and "Physics of Solid Nanostructures"), and the Russian Federation Government Program for Support of Leading Scientific Schools (project no. 00-15-96568). Mukhamedzhanov and Chuev thank the Foundation for Support of Russian Science.

REFERENCES

1. D. K. Kayak, K. Got, A. Yutani, *et al.*, IEEE Trans. Electron Devices **43**, 1709 (1996).
2. M. Arafa, K. Ismail, J. O. Chu, *et al.*, IEEE Trans. Electron Device Lett. **17**, 586 (1996).
3. A. P. Boltaev, M. M. Rzaev, and N. N. Sibel'din, Izv. Akad. Nauk, Ser. Fiz. **63** (2), 262 (1999).
4. T. E. J. Whall, J. Cryst. Growth **157**, 353 (1991).
5. C. J. Emeleus, T. E. Whall, D. W. Smith, *et al.*, J. Appl. Phys. **73**, 3852 (1993).
6. R. J. P. Lander, M. J. Kearney, A. I. Horrel, *et al.*, Semicond. Sci. Technol. **12**, 1064 (1997).
7. A. M. Afanas'ev, M. A. Chuev, R. M. Imamov, *et al.*, Kristallografiya **42** (3), 514 (1997) [Crystallogr. Rep. **42**, 467 (1997)].
8. A. M. Afanas'ev, M. A. Chuev, R. M. Imamov, and A. A. Lomov, Kristallografiya **45** (4), 715 (2000) [Crystallogr. Rep. **45**, 655 (2000)].
9. E. Kh. Mukhamedzhanov, C. Bocchi, S. Franchi, *et al.*, J. Appl. Phys. **87**, 4234 (2000).
10. A. M. Afanas'ev, M. A. Chuev, R. M. Imamov, *et al.*, Pis'ma Zh. Éksp. Teor. Fiz. **74** (10), 560 (2001) [JETP Lett. **74**, 498 (2001)].
11. J. P. Dismukes, L. Ekstrom, and R. J. Paff, J. Phys. Chem. **68** (10), 3021 (1964).

Translated by T. Safonova

Crystallography Reports, Vol. 47, No. 6, 2002, pp. 1063–1071. Translated from Kristallografiya, Vol. 47, No. 6, 2002, pp.1135–1143.

SURFACE, THIN FILMS, AND NANOMATERIALS

Structural Inhomogeneities and Magnetic Properties of Co/Cu Multilayer Films

V. F. Meshcheryakov*, A. G. Vasil'ev*, K. V. Timonin, and I. A. Khorin*****

** Moscow State Institute of Radioengineering, Electronics, and Automation (Technical University), pr. Vernadskogo 78, Moscow, 117454 Russia*

*** Shubnikov Institute of Crystallography, Russian Academy of Sciences, Leninskiĭ pr. 59, Moscow, 119333 Russia*

**** Institute of Physics and Technology, Russian Academy of Sciences, Nakhimovskiĭ pr. 36, Moscow, 117218 Russia*

e-mail: niin@ranet.ru

Received January 22, 2002

Abstract—The polycrystalline Co/Cu multilayer films are prepared by magnetron sputtering onto Si/SiO_2 substrates. The static magnetization and the ferromagnetic resonance (FMR) spectra of these films are investigated. The microscopic cross-sectional structure of the films is examined using transmission electron microscopy. It is demonstrated that the differences in the magnetization curves and the ferromagnetic resonance spectra are associated with the specific structural features governed by the technological parameters of the film sputtering. The possible structural features that arise during the formation of layered structures and are responsible for the appearance of additional lines in the FMR spectra are discussed. *© 2002 MAIK "Nauka/Interperiodica".*

INTRODUCTION

Ultrathin multilayer metallic structures in which ferromagnetic layers are separated by a nonmagnetic interlayer possess a giant magnetoresistance. This phenomenon was revealed in films of compositions Fe/Cr [1] and Co/Cu [2]. Apart from the interlayer thickness [3], the structure of an interface—the region separating magnetic and nonmagnetic layers—has a decisive effect on the properties of these films. Puik *et al.* [4] and Vemon *et al.* [5] showed that even the power of the evaporation source affects the atomic distribution at the interface. As a consequence, even insignificant variations in the preparation conditions of layered structures can lead to a qualitative change in their properties. In particular, such a high sensitivity to preparation conditions of layered structures manifests itself in measurements of the static magnetization and the ferromagnetic resonance (FMR). The elucidation of the physical nature of the interactions arising in these structures necessitates a detailed investigation into the crystal structure of films and their physical parameters.

For multilayer films, one of these parameters is the uniaxial anisotropy of magnetic layers. This anisotropy, apart from the anisotropy typical of bulk materials, involves the surface component controlled by the layer thickness and the interface structure. The uniaxial anisotropy determines the proportionality coefficient in a linear dependence of the magnetization measured in the direction perpendicular to the film plane on the magnetic field and the position of the absorption line for the acoustic branch of the ferromagnetic resonance. Another factor affecting the properties of the structures under consideration is the exchange interaction between magnetic layers. If this interaction has an antiferromagnetic nature, the dependence of the magnetization measured in the direction parallel to the film plane on the magnetic field exhibits a nonlinear behavior. In the case of resonance measurements, the exchange interaction affects only the location of additional resonance lines—the so-called optical modes whose intensity is substantially less than that of the acoustic modes [6]. Apart from these modes, there can arise lines associated with the spin-wave resonance [7].

We investigated the ferromagnetic resonance in multilayer structures prepared under slightly different conditions and observed the qualitative difference in the experimental spectra. This difference manifests itself not only in a change in the position of the resonance lines but also in the appearance of additional lines in the magnetic field directed along the normal to the film plane. This circumstance lent impetus to a thorough investigation into the microstructure, the FMR spectra, and the static magnetization of the prepared samples. The aim of the present work was to investigate the possible inhomogeneities formed in layered structures and their influence on the magnetic properties.

SAMPLE PREPARATION

In this work, we studied the structural inhomogeneities and magnetic properties of the Co/Cu multilayer films prepared by magnetron sputtering onto single-crystal Si/SiO_2 substrates. A vacuum chamber for sam-

1063-7745/02/4706-1063$22.00 © 2002 MAIK "Nauka/Interperiodica"

Table 1. Characteristics of the prepared samples and magnetron source powers used for their sputtering

Sample no.	Number of layer pairs	Source power, W	Co layer thickness, Å		Cu layer thickness, Å
			sputtering	magnetization	sputtering
1	15	Co – 300 Cu – 300	30	33	9
1a	15	Co – 300 Cu – 300	30	47	9
2	15	Co – 200 Cu – 200	30	57.3	12
3	20	Co – 300 Cu – 200	6	4	4.8

ple sputtering was pumped with a thurbomolecular pump, which provided a way of producing a residual pressure of 10^{-6} mbar. The argon pressure in the course of sputtering was equal to 10^{-2} mbar. The films were sputtered using two independent magnetron sources operating in a dc or ac mode. Sample nos. *1, 2*, and *3* were sputtered with a magnetron source operating in the dc mode, and the source was operated in the ac mode in the course of sputtering sample no. *1a*. Single-crystal Si(100) wafers 50 mm in diameter with applied SiO_2 layers served as substrates. Three samples (nos. *1*, *1a*, and *2*) were sputtered onto the substrate placed above the source. In this case, 15 pairs of Co/Cu layers were deposited onto the substrate. The substrate was continuously rotated at a rate of 2.5 rpm during sputtering of sample no. *3*, which involved 20 pairs of Co/Cu layers. Al the samples were prepared at room temperature. The sputtering rate of the films varied from 1 to 2 Å/s.

The cobalt and copper layer thicknesses given in the column "sputtering" in Table 1 were calculated from the times and rates of sputtering. The sputtering rate of cobalt was refined using the preliminarily obtained dependences of the magnetization of monolayer films on the source power and the sputtering time. In these dependences, the saturation magnetization was taken to be equal to the saturation magnetization of a bulk sample $M_S = 1420$ G. The dependences of the film thickness on the source power and the sputtering time exhibit a linear behavior and passed through zero at finite powers and times of sputtering. With the use of these data and the results of FMR measurements, it was found that a continuous film is formed on the substrate surface when the amount of the sputtered material corresponds to a thickness of 20–25 Å. Most likely, this is the reason why the giant magnetoresistance was not observed in our layered structures.

The Co layer thicknesses listed in the column "magnetization" in Table 1 were calculated under the assumption that the maximum measured magnetization of the layered films was equal to the saturation magnetization of the bulk sample. The power of the source used for the sample sputtering is also presented in Table 1. Sample no. *1a* differed from sample no. *1* only in the operating mode of the magnetron source. Sample no. *2* differed from sample no. *1* in the thickness of the copper interlayer. The thicknesses of the cobalt and copper layers in sample no. *3* prepared under dynamic conditions were considerably smaller and equal to 5 and 6 Å, respectively.

RESULTS OF MAGNETIC MEASUREMENTS AND THEIR INTERPRETATION

The magnetization was measured on a vibrating-sample magnetometer. The FMR spectra were recorded on a spectrometer operating at a frequency of 9.55 GHz. The magnetic component of the microwave field was always perpendicular to the constant magnetic field and lay in the substrate plane. All the measurements were carried out at room temperature.

Sample no. *3*. The magnetization curves obtained for the samples in the magnetic fields aligned parallel and perpendicular to the substrate plane are depicted in Fig. 1. The dependences of the magnetization on the magnetic field for sample no. *3* prepared under dynamic conditions are linear and identical for both directions (Fig. 1d). The absence of a spontaneous moment indicates that the film in this sample is composed of individual Co clusters, which are not coupled by the exchange interaction. The cluster size (the number n of atoms per cluster) can be estimated using the Curie formula for the magnetization M, that is,

$$M = \frac{(N_A\rho/\mu n)[g\mu_B n]^2 S(S+1)}{3kT}H,$$

where N_A is the Avogadro number, μ is the molecular weight, ρ is the density, μ_B is the Bohr magneton, k is the Boltzmann constant, and T is the temperature. From this formula, at the value of $g = 2$ and the spin $S = 1/2$, we have $n = 1600$, which corresponds to a linear cluster size of ~40 Å. No resonance absorption is observed for this sample.

Sample nos. *1, 1a*, and *2*. The magnetizations of sample nos. *1*, *1a*, and *2* in the parallel geometry only slightly differ from each other, are close to the saturation magnetization, and weakly increase with an increase in the magnetic field (Figs. 1a–1c). This increase suggests that the samples also contain Co clusters. In the perpendicular configuration, the dependences $M(H)$ are linear and differ for different samples. The FMR spectrum at the magnetic field lying in the film plane consists of single absorption lines, whose widths and positions are listed in Table 2. At the perpendicular orientation, the FMR spectra, which for

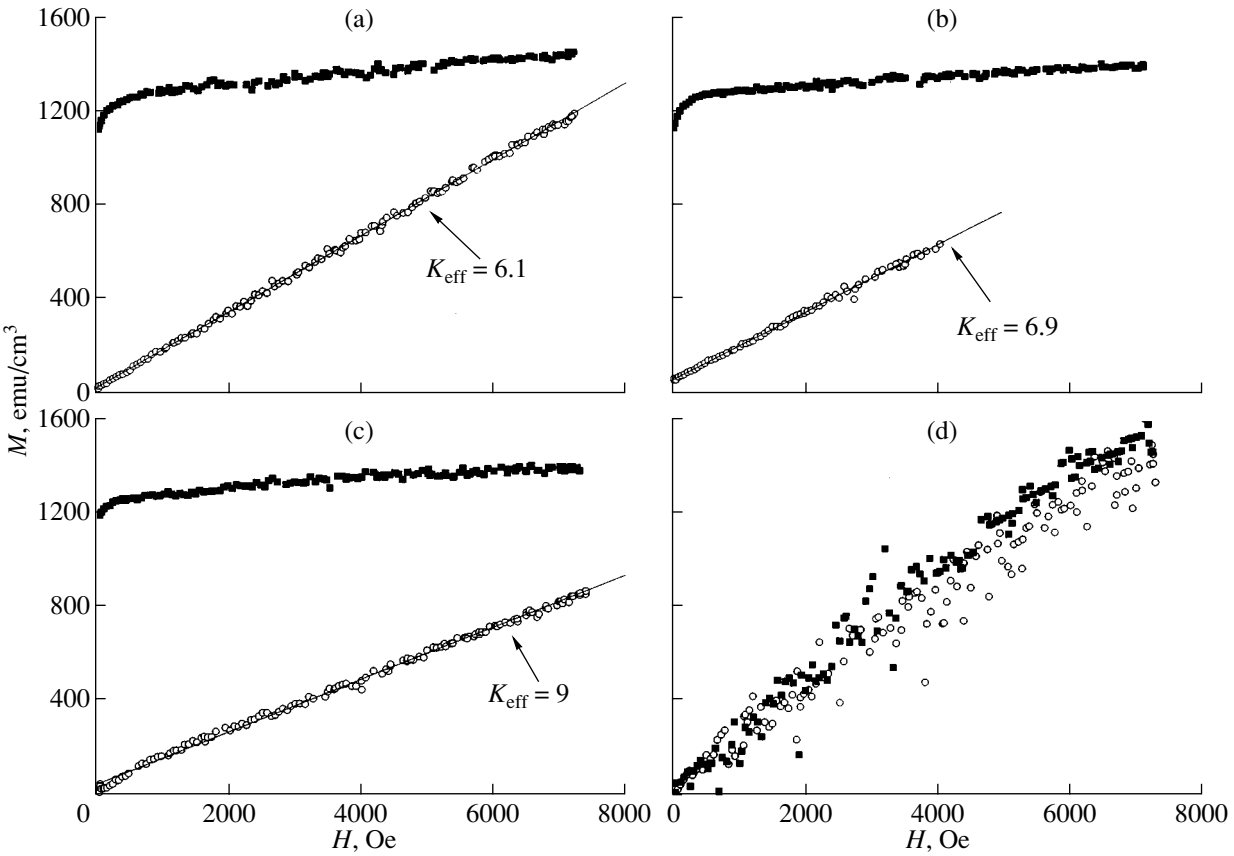

Fig. 1. Magnetization curves for sample nos. (a) *1*, (b) *1a*, (c) *2*, and (d) *3* in magnetic fields aligned parallel (closed symbols) and perpendicular (open symbols) to the substrate plane.

sample nos. *1* and *2* are shown in Fig. 2, differ considerably. The single absorption line is observed in the spectrum of sample no. *1a*. The spectrum of sample no. *1* involves the main line and several additional lines with a lower intensity on the left. The FMR spectrum of sample no. *2* exhibits several narrow lines with close intensities. The lines observed for sample nos. *1* and *2* in the perpendicular configuration differ qualitatively. The width of these lines for sample no. *1* is almost ten times larger than that for sample no. *2*. The spacing between the lines monotonically decreases with a decrease in the resonance field. The additional absorption lines for sample nos. *1* and *2* appear only in the case when the deviation of the magnetic field direction from the normal to the film is less than 8°. The experimental angular dependences of the location of the uniform resonance lines are plotted in Fig. 3. In this case, at the perpendicular orientation, the high-field line is chosen as the line of the uniform resonance for sample no. *2*.

The results obtained demonstrate that the FMR spectra of sample nos. *1* and *1a* are characterized by close parameters and differ in that there are additional absorption lines for sample no. *1a* in the perpendicular configuration. At the same time, the FMR spectrum of sample no. *2* and the line width differ from those observed for sample nos. *1* and *1a*. It should be noted that the FMR spectra of all the samples taken from different regions of the substrate completely coincide with each other. This suggests that the film has a good uniformity along the surface and the difference observed in

Table 2. Magnetic characteristics of the samples

Sample no.	g factor	K_{eff}		Location of FMR line, Oe		FMR line width, Oe	
		FMR	magnetization	$H_{\|\|}$	$H_{\perp}$	$H_{\|\|}$	$H_{\perp}$
1	1.99	6.25	6.1	1160	12300	380	380
1a	2.02	6.55	6.9	1100	12710	300	800
2	1.97	9.58	9.0	830	17080	180	40

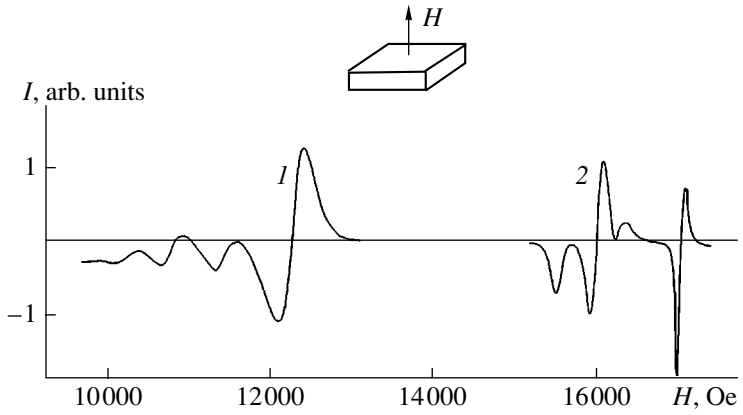

Fig. 2. FMR spectra of sample nos. *1* and *2* in the perpendicular geometry.

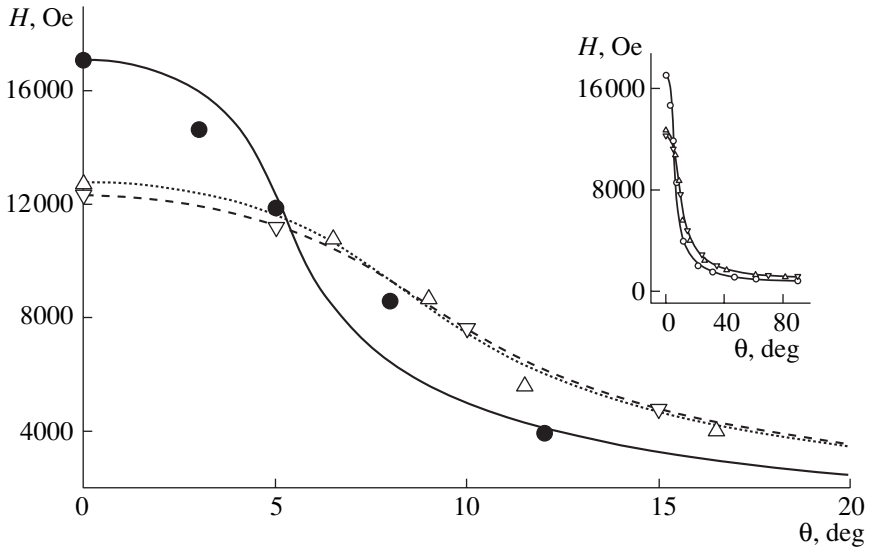

Fig. 3. Theoretical (lines) and experimental (symbols) angular dependences of the location of the FMR lines for sample nos. *1* (△, solid line), *1a* (▽, dashed line), and *2* (●, solid line). The inset shows the same dependences on the other scale.

the sample properties is determined by the difference in the transverse structure.

Since the magnetization of the samples reaches saturation already in low magnetic fields (Fig. 1), the magnetic moments of ferromagnetic layers lie in the film plane and are parallel to each other. In this case, the layers can be considered monolayer films. Under the assumption that the *z* axis is aligned along the normal to the plane of the film, the density of its energy (including the Zeeman, demagnetization, and uniaxial anisotropy contributions) can be written in the form [8]

$$E = \left(2\pi + \frac{K_U}{M_S^2}\right)M_Z^2 - \mathbf{M}\cdot\mathbf{H}, \qquad (0)$$

where M_S is the saturation magnetization and K_U is the uniaxial anisotropy energy constant. Now, we introduce the designations $K_{\text{eff}} = 4\pi + 2K_U/M_S^2$, θ_H is the angle between the magnetic field direction and the normal to the film plane, and θ is the angle between the magnetic moment direction and the normal to the film plane. Then, the equilibrium position of the magnetic moment is defined by the relationship

$$H\sin(\theta_H - \theta) = K_{\text{eff}}M_S\sin\theta\cos\theta. \qquad (1)$$

From this expression, it follows that the dependence of the film magnetization on the magnetic field aligned along the normal to the film plane can be described by the formula

$$M = H/K_{\text{eff}}. \qquad (2)$$

The relationship for the uniform resonance absorption spectrum can be derived from expression (1) in the

following form:

$$(\omega/\gamma)^2 = [H\cos(\theta_H - \theta) - K_{\text{eff}}M_S\cos 2\theta] \times [H\cos(\theta_H - \theta) - K_{\text{eff}}M_S\cos\theta], \quad (3)$$

where ω is the frequency and γ is the gyromagnetic ratio.

With the use of expressions (4) at $\theta = 0°$ and 90° and experimental data on the magnetization, we determined the values of K_{eff} and the *g* factors (Table 2). The K_{eff} values evaluated from the results of static and resonance measurements are in rather good agreement with each other. This indicates the adequacy of the model used to interpret our results. Within the limits of experimental error, the *g* factors for all the samples coincide with each other and are equal to 2.0. However, this value differs from $g = 2.16$ obtained for Co/Cu multilayer films under ultrahigh vacuum with a residual pressure of 10^{-8} mbar in [9] and $g = 2.20$ determined in [10]. On the other hand, the *g* factor for cobalt monolayer films prepared under vacuum with a residual pressure of 10^{-6} mbar varies from 1.9 to 2.2 [11]. The large spread of the *g* factors is explained by the presence of stresses.

The theoretical (lines) and experimental angular dependences of the location of the FMR lines for three samples studied [the theoretical dependences were calculated using relationship (4)] are compared in Fig. 3. The experimental data for sample nos. *1* and *1a* fit the calculated curves well, whereas the deviation between the experimental and calculated data for sample no. *2* appears to be considerable in the vicinity of $\theta = 90°$. This suggests that the high-field FMR line observed for sample no. *2* in the perpendicular orientation of the magnetic field is not the uniform resonance line.

According to Heinrich and Cochran [3], the minimum width of the uniform resonance line for single-crystal Co/Cu films is equal to 20 Oe. The line width for our samples varies from 40 to 800 Oe. The line widths in the spectra of sample no. *1* for different geometries are identical and equal to 380 Oe. At the same time, for sample no. *1a*, the resonance line is broadened by a factor of 2.7 with a change in the magnetic field direction from the parallel ($\Delta H_{\parallel} = 300$ Oe) to perpendicular configuration. The broadening of the FMR line observed for these samples can be caused by the following factors. In the parallel configuration, the polycrystalline nature of the samples should lead to the broadening of the order of the anisotropy field. The broadening can also be due to the scatter in the values of K_{eff} owing to the dipole interactions in the interface region. In the perpendicular geometry, owing to the strong angular dependence (Fig. 3), the broadening can be associated with the variations in the directions of the magnetization of different macroscopic regions. Reasoning from the aforesaid, we can infer that the misorientation of the magnetizations in different layers in sample no. *1a* in perpendicular geometry is substantially larger than that in the other samples. A change in the line width for sample no. *2* depending on the orientation qualitatively differs from that observed for the above samples. The line width for the perpendicular direction is almost five times less than the line width (180 Oe) for the parallel direction. Analysis of the line widths for the samples under investigation demonstrates that the relaxation mechanism responsible for the line width observed in the spectra of sample no. *2* in the perpendicular geometry essentially differs from the relaxation mechanism in sample nos. *1* and *1a*.

There exist two approaches to the description of additional modes arising in ferromagnetic films. One approach uses the concept of spin waves, which occur in multilayer structures only in the case when the magnetic field is aligned normally to the film plane and whose spectrum at $\theta_H = \theta = 0$ is described by the equation [12]

$$\frac{\omega}{\gamma} = H - K_{\text{eff}}M_S - \frac{A}{M_S}\mathbf{k}^2, \quad (4)$$

where *A* is the constant of the order of the exchange interaction constant and **k** is the wave vector with a magnitude proportional to an integer squared. Similar modes were observed by Wigen and Zhang [10] in Co/Cu multilayer samples at magnetic field orientations close to the perpendicular orientation. Their spectrum was well represented by relationship (5), and the intensities of these modes were considerably lower than the intensity of the uniform resonance line. In our case, the additional modes in sample no. *1* are also observed only at orientations close to the perpendicular orientation; however, the condition of the proportionality to the integer squared is not satisfied. According to the second approach, at resonance, the magnetic moments in each layer are parallel to one another and oscillate in a certain phase with respect to the moments in other planes [13]. The narrow lines observed in the spectrum of sample no. *2* (Fig. 2) are possibly associated with excitation of oscillations of the magnetic moments in particular planar formations occurring in the film, which is nonuniform in thickness. This is evidenced by the fact that the resonance lines in the spectrum of sample no. *2* in the perpendicular configuration are substantially narrower than those of sample no. *1*.

FILM STRUCTURE AND ITS INFLUENCE ON THE MAGNETIC PARAMETERS

Film structure. The planar images and the images of cross-sectional cleavages of all the samples were obtained using transmission electron microscopy. An examination was performed on a Philips LM430ST microscope at an accelerating voltage of 200 kV. Judging from the electron diffraction patterns recorded for different regions in the plane and cross section of the films (Fig. 4), the samples have a polycrystalline structure with a face-centered cubic lattice. The images were

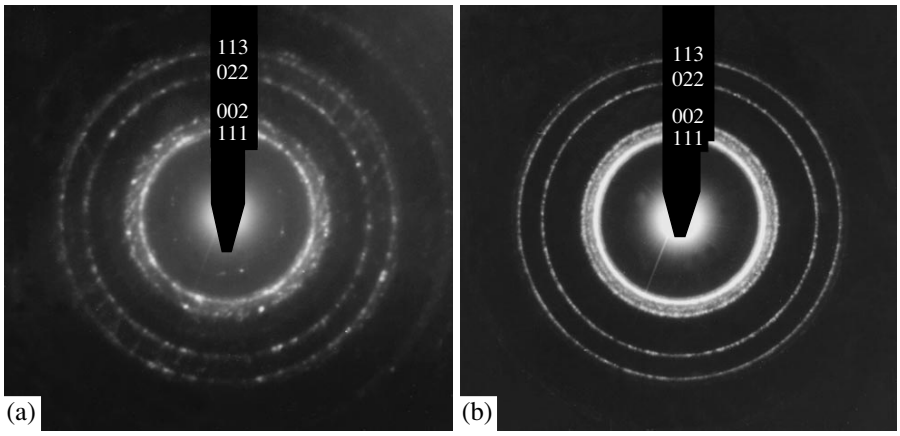

Fig. 4. Diffraction patterns of (a) planar and (b) cross-sectional samples of film no. *1a*. The diffraction patterns correspond to a polycrystalline structure with the parameters of the face-centered cubic lattices of cobalt and copper.

slightly defocused in order to increase the contrast. The micrographs of cross-sectional cleavages of all the samples at different magnifications are shown in Figs. 5 and 6. It is clearly seen that all four samples have a layered structure. For sample nos. *1*, *1a*, and *3*, the layering is sufficiently uniform and the number of layers corresponds to their number specified in the course of sputtering (Figs. 5a, 5b, 5d). The thickness of individual layers is equal to 30–50 Å. However, as can be seen from Fig. 5c, only four layers of different thicknesses can be assigned to the contrasts observed for sample no. *2*.

There are three characteristic features distinguishing the structure of the samples: the layering, the presence of crystal grains, and the formation of a columnar structure corresponding to two vertical contrasts. The wide dark contrasts are due to columns consisting of grains 100–200 Å in size. The investigation of the surface of epitaxial multilayer films under a tunneling microscope [14] revealed that the columnar structure observed in our case manifests itself as a bumpy surface. The narrow bright contrasts indicated by arrows in Figs. 6a–6c can be associated either with grains of size 30–50 Å (with orientation differing from the orientation of grains corresponding to the wide contrasts) or with holes.

Sample no. *1* (Figs. 5a, 6a) is characterized by a well-defined layering. The columnar structure and the related narrow contrasts are weakly pronounced. No crystal grains are found, and the size of polycrystals varies from 100 to 200 Å.

The structure of sample no. *1a* (Figs. 5b, 6c) is also layered, but the boundaries between the layers are not as sharp as in sample no. *1*. Moreover, the structure formed by regularly arranged and approximately identical columns is observed in the film. The column diameter is equal to 150–200 Å. The columns consist of crystal grains. The channels that manifest themselves as bright contrasts and disturb the layer homogeneity are clearly seen. The sizes of the bright contrasts are equal to ~5–10 Å. At a large magnification (Figs. 7a, 7b), it is seen that the columns have a twin structure and the crystal grain faces are tilted at different angles with respect to the substrate plane. This sample is characterized by the most regular structure built up of the columns separated by the regions corresponding to the vertical narrow contrasts.

Sample no. *2* has an irregular, weakly pronounced, layered structure, which most likely can be formed owing to growth processes during the sputtering of the film. No regular alternation of layers takes place in this weakly pronounced layered structure. The columnar structure is observed in sample no. *2*. However, unlike sample no. *1a*, the columns occur as irregular inclusions. The boundaries of the columns are considerably sharper than those in the above samples. The crystal grains forming the columns are clearly seen. The sizes of these grains, like the column diameter, vary in a wide range from 30 to 300 Å.

In sample no. *3* prepared under dynamic conditions, the observed layered structure is amorphous and involves Co and Cu individual clusters 30–50 Å in size. The layer thicknesses are substantially smaller than those in the other samples. No vertical contrasts and crystal grains are found.

Relation between the magnetic characteristics and the structure of samples. Let us analyze the relation between the magnetic properties of the samples and the characteristics of their transverse structure. The magnetization of sample no. *3* composed of Co and Cu individual particles is isotropic and proportional to the magnetic field. Despite the layered structure, the magnetization is determined only by the paramagnetic susceptibility of these particles due to the absence of the interparticle interaction. The physical parameters of sample nos. *1* and *1a* are close to each other. The sole difference resides in the fact that the FMR spectrum of sample no. *1* at the perpendicular orientation of the

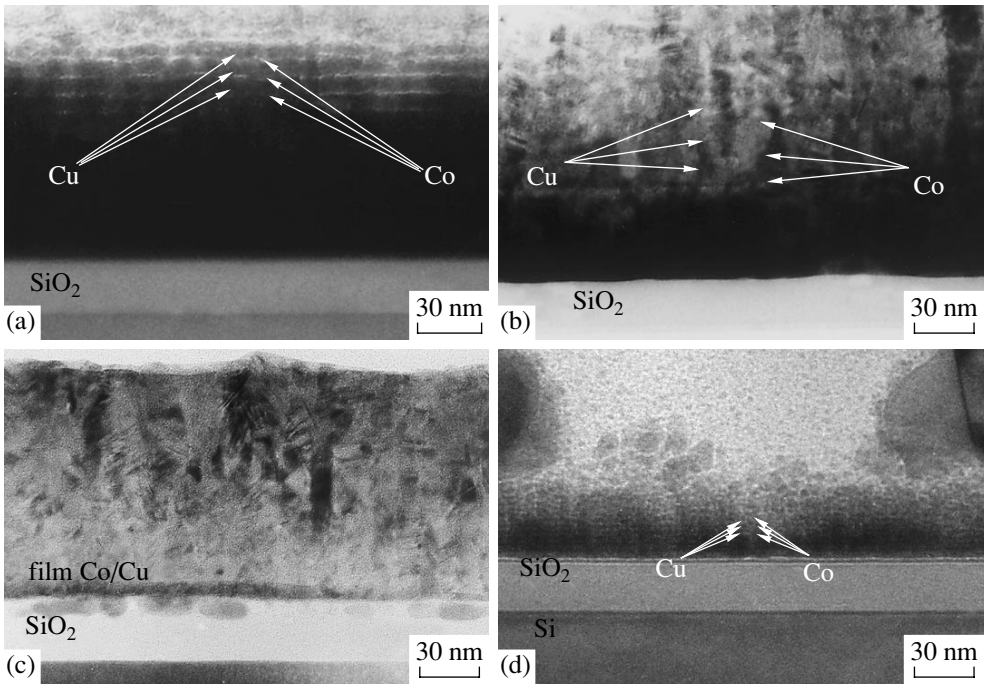

Fig. 5. Micrographs of cross-sectional cleavages of sample nos. (a) *1*, (b) *1a*, (c) *2*, and (d) *3* on the Si/SiO_2 substrate. Film layers with dark-field and bright-field contrasts correspond to copper and cobalt, respectively.

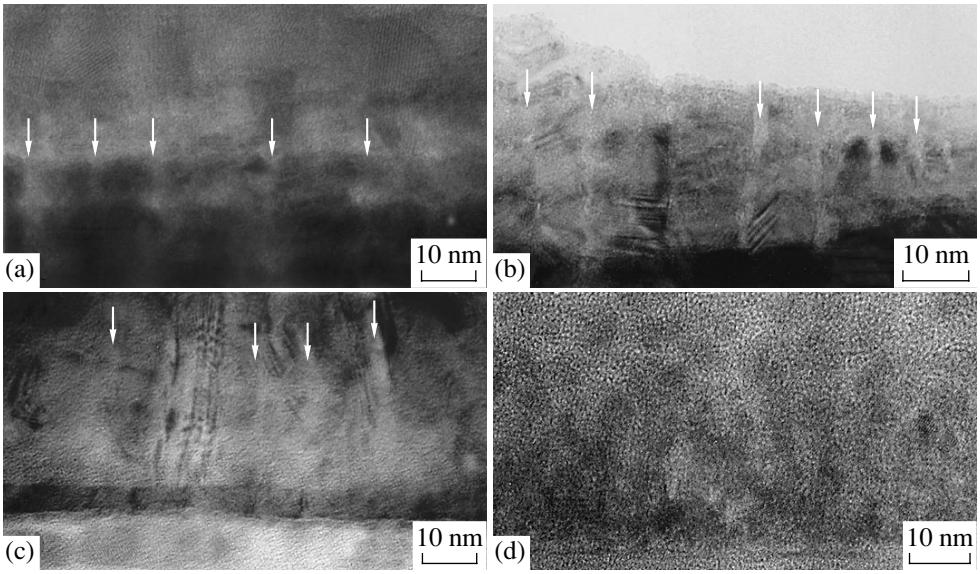

Fig. 6. Micrographs of cross-sectional cleavages of sample nos. (a) *1*, (b) *2*, (c) *1a*, and (d) *3* at a larger magnification.

magnetic field exhibits additional resonance lines located at regular intervals. Structurally, sample no. *1* differs from sample no. *1a* in that it has a sharper boundary between the layers and a less pronounced columnar structure. Owing to the well-defined columnar structure of sample no. *1a*, the FMR line measured in the perpendicular geometry is broadened and the additional resonance lines cannot be observed. Unlike sample nos. *1* and *1a*, only four layers with different thicknesses can be distinguished in sample no. *2*. The columns are represented by randomly oriented crystal grains. Most likely, as a result, the lines observed in the perpendicular configuration and located at irregular intervals are not the uniform resonance lines and the FMR line width for this sample is one order of magnitude less than those for sample nos. *1* and *1a*.

The question as to the occurrence of narrow resonance lines in the spectrum of the inhomogeneous

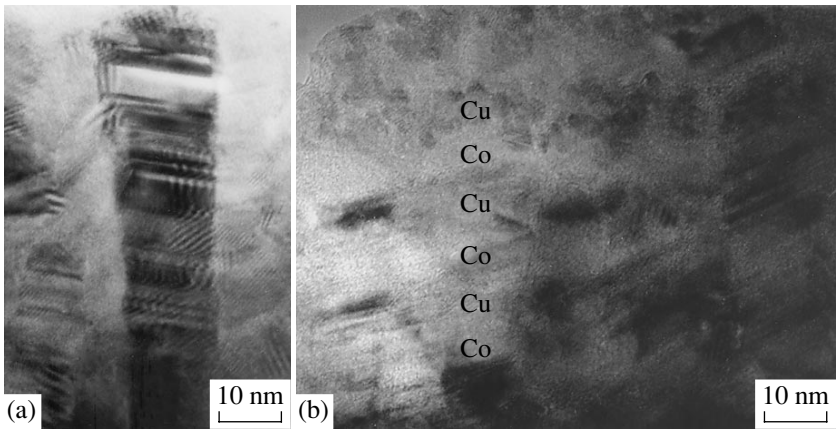

Fig. 7. Micrographs of two characteristic regions of cross-sectional cleavage of sample no. *1a* with (a) a columnar structure composed of twinned grains and (b) grain boundaries tilted with respect to the substrate plane.

structure remains open. Note that these lines in the spectra of the high-quality layered films at an orientation of the magnetic field that is close to the perpendicular orientation become strongly broadened and disappear at $\theta_H = 0$. As far as we know, research dealing with the observation of the FMR spectra of multilayer structures in the perpendicular geometry is lacking. In our earlier work [6], an attempt to observe these spectra for [Fe/Cr]*n* films also failed. Taking into account the results obtained in the present work, this can be associated with the formation of the columnar structure. Owing to the strong angular dependence of the location of the FMR lines at orientations of the magnetic field close to the perpendicular orientation, even an insignificant misorientation of crystal grains in the adjacent magnetic layers can lead to a substantial broadening of the FMR lines.

Specific structural features of the layered structures and their effect on the magnetic properties of the studied films. Investigation into the morphology of the prepared structures has revealed that the results of the magnetic measurements of multilayer films should be interpreted with due regard for the following specific features. First, the interlayer thickness under the same sputtering conditions can vary with an increase in the number of layers. Second, the formation of the columnar structure leads to the necessity of allowing for the number and width of the inhomogeneities within the layer. Third, there is a scatter in the directions of the uniaxial anisotropy field in different layers. Furthermore, the samples can contain noninteracting nanoparticles and each nanoparticle has a giant magnetic moment. At sufficiently small thicknesses of magnetic layers, the film consists of a mixture of these particles.

The aforementioned specific features can affect the magnetic characteristics as follows. For the spectra in the perpendicular configuration, the occurrence of the layered structure results in the appearance of additional resonance lines located at regular intervals at magnetic fields lower than the field of the uniform resonance (sample no. *1*). In the case of the columnar structure formed by crystal grains, the line width in these spectra can appreciably increase, because the planes of crystal grains are not parallel to the substrate plane (sample no. *1a*). In this case, each layer is characterized by discontinuities due to the columnar structure of the films. The formation of irregular layers can lead to the appearance of nonuniform FMR resonance lines with a width that is considerably less than that of a uniform resonance line.

CONCLUSIONS

The results of the above investigation allowed us to draw the following inferences regarding the influence of the structure on the magnetic characteristics of the multilayer films.

(i) The *g* factors for all the samples are determined to be $g = 2.0 \pm 0.05$, which differs from the value $g = 2.2$ obtained in [9, 10]. The coincidence of the *g* factors for all the samples indicates that this parameter, as well as the magnetization, is less dependent on the structure as compared to the other FMR parameters.

(ii) The K_{eff} values determined from the FMR data agree with those obtained from the experimental data on the static magnetization and are governed by the thickness of the nonmagnetic interlayer.

(iii) Owing to the strong angular dependence of the location of the FMR lines at orientations of the magnetic field close to the perpendicular orientation, the misorientation of crystal grains with respect to each other in columns leads to a significant broadening of the FMR lines.

(iv) The FMR spectrum of the strongly inhomogeneous sample at the perpendicular orientation of the magnetic field exhibits several narrow resonance lines that are not uniform FMR resonance lines. Possibly, the observed lines are the nonuniform resonance lines asso-

ciated with the presence of layers that are nonuniform in thickness.

ACKNOWLEDGMENTS

This work was supported by the Russian Foundation for Basic Research (project no. 00-02-17162) and the Program "Russian Universities" of the Ministry of Education of the Russian Federation.

REFERENCES

1. M. N. Baibich, J. M. Broto, A. Fert, *et al.*, Phys. Rev. Lett. **61**, 2472 (1988).
2. S. S. P. Parkin, Z. G. Li, and D. J. Smith, Appl. Phys. Lett. **58**, 2710 (1991).
3. B. Heinrich and J. F. Cochran, Adv. Phys. **42**, 523 (1993).
4. E. J. Puik, M. J. van der Wiel, H. Zeijltemaker, and J. Verhoeven, Appl. Surf. Sci. **47**, 251 (1991).
5. S. P. Vemon, D. G. Stearns, and R. S. Rosen, Appl. Opt. **32**, 6969 (1993).
6. A. B. Drovosekov, O. V. Zhotikova, N. M. Kreĭnes, *et al.*, Zh. Éksp. Teor. Fiz. **116**, 1817 (1999) [JETP **89**, 986 (1999)].
7. Z. J. Wang, S. Mitsudo, and K. Watanabe, J. Magn. Magn. Mater. **176**, 127 (1998).
8. C. Chappert, K. L. Dang, P. Beauvillain, *et al.*, Phys. Rev. B **34**, 3192 (1986).
9. B. Heinrich, J. F. Cochran, M. Kowalewski, *et al.*, Phys. Rev. B **44**, 9348 (1991).
10. P. E. Wigen and Z. Zhang, Braz. J. Phys. **22** (4), 267 (1992).
11. S. Fraim, in *Ferromagnetische dünne Schichten* (Berlin, 1963; Mir, Moscow, 1964), p. 264.
12. R. P. van Stapele, F. J. A. M. Greidanus, and J. W. Smits, J. Appl. Phys. **57**, 1282 (1985).
13. A. B. Drovosekov, N. M. Kreĭnes, V. F. Meshcheryakov, *et al.*, Pis'ma Zh. Éksp. Teor. Fiz. **67**, 690 (1998) [JETP Lett. **67**, 727 (1998)].
14. D. T. Pierce, J. Unguris, R. J. Celotta, and M. D. Stiles, J. Magn. Magn. Mater. **200**, 290 (1999).

Translated by O. Borovik-Romanova

Crystallography Reports, Vol. 47, No. 6, 2002, pp. 1072–1075. Translated from Kristallografiya, Vol. 47, No. 6, 2002, pp. 1144–1148.

CRYSTAL GROWTH

On the Thermodynamics of Homogeneous Crystal Nucleation

E. B. Treĭvus

Institute of the Earth's Crust, St. Petersburg State University,
Universitetskaya nab. 7/9, St. Petersburg, 199034 Russia
e-mail: treivus@cryst.geol.pu.ru

Received February 8, 2002

Abstract—A correct phenomenological consideration is given to the change in the Gibbs thermodynamic potential in the course of crystal nucleation. It is proved that this process is described by two activation barriers.

There is a great number of works devoted to the thermodynamic investigation of crystal nucleation. Although the first investigations in this direction were performed by J.W. Gibbs almost 125 years ago, the problem remains topical up to now. However, the discrepancy observed in the results obtained and their insufficiently adequate presentation call for further investigation. In this respect, we attempted to take a fresh look at this problem in the framework of macroscopic thermodynamics.

The initial stage of crystal nucleation can be considered in terms of two concepts. According to the first concept, even initially formed particles have a regular crystal structure. This implies that an accidental approach of a number of atoms constituting a nucleus proceeds rather slowly and they immediately form a crystal building. In other words, no chaotic aggregates of atoms, which, hereafter, will be referred to as clusters, are formed within this concept of the nucleation.

Crystals should have rounded apices and rounded edges due to the thermal smoothing of these surface elements. The edges of a real crystal cannot be formed by individual rows of atoms, and its apices cannot be represented by single atoms. The edges of microcrystals were treated as rounded even by Gibbs [1]. The higher the temperature of the crystal and the closer the temperature to the melting point of a particular compound, the more pronounced the above smoothing. Note that the smoothing in solutions, which will be considered in the present work, is expected to be stronger than that in vapors. The degree of smoothing should depend on the nature of a given material and, apparently, should increase with an increase in its solubility. The size of curved segments considerably exceeds sizes of individual atoms.

According to the Gibbs–Curie principle [2], the rounding of crystal nuclei is even more probable in the case when their surface energy is characterized by a relatively weak anisotropy. The rounding should be especially pronounced under conditions of crystal nucleation in solutions at temperatures close to their melting point and in melts.

The pressure in the crystal nucleus with planar faces and sharp edges should be equal to the pressure of an environment [3]. However, the pressures in two phases in contact are different if they have a curved interface. Therefore, the pressure in the crystal should be higher than that in the surrounding solution when planar surface regions of the nucleus are small in area. Taking into account the possible scale of the edge smoothing, the size of the crystal nucleus with an increased pressure most likely does not exceed ten nanometers.

The crystal nucleation can be described in another way. An accidental approach of atoms constituting an original nucleus occurs so rapidly that these atoms at the initial stage of nucleation have no time to form a crystal and the nucleus can be represented as an amorphous liquidlike particle (cluster). Only with time, this cluster begins to transform into the crystal. At present, the existence of clusters in supersaturated solutions can be considered proved by numerous investigations [4–7]. Clusters decay and arise again and, probably, initially have a diffuse interface. However, they exist for a physically appreciable time. Only a small number of the clusters transform into crystals. It is currently believed that crystal nucleation in solutions most probably proceeds through the cluster mechanism.

By virtue of its amorphism, a cluster should be spherical in shape. Therefore, as in the crystal subnucleus with rounded edges, the pressure in the cluster should be higher than that in the surrounding solution.

According to the most frequently used technique of thermodynamic analysis of new-phase nucleation, which goes back to Gibbs, the internal region of the nucleus and its surface layer are treated as a single system. With due regard for the increased pressure in submicroscopic particles, the equilibrium internal state of this system at a constant temperature is described by the equation [8, p. 320]

$$Sd\sigma = Vdp - md\mu, \quad (1)$$

where S, V, and m are the surface area, volume, and mass of the particle, respectively. The quantities σ, p, and μ under the differential sign are the surface tension, pressure, and chemical potential of the particle. Unlike the equation in [8], Eq. (1) for simplicity is written for a single-component material.

Although the crystal nucleus is rounded, it is not a sphere. However, we assume that the nucleus is a sphere with a certain mean radius of curvature r. As applied to this nucleus, Eq. (1) can be rearranged into the form

$$3\sigma' = rp' - \frac{r}{\Omega}\mu', \tag{2a}$$

where the prime indicates the derivatives of the corresponding quantities with respect to r and Ω is the molar volume of the crystal. This equation also holds for the cluster.

For a larger sized nucleus in the form of a faceted crystal, the influence of the curvature of edges and apices can be ignored and the pressure in the crystal is equal to the pressure in the environment. For simplicity, it is assumed that, in this case, the nucleus is a cube with the edge length r. For this nucleus, we have

$$p' = 0; \quad \mu' \approx \sigma' \approx 0. \tag{2b}$$

As a rule, the crystal nucleation is considered on the basis of the Gibbs thermodynamic potential G. The increments of this potential ΔG and its differential $d\Delta G$ in the course of nucleation of a new phase were rigorously derived by Rusanov [8] in the form

$$\Delta G = (p_l - p)V - (\mu_l - \mu)m + \sigma S, \tag{3a}$$

$$d\Delta G = (p_l - p)dV - (\mu_l - \mu)dm + \sigma dS. \tag{3b}$$

Here, the subscript l indicates that the corresponding quantity refers to the solution.

Equations (3) are the simplified variants of the corresponding relationships obtained in [8], because they are written under the assumption that the volume of the system is considerably larger than the nucleus volume. This means that the chemical potential μ_l of the crystallized compound in the solution remains constant during the crystal nucleation and is equal to the chemical potential of the initial homogeneous medium.

In Eqs. (3), the term associated with the difference between the pressures in the medium and the crystal nucleus is usually omitted (see, for example, [2, 9]). Note that authors ignoring this difference do not justify this approach. In particular, Nishioka and Maksimov [9] examined crystal nuclei in the form of spherical clusters. They noted that the chemical potential of a compound depends on the pressure, but the corresponding term in the equation describing the change in the thermodynamic potential of the nucleus was absent.

The relationship similar to formula (3b) for crystal nucleation was derived by Semenchenko [10], and the expression for ΔG was obtained by Skripov and Koverda [11]. The authors of these works allowed for the pressure difference by considering a flat-faced nucleus. However, this requires an explanation. Let us now assume that the crystal is so small that it can be represented as a surface layer. As was noted above, if this crystal had sharp edges, the pressure in the crystal would be equal to that in the surrounding medium. Gibbs [1] assumed that the pressures in the crystal nucleus and the solution are equal to each other. He accounted for the pressure difference only in the case of the "isotropic" nucleus phase, which was treated as an amorphous material whose particles were characterized by a radius of curvature. The difference between the pressures in the crystal and liquid phases can be explained only within the concept described above.

It is necessary to analyze, if only qualitatively, the dependence of the surface tension of the crystal nucleus on its size. In [6, 12], under the assumption that the crystal nucleus at the early stage is the cluster, this dependence was described by the Tolman equation, which was derived for an equilibrium liquid droplet. As follows from this equation, the surface tension σ monotonically increases from zero to a certain asymptotic value with an increase in the radius of curvature of the particle. However, the dependence of the surface tension of the nucleus on the nucleus size varying in a wide range should be more complex in the case of both the crystal subnucleus and the cluster.

Let the initial crystal nucleus be so small that the entire nucleus surface is thermally smoothed and faces are absent. As long as the nucleus grows, remaining in this state, the curvature of the nucleus surface decreases and the surface tension increases ($\sigma' > 0$) [8]. The edges and apices of the crystal have an increased surface energy. We assume that they make a certain contribution to the surface tension σ; i.e., the value of σ in Eqs. (3) is the surface tension averaged over the crystal. At a certain growth stage, the faces arise in the crystal and a decrease in the contribution from the energy of the edges and apices leads to a decrease in the mean surface tension of the crystal ($\sigma' < 0$) [8]. With further crystal growth, the surface tension asymptotically tends to a limiting value ($\sigma' \approx 0$) even at small radii r, because the contribution of the apices and edges rapidly becomes insignificant. The same behavior of the dependence of the surface tension σ should be observed in the case when the crystal nucleus at the initial stage is the cluster. Actually, the surface energy of the cluster is higher than that of the real faces of the crystal formed from the cluster. The aforementioned dependence of the surface tension of the crystal nucleus is displayed in Fig. 1a. Undeniably, this dependence is obtained under the conditions that the temperature, pressure, and concentrations of solution components remain unchanged. Note that the nucleus is a nonequilibrium formation. At the same time, the thermodynamic approach is restricted to the interpretation of the surface tension of the crystal that is in equilibrium with the medium.

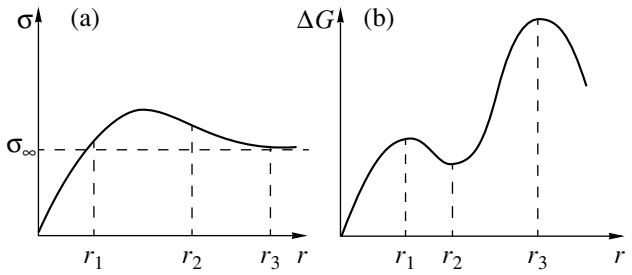

Fig. 1. The most probable dependences of (a) the surface tension and (b) the Gibbs thermodynamic potential for a crystal nucleus on the nucleus size.

Therefore, the thermodynamic inferences can be treated only as qualitative.

Equation (3b) has the following roots:

$$(p_1 - p_l)dV = \sigma_1 dS, \quad \mu_1 = \mu_l; \tag{4.I}$$

$$(p_2 - p_l)dV = (\mu_2 - \mu_l)dm + \sigma_2 dS; \tag{4.II}$$

$$p_3 = p_l, \quad (\mu_l - \mu_3)dm = \sigma_3 dS. \tag{4.III}$$

The first two roots correspond to the above spherical nucleus, and root (4.III) refers to the cubic nucleus. Therefore, relationships (4) can be rewritten in the form

$$p_1 - p_l = \frac{2\sigma_1}{r_1}, \quad \mu_1 = \mu_l; \tag{5.I}$$

$$p_2 - p_l = \frac{2\sigma_2}{r_2} + \frac{\mu_2 - \mu_l}{\Omega}; \tag{5.II}$$

$$p_3 = p_l, \quad \frac{\mu_l - \mu_3}{\Omega} = \frac{4\sigma_3}{r_3}. \tag{5.III}$$

Here, r_1 and r_2 are the sphere radii and r_3 is the edge length of the cube.

Conditions (5.I) were given in [8] without limitation imposed on the character of a new phase. Conditions (5.I) and (5.III) were obtained by Semenchenko [10], who applied them to describe the equilibrium of a faceted crystal with a medium. Root (5.I) for crystal nuclei was found in [11]. Volmer [13] revealed conditions (5.II) for a liquid droplet in a vapor. He used conditions (5.III) as a "further simplification" of Eq. (5.II) [13] and, without any assumptions, changed over to analysis of the crystal nucleation. In other works (see, for example, [2, 14]), consideration was given only to conditions (5.III) as corresponding to the potential G at a maximum and a critical crystal nucleus without mention of the other roots of Eq. (3b). This is the most widely used variant of analysis of crystal nucleation. Note that Gibbs [1] treated only the flat-faced nucleus corresponding to conditions (5.III).

Substitution of conditions (5) into Eq. (3a) gives the relationships

$$\Delta G_1 = (4/3)\pi r_1^2 \sigma_1; \tag{6.I}$$

$$\Delta G_2 = (4/3)\pi r_2^2 \sigma_2; \tag{6.II}$$

$$\Delta G_3 = 2r_3^2 \sigma_3. \tag{6.III}$$

It is seen from these expressions that, in all three cases, the increment ΔG is positive and does not depend on the relation between σ and r. Therefore, the increment ΔG cannot be negative. The negative values of ΔG found in [6, 12] are explained by the fact that the authors took into account the dependence of the surface tension σ on the size r by assuming that the chemical potential μ of the nucleus is constant. However, these quantities are related to each other by Eq. (1).

Therefore, the dependences of ΔG on r exhibits three particular points, which can be either inflection points or extrema. It is evident that their character can be revealed by examining the second differential of ΔG. As far as we know, only Rusanov [8] considered $d^2\Delta G$ and analyzed only conditions (5.I). Hereafter, for brevity, we will manipulate with the second derivative of ΔG.

For the spherical subnucleus, we have

$$\Delta G'' = 8\pi(p_l - p)r - \frac{8\pi}{\Omega}(\mu_l - \mu)r + 8\pi\sigma - 4\pi r\left(rp' - \frac{r}{\Omega}\mu' - 2\sigma'\right). \tag{7}$$

Substitution of relationship (2a) into this equation leads to the expressions

$$\Delta G'' = 8\pi(p_l - p)r - \frac{8\pi}{\Omega}(\mu_l - \mu)r + 8\pi\sigma - 4\pi r\sigma'. \tag{8}$$

With due regard for relationships (2b), for the cubic faceted nucleus, we find

$$\Delta G'' = \frac{6r}{\Omega}(\mu_l - \mu) + 12\sigma. \tag{9}$$

Substituting roots (5.I) and (5.II) into Eq. (8) gives

$$\Delta G_1'' = -16\pi\sigma_1 - 4\pi r_1\sigma_1'; \tag{10.I}$$

$$\Delta G_2'' = -16\pi\sigma_2 - 4\pi r_2\sigma_2'. \tag{10.II}$$

Let us consider root (5.III). In this case, the equality of the pressures means that the nucleus is already flat faced and relatively large. Consequently, root (5.III) corresponds to the nucleus with the maximum size. According to the second condition for root (5.III), the inequality $\mu_3 < \mu_l$ is satisfied, because the other variables in this expression are positive. After substitution

of this root (5.III) into Eq. (9), we obtain

$$\Delta G'' = \frac{3r_3}{\Omega}(\mu_3 - \mu_l). \quad (10)$$

Since we have $\mu_3 < \mu_l$, the maximum of ΔG takes place in the case of root (5.III).

Now, we examine roots (5.I) and (5.II). Since root (5.III) is associated with the maximum of ΔG, roots (5.I) and (5.II) [or (5.II) and (5.I)] correspond either to ΔG at a maximum and a minimum or to inflection points in the dependence of ΔG. We make the sole assumption that one of these roots falls in the range of spherical-nucleus sizes in which $\sigma' > 0$. This implies that the corresponding root indicates the maximum of ΔG. Two maxima should be separated by a minimum. Consequently, the other root is associated with this minimum, which most likely lies in the range of the sizes r in which $\sigma' < 0$.

The other variant is the occurrence of two inflection points in the dependence of ΔG below the maximum corresponding to conditions (5.III). In this case, the values of $\Delta G_1''$ and $\Delta G_2''$ should be equal to zero. This imposes rigid limitations on the quantity σ', which cannot be explained physically.

The first activation barrier corresponds to the transformation of either the rounded crystal to the faceted crystal or the cluster to the crystal nucleus and, probably, has a relatively small height. In the former case, the barrier height should strongly depend on the degree of the thermal smoothing of apices and edges. This barrier should be lower than the barrier described by conditions (5.III) (Fig. 1b).

Two barriers in the thermodynamic potential for crystal nucleation were also found by Pervushin [15] with the use of statistical thermodynamics. Moreover, the computer simulation of a change in the Gibbs thermodynamic potential during crystal nucleation also revealed that the number of these barriers should be more than one [16]. These data confirm the validity of the results of the aforementioned phenomenological analysis of this potential.

CONCLUSION

Thus, it was demonstrated that the term associated with the difference between the pressures in the initial crystal nucleus and the environment cannot be ignored in the equation that describes the dependence of the Gibbs potential on the size of the nucleus, irrespective of whether it has a regular crystalline or amorphous structure. With allowance made for this term, the equation for the differential of the change in the Gibbs potential has three roots. This indicates that the crystal nucleation is characterized by two activation barriers rather than by one barrier.

ACKNOWLEDGMENTS

This work was supported by the Russian Foundation for Basic Research, project no. 00-05-65183.

REFERENCES

1. J. W. Gibbs, *The Scientific Papers*, Vol. 1: *Thermodynamics* (Dover, New York, 1961; Nauka, Moscow, 1982).
2. A. A. Chernov, in *Modern Crystallography*, Vol. 3: *Crystal Growth*, Ed. by B. K. Vainshtein, A. A. Chernov, and L. A. Shuvalov (Nauka, Moscow, 1980; Springer-Verlag, Berlin, 1984), p. 3.
3. A. I. Gusev and A. A. Rempel', *Nanocrystalline Materials* (Fizmatgiz, Moscow, 2001).
4. É. M. Kol'tsova, A. V. Aganina, and L. S. Gordeev, Zh. Fiz. Khim. **74** (5), 888 (2000).
5. Y. Georgalis, A. M. Kiersek, and W. Saenger, J. Phys. Chem. **104** (15), 3405 (2000).
6. A. M. Askhabov, Tr. Inst. Geol., Ross. Akad. Nauk, Ural. Otd., Komi Nauchn. Tsentr, No. 107, 14 (2001).
7. E. B. Treĭvus, Kristallografiya **46** (6), 1114 (2001) [Crystallogr. Rep. **46**, 1039 (2001)].
8. A. I. Rusanov, *Phasengleichgewichte und Grenzflachenerscheinungen* (Khimiya, Leningrad, 1967; Academie, Berlin, 1978).
9. K. Nishioka and I. L. Maksimov, J. Cryst. Growth **163** (1–2), 1 (1996).
10. V. K. Semenchenko, *Selected Chapters of Theoretical Physics* (Prosveshchenie, Moscow, 1966).
11. V. P. Skripov and V. P. Koverda, *Spontaneous Crystallization of Supercooled Liquids* (Nauka, Moscow, 1984).
12. M. A. Larson and J. Garside, J. Cryst. Growth **76** (1), 88 (1986).
13. M. Volmer, *Kinetik der Phasenbildung* (Steinkopff, Dresden, 1939; Nauka, Moscow, 1986).
14. J. Nyvlt, O. Söhnel, M. Matuchova, and M. Broul, *The Kinetics of Industrial Crystallization* (Academia, Prague, 1984).
15. Yu. V. Pervushin, Zh. Fiz. Khim. **62** (4), 900 (1988).
16. T. N. Drebushchak, Author's Abstract of Candidate's Dissertation in Chemistry (Novosibirsk, 2000).

Translated by O. Borovik-Romanova

Crystallography Reports, Vol. 47, No. 6, 2002, pp. 897–900. Translated from Kristallografiya, Vol. 47, No. 6, 2002, pp. 967–970.

CRYSTALLOGRAPHIC SYMMETRY

Plane Decagonal Quasicrystals with 3-Coordinated Atoms

V. A. Chizhikov

Institute of Crystallography, Russian Academy of Sciences, Moscow, 119333 Russia
e-mail: chizhikov@ns.crys.ras.ru
Received March 19, 2002

Abstract—A plane decagonal tiling with 3-connected nodes, which is obtained by decorating the Penrose tiling, is proposed as the structure of a two-dimensional covalent quasicrystal. The mean energy of the atoms in the given structure, calculated using the model Tersoff potential for carbon, is found to be close to the energy of the atoms in fullerene. An octagonal tiling containing 3-connected nodes and even cycles only is also proposed. © *2002 MAIK "Nauka/Interperiodica".*

In 1979, the mathematician Rodger Penrose proposed a new class of plane aperiodic pentagonal tilings formed by rhombi with acute angles of $2\pi/5$ and $2\pi/10$ [1, 2]. This initiated discussions on the possibility of using this tiling in crystallography [3, 4]. It is therefore not surprising that in 1985, when decagonal phases were detected in Al–Mn and Al-Fe, the authors of this discovery ascribed them to Penrose tiling [5, 6]. The only way of connecting the Penrose tiling with the structure of a decagonal quasicrystal is to set a certain arrangement of atoms in the bulk and at the boundaries of the two rhombi forming the tiling, which play, in this case, a role similar to that of a unit cell in a crystal. In this paper, we apply this method to describe the structure of a hypothetical decagonal plane quasicrystal whose atoms, all have the same coordination number (three).

In order to obtain a 3-coordinated structure on a plane, we can divide the plane into triangles and place one atom in each triangle, assuming that only the atoms belonging to adjacent triangles are connected. The perfection of this structure depends on the ratio of the sides of the triangles. The structure of graphite in which the lengths of the bonds, as well as the angles formed by them, are identical corresponds to the division of the plane into equilateral triangles. Generally, the closer the triangles are to equilateral, the more perfect the structure. For this reason, to apply this method to the Penrose tiling we must divide the rhombi into triangles along the shorter diagonal. After completing this procedure, we obtain a tiling with 3-connected nodes, which is formed by pentagons, hexagons, and heptagons. Pentagons and heptagons are encountered in this structure with the same frequency by virtue of a general theorem analogous to the Euler relation for polyhedra [7]. This structure obtained from the Penrose tiling obviously possesses the decagonal symmetry of the crystallographic sense. Another method of obtaining a structure topologically equivalent to the given structure (except for the lengths of bonds and their directions) is the splitting of the Penrose tiling into Voronoi domains (the polygons in the present case) [3].

Let us consider the possibility of the existence of a natural quasicrystal whose structure is based on such a tiling. At present, many structures based on plane 3-connected nets are known [7]. Most structures of this type are based on a plane hexagonal lattice. Among such substances, we can find suitable materials for creating a decagonal 3-connected quasicrystal. It is well known that pentagon-heptagon pairs can be formed in graphite; such defects were observed, for example, in carbonic nanotubes. A plane carbonic structure formed only by pentagons and heptagons was also proposed [8]. Obviously, the energy of a decagonal carbonic structure will be "worse" than that of graphite. Another possibility is associated with substances having the structural formula A_2X_3, in which A atoms occupying the sites of a plane hexagonal lattice are connected through X atoms. Among such substances, we can mention B_2O_3 and As_2S_3 (mineral orpiment).

Let us consider the first case, when the nodes of a tiling are occupied by carbon atoms. In compliance with the above arguments, we specify the positions of the two nodes in each rhombus, each of which has three bonds: one with another node in the rhombus and two with the nodes in the adjacent rhombi (Fig. 1). For the sake of convenience, we will distinguish between the two types of nodes, *B* and *W*, which are presented by black and white circles, respectively, in the figure. Figure 2a shows a region of the Penrose tiling decorated by nodes in accordance with the rules illustrated in Fig. 1. All *W* nodes lie at the same distance x from the corresponding vertices of the rhombi; for this reason, these nodes form regular (shaded) pentagons. Parameter y is chosen so that all *BW* bonds have the same length. If we assume that the length of the edges of the initial rhombi is equal to unity, then $y = 1/\tau$, where $\tau = (\sqrt{5} + 1)/2$ is the golden mean. Henceforth, we assume that $x = 1/2$. The structure contains three types of bonds: *WW* =

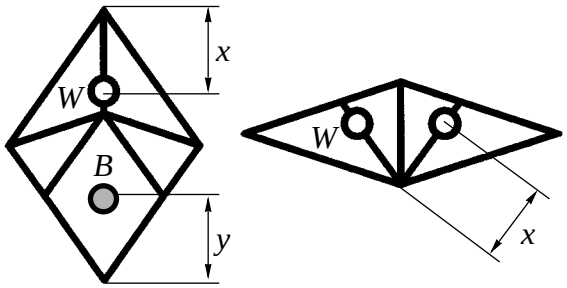

Fig. 1. Decoration by atoms belonging to the rhombi of the initial Penrose tiling. Lines indicate the edges of the rhombi and the inflation rules for Penrose tilings.

$2x\sin(2\pi/10) = (1/2)\sqrt{3-\tau}$, $BB = 2y\sin(2\pi/10) = (1/\tau)\sqrt{3-\tau}$, and $BW = 2\cos(2\pi/10) - x - y = 1/2$. A noticeable disadvantage of this structure is the considerable spread in the length of the bonds. This difference can be partly compensated, assuming that the atoms have a nonzero coordinate in the direction perpendicular to the plane. For this purpose, we raise or lower each *W* atom by $h = 1/(2\tau)$ depending on the orientation of the regular pentagon containing this atom. *B* atoms remain on the plane. In this case, the length of the *BW* bonds becomes equal to that of the *WW* bonds, and all hexagons *WWBWWB* become regular. In the structure obtained in this way (Fig. 2b), the angles formed by the bonds in most atoms are the same as in fullerene, while in the rest these angles are the same as in graphite. However, the lengths of the *BB* and *WW* (*BW*) bonds still differ significantly: $BB = (2/\tau)WW$. If we continue this geometrical analysis, this difference can probably be minimized at the expense of a certain spread in the angles.

However, we will confine our analysis to the relaxation structure, using the model interatomic Tersoff potential for carbon [9, 10]. To this end, we must preliminarily scale the tiling so that the distances between the bonds become typical of carbon. For example, we can assume that the length of the *WW*(*BW*) bond is equal to the atomic spacing in graphite (1.46 Å); in this case, the length of the rhombus edge is 2.48 Å. For the region of the structure for relaxation, we can choose, for example, a unit cell of a periodic approximant of the Penrose tiling. However, for this purpose it is more natural and methodically much more useful to use a rhombus of the Penrose tiling, e.g., a rhombus with an acute angle $2\pi/5$ to which the inflation operation is applied several times.

Here, we must explain the term inflation. Inflation of a tiling is one of the most frequently used methods for obtaining a quasi-periodic tiling. In this method, all figures of the given tiling are divided, according to certain rules, into similar smaller figures, after which the obtained tiling is inflated uniformly so that the figures constituting it acquire the initial size. Multiple applications of inflation make it possible to obtain arbitrarily large regions of a tiling starting from one or several unit

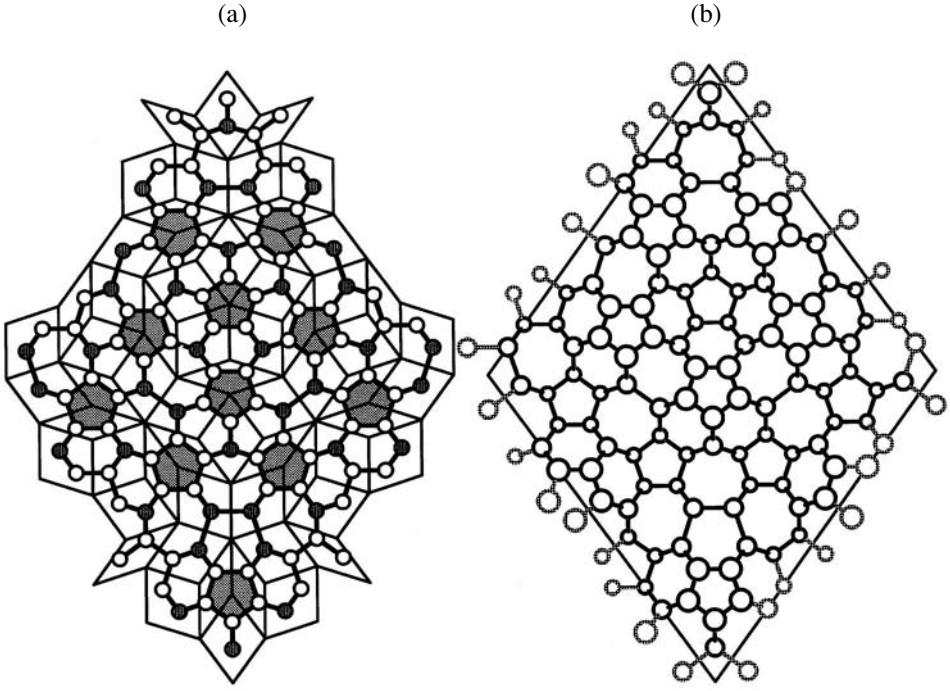

Fig. 2. (a) The rhombus obtained as a result of four-fold application of inflation to a unit rhombus of a Penrose tiling with an acute angle of $2\pi/5$, decorated by nodes in compliance with the rules depicted in Fig. 1. (b) The same rhombus decorated by atoms. All bonds for 110 atoms belonging to the rhombus, including those with atoms belonging to other rhombi, are indicated.

tiles. Lines in Fig. 1 show the inflation rules for the unit rhombi of the Penrose tiling. The rhombus in Fig. 2 is obtained from a unit rhombus with an acute angle of $2\pi/5$ as a result of four-fold inflation.

It can easily be seen that periodic boundary conditions are inapplicable to the rhombus depicted in Fig. 2. However, in this case we can use other boundary conditions, which will be conditionally referred to as quasi-periodic. These conditions are just the matching rules for rhombi in the initial Penrose tiling. According to these rules, the opposite sides of the rhombi are not matched as in the case of periodic boundary conditions, but adjacent sides are; for the given rhombus, these are the edges forming angles of $2\pi/5$. The use of a rhombus with quasi-periodic boundary conditions as an object for relaxation may have some disadvantages, which will be discussed below.

After the relaxation of the structure of the rhombus in Fig. 2b, which was carried out with the help of the Tersoff potential, we obtained the following results. The rhombus containing 110 atoms has an edge length of 17.14 Å. This corresponds to the length of the edge of a unit rhombus equal to 2.5 Å, which is approximately equal to the initially chosen value of 2.48 Å. The distances between neighboring atoms vary from 1.40 to 1.57 Å. The average length of the bond is 1.48 Å. In spite of the fact that some atoms have a "poor" energy of –6.27 eV, the average energy of the structure is –6.89 eV/atom. It should be mentioned, for comparison, that the energy of fullerene calculated with this potential is equal to –6.73 eV/atom (the numerical parameters of the potential were chosen so that the energy of graphite coincided with the experimental value of –7.40 eV/atom [10]).

We must now consider the applicability of quasi-periodic boundary conditions in our analysis. It should be noted above all that, using these boundary conditions, it is impossible to fill the plane with a single rhombus having an acute angle $2\pi/5$. In order to describe the entire structure, we need both rhombi of the Penrose tiling with angles $2\pi/5$ and $2\pi/10$. The relaxation of these rhombi must be carried out simultaneously so as to minimize the energy of the entire tiling as a whole. Here, we must take into account the frequency of the appearance of each rhombus and their common edges in the structure. In this paper, we confine our analysis to only a small region of the tiling, which, however, contains all main features of the entire structure.

The boundary conditions weakly affect the state of the atoms located at large distances from the boundaries if the size of the chosen spatial region is large enough. In the case of periodic boundary conditions, which are valid for a unit cell of the crystal, we can always carry out a parallel translation of the boundaries so that an arbitrarily chosen atom is at the center of a unit cell. This means that the energy of an individual atom in a crystal with a large unit cell weakly depends on the periodicity. On the contrary, the boundaries of the rhombi in the Penrose tiling cannot be displaced arbitrarily since it would lead to certain stresses in the structure. Such stresses must appear at the vertices of the rhombi, since the atoms located at these sites adjoin the equivalent atoms in adjacent rhombi. The positions of equivalent atoms belonging to different unit cells cannot be changed independently. In particular, this means that these atoms must have identical coordinates along the direction perpendicular to the plane. Fortunately, by virtue of the decoration method proposed by us here, it is advantageous from the energy viewpoint that the regular pentagons of atoms located at the vertices of the rhombi be parallel to the plane, which confirms the self-consistency of the approach used by us here.

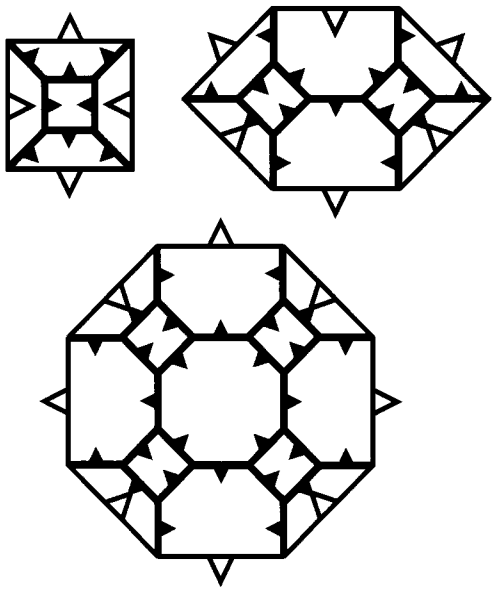

Fig. 3. Inflation rules for an octagonal tiling formed by squares, regular octagons, and equilateral hexagons with angles of 90° and 135°.

The structure with 3-coordinated atoms considered above contains, apart from hexagons, closed chains consisting of five and seven atoms. It was mentioned above that cycles of 5 and 7 atoms might be contained as defects in graphite and carbonic nanotubes. However, the formation of odd cycles is forbidden for a number of substances with 3-coordinated atoms. For example, in crystal with the general structural formula *AB* (boron nitride BN, GeS, SnS, etc.) this is due to the required alteration of the *A* and *B* atoms. In this case, cycles of 4 and 8 atoms should be introduced as defects. An increase in the number of such defects may obviously elevate the macroscopic symmetry of the structure, e.g., to the octagonal symmetry.

By way of an example, let us consider an octagonal tiling composed of squares, regular octagons and equilateral hexagons with angles of 90° and 135°; the infla-

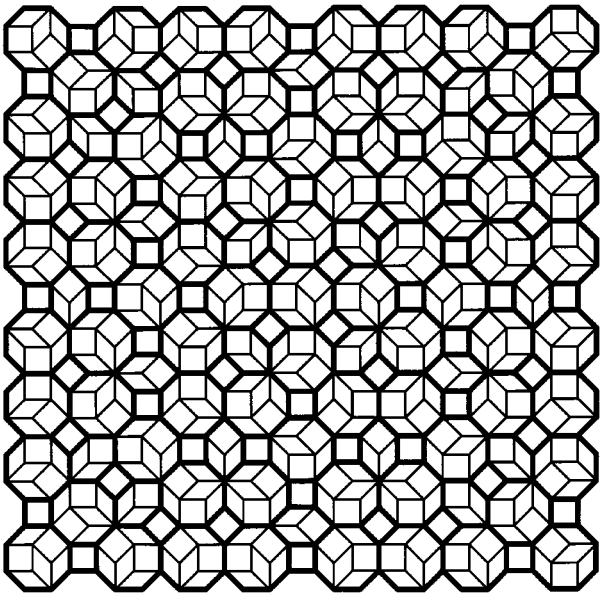

Fig. 4. A region of an octagonal tiling with 3-connected nodes, obtained according to the inflation rules presented in Fig. 3. Thin lines show the Ammann-Beenker tiling.

tion rules for such a structure are illustrated in Fig. 3. The splitting of figures occurs in accordance with their orientations in the plane, which are depicted with the help of auxiliary triangles plotted on their sides. The inflation coefficient $\alpha = (1 + \sqrt{2})$.

The obtained tiling has an octagonal macroscopic symmetry and is formed by figures with an even number of sides connected in triples at each vertex of the tiling (Fig. 4). Squares and octagons are encountered with equal frequency by virtue of the above-mentioned principle [7]. The numbers of octagons and hexagons n_o and n_h are connected through the relation $n_o/n_h = (4 + 2\sqrt{7})/3 \approx 3.097$. It is interesting to establish the relation between the given tiling and other octagonal tilings. Hexagons and octagons can be split in such a way that they form a tiling consisting of squares and rhombi with acute angles of 45°. Such a splitting lowers the symmetry of the initial figures (the symmetry of a hexagon is lowered by half and that of octagon by a factor of 8). Consequently, using different splitting modes, one can obtain an infinitely large number of different tilings, including the well-known Ammann-Beenker octagonal tiling (see Fig. 4) [11, 12].

ACKNOWLEDGMENTS

The author thanks V.E. Dmitrienko, M. Kleman, and F. Mauri for helpful discussions. This study was supported financially by Centre National de la Recherche Scientifique (France) (CNRS-RAS agreement, project no. 4058) and the Russian Foundation for Basic Research, project no. 02-02-16275-a.

REFERENCES

1. R. Penrose, Math. Intell. **2**, 32 (1979).
2. M. Gardner, *Penrose Tile to Trapdoor Ciphers* (Freeman, New York, 1989; Mir, Moscow, 1993).
3. A. L. Mackay, Kristallografiya **26** (5), 910 (1981) [Sov. Phys. Crystallogr. **26**, 517 (1981)].
4. A. L. Mackay, Physica A (Amsterdam) **114**, 609 (1982).
5. L. Bendersky, Phys. Rev. Lett. **55** (14), 1461 (1985).
6. K. K. Fung, C. Y. Yang, Y. Q. Zhou, *et al.*, Phys. Rev. Lett. **56** (19), 2060 (1986).
7. A. Wells, *Structural Inorganic Chemistry* (Clarendon, Oxford, 1984; Mir, Moscow, 1987), Vol. 1.
8. V. H. Crespi, L. X. Benedict, M. L. Cohen, and S. G. Louie, Phys. Rev. B **53** (20), R13303 (1996).
9. J. Tersoff, Phys. Rev. B **37** (12), 6991 (1988).
10. J. Tersoff, Phys. Rev. Lett. **61** (25), 2879 (1988).
11. F. P. M. Beenker, Eindhoven Univ. Technical Report 82-WSK-04 (1982).
12. R. Ammann, B. Grunbaum, and G. C. Shephard, Discrete Comput. Geom. **8**, 1 (1992).

Translated by N. Wadhwa

Crystallography Reports, Vol. 47, No. 6, 2002, pp. 901–906. Translated from Kristallografiya, Vol. 47, No. 6, 2002, pp. 971–975.

THEORY OF CRYSTAL STRUCTURES

Planar Complication Schemes of Binary Ratios

N. L. Smirnova

Moscow State University, Vorob'evy gory, Moscow, 119899 Russia

Received January 10, 2002

Abstract—The planar and linear complication schemes are constructed for the compositions corresponding to the phase diagram of $BaO : BiO_{1.5}$, the compositions of borate radicals, the symbols of reflections with the intensity 100, the symbols of simple forms, the symbols of planes with a high density of atoms in planar bilayer structures, the theoretical and realized formulas of binary compounds, and the ratios between the chemical coefficients of two different cations in oxides. The schemes of silicate and borate radicals are compared. It is confirmed that the binary ratios obey the law of small numbers. *© 2002 MAIK "Nauka/Interperiodica".*

As was shown earlier in [1], in any system, there exist attributes according to which it is possible to separate essentially different constituents that are different in rank and whose combinations can represent all objects of a four-level system. Goldschmidt [2] proposed to use four series as four constituents that are most probably realized in the planar complication scheme. The planar complication scheme is constructed using the Weiss law. According to this law, a new symbol of the zone, for example, 12, is formed using the term-by-term summation of two initial symbols 11 and 01, namely, 1 + 0 = 1 and 1 + 1 = 2. Moreover, Goldschmidt introduced a shift of new elements downward by a step. In our previous work [3], the thus obtained system of ratios between mutually prime numbers was, on the one hand, simplified (we used only half the scheme and removed repeated ratios) and, on the other hand, complicated (we introduced the ratios between numbers involving the greatest common divisors). As a consequence, we derived the system of ratios between arbitrary numbers. The complication included the addition of exponents (n = 2, 3, 4, …) to each ratio. Numbers involved in the ratios between mutually prime numbers should be multiplied term by term by these exponents. For example, $11^{1, 2, 3, 4}$ means the ratios 11, 22, 33, and 44 (1 : 1, 2 : 2, 3 : 3, and 4 : 4). In the planar complication scheme, the exponents exist in an implicit form and are given only for the realized ratios.

Goldschmidt believed that it would make no sense to consider symbols of the fifth and higher series. In [3], we analyzed most, if not all, the symbols. As a result, we established the regularities of the formation of arithmetic series and Fibonacci sequences and revealed the furcation (differentiation–integration) points. The application series were represented in the form of arithmetic sequences with the least initial terms and small differences. Therefore, many specific features discussed in Goldschmidt's work manifested themselves in the planar complication scheme. Goldschmidt would have found them by himself if his consideration had not been restricted to the realization of four series in the planar complication scheme.

In this work, we constructed the planar complication scheme for the compositions of the phase diagram of $BaO : BiO_{1.5}$ (Fig. 1), which was investigated by three methods [4]. We obtained the ratios (formulas) for 19 phases identified by electron microscopy, 17 phases determined by visual polythermal analysis, and 10 phases revealed by differential thermal and thermogravimetric analyses. As can be seen from the planar complication scheme (Fig. 2a), electron microscopy, visual polythermal analysis, and differential thermal and thermogravimetric analyses identified phases up to the twelfth, eighth, and sixth series, respectively. The first three series are filled completely. The bifurcation points are as follows: 12, 13, 23, and 34. The sequences of layers containing Ba or only Bi atoms were found for four phases in [4]. Let us designate the layers composed of Ba atoms by the letter *k* and the layers comprised of Bi atoms by the letter *g*. Then, for the compositions 11, 45, 49, and 13, we obtain the sequences *kg*, $(kg)_3kgg$, *kggkgkggkgggg*, and *kggkgggg*, which are described by the Zhdanov formulas 2, 2223, 3235, and 35. The sequences consist of the previously found dominant modules *kg* and *kgg* and the recessive module *kgggg* (or 2, 3, and 5).

In order to assign silicates to subclasses, Bokiĭ [5] proposed to use the binary ratios Si : O. The formulas obtained in [5] are represented in the planar complication scheme (Fig. 2b). By analogy with silicates, for borates, we determined the ratios B : (O + OH), B : O, and O : OH (Fig. 2b). Compared to silicates, the ratios for borates vary in a considerably wider range. Silicate radicals virtually do not contain OH groups, whereas the O : OH ratio in borates varies from 10 to 0.1. The Si : O ratio in silicates changes from 1 : 2 to 1 : 4, while the B : (O + OH) ratio in borates varies in a wider range

1063-7745/02/4706-0901$22.00 © 2002 MAIK "Nauka/Interperiodica"

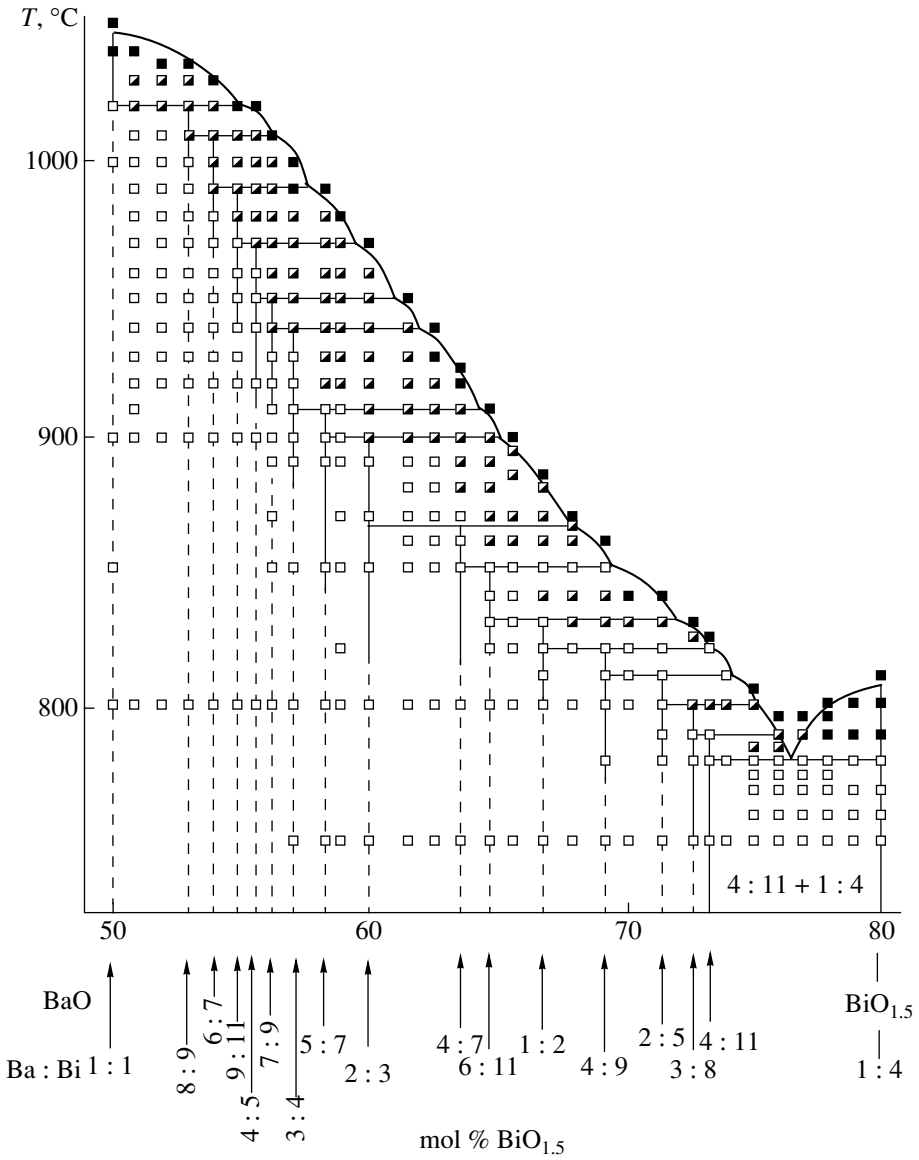

Fig. 1. Phase diagram of BaO : $BiO_{1.5}$ according to visual polythermal analysis [4]. Squares are the experimental points.

(from 8 : 11 to 2 : 7). At the same time, the number of the Si : O ratios in silicates is equal to 25, whereas the number of the B : (O + OH) ratios in borates is equal to 18, i.e., is smaller, even though silicate radicals contain only O atoms, while borates involve O atoms and OH groups.

When analyzing the formulas (symbols) of the faces of simple forms and the formulas of reflections (symbols of reflections with the intensity 100) in our earlier work [3], we did not consider many formulas involving numbers larger than nine. For completeness of the pattern, all the formulas previously omitted are included in the planar complication scheme (Fig. 2c). The first five series of the planar complication scheme are filled by the formulas of reflections and faces. Then, as before, the formulas occur when going along arithmetic series. The longest series have the form 110(010), 120, 130, …, and 120(110), 230, 340, …. It is easy to separate several shorter series. The former series is fused (without gaps) to the formula 1.12.0. Then, the series involves gaps. The range of new realized formulas is regularly complemented when going along arithmetic sequences in the nearest series. Reflections with orders larger than unity are not given in the planar complication scheme. In this respect, we present them as a linear complication series. This series can be obtained by projecting the formulas of the planar complication scheme onto a line. The curly, square, and slant brackets are used for the formulas of the first four, fifth, and sixth series, respectively. The exponents are written in angle brackets. The linear complication series obtained is as

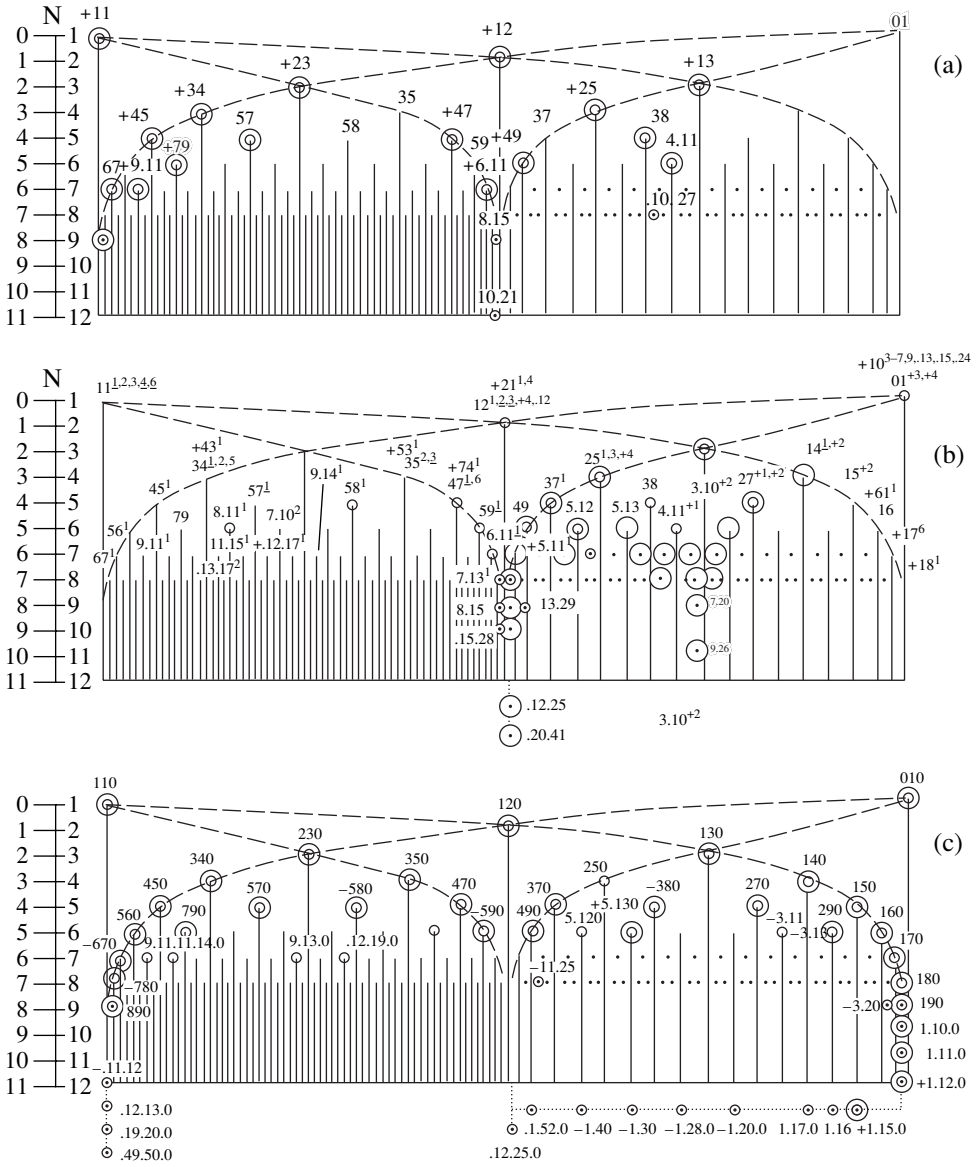

Fig. 2. Planar complication schemes for (a) the formulas of compositions of the compounds determined in the phase diagram of $BaO : BiO_{1.5}$ by visual polythermal analysis (large circles), electron microscopy (small circles), and differential thermal and thermogravimetric analyses (plus signs); (b) the formulas of the ratios Si : O (large circles) for silicates and the ratios B : (O + OH) (small circles), B : O (exponents), O : OH (coinciding with the ratios B : O) (underlined exponents), and O : OH (plus signs) for borates; (c) the formulas for the reflections *hk*0 with the intensity 100 (large circles) and the symbols *hk*0 of faces (small circles) (the formulas composed of two indices revealed only in the symbols *hkl* of reflections and in the symbols *hkl* of faces are marked by the plus and minus signs, respectively); (d) the formulas of the compositions determined from the coordination numbers of binary compounds (the realized compositions are in bold type); and (e) the formulas of the quantitative ratios between the coefficients of two different cations in oxides.

follows: {110} ⟨1–10⟩; 890; 780; 670; /560/; [450]; 790; {340} ⟨1, 2⟩; [570]; {230} ⟨1, 2, 3⟩; [580]; {350}; [470]; /590/; {120} ⟨1, 3, 4⟩; /490/; [370]; [380]; {130} ⟨1, 3⟩; [270]; {140} ⟨1, 2, 4⟩; /290/; [150] ⟨1, 2⟩; /160/; 170; 180; 190; 1.10.0; {010} ⟨1–18⟩.

In [6], the crystallographic planes characterized by a high degree of occupation with atoms were revealed in planar structures of sulfides with the symmetry group *Pnma*. The symbols of these planes will be considered without regard for signs. The indices (except for zero) are written in increasing order. The formulas are represented in the form of the linear complication series. The curly, square, and slant brackets are used for the formulas of the first four, fifth, and sixth series, respectively. The exponents are written in angle brackets. The third (smaller) significant indices are given in parentheses. The linear complication series is represented as {110} ⟨1(1), 2(1), 5(0)⟩; [450]; {340}; {230} ⟨1(0, 1), 2(0)⟩;

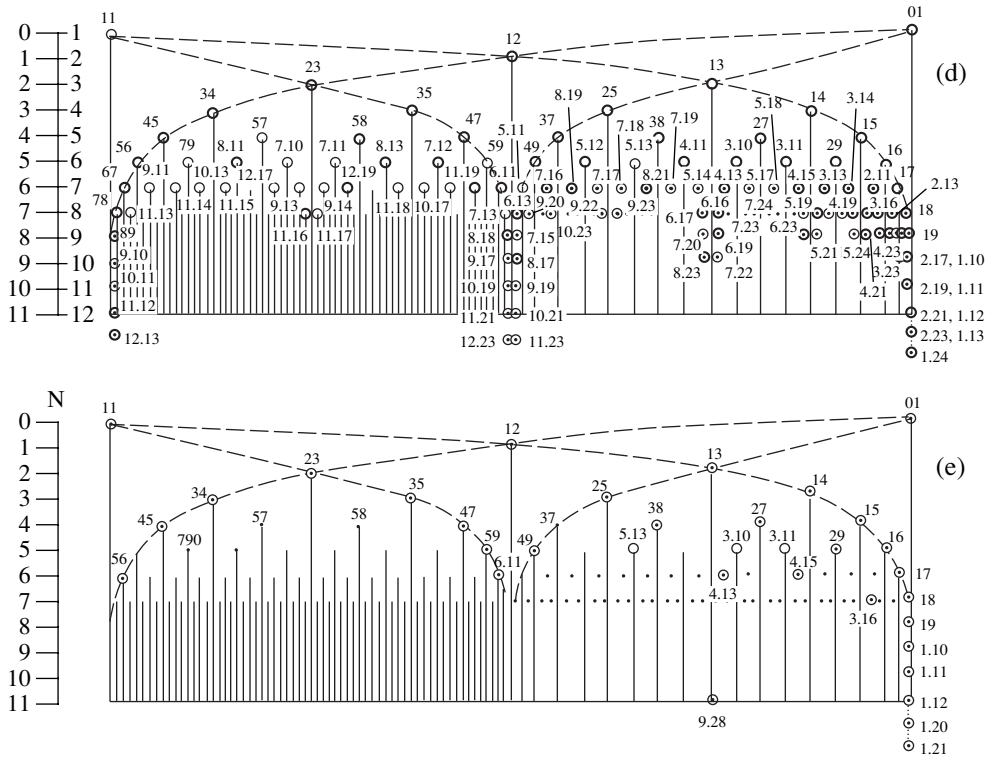

Fig. 2. (Contd.)

{350} ⟨1(0, 1)⟩; {120} ⟨1(0, 1), 2(0, 1), 3(0, 1)⟩; [370]; {250} ⟨1, 2⟩, {130} ⟨1(0, 1), 2(0)⟩; {140}; [150]; /160/ ⟨1(0, 1)⟩; 170; 180; 190; {010} ⟨2, 4, 6, 8, 10⟩. For example, the removal of brackets for {110} ⟨1(1), 2(1), 5(0)⟩ gives 111, 122, and 550. The basic formulas of the sequence almost completely enter into the composition of the first four series of the planar complication scheme.

Finally, let us examine the possible compositions calculated from the coordination numbers of binary compounds. As is known, for binary compounds A_mB_n, the coefficients m and n ($n \geq m$) can be calculated from the coordination numbers r and s ($r \geq s$) of the constituent atoms A and B. This is possible, because the ratio $m : n$ between the coefficients for crystal structures of binary compounds is inversely proportional to the ratio $r : s$ [e.g., for CaF_2, $m : n = 1 : 2$ and $r : s = 8 : 4 = k(2 : 1)$, where $k = 4$]. Unlike the ratios $m : n$, the ratios $r : s$ can have higher orders k ($kr : ks$). However, the number of orders of a larger coordination number is restricted by the upper limit whose experimental value even for intermetallic compounds does not exceed 24, and a smaller coordination number is less than or equal to 12 [7]. Therefore, the number of orders decreases with an increase in the maximum coordination number r and cannot exceed 24. At the composition 1 : 1, both coordination numbers can be equal to unity but also can have higher orders ⟨2, 3, 4, 5, 6, …, 24⟩, i.e., be characterized by the ratios 2 : 2, 3 : 3, 4 : 4, etc. For the composition 1 : 2, the ratio between the coordination numbers is equal to 2 : 1 and the number of orders decreases to 12 ($r : s = 24 : 12$). At the compositions 1 : 3 and 2 : 3, the number of orders decreases to eight ($r : s = 24 : 8$ and 24 : 16). Figure 2d displays the planar complication scheme for the formulas of the theoretical ratios $m : n$ corresponding to mutually prime numbers. This is also the planar complication scheme for the ratios $s : r$. All the first five series are completely filled with formulas. It should be noted that the ratios of the first several series most frequently occur when ordering; i.e., these ratios correspond to the minimum information entropy. This especially holds true for the compositions of the first two series: 01, 11, 12, 13, and 23. The orders are not presented in the planar complication scheme, because the larger coordination number [1 (24), 2 (12), 3 (8), 4 (6), 5 and 6 (4), 7 and 8 (3), 9–12 (2), and 13–24 (1)] in the formula determines its maximum order (given in parentheses). For smaller coordination numbers, the maximum order is two times smaller: 1(12)… .

In the case when the A and B atoms each occupy one position, the coordination sphere of the A atom is composed of the B atoms, the coordination sphere of the B atom consists of the A atoms, and these coordination spheres are simple. If the A atom occupies one position and the B atom occupies several positions, the A atom has a complex (combined) coordination sphere. When the coordination numbers of the A and B atoms are equal to one out of ten position multiplicities (1, 2, 3, 4, 6, 8, 12, 16, 24, and 48), their coordination spheres can

be comprised of atoms of the same sort, i.e., can be simple. If the coordination number of at least one of the atoms, for example, the *B* atom, differs from these ten multiplicities, the coordination sphere of at least the *A* atom will be complex (combined).

A change in the coordination number equal to the above multiplicities due to the multiplication by the order can lead to a changeover from the simple coordination sphere to the complex coordination sphere. At a coordination number of 1 and an order of 5, the coordination number becomes equal to 5. As a result, the coordination sphere that is simple at a coordination number of 1 can be only complex at a coordination number of 5. The coordination numbers equal to the multiplicities and the orders, the product of which by the coordination number leads to complex coordination spheres instead of simple spheres, are listed below (the coordination numbers are marked in bold type, and the orders are given in angle brackets): **1** ⟨5, 7, 9–11, 13–15, 17–23⟩; **2** ⟨5, 7–11⟩; **3** ⟨3, 5–7, 9–11⟩; **4** ⟨5⟩; **6** ⟨3⟩.

Simple binary structural types—ancestors—involve atoms that each occupy one position. A.V. Shubnikov [8] determined the compositions of 13 simple binary structural types (1 : 1, 1 : 2, 1 : 3, 1 : 4, 1 : 6, 1 : 8, 1 : 12, 1 : 16, 1 : 24, 1 : 48, 2 : 3, 3 : 4, and 3 : 8, where 1, 2, 3, 4, 6, 8, 12, 16, 24, and 48 are the multiplicities). Simpler structural types, such as NaCl and CaF_2, have the highest cubic symmetry. The formulas of pseudobinary structural types in which at least one atom occupies one position and the second atom occupies two or more positions (for example, $FeFe_2O_4$) are assigned to the formulas of simple structural types of second rank. In this case, the chemical compound involves atoms of two sorts and one of them (O) has a complex (combined) coordination sphere. These formulas can be represented using the linear complication series. The curly, square, and slant brackets are used for the formulas of the first four, fifth, and sixth series, respectively. The Shubnikov ratios between the coefficients of atoms are marked in bold type. The coefficients that can correspond to one position whose multiplicity is equal to one of the aforementioned ten multiplicities are also marked in bold type. The second coefficients that are not equal to the multiplicity of one position are printed in plain type. The sign plus indicates the realized formulas [9]. The formulas in which numbers marked in bold type can correspond to one position are denoted by exclamation points.

The linear complication series is as follows: +!{**11**}, .**12**.13, .11.**12**, +.10.11, 9.10, +**8**9, +7**8**, +**6**7, .11.13, +!/5**6**/, +9.11, +![**4**5], .11.14, /79/, +.10.13, +!{**34**}, .11.15, +/**8**.11/, +[57], .**12**.17, +/7.10/, +9.13, .11.**16**, +!{**23**}, .11.17, 9.14, /7.11/, +.**12**.19, +[5**8**], /**8**.13/, .11.18, +!{**3**5}, +.10.17, +/.7.**12**/, +.11.19, +[**4**7], 9.**16**, +/59/, +.11.20 +**6**.11, +7.13, +**8**.15, +9.17, .10.19, +.11.21, .**12**.23, +!{**12**}, .11.23, +.10.21, 9.19, **8**.17, +7.15, +**6**.13, 5.11, 9.20, +/**4**9/, +7.**16**, .10.23, +[**3**7], 8.19, +/5.**12**/, 7.17, 9.22, +!{**2**5}, 9.23, 7.18, +/5.13/, +**8**.21, +![**38**], 7.19, +/**4**.11/, +5.14, **6**.17, +7.20, +**8**.23, +!{**13**}, 7.22, +!**6**.19, 5.**16**, +**4**.13, 7.23, +!/**3**.10/, 5.17, 7.**24**, +![**2**7], 5.18, +/**3**.11/, +!**4**.15, +5.19, +!**6**.23, +!{**14**}, 5.21, +**4**.17, +**3**.13, +5.22, +!/**2**9/, 5.23, +**3**.14, +**4**.19, 5.**24**, +![**1**5], **4**.21, +**3.16**, +!**2**.11, +!**3**.17, +**4**.23, +!/**16**/, +**3**.19, **2**.13, +!**3**.20, +**1**7, +**3**.22, +!**2**.15, +**3**.23, +!**18**, +!**2**.17, +!**1**9, **2**.19, +!**1**.10, +**2**.21, +!**1**.11, **2**.23, +!**1.12**, +!**1**.13, **1**.14, +!**1**.15, +!**1.16**, **1**.17, **1**.18, +!**1**.19, **1**.20, **1**.21, **1**.22, **1**.23, **1.24**.

Analysis of 516 of Shubnikov's formulas for 1073 binary structural types [10] demonstrated that there are only 128 of Shubnikov's formulas (25%) that correspond to the occupation of one position by either of two atoms with the following multiplicities: 1 (56, 44%), 2 (23, 18%), 3 (23, 18%), 6 (18, 14%), 4 (7, 6%), and 12 (1, 1%). Consequently, complex coordination spheres are characteristic of structural types described by 75% of Shubnikov's formulas. These are either binary structural types of third rank or pseudoternary structural types. However, 320 of Shubnikov's formulas include multiplicities with indices of 1 or 2. As a consequence, together with 128 of Shubnikov's formulas, we have 448 of Shubnikov's formulas (87%). Therefore, it is worth noting that binary compounds are only "pseudobinary" compounds. It is also interesting to note that all the formulas of reflections (without regard for the orders) are included in many theoretical formulas of compositions of binary chemical compounds.

With the use of the data taken from [5], we determined different quantitative ratios between coefficients of cations in oxides containing two cations (Fig. 2e). Except for several formulas, all these ratios correspond to the theoretical binary ratios derived from the coordination numbers. Four series are completely filled in the planar complication scheme.

Thus, planar complication schemes were constructed for a number of systems. The data obtained are generalized. This allows one to consider these systems from a different viewpoint. The schemes are prognostic. All new results will fall into the schemes with due regard for the law of small numbers.

ACKNOWLEDGMENTS

I am grateful to N.G. Furmanova for her assistance in preparing the manuscript.

REFERENCES

1. N. L. Smirnova, Kristallografiya **46** (1), 10 (2001) [Crystallogr. Rep. **46**, 4 (2001)].
2. V. Goldschmidt, *Über Complikation und Displikation* (Carl Winters Universitat, Heidelberg, 1921; Geol. Inst.

Kol'skogo Nauchn. Tsentra Ross. Akad. Nauk, Apatity, 1998).
3. N. L. Smirnova and N. V. Belov, Dokl. Akad. Nauk SSSR **279**, 633 (1984) [Sov. Phys. Dokl. **29**, 866 (1984)].
4. L. A. Klinkova, V. I. Nikolaĭchik, L. V. Zorina, *et al.*, Zh. Neorg. Khim. **41** (5), 709 (1996).
5. G. B. Bokiĭ, *Systematization of Natural Silicates* (VINITI, Moscow, 1997).
6. S. V. Borisov, S. A. Magarill, N. V. Pervukhina, and N. V. Podberezskaya, Zh. Strukt. Khim. **41** (2), 324 (2000).
7. P. I. Kripyakevich, *Structural Types of Intermetallic Compounds* (Nauka, Moscow, 1977).
8. A. V. Shubnikov, Izv. Ross. Akad. Nauk, Ser. 6 **16**, 515 (1922).
9. N. L. Smirnova, Kristallografiya **46** (6), 979 (2001) [Crystallogr. Rep. **46**, 898 (2001)].
10. N. L. Smirnova, in *Noncrystalline State of Solid Mineral Materials* (Nauchn. Tsentr Ural. Otd. Geol. Inst. Ross. Akad. Nauk, Syktyvkar, 2001), p. 25.

Translated by O. Borovik-Romanova

Crystallography Reports, Vol. 47, No. 6, 2002, pp. 907–912. Translated from Kristallografiya, Vol. 47, No. 6, 2002, pp. 976–981.

THEORY OF CRYSTAL STRUCTURES

Growth of Random Plane Graphs and Packings

V. G. Zhuravlev, A. V. Maleev, V. G. Rau, and A. V. Shutov

Vladimir State Pedagogical University, Vladimir, Russia

e-mail: andr_mal@mail.ru

Received July 11, 2001; in final form, January 17, 2002

Abstract—The process of growth of random graphs with the vertices lying at the points of the plane (i, j) with integral coordinates has been considered. Computer simulation of the process allowed us to establish that random graphs grow in the self-similar mode. The sectorial growth proceeds in such a way that the growth boundary in four sectors consists of two horizontal and two vertical linear segments; in the other four sectors, the boundary is a part of an ellipse; the real growth boundary lags behind the limited form to which it tends; the scatter interval along the principal growth diagonal is proportional to the cubic root of the number of the coordination sphere. © *2002 MAIK "Nauka/Interperiodica".*

INTRODUCTION

The process of crystal formation can be simulated with the aid of the following simple purely geometric model. Let a periodic packing of closed domains (e.g., polyhedra which should not necessarily be convex) be set in a three-dimensional space and choose arbitrarily one or several domains in this packing which would play the role of a seed. The "growth process" is then considered as the successive addition to the seeding set of its coordination sphere—a set of domains neighboring the seeding set. The neighborhood ratio is determined by the local rules. For example, a domain neighboring the seeding set is a domain that shares a point, an edge, or a face with the seeding set. The packing with the given neighborhood ratio of various domains determines a three-dimensional periodic graph to each vertex of which there corresponds one domain of the packing. The edges connect those vertices to which the neighboring domains correspond.

Despite the simplicity of the above model, it allowed us to reveal certain characteristics that are rather similar to the well-known characteristics of real processes of crystal formation. Thus, we revealed and rigorously proved [1] the self-similar nature of "growth" of a three-dimensional periodic graph [1], with the growth form being a convex polygon (to which the growth structure tends) independent of the choice of the seed and dependent only on the graph structure. The proof of the self-similarity of the growth form is based on the sectorial nature of growth of a periodic graph proven in [1]. These facts are consistent with the concepts of ideal crystal growth commonly accepted in crystallography. It was indicated that, in the case of ideal growth, where a crystal remains to be self-similar from the moment of its nucleation, it is possible to single out the domains in the shape of pyramids in the center of the crystal, the so-called overgrowth pyramids or simply growth pyramids [2].

The study of the process of crystal formation under varying growth conditions gave very interesting results in terms of the geometry of crystal formation. We recollect here the well-known studies performed by G.G. Lemmlein, including the studies of the effect of impurities on crystal habit (Maltese cross). Therefore, we believe, that the natural extension of the metric approach is the incorporation of randomness elements into the process of crystal formation. These considerations, and also the prognosis of crystallinity (regularity) in the Delaunay (Delone) *r–R* systems formulated by Galiulin [3], gave an impetus to the formulation of the problem of studying the growth of the graph *G* in which the boundedness of vertices is determined by the local rules with fixed probabilities. In this article, we limit our consideration to the two-dimensional case.

We chose *G* as a graph with a set of vertices $V(G)$ from the points lying in the plane (i, j) and having the integral coordinates $i, j = 0, \pm1, \pm2, \ldots$. Any neighboring vertices along the vertical or the horizontal are connected by edges with 100% probability, whereas the vertices (i, j), $(i, j) \pm \mathbf{e}$ and (i, j), $(i, j) \pm \mathbf{e}^-$ (where $\mathbf{e} = (1, 1)$ and $\mathbf{e}^- = (-1, 1)$) are connected by edges with probability *p*. Thus, the vertices of the graph *G* which form a square lattice can have one of $2^4 = 16$ possible first environments with the probabilities $p^k(1 - p)^{4-k}$, $0 \le k \le 4$ (local rules). The graph *G* can be brought into correspondence with the aperiodic packing of closed figures in the plane. Figure 1 shows a fragment of the packing corresponding to the random graph *G* with $p = 0.3$. The graph vertices are the points lying inside the figures. The boundaries of these figures are indicated by solid lines, whereas the edges of the graph *G*, by thin lines.

Now, select the origin of the coordinate system (0, 0) to be a seed and form around this seed the 1st, 2nd, …, *n*th coordination environments, $eq(1, G)$, $eq(2, G)$, …, $eq(n, G)$. Limiting ourselves to the periodic

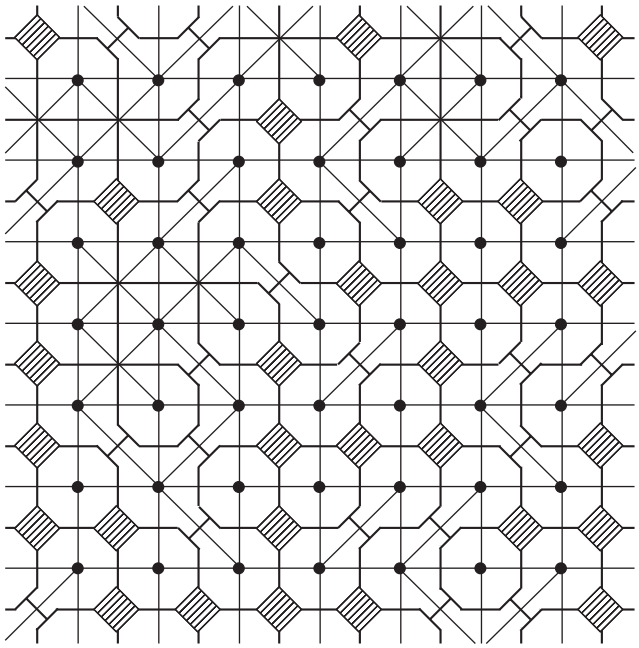

Fig. 1. Fragment of the aperiodic packing of closed figures in the plane (the figure boundaries are depicted by solid lines, the hatched squares indicate the voids) and the corresponding random graph with the probability $p = 0.3$ (graph vertices are depicted by the points inside the figures; thin lines indicate the graph edges).

graph G_{per}, as was indicated earlier, we see that the set $eq(n, G_{per})$ grows in a self-similar way as a certain polygon $Pol(n, G_{per})$, with $eq(n, G_{per})$ deviating from it at $n \longrightarrow \infty$ by not more than the constant $c(G_{per})$ [1]. The periodicity is characterized by a multigonal growth form in the plane and a multifacial growth form in the space.

The computer experiment showed that, for a random graph G, the coordination circumference $eq(n, G)$ at $n \longrightarrow \infty$ also grows in a self-similar way, $eq(n, G) \longrightarrow n\Gamma$. In the first quarter, the growth boundary Γ consists of two rectilinear segments, γ_1 and γ_3, and the arc of an ellipse, γ_2 (Fig. 2). The growth boundary Γ is extended to other three quarters by the fourfold axis passing through the origin of the coordinate system. To prove the reliability of the results obtained in the computer experiments, we analyze mathematically both the formulation of the problem of the growth form of the suggested random graphs and its solution.

1. LAYER GROWTH OF GRAPHS

1.1. Probabilistic measure. Denote the denumerably-dimensional random quantity by $\xi = (\xi_{ij})$. Its components ξ_{ij} are the independent equivalently distributed random Bernoulli quantities with the distribution

$$P(\xi_{ij} = 1) = p, \quad P(\xi_{ij} = 0) = q, \quad p + q = 1. \quad (1)$$

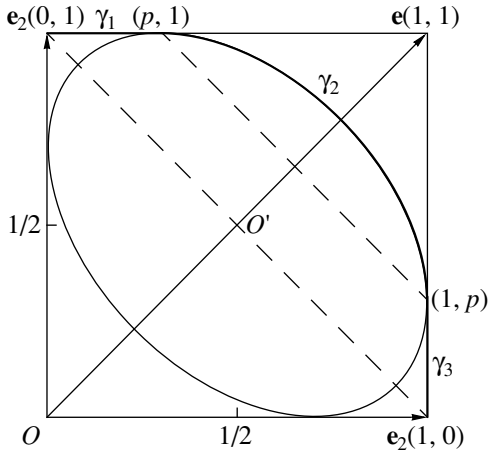

Fig. 2. The structure of the growth boundary Γ in the first quarter; it consists of two linear segments, γ_1 and γ_3, and the arc of the ellipse, γ_2.

By definition, the random quantity ξ takes the values from the space Ω of all the number sequences $\omega = (\omega_{ij})$ consisting of the elements $\omega_{ij} = 0$ or 1. The Bernoulli measure, i.e., the measure–product of the probabilistic measures (1) in the space Ω is denoted by P [4],

$$P(\xi : \xi_{i_1 j_1} = \omega_{i_1 j_1}, \ldots, \xi_{i_n j_n} = \omega_{i_n j_n}) = p^{\Sigma} q^{n-\Sigma}, \quad (2)$$

where Σ equals the sum $\omega_{i_1 j_1} + \ldots + \omega_{i_n j_n}$.

1.2. Random graphs. Consider the set $Gr = Gr(Z_+^2)$ of graphs G (the transition from graphs with a set of integral vertices in the plane Z^2 to the graph with the vertices from the first quarter of Z_+^2 is possible because growth proceeds independently in each quarter). Each graph G has a set of vertices $V = Z_+^2$, and any two neighboring vertices (along the horizontal or the vertical) are connected by an edge. The vertices (i, j) and $(i + 1, j + 1)$ can be either connected or not connected by an edge depending on the choice of the graph G. The graphs from Gr are enumerated by the points $\omega = (\omega_{ij})$ of the space Ω with the aid of the mapping

$$\Omega \ni \omega \xrightarrow{G} G(\omega) \in Gr. \quad (3)$$

The vertices (i, j) and $(i + 1, j + 1)$ in the graph $G = G(\omega)$ are connected by a diagonal only if $\omega_{ij} = 1$. This mapping allows one to transfer the measure P onto the set Gr of random graphs $G = G(\xi)$ and, thus, sets the isomorphism of the probabilistic spaces

$$(Gr, P) \approx (\Omega, P). \quad (4)$$

1.3. Growth curve. A chain $x' \longrightarrow \ldots \longrightarrow x$ with the minimum number of edges from $E = E(G)$ of the graph G which connects the vertex x' with x is called the geodesic g at fixed $\omega \in \Omega$. The number of edges $d(x', x) = d(x', x; G)$ sets the metrics on the set of verti-

ces $V = Z_+^2$; the nth coordination circumference or the equidistant set with the center at the origin

$$eq(n, G) = \{x \in Z_+^2 : d(0, x; G) = n\}, \quad n = 1, 2, 3, \ldots \tag{5}$$

is the set of vertices spaced by a distance n from the vertex $x' = 0$. Naturally, $eq(n, G)$ depends on the choice of random metrics d, i.e., on the choice of an element ω from the space Ω. Our main goal is to show that $eq(n, G)/n$ at $n \longrightarrow \infty$ for almost all the graphs $G \in Gr$ tends to the curve

$$\gamma = \gamma_1 + \gamma_2 + \gamma_3, \tag{6}$$

consisting of the vertical segment γ_1 with the ends $(1, 0)$, $(1, p)$ (Fig. 2), the horizontal segment γ_3 with the ends $(0, 1)$ and $(p, 1)$, and the arc of the ellipse

$$\frac{\delta^2}{p} + \frac{d^2}{q} = 1, \tag{7}$$

where $\delta = x + y - 1$, $d = x - y$ lies between the points $(1, p)$ and $(p, 1)$ in the coordinate system $\mathbf{e}_1 = (1, 0)$, $\mathbf{e}_2 = (0, 1)$. This ellipse can conveniently be written in the coordinate system (δ, d) with the center at $O' = (1/2, 1/2)$ and the basis $\mathbf{e}_1' = (1/2, -1/2)$, $\mathbf{e}_2' = (1/2, 1/2)$.

1.4. The strong law of large numbers. In order to formulate rigorously the above statement about the behavior of the growth boundary $eq(n, G)$, introduce one more metrics $\rho(A, B)$—the distance between the close subsets A and B of the conventional Euclidean plane R^2. For any $\varepsilon \geq 0$ and point $a \in A$, the circle of radius ε with the center a is denoted as $r(a, \varepsilon)$. Then, determine the ε neighborhood A_ε of the set A as the combination of the circles $r(a, \varepsilon)$ for all the points $a \in A$. The distance $\rho(A, B)$ is assumed to be $inf\,\varepsilon$ for which the inclusions $B \subset A_\varepsilon$ and $A \subset B_\varepsilon$ are valid.

The computer experiment showed that for the growth boundary $eq(n, G)$ at $n \longrightarrow \infty$ in the metrics ρ the strong law of large numbers is fulfilled, i.e., the following statement is valid:

$$\frac{1}{n} eq(n, G) \longrightarrow \gamma. \tag{8}$$

If one uses the metrics ρ in explicit form, the latter statement can be written in the form

$$\rho\left(\frac{1}{n} eq(n, G), \gamma\right) \longrightarrow 0. \tag{9}$$

For any $\varepsilon > 0$ and $\varepsilon_1 > 0$, there exists the natural number N dependent on ε and ε_1 such that the inequality

$$\rho\left(\frac{1}{n} eq(n, G(\omega)), \gamma\right) < \varepsilon \tag{10}$$

is fulfilled for all $n \geq N$ with the probability

$$P \geq 1 - \varepsilon_1. \tag{11}$$

1.5. Self-similar growth. Consider two important corollaries of statement (8), namely:

—the random graph $G = G(\xi)$ grows in a self-similar way;

—the appropriate averaging $\langle eq(m, G)\rangle$ of the number of vertices of the nth coordination environment $|eq(n, G)|$ also satisfies the strong law of large numbers.

The self-similar growth of the graph G signifies the inclusion

$$eq(n, G) \subset (n\gamma)_{\varepsilon(n)}. \tag{12}$$

The right-hand side includes the $\varepsilon(n)$ neighborhood of the homothetic image $n\gamma$ of the curve $\gamma \subset R^2$ with the coefficient n, and the radius of the neighborhood $\varepsilon(n)$ grows as $o(n)$, i.e., $\varepsilon(n)/n \longrightarrow 0$ and $n \longrightarrow \infty$.

We choose averaging of the number of vertices $|eq(n, G)|$ over the width $\Delta n = 2\varepsilon(n)$ for $\varepsilon(n)$ from inclusion (12)

$$\langle eq(n, G)\rangle = \frac{1}{\Delta n} \sum_{n - \varepsilon(n) \leq m \leq n + \varepsilon(n)} |eq(m, G)|.$$

Then, the property of self-similar growth of graphs G (12) for averaging $\langle eq(n, G)\rangle$, yields the convergence

$$\frac{1}{n}\langle eq(n, G)\rangle \longrightarrow 1 + p + \sqrt{pq}\arcsin\sqrt{q}. \tag{13}$$

1.6. Periodic graphs. Let us separate a sublattice L of the finite index in an integral square net Z^2. We assume that the sequence $\omega \in \Omega$ (Sect. 1.1) is periodic with respect to the translations from the sublattice L: $\omega_{ij} = \omega_{i_1 j_1}$ if the difference $(i, j) - (i_1, j_1)$ belongs to L. Periodic graphs grow in the form of convex polygons Pol_G with a finite number of vertices [1]. In our case, Pol_G is a polygon whose boundary consists of vectors $\mathbf{e}_1$, $\mathbf{e}_2$ and a convex (upward) broken line $\hat{\gamma} = \hat{\gamma}(\omega)$ connecting the vertices $(1, 0)$ and $(0, 1)$ (Fig. 2). We limit our consideration to square sublattices $L^N = NZ^2$ with the basis $N\mathbf{e}_1$, $N\mathbf{e}_2$ and the scale coefficient $N = 1, 2, 3, \ldots$. At fixed N, any sequence $\omega \in \Omega$ uniquely determines the periodic sequence ω^N, namely, $\omega_{ij}^N = \omega_{ij}$ for any i, $j < N$; $\omega_{ij}^N = \omega_{i_1 j_1}^N$ if the differences $i - i_1$ and $j - j_1$ are divisible into N.

With due regard for (3), inclusion (12) provides the following properties of periodic-graph growth $G^N = G(\omega^N)$. For any $\varepsilon > 0$ and $\varepsilon_1 > 0$, there exists such a natural number $N = N(\varepsilon, \varepsilon_1)$ that the following inequality is valid

$$P\{\omega \in \Omega: \rho(\hat{\gamma}(\omega^N), \gamma) \leq \varepsilon\} \geq 1 - \varepsilon_1. \tag{14}$$

Inequality (14) shows that if one chooses a sufficiently large period N, then the polygonal growth boundary $\hat{\gamma}$ of a random periodic graph $G^N = G(\xi^N)$ approximates a

smooth growth boundary γ of a random graph $G = G(\xi)$ quite well.

2. LOWER AND UPPER ESTIMATES OF GROWTH BOUNDARIES

Up to now, all attempts to prove the strong law of large numbers considered in Sect. 1.4 for the growth boundary $eq(n, G)$ of random graphs G by the conventional methods of the probability theory have failed. We give here the upper and lower boundaries of the growth curve γ (6).

2.1. Upper estimates and entropy. We first consider the simpler upper estimates. With this aim, we consider an arbitrary vertex $x = (x_1, x_2)$ from the set of vertices V of the graph $G = G(\omega)$, all the possible paths of this graph w, and the lengths $d(w) = n$ of the paths connecting the initial vertex Q with the vertex x. We assume all the paths w to be real if the motion along w is performed only along the directions $\mathbf{e}_1$ and $\mathbf{e}_2$ and along the diagonal direction $\mathbf{e} = (1, 1)$ in the case where the corresponding diagonal edge belongs to the graph G. The latter condition can be written as $w \in G$. We consider here not only the geodesic paths, but all the paths w of the graph G. Denote the number of edges in the path w of the type $\mathbf{e}_1$, $\mathbf{e}_2$, and $\mathbf{e}$ as n_1, n_2, and n_3, respectively. These edges can be uniquely restored from the coordinate of the path end x and its length n: $n_1 = n - x_2$, $n_2 = n - x_1$, and $n_3 = x_1 + x_2 - n$. In the maximum graph $G_{\max} = G(\omega_1)$, the number of paths $w \in G_{\max}$ for the unit sequence ω_1 with the elements $\omega_{ij} = 1$ for all i, j is described as

$$\frac{n!}{(n - x_1)!(n - x_2)!(x_1 + x_2 - n)!}.$$

Therefore, the mathematical expectation of the number of all the paths is $w(x, n) = \sum_{\omega \in \Omega^n} |\{w: w \in G(\omega)\}| P(\omega)$, where the summation is performed over the square $\Omega^n = \{\omega = (\omega_{ij}): i, j \le n, \omega_{ij} = 0 \text{ or } 1\}$ and the probability P determined by (2) is calculated by the formula

$$w(x, n) = \frac{n!}{(n - x_1)!(n - x_2)!(x_1 + x_2 - n)!} p^{x_1 + x_2 - n}. \quad (15)$$

Now, single out the upper triangle C^+ containing the points $\alpha = (\alpha_1, \alpha_2)$ with the coordinates $0 < \alpha_1, \alpha_2 \le 1$, $\alpha_1 + \alpha_2 \ge 1$ in the single square C stretched onto $\mathbf{e}_1$ and $\mathbf{e}_2$. To each point $\alpha \in C^+$ there corresponds the probability distribution $p_1 = 1 - \alpha_1$, $p_2 = 1 - \alpha_2$, $p_3 = \alpha_1 + \alpha_2 - 1$, where $p_i \ge 0$ and $p_1 + p_2 + p_3 = 1$. The quantity $H(\alpha) = -(1 - \alpha_1)\ln(1 - \alpha_1) - (1 - \alpha_2)\ln(1 - \alpha_2) - (\alpha_1 + \alpha_2 - 1)\ln(\alpha_1 + \alpha_2 - 1)$ is called the entropy of the distribution p_1, p_2, p_3, which, as is well known, determines the probability $\exp(-nH)$ of the motion along the typical paths w of the maximum graph $G_{\max}$ with the probabilities p_1, p_2, p_3 of transitions along the $\mathbf{e}_1$, $\mathbf{e}_2$, $\mathbf{e}$ edges. The quantity $H(\alpha)$ is the function varying within the range $0 \le H(\alpha) \le \ln 3$ and taking the minimum value $H(\alpha) = 0$ at the vertices of the C^+ triangle and the maximum value $H(\alpha) = \ln 3$, at its center of gravity $\alpha = (2/3, 2/3)$. The inequality $H(\alpha, p) = H(\alpha) + (\alpha_1 + \alpha_2 - 1)\ln p \le 0$ singles out the domain $C^+(p)$ in the triangle C^+. This is the domain in C^+ which is intersected by the curve γ_2^+

$$H(\alpha, p) = 0 \quad (16)$$

and containing the vertex (1, 1). Let us agree on a condition that the boundary γ_2^+ would not be included in the domain $C^+(p)$. The important part played by the triangle C^+ is also emphasized by one more important property. According to (5), for any graph $G \subset Gr$ and any n, the inclusion $\frac{1}{n} eq(n, G) \subset C^+$ is fulfilled.

Theorem 1. If the vertex $x = (x_1, x_2)$ has the form $(\alpha_1(n)n, \alpha_2(n)n)$, where $\alpha_i(n) = [\alpha_i n]/n$, $i = 1, 2$ and $\alpha = (\alpha_1, \alpha_2)$ belong to the triangle C^+, then the mathematical expectation of the number of all the paths of the random graph $G \subset Gr$ tends to zero

$$w(x, n) \longrightarrow 0 \quad \text{for} \quad n \longrightarrow \infty, \quad (17)$$

if α belongs to the domain $C^+(p)$.

2.2. The optimum single-step strategy. The method of obtaining lower estimates for the growth boundary $eq(n, G)$ is illustrated by the example of estimating the growth rate along the main diagonal $\mathbf{e} = (1, 1)$.

We fix the graph $G = G(\omega)$ for a certain sequence $\omega \in \Omega$ and construct on it the path

$$w_k = w_k(\omega) = w(i_1, j_1) + \ldots + w(i_k, j_k), \quad (18)$$

originating at the zeroth vertex and consisting of k atomic chains $w(i_s, j_s)$, $s = 1, \ldots, k$ chosen according to the same repeating principle. The only requirement for this path is that it should provide the fastest motion along the diagonal $\mathbf{e}$. Now, consider the linear order on the set of vertices $V = Z_+^2$ of the graph G

$$(i, j) \lhd (i_1, j_1) \quad (19)$$

by the two following conditions: $i + j < i_1 + j_1$ and if $i + j = i_1 + j_1$, then $j < j_1$. The initial $\lhd$ sequence of the vertices has the form

$$(0, 0) \lhd (1, 0) \lhd (0, 1) \lhd (2, 0) \lhd (1, 1) \lhd (0, 2) \lhd \ldots. \quad (20)$$

Thus, to each vertex $(i, j) \in V$ is attributed an ordinal number from the sequence 1, 2, 3, ….

Order (19) determines the $\lhd$-strategy: we find the first vertex (i_1', j_1') with the condition $\omega_{i_1' j_1'} = 1$ in sequence (20), i.e., the vertices (i_1', j_1') and $(i_1, j_1) = (i_1', j_1') + \mathbf{e} = (i_1 + 1, j_1 + 1)$ are connected by the edge

in the graph $G = G(\omega)$. Knowing the vertex (i_1', j_1'), we can construct the first atomic chain

$$w(i_1, j_1) = (0, 0) \longrightarrow \ldots \longrightarrow (i_1', 0) \longrightarrow \ldots \longrightarrow (i_1', j_1') \longrightarrow (i_1, j_1). \quad (21)$$

The second chain $w(i_2, j_2)$ with the origin at the vertex found (i_1, j_1) is constructed by the same rule (21), etc. Within k steps, we construct the path $w_k = w_k(\omega)$ (18). It is seen from the definition that the $\triangleleft$-strategy is the optimum single-step strategy. It is nonlocal because it admits the atomic chains $w(i_s, j_s)$ of an arbitrarily large length $d(w(i_s, j_s))$. The local strategies admit individual steps based on the information on the finite part of graph G in a circle with the center at the initial vertex (i_s, j_s) and constant radius R (the observation radius, R, is constant at all the steps).

From the definition of the probability P in Sect. 1.1, it follows that $d(1, \xi) = d(w(i_1, j_1)), \ldots, d(k, \xi) = d(w(i_k, j_k))$ are the independent equivalently distributed random quantities. Therefore, the inequality $d(w_k(\omega)) = \sum_{1 \le s \le k} d(w(i_s, j_s))$ yields the mathematical expectations

$$M(d(w_k(\xi))/k) = M(d(1, \xi)). \quad (22)$$

At $x = (x_1, x_2)$ from R^2, we denote the projection of x on the principal diagonal along the orthogonal vector $(1, -1)$ as $pr_e(x) = \left(x, \frac{\sqrt{2}}{2}\mathbf{e}\right) = \frac{\sqrt{2}}{2}(x_1 + x_2)$ and, in a similar way, the projection of the final vertex of the path $w_k(\omega)$ as $pr_e(w_k(\omega))$. Using this notation, we can write

$$M\left(\frac{pr_e(w_k(\xi))}{d(w_k(\xi))}\right) = \frac{\sqrt{2}}{2} + \frac{\sqrt{2}}{2} M\left(\left(\frac{d(w_k(\xi))}{k}\right)^{-1}\right).$$

Now, use the following inequality for the mathematical expectations of the direct and reciprocal quantities

$$M\left(\left(\frac{d(w_k(\xi))}{k}\right)^{-1}\right) \ge \left[M\left(\frac{d(w_k(\xi))}{k}\right)\right]^{-1}$$

and use equality (22) to obtain the lower estimate

$$\lim_{k \to \infty} M\left(\frac{pr_e(w_k(\xi))}{d(w_k(\xi))}\right) \ge \frac{\sqrt{2}}{2} + \frac{\sqrt{2}}{2}[M(d(1, \xi))]^{-1}.$$

To formulate the final result, introduce the following additional notation: $n_k(\omega) = d(w_k(\omega))$ is the path length $w_k(\omega)$ (18) and $\max pr_e(eq(n_k(\omega)), G(\omega))$ is the maximum projection onto the principal diagonal of all the vertices of the nth coordination circumference (5) of the graph $G = G(\omega)$.

Theorem 2. The lower estimate of the rate of the diagonal growth of random graphs $G \in Gr$ has the form:

$$\lim_{k \to \infty} M\left[\frac{\max pr_e(eq(n_k(\xi), G(\xi)))}{n_k(\xi)}\right] \ge \frac{\sqrt{2}}{2} + \frac{\sqrt{2}}{2} M(p)^{-1}. \quad (23)$$

The mathematical expectation $M(p) = M(d(1, \xi))$ is calculated by the formula

$$M(p) = \sum_{n=1}^{\infty} q^{(n)} = \frac{q^{-1/8}}{2}\theta_2(z/2), \quad (24)$$

where $(n) = n(n-1)/2$, $\theta_2(z) = \Theta_{Z+1/2}(z)$, θ is the Jacobi function on the set of shifted integers $Z + 1/2$, and the variable z is related to q by the exponential dependence $q = \exp(\pi i z)$.

3. DYNAMICS OF FORMATION OF GROWTH BOUNDARY

3.1. Quasinormal distribution. Let us choose again the direction of the principal diagonal $\mathbf{e} = (1, 1)$ and relate the graph G to a random quantity

$$S(n, \xi) = \max\{\sqrt{2}x: (x, x) \in eq(n, G)\}. \quad (25)$$

The computer simulation on cellular automata results in the following hypothetical limiting theorem for this random quantity

$$p\left\{\frac{S(n, \xi) - MS(n, \xi)}{\sqrt{DS(n, \xi)}} \le x\right\} \longrightarrow \Phi_{quasi}(x), \quad n \longrightarrow \infty. \quad (26)$$

In the first approximation, the distribution $\Phi_{quasi}(x)$ (Fig. 3) is a normal Gaussian distribution $\Phi(x)$. The mathematical expectation $MS(n, \xi)$ is

$$MS(n, \xi) = nm_e - \Delta(n) \quad (27)$$

with the coefficient $m_e = \frac{\sqrt{2}}{2}(1 + \sqrt{p})$ being determined by ellipse (7) and the dispersion $DS(n, \xi)$, by

$$\sqrt{DS(n, \xi)} = \sigma(p)n^{\alpha}. \quad (28)$$

The exponent equals $\alpha = 1/3$, and $\sigma(p)$ is the positive constant dependent only on the probability p.

3.2. Long-range order. In formula (27), $\Delta(n)$ is the positively defined nonlinear function n of the same order as that of dispersion (28). The dependence of the average value of the mathematical expectation on n, $MS(n, \xi)/n = m_e - \Delta(n)/n$, indicates that $S(n, \xi)$ cannot be expanded into a sum of independent random quantities. The inequality of degree $\alpha < 1/2$ in dispersion formula (28) can be interpreted as the existence of self-organization elements in the process of growth of the coor-

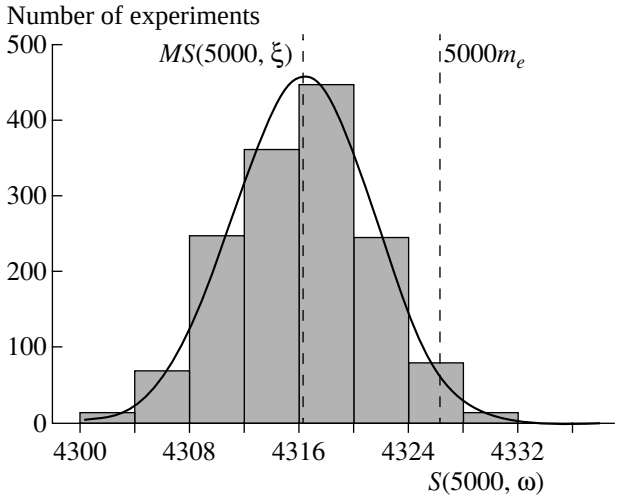

Fig. 3. Histogram of the distribution of the random quantity $S(5000, \xi)$ for the probability $p = 0.05$ constructed from the results of 1500 independent experiments.

dination circumferences $eq(n, G)$ (5). Since the ratio tends to zero, $\Delta(n)/n \longrightarrow 0$, at $n \longrightarrow \infty$, then the limiting distribution (26) yields the strong law of large numbers (8) along the principal diagonal **e**.

RESULTS AND CONCLUSIONS

The present study allowed us to reveal the following phenomena inherent in the growth process of the random graph $G = G(\xi)$:

(1) The growth of coordination circumferences $eq(n, G)$ is linearized or, in other words, $eq(n, G)$ is approximated by the curve $n\gamma$, and the random graph $G = G(\xi)$ grows in a self-similar way.

(2) The growth has a sectorial nature, i.e., the coordination circumferences $eq(n, G)$ are divided into two crystal sectors, γ_1 and γ_3, and one elliptical sector, γ_2.

(3) The lag of the mathematical expectation $MS(n, \xi)/n$ behind its limiting value $\lim_{n \to \infty} MS(n, \xi)/n = m_e$.

(4) The narrowing of the range of scatter in $\sqrt{DS(n, \xi)}$ down to the quantity $\sigma(p)n^{1/3}$.

We believe that the main result of our study is the establishment of the fact that random graph G grows in a self-similar way, with the growth form being rather simple and consisting of first- and second-order lines.

Moreover, it is also established that the formation of the periodic and random structures is characterized by the following common phenomena: self-similar growth, sectorial growth, the lag behind the limiting growth boundary, and the narrowing of the range of scatter down to cn^{α} with the exponent $\alpha < 1/2$ (in the case of periodic structures, $\alpha = 0$, for a random graph, $\alpha = 1/3$).

REFERENCES

1. V. G. Zhuravlev, Algebra Analiz **13** (2), 1 (2001).
2. I. Kostov, *Crystallography* (Mir, Moscow, 1965).
3. R. V. Galiulin, Kristallografiya **43** (2), 366 (1998) [Crystallogr. Rep. **43**, 332 (1998)].
4. A. I. Shiryaev, *Probability* (Nauka, Moscow, 1980).

Translated by L. Man

Crystallography Reports, Vol. 47, No. 6, 2002, pp. 913–917. Translated from Kristallografiya, Vol. 47, No. 6, 2002, pp. 982–986.

CRYSTAL CHEMISTRY

Morphotropic Series of Bi-containing Layered Perovskite-Like Oxides and Principles of Their Systematics[1]

G. A. Geguzina

Research Institute of Physics, Rostov State University, pr. Stachki 194, Rostov-on-Don, 344090 Russia

e-mail: denis@ip.rsu.ru

Received January 10, 2002

Abstract—The well-known bismuth-containing layered perovskite-like oxides (BLPO) of composition $A_{m-1}Bi_2B_mO_{3m+3}$ are divided into morphotropic series. In these series, the *a*, *b*, and *c* parameters of the orthorhombic unit cells and the Curie temperature (T_c) change monotonically with increasing unstrained interatomic *A*–O bond lengths, when *A* are *s* elements. For compounds in which *A* are *p* elements (Pb^{II} or Bi^{III}), the *a* and *b* unit-cell parameters and T_c, unlike the *c* unit-cell parameter, deviate substantially from these correlations, with the deviations decreasing with an increase of the *m* parameter. These facts must be taken into consideration in the search for new BLPO, whose compositions are predicted with the use of the systematics. © *2002 MAIK "Nauka/Interperiodica".*

INTRODUCTION

Bismuth-containing layered perovskite-like oxides (BLPO) of the general formula

$$A_{m-1}Bi_2B_mO_{3m+3} \quad (1)$$

are considered. More than 70 individual BLPO containing one or two different elements in the *A* position and up to three different elements in the *B* position are known. All BLPO possess ferroelectric properties and are characterized by phase transitions at rather high Curie temperatures (T_c). For some representatives, T_c are higher than 1200 K. The compositions, structures, and properties of BLPO were surveyed in a number of reviews (see, for example, [1–16]), where the authors proposed different interpretations of BLPO behavior depending on their composition.

The main aim of this study is to divide the BLPO family into morphotropic series, which allow one to reveal the atomic characteristics exerting an effect on the lattice parameters and T_c. The so-called unstrained interatomic *A*–O bond lengths [17–21] can be used as such atomic characteristics. In morphotropic series, these bond lengths vary depending on the composition of the *A* position. The Curie temperature and the *a*, *b*, and *c* parameters of the orthorhombic unit cell can be represented as a function of the composition of the BLPO in the morphotropic series. Hence, the unstrained interatomic *A*–O bond length can be used as a numerical argument of the atomic composition. In this study, the principles for an adequate systematics of the known and hypothetical compositions are proposed for the search for new BLPO.

[1] This study was presented at the Symposium "Order, Disorder, and Properties of Oxides" (ODPO), Sochi, Russia, 2001.

MORPHOTROPIC SERIES OF BLPO AND LATTICE PARAMETERS

A system of unstrained interatomic *A*–O and *B*–O bond lengths for perovskite-like complex oxides was proposed earlier in [17–21]. The perovskite structure is a parent structure of all perovskite-like compounds composed of oxygen octahedra. Hence, this self-consistent system of unstrained interatomic bond lengths (UIBL) can also be used in the case of BLPO, because the *A* and *B* atoms in their perovskite-like layers occupy positions with the coordination numbers 12 and 6, respectively, as in perovskite-type structures. For each particular pair of *A* and O atoms or pair of *B* and O atoms, UIBL were determined [19–21] and are constant.

Let us denote the unstrained interatomic *A*–O and *B*–O bond lengths as L^0_{AO} and L^0_{BO}, respectively. In a complicated structure, the corresponding interatomic bonds are deformed as compared to L^0_{BO} and L^0_{AO}, and, hence, these bonds are strained. Strained interatomic bond lengths are denoted as L_{AO} and L_{BO}. In the vast majority of perovskite-like complex oxides, the *A*–O are elongated, whereas the *B*–O bonds are shortened within certain limits [21–23].

It is of most interest to consider the morphotropic series in relation to the composition of the *A*-position (Bi^{III} can also occupy the *A*-position), because the *A*–O bonds are elongated and most strained, due to which they are the least stable and most sensitive to changes in composition [21]. The shortened *B*–O bonds, which stabilize the structure as a whole, are more stable and less strained. The degree of their strain depends only slightly on the composition as compared to the *A*–O bonds. The strains in the *A*–O and *B*–O bonds exert an

1063-7745/02/4706-0913$22.00 © 2002 MAIK "Nauka/Interperiodica"

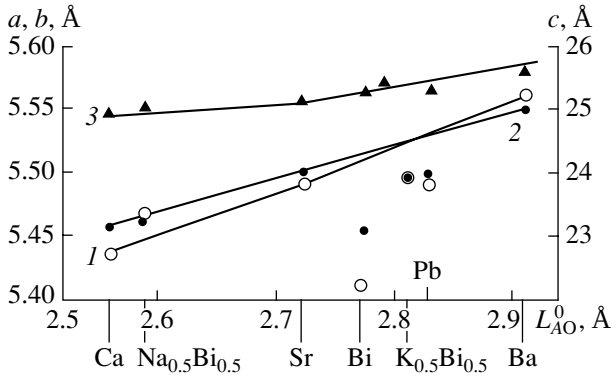

Fig. 1. Plots of the (*1*) *a*, (*2*) *b*, and (*3*) *c* unit-cell parameters vs. unstrained interatomic bond lengths (L^0_{AO}) in the morphotropic series $A^{II}Bi_2Nb_2O_9$ (m = 2). The data for $Bi_3^{III}TiNbO_9$ are included.

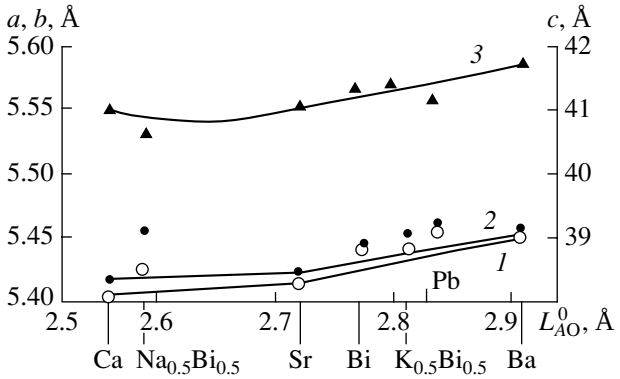

Fig. 2. Plots of the (*1*) *a*, (*2*) *b*, and (*3*) *c* unit-cell parameters vs. unstrained interatomic bond lengths (L^0_{AO}) in the morphotropic series $(A^{II}Bi_2)Bi_2Ti_4O_{15}$ (m = 4). The data for $Bi_5^{III}FeTi_3O_{15}$ are included.

effect on the physical properties of BLPO, in particular, on their Curie temperatures. This effect was observed in perovskite-like complex oxides [24].

In the known BLPO, large divalent (Ca, Sr, Pb, or Ba), trivalent (Ho, Pr, La, or Bi), and/or monovalent (Na or K) atoms are located in the *A* positions. The *B* positions are occupied by small trivalent (Fe or Ga), tetravalent (Ge, Ti, or Mn), pentavalent (Nb or Ta), and/or heptavalent (W or Mo) atoms.

Each morphotropic series proposed in this study includes BLPO containing a variable *A* atom with the same average valence, all other atoms in formula (1) being constant. An example is the morphotropic series with $m = 2$ and the variable A^{II} atom. This series includes members with the general formula $A^{II}Bi_2Nb_2O_9$, namely, $Ca^{II}Bi_2Nb_2O_9$, $(Na_{0.5}Bi_{0.5})^{II}Bi_2Nb_2O_9$, $Sr^{II}Bi_2Nb_2O_9$, $(K_{0.5}Bi_{0.5})^{II}Bi_2Nb_2O_9$, $Pb^{II}Bi_2Nb_2O_9$, and $Ba^{II}Bi_2Nb_2O_9$. In some cases, it is reasonable to consider the morphotropic series involving BLPO exclusively with Bi^{III} as the *A* atom. The morphotropic series under consideration already contains a compound with a *p*-type atom (Pb^{II}). The addition of BLPO with Bi^{III}, namely, Bi_3TiNbO_9, allows one to follow the influence of the valence and electronic configuration of the *A* atom on the unit-cell parameters and Curie temperature. In such BLPO, the presence of *B* atoms of another type as compared to that typical of this morphotropic series has a less significant effect than the presence of the Bi^{III} atom in the *A* positions.

The behavior of compounds containing Pb^{II} and Bi^{III} atoms with *p*-type electronic configurations of the valence shells differs from the behavior of compounds with *s*-, *ds*-, or *sp*-type atoms, as has been demonstrated in studies of perovskite-like structures [21–23]. The characteristic features of the electron shells of Pb^{II} and Bi^{III} atoms are responsible for the occurrence of the directed and nonequivalent interatomic distances in the structure. This fact could have an impact not only on the possibility of formation of the structure and its characteristic features but also on the physical properties of the compound.

For all possible morphotropic series, the *a*, *b*, and *c* parameters of the orthorhombic unit cell were plotted vs. the unstrained interatomic *A*–O bond lengths (see, for example, Figs. 1 and 2). For BLPO with $m = 2$ (Fig. 1), the *a*, *b*, and *c* parameters increase monotonically as L^0_{AO} increases, if the *A* position is occupied by *s* elements. The monotony of this dependence is broken at points corresponding to *p* elements (Pb^{II} and Bi^{III}). The *a* and *b* parameters of the corresponding BLPO are substantially smaller than those expected from the plot for BLPO containing *s* elements in the *A* position. The maximum deviations from the general monotonic dependences are observed for the points corresponding to the Bi_3TiNbO_9 compound. Smaller deviations are observed for BLPO characterized by the mixed composition of the *A* position, namely, for $(Na_{0.5}Bi_{0.5})$ and $(K_{0.5}Bi_{0.5})$.

In the morphotropic series with $m = 4$ and the general formula $A^{II}Bi_4Ti_4O_{15}$ containing the same A^{II} atoms, drops of the *a* and *b* parameters at points corresponding to $A = Pb^{II}$ or Bi^{III} are much smaller (Fig. 2) than those observed in the above-considered series. For the morphotropic series with $m = 5$, no dropouts from the general dependence are observed. This behavior of the *a* and *b* parameters is manifested in all morphotropic series to a greater or lesser extent. The *c* parameter shows no essential anomalies at any *m* and in any oxidation states of the *A* atoms. Thus, this parameter increases slightly and monotonically in each morphotropic series as the unstrained interatomic *A*–O bond length increases. Consequently, the *c* parameter is vir-

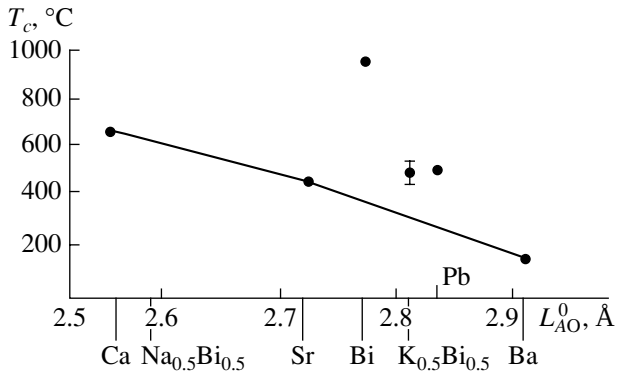

Fig. 3. Curie temperature vs. unstrained interatomic bond distances (L^0_{AO}) in the morphotropic series $A^{II}Bi_2Nb_2O_9$ (m = 2). The data for $Bi^{III}_3TiNbO_9$ are included.

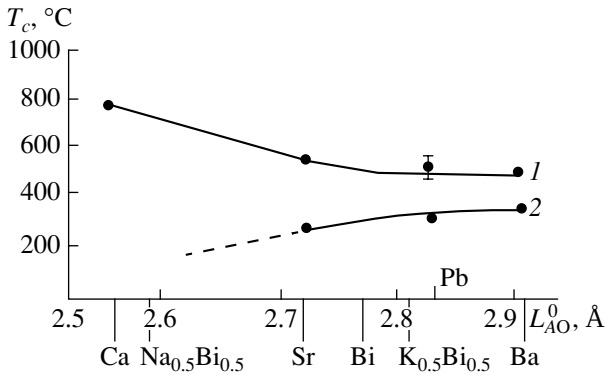

Fig. 4. Curie temperature vs. unstrained interatomic bond distances (L^0_{AO}) in two morphotropic series (m = 5): (*1*) $(A^{II}Bi_3)Bi_2B_5O_{18}$ and (*2*) $(A^{II}_2Bi_2)Bi_2B_5O_{18}$ [18].

tually independent of the oxidation state and electronic configuration of the *A* atoms but depends on their dimensional characteristics.

CURIE TEMPERATURE IN MORPHOTROPIC SERIES

The relationships between the Curie temperature, on the one hand, and various crystal-chemical characteristics of the atoms and structure, on the other, were discussed in several reviews (see, for example, [1–3, 9–12, 20]) and in some original publiatoms. In these studies, the ionic radii, tolerance factor (t), electronegativities, and other characteristics were examined with the aim of revealing correlations. In the present study, the relationships between the unstrained interatomic *A*–O bond lengths and T_c are considered. As an example, the plots of the Curie temperature vs. the unstrained interatomic *A*–O bond lengths for three different morphotropic series are shown in Figs. 3 and 4. If one *s*-type *A* atom in the morphotropic series is replaced by another atom, the Curie temperature changes monotonically as the unstrained interatomic A^{II}-O bond length increases. When an *s*-type atom is replaced by a *p*-type atom (for example, by Pb^{II} or Bi^{III}), the monotony is broken.

At m = 2 (Fig. 3), the Curie temperature of $PbBi_2Nb_2O_9$ is higher than that following the general tendency for *s*-type atoms. Bismuth-containing layered perovskite-like oxide containing a Bi^{III} atom in a mixed *A* position and especially $Bi_3TiNb_2O_9$ containing exclusively Bi^{III} in the *A* position possess even higher Curie temperatures. However, the observed jumps of the Curie temperature for such BLPO are diminished as m increases and virtually disappear at m = 5 (Fig. 4). The reasons for these phenomena remain unclear and call for further investigation.

However, it can be assumed that the BLPO structure becomes more similar to the perovskite structure as the thickness of the perovskite-like layer in the BLPO structure increases with increasing m, on the assumption that the perovskite structure contains an infinite number of perovskite-like layers (as compared to the BLPO structures) in the absence of particular interlayer constructions. Probably, m = 5 is the limiting value for BLPO. In addition, the interlayer Bi atoms in BLPO differ from the Bi atoms in the perovskite-like layers.

It can be assumed that small values of m and the presence of *p*-type atoms (Pb^{II} or Bi^{III}) in the perovskite-like layers lead to an increase in the number of nonequivalent and directed bonds between these atoms and the oxygen atoms, as well as in the number of the bonds between different *p*-type atoms resulting in substantial strains in the interatomic bonds. The presence of strongly strained interatomic bonds in the structure may facilitate an increase in the Curie temperature [24]. Strains in the interatomic distances, which give rise to distortions of the BLPO lattice, and a contraction of the oxygen octahedral framework of the perovskite structure containing the Pb and Bi atoms are responsible for the disproportionately small a and b parameters of the corresponding BLPO structures. The role of interlayer constructions and interlayer Bi^{III} atoms remains unclear.

The dependence of the Curie temperature on m deserves attention. When constructing the corresponding plots, the difference in the electron shells of all *A* and *B* atoms must be taken into account. For BLPO compositions containing different *A* atoms, the Curie temperature changes variously as m changes, even if the valence shells of the *A* atoms have similar electronic configurations [12]. For Ca-containing BLPO, the Curie temperature gradually, though slightly, increases as m increases. For Sr- and Ba-containing BLPO, the Curie temperature first increases (with a noticeable peak at about m = 2.5) and then sharply decreases. At small m, lead-containing BLPO have Curie tempera-

tures at approximately the same level, although T_c slightly increases at $m = 4$ and then slightly decreases. For BLPO containing exclusively Bi^{III} atoms in the A position, the Curie temperature sharply decreases as m increases, but T_c still remains rather high.

CHOICE OF COMPOSITIONS AND PRINCIPLES OF THEIR SYSTEMATICS

The number of known bismuth-containing layered perovskite-like oxides is rather small (less than 100), whereas more than 1000 perovskite-like binary and ternary oxides are available [18]. It is expected that the search for new compositions and the synthesis of new compounds will lead to an increase in the number of BLPO. The synthesis must be carried out with consideration for the changes in the structure and properties revealed from the consideration of the known BLPO. The directed search for new compounds was developed in sufficient detail and applied to the perovskite- and pyrochlore-type structures [25]. The first step of this procedure involves the choice of a new hypothetical composition. For this purpose, the systematics of all the possible compositions of the structures under examination is called for. To be more precise, a list of general formulas of the type (1) is required. These formulas are convenient to use for a choice of appropriate chemical elements in the desired oxidation states.

It is appropriate to divide BLPO compositions with the use of the principles that were initially proposed for perovskite-type structures [18]. These principles are based on the general conditions for the formation of complex oxides with various compositions. These principles are as follows:

(i) the valence-balancing principle for the chemical formula of BLPO (an analogue of the electroneutrality principle for purely ionic compounds);

(ii) the principle of the difference in valences of the atoms occupying the identical A and/or B positions in the crystal lattice of complex BLPO;

(iii) the principle of compatibility of oxidation states in high-temperature solid-state synthesis.

Formula (1) can be transformed into a more general formula taking into account that A and B can denote several different atomic sorts simultaneously:

$$Bi_2(A^1_{\alpha_1}\ldots A^i_{\alpha_i}\ldots A^p_{\alpha_p})(B^1_{\beta_1}\ldots B^j_{\beta_j}\ldots B^q_{\beta_q})O_{3m+3}, \quad (2)$$

where

$$\sum_{i=1}^{p}\alpha_i = m-1; \quad \sum_{j=1}^{q}\beta_j = m. \quad (3)$$

Then, taking into account the valences of the atoms $A^i(n_{A^i})$ and $B^j(n_{B^j})$, the valence-balancing condition can be written as follows:

$$\sum_{i=1}^{p}\alpha_i n_{A^i} + \sum_{j=1}^{q}\beta_j n_{B^j} = 6m. \quad (4)$$

The second condition is required to exclude solid-solution compositions of isovalent substitutions in the A and/or B sublattices in structures of complex BLPO, when $p > 1$ and/or $q > 1$. The fulfillment of this condition leads to a substantial decrease in the number of possible general formulas in the formal (without this condition) systematics. This condition involves the simultaneous fulfillment of two series of inequalities:

$$n_{A^1} \neq n_{A^2} \neq \ldots \neq n_{A^i} \neq \ldots \neq n_{A^p}, \quad (5)$$

$$n_{B^1} \neq n_{B^2} \neq \ldots \neq n_{B^i} \neq \ldots \neq n_{B^q}. \quad (6)$$

In this case, such compounds are allowable in which the valences of particular atoms located in different positions in the lattice, for example, those of A^k and B^l, are equal:

$$n_{A^k} = n_{B^l}. \quad (7)$$

The two first conditions concern the deduction of general chemical formulas that describe the compositions of hypothetical compounds, including the fixation of the oxidation states of the A and B components. The third condition must be taken into account in the choice of a particular chemical composition of the desired BLPO. The intended oxidation states of the selected chemical elements must be stable and compatible under real synthesis conditions [18]. For example, chemical elements, whose oxidation states are stable under different atmospheric conditions, cannot be used simultaneously in the composition of particular BLPO.

A system for the determination of the characteristics of compositions, namely, of the valences and fractions of the atoms, can be formulated from Eqs. (3), (4), and some other equations (if the compositions are more complicated). The elaboration of this systematics of compositions is a problem with the following variables, which can be changed within certain limits:

(i) the parameter m, which, at first glance, has no limitations;

(ii) the parameters p and q, which can be limited;

(iii) valences n_{A^i} and n_{B^j};

(iv) the fractions (α_i and β_j) calculated according to the corresponding equations.

These variables can be considered as numerical parameters in the systematics of compositions, and the ranges of their changes can be reasonably restricted.

Bismuth-containing layered perovskite-like oxides with $m = 1$, 1.5, 2, 2.5, 3, 3.5, 4, and 5 are known. The synthesis of one BLPO with $m = 8$ [9] and the preparation of one BLPO with $m = 10$ [26] were reported. However, these data were not confirmed in subsequent

studies. Hence, it seems reasonable to use $m = 5$ as the upper limit of this parameter. In addition, the general tendency of a decrease in the Curie temperature of the known BLPO with increasing m should be remembered. An increase in m generally requires an increase in the number of atomic sorts in the A and/or B positions, which may also lead to a decrease in the Curie temperature and complication of the procedure for the preparation of the corresponding compounds.

The known BLPO contain a limited number of atoms of different sorts in the A and/or B positions. Conceivably, this is due to the fact that the compositions of the individual BLPO cannot include a larger number of different atomic sorts. It is also not improbable that no efforts to synthesize more complicated compositions were made. It seems reasonable to restrict the number of different sorts of atoms, i.e., to use $p = 0$, 1, 2, or 3 and $q = 1$, 2, or 3. In the known BLPO with different m, the valences of the A^i atoms $n_{A^i} = 1$, 2, 3, or 4 and the valences of the B^j atoms $n_{B^j} = 3$, 4, 5, or 6. These values are used in the present study as the restrictions imposed on the valences of the A^i and B^j atoms in the systematics of compositions. The corresponding fractions of the A^i (α_i) and B^j (β_j) atoms are determined from the solution of Eqs. (3) and (4) taking into account inequalities (5) and (6).

Evidently, combinations of these parameters are not all possible in BLPO compositions. The goal of the systematics is to choose general formulas for BLPO. As an example, let us consider the determination of the general formulas for BLPO with $m = 2$ by solving the system of Eqs. (3) and (4) at $p = 1$ and $q = 1$ and the valence of the A atom $n_A = 2$ and then at $p = 1$ and $q = 2$ and the valence of the A atom $n_A = 3$:

(1) $\alpha = 1$; $\beta = 2$; $n_A + 2n_B = 12$; if $n_A = 2$, $n_B = 5$; the general formula of BLPO is $A^{\mathrm{II}}\mathrm{Bi}_2B_2^{\mathrm{V}}\mathrm{O}_9$.

(2) $\alpha = 1$; $\beta_1 + \beta_2 = 2$; $\beta_1 = 2 - \beta_2$; $n_A + (2 - \beta_2)n_{B^1} + \beta_2 n_{B^2} = 12$; $n_A = 3$; $2n_{B^1} - \beta_2 n_{B^1} + \beta_2 n_{B^2} = 9$; if $n_{B^1} = 6$ and $\beta_1 = 1$, $\beta_2 = 1$ and $n_{B^2} = 3$; the general formula of BLPO is $A^{\mathrm{III}}\mathrm{Bi}_2B^{\mathrm{VI}}B^{\mathrm{III}}\mathrm{O}_9$.

The compositions of certain known BLPO satisfy the formulas obtained in this study.

ACKNOWLEDGMENTS

This study was supported by the Ministry of Education of the Russian Federation, grant no. E00-3.4-560.

REFERENCES

1. E. C. Subbarao, J. Phys. Chem. Solids **23**, 665 (1962).
2. *Ferroelectrics and Antiferroelectrics*, Ed. by G. A. Smolenskiĭ (Nauka, Leningrad, 1971).
3. *The Physics of Ferroelectric Phenomena*, Ed. by G. A. Smolenskiĭ (Nauka, Leningrad, 1985).
4. M. E. Lines and A. M. Glass, *Principles and Applcations of Ferroelectrics and Related Materials* (Clarendon, Oxford, 1977; Mir, Moscow, 1981).
5. G. A. Smolenskiĭ, V. A. Isupov, and A. I. Agranovskaya, Fiz. Tverd. Tela (Leningrad) **3**, 895 (1971) [Sov. Phys. Solid State **3**, 651 (1971)].
6. T. Kikuchi, A. Watanabe, and K. Uchida, Mater. Res. Bull. **12**, 299 (1977).
7. V. G. Osipyan, *Structure and Properties of Ferroelectrics* (Latviĭsk. Gos. Univ. im. P. Stuchki, Riga, 1983), p. 3.
8. V. G. Osipyan, L. I. Savchenko, and I. B. Avakyan, *Dielectrics and Semiconductors* (Kievsk. Politekh. Inst., Kiev, 1988), Vol. 33, p. 16.
9. V. A. Isupov, Ferroelectrics **189**, 211 (1996).
10. V. A. Isupov, Izv. Akad. Nauk, Neorg. Mater. **33**, 1106 (1997).
11. L. A. Reznichenko, O. N. Razumovskaya, L. A. Shilkina, and N. V. Dergunova, Izv. Akad. Nauk, Neorg. Mater. **32**, 474 (1996).
12. G. A. Geguzina, E. G. Fesenko, and E. T. Shuvaeva, Ferroelectrics **167**, 311 (1995).
13. B. Aurivillius, Ark. Kemi **1**, 463 (1949).
14. B. Aurivillius, Ark. Kemi **1**, 499 (1949).
15. B. Aurivillius, Ark. Kemi **2**, 512 (1950).
16. B. Aurivillius and P. H. Fang, Phys. Rev. **126**, 893 (1962).
17. V. P. Sakhnenko, E. G. Fesenko, A. T. Shuvaev, *et al.*, Kristallografiya **17** (2), 316 (1972) [Sov. Phys. Crystallogr. **17**, 268 (1972)].
18. E. G. Fesenko, *Perovskite Family and Ferroelectricity* (Atomizdat, Moscow, 1972).
19. G. A. Geguzina, V. P. Sakhnenko, E. G. Fesenko, *et al.*, Available from VINITI, No. 3049-76 (1976).
20. V. P. Sakhnenko, N. V. Dergunova, and L. A. Reznichenko, *Energy Crystal Chemistry of Solid Solutions of Oxyden-Octahedral Type Compounds and Simulation of Piezoceramic Materials* (Rostovsk. Pedagogich. Univ., Rostov-on-Don, 1999).
21. G. A. Geguzina, in *Advances in Structure Analysis* (Chech and Slovak Crystallographic Association, Prague, 2000), p. 223.
22. G. A. Geguzina and E. G. Fesenko, Izv. Akad. Nauk SSSR, Neorg. Mater. **20**, 1394 (1984).
23. Ya. E. Cherner, G. A. Geguzina, and E. G. Fesenko, Izv. Akad. Nauk SSSR, Neorg. Mater. **19**, 287 (1983).
24. G. A. Geguzina, O. A. Zhelnova, and A. A. Bokov, Ferroelectrics **153**, 85 (1994).
25. G. A. Geguzina and Ya. E. Cherner, Izv. Akad. Nauk SSSR, Neorg. Mater. **27**, 1881 (1991).
26. G. I. Ismailzade, V. I. Nesterenko, F. A. Mirishli, and P. G. Rustamov, Kristallografiya **12** (3), 468 (1967) [Sov. Phys. Crystallogr. **12**, 400 (1967)].

Translated by T. Safonova

Crystallography Reports, Vol. 47, No. 6, 2002, pp. 918–924. Translated from Kristallografiya, Vol. 47, No. 6, 2002, pp. 987–993.

CRYSTAL CHEMISTRY

In memory of V.Ya. Khaimov-Mal'kov

Diffusion of Intrinsic Defects in Dielectric and Semiconductor Crystals with Impurities

E. M. Akulenok*, Kh. S. Bagdasarov*, Yu. K. Danileĭko, T. P. Lebedeva**, and A. A. Manenkov****

** Shubnikov Institute of Crystallography, Russian Academy of Sciences, Leninskiĭ pr. 59, Moscow, 119333 Russia*

e-mail: dyuk@ran.gpi.ru

*** Institute of General Physics, Russian Academy of Sciences, ul. Vavilova 38, Moscow, 117942 Russia*

Received February 27, 2002

Abstract—This paper reports on the results of detailed theoretical investigations into the diffusion of intrinsic defects in impurity crystals doped with mixed-valence ions. The special case of diffusion stimulated by variations in the redox properties of the atmosphere at the crystal boundary during high-temperature annealing is analyzed. The major consideration is given to the following fundamental problems: (i) the dynamics of valence transitions and the structure of the chemical reaction zone, (ii) the possibility of determining the type of chemical reaction at the crystal–atmosphere interface and the type of diffusing defects, (iii) the effect of dilatation mechanical stresses arising in the reaction zone on the reaction-zone structure and on the dynamics of diffusion processes, and (iv) the determination of the diffusion parameters of intrinsic defects and the constants of their interaction with impurity centers. *© 2002 MAIK "Nauka/Interperiodica".*

INTRODUCTION

Among the large number of theoretical and experimental investigations into the problem of point-defect diffusion, the studies performed under the supervision and with the direct participation of V.Ya. Khaimov-Mal'kov are of fundamental importance [1–3]. The majority of these studies dealt with the diffusion in sapphire crystals. However, the inferences made in these works can be applied to other crystalline media in which the diffusion of intrinsic defects in the presence of impurity atoms is stimulated by concentration inhomogeneities, temperature gradients, and force effects (electric fields and mechanical stresses) [4, 5]. In the present paper, we consider in more detail the case described earlier in [1], where the intrinsic point defects can interact with impurity atoms (centers), change their valence state and the spatial configuration of the surrounding lattice, and form an impurity–defect complex with a low mobility [6]. This interaction leads to the formation of impurity centers that can appear stable and not very mobile at a specified temperature; as a result, the diffusing defects can get out of diffusion. As a rule, this interaction is described in terms of a solid-phase chemical reaction. The solid-phase chemical reaction can considerably change the spatial pattern of intrinsic-defect diffusion and, therefore, must be taken into consideration [1]. It should be noted that the solid-phase chemical reaction can affect the diffusion proceeding not only in doped crystals but also in crystals with low concentrations of background impurities, which in many practical cases substantially exceed the concentration of intrinsic defects. In the subsequent discussion, the diffusion attended by a solid-phase chemical interaction between mobile intrinsic defects and low-mobility impurity centers will be referred to as diffusion with traps, as was done in our earlier work [1].

The aim of the present work is to develop the diffusion theory of intrinsic defects, which was proposed in [1]. The diffusion of intrinsic defects involved in the solid-phase chemical reaction with impurity atoms is considered with due regard for the effect of mechanical stresses arising in this process.

In actual fact, a change in the valence state of an impurity and, consequently, in the configurational state of impurity centers leads to a change in their dilatation volume. In turn, the change in the dilatation volume can give rise to mechanical stresses that exhibit considerable gradients and affect the course of the diffusion. This is particularly true with regard to the chemical reaction occurring with a well-defined front. Note that the distribution of mechanical stresses can be determined not only by a local distribution of stress sources but also by the sample shape and external forces acting on the sample due to a reaction at the support.

From the foregoing, it follows that a theoretical treatment of diffusion with traps is a complicated nonlinear (by virtue of the chemical reaction) problem in

1063-7745/02/4706-0918$22.00

mathematical physics. This problem is topical both in solid-state physics and in practical terms. First of all, this is the case with the growth of crystals and, especially, their heat treatment. With knowledge of the regularities of the process of diffusion with traps, it is possible to choose properly the temperature, time, annealing atmosphere, and partial pressures of the different gases involved in this processes. It should be noted that diffusion with traps controls important processes, such as the oxidation of dyes with atmospheric oxygen in solid polymer matrices and the oxidation of drugs in solid fillers. The elucidation of the mechanisms of these processes will permit the correct evaluation of the oxidation rates and the development of appropriate methods for suppressing oxidation for a given time through the proper choice of the composition and thickness of the protective shell.

THEORETICAL ANALYSIS

A diffusion process with traps will be analyzed theoretically in the framework of the following model. For simplicity, we consider an isotropic (with respect to diffusion) crystal with a doping impurity that enters into interactions with intrinsic lattice defects to change the valence state according to the chemical reaction $A + B \rightleftarrows H$, where A is a mobile (migrating) intrinsic Schottky defect, B is a substitutional impurity atom, and H is a defect–impurity center. In what follows, we assume that the components B and H possess a low mobility and do not participate in diffusion. Moreover, it is assumed that an ensemble of defects in the crystal is in thermodynamic equilibrium with the atmosphere surrounding the crystal. The equilibrium is disturbed at the instant of time $t = 0$ with a change in the conditions at the interface. This can be either a change in the composition of the atmosphere surrounding the crystal (up to the complete evacuation of the atmosphere) or an external action, for example, as a result of ionic bombardment.

Within the above approximations (for a planar interface), we can write the system of equations

$$\begin{aligned} \frac{\partial N}{\partial t} &= D\frac{\partial^2 N}{\partial x^2} - w(N)C + \frac{C_0 - C}{\eta}, \\ \frac{\partial C}{\partial t} &= -w(N)C + \frac{C_0 - C}{\eta} \end{aligned} \quad (1)$$

with the following initial and boundary conditions:

$$t = 0 \text{ and } x > 0 \quad N(x, 0) = 0 \quad C(x, 0) = C_0, \quad (2)$$

$$t > 0 \text{ and } x = 0 \quad N(0, t) = N_0. \quad (3)$$

Here, N is the concentration of diffusing defects in the initial chemical state, C is the concentration of impurities in the initial chemical state, C_0 is the initial concentration of impurities in the initial valence state, N_0 is the concentration of defects at the interface between the crystal and the surrounding atmosphere (the physical meaning of the parameter N_0 and the processes determining its magnitude will be considered below), $w(N)$ is the probability of trapping (chemical reaction) a mobile defect by an impurity atom per unit time with the formation of a defect–impurity center, and η^{-1} is the probability of the inverse process occurring.

The system of equations (1) is written for a simple cubic lattice without regard for the aforementioned mechanical stresses.

Now, we perform a phenomenological analysis of the dependence $w(N)$. For this purpose, we assume that "a narrow bottleneck" determining the reaction rate is the mean-statistic time required for a defect to meet an impurity atom during a random walk over the bulk of the crystal rather than the time required for the interaction between the defect and the impurity atom (the time of spatial transformation of the impurity center). In order to define more concretely the dependence $w(N)$, we will proceed from the following reasoning. Let us consider the model of an infinite medium (for simplicity, with cubic symmetry) in which impurity atoms with the mean concentration N are arranged in a random manner. A single defect will be thrown into the volume of this medium at random. This defect is able to execute a random walk (i.e., equally probable jumps with the frequency ν and with a shift by one lattice constant a_0) along the six crystallographic directions. In the case when the dilatation energies of the single defect and the impurity atom are of opposite signs, these particles are attracted together owing to the elastic interaction. It is this interaction that causes the impurity atom and the defect to rapidly approach each other when the defect executes the random walk and that brings about a change in the valence state of the impurity due to the electromagnetic interaction when this interaction becomes thermodynamically possible. Let r_d be the radius of this elastic interaction. Hereafter, this radius will be termed the radius of a black sphere in which the defect becomes bound and, thus, gets out of diffusion. In our consideration, we introduce the time-dependent random quantity $V_i(t)$, which is equal to the volume of a tube of radius r_d. The axis of this tube is the mechanical trajectory of the defect executing the random walk in the crystal. The tube length is equal to the path covered by the defect beginning with the instant it is thrown in and ending with the instant of its capture by an impurity. We leave out cumbersome calculations and average the random quantity $V_i(t)$ over all the possible realizations of the random walk with allowance made for the correlation. For the average value $V(t)$, we obtain the relationship

$$V(t) = \xi r_d^2 a_0 \nu t. \quad (4)$$

Here, ξ is the coefficient characterizing the correlation effects for the quantity $V(t)$ in the course of the random walk. The correlation coefficient ξ was calculated by Monte Carlo numerical simulation of the random walk

process. As a result, we obtained the correlation coefficient $\xi \cong 0.67$ in the case when the radius r_d of the black sphere coincided with the radius of the first coordination sphere, $\xi \cong 0.2$ when the radius r_d coincided with the radius of the second coordination sphere, and $\xi \cong 0.12$ if the radius r_d coincided with the radius of the third coordination sphere. Taking into account relationship (4), the probability $P(t < T)$ of entering a single itinerant defect into an interaction (reaction) with an impurity atom within the time interval $0 < t < T$ can be determined as the probability that at least one impurity atom involved in an ensemble with the concentration N will occur in the volume $V(T)$ [7, 8]:

$$P(t < T) = 1 - \exp(-V(T)N). \quad (5)$$

In this case, the probability $w(N)$ can be defined as $\langle T \rangle^{-1}$. By averaging the time T with the use of the probability density $\frac{\partial P(t < T)}{\partial T}$, we obtain $w(N) = kN$, where k is the chemical reaction constant (expressed in units of $cm^3\ s^{-1}$):

$$k = \xi r_d^2 a_0 \nu. \quad (6)$$

Let us now turn our attention to the discussion of the physical meaning of the parameter N_0. As a rule, physical processes occurring at the interface between a crystal and the surrounding atmosphere, for example, in the course of evaporation or ionic (atomic) bombardment, can be characterized by the rate of defect formation F_0 at the crystal boundary. The rate of defect formation F_0 is defined as the number of defects escaping from a unit interfacial area into the crystal bulk in a unit time. In order to estimate the volume concentration of defects in the surface layer N_0 (in what follows, N_0 will be treated as the boundary value of the concentration of diffusing defects N), we will proceed from the following considerations. It is assumed that structural defects are formed at the rate F_0 on the surface of a crystal occupying a half-space. These defects diffuse into the crystal bulk and execute a three-dimensional random walk. According to the theory of Brownian motion, each particle escaping from a certain surface with a probability equal to unity must necessarily return to this surface [9]. In real situations, a structural defect, as a rule, disappears after escaping from the bulk of the crystal to its surface. Therefore, a structural defect that was created on the surface and then diffused into the crystal bulk has a finite lifetime because of its return to the initial surface. On this basis, after summing the fluxes of defects that escape from and arrive at the crystal surface and making these fluxes equal to the rate of defect formation F_0, we obtain the following estimate of the surface concentration:

$$N_0 \cong \frac{F_0}{\nu_{surf} a_0}. \quad (7)$$

Here, ν_{surf} is the mean frequency of return of the defect to the initial surface. It should be noted that, owing to the elastic interaction of a particular defect with the free surface, the mean frequency ν_{surf} can differ significantly (toward larger values) from the frequency ν of random jumps in the bulk of the crystal.

For a further analysis, in the system of equations (1), we will change over to the dimensionless quantities

$$\tau = kN_0 t, \quad y = \left(\frac{kC_0}{D}\right)^{\frac{1}{2}} x, \quad \beta = \frac{N_0}{C_0},$$

$$u = \frac{C}{C_0}, \quad v = \frac{N}{N_0}, \quad \theta = \frac{1}{k\eta N_0}$$

and the new function $\varphi(y, \tau)$ defined by the equations

$$v = \frac{\partial \varphi}{\partial t}, \quad u = \exp(-\varphi) \quad (8)$$

with the following initial and boundary conditions:

$$\tau = 0, \quad y > 0: \varphi(0, y) = 0, \quad \left.\frac{\partial \varphi}{\partial \tau}\right|_{y = +0} = 0;$$
$$y = 0, \quad \tau > 0: \varphi(\tau, 0) = \tau. \quad (9)$$

As a consequence, the system of equations (1) becomes equivalent to the dimensionless equation

$$\beta \frac{\partial \varphi}{\partial \tau} = \frac{\partial^2 \varphi}{\partial y^2} - 1 + \exp(-\varphi - \theta\tau) + \theta \exp(-\varphi - \theta\tau) \int_0^\tau \exp(\varphi + \theta t')\, dt'. \quad (10)$$

Equation (10) describes the diffusion of point defects entering into the second-order reaction with an immobile impurity particle and represents a nonlinear integro-differential equation that has defied exact analytical solution. However, in the most frequently occurring real situations, we deal with an impurity concentration that is considerably higher than the concentration of point defects ($\beta \ll 1$) and with a low probability of the decomposition of the defect–impurity centers formed as a result of the reaction ($\theta \ll 1$). In this case, the approximate solution to the problem defined by expressions (9) and (10) can be obtained in the form of an implicit function, that is,

$$y = \int_{\varphi(y, \tau)}^{\tau} \frac{dz}{\sqrt{2(\exp(-z) + z - 1)}}, \quad (11)$$
$$u(y, \tau) = \exp(-\varphi(y, \tau)).$$

Figure 1 shows the spatial distributions of the impurity concentration $u(y, \tau)$ and the concentration of diffusing defects $v(y, \tau)$ for two instants of time τ, which were calculated using relationships (11). It is worth noting that the functions $u(y, \tau)$ and $v(y, \tau)$ are independent of any parameter of the problem under consideration. Therefore, the changeover to arbitrary dimen-

sional variables (within the approximations $\beta \ll 1$ and $\theta \ll 1$) can be treated to be equivalent to a linear deformation along the y axis of the concentration distributions shown in Fig. 1.

By using relationships (11), we found that the position y_f of the reaction front at $\left.\frac{\partial^2 u}{\partial y^2}\right|_{y=y_f} = 0$ corresponds to the concentration $u(y_f, \tau) \cong 0.417$. In this case, the slope of the spatial distribution of the impurity concentration at the reaction front is determined as $\left.\frac{\partial u}{\partial y}\right|_{y=y_f} \cong 0.318$.

Note that these quantities are universal and independent of the distance covered by the reaction front beginning from the crystal boundary. This means that the size (thickness) of the reaction zone remains unchanged upon its displacement into the bulk of the sample. The displacement of the reaction front with time can be determined from the relationship

$$y_f(\tau) = \int_{0.874}^{\tau} \frac{dz}{\sqrt{2(\exp(-z) + z - 1)}}. \quad (12)$$

At $\tau \gg 1$ (i.e., after the separation of the reaction front from the crystal boundary), we obtain $y_f = \sqrt{2\tau}$. The concentration of diffusing defects at the reaction front in the course of its displacement deep into the sample decreases according to the law $v(y_f, \tau) \cong 0.54\tau^{-1/2}$.

An important remark on the applicability of the approximate solution (11) needs to be made, because the use of these relationships in the calculations can substantially affect the physical picture of the occurrence of the reaction under investigation. Reasoning from the analysis of the dimensionless equation (10), we can formulate the following mathematical statement: for an arbitrarily small parameter θ, there exists an instant of time τ_s beginning from which the solution to the dimensionless equation (10) will be significantly different from the solution defined by formulas (11). The time τ_s can be estimated from the relationship $\tau_s \cong \theta^{-1}$. Analysis demonstrates that, in the case of the dimensionless equation (10), unlike relationship (12), the slope of the spatial distribution of the impurity concentration at the reaction front becomes dependent on the position of the reaction front at $\tau \gg \tau_s$ and decreases in the course of its displacement according to the law $\left.\frac{\partial u}{\partial y}\right|_{y=y_f} \cong \frac{1}{5.7\theta y_f}$, whereas the spatial distribution of impurities with concentrations up to $u(y, \tau) \cong 0.5$ changes according to the formula $u(y, \tau) \cong \frac{\theta y_f}{y_f(1+\theta) - y}$, where $y_f \cong \sqrt{2(1+\theta)\tau}$.

It should be noted that, in the case of a sample in the form of a thin plate when defects are formed only on one surface of the plate and escape from the opposite surface, there exists a certain layer in the vicinity of the latter surface in which impurities occur in the initial chemical state. The concentration of impurities on this surface is equal to the initial concentration. The length of this layer can be estimated to be $\Delta y \cong \theta L$, where L is the thickness of the plate [10].

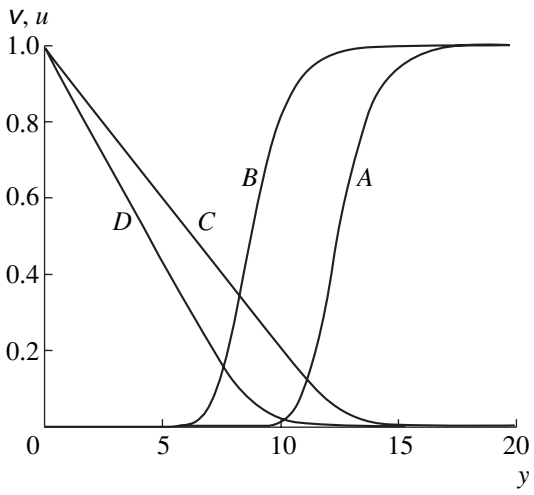

Fig. 1. Dependences of (*A*, *B*) the normalized concentration of impurities in the initial state $u(y, \tau)$ and (*C*, *D*) the normalized concentration of diffusing defects $v(y, \tau)$ on the longitudinal coordinate y for two instants of time: (*B*, *D*) $\tau = 20$ and (*A*, *C*) $\tau = 80$.

In the above analysis, we ignored the effect of mechanical stresses (arising in the reaction zone) on the diffusion process. The origin of these stresses can be explained in terms of the following two factors: (1) the difference between the total dilatation volumes of the reacting defects and the reaction products and (2) the small size of the chemical reaction zone and, as a consequence, large concentration gradients of the reacting components and the reaction products.

In the subsequent consideration, we will take into account the dilatation energy U_{elas} of the diffusing defect A in an external (with respect to the defect) elastic field: $U_{elas} = -\omega_A P$, where $P = -\frac{1}{3}\sigma_{kk}$ is the mean hydrostatic pressure, σ_{kk} is the trace of the elastic constant tensor, and ω_A is the dilatation volume of the diffusing defect A. In this case, the flux of defects J_A in the elastic force field σ_{kk} can be represented by the relationship $J_A = -\mu\omega_A N \mathrm{grad} P$, where μ is the mobility of the diffusing defect A in the elastic force field.

One more remark on the applicability of the subsequent treatment is necessary. In many cases, a considerable diffusion of defects in crystals occurs at high temperatures and, owing to concentration gradients, stresses arising in the diffusion zone can be very strong. Consequently, in the diffusion zone and especially in the chemical reaction zone, there arise effects of stress

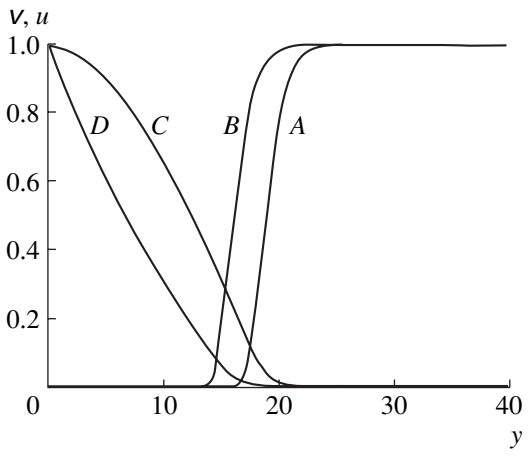

Fig. 2. Dependences of (*A*, *B*) the normalized concentration of impurities in the initial state $u(y, \tau)$ and (*C*, *D*) the normalized concentration of diffusing defects $v(y, \tau)$ on the longitudinal coordinate y for two dilatation parameters: (*B*, *D*) $\gamma = 0.02$ and (*A*, *C*) $\gamma = -0.02$.

relaxation. These effects can bring about the formation (or the spatial redistribution) of an ensemble of structural defects of a dislocation nature [11]. The discussion of these processes does not enter into the scope of the present paper. In this respect, we will restrict our consideration to the case of a comparatively low-temperature diffusion that does not lead to stress relaxation.

As was already mentioned, the nonlinear diffusion-elastic problem has defied analytical solution. For this reason, the subsequent treatment will be reduced to a numerical analysis of the process in the geometry of a thin long plate. In this case, the system of equations (1) in the aforementioned dimensionless variables with allowance made for the fluxes caused by mechanical stresses takes the form

$$\beta\frac{\partial v}{\partial \tau} = \frac{\partial^2 v}{\partial y^2} - uv + \frac{\partial J_A}{\partial y},$$
$$\frac{\partial J_A}{\partial y} = \gamma\left[\frac{\partial v}{\partial y}\left(\frac{\partial u}{\partial y} - \frac{12}{\tilde{L}^3}\int_0^{\tilde{L}}\left(y - \frac{\tilde{L}}{2}\right)u(y)dy\right) + v\frac{\partial^3 u}{\partial y^3}\right], \quad (13)$$

where

$$\gamma = \frac{2\omega_A(\omega_B - \omega_H)EC_0}{9\Theta(1-\vartheta)},$$

E is the Young's modulus, ϑ is the Poisson ratio, Θ is the temperature of the crystal (expressed in terms of energy), and $\tilde{L}$ is the thickness of the plate (expressed in terms of $\sqrt{\frac{D}{kC_0}}$). Equation (13) is written for the distribution of mechanical stresses over the plate, which was determined within the membrane approximation [12].

The results of the numerical solution to Eq. (13) for $\beta \ll 1$ at different values of the parameters γ and $\tilde{L}$ are presented in Fig. 2. It is worth noting that the distance covered by the reaction front depends on the parameter γ, its sign, and the plate thickness L (i.e., this is a manifestation of the so-called size effect).

RESULTS AND DISCUSSION

It follows from relationship (12) that, in the absence of mechanical stresses and recombination effects, the displacement of the reaction front occurs in accordance with the expression $y_f = \sqrt{2\tau}$. In dimensional variables, this expression corresponds to the relationship $x_f = \sqrt{2D\frac{N_0}{C_0}t}$. We used the results obtained in [1] for the $Ti^{3+} \longrightarrow Ti^{4+}$ valence transition, which is observed in sapphire crystals upon the interaction of Ti^{3+} ions with aluminum vacancies, and found that, in the case when the temperature in the reaction zone is 1500°C, the quantity DN_0 is approximately equal to 1.9×10^{14} cm^{-1} s^{-1}. Unfortunately, it is impossible to determine the individual quantities D and N_0 from the results reported in [1]. Moreover, the activation energy estimated at 80 kcal mol^{-1} [1] can be assigned only to the quantity DN_0. Nonetheless, we can use relationship (7) for N_0 and $D \cong \nu a_0^2$ and obtain the estimate $DN_0 \approx F_0 a_0 \frac{\nu}{\nu_{surf}}$.

It should be noted that the rate of defect formation F_0 at the crystal boundary is an anisotropic quantity and depends on the crystallographic orientation of this boundary. Moreover, the rate of defect formation F_0 can strongly depend on the degree of structural perfection of the crystal surface (the surface relief on the atomic level). These dependences must always be kept in mind in the interpretation of the results obtained in quantitative investigations of diffusion processes.

Note also that the atmosphere surrounding the crystal under investigation can affect the diffusion of intrinsic defects through variations in the rate of defect formation F_0 due to chemical reactions proceeding on the crystal surface. This effect is rather difficult to interpret because of the great diversity of chemical reactions occurring on the surface of crystals. In particular, we analyzed the dependences of the velocity of the chemical reaction front on the partial oxygen pressure and the external electric field strength for sapphire crystals [1] and revealed that the most probable reactions proceeding on the surface are as follows:

$$O_2 \rightleftharpoons 2O_{surf},$$
$$O_{surf} + Al_{lat}^{+3} \rightleftharpoons AlO^{+1}\uparrow + V_{Al}^{+n}$$

$$+\begin{cases}(2-n)h^+, & \text{at } 0 \le n \le 2\\ e^-, & \text{at } n = 3,\end{cases}$$

$$Al_{lat}^{+3} \rightleftharpoons Al\uparrow + V_{Al}^{+n} + (3-n)h^+.$$

Here, O_{surf} is the atomic oxygen absorbed by the surface, Al_{lat}^{+3} is the lattice aluminum, V_{Al}^{+n} is the aluminum vacancy with a positive charge $+n$, h^+ is the hole in the valence band, and e^- is the electron in the conduction band.

The existence of an AlO^{+1} ionized molecule in sapphire vapors was confirmed by mass spectrometric investigations [10]. The ratio between the rates of the second and third reactions determines the dependence of the parameter F_0 (the rate of formation of V_{Al}^{+n} aluminum vacancies) on the partial oxygen pressure. According to the results obtained in [1] and the mass action law, this ratio proves to be approximately equal to 0.6. The charge of V_{Al}^{+n} vacancies can be determined from the experiment on diffusion in an electric field. Unfortunately, this could not be done in [1], because there was an uncertainty in the mobility of aluminum vacancies in sapphire crystals. It was found with confidence that these vacancies possess an electric charge. Most probably, this charge is equal to +3.

Now, we return to the analysis of the size of the chemical reaction zone Δx_f. As follows from the above discussion, the size of the reaction zone does not depend on the position of the reaction front and, in dimensionless variables, is equal to 3.145. In dimensional variables, this value corresponds to the quantity $\Delta x_f = 3.145\sqrt{\frac{D}{kC_0}}$. By using formula (6) and assuming that $r_d = 2a_0$, we obtain the estimate $\Delta x_f \cong 0.345l\left(\frac{l}{a_0\xi}\right)^{1/2}$. Here, l is the mean distance between impurity atoms. Note that the quantity Δx_f is very small.

For example, at the content $C_0 = 10^{-4}$ at. %, we have $\Delta x_f \cong 3 \times 10^{-6}$ cm.

Such an abrupt front of the chemical reaction virtually cannot be experimentally investigated using optical methods. A different situation arises with semiconductor crystals in which the *p–n* transition can occur at the front of interaction between diffusing defects and a doping impurity [13]. In this case, the thickness of the reaction front can be determined by electrical methods, for example, from its amplitude–frequency and voltage–capacitance characteristics.

One additional essential remark needs to be made. In the case of a high concentration of doping impurities when the thickness of the reaction front is small (of the order of several tens or hundreds of the lattice constants), the description of the diffusion in the interaction region in terms of the parabolic equation can turn out to be a very rough approximation. This situation requires a more rigorous treatment, for example, in the framework of the kinetic equation or direct simulation.

As was noted above, mechanical stresses caused by variations in the dilatation volumes of the interacting components in the course of the chemical reaction can substantially affect the diffusion processes under investigation. This effect is especially pronounced in the case of low-temperature diffusion. As an illustration, we consider the low-temperature diffusion of interstitial silicon in single-crystal silicon doped with boron [13]. In our consideration, we will use the following constants of the diffusion process: $E \cong 10^{12}$ dyn cm^{-2}, $\vartheta = 0.3$, $\omega_{Si}^* = 4 \times 10^{-23}$ cm^{-3}, $\omega_B - \omega_B^* \cong 4.6 \times 10^{-23}$ cm^{-3}, and $C_0 = 10^{18}$ cm^{-3}. Here, ω_{Si}^* and ω_B^* are the dilatation volumes of interstitial silicon and boron, respectively, and ω_B is the dilatation volume of boron at the lattice site [14]. For these constants, we obtain the parameter $\gamma \cong -0.02$ [see Eq. (13)]. The thickness of the plate was taken to be equal to 3×10^{-2} cm, which, in dimensionless variables, corresponds to the quantity $\tilde{L} \cong 10^4$.

Figure 3 presents the calculated time dependences of the reaction front coordinate for the transition of boron from a substitutional position to an interstitial position in two plates of different thicknesses. The dependence calculated in the absence of mechanical stresses in the sample is also shown in this figure for comparison. It can be seen from Fig. 3 that stresses arising from the difference between the dilatation volumes $\omega_B - \omega_B^*$ bring about an appreciable increase in the velocity of the reaction front and that, in the presence of mechanical stresses, the velocity of the reaction front depends on the plate thickness.

One more manifestation of mechanical stresses that can be observed not only in platelike samples is noteworthy. The case in point is the instability of the stress distribution over the reaction front upon its separation from the surface of the sample. As follows from the analysis performed in this work, the instability of the stress distribution over the reaction front stems from the inhomogeneity of the distribution of lattice-defect generation centers over the sample surface, which, in turn, gives rise to sources of local stresses. The local stresses create channels through which defects can rapidly escape from local surface sources of their generation. For a unidirectional generation of intrinsic defects, a similar situation is observed on the outcropping surface. On this surface, a boron layer is retained in the initial state owing to the reverse transition of boron from an interstitial position to a substitutional position (the parameter $\theta \neq 0$). This also gives rise to an instability of the distribution of mechanical stresses due to the formation of local centers (either on the surface or in its immediate vicinity) through which silicon can effi-

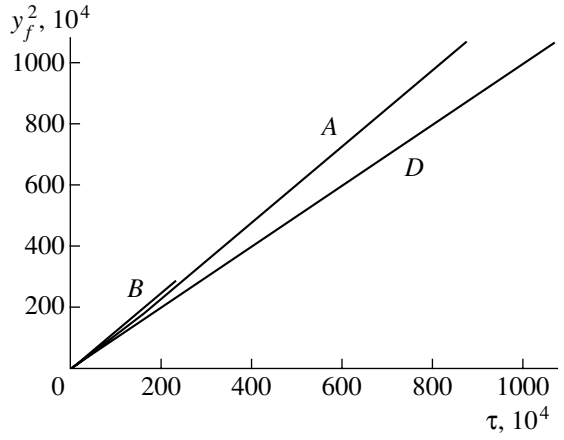

Fig. 3. Dependences of the square of the reaction front displacement on the time τ for plates of thicknesses $\tilde{L} = 1.0 \times 10^4$ (curve *A*) and $\tilde{L} = 0.6 \times 10^4$ (curve *B*). For comparison, straight line *D* shows the dependence calculated in the absence of mechanical stresses in the sample.

ciently escape from the interstitial position. The stationary distribution of stresses separates the flow of interstitial silicon (diffusing from the crystal bulk) into individual channels that are directed to local centers. This pattern bears some resemblance to the breakdown phenomenon. Most likely, a similar situation was observed in [13].

CONCLUSION

Thus, the investigations performed have demonstrated that the interaction between impurity atoms and intrinsic Schottky defects diffusing in a crystalline solid can substantially change the diffusion pattern. This interaction can be adequately described in terms of the chemical reaction, can manifest itself in a large variety of ways, and must always be taken into account in the interpretation of the experimental data on diffusion in solids.

REFERENCES

1. E. M. Akul'onok, Yu. K. Danileiko, V. Ya. Khaimov-Mal'kov, *et al.*, J. Solid State Chem. **26**, 17 (1978).
2. E. M. Akulenok, Yu. K. Danileĭko, V. S. Papkov, and V. Ya. Khaimov-Mal'kov, Kristallografiya **15** (6), 1200 (1970) [Sov. Phys. Crystallogr. **15**, 1048 (1970)].
3. E. M. Akulenok, Yu. K. Danileĭko, V. V. Panteleev, *et al.*, Kristallografiya **18** (5), 1044 (1973) [Sov. Phys. Crystallogr. **18**, 654 (1973)].
4. J. R. Manning, *Diffusion Kinetics for Atoms in Crystals* (Van Nostrand, Princeton, 1968).
5. Ya. E. Geguzin and M. A. Krivoglaz, *Motion of Macroscopic Inclusions in Solids* (Metallurgiya, Moscow, 1971).
6. F. A. Kroger, *The Chemistry of Imperfect Crystals* (North-Holland, Amsterdam, 1964).
7. Yu. K. Danileĭko, Yu. P. Minaev, and A. V. Sidorin, Kristallografiya **30** (5), 950 (1985) [Sov. Phys. Crystallogr. **30**, 551 (1985)].
8. Yu. K. Danileĭko, Izv. Akad. Nauk SSSR, Ser. Fiz. **46**, 1119 (1982).
9. W. Feller, *An Introduction to Probability Theory and Its Applications* (Wiley, New York, 1968; Mir, Moscow, 1984), Vol. 1.
10. T. Sasamoto and T. Sata, J. Chem. Soc. Jpn. **74**, 578 (1971).
11. Ya. E. Geguzin, *Diffusion Zone* (Nauka, Moscow, 1979).
12. A. D. Kovalenko, *Thermoelasticity* (Vishcha Shkola, Kiev, 1975).
13. A. N. Buzynin, A. E. Luk'yanov, V. V. Osiko, and V. V. Voronkov, Mater. Res. Soc. Symp. Proc. **510**, 281 (1998).
14. F. H. Horn, Phys. Rev. **97**, 1521 (1955).

Translated by O. Borovik-Romanova

Crystallography Reports, Vol. 47, No. 6, 2002, pp. 925–933. Translated from Kristallografiya, Vol. 47, No. 6, 2002, pp. 994–1003.

DIFFRACTION AND SCATTERING OF IONIZING RADIATION

Determination of the Parameters of a Rough Surface from the Dynamical X-ray Diffraction Data

V. L. Nosik

Center on Innovation and Technology "Crystal Growth," Russian Academy of Sciences, Moscow, 119333 Russia
e-mail: valnosik@mtu-net.ru

Received January 30, 2002

Abstract—A new method is proposed for determining the roughness parameters from X-ray diffraction data. The method is based on a controllable displacement of reflecting planes under an external tangential pressure. It is shown that the displacement of atomic planes near the rough surface upon sample compression increases in proportion to the applied stress and strongly depends on the roughness parameters. Rough surfaces with determinate periodic and random reliefs are considered together with the corresponding features of X-ray rocking curves. © *2002 MAIK "Nauka/Interperiodica".*

INTRODUCTION

Since the beginning of the twentieth century, X rays have been widely used for determining the structure parameters of various crystalline materials. Such experiments usually provide information on the periodic arrangement of molecules averaged over large volumes of substances.

Surface studies are usually carried out by the methods of atomic-force and electron microscopy, which are characterized by their small depth of penetration into the sample. The application of X-ray methods for this purpose requires either the grazing geometry of the sample or detection of secondary processes with a small escape depth, e.g., photoelectrons in the method of standing X-ray waves [1–3]. Relatively recently, three-crystal X-ray diffractometry was used for the diagnostics of submicrometer layers [2, 3]; this method makes it possible to judge the parameters of the stressed layer and surface of the crystal from the measurements of amplitude and width of the main peak and pseudopeak. However, these methods cannot be used if the crystal has no volume defects, disoriented films, or plastic deformations at the surface.

Under standard conditions, roughness affects the diffraction reflection of X rays so weakly that the crystal surface can be regarded as absolutely plane. Attempts to introduce a transition layer with smoothly varying parameters (density, interplanar spacing, etc.) usually led to physically incorrect results. In this respect, the following citation is illustrative: although "the actual structure of the surface (with its steps, oxide and adsorbed films, and other departures from an idealized pattern) may introduce a considerable distortion in the boundary condition scheme, … the problem is solved experimentally" [4].

This is due to the fact that X rays penetrate a crystal to a depth of the order of the extinction length (2–20 μm) even under dynamical diffraction conditions, while the thickness of atomic layers disordered by roughness is much smaller. In some cases, the contribution of the surface (or surface region) may become comparable with the bulk contribution. For example, in the grazing geometry of scattering, the main contribution to the intensity of the scattered wave comes from the inhomogeneous and damaged surface layer (Yoneda effect) [5], while substrates that repeat and enhance morphological features play the leading role in the reflectometry of multilayerd epitaxial structures [6].

It is well known that in the case of homogeneous shearing strain, the roughness of the surface relief of the sample generates supplementary strains in the surface regions of the crystal. It will be shown below that the high sensitivity of X rays to the elastic distortions of reflecting planes under diffraction conditions makes it possible to determine the parameters of the deformed surface layer and to connect them with the rough surface characteristics.

Under loading, the surface relief peculiarity becomes a source of elastic stresses; in accordance with Hooke's law, the induced displacements are directly proportional to the applied force. As a result of the statistical action of the entire relief, a certain distribution of elastic displacements of reflecting planes is formed, which results in considerable changes in the shape and position of the rocking curve.

ROUGHNESS PARAMETERS

In spite of the fact that roughness strongly affects the user properties of articles, a quality criterion for estimating roughness was introduced in Russian industry only in 1928: rough surfaces with traces of machining are marked by △, surfaces with almost indistinguishable traces of finishing correspond to △△, finished

1063-7745/02/4706-0925$22.00 © 2002 MAIK "Nauka/Interperiodica"

Table 1. Roughness parameters and grades of finishing

Finishing class	R_a, μm	R_z, μm
Δ1	80	320
Δ2	40	160
Δ3	20	80
Δ4	10	40
Δ5	5	20
Δ6	2.5	10
Δ7	1.25	6.3
Δ8	0.63	3.2
Δ9	0.32	1.6
Δ10	0.16	0.8
Δ11	0.08	0.4
Δ12	0.04	0.2
Δ13	0.02	0.1
Δ14	0.01	0.05

surfaces are marked by △△△, and finely finished surfaces, by △△△△.

At present, the following two numerical parameters are commonly used: the arithmetic mean deviation of the profile from the mean line over length l,

$$R_a = \frac{1}{l}\int_0^l |H|dx \approx \frac{1}{n}\sum_{i=1}^{n}|z_i| \quad (1)$$

and the height of profile roughness, which is equal to the mean distance between the five highest and five lowest points of the profile over length l,

$$R_z = \frac{1}{5}\sum_{i=1}^{5}(H_i^{\max} - H_i^{\min}), \quad (2)$$

where the profile $H(x)$ of the surface is a function of the coordinate x along the surface. Usually, the category of finishing to which certain values of R_a and R_z correspond is indicated (Table 1).

In addition, the mean-square deviation (R_s^2), the number of intersections with the level, the number of peaks over the interval, the mean slope of the curve, the duration of the process occurring above the level, as well as some other parameters are also sometimes used.

It is assumed that a determinate (usually periodic) relief and a random component, the relation between which may change over a wide range, appear on the finished surface of a material.

We will confine our analysis to a one-dimensional relief for which the surface profile depends only on the coordinate x along the chosen axis. This kind of roughness is formed as a result of the back and forth movement of the tool during polishing. An analysis of the rough surface formed as a result of circular motion of the polishing tool requires a 2D mathematical apparatus and will be carried out later.

In the general case, the description of the relief of a rough surface should be based on finite functions of two variables $H(x, r)$, where r is an elementary event from a certain probabilistic space and x is the coordinate along the surface. Having fixed the variable r, we obtain a certain realization of the surface $H_r(x)$; conversely, by fixing x, we can determine the statistical set of possible positions of the surface $H_x(r)$ at this point.

The roughness profile can be presented in the form of a Fourier integral,

$$H(x) = \int \exp(iqx)dZ(q), \quad (3)$$

in which the contribution of each harmonic is determined by the statistical weight $dZ(q)$.

In order to determine the random function $H(x)$, we must specify all the momenta of its distribution. However, the analysis is usually confined to the introduction of a correlation function K (or the covariation function) and the mean value $m(x)$:

$$\begin{aligned} m(x) &= E[H(x)], \\ K(x, x') &= E[(H(x) - m)(H(x') - m)]. \end{aligned} \quad (4)$$

We will consider below the following two cases of practical importance: a rough surface with a determinate relief, when $m(x) = m_0(q_* x)$, and a completely random relief, when $m(x) = 0$.

We assume that the correlation function depends only on the coordinate difference $\tau = x - x'$, which enables us to use in some cases the Birkhoff-Khinchine theorem

$$K(\tau) = \int_{\infty}^{-\infty} \exp(iq\tau)s(q)dq. \quad (5)$$

Table 2 contains the correlation function used here and the corresponding spectral densities $s(q)$. The correlation length a introduced in Table 2 is an important parameter. In order to obtain qualitative estimates of roughness with a determinate relief, we can use the relation $R_{a,s} \approx m_0 + a$.

ELASTIC STRAINS IN THE VICINITY OF A ROUGH SURFACE

Let us suppose that the width and length of the sample under investigation (x and y axes) are much larger than its height (z axis), its rough surface has a certain relief $H(x)$, and it is elastically compressed along the x axis so that $\sigma_{xx} = \sigma_0$ in the bulk of the sample. Figure 1 shows the simplest experimental setup in which the

sample is compressed by the force of gravity of the load. In order to eliminate bending of the reflecting planes, it is important to avoid twisting the sample under loading.

Since the normal **n** to the rough surface is not directed strictly along the z axis, $\mathbf{n} = (n_x, 0, n_z)$, the boundary conditions [7–9]

$$n_i\sigma_{ik} = 0 \tag{6}$$

lead to the following equation for determining the stress tensor:

$$\sigma_{kz} - \sigma_{kx}\frac{\partial H}{\partial x} = 0. \tag{7}$$

The solution of this equation can be sought in the perturbation theory as the sum of the large bulk term $\sigma_{xx} = \sigma_0$ and the small term σ^s_{kz} emerging as a result of the inclusion of the term linear in H:

$$\sigma^s_{kz} = \sigma_0\frac{\partial H}{\partial x}. \tag{8}$$

In the general case of a 2D roughness, such a problem is solved by introducing a local system of coordinates $R = R(x', y', z')$, in which the region of the surface under investigation lies at a height z'. In this system, the normal to the surface has the form [7]

$$\mathbf{n} = \mathbf{e}_z - \frac{\mathbf{e}_x}{H_1}\frac{\partial H}{\partial x'} + \frac{\mathbf{e}_y}{H_2}\frac{\partial H}{\partial y'}, \tag{9}$$

where H_k are the Lamé coefficients. Substituting this expression into Eq. (6), we can derive a more general expression for the surface stress tensor components.

Expressions (7) and (8) can be used for an isotropic as well as anisotropic solid (crystal). We will confine our subsequent analysis to the case when stresses are applied along the principal axes of the crystal, and elastic parameters of the crystal and the isotropic material coincide.

In the case of symmetric Bragg diffraction, the diffraction vector **h** is directed along the normal to the surface (z axis), and the solution of averaged Takagi–Taupin equations requires knowledge of the momentum's set of distribution of only one component of the displacement vector. The Fourier component of the polarizability of the deformed crystal assumes the form

$$\begin{aligned}\chi^d_h &= \chi_h\overline{\exp(ihu_z)}\\ &\approx \chi_h\exp(ih\bar{u}_z)\exp\{-h^2(\overline{u_z^2} - \bar{u}_z^2)\},\end{aligned} \tag{10}$$

where χ_h is the value for a perfect crystal.

Hooke's law makes it possible to determine easily the displacement of the reflecting planes of the sample under the action of the external bulk load σ_0:

$$u_{xx} = \sigma_0/E, \quad u_{yy} = u_{zz} = -\nu\sigma_0/E, \tag{11}$$

Table 2. Correlation functions in direct and reciprocal spaces

$K(\tau)$	$s(q)$
$K_1 = R_s^2\exp(-\alpha_1\lvert\tau\rvert)$	$s_1 = \dfrac{R_s^2\alpha_1}{\pi(\alpha_1^2 + q^2)}$
$K_2 = R_s^2\exp(-\tau^2/a^2)$	$s_2 = \dfrac{aR_s^2}{2\sqrt{\pi}}\exp(-4q^2a^2)$

where E is the Young modulus and ν is the Poisson ratio.

We assume that the external force is applied to one of the sides of the sample whose length along the direction of force is equal to L, and the opposite side of the crystal is pressed; in this case, the displacements have the form

$$u_x = \sigma_0 x/E, \quad u_z = u_0 - \nu\sigma_0 z/E. \tag{12}$$

The value of the induced strain can easily be controlled either from the displacement of the sample edge,

$$u_x(L) = \sigma_0 L/E \tag{13}$$

or from the change in the Bragg angle,

$$\delta\theta \sim u_{zz}, \tag{14}$$

which is defined as the center of the rocking curve during reflection or transmission diffraction taking refraction into account.

Thus, we can assume that the tangential force

$$F_x = \sigma^s_{xz}dxdy \tag{15}$$

is applied to a small element $dxdy$ on the sample surface, and we must determine the displacements.

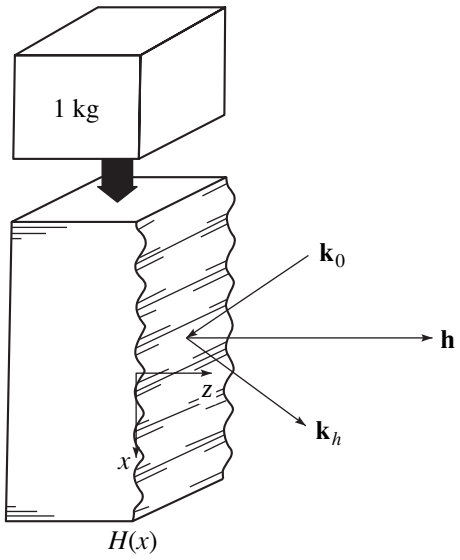

Fig. 1. Diffraction geometry and experimental setup.

There exist several approaches to the solution of this problem [8–10]. We will use the most physically feasible approach [9], in which the solution is constructed on the basis of the formalism of point sources (Green's tensors) for the equilibrium equation for a semi-infinite medium.

Under the action of the point force

$$F_x = \sigma_0 \frac{dH}{dx}\delta(x')\delta(y'). \quad (16)$$

The atomic planes are deformed along all the three axes ($i = x, y, z$):

$$u_i(x, y, z) = G_{ix}(x - x', y - y', z - z')F_x(x', y', z'). \quad (17)$$

We are interested only in the displacements u_z, for which Green's function has the form [9]

$$G_{zx} = xT(r), \quad T(r) = \alpha\left(\frac{1-2\nu}{r(r+z)} + \frac{z}{r^3}\right), \quad \alpha = (1+\nu)/2\pi E, \quad (18)$$

where

$$r = \sqrt{x^2 + y^2 + z^2}.$$

Summing over all point sources on the surface, we obtain

$$\bar{u}_z(r) = \sigma_0 \int iqF(r, q)dZ(q),$$
$$\overline{|u_z(r)|^2} = \sigma_0^2 \int s(q)q^2 dq|F(r, q)|^2. \quad (19)$$

While writing this expression, we have used the spectral representation (3) and introduced the notation

$$F(r, q) = \int_{-\infty}^{\infty} dx' \int_{-\infty}^{\infty} dy'(x - x')\exp(iqx')T(x - x', y - y', z). \quad (20)$$

Taking into account the translation symmetry of the problem along the y axis, we will consider the displacements at point $y = 0$ and carry out integration with respect to y'; this gives

$$F(r, q) = \int_{-\infty}^{\infty} dx' G(x - x', z)\exp(iqx'), \quad (21)$$

where

$$G(x - x', z) = \int_{-\infty}^{\infty} dy' T(x - x', y', z)$$
$$= -2\alpha\{(1-2\nu)\,\mathrm{sgn}(x - x')\arccos(z/A) + z(x - x')/A^2\}, \quad (22)$$
$$A^2 = (x - x')^2 + z^2.$$

DETERMINATE RELIEF

Let us suppose that we can single out in the Fourier expansion (3) of the random function describing the surface relief an anomalously large harmonic,

$$H(x') \approx m_0 \sin(q_* x'),$$
$$dZ(q) \approx -0.5im_0(\delta(q - q_*) - \delta(q + q_*)). \quad (23)$$

In this case, statistical average displacements of the reflecting planes have the form

$$\bar{u}_z(r) = 0.5\sigma_0 m_0 q_*(F(r, q_*) + F(r, -q_*)). \quad (24)$$

Figure 2 shows the calculated 3D curves describing the functions

$$f(z, q) = \bar{u}_z(r)/\sigma_0 m_0 \alpha \quad (25)$$

in dimensionless coordinates (in units of $a = 2\pi/q_*$). It should be noted that the form of the function G weakly depends on the type of the sample under investigation. The Poisson ratio is approximately equal to 0.3 for almost all solids. For example, for germanium (silicon) subjected to an external action along the crystallographic axes, we obtain $\nu = 0.273$ (0.278) and $E = 0.85$ (1.017) $\times 10^7$ N/cm^2 [11].

Figure 2a corresponds to the typical value of the Poisson ratio $\nu = 0.3$. Figure 2b shows the graph for $\nu = 0.5$, which corresponds to an incompressible solid. It can be seen from the figures that the emerging displacements are periodic functions of x (coordinate along the surface) and decrease quite rapidly in the bulk of the crystal. It will be shown in the Appendix that the following expression can be used for approximate calculations:

$$\bar{u}_z(r) \approx 0.5\sigma_0 m_0 q_*(f_0(z) + f_1(z)\sin(q_* x)). \quad (26)$$

It is interesting to note that, in addition to the damaged surface layer, one more stressed region is formed in the sample at a depth of the order of $3a$; between these regions, the crystal lattice is practically perfect. Thus, the higher the quality of finishing of the surface (the larger the parameter a), the more uniform the distribution of emerging stresses over the volume, which improves the quality of the working surface.

Let us estimate the effective influence of a periodic relief on the X-ray diffraction. An estimate of the mean displacement gives

$$h\bar{u}_z \le Mf^m, \quad M = (1+\nu)hm_0\frac{\sigma_0}{2\pi E}, \quad (27)$$

where f^m is the maximum of function f (a number of the order of unity).

Let the characteristic amplitude of the relief be $m_0 =$ 1 μm ($hm_0/2\pi = m_0/d = 10^4$, where d is the interplanar spacing); in this case, displacements become large even under insignificant loads,

$$M = 10^4\sigma_0/E. \quad (28)$$

Let us estimate such loads. We assume that the theoretical limit of the material strength is approximately equal to $0.1E$. However, the breakdown is usually observed for a load two or three orders of magnitude smaller owing to the inhomogeneities of the structure. The critical loads for single crystals are higher. For example, for a sapphire whisker, the tensile strength is $\sigma_t/E = 0.028$. In order to create displacements with $M = 0.05$ that are detectable in X-ray experiments, we must apply to a crystal a pressure $\sigma_0 = 5 \times 10^{-6}E$, which amounts to 5 kgf/cm^2 (50 N/cm^2) in the case of germanium.

Disregarding the terms quadratic in $h\bar{u}_z$ in Eq. (10) and using the well-known expansion, we can present the polarizability of the crystal in the form

$$\chi_h^d \approx \chi_h \exp(ih\bar{u}_z) = \chi_h \sum_{n=-\infty}^{\infty} J_n(Mf_1(z))\exp(inq_* x), \quad (29)$$

where J_n is an integer-order Bessel's function. The scattering potential of this form is typical of superlattices [10]; the only specific feature is the dependence of the contribution from each harmonic on coordinate z.

In the case of X-ray scattering from a crystal with a superlattice, the Takagi–Taupin equations defining the amplitudes of the transmitted (E_0) and diffracted (E_h) waves,

$$E = E_0 \exp(i\mathbf{k}_0\mathbf{r}) + E_h \exp(i\mathbf{k}_h\mathbf{r}) \quad (30)$$

split into an infinitely large system of equations in the new components

$$E_{0,h} = \sum_{n=-\infty}^{\infty} E_{0,h}^n \exp(inq_* x). \quad (31)$$

Thus, the initial reflection splits into n individual reflections that correspond to scattering with the diffraction vector $\mathbf{h} + nq_*\mathbf{e}_x$. In the case when the angular half-width of the principal reflection

$$\Delta\theta = \frac{2C|\chi_h|}{\sin 2\theta} \quad (32)$$

(θ is the Bragg angle) is smaller than the angular displacement of the supplementary reflection

$$\delta\theta_n = nq_*/k_0 \cos\theta \quad (33)$$

additional reflections called satellites appear on the rocking curve.

The fact that satellites emerge indicates that the relief of the rough surface contains a harmonic with the period

$$a = 2\pi/q_* < \pi/k_0 \cos\theta\Delta\theta. \quad (34)$$

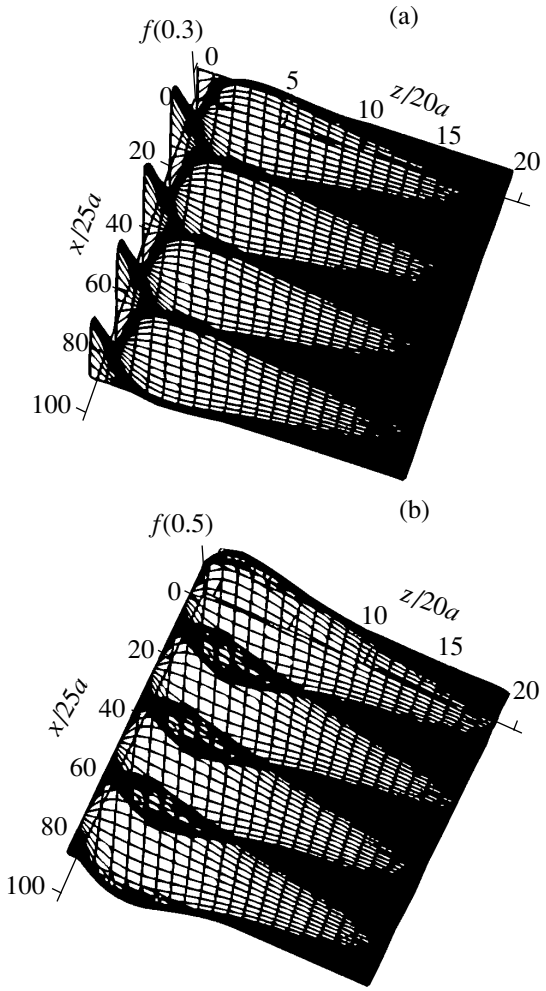

Fig. 2. Calculated 3D plots describing the dependence of displacements induced by roughness on coordinates x and z.

For example, for reflection Si(111) of CuK_α radiation, the width of the rocking curve is $\Delta\theta \approx 1.6 \times 10^{-5}$, and the minimal period of the harmonic being detected is $a_{\min} \approx 70$ μm. Thus, the value of q_* can be determined from the angular position of a satellite, and the measurement of its angular width proportional to

$$J_1(Mf_1) \approx Mf_1/2, \quad (35)$$

makes it possible to determine m_0.

By way of an example, Fig. 3 shows the calculated rocking curves with resolved satellites for the reflection Si(111) of monochromatic CuK_α radiation, where

$$p = 2 \times 10^6 \Delta\theta. \quad (36)$$

Figure 3a shows the theoretical rocking curves for $\delta\theta_n = \Delta\theta$ (the extinction length is equal to two roughness periods) and $M = 0.1$ and 0.5 (curves *1* and *2*). It can be seen that the contribution from a second-order satellite ($n = 2$) is negligibly small. Figure 3b illustrates the change in the theoretical rocking curves upon a

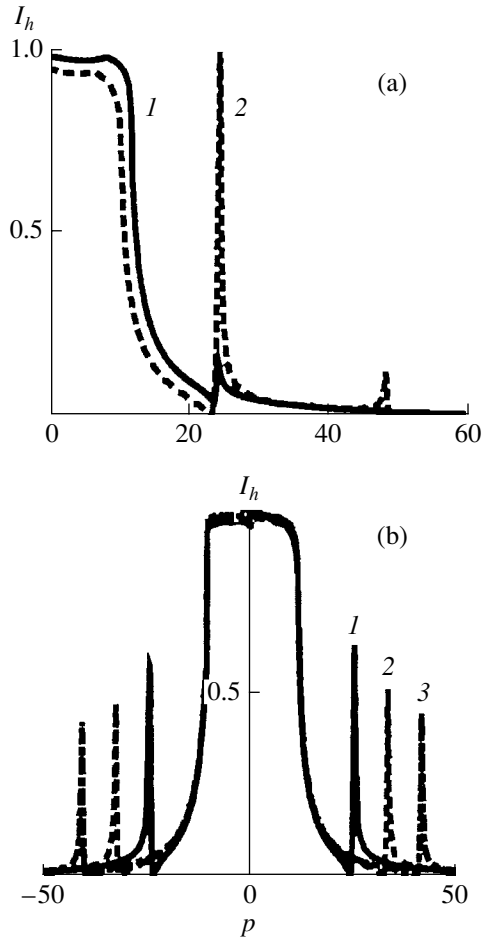

Fig. 3. Calculated rocking curves with resolved satellites for reflection Si(111); CuK_α radiation, determinate relief: (a) extinction length is equal to two roughness periods, M = 0.1 and 0.5 (curves *1* and *2*); (b) variation of the roughness period, $\delta\theta_n/\Delta\theta$ = 3, 4, and 5 (curves *1*, *2*, and *3*), M = 0.4 (m_0 = 1 μm, σ_0 = 400 N/cm^2).

variation of the roughness period $\delta\theta_n/\Delta\theta$ = 3, 4, and 5 (curves *1*, *2*, and *3*) for M = 0.4.

The diffraction fields in the region of a satellite were calculated in perturbation theory, disregarding their effect on the principal reflection. For better visualization, the displacement of the center of the rocking curve (14) was neglected. If the layer in which displacements are concentrated is comparable with the extinction length for the given reflection, $\Lambda_n \sim \lambda/\Delta\theta J_n$, the reflection is dynamic. For such a reflection, for the exact Bragg angle, the intensity of the reflected wave is equal to the intensity of the incident wave, although its angular width may be very small.

Till now, we have disregarded the terms quadratic in $h\bar{u}_z$ in view of their smallness for relatively small applied pressures. In the case of an indeterminate relief, their effect on the X-ray diffraction must be taken into account consistently.

INDETERMINATE RELIEF

In the case of a rough surface without a determinate relief ($m_0 = 0$), the polarizability of the crystal assumes the form

$$\chi_h^a \approx \chi_h \exp(-h^2\overline{u_z^2}). \tag{37}$$

Let the correlation function be defined in the form K_2 (Table 2). We can simplify the calculation of $\langle|u_z|^2\rangle$ by carrying out first the integration with respect to q in Eq. (19):

$$\langle|u_z(x,z)|^2\rangle = \sigma_0^2\int_{-\infty}^{\infty}dx'\int_{-\infty}^{\infty}dx''G(x-x',z)G^*(x-x'',z)J(x'-x''); \tag{38}$$

here, we have introduced a function defining the correlation of the first derivative of displacements:

$$J(x'-x'') = \int_{-\infty}^{\infty}\lambda^2 d\lambda s_2(\lambda)\exp(i\lambda(x'-x'')) = \frac{R_s^2}{a^2}(1+(x'-x'')^2/4a^2)\exp(-(x'-x'')^2/a^2). \tag{39}$$

As the argument increases, the function $J(x'-x'')$ decreases at a slightly lower rate than the function $K(x'-x'')$ (Fig. 4). In the limiting case of "coarse" roughness $a \ll R_s$, we can make the substitution

$$J(x'-x'') \approx j\delta(x'-x''), \quad j = \frac{R_s^2\sqrt{\pi}}{2a},$$

leading to the expression

$$\langle|u_z^0(r)|^2\rangle = j\sigma_0^2\lim_{r_c\to\infty}\int_{-r_c}^{r_c}dx'|G(x-x',z)|^2. \tag{40}$$

In the case of integration between infinitely large limits, expression (40) diverges for any external pressure. If we use the exact function $J(x'-x'')$, the integral diverges even more rapidly. This is due to the fact that Green's functions in Eq. (18) decrease slowly with increasing distance from the point source, and the integration itself is distributed over the entire surface of the crystal.

Such a divergence contradicts the experimental data even if we take into account the fact that we consider the square of displacements and that computations are statistical by nature. Although the stresses at the surface increase upon the application of a load, breakdown usually occurs along 3D fracture surfaces as a result of crack initiation and growth. Cleavage occurs along the crystallographic cleavage planes in the case of a brittle fracture and through coalescence of microvoids and

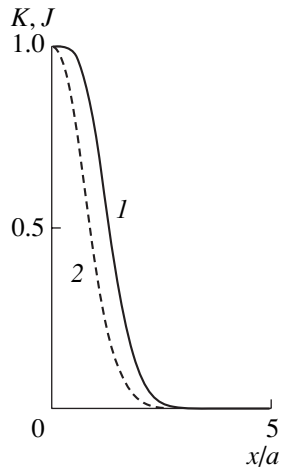

Fig. 4. Curves describing the functions $K(x)$ (*1*) and $J(x)$ (*2*).

slip due to plastic deformation in the case of a ductile fracture.

Expression (38) describes displacements only in a perfect elastic solid; in actual practice, the structure always contains inhomogeneities. Polycrystalline materials contain grain boundaries, while single crystals have clusters, impurity inclusions, and cleavage and twinning planes.

As the external force increases (during sample preparation or under repetitive loading), individual groups of atoms, especially those constituting defects in crystals, usually experience rearrangements including plastic deformation, during which the local stresses decrease ("relax"). If the local stress on a certain surface in the bulk of the crystal is higher than the ultimate strength σ_t, a microcrack will pass through this surface element. The larger the size of the crack, the higher the stress concentration. The limiting size of the cluster (Griffith crack) is determined from the condition that the energy liberated during the growth of the crack compensates the expenditures on the formation of the crack surface,

$$r_c \approx E\gamma/\sigma^2, \tag{41}$$

where γ is the energy corresponding to the unit surface area of the material. If a stress σ is applied to the sample, it is deformed first elastically and then plastically. In this case, considerable local stresses appear in the vicinity of structural inhomogeneities (including the rough surface). The applicability of the theory developed above is determined precisely by the transition from elastic to plastic deformation.

Thus, for the limit of integration in Eq. (40), we can use the length r_c, while still remaining in the limits of applicability of the theory of elasticity. In this approximation, quadratic displacements can be estimated by the following expression for s^2, which does not depend on the applied stress:

$$h^2\overline{\left|u_z^0\right|^2} \le s^2,$$
$$s^2 = (1+\nu)^2\left(\frac{h\sigma_0}{2\pi E}\right)^2 r_c R_s^2/a = (1+\nu)^2\frac{h\gamma}{4\pi^2 E}hR_s^2/a. \tag{42}$$

Under standard conditions, the length r_c for crystals is much larger than the extinction length (2–20 μm) and does not significantly affect the diffraction.

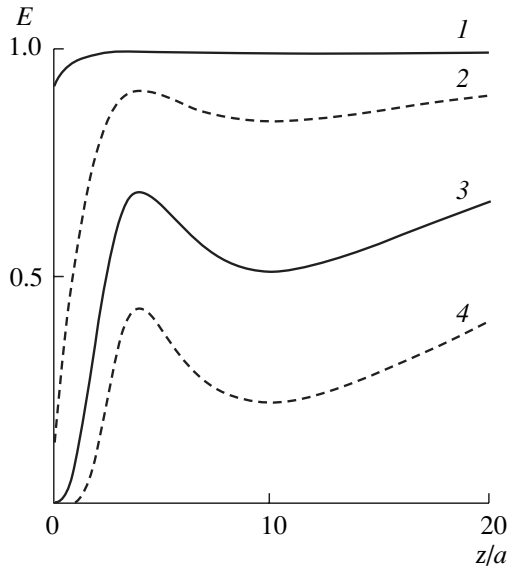

Fig. 5. Calculated dependences of the Debye–Waller factor E on the depth z; s = 0.1, 0.5, 1, and 1.5 (curves *1*, *2*, *3*, and *4*).

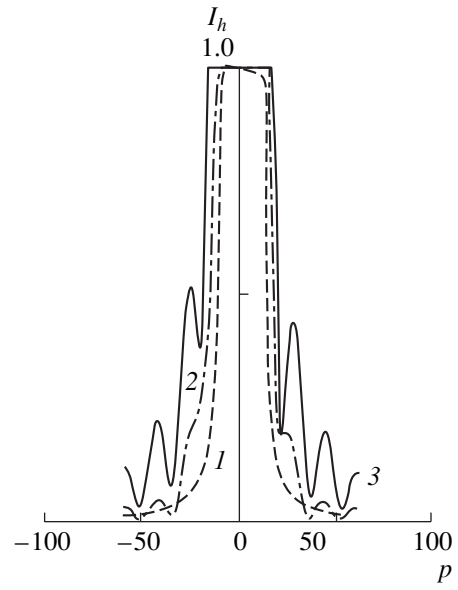

Fig. 6. Calculated rocking curves for reflection Si(111), CuK_α radiation, and indeterminate relief.

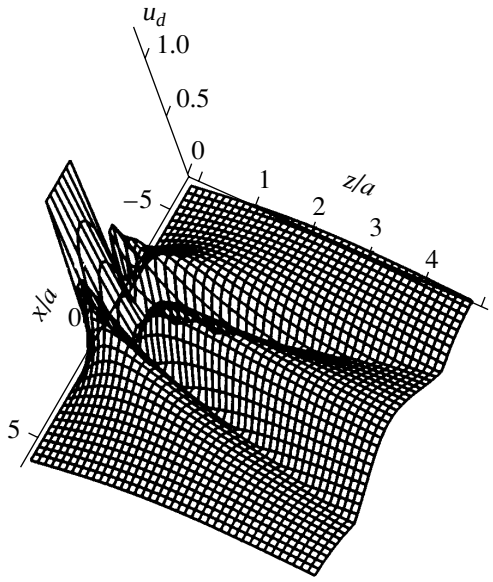

Fig. 7. Two-dimensional displacement field around the "dipole" created by the period of the relief.

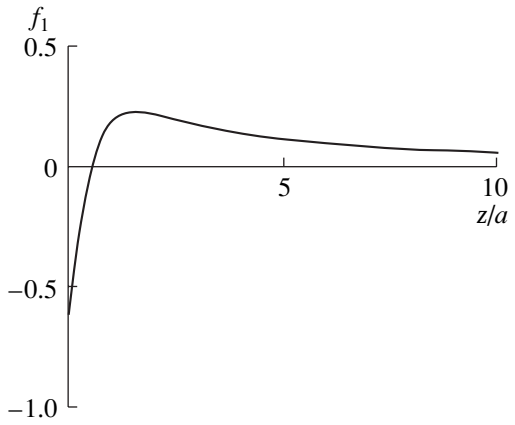

Fig. 8. Curve describing the dependence of the Fourier component $f_1(z)$ on the depth.

Figure 5 shows the theoretical dependences of the Debye–Waller factor

$$E = \exp(-s^2 N(z)),$$
$$N(z) = \frac{1}{2\alpha^2 r_c}\int_{-r_c}^{r_c} dx|G(x,z)|^2 \quad (43)$$

for s = 0.1, 0.5, 1, and 1.5 (curves *1*, *2*, *3*, and *4*) obtained as a result of integration over the surface. It should be observed that the displacement of atomic planes increases at a depth of the order of $10a$ in this case also. Unfortunately, only qualitative estimates are available for r_c since the surface energy γ in relation (41) depends considerably on plastic strain and on temperature effects. For example, for a roughness height R_s = 0.1 μm, correlation length a = 200 μm, reflection Si (111), and r_c = 602 μm, we obtain s = 1.

Figure 6 shows the theoretical rocking curves for a symmetric Bragg reflection Si(111) of CuK_α radiation corresponding to s = 0, 0.01, and 0.1 (curves *1*, *2*, and *3*). The calculations were based on a layer-by-layer solution of the Takagi–Taupin equations on a segment of z from 0 to a according to the method described in [12] (the number of layers is 200). It can be seen that as the applied stresses increase, the rocking curve becomes broader and displays oscillations that can be used for numerically determining the rms roughness R_s.

It should be noted that the theory developed here is applicable for characterizing a surface with the displacement correlation parameter a larger than the extinction length. Otherwise, the scattering in the surface region is of a kinematic type.

CONCLUSIONS

We have proposed a method for determining the statistical parameters of a real surface subjected to an external load creating a macroscopic elastically deformed layer near the crystal surface. It is shown that the rocking curve changes significantly when the rough surface parameters change and a load is applied in the case of Bragg reflection.

Surfaces with a determinate periodic relief were considered. It is shown that the rocking curve acquires satellites if the period of a relief is smaller than its extinction length. The angular deviation of a satellite from the exact Bragg angle makes it possible to determine unambiguously the period of the relief.

The X-ray express method of diagnostics of a rough surface is attractive in view of the nondestructive action of X rays and the availability of the X-ray equipment. It should be noted that, in most cases, the user is interested in certain averaged parameters of a rough surface rather than in a detailed pattern of the relief, which is provided, for example, by atomic-force and electron microscopy. Consequently, the drawback of all X-ray methods associated with the averaging of X-ray data over the area illuminated by an X-ray beam becomes its advantage. In addition, modern X-ray optics makes it possible to vary the beam cross section over a wide range.

In a number of cases, it is more important (from the user's point of view) to obtain not an ultrasmooth surface, but a roughness with given (or controllable) parameters. For example, the flat-top honing of cylinders of internal combustion engines is usually carried out in two stages [13]. First, a basic roughness with deep indentations (R_s = 20–30 μm), which are filled with oil during the engine operation, is created with the help of coarse-grain hones (a = 100–120 μm). Then, the protrusions are smoothed with the help of small-grain hones (12–40 μm) to create the bearing surface. By way of another example, we consider epitaxial processes,

which are determined not only by the atomic structural and geometric correspondence between the film and the substrate, the process temperature, etc., but also by the perfection of the substrate and the finishing of its surface [14]. The epitaxy begins with the emergence of individual crystallites on the substrate, which coalesce to form a continuous film. At the initial stage of coalescence, it is the indentations of the rough surface that may serve as active centers of crystallization. Epitaxy can also take place on a pseudoamorphous substrate with a crystallographically symmetric microrelief (graphoepitaxy).

The samples subjected to investigation by X-ray methods are often under the action of uncontrollable external loads. The sources of such deformations include

(i) deformations emerging during the fixation of crystals (gluing, clamping, etc. [15]);

(ii) mismatch between lattice parameters between the layers in crystalline multilayered systems and systems using crystalline substrates; and

(iii) the nonuniform heating of samples under high-power synchrotron radiation beams.

In this case, the surface roughness may lead to the formation of macroscopic deformed layers in the crystal, which may considerably deteriorate the interpretation of the obtained results.

APPENDIX

The form of the calculated field of displacements (Fig. 2) suggests that the integration over the roughness period can be replaced by summation over two point sources located at the points $\pm\pi/2q = \pm a/4$:

$$\begin{aligned} 2\bar{u}_z(r)/\sigma_0 m_0 &= F(r, q_*) + F(r, -q_*) \\ &= \int_{-a/4}^{a/4} dx' G(x - x', z)\sin(qx') \qquad \text{(A.1)} \\ &\approx \pi/q_*\{G(x + \pi/2q_*, z) - G(x - \pi/2q_*, z)\}. \end{aligned}$$

Figure 7 shows the displacement field around such a "dipole." It can be verified that the field of the "dipole" decreases in the bulk of the crystal in proportion to $1/z^2$, i.e., much more rapidly than the function G proper.

Summing over the "dipoles" closest to the point of observation, we can easily obtain the analytic expression

$$\begin{aligned} &F(r, q_*) + F(r, -q_*) \\ &\approx \pi/q_* \sum_N G(x + \pi/2q_* + Na, z) \qquad \text{(A.2)} \\ &\quad - G(x - \pi/2q_* + Na, z), \end{aligned}$$

which is in good agreement with the results of calculations. Taking into account the periodicity of displacements along the surface (x axis), we apply again the approximate integration formula (A.1) to obtain the Fourier function series

$$F(r, q_*) + F(r, -q_*) \approx f_0(z) + f_1(z)\sin(q_* x).$$

In this approximation, we obtain $f_0 = 0$,

$$\begin{aligned} f_1(z) &= q_*/2\pi \int_{-\pi/q_*}^{\pi/q_*} dx \sin(q_* x)(F(r, q_*) + F(r, -q_*)) \\ &= 1/2\{G(\pi/q_*, z) + G(-\pi/q_*, z)\} \\ &\quad - 2\alpha\{(1 - 2\nu)\arccos(z/A_0) + (z\pi/q_*)A_0^2\}, \end{aligned}$$

where

$$A_0^2 = z^2 + (\pi/q_*)^2. \qquad \text{(A.3)}$$

Figure 8 shows the curve describing the dependence $f_1(z)$.

REFERENCES

1. V. L. Nosik and M. V. Kovalchuk, Nucl. Instrum. Methods Phys. Res. A **405**, 480 (1998).
2. A. M. Afanas'ev, P. A. Aleksandrov, and R. M. Imamov, *X-ray Diffraction Diagnostics of Submicron Layers* (Nauka, Moscow, 1989).
3. A. M. Afanas'ev, P. A. Aleksandrov, and R. M. Imamov, *X-ray Structural Diagnostics in Researching Near-Surface Layers of Single Crystals* (Nauka, Moscow, 1986).
4. Z. G. Pinsker, *X-ray Crystal Optics* (Nauka, Moscow, 1982).
5. S. K. Sinha, E. B. Sirota, S. Garoff, and H. B. Stenley, Phys. Rev. B **38**, 2297 (1988).
6. S. I. Zheludeva, M. V. Kovalchuk, N. N. Salaschenko, *et al.*, Rev. Sci. Instrum. **63** (1), 1519 (1992).
7. V. A. Pal'mov, Izv. Akad. Nauk SSSR, Mekh. Mashinostr. **5**, 1 (1963).
8. A. P. Khusu, Yu. R. Vitenberg, and V. A. Pal'mov, *Surface Roughness (Probability-Theoretical Approach)* (Nauka, Moscow, 1975).
9. L. D. Landau and E. M. Lifshitz, *Course of Theoretical Physics*, Vol. 7: *Theory of Elasticity* (Nauka, Moscow, 1987; Pergamon, New York, 1986).
10. A. I. Lur'e, *Three-Dimensional Problems of Theory of Elasticity* (Gostekhizdat, Moscow, 1955).
11. K. Brugger, Phys. Rev. A **133**, 1611 (1964).
12. V. L. Nosik, Kristallografiya **38** (1), 4 (1993) [Crystallogr. Rep. **38**, 1 (1993)].
13. A. É. Khrulev, *Repair of Foreign Car Engines* (Izd. "Za Rulem," Moscow, 2000).
14. L. S. Palatnik and I. I. Papirov, *Epitaxial Films* (Nauka, Moscow, 1971).
15. M. V. Kovalchuk, E. V. Suvorov, O. P. Aleshko-Ozhevskii, *et al.*, Nucl. Instrum. Methods Phys. Res. A **405**, 449 (1998).

Translated by N. Wadhwa

Crystallography Reports, Vol. 47, No. 6, 2002, pp. 934–938. Translated from Kristallografiya, Vol. 47, No. 6, 2002, pp. 1004–1008.

STRUCTURE OF INORGANIC COMPOUNDS

Phase Separation in High-T_c Superconductors, Copper Oxides, and Related Antiferromagnetic Phases CuO and Y_2BaCuO_5[1]

S. G. Titova*, A. N. Titov, D. O. Shorikov*, D. I. Kochubeĭ***, S. G. Nikitenko***, V. F. Balakirev*, P. P. Pal'-Val'****, L. N. Pal'-Val'****, and T. I. Arbuzova****

** Institute of Metallurgy, Ural Division, Russian Academy of Sciences, ul. Amundsena 101, Yekaterinburg, 620016 Russia*

e-mail: titova@imet.sco.ru

*** Institute of Metal Physics, Ural Division, Russian Academy of Sciences, ul. S. Kovalevskoĭ 18, Yekaterinburg, 620219 Russia*

**** Boreskov Institute of Catalysis, Siberian Division, Russian Academy of Sciences, pr. Akademika Lavrent'eva 5, Novosibirsk, 630090 Russia*

***** Verkin Institute for Low Temperature Physics and Engineering, National Academy of Sciences of Ukraine, pr. Lenina 47, Kharkov, 61103 Ukraine*

Received January 10, 2002

Abstract—The acoustic properties and crystal structure of high-T_c superconducting cuprates and the related antiferromagnetic phases CuO and Y_2BaCuO_5 exhibit similar properties at a temperature of about 160 K and 240 K. These properties can be associated with the formation of inhomogeneous state of phase separation. Analysis of the magnetic properties of Y_2BaCuO_5 shows that these effects are of a nonmagnetic nature. The results of EXAFS data for the high-T_c superconducting compound $Hg_{0.8}Tl_{0.2}Ba_2Ca_2Cu_3O_{8.10}$ show that the phenomenon of phase separation is suppressed by superconductivity. *© 2002 MAIK "Nauka/Interperiodica".*

INTRODUCTION

The inhomogeneous state (phase separation) in CuO_2 planes in high-T_c superconducting cuprates was first observed in 1993 by Bianconi [1]. Up to now, the state of phase separation in the form of stripes was found in $La_{2-x}Nd_xCuO_4$, $La_{2-x}Sr_xCuO_{4+\delta}$ [2, 3], $Bi_2Sr_2CaCu_2O_{8+\delta}$ [4], and $YBa_2Cu_3O_{7-\delta}$ [5]. However, no such state was observed in mercury-based high-T_c cuprates possessing the highest critical temperature and the smallest distortion of the CuO_2 planes [3]. In this connection the question arises of whether the superconducting properties and the state of phase separation are related, i.e., whether the interactions responsible for these effects are independent, compete, or provide each other. To find the answer to this question, we studied the temperature evolution of the crystal structure in the mercury-based high-T_c compound of the composition $Hg_{0.8}Tl_{0.2}Ba_2Ca_2Cu_3O_{8.10}$ in the vicinity of the superconducting transition by EXAFS spectroscopy.

Another important problem is the nature of the state of phase separation. This state can be of either magnetic [6] or polaron [7] origin. To analyze this problem, we measured the acoustic and structural parameters and also the magnetic susceptibility in a wide temperature range for two Cu(II)-containing antiferromagnetic materials—CuO and Y_2BaCuO_5.

[1] This work was presented to the Symposium "Order, Disorder, and Properties of Oxides" (ORDPO), Sochi, Russia, 2001.

RESULTS AND DISCUSSION

The Y_2BaCuO_5 ceramic and CuO samples were prepared by a solid-state reaction in air at 950°C from Y_2O_3, $BaCO_3$, and CuO (of 99.99% purity). The synthesis and the parameters of the $Hg_{0.8}Tl_{0.2}Ba_2Ca_2Cu_3O_{8.10}$ samples were reported in [8]; their critical temperature T_c was close to 125 K. The EXAFS measurements were made in the Novosibirsk Center of Synchrotron Radiation at the VEPP-3 reactor.

The crystal structure of CuO and Y_2BaCuO_5 is well known [9, 10]. Copper (II) oxide has a centrosymmetric structure and is described by the monoclinic space group $C2/c$. Each in-plane copper atom is surrounded by four oxygen atoms forming an almost regular parallelogram, whereas the oxygen coordination corresponds to a distorted tetrahedron formed by copper atoms. The CuO_4 parallelograms are elongated in the [110] and $[\bar{1}10]$ directions and form two types of Cu–O–Cu chains in the [101] and $[10\bar{1}]$ directions.

In Y_2BaCuO_5, copper atoms are coordinated by five oxygen atoms forming almost square pyramids, which, in turn, form layers alternating with Y–O–Y–chains. Thus, in contrast to high-T_c superconducting phases and CuO, here, the copper–oxygen clusters do not form a bound structure that is separated by the Ba–O and Y–O fragments inside and outside the layers, respectively. We failed to find any data on possible structural trans-

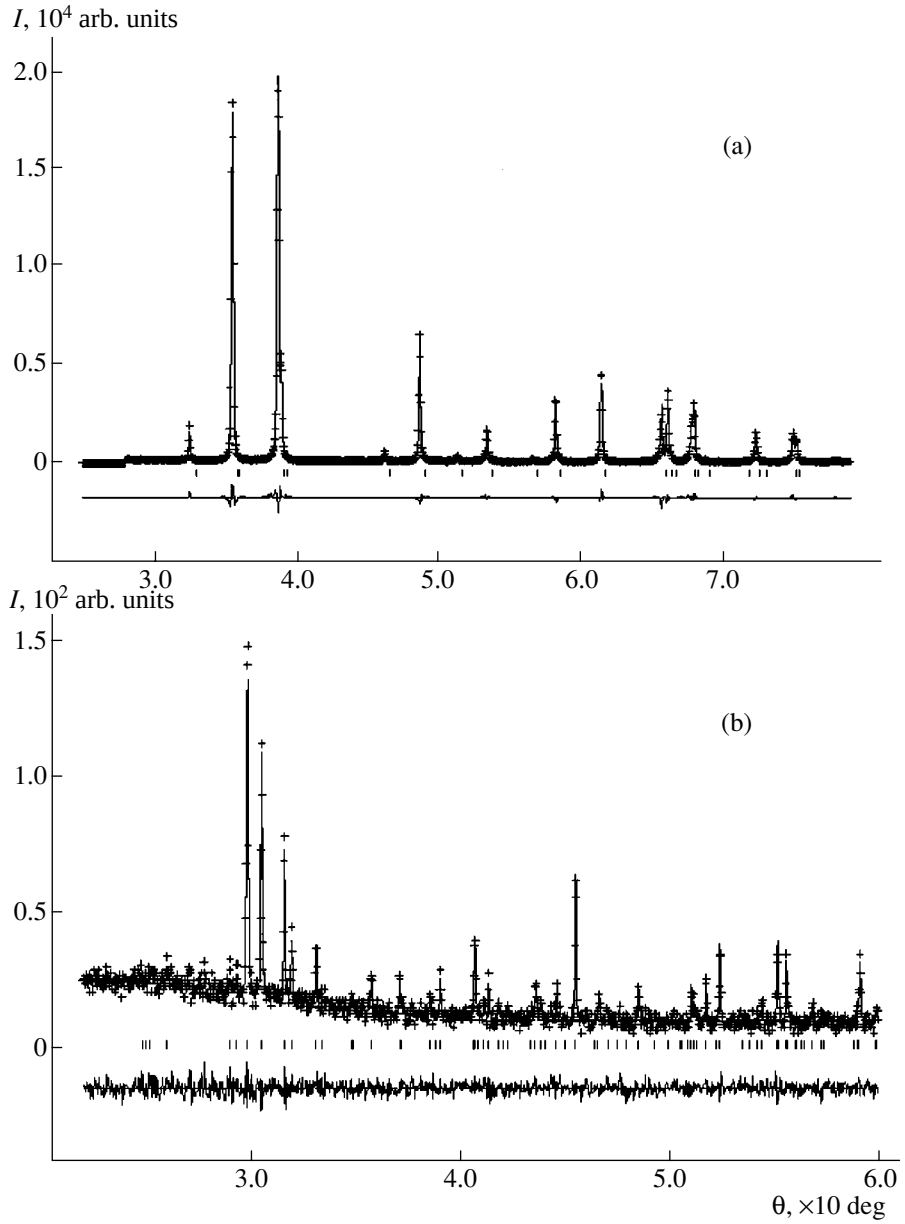

Fig. 1. X-ray diffraction patterns of (a) CuO and (b) Y_2BaCuO_5 at room temperature. The experimental, calculated, and difference curves are presented. I is the reflection intensity, $\lambda = 1.5405$ Å.

formations in CuO and Y_2BaCuO_5 during cooling down to 4.5 K.

The low-temperature structural studies were performed on a STOE diffractometer (graphite monochromator, Cu$K_{\alpha 1}$ radiation, the 2ϑ range was 20°–60° for Y_2BaCuO_5 and 20°–80° for CuO, 5° linear position-sensitive detector, transmission mode) in a cryostat manufactured by Oxford Instruments. The sample was placed into a helium atmosphere, the temperature ranged within 100–300 K, the measurements were performed during sample cooling, the temperature step was equal to 3–5 K, the cooling rate between the measurements was about 1 K/min, the average time of one measurement was about 40 min. The structural parameters were refined using the GSAS program package. The first-king Chebyshev polynomial with eight parameters was used to fit the background. The profile function (the Simpson modification of the pseudo-Voigt function [11]) had 12 coefficients, of which nine were adjustable. The X-ray diffraction patterns obtained at room temperature are shown in Fig. 1.

The structure model described in [10] was used as the initial model of Y_2BaCuO_5: sp. gr. *Pbnm*, four Ba in the (0.93, 0.90, 1/4) position, four Y1 in the (0.12, 0.29, 1/4) position, four Y2 in the (0.40, 0.07, 1/4) position, four Cu in the (0.71, 0.66, 1/4) position, eight O1 in the

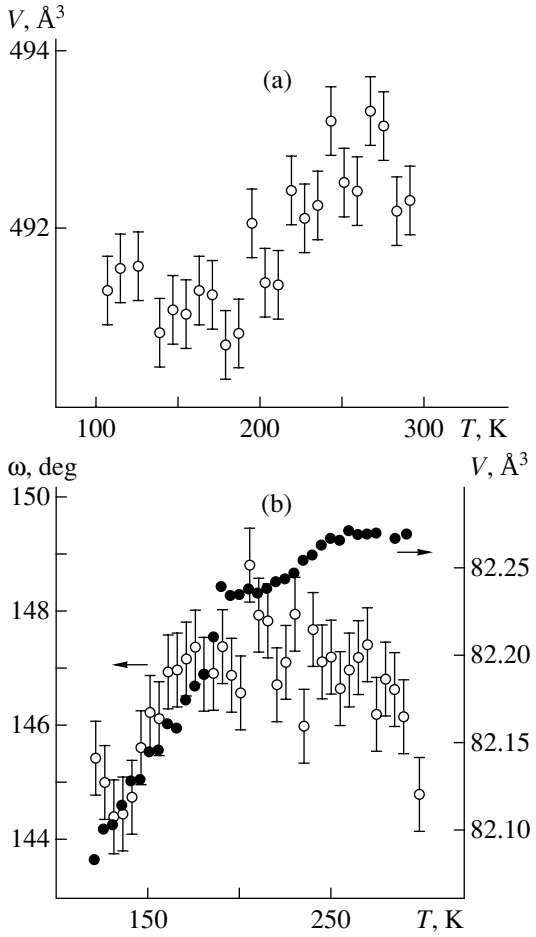

Fig. 2. The temperature dependence of the unit-cell volume V for (a) Y_2BaCuO_5 and (b) CuO. For CuO, the Cu–O–Cu bond angles are also indicated (empty symbols). Hereafter, the error bars are not shown if the error does not exceed the symbol size.

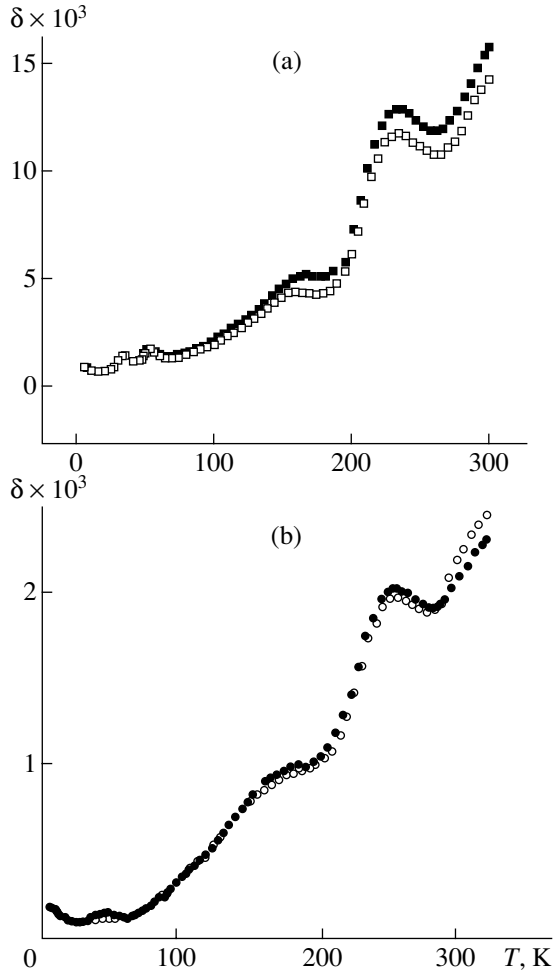

Fig. 3. The temperature dependence of the internal friction δ for (a) CuO and (b) Y_2BaCuO_5. Empty and filled symbols correspond to cooling and heating, respectively.

(0.16, 0.43, 0) position, eight O2 in the (0.36, 0.23, 0.5) position, and four O3 in the (0.03, 0.10, 1/4) position. Unfortunately, for this phase we managed to determine only the temperature dependence of the unit cell parameters owing to the insufficient accuracy of the X-ray diffraction method for determining the oxygen position. The temperature dependence of the unit-cell volume is shown in Fig. 2a.

The structure model described in [9] was used as the initial model for CuO: sp. gr. $C2/c$, four Cu in the 4*a* position (0, 0, 0), and four O in the 4*b* position (1/2, 1/2, z). The isotropic thermal parameters of oxygen atoms were not refined and were taken to be equal to 0.03 Å, whereas the thermal parameters for copper atoms were calculated in the anisotropic approximation as $\exp[-2\pi^2(U_{11}a^*h^2 + 2U_{12}a^*b^*hk + \ldots]$. The reliability factors for all the temperature points were $wR_p \sim 13$–14 and 8–9%, $R_p \sim 10$–11 and 6.6–6.7%; $\chi^2 \sim 0.30$–0.35 and 2.90–2.97 for Y_2BaCuO_5 and CuO, respectively. The temperature dependences of the unit-cell volume and of the Cu–O–Cu bond angle for CuO are shown in Fig. 2b. The results of the structure analysis for the mercury-based high-Tc compound are described in detail in [8, 12, 13].

The acoustic properties of Y_2BaCuO_5 and CuO (internal friction coefficient and sound velocity) were measured by a double built-up vibrator at a frequency of 90–100 kHz. The results are shown in Fig. 3. It is apparent that the acoustic characteristics of both materials are similar at temperatures of about 160 and 230–240 K. Furthermore, at these temperatures, the peaks of ultrasonic absorption were also observed for high-T_c compounds [14, 17], where they were attributed to the spin and charge inhomogeneities corresponding to the phase separation. These phenomena seem to occur in a similar way in both high-T_c compounds and in the related antiferromagnetic phases.

The parameters of the crystal structure for the samples under study exhibit anomalous behavior at the same temperatures at which the ultrasonic absorption

peaks were observed (about 160 and 240 K) (Fig. 2). We should also mention the unstable behavior of the Cu–O–Cu bond angle in the vicinity of 200 K. Earlier, the unusual behavior of magnetostriction in various magnetic fields was reported at a temperature of about 203 K [18], where it was explained by the effect of domain structure.

The magnetic properties of CuO were described in detail in [19–21]. At $T_{N1} < 230$ K, this material becomes a collinear three-dimensional antiferromagnet with the spin $S = 1/2$ directed along the crystallographic *b* axis. At temperatures below $T_{N2} = 212$ K [20], the direction of the magnetic moment lies in the *ac* plane [21]. Above T_{N1} (up to about 540 K), we observed an increase in magnetic susceptibility that can be explained by a quasi-one-dimensional magnetic order in the antiferomagnetic Cu–O–Cu chains oriented along the $[10\bar{1}]$ direction. In these chains, magnetic correlations exist above the Néel temperature [19].

The magnetic susceptibility of Y_2BaCuO_5 was measured by the Faraday balance technique in the temperature range 55–600 K in fields up to 13 kOe. The results obtained for CuO turned out to be in good agreement with those described above and reported in [20]. In the temperature range under study, the magnetic susceptibility of Y_2BaCuO_5 exhibits paramagnetic behavior, $\chi = C/(T - \theta)$ with $C = (8.9 \pm 0.3) \times 10^{-5}$ K and $\theta = -31.7 \pm 4.0$ K. The calculated effective moment equals $m_{eff} = 1.79\ \mu_B$ and corresponds to the spin S = 1/2 for Cu^{2+}.

The radial distribution function (RDF) for $Hg_{0.8}Tl_{0.2}Ba_2Ca_2Cu_3O_{8.10}$ determined by the Fourier transform of the EXAFS spectra (Cu*K*-edge) at 300, 140, and 110 K is shown in Fig. 4. It is clear that for all RDF maxima, except for the first one, attributed to the contribution of Cu–O bonds in the CuO_2 planes, the intensity recorded on cooling is associated with the temperature factor. However, the maximum intensity of the first peak (corresponding to the most ordered state of the corresponding bonds) is observed at 300 K and the minimum, at about 140 K. Note also that on further cooling down to the superconducting-transition temperature, the peak height increases again (the degree of disorder of Cu–O bonds becomes lower).

The anomalous properties of CuO and high-T_c cuprates in the 160–240 K range are often interpreted in terms of the phase separation because of spin correlations of the antiferromagnetic type. This idea is associated with the Néel temperature of CuO in this range and of spin correlations in high-T_c cuprates in wide ranges of compositions and temperatures. In this study, we showed that both anomalies, at ~160 and 240 K, are determined in Y_2BaCuO_5 in a pure paramagnetic state, and, therefore, we prefer to suggest another mechanism of phase separation, for example, the polaron one [7] or the model of polar Jahn–Teller centers [22].

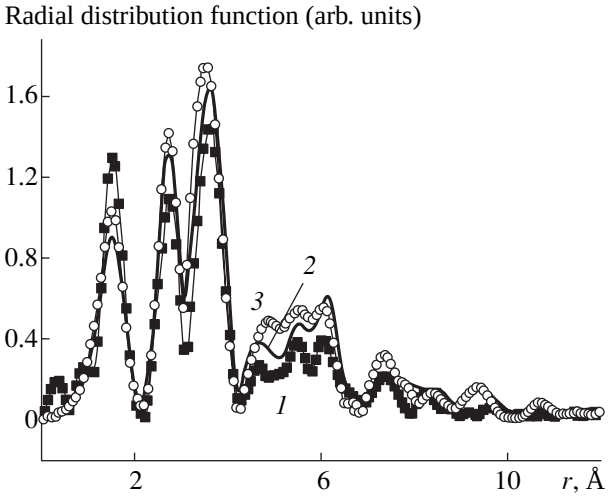

Fig. 4. The radial distribution function obtained by EXAFS spectroscopy for $Hg_{0.8}Tl_{0.2}Ca_2Cu_3O_{8.10}$ at (*1*) 300, (*2*) 140, and (*3*) 110 K; Cu*K* edge.

Discussing the results of the EXAFS spectroscopy for high-T_c materials, we should note that a pronounced distortion of the CuO_2 planes is observed in $Bi_2Sr_2CaCu_2O_{8+\delta}$, $LaCuO_{4.1}$ [3, 4], and $YBa_2Cu_3O_y$ [5] below the temperature of the superconducting transition. This distortion, which even increases on cooling in some cases, was attributed to phase separation. Such a behavior gave rise to the hypothesis of the existence of a quantum critical point because of the formation of the self-organized structure of charged stripes in the high-T_c compounds. The hypothesis leads to the conclusion that the critical charge and spin fluctuations in the vicinity of this point determine the charge-carrier interactions and superconductivity [2]. Our EXAFS spectroscopy data (Fig. 4) and high-resolution X-ray diffraction data [8, 13] unambiguously show that the degree of distortion in CuO_2 planes drastically decreases at $T < T_c$. Probably, the difference between our data and the results reported in [4, 5] is explained by the fact that the samples used in [4, 5] were heavily irradiated with a photon flux of the order of 10^{11} s^{-1}. Earlier, we showed that the observed distortion can be photoinduced [12] and, therefore, we used a flux that was less intense by two orders of magnitude.

Thus, the mercury-based high-T_c materials characterized by the highest critical temperatures have much smaller distortions of CuO_2 planes as compared to other high-T_c systems. These distortions do not increase on cooling without strong irradiation. This leads to the conclusion that the formation of stripe structure and phase separation are not related to the mechanism of superconductivity.

One of the well-known theories describing the properties of high-T_c cuprates is based on the concept of polarons and bipolarons [23]. In the case where the polaron density is high, the contribution of polarons

and bipolarons to the thermodynamic potentials can exceed the contribution from the crystal lattice. The characteristic feature of such systems is a nonmonotonic temperature dependence of the polaron bandwidth. As was shown in [7], close to the temperature corresponding to the maximum polaron localization (the collapse point for the polaron band), there exists a certain stability limit of the homogeneous state of the material. If the Fermi level in this material is located between the bottom and the middle of the polaron band, the homogeneous state decomposes into phases enriched with and depleted of charge carriers, which can be explained follows. At the collapse of the polaron band, the Fermi level of the initial material should go up, which is equivalent to the negative contribution of charge carriers to the total entropy. If this contribution is not compensated with the contribution of the crystal lattice, decomposition takes place. In the case of the impurity polarons discussed in [7], the compensation of the electric-charge redistribution occurs because of the diffusion-induced redistribution of impurities. In the case where the temperature corresponding to the collapse of the polaron band is rather low and the mobility of the impurity (oxygen in high-T_c materials) is insufficient, the segregation in the form of phase separation can take place. Of course, the geometric shape of the stripes for the fractions formed requires additional interpretation. Alexandrov and Kabanov demonstrated theoretically [6] that Fröhlich interaction favors the formation of such stripes in doped antiferromagnetic insulators under the condition that the dielectric constant has a high value; in other words, the Fröhlich interactions enhance the role of short-range antiferromagnetic and electron–phonon interactions.

Thus, we suggest that the processes occurring at $T \sim$ 240 and 160 K are associated with the formation and redistribution of charge in the separation state. Both these features are of a nonmagnetic nature. The inhomogeneous state with domains (stripes) with different charge-carrier concentrations and different distortions of CuO_2 planes is the most favorable at temperatures slightly exceeding the temperature of the superconducting transition, and it is suppressed during further cooling. The "stripe state" cannot induce superconductivity, but both these effects are explained by the polaron nature of the materials under discussion.

ACKNOWLEDGMENTS

This work was supported by the Russian Foundation for Basic Research, projects nos. 01-03-32620, 00-15-96575, and 00-15-97388 and by the Civilian Research and Development Foundation, project no. REC-005.

REFERENCES

1. A. Bianconi, Solid State Commun. **89**, 933 (1994).
2. *Proceeding of the Second International Conference on Stripes and High-T_c Superconductivity in "Stripes and Related Phenomena,"* Ed. by A. Bianconi *et al.* (Academic, New York, 2000).
3. A. Bianconi, G. Bianconi, S. Caprara, *et al.*, J. Phys.: Condens. Matter **12**, 10655 (2000).
4. N. L. Saini, A. Lanzara, A. Bianconi, and H. Oyanagi, Eur. Phys. J. B **18**, 257 (2000).
5. H. Oyanagi, N. L. Saini, and A. Bianconi, Int. J. Mod. Phys. B **29–31**, 3623 (2000).
6. A. S. Aleksandrov and V. V. Kabanov, Pis'ma Zh. Éksp. Teor. Fiz. **72**, 825 (2000) [JETP Lett. **72**, 569 (2000)].
7. A. N. Titov and A. V. Dolgoshein, Fiz. Tverd. Tela (St. Petersburg) **42**, 425 (2000) [Phys. Solid State **42**, 434 (2000)].
8. S. Titova, I. Bryntse, J. Irvine, *et al.*, J. Supercond. **11**, 571 (1998).
9. S. Asbrink and L.-J. Norrby, Acta Crystallogr., Sect. B: Struct. Crystallogr. Cryst. Chem. **26**, 8 (1970).
10. C. Michel and B. Raveau, J. Solid State Chem. **43**, 73 (1982).
11. A. C. Larson and R. B. Von Dreele, LANSCE, MS-H805 (Los Alamos National Laboratory, 1986).
12. S. G. Titova, D. O. Shorikov, V. F. Balakirev, *et al.*, Physica B (Amsterdam) **284–288**, 1091 (2000).
13. S. Titova, I. Bryntse, A. Titov, and V. Voronin, Izv. Akad. Nauk, Ser. Fiz. **65**, 854 (2001).
14. L. N. Pal-Val, P. P. Pal-Val, V. D. Natsik, and V. I. Dotsenko, Fiz. Nizk. Temp. **18**, 126 (1992) [Sov. J. Low Temp. Phys. **18**, 86 (1992)].
15. S. G. Titova, T. I. Arbuzova, V. F. Balakirev, *et al.*, Fiz. Nizk. Temp. **22**, 1226 (1996) [Low Temp. Phys. **22**, 938 (1996)].
16. S. G. Titova, V. F. Balakirev, P. P. Pal-Val, *et al.*, Czech. J. Phys., Suppl. S3, 1417 (1996).
17. Y. N. Wang, Y. N. Huang, and H. M. Shen, Supercond. Sci. Technol. **7**, 441 (1994).
18. I. V. Krynetskiĭ, A. S. Moskvin, S. V. Naumov, and A. A. Samokhvalov, Pis'ma Zh. Éksp. Teor. Fiz. **56**, 584 (1992) [JETP Lett. **56**, 566 (1992)].
19. T. I. Arbuzova, A. A. Samokhvalov, I. B. Smolyak, *et al.*, J. Magn. Magn. Mater. **95**, 168 (1991).
20. J. B. Forsyth, P. J. Brown, and B. M. Wanklyn, J. Phys. C **21**, 2917 (1988).
21. B. X. Yang, T. R. Thurston, J. M. Tranquada, and G. Shirane, Phys. Rev. B **39**, 4343 (1989).
22. A. S. Moskvin, N. N. Loshkareva, Yu. P. Sukhorukov, *et al.*, Zh. Éksp. Teor. Fiz. **105**, 967 (1994) [JETP **78**, 518 (1994)].
23. A. S. Alexandrov and N. F. Mott, *Polarons and Bipolarons* (World Scientific, Singapore, 1995).

Translated by K. Kugel

Crystallography Reports, Vol. 47, No. 6, 2002, pp. 939–945. Translated from Kristallografiya, Vol. 47, No. 6, 2002, pp. 1009–1015.

STRUCTURE OF INORGANIC COMPOUNDS

X-ray Diffraction and IR Spectroscopy Study of Labuntsovite-Group Minerals[1]

R. K. Rastsvetaeva* and N. V. Chukanov**

** Shubnikov Institute of Crystallography, Russian Academy of Sciences, Leninskiĭ pr. 59, Moscow, 117333 Russia*

e-mail: rast@ns.crys.ras.ru

*** Institute of Problems of Chemical Physics in Chernogolovka, Russian Academy of Sciences, Chernogolovka, Moscow oblast, 142432 Russia*

Received January 10, 2002

Abstract—The distribution of cations over the positions in the structures of labuntsovite-group minerals was studied by X-ray diffraction analysis and IR spectroscopy. Several types of cation order over the five key positions are established depending on cation composition and their force characteristics. © *2002 MAIK "Nauka/Interperiodica".*

INTRODUCTION

Minerals of the labuntsovite group are promising ion exchangers, sorbents, and catalyst carriers and therefore can be used in chromatography, catalysis, water purification, etc. Efforts were made to synthesize meso- and microporous materials [1–4] with the use of minerals of the nenadkevichite (representative of the labuntsovite group) structure type taking into account the available data on the natural specimens.

Zeolite properties of many Ti-, Nb-, and Zr-alkali silicates are associated with the differences in the force characteristics of the cation–oxygen chemical bonds. It is well known that a quantitative characteristic of a bond is the force constant derived from the second partial derivative of the total potential energy with respect to the deviation of the bond length from its equilibrium value. The corresponding stretching frequencies determined from IR spectra can be considered as a measure of force characteristics. The classification of the force characteristics into "high" and "low" ones is arbitrary. In this study, the force characteristics of the bonds, whose cation–oxygen stretching frequencies are either lower than 400 cm^{-1}, range from 400 to 700 cm^{-1}, or are higher than 700 cm^{-1} will be referred to as low, moderate, and high, respectively. It should be noted that the values of the force characteristics decrease with an increase in the coordination number and the elongation of the bond.

Transition elements (along with silicon) possessing high force characteristics of the bonds with oxygen play the key role in the structures of most of the minerals under consideration and provide the formation of three-dimensional frameworks, whereas the cations with low force characteristics and water molecules are located in their cavities.

CRYSTAL CHEMISTRY OF LABUNTSOVITE-GROUP MINERALS

The general crystallochemical formula of the monoclinic members of the labuntsovite group with ordered cations can be written as (Z = 1): $A_4B_4C_{4-2x} \cdot [D_x(H_2O)_{2x}][M_8(O,OH)_8][Si_4O_{12}]_4 \cdot nH_2O$, where $n \approx 8$, x = 0–2, A = Na, Ca, Sr, H_3O, or □; B = K, Na, H_3O, or □; C = K, Ba, H_3O, or □; D = Mn^{2+}, Fe^{2+}, Mg, Zn, or □; M = Ti or Nb; and □ is a vacancy (letters A, B, C, and D not only denote the particular set of cations but also correspond to certain structure positions or groups of positions, if the latter are split).

The labuntsovite group includes more than twenty minerals, which are widespread in the massifs of the Kola Peninsula and Greenland. Fourteen minerals of this group were recognized by the Commission on New Minerals and Mineral Names of the International Mineralogical Association. Their chemical compositions (wt %) lie within the following ranges: Na_2O, 0–14; K_2O, 0–15; CaO, 0–7; Sr–O, 0–8; BaO, 0–17; MgO, 0–2; FeO, 0–5; MnO, 0–7; ZnO, 0–7; TiO_2, 1–27; and Nb_2O_5, 0–39. Some structurally studied minerals of the labuntsovite group are listed in Table 1.

The structures of all the minerals of the labuntsovite group can be described as mixed frameworks consisting of infinite chains of titanium- or niobium-octahedra sharing vertices along the a axis. The chains are linked to each other via the $[Si_4O_{12}]$-rings along two other directions. The SiO_4-tetrahedra share vertices with the $Ti(Nb)O_6$-octahedra. The structural similarity of the mixed frameworks is seen from the fact that their unit-

[1] This study was presented at the Symposium "Phase Transitions in Solid Solutions and Alloys," Sochi, Russia, 2001.

Table 1. Symmetry and unit-cell parameters of some structurally studied minerals of the labuntsovite group

Mineral	Sp. gr.	*a*, Å	*b*, Å	*c*, Å	β, deg	Reference
Nenadkevichite	*Pbam*	7.41	14.20	7.15	90	[5]
Korobitsynite	*Pbam*	7.35	14.15	7.12	90	[6]
Abuntsovite	*C2/m*	14.18	13.70	7.74	117.0	[7]
Labuntsovite-Mn	*C2/m*	14.29	13.85	7.78	116.8	[8]
Labuntsovite-η	*C2/m*	14.30	13.82	7.79	116.8	[9]
Lemmleinite-K(1)	*C2/m*	14.33	13.83	7.79	117.1	[10]
Lemmleinite-K(2)	*C2/m*	14.42	13.91	7.80	116.9	[10]
Lemmleinite-Ba	*C2/m*	14.22	13.75	7.77	116.7	[11]
Paralabuntsovite	*I2/m*	14.24	13.77	15.57	116.8	[8]
Niobium-rich analogue of labuntsovite	*Cm*	14.45	13.91	7.836	117.4	[12]
Lemmleinite-K(3)	*C2/m*	14.39	13.90	7.83	117.6	[13, 14]
"Monoclinic nenadkevichite"	*C2/m*	14.75	14.37	8.01	117.4	[15]
Vuoriyarvite-K	*Cm*	14.69	14.16	7.86	117.9	[16]
Kuzmenkoite-Mn	*Cm*	14.37	13.91	7.81	117.1	[17, 18]
Alsakharovite	*Cm*	14.45	13.91	7.836	117.4	[19]
Karupmollerite-Ca	*C2/m*	14.64	14.21	7.91	117.4	[20]
Gutkovaite-Mn	*Cm*	14.36	13.89	7.814	117.4	[21]
Tsepinite-Na	*Cm*	14.60	14.27	7.93	117.4	[22]

Note: Data for the monoclinic members of the labuntsovite group are given in the unified setting, which corresponds to the monoclinic angle β.

cell parameters are comparable, even if the representatives of this mineral group are described by different symmetries (Table 1). Large alkali and alkaline-earth cations and water molecules occupy the cavities of the structures.

Framework consisting of the Ti(Nb)O_6-octahedra and four-membered rings of the SiO_4-tetrahedra. The framework of the composition $[M_4(O,OH)_4(Si_4O_{12})_2]$ is negatively charged depending on the Ti : Nb ratio in the *M*-octahedra. The axes of the *M*-octahedra in the chains are tilted with respect to each other in the *ac*-plane, which imparts the zigzag shape to these chains. The *M*–O–*M* angles characterizing the mutual inclination of octahedra in the chains are approximately equal to (135°–138°) for all the minerals of the labuntsovite group. However, the directions of inclination substantially differ as well as the angles of mutual rotation of octahedra. In orthorhombic structures, the chains are straightened in the *ac*-plane, so that the chain axis is parallel to the *x* axis of the unit cell. In monoclinic structures, these structural elements are more complicated because of the rotation of the octahedra about their axes and the additional inclination with respect to each other in the *ab*-plane, so that the axis of the chain passing through the shared vertices of the octahedra is bent in a wavelike fashion. In this case, there are prerequisites for the formation of additional octahedra at the sites of mutual approach of the chains, so that the additional octahedra share edges with the chain octahedra. This transformation of the chains in the monoclinic structures leads to deformation of the silicon–oxygen rings. As a result, these rings are no longer planar and symmetrical cycles with Si–O–Si angles of 150° and 172° (orthorhombic structures). The angles of rotation of the tetrahedra in the monoclinic structures now range within 135°–154°, which offers the possibilities of identifying the minerals of the labuntsovite group from their IR spectra.

Zeolite-like cavities. The differences in the frameworks of the orthorhombic (Fig. 1) and monoclinic (Fig. 2) minerals of the labuntsovite group are reflected in the character of filling of the zeolite-like cavities. The orthorhombic minerals (sp. gr. *Pbam*) include niobium-rich nenadkevichite [5] and its titanium analogue korobitsynite [6] with the idealized general formula $Na_8(Nb,Ti)_4(O,OH)_4[Si_4O_{12}]_2 \cdot nH_2O$, where $n \approx 8$ ($Z = 1$). These structures have relatively small similar cavities, in which sodium atoms substantially dominate over other cations. The Na atoms are located in eight- and nine-vertex coordination polyhedra with the shortest Na–O distance of 2.2 Å, which hinders the incorporation of large cations such as K^+ and Ba^{2+} into the structures of the orthorhombic members of the labuntsovite group. All the other members of this group belong to the monoclinic system. Their structures contain large cavities of different shapes and sizes, which are denoted by the letters *A*, *B*, and *C* according to the nomenclature used for this mineral group [23] and the letter by *D* in the case of the formation of additional octahedral complexes. In all the structurally studied

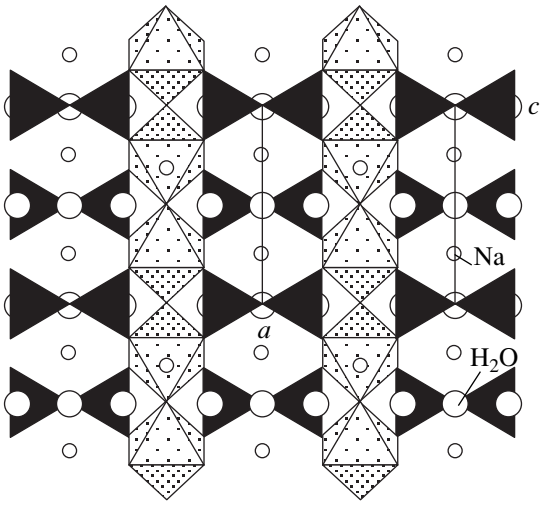

Fig. 1. Structure of the orthorhombic representatives of the labuntsovite group.

minerals of the labuntsovite group, the selective incorporation of extraframework cations into the *A*, *B*, *C*, and *D* positions was observed. This makes it possible to reveal the following characteristic features of the ordering of cations and water molecules in the series of structurally studied minerals of the labuntsovite group.

The *A* position is occupied predominantly by sodium atoms. It should be noted that four sodium atoms provide the maximum possible occupancy. Although the multiplicity of the *A* position is equal to 8, the pairs of crystallographically equivalent positions are located at such close distances (2.5 Å) that they cannot be simultaneously occupied by cations. In the monoclinic structures, the single *A* position can be split into the *A*(1) and *A*(2) subpositions spaced by 1.6–1.7 Å. One of these positions is still occupied by Na cations, whereas the other position is occupied by larger cations, such as Sr in the structure of the Zn, Ti-containing representative of the labuntsovite group [19], K in niobium-rich labuntsovite [12], and H_3O in tsepinite-Na [22]. In most of the labuntsovites, the *A*(2) position is occupied by H_2O molecules and is involved in the coordination environment around the *A*(1) position displaced for a longer distance.

The main difference between kuzmenkoite $K_4[Mn_2(H_2O)_4][(Ti,Nb)_8(O,OH)_8][Si_4O_{12}]_8 \cdot 8H_2O$ [17, 18] and the minerals with the labuntsovite structure is that the *A*(1) position in the former mineral is vacant because of the low sodium concentration, with the *A*(2) position being partly occupied by H_3O and H_2O. In the structurally studied calcium-rich labuntsovite-like minerals [15], the *A* position is vacant to a large degree because calcium is not incorporated into this position at a low sodium concentration. An analogous situation was also observed in the structure of karupmollerite-Ca $\square_4(K_{1.03}Na_{0.87})(Ca_{0.57}Na_{0.30}Ba_{0.02})(Ca_{1.39}Mn_{0.02}) \cdot (Nb_{2.71}Ti_{1.20}Fe_{0.05})(Nb_{2.63}Ti_{1.28}Fe_{0.05})[Si_4O_{12}]_4(O,OH)_8 \cdot 11H_2O$ studied by the Rietveld method [20].

An essentially different distribution of the extraframework cations is observed in the structure of gutkovaite-Mn, which is a low-sodium and, at the same time, Ca-containing representative of the labuntsovite group [21]. The Ca atoms in this mineral are ordered and occupy one of two positions related by a twofold axis, whereas these two positions in the structures of typical labuntsovites are statistically occupied by sodium. Compared to the Na-nine-vertex polyhedron (the average Na–O distance is 2.65 Å) in the labuntsovite structure, the Ca-polyhedron in gutkovaite-Mn is reduced to a seven-vertex polyhedron (the average Ca–O distance is 2.48 Å). In low-potassium ($K \le 4$) labuntsovites, all the potassium atoms are located in the *B* position [10, 23], which can also be split into partly

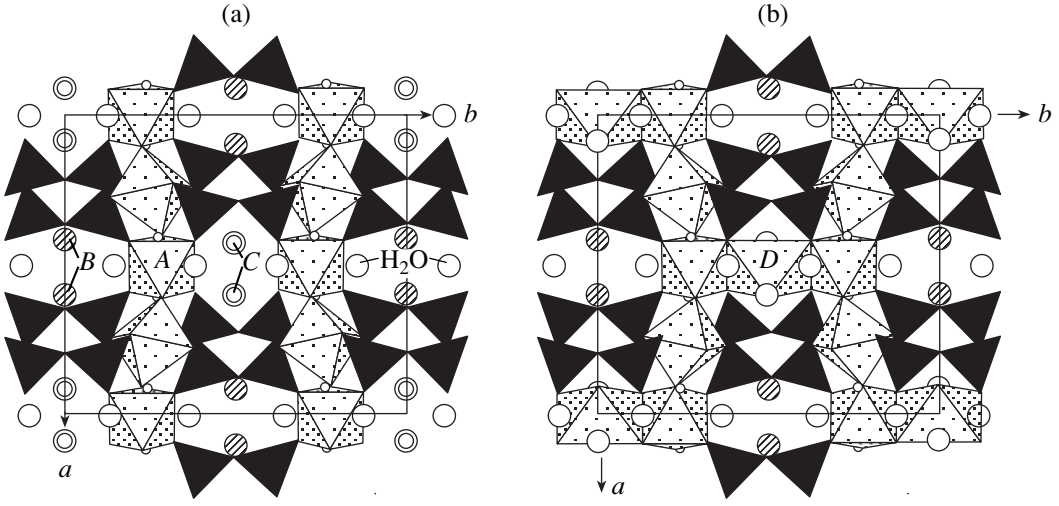

Fig. 2. Structure of the monoclinic representatives of the labuntsovite group (a) without an additional complex between the chains of the MO_6-octahedra and (b) with the additional $D(H_2O)_2$ complexes.

occupied subpositions. The structure of vuoriyarvite-K [16], which differs from most of the other minerals of the labuntsovite group, is characterized by the presence of a large number of extraframework positions spaced by close distances, including the positions around the *B* position. The disorder in the structure of this mineral is seen from the nonequivalence of all the four tetrahedra of the silicon–oxygen ring and all Nb(Ti)–O bonds in all the octahedra, the nonsymmetric splitting of the extraframework partly vacant positions, and, as a consequence, the absence of a center of inversion.

Vuoriyarvite-K is structurally similar to its Na,Ti-rich analogue—tsepinite-Na (Na, H_3O, K, Sr, Ba)$_2$ (Ti,Nb)$_2$[Si_4O_{12}](OH,O)$_2 \cdot 3H_2O$ [22] from the Khibiny massif. In particular, the structure of tsepinite-Na has eight extraframework positions occupied by large cations (Na, K, Ba, Sr, Ca, and H_3O^+). However, six of these positions are usually vacant. Two positions have occupancies of ~0.6. Three other positions contain H_3O^+ ions with occupancies of 0.35, 0.26, and 0.39 (the H_3O–O distances are 3.12, 3.19, and 2.93 Å, respectively).

The partial replacement of K by H_3O was observed in some other members of the labuntsovite group, for example, in the Zn,Ti-containing representative [19]. Direct evidence of the incorporation of oxonium ions into the labuntsovite structure is lacking. At the same time, the presence of H_3O^+ ions in labuntsovites is consistent with the chemical compositions of many specimens (a deficiency of extraframework cations often accompanied by a high water content), which is confirmed by the IR spectroscopy data. The IR spectrum of the structurally studied specimen of tsepinite-Na [24] has additional bands at 3250, 2940, and 1700 cm^{-1} and is characterized by high absorption intensity in the region of Si–O–Si stretching vibrations (1000–1200 cm^{-1}). For the H_3O^+ ion with the symmetry C_{3v}, the calculated frequencies (cm^{-1}) are as follows: $\nu_1(A_1) = 3160$; $\nu_{2\delta}(A) = 1050$–1140; $\nu_3(A) = 3320$, and $\nu_{4\delta} = 1730$–1740. Apparently, the involvement of the oxonium cations in hydrogen bonding leads to a lowering of their symmetry and induces low-frequency shifts of their spectral bands. Since the $\nu_{2\delta}(A)$ band overlaps with the ν(Si–O–Si) band, the precise determination of its position is difficult.

The *B* position is most often surrounded by two water molecules, $H_2O(1)$ and $H_2O(2)$, involved in the coordination sphere of the sodium atoms, and each of these water molecules is also bound to one of the large cations (K or Ba).

In monoclinic structures, the chains of the (Ti,Nb)-octahedra can be cross-linked via additional octahedra located at the sites where the chains approach each other (Fig. 2b). These additional octahedra share edges with the octahedra of the chains. The "cross-linking" *D* position can be occupied by both $R = Mn^{2+}$, Fe^{2+}, Mg, or Zn ions and the larger ions, such as Ca, Na, or Sr. It should be noted that divalent cations R^{2+}, i.e., the cations with relatively high force characteristics, are incorporated into this position as $[R(H_2O)_2]^{2+}$ complexes. The water molecules involved in these complexes are located at the vertices of the "cross-linking" octahedron and occupy the *C* position. If the positions of the H_2O molecules and *C* cations in the labuntsovite structure virtually coincide (the distance between these positions is no larger than 0.3 Å), an interesting instance of alternative isomorphism is observed:

$$2(\mathrm{K, Ba}) + \square \longleftrightarrow 2H_2O + (\mathrm{Mn, Fe, Mg, Zn}).$$
$$C \qquad D \qquad C \qquad D$$

For the labuntsovite group, the continuous isomorphism according to this scheme occurs throughout the range of the occupancies of the *C* and *D* cation positions (i.e., from 0 to 4 and from 2 to 0, respectively). Of the "*D*-occupied" (and, consequently, "*C*-vacant") minerals with a labuntsovite structure, labuntsovite-Mn, labuntsovite-Fe, and labuntsovite-Mg have already been described [23].

The fact that the additional (cross-linking) octahedral positions are occupied mainly by the divalent Fe, Mn, Mg, and Zn cations was confirmed in a series of structural studies [10, 11]. However, the *D* position is often vacant (lemmleinite [13] and tsepinite [22]) and can also be occupied mainly by sodium (vuoriyarvite [16]) or calcium (monoclinic nenadkevichite [15]) cations. The unusual position occupied by strontium with the occupancy of 0.22 was observed in tsepinite-Na. This position can be interpreted as octahedral (an analogue of the *D* position). However, compared to the usual cross-linking cations, the strontium atoms are displaced from the centers of the squares that are formed by the oxygen atoms shared by the Ti,Nb-octahedra. The average, minimum, and maximum Sr–O distances are 2.35, 2.16, and 2.50 Å, respectively.

The shape of the chain (or the degree of its straightening) depends on the size of the cation in the key *D* position. This is reflected in the change in the unit-cell parameter *a* along the chain and, to a lesser extent, in the change in the unit-cell parameter *b*, which is exemplified by several structurally studied minerals of the labuntsovite group [22]. In particular, the average distances in the *D*-octahedra and the unit-cell parameter *a* are as follows (*A*): 2.0–2.1 and 14.2–14.3 in labuntsovites, 2.2 and 14.4 in kuzmenkoite-Mn, 2.3 and 14.7 in vuoriyarvite-K (containing Na in the *D* position), 2.3 and 14.75 in monoclinic nenadkevichite (Ca), and 2.35 (for Sr) and 14.6 in tsepinite-Na (Sr + vacancy).

As was mentioned above, the *B* position is occupied mainly by potassium cations. The excessive (above four atoms per unit cell) potassium atoms are incorporated into the *C* position where they compete with barium atoms and water molecules. It should be noted that the potassium atoms virtually share their positions with the H_2O molecules located at the vertices of the *D*-octahe-

dra, whereas the heavy barium atoms are more rigidly fixed at distances of 0.3 Å from the H_2O positions. In a labuntsovite structure with the more than two Ba atoms (lemmleinite-Ba) [11], the Na, K, and Ba cations were demonstrated to be completely ordered in the *A*, *B*, and *C* positions, respectively, with barium atoms in the latter position being dominant.

Karupmollerite-Ca [20] is characterized by a substantial deficiency of extraframework cations (2.8 out of 12 theoretically possible cations) with a simultaneous increase in the H_2O content. Although this mineral is structurally similar to kuzmenkoite-Mn, the *C* position in its structure is occupied by the Ca and Na cations in contrast to other minerals of the labuntsovite group, in which this position is occupied by Ba and K cations. In the structure of karupmollerite-Ca, the *C* position is displaced from the *D* position ("moves apart" from it, with the *D*–*C* distance being 2.41 Å) and from the H_2O position in the vertex of the *D*-octahedron (the *C*–H_2O distance is 0.82 Å). For comparison, the corresponding distances in lemmleinite-Ba are 2.11 and 0.29 Å, respectively. The Ca and Na cations (partly, Ba cations) statistically (by ~23%) occupy the *C* position and alternate with the *D* cations, with *D* dominating over *C* (~70 and 23%, respectively).

Lemmleinite-K [10] occupies a special place among minerals with a labuntsovite structure. This mineral is the potassium-limiting member of the isomorphous family described by the above scheme, i.e., contains no cations in the *D* positions, whereas the *C* position is almost fully occupied by K.

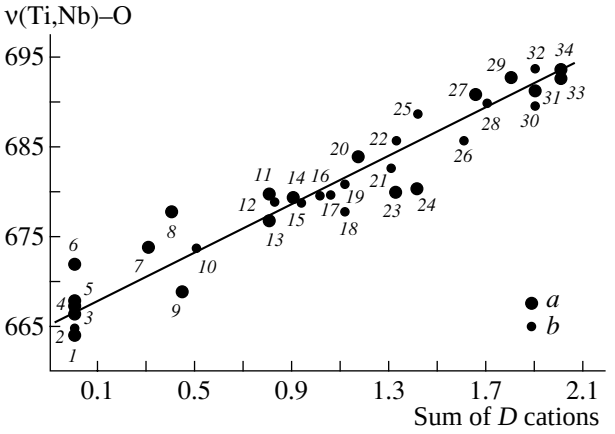

Fig. 3. Dependence of the position of the (Ti,Nb)-O stretching-vibration band on the content of *D*-cations in the minerals of the labuntsovite group according to the data of (*a*) structural studies and (*b*) chemical analysis. The experimental points are numbered in correspondence with the following specimens: *1*, *2*, and *3* (korobitsynite); *4* and *5* (nenadkevichite); *6*, *7*, *8*, and *10* (lemmleinite-K); *9* (tsepinite-Na); *11* (paralabuntsovite-□); *12*, *14*, and *15* (labuntsovite-□); *13* (lemmleinite-Ba); *16* (labuntsovite-Fe); *17*, *21*, *22*, and *26* (labuntsovite-Mg); *18* (paralabuntsovite-Mg); *19*, *21*, and *23* (labuntsovite-Mn); *20* (vuoriyarvite-K); *24* (karupmollerite-Ca); *25*, *27*, and *30* (kuzmenkoite-Mn); *28* (kuzmenkoite-Zn); *29* (organovaite-Mn); *31* (gutkovaite-Mn); *32* and *33* (organovaite-Zn); *34* (parakuzmenkoite-Fe).

IR SPECTROSCOPY

The fact that the constituent elements of labuntsovites have different force characteristics of the cation–oxygen bonds enables one to successfully use both IR spectroscopy and X-ray diffraction analysis. Thus, the force constants can be directly determined from IR spectroscopic data, because these constants are proportional to the ratio of the squared frequency of the corresponding normal vibrations to the reduced mass of these vibrations.

The minerals of the labuntsovite group can be identified from their IR spectra because of the differences in the Si–O–Si angles in the four-membered silicon–oxygen rings, which, in turn, depend on the deformation of the octahedra in the chains. In the region of Ti(Nb)–O stretching vibrations (660–700 cm^{-1}), the IR spectra of minerals of the labuntsovite group have a strong narrow band. The fact that this band is not split in the spectra of multiphase samples throughout the entire range of the Ti : Nb ratio indicates that the Ti- and Nb-octahedra are involved in normal chain vibrations as virtually indistinguishable oscillators. The Ti(Nb)–O stretching frequencies depend primarily on the occupancy *x*/2 of the cross-linking *D*-octahedra (see the crystallochemical formula). The interactions between Ti(Nb)-octahedra in the chains are stronger than those between chain octahedra and *D*-octahedra. Therefore, the latter interactions can be considered as perturbations.

According to the theory of vibrations in the cluster approximation [25], these perturbations for a chain consisting of *N* links are described by the dynamic matrix $\Delta\check{D}$. This matrix has the dimensionality $N \times N$, and the elements of its principal diagonal are equal to Δd_0 (with a probability of *x*/2) or 0 (with a probability of $1 - x/2$). According to the first-order perturbation theory, the shift of the *k*th (Ti,Nb)–O stretching band is described by the following equation [26]:

$$\Delta\nu_k(N, x)^2 = g_{0k}^* \Delta\check{D}\mathbf{g}_{0k},$$

where $\mathbf{g}_{0k}$ is the *k*th zeroth-order eigenvector, whose *i*th component (with due regard for only the short-range interactions between the octahedra) is $\mathbf{g}_{0k}^i = [2/(N + 1)]^{1/2}\sin[ik\pi/(N + 1)]$. In the IR spectrum, the edge mode of the frequency branch with $k = 1$ is active. Consequently, the following equation can be written:

$$\Delta\nu(N, x)^2 = [2/(N + 1)]\sum_{i=1}^{N}(x/2)\Delta d_0 \sin^2[(i\pi)/(N + 1)]. \quad (1)$$

Table 2. Crystallochemical role of cations with different force characteristics of the cation–oxygen bond

Cations	Isomorphism	Presence of vacancies	Splitting of positions	Stretching frequencies, cm^{-1}
Si	–	–	–	900–1100
Ti, Nb, Zr, $^{[4]}Fe^{2+}$, Fe^{3+}	+	–	–	660–700
Mn, $^{[6]}Fe^{2+}$, Mg, Zn, $^{[6]}Ca$	+	+	–	440–470
Na, K, $^{[>6]}Ca$, Sr, Ba, H_3O^+	+	+	+	<400

Summing up from $i = 1$ to $i = N$ at $N \longrightarrow \infty$, we obtain

$$\Delta\nu^2(x) = \nu^2(x) - \nu_0^2 = cx,$$

where ν_0 is the Ti(Nb)–O stretching frequency in the case of a completely vacant *D* position, *x* is the number of atoms (per unit cell) in the *D* position, and *c* is a constant. If the nondiagonal elements of the dynamic matrix $\check{D}$ that describes the interactions between oscillators are much smaller than the diagonal elements, i.e., $\nu(x) - \nu_0 \ll \nu_0$, the latter equation can be rewritten as $\nu(x) = \nu_0 + (c/2\nu_0)x$.

Thus, the position of the Ti(Nb)–O stretching band must linearly correlate with the occupancy of the *D* position. This conclusion was experimentally confirmed. We measured IR spectra of all the minerals of the labuntsovite group characterized either chemically or structurally. The spectra were recorded on a Specord 75 IR spectrophotometer with the spectral slit width of 1.2 cm^{-1} (for the wave numbers ranging from 400 to 1200 cm^{-1}). The samples were prepared as pellets with potassium bromide. The wave numbers were determined with the use of polystyrene and gaseous ammonia as the standards. For the structurally studied specimens, the occupancies of the *D* positions plotted on the graph (Fig. 3) were determined from the experimental structural data. For the remaining specimens, the occupancies were determined as an excessive (above eight atoms per unit cell) number of the octahedrally coordinated atoms (Ti, Nb, Fe, Mg, Mn, Zn).

The idealized dependence (1) was determined on the assumption that the perturbing cross-linking octahedra in the *D* position are identical, whereas other perturbing factors are absent. The first condition implies that the cross-linking octahedra possess close force characteristics, thus giving rise to approximately equal elements of the vibrational dynamic matrix responsible for the interactions between the links of the adjacent chains via the cross-linking octahedra. Most likely, the scatter in the points plotted on the graph in Fig. 3 results primarily from the differences in the arrangement and occupancies of the extraframework positions.

The correlation between the stretching frequencies for the chains and the occupancy of the *D* position allows one to make some preliminary conclusions about the character of the structures of new minerals belonging to the labuntsovite group without resorting to X-ray diffraction analysis.

The differences in the force characteristics of the cation–oxygen bonds determining the role of the cations in the structures of the specimens of the labuntsovite group can be seen from Table 2, where the cations are arranged in order of decreasing stretching frequencies. The last column in Table 2 indicates the ranges of the characteristic stretching vibration frequencies of the corresponding polyhedra, which reflect the force characteristics of four groups of cations (according to the IR spectroscopic data). In particular, this table accounts for the ever more pronounced tendency of Group IV elements to be replaced by vacancies. Probably, this tendency is associated with specimen decationization (in this case, the charge is compensated with the replacement of H_2O with H_3O^{+1} or, e.g., by the oxidation of iron or manganese to the trivalent state). For Group III elements, the complex isomorphism involves not only the replacement of both atoms by other atoms but also the replacement of complexes by other complexes.

CONCLUSIONS

To summarize, the following conclusions can be drawn.

The *D* cations give rise to substantial local perturbations of the force field (in the case of complete occupancy of the *D* position, the observed shifts of the (Ti,Nb)–O stretching bands in the IR spectra under the influence of the *D* cations reach 30 cm^{-1}), so that their effect must be taken into account, in particular, in the interpretation of the ion-exchange properties of the labuntsovite-group minerals.

Perturbations induced by the *D* cations only slightly depend on the nature of these cations. Thus, the *D* position can be occupied by Ca, Sr, and Na cations along with "typical" *D* cations (Mg, Mn, Fe, and Zn) that have close ionic radii and a coordination number of 6.

In some cases, IR spectroscopy enables one to obtain information on the distribution of the cations that play a dual role in the structures of zeolite-like minerals, without resorting to X-ray diffraction analysis. This is of particular importance in the cases where X-ray diffraction studies cannot be performed because of the poor quality of the crystals. In particular, such cations as Ca, Sr, or Na can occupy both the *D* position (at low coordination numbers) and large cavities of the framework, where they are characterized by high coor-

dination numbers. This is particularly true for the representatives of the labuntsovite group that are virtually free of Mg, Mn, Fe, and Zn ions and contain about two atoms, Ca + Sr, for every 16 Si atoms. The frequencies in the maxima of the (Ti,Nb)–O stretching bands for different specimens vary over a wide range, which corresponds to the distribution of these cations both over the *D* position and the extraframework positions.

Along with the Ca, Sr, and Na cations, some transition-metal cations can also play a dual role in the structures of labuntsovite-like minerals. For example, the total amount of manganese and zinc in some specimens is substantially higher than the theoretical limit for the *D* cations (two atoms for every 16 silicon atoms) and can be equal to three or more atoms. The presence of excessive Mn + Zn ions does not lead to a substantial increase in the ν(Ti,Nb–O) frequency, and, hence, the excessive ions act as typical extraframework ions. Apparently, in this case the potassium or barium ions in the *C* position are replaced by complexes of the $[Zn(H_2O)_2]^{2+}$ type.

ACKNOWLEDGMENTS

This study was supported by the Russian Foundation for Basic Research, project no. 02-05-64080.

REFERENCES

1. J. Rocha, P. Brandao, Z. Lin, *et al.*, J. Phys. Chem. **100** (36), 14978 (1996).
2. J. Rocha, P. Brandao, Z. Lin, *et al.*, Chem. Commun., No. 5, 669 (1996).
3. A. I. Bortun, L. N. Bortun, S. A. Khainakov, *et al.*, Solvent Extr. Ion Exch. **17** (3), 649 (1999).
4. G. Cruciani, P. Deluca, A. Nastro, and P. Pattisson, Micropor. Mesopor. Mater. **21** (1–3), 143 (1998).
5. G. Perrault, C. Boucher, J. Vicat, *et al.*, Acta Crystallogr., Sect. B: Struct. Crystallogr. Cryst. Chem. **29** (7), 1432 (1973).
6. R. K. Rastsvetaeva, N. V. Chukanov, and I. V. Pekov, Dokl. Akad. Nauk **357** (3), 364 (1997).
7. N. I. Golovastikov, Kristallografiya **18** (5), 950 (1973) [Sov. Phys. Crystallogr. **18**, 596 (1973)].
8. N. I. Organova, D. K. Arkhipenko, Yu. P. Dikov, *et al.*, Mineral. Zh. **3** (2), 49 (1981).
9. K. A. Rozenberg, R. K. Rastsvetaeva, I. V. Pekov, and N. V. Chukanov, Kristallografiya **47** (2), 265 (2002) [Crystallogr. Rep. **47**, 229 (2002)].
10. R. K. Rastsvetaeva, N. V. Chukanov, I. V. Pekov, *et al.*, Kristallografiya **43** (5), 874 (1998) [Crystallogr. Rep. **43**, 820 (1998)].
11. R. K. Rastsvetaeva, N. V. Chukanov, and I. V. Pekov, Dokl. Akad. Nauk **357** (1), 64 (1997).
12. K. A. Rozenberg, R. K. Rastsvetaeva, I. V. Pekov, and N. V. Chukanov, Kristallografiya **47** (3), 449 (2002) [Crystallogr. Rep. **47**, 408 (2002)].
13. R. K. Rastsvetaeva, A. V. Arakcheeva, and A. P. Khomyakov, Dokl. Akad. Nauk **351** (2), 207 (1996).
14. R. K. Rastvetaeva, R. A. Tamazyan, D. Yu. Pushcharovsky, *et al.*, Eur. J. Mineral. **6**, 503 (1994).
15. N. I. Organova, Z. V. Shlyukova, N. I. Zabavnikova, *et al.*, Izv. Akad. Nauk SSSR, Ser. Geol., No. 2, 98 (1976).
16. R. K. Rastsvetaeva, R. A. Tamazyan, D. Yu. Pushcharovskiĭ, *et al.*, Kristallografiya **39** (6), 994 (1994) [Crystallogr. Rep. **39**, 908 (1994)].
17. N. I. Golovina, G. V. Shilov, N. V. Chukanov, and I. V. Pekov, Dokl. Akad. Nauk **362** (3), 350 (1998).
18. R. K. Rastsvetaeva, N. V. Chukanov, and I. V. Pekov, Kristallografiya **45** (5), 830 (2000) [Crystallogr. Rep. **45**, 759 (2000)].
19. K. A. Rozenberg, R. K. Rastsvetaeva, I. V. Pekov, and N. V. Chukanov, Dokl. Akad. Nauk **383** (5), 657 (2002).
20. N. A. Yamnova, I. V. Pekov, Yu. K. Kabalov, *et al.*, Dokl. Akad. Nauk **375** (4), 487 (2000).
21. R. K. Rastsvetaeva, I. V. Pekov, and Yu. V. Nekrasov, Kristallografiya **46** (3), 415 (2001) [Crystallogr. Rep. **46**, 365 (2001)].
22. R. K. Rastsvetaeva, N. I. Organova, I. V. Rozhdestvenskaya, *et al.*, Dokl. Akad. Nauk **371** (3), 336 (2000).
23. N. V. Chukanov, I. V. Pekov, and A. P. Khomyakov, Eur. J. Mineral. **14** (1), 165 (2002).
24. N. V. Chukanov, I. V. Pekov, R. K. Rastvetaeva, *et al.*, Can. Mineral. **37** (4), 901 (1999).
25. N. V. Chukanov and I. V. Kumpanenko, Chem. Phys. Lett. **146** (3–4), 211 (1988).
26. N. V. Chukanov, Doctoral Dissertation in Physics and Mathematics (Inst. Khim. Fiz. Akad. Nauk SSSR, Chernogolovka, 1992).

Translated by T. Safonova

Crystallography Reports, Vol. 47, No. 6, 2002, pp. 946–949. Translated from Kristallografiya, Vol. 47, No. 6, 2002, pp. 1016–1019.

STRUCTURE OF INORGANIC COMPOUNDS

Mechanism of Formation of Barium Cuprate-Based Solid Solutions with Perovskite-like Structure Doped with Cadmium and Yttrium Oxides[1]

L. P. Lyashenko

Institute of Problems of Chemical Physics, Russian Academy of Sciences, Chernogolovka, Moscow oblast, 142432 Russia

e-mail: kaplunov@icp.ac.ru

Received May 11, 2002

Abstract—The influence of Y_2O_3 and CdO content on the phase composition, structure, and electrical properties of Y_2O_3–CdO–BaO–CuO ceramics was studied. The concentration limits of the existence of the orthorhombic perovskite-like $Y_xBa_{2-x}Cd_yCu_{1-y}O_{3+\delta}$ solid solutions (where $0.20 \le x \le 0.37$ and $y \le 0.2$) and their unit-cell parameters are determined. *© 2002 MAIK "Nauka/Interperiodica".*

INTRODUCTION

The compound Ba_2CuO_3, one of the components for synthesis of high-temperature superconductors, is hygroscopic and readily decomposes in the presence of a small quantity of carbon dioxide and water [1, 2]. At 810°C, this barium cuprate undergoes a phase transition (associated with the change in the oxygen content) from the orthorhombic (Sr_2CuO_3 structural type) to the tetragonal (K_2NiF_4 structural type) phase, melting incongruently at 920°C [3, 4]. The stabilization of the perovskite-like Ba_2CuO_3 structure by various dopants was observed earlier [5] and was then studied in detail for barium cuprate doped with rare-earth oxides [6–8].

Below we describe the study of the existence ranges and crystallographic parameters of stable barium cuprate-based perovskite-like $Y_xBa_{2-x}Cd_yCu_{1-y}O_{3+\delta}$ solid solutions.

EXPERIMENTAL

The solid solutions based on Ba_2CuO_3 were synthesized by the standard ceramic technique from a charge of composition $(x'/2)Y_2O_3 \cdot (2 - x')BaO \cdot y'CdO \cdot (1 - y')CuO$ (where x' ranges from 0.2 to 0.4 and y', from 0 to 0.4 at a step of 0.01 both for x' and y'). The necessary quantities of BaO_2 (analytical grade), Y_2O_3 (Y–1), CuO (high-purity grade), and CdO (high-purity grade) were mixed in an agate mortar with the addition of ethyl alcohol and then the mixture was annealed for 40 h in air at 930°C. The samples were cooled to 20°C in a furnace and quenched in an ice-cooled oil of the trademark D-1.

The synthesized phases were identified on a DRON-3M X-ray powder diffractometer at 20°C (CuK_α radiation, Ni filter). The accuracy of the determination of the unit-cell *a*, *b*, and *c* parameters and unit-cell volume *V* was ±0.002, ±0.003, ±0.006 Å, and ±0.20 Å^3, respectively.

The phase composition and microstructure of the samples were studied by electron-probe microanalysis on a JEOL Superprobe instrument (probe diameter 1 μm; accelerating voltage 20 kV; accuracy of cation identification 1%). The standards were polycrystalline $YBa_2Cu_3O_{6.9}$ and CdO samples. The conducting layer was a ~200-Å-thick aluminum foil deposited onto the sample surface in vacuum. Quantitative calculations were performed using the ZAF-program for metals, which was applied to the instrument.

RESULTS AND DISCUSSION

The doping of barium cuprate with yttrium oxide results in the formation of two types of substitutional solid solutions of the type $Y_xBa_{2-x}CuO_{3+\delta}$ with a perovskite-like structure: (1) the tetragonal structure ($0.20 \le x \le 0.25$) and (2) the orthorhombic structure ($0.33 \le x \le 0.38$) with the doubled *c*-parameter existing within a wide temperature range [8]. The transition from the tetragonal to orthorhombic phase is accompanied by a change in the yttrium content. The samples obtained from a charge of composition $0.25 < x' < 0.33$ consisted of a mixture of the tetragonal and orthorhombic phases. For the monophase samples, the *x* and x' values coincide.

The X-ray diffraction and electron-probe data showed that the interaction of the $Y_xBa_{2-x}CuO_{3+\delta}$ solid solutions with CdO at high temperatures results in the formation of the substitutional solid solutions

[1] This work was presented to the Symposium "Order, Disorder, and Properties of Oxides" (ODPO), Sochi, Russia, 2001.

$Y_xBa_{2-x}Cd_yCu_{1-y}O_{3+\delta}$ (where $0.20 \le x \le 0.37$ and $y \le 0.2$) with a perovskite-like orthorhombic structure. Yttrium ions incorporated into the Ba_2CuO_3 structure occupy the barium positions, whereas cadmium ions occupy the copper positions, thus stabilizing the perovskite-like orthorhombic structure. It is worth noting that no perovskite-like phases were formed upon replacement of barium by cadmium ions in the sample obtained from the $1.67BaO \cdot 0.33CdO \cdot CuO$ charge.

Typical X-ray diffraction patterns of the studied solid solutions with tetragonal and orthorhombic structures are shown in Fig. 1 (curves *1–3*). In the composition range $0.20 \le x \le 0.25$, upon the replacement of some copper ions by larger cadmium ones (Fig. 1, curves *1*, *2*) the tetragonal structure $Y_xBa_{2-x}CuO_{3+\delta}$ is transformed into an orthorhombic one. In the composition range of the charge $0.25 < x < 0.33$, the samples consisted, in the absence of cadmium, of a mixture of tetragonal and orthorhombic phases; doping with cadmium oxide resulted in the formation of the orthorhombic phase alone. Figure 1 shows that the diffraction maxima of the cadmium-doped orthorhombic phase (curve *2*, $x = 0.2$ and $y = 0.2$) and the tetragonal phase without cadmium (curve *1*, $x = 0.2$ and $y = 0$) are slightly broadened. With the approach of the solubility limit of yttrium and cadmium in barium cuprate, the diffraction reflections of the solid solutions narrowed with the $K_{\alpha_{1,2}}$ doubles being resolved at large diffraction angles, which indicates a higher degree of order (Fig. 1, curve *3*).

The solubility limit of cadmium in the solid solutions studied was determined by local X-ray spectroscopic microanalysis of the samples synthesized by the ceramic technique ($T = 930$°C and $t = 40$ h) from the $Y_xBa_{2-x}CuO_{3+\delta}$: CdO = 1 : 1 charge. The X-ray phase analysis showed that the samples obtained from this charge were mixtures of the P, CdO, and CuO (trace amount) phases. The electron-probe microanalysis showed that an increase in the yttrium content (x) in the solid solutions reduced the solubility limit of cadmium. At $x = 0.2$ and 0.33, the solubility limit was 0.2 and 0.15 atomic fractions, respectively.

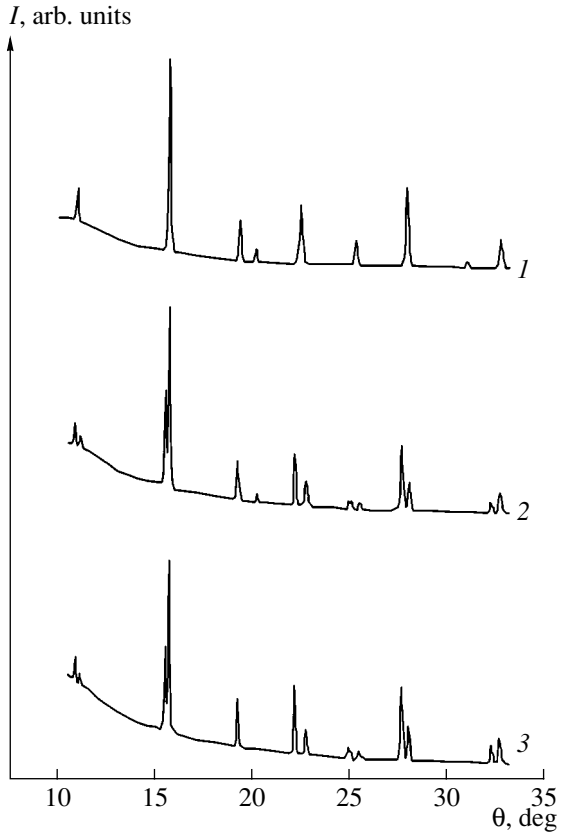

Fig. 1. X-ray diffraction patterns of $Y_xBa_{2-x}Cd_yCu_{1-y}O_{3+\delta}$ solid solutions synthesized for 40 h at 930°C and cooled in the furnace: (*1*) the tetragonal phase with $x = 0.2$ and $y = 0.0$ and the orthorhombic phases with (*2*) $x = 0.2$ and $y = 0.2$ and (*3*) $x = 0.33$ and $y = 0.15$.

The X-ray diffraction patterns of all the solid solutions were indexed by analogy with the $Y_xBa_{2-x}CuO_{3+\delta}$ solid solutions studied earlier [8]. The unit-cell parameters of the solid solutions determined from the set of diffraction reflections recorded in the range of 2ϑ angles 30°–75°, the unit-cell volumes, and the b/a ratios are listed in the table. For comparison, this table also lists the crystallographic data of the ini-

Crystallographic parameters and resistivity of the $Y_xBa_{2-x}Cd_yCu_{1-y}O_{3+\delta}$ solid solutions with a perovskite-like structure depending on the yttrium and cadmium content at 20°C

$Y_xBa_{2-x}Cd_yCu_{1-y}O_{3+\delta}$		a, Å	b, Å	c, Å	V, Å^3	b/a	ρ, Ω m
x	y						
0.20	0.00	4.045	4.047	8.092	132.47	1.0005	1.1
0.20	0.10	4.003	4.109	8.223	135.25	1.0265	17.9
0.20	0.20	4.000	4.106	8.209	134.83	1.0265	212.0
0.33	0.00	3.997	4.095	8.195	134.13	1.0245	30.9
0.33	0.10	4.000	4.107	8.215	134.96	1.0268	13.1
0.33	0.15	4.005	4.102	8.205	134.80	1.0242	11.4

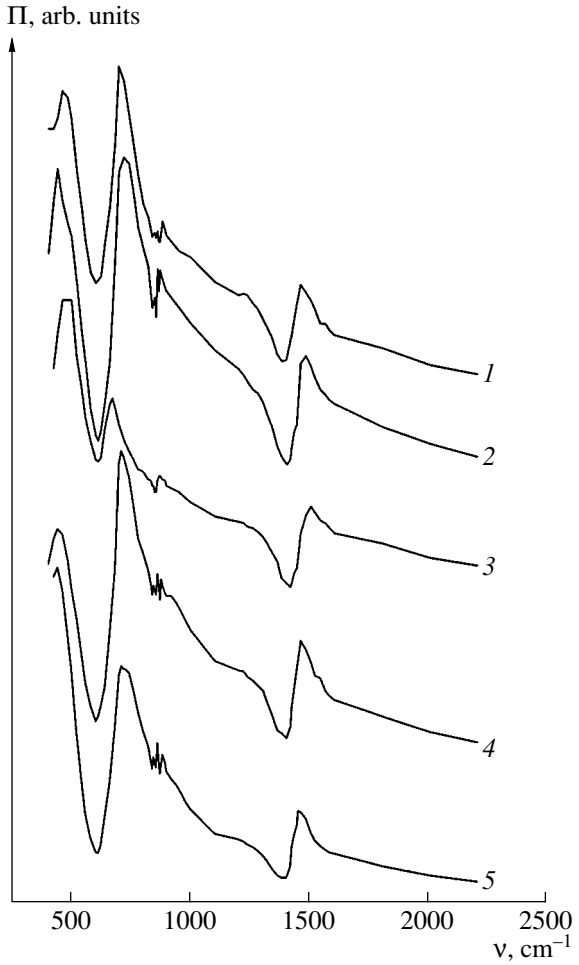

Fig. 2. Infrared spectra of $Y_xBa_{2-x}Cd_yCu_{1-y}O_{3+\delta}$ solid solutions synthesized for 40 h at 930°C and cooled in the furnace (KBr pellet and 4-mg weight): (*1*) $x = 0.2$ and $y = 0.0$, (*2*) $x = 0.33$ and $y = 0.0$, (*3*) $x = 0.2$ and $y = 0.1$, (*4*) $x = 0.27$ and $y = 0.1$, and (*5*) $x = 0.33$ and $y = 0.1$.

tial tetragonal and orthorhombic phases with $x = 0.20$ and 0.33, respectively.

The replacement of Cu^{2+} ions by larger Cd^{2+} ions in the solid-solution structure results in an increase in the unit-cell volume and a higher degree of its orthorhombicity. For example, the unit-cell volume and the orthorhombicity are 132.47 Å^3 and 1.0005 and 135.25 Å^3 and 1.0265 at $x = 0.2$, $y = 0$ and at $x = 0.2$, $y = 0.1$, respectively. The observed unit-cell expansion is consistent with the ratio of the Cu^{2+} and Cd^{2+} ionic radii equal to 0.62 and 0.84 Å at the coordination number 4 [9]. A further increase in the cadmium content in the solid solutions at x = const results in an anomalous unit-cell "compression" along the c axis. For example, the volumes V are 135.25 and 134.83 Å^3 at $x = 0.2$, $y = 0.1$ and $x = 0.2$, $y = 0.2$, respectively. This compression can be attributed to microstresses caused by the large difference in the ionic radii of the cations and, hence, the rearrangement of the electronic structure of the crystal lattice.

The X-ray diffraction pattern of the $Y_xBa_{2-x}Cd_yCu_{1-y}O_{3+\delta}$ solid solutions hardened from the experimental temperature down to 20°C and then slowly cooled in the furnace showed that the orthorhombic perovskite-like structure is stable in the range from the temperature of synthesis to room temperature.

The structural studies of the yttrium and cadmium oxide-doped barium cuprate-based solid solutions are complemented by the infrared (IR) spectra in the range 400–2200 cm^{-1} at 20°C (Specord 75 spectrometer, KBr pellets, 4-mg weight). The infrared spectra of the solid solutions with and without cadmium contain a broad (460–700 cm^{-1}) intense absorption band at 600–610 cm^{-1} corresponding to the Cu–O vibrations and three weak absorption bands at 840, 850, and 870 cm^{-1} attributed to the appearance of oxygen incorporated into the lattice as a result of the heterovalent replacement of Ba^{2+} by Y^{3+} ions to provide the electrical neutrality of the system (Fig. 2, curves *1–5*). The absorption band at 1400 cm^{-1} corresponds to vibrations of the adsorbed OH group [10]. The frequency position of the IR absorption bands (ν) is almost independent of the yttrium and cadmium content, which only changes the intensity of these bands.

The incorporation of oxygen into the barium cuprate lattice during the heterovalent replacement of some Ba^{2+} ions by Y^{3+} ions and the replacement of Cu^{2+} ions by larger Cd^{2+} ions result in the formation of a stable perovskite-like orthorhombic structure within wide concentration and temperature ranges.

$Y_xBa_{2-x}Cd_yCu_{1-y}O_{3+\delta}$ solid solutions are semiconductor ceramics with a resistivity ranging within 1.1–212.0 Ω m depending on their composition at 20°C (see table).

CONCLUSIONS

Thus, the formation of barium cuprate-based $Y_xBa_{2-x}Cd_yCu_{1-y}O_{3+\delta}$ solid solutions is established and ranges of their homogeneity are determined. The X-ray diffraction and electron-probe studies showed that in these solid solutions a perovskite-like structure with different degrees of order is stabilized in the composition range $0.20 \le x \le 0.37$ and $y \le 0.20$ with the double c-period in a wide temperature range (up to 930°C).

The concentration dependence of the crystallographic parameters of $Y_xBa_{2-x}Cd_yCu_{1-y}O_{3+\delta}$ solid solutions was also studied.

It is established that the above solid solutions studied are semiconductor materials.

ACKNOWLEDGMENTS

The author is grateful to M.G. Kaplunov for his help in recording IR spectra and their interpretation.

REFERENCES

1. R. S. Roth, K. L. Davis, and J. R. Dennis, Adv. Ceram. Mater. **2** (3B), 303 (1987).
2. A. R. Armstrong, PhD Thesis (Magdalene College, University of Cambridge, 1990).
3. W. Zhang, K. Osamura, and S. Ochiai, J. Am. Ceram. Soc. **73** (7), 1958 (1990).
4. W. Zhang and K. Osamura, Jpn. J. Appl. Phys. **29** (7), L1092 (1990).
5. G. Wang, S.-J. Hwu, S. N. Song, *et al.*, Adv. Ceram. Mater. **2** (3B), 313 (1987).
6. L. P. Lyashenko, N. V. Sachkova, V. N. Molchanov, *et al.*, Neorg. Mater. **32** (12), 1502 (1996).
7. L. P. Lyashenko, N. V. Sachkova, and L. G. Shcherbakova, Neorg. Mater. **32** (12), 1511 (1996).
8. L. P. Lyashenko and L. G. Shcherbakova, Materialovedenie, No. 2, 30 (2001).
9. R. D. Shanon and C. T. Prewitt, Acta Crystallogr., Sect. B: Struct. Crystallogr. Cryst. Chem. **25** (5), 925 (1969).
10. A. N. Lazarev, *Vibration Spectra and Structure of Silicates* (Nauka, Leningrad, 1968).

Translated by A. Zolot'ko

Crystallography Reports, Vol. 47, No. 6, 2002, pp. 950–956. Translated from Kristallografiya, Vol. 47, No. 6, 2002, pp. 1020–1026.

STRUCTURE OF INORGANIC COMPOUNDS

Structure Model of Al,K-Substituted Tobermorite and Structural Changes upon Heating*

N. I. Organova[1], E. V. Koporulina[1], A. G. Ivanova[2], N. V. Trubkin[1], A. E. Zadov[3], A. P. Khomyakov[4], I. M. Marcille[1], N. V. Chukanov[5], and A. N. Shmakov[6]

[1] *Institute of Geology of Ore Deposits, Petrography, Mineralogy, and Geochemistry (IGEM), Russian Academy of Sciences, Staromonetnyĭ per. 35, Moscow, 109017 Russia*
e-mail: natalia@igem.ru

[2] *Moscow State University, Vorob'evy gory, Moscow, 119899 Russia*

[3] *NPO Regenerator, Moscow, Russia*

[4] *Institute of Mineralogy, Geochemistry, and Crystal Chemistry of Rare Elements, ul. Veresaeva 15, Moscow, 121327 Russia*

[5] *Institute of Problems of Chemical Physics in Chernogolovka, Russian Academy of Sciences, Chernogolovka, Moscow oblast, 142432 Russia*

[6] *Boreskov Institute of Catalysis, Siberian Division, Russian Academy of Sciences, pr. Akademika Lavrent'eva 5, Novosibirsk, 630090 Russia*

Received January 16, 2002

Abstract—A structure model of Al and K-containing tobermorite is proposed based on the results obtained by different methods—powder X-ray diffraction analysis, microdiffraction in an electron microscope, etc. The factors responsible for the stability of the structure modules typical of the specimens of this family are discussed. Most of the microcrystals were demonstrated to consist of two phases characterized by a high degree of silicon–oxygen radical condensation. The examination of two-phase microcrystals in an electron microscope by the method of diffraction contrast allowed us to propose the mechanism of change of the degree of condensation of the tobermorite structures under an electron beam. Heating the starting crystals results in their transformation into an amorphous state with a simultaneous increase in the degree of condensation of the silicon–oxygen ribbons in the structure. *© 2002 MAIK "Nauka/Interperiodica".*

INTRODUCTION

Early structural studies. Mineral tobermorite is a potassium hydrosilicate of practical interest in view of the fact that its synthetic analogue is one of the components of portlandcement. Until recently, the detailed structure of this mineral was unknown. In the late 1990s, S. Merlino *et al.* [1–4] reported structural data on several varieties of the so-called 11-Å tobermorites. Besides these, there exist 14- and 9-Å varieties (plombierites and riversideites, respectively).

The first structure model of tobermorite was proposed by Megow [5] in 1956. However, the first complete structure solution was reported only in 1997. The lapse of more than 40 years between these two investigations is explained by the fact that the crystals of most specimens are imperfect, and the corresponding single crystals are either absent or occur very rarely.

In [6] (published prior to the structure determination), natural specimens of the mineral were examined by the diffraction (X-ray diffraction and microdiffraction), chemical (electron microprobe, Kevex), IR spectroscopic, optical, and thermal methods. It was demonstrated that the major absorption band (almost at 1000 cm^{-1}) associated with the silicon–oxygen motif does not preserve its position in the IR spectra from different mineral specimens. The frequency of this band depends on the degree of condensation of the silicon–oxygen tetrahedra. It was concluded that the latter characteristic slightly varies in different tobermorites. Thus, 11-Å tobermorites contain double three-membered silicon–oxygen chains that are like those observed in xonotlite but have a different configuration. In some specimens, the degree of their binding to each other is higher, which is equivalent to an increase in the degree of silicon–oxygen tetrahedra condensation.

Microdiffraction studies of microcrystals of various tobermorites accompanied by the determination of their chemical composition (Kevex attachment) confirmed that the structures of microcrystals are often imperfect [7]. In all cases, microtwinning perpendicular to the (100) or (010) planes was observed as well as characteristic blurring of the reflections with $k \neq 2n$ in the (hk0) section of the reciprocal lattice. In addition, infinite diffuse rods along the Z^*-direction were found in the patterns of many microcrystals. If microcrystals are

* This study was presented at the Symposium "Phase Transitions in Solid Solutions and Alloys," Sochi, Russia, 2001.

1063-7745/02/4706-0950$22.00 © 2002 MAIK "Nauka/Interperiodica"

rotated about the X^* axis, the reflections with $k \neq 0$ are continuous, which is associated with the disorder in the mutual arrangement of the structure modules, namely, with a possible displacement by $\pm b/2$ of the ribbons with respect to the core or with variations in the structural motif in the (001) plane. The existence of parallel atomic planes that are equidistant from each other and possess the same translational characteristics within the layer leads (according to Guinier [8]) to the formation of diffuse rods in the reciprocal space in the direction normal to these planes. Such rods are often observed in diffraction patterns of many microcrystals.

Prior to the studies performed by Merlino, Hamid [9] made the second (after Megow) step toward a better understanding of the characteristic features of the structure of tobermorite. Hamid determined the structure of tobermorite for a subunit with unit-cell parameters a and b that were twice as small (the most widespread true unit cell has the parameters $a = 5.2 \times 2$ Å, $b = 3.68 \times 2$ Å, $c = 22.7$ Å).

The results of the studies performed by Hamid and Merlino confirmed the assumptions made by Megow [5]. The structure of tobermorite contains a core of Ca-polyhedra, which, within the first approximation, are trigonal prisms. The Ca atoms are located at two levels. The three-membered ribbons of the silicon–oxygen tetrahedra are on the opposite sides of the core. The ribbons can be displaced by $\pm b/2$ with respect to each other. Megow believed that these structure elements are single chains rather than ribbons. In the model proposed by Hamid, both chains and ribbons are equally probable because of the probable displacement of the chains. Such a displacement can occur because the translation characterizing the three-membered silicon-oxygen ribbon in tobermorite (7.3 Å) is equal to the size of two Ca-polyhedra of the core.

Merlino was the first to state that all the specimens consisted of at least two components belonging to the same group of OD structures. The existence of more than one mineral variety in all our specimens was indicated in [6]. We also noted that specimens characterized by a higher degree of condensation belong to Al-containing tobermorites. Unfortunately, this variety is most difficult to uncrystallize, so its single crystals have not been found as yet. However, its structure is of special interest because of the ability of this variety to absorb and retain cesium [10].

THERMAL TRANSFORMATIONS IN TOBERMORITE

Heating 14-Å tobermorite to 90 and 300°C led to its transformation into 11-Å tobermorite and 9-Å riversideite, respectively, with its main structure modules being retained [11]. In all cases, the Ca-core remained intact. The double three-membered chains are adjacent to the core both in plombierite and tobermorite. The three-membered chains in riversideite are linked to the core in a similar fashion. The minerals differ in the number of water molecules and Ca cations located between their layers. Decondensation of the double chains into single chains was first observed by IR spectroscopy. Recently, this fact was confirmed by Merlino *et al.* [3], who determined the structure of tobermorite. The structure of plombierite remains to be studied. However, it is evident that the silicon–oxygen motif in the latter mineral is similar to that in tobermorite.

The 11-Å tobermorites are classified into two groups (normal and anomalous). The aluminum-containing varieties belong to anomalous tobermorites and are not transformed into riversideite upon calcination. In addition, specimens of 11-Å minerals have different numbers of interlayer Ca cations and water molecules.

Our studies [12] of the thermal behavior of tobermorites demonstrated that these minerals underwent various structural changes during heating. However, the characteristic features of these changes are still unknown.

Generally, the Al-containing tobermorites incorporate not only Al but also K. All the Al,K-containing tobermorites are formed at higher temperatures and belong to the anomalous minerals more often than tobermorites that are free of these elements. In addition, the Al,K-containing tobermorites are more condensed. Their powder X-ray patterns differ from those of all the other specimens only in that they have weak reflections, with the d_{001} distance remaining constant (11.3 Å).

A representative collection of tobermorites of various compositions was examined in [12]. The products of their hydration, dehydration, and heating were investigated. The results of this study demonstrated that the changes in the structure of the silicon–oxygen radical occurring in these processes can lead to either the decondensation or the further condensation of the silicon–oxygen tetrahedra. In some instances, these processes occur simultaneously. The pathway of these processes depends on the quantitative ratio between two crystallographically nonequivalent hydroxy groups in different specimens. One hydroxy group is bound to the calcium cation, whereas the other one is bound to the free vertex of a silicon–oxygen tetrahedron. All these low-energy processes take place at ~300°C. These conclusions were made based on the results of X-ray phase analysis, IR spectroscopy, derivatography, and microdiffraction study, together with data on the chemical compositions of the specimens. In the case of tobermorites with a high Al and K content, the degree of condensation increased upon heating to 300–400°C. However, this change of the structure was not significantly reflected in the powder X-ray diffraction patterns. Only an overall decrease in the line intensities was observed at the early stages. Subsequent heating caused the transformation of the compound into an amorphous state.

In this study, we examined the topotaxial transformation observed for microcrystals of Al,K-containing

tobermorites in an electron microscope and constructed the model of a possible mechanism of this transformation.

STRUCTURE MODEL OF (Al,K)-CONTAINING TOBERMORITE

The averaged crystallochemical formula of Al-containing tobermorite is $Ca_{4.5}[(Si_{6-x},Al_x)O_{15}(OH)_{2-y}] \cdot nH_2O$, where $n = 5–6$, $0.5 < x < 1.2$, and the y value is determined by the valence balance (for the normal and maximum condensed tobermorites, y is 0 and 1, respectively). According to the IR spectroscopy data, the degree of condensation of the silicon–oxygen chains in all the Al-containing tobermorites is higher than that in the normal tobermorite.

We studied three natural specimens of Al-containing tobermorite from different deposits. The specimens were examined by electron microscopy (microdiffraction and an approximate estimation of the chemical composition). In each specimen, three types of microcrystals were revealed, namely, usual tobermorite with a *C*-pseudocentered unit cell ($a = 11.8$ Å, $b = 7.3$ Å, $c = 22.7$ Å), unknown condensed tobermorite with a *C*-centered orthorhombic unit cell (the doubled a parameter), and microcrystals containing the above-described phases twinned along the (100) plane. The new variety of tobermorite has a different arrangement of reflections on both odd and even layer lines. The twinned microcrystals constitute the major portion of the specimen. All three types of microcrystals contain Al and K atoms. Each of these types has its own characteristic features. Thus, the reflections with any indices in the X-ray patterns of usual tobermorite are generally sharp and have the shape of spots, which indicates that the corresponding crystals are obviously crystallized. Microcrystals with two components are usually characterized by reflections with $k = 2n \pm 1$, which are blurred and elongated in the direction perpendicular to the Y^* axis. Apparently, this corresponds to the small thickness of the microvolumes of the twinned phase with the doubled unit cell. Initially, we characterized the crystals providing the above-mentioned sharp spot reflections as single crystals. However, the subsequent microdiffraction studies demonstrated that all these crystals were twins. In the X-ray patterns of microcrystals of the second and third groups, the strongest reflections with $k = 2n$ (in the X-ray patterns of microcrystals of the first group, only the reflections with $k + h = 4n$ are present) are surrounded by satellites, which remove the restrictions inherent in the first group of crystals within the same metrics.

The disorder in the structures of tobermorite is explained by the displacement of the layers parallel to the (001) plane with respect to each other and also by their possible nonequivalence. This is associated with the fact that, as mentioned above, having the same dimensions of the elementary rectangle and density of the silicon–oxygen tetrahedra, the double silicon–oxygen chains may have different mutual displacements, orientations, and mutual arrangement.

Consideration of the possible mutual arrangement of the tobermorite ribbons enabled us to construct a structure model of Al-containing tobermorite with the maximum possible degree of condensation. When constructing the model, we assumed that all the structures contain doubled CaO_2-networks composed of oxygen polyhedra, double chains linked with the Ca-core in the same fashion, and ambiguity in the mutual linkage of the ribbons and the core in the case of their mutual displacement by $\pm b/2$. Two projections of the known 11-Å tobermorites are schematically shown in Figs. 1 and 2 together with a new model for the Al-containing variety.

The new model is characterized by broad channels along the Y axis, which can incorporate both alkali cations and water molecules, because the width of the channels is 1.5 times larger than in the conventional tobermorite variety (Fig. 2). The channels can be formed via additional cross-linking of the adjacent ribbons along the X axis after the rearrangement of the chains of tetrahedra linking the silicate diortho groups. The possibility of such cross-linking correlates with an increase in the average size of a tetrahedron in the tobermorite ribbons because of incorporation of Al atoms. The resulting structure has more pronounced zeolite properties than conventional tobermorite.

The structure model was tested and refined by two diffraction methods. The intensities of the $hk0$ reflections were estimated by single-crystal electron microdiffraction and then were used in the refinement of the atomic positions on the $xy0$ projection using the AREN program. All the atomic parameters of the model were refined by the Rietveld method (the JOUNG-98 program) based on powder X-ray diffraction data (synchrotron radiation, $\lambda = 1.5423$ Å; the Novosibirsk Research Center).

The refinement with the use of single-crystal X-ray data showed that the crystals are microtwinned.

The Rietveld refinement of the atomic coordinates was performed for a two-phase specimen within the sp. gr. *Imm*2 based on the subcell of Hamid's model [9]. The refinement converged to $R = 15.25\%$. One phase was shown to be usual tobermorite, whereas the other phase was highly condensed tobermorite. The results obtained in the refinement can be improved if one determines the coordinates of the interlayer calcium atoms and water molecules in the condensed tobermorite specimen.

INFLUENCE OF TEMPERATURE ON THE STRUCTURAL CHARACTERISTICS OF (Al,K)-CONTAINING TOBERMORITES

The thermal transformations of the structure were examined [13] for two microcrystals (courtesy of

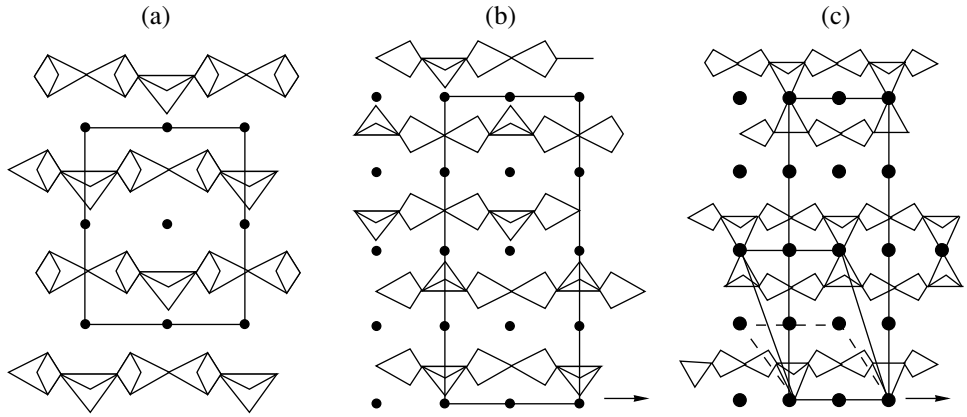

Fig. 1. Schemes of the elementary structure modules of Al-containing tobermorites projected onto the (001) plane: (a) usual tobermorite; (b) one of the possible modes of the ordered arrangement of double ribbons; (c) the proposed model of the structure of highly condensed tobermorite; calcium atoms are indicated by solid circles.

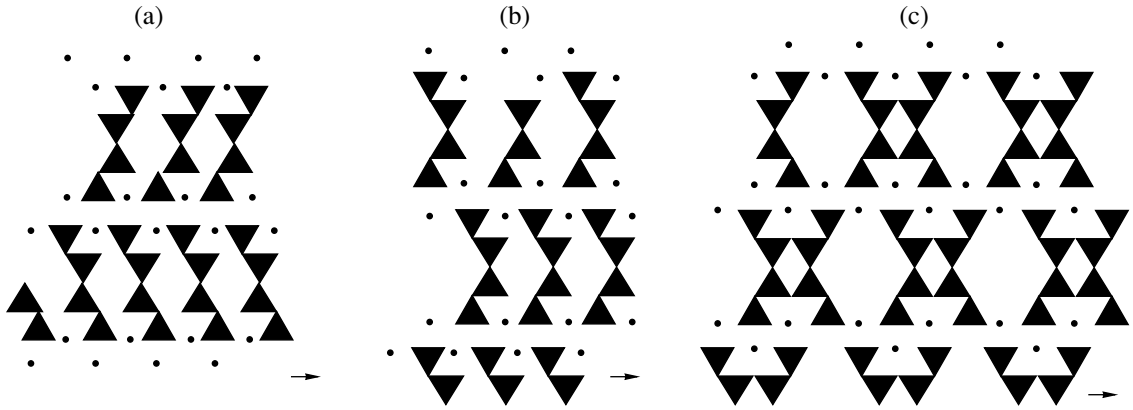

Fig. 2. Scheme of the mutual arrangement of the tobermorite ribbons along the [010] direction: (a) clinotobermorite; (b) usual tobermorite; (c) highly condensed tobermorite.

A.P. Khomyakov). The microdiffraction study revealed the presence of both phases not only by the X-ray diffraction method but also by the method of diffraction contrast [14]. The latter technique allows one to study different defects, including the defects in a real crystal, using a beam incident onto the crystal and reflected from the surface plane. The images were obtained in the (600) reflection indicated by an arrow (Fig. 3b) located before the first intense reflection, (800).

This method proved to be very fruitful for examining our specimens. The microdiffraction patterns and the images with the diffraction contrast obtained in the transmission mode are shown in Fig. 3. The microdiffraction pattern can be interpreted as the pattern from two epitaxially intergrown phases. Each basic reflection with $k = 2n$ from the unit cell with $a = 11.3$ Å is accompanied by several less intense satellite reflections, which lead to unit-cell doubling along the X axis. At $k = 2n + 1$, the basic reflections from a single unit cell are sharp, whereas the reflections giving rise to the doubling of the unit-cell parameter a are elongated along the X^* axis. The image with the diffraction contrast showed that the phase with the doubled parameter a is the accumulation of dark regions elongated in the direction of the Y axis and incorporated into a lighter matrix of usual tobermorite. All the microcrystals examined in an electron microscope were heated, which could change their state upon irradiation with an electron beam in vacuum. Actually, the dark regions partly vanished, which was accompanied by corresponding changes in the diffraction pattern (Fig. 3d). Thus, the main portion of the satellite reflections with odd k of the second phase disappeared. The satellite reflections with even k were retained. This indicates that the modulation superimposed on the structure of Hamid's single unit cell was retained. The most probable mechanism of modulation involves ordering the core cations, including ordering the vacancies, together with the characteristic features of the structure of the silicon–oxygen radical with a high degree of condensation.

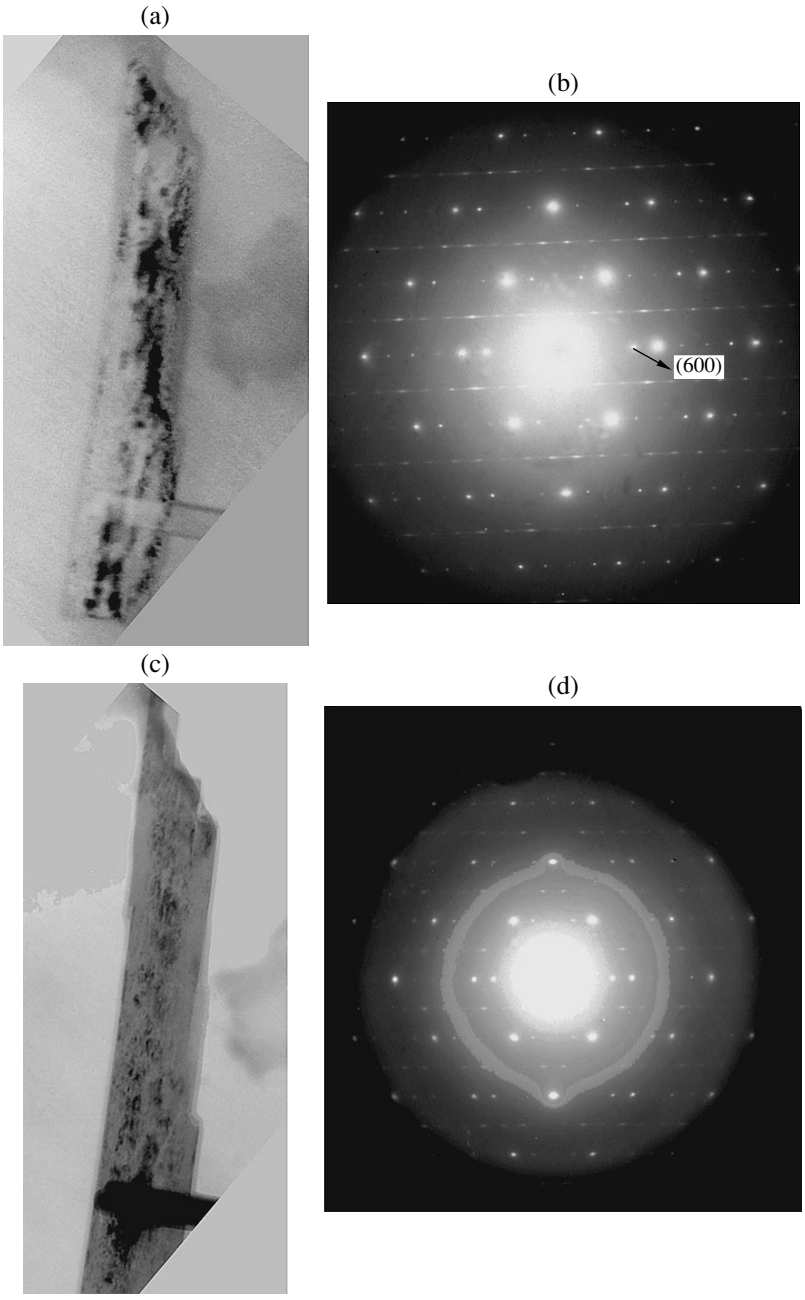

Fig. 3. Electron microscopy study of a microcrystal of tobermorite from the Khibiny massif: (a) image obtained by the method of diffraction contrast and (b) the microdiffraction patterns of the unirradiated crystal; analogous (c) image and (d) microdiffraction pattern of the irradiated crystal.

The *hk*0 reflections for the highly condensed phase could be indexed with due regard for twinning in the *C*-centered monoclinic unit cell. The vectors of the orthorhombic lattice with the doubled unit-cell parameter *a* are related to those of Hamid's lattice characterizing the epitaxial insertion as follows: / 4 1 0 /, / 0 1 0 /, / 0 0 1 /.

It is essential that the number of sharp satellite reflections with even *k* are consistent with the "new" unit cell. The contributions of these reflections must be summed with due regard for their intensities. For the orthorhombic unit cell with $a = 22.536$ Å, $b = 7.384$ Å, $c = 22.961$ Å, all the angles are right. For the monoclinic unit cell derived on the condition of centering the large orthorhombic unit cell, we obtain $a = 5.884$ Å, $b = 7.392$ Å, $c = 22.9601$ Å, $\beta = 108.32°$.

The comparison of this unit cell with the unit cells of the known structures of 11-Å tobermorites allowed us to draw the conclusion that the observed reduction of the number of satellite reflections is associated with the changes occurring in the most mobile portion of the structure of tobermorite, namely, in the interlayer space occupied by cations and water molecules.

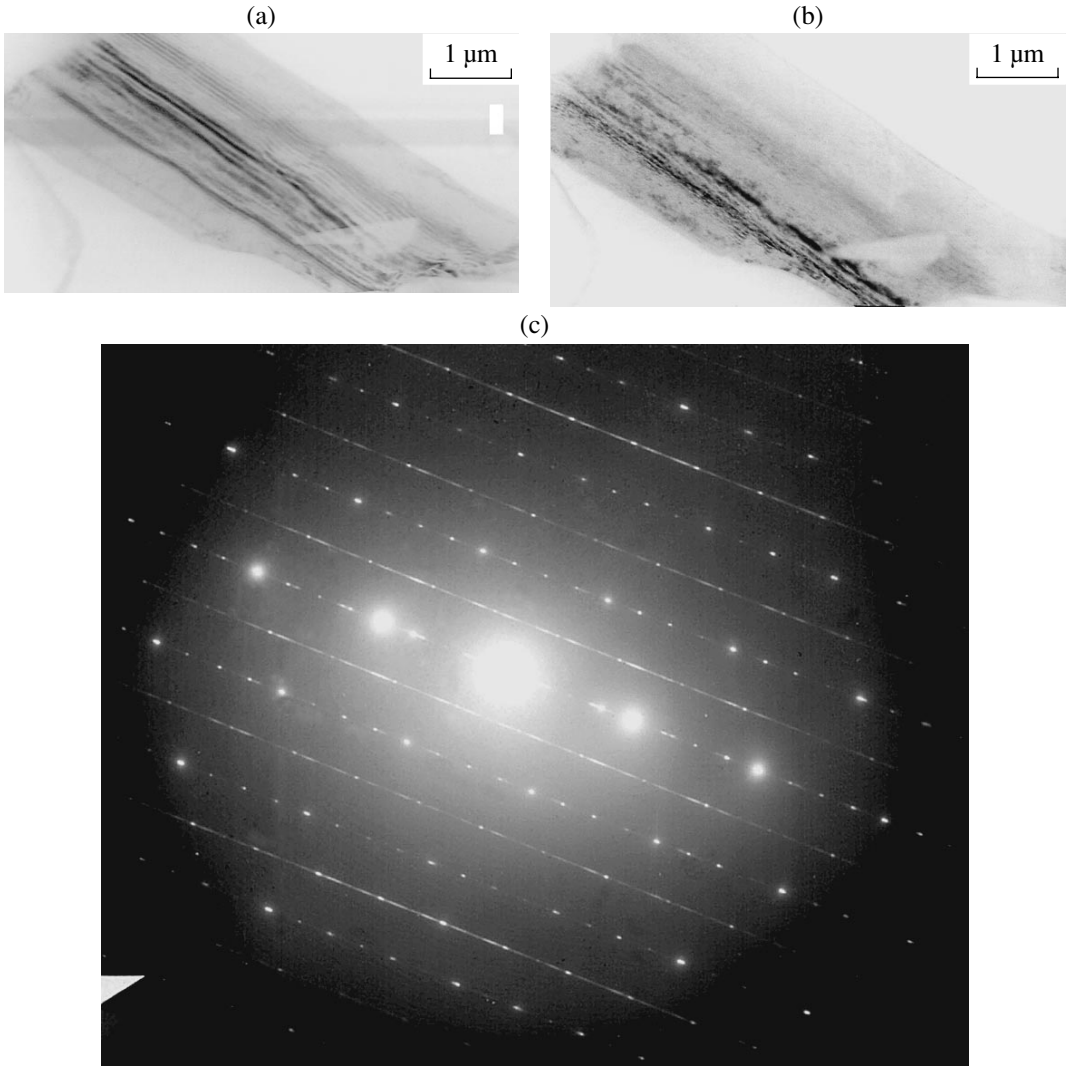

Fig. 4. Electron microscopy of the second tobermorite crystal from the Khibiny massif: (a) and (b) images of the crystal obtained by the method of diffraction contrast (a) before and (b) after irradiation; (c) microdiffraction pattern of the crystals.

In all the known tobermorite structures, the arrangement of these cations and water molecules projected onto the (001) plane agrees with the metrics determined in the microdiffraction study.

An inconsistency of the reflections with odd and even k can be attributed to the fact that the interlayer space includes a fragment of the structure possessing its own unit-cell parameters that difffer from those of the framework. This fragment is epitaxially related to this framework.

The presence of satellite reflections in Al-containing specimens indicates that the most mobile portions of their structures are determined by a high degree of condensation of the (Si,Al)-tetrahedra.

Another example of the behavior of a microcrystal containing condensed silicon–oxygen radicals is shown in Fig. 4. This microcrystal was also examined with the use of the diffraction contrast method. Unlike the crystal considered above, the photograph shown in Fig. 4 revealed that a crystal characterized by a high degree of condensation of tetrahedra is, on the one hand, more perfect and, on the other hand, provides the formation of additional reflections on the diffraction patterns along the A^* axis, incommensurate with the main unit cell. Most likely, these reflections are associated with the presence of a large potassium cation. One of these reflections was used along with the (600) reflection in the electron microscopy study with the use of diffraction contrast.

Dark regions are arranged strictly parallel to the Y axis and regularly alternate along the X axis. These regions form two groups in different regions of the crystal with periods of 200 and 450 Å. This fact indicates regular changes in the conditions of crystal growth. Heating the crystal results in the destruction of dark regions but without noticeable changes in the cor-

responding diffraction patterns. Hence, it can be concluded that the presence of potassium stabilizes the structure.

CONCLUSIONS

We proposed a model of the hypothetical structure of Al,K-containing tobermorite characterized by a high degree of condensation. The structural formula of this mineral variety is changed, because the silicon–oxygen tetrahedra share their free vertices. As a result, the structure has broad channels along the *Y* axis. These channels can be occupied by large cations. Apparently, the matrix of usual tobermorite also has inclusions of this variety.

The structures of tobermorites are complex formations. They show the following features: displacement of the silicon–oxygen radical with respect to the Ca-core by *b*/2, widespread microtwinning along the (100) plane, parallel displacements of the core, and the probable ordering of the vacancies in the core.

The examination of the structural changes in microcrystals upon heating at 300–400°C demonstrated that the initial stage of the structural changes is associated with the most mobile structure portion, namely, with the interlayer cations and water molecules. Amorphization of Al,K-containing tobermorite occurs at 300–400°C.

The next stage is, apparently, associated with changes in the silicon–oxygen radical. This characteristic feature was indicated by Taylor [15, 16]. The fact that "hoppings" of silicon atoms in silicate structures frequently occur was repeatedly indicated by N.V. Belov [17]. Recently, Bailay observed this phenomenon [18] in layered silicates. The latter minerals undergo the serpentine–chlorite transformation accompanied by the rotation of the silicate layer. Like the specimen from the Khibiny massif, the specimen from Mokraya Synya showed an increase in the degree of condensation of the silicon–aluminum–oxygen radical during subsequent heating.

Apparently, the fact that sharp satellites of reflections with $k = 2n$ are preserved upon heating indicates the retention of the framework structure, the most stable portion of the structure of the tobermorite minerals.

ACKNOWLEDGMENTS

This study was supported by the Russian Foundation for Basic Research, project no. 00-05-64588.

REFERENCES

1. S. Merlino, E. Bonnacorsi, and T. Amrbruster, in *Modular Aspects of Minerals* (1997), Vol. 1, p. 29.
2. S. Merlino, E. Bonnacorsi, and T. Amrbruster, Am. Mineral. **84**, 1613 (1999).
3. S. Merlino, E. Bonnacorsi, and T. Amrbruster, Eur. J. Mineral. **12**, 411 (2000).
4. S. Merlino, E. Bonnacorsi, and T. Amrbruster, Eur. J. Mineral. **13**, 577 (2001).
5. H. D. Megow and C. H. Kesley, Nature **177**, 390 (1956).
6. A. E. Zadov, N. V. Chukanov, N. I. Organova, *et al.*, Zap. Vses. Mineral. O–va **124**, 36 (1995).
7. O. A. Gard and H. F. W. Taylor, Miner. Mag. **31** (236), 361 (1957).
8. A. Guinier, *Théorie et technique de la radiocristallographie* (Dunod, Paris, 1956; Fizmatgiz, Moscow, 1961).
9. S. A. Hamid, Z. Kristallogr. **154**, 189 (1981).
10. S. Komarneni and D. M. Entory, Nature **221** (4611), 647 (1983).
11. *Minerals* (Nauka, Moscow, 1981), Vol. 3, iss. 3, p. 322.
12. A. E. Zadov, N. V. Chukanov, N. I. Organova, *et al.*, Zap. Vses. Mineral. O–va **130** (2), 26 (2001).
13. N. I. Organova, N. V. Trubkin, and A. P. Khomyakov, in *Proceedings of the International Conference on Genesis and Crystal Growth* (Sankt-Peterb. Gos. Univ., St. Petersburg, 2001), p. 269.
14. O. Van der Biest and G. Thomas, in *Electron Microscopy in Mineralogy*, Ed. by H. R. Wenk (Springer-Verlag, Berlin, 1976; Mir, Moscow, 1979).
15. *The Chemistry of Cements*, Ed. by H. F. W. Taylor (Academic, London, 1964; Stroĭizdat, Moscow, 1969).
16. H. F. W. Taylor, *Cement Chemistry* (T. Telford, London, 1997, 2nd ed.; Mir, Moscow, 1996).
17. N. V. Belov, *Essays on Structural Mineralogy* (Nedra, Moscow, 1976).
18. J. Banfield and S. W. Bailay, Am. Mineral. **81**, 79 (1996).

Translated by T. Safonova

Crystallography Reports, Vol. 47, No. 6, 2002, pp. 957–960. Translated from Kristallografiya, Vol. 47, No. 6, 2002, pp. 1027–1030.

STRUCTURE OF INORGANIC COMPOUNDS

Modulation in the Murataite Structure[1]

O. V. Karimova*, N. I. Organova*, and V. G. Balakirev**

** Institute of Geology of Ore Deposits, Petrography, Mineralogy, and Geochemistry (IGEM), Russian Academy of Sciences, Staromonetnyĭ per. 35, Moscow, 109017 Russia*

*** All-Russia Research Institute of Synthesis of Mineral Raw Materials, Institutskaya ul. 1, Aleksandrov, Moscow oblast, 601600 Russia*

Received January 16, 2002

Abstract—Synthetic varieties of murataites (*M*5 and *M*8) were studied by transmission electron microscopy. One of the varieties was additionally investigated by high-resolution electron microscopy. It was demonstrated that the atoms possessing the strongest scattering properties are nonuniformly distributed over the unit cells of both varieties, and the distribution follows the laws of replacement and displacement modulations of cations in the ideal fluorite structure. © *2002 MAIK "Nauka/Interperiodica".*

Murataite is a very rare mineral belonging to a group of complex oxides of titanium, niobium, rare-earth elements, calcium, and zinc. Chemical analysis of this mineral and its structure solution [1] gave the formula $(Y, Na)_6(Zn, Fe)_5Ti_{12}O_{29}(O, F)_{10}F_4$.

The structure of the mineral belongs to the cubic system (space group $F4–3m$) with the unit-cell parameter $a = 14.86 \pm 0.01$ Å.

Synthetic murataite was first found in ceramics developed for the conservation of highly active arms waste [2–4]. Later on, synthetic murataite was also discovered in molten ceramic destined for the immobilization of highly active waste [5].

The compositions of synthetic murataites are transformed into the formula $A_4B_2C_7O_{22}$, where A = Ca, Mn, *TR*, or U; B = Mn, Ti, or Zr; and C = Ti, Al, or Fe. This formula differs from that of natural murataite.

The structure of natural murataite [1] is composed of 12-membered clusters formed from the $M1O_6$ octahedra, where *M*1 = Ti, Nb, or Na. Previously, this fundamental structural unit was known as the Keggin unit present in synthetic molybdates and tungstates [6]. The tetrahedral cavities present in the centers of the clusters (*T* positions) are occupied by Zn and Si atoms [4]. The 12-membered clusters are linked to form a zeolite-like framework. The octahedral cavities in the framework (*X* positions) each contain six Y atoms occupying the vertices of the octahedra.

It is evident, that the structure of natural murataite belongs to the fluorite type with a sublattice $a/3$ possessing oxygen and metal vacancies, which are accompanied by atomic displacements. Hence, we proposed that the varieties of murataite (three varieties are presently known, namely, one natural murataite and two synthetic phases) be denoted with respect to the size of the fluorite unit cell. Thus, natural murataite was denoted as *M*3. This characteristic feature is well manifested in the X-ray diffraction patterns, which show all X-ray lines from the sublattice and only some weak lines from the superlattice. Strong reflections observed in the X-ray patterns determine the cubic sublattice, whose parameters are close to those of fluorite. Weaker reflections define the true unit-cell parameters [7].

Microdiffraction patterns of a synthetic specimen obtained on a JEM100C + KEVEX5100 transmission electron microscope [5, 8] demonstrated that this specimen contained new varieties of murataite as major phases (Figs. 1–3).

Some ceramics contain not only the major varieties of fluorite-type murataites with fivefold and eightfold unit cells (5*a* and 8*a*, respectively), but also single microcrystals characterized by a different arrangement of superstructure reflections. Both quantitatively predominant phases can be considered as superstructures of the face-centered unit cell of fluorite, as a result of which the most intense reflections observed in the

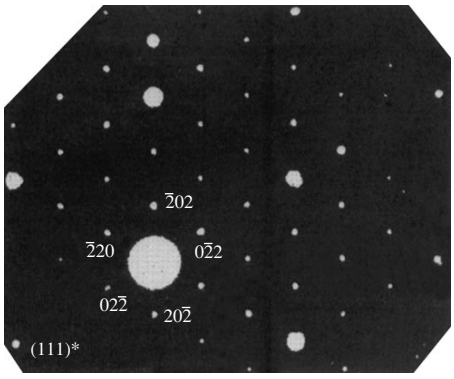

Fig. 1. Microdiffraction pattern from murataite *M*3 along the [111] axis.

[1] This study was presented at the Symposium "Order, Disorder, and Properties of Oxides" (ODPO), Sochi, Russia, 2001.

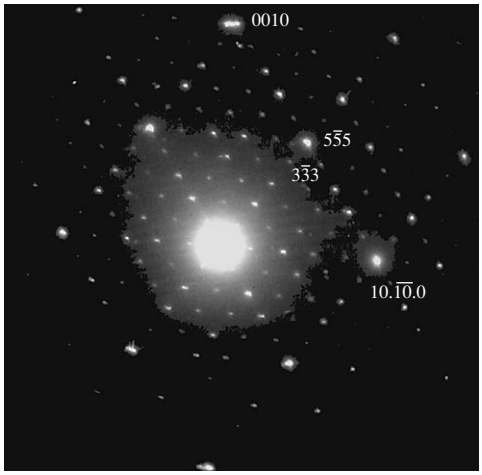

Fig. 2. Microdiffraction pattern from muratite *M*5 along the [110] axis.

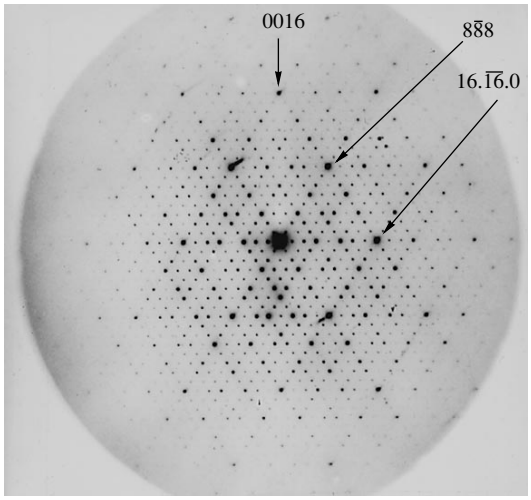

Fig. 3. Microdiffraction pattern from muratite *M*8 along the [110] axis.

X-ray and microdiffraction patterns belong to the sublattices (due to differences in the chemical composition, the sublattices have different dimensions resulting in the splitting of sublattice reflections). The splitting of reflections in the small-angle region is insignificant because of a small difference in the sublattice dimensions.

Along with the above-mentioned evident difference in intensities of the reflections of different types, yet another characteristic feature of each sample was observed in the microdiffraction patterns of the phases measured along the [110] direction (Figs. 2 and 3). Thus, among weak superstructure reflections, the reflections with $hkl = 5n \pm 2$ and $hkl = 5n \pm 3$ appeared to be systematically strong in the X-ray patterns of muratite 5*a* (*M*5). In the X-ray patterns of muratite 8*a* (*M*8), the reflections with $hkl = 8n \pm 3$ and $hkl = 8n \pm 5$ were systematically strong.

The analysis showed that the reflections with the above-mentioned indices can be considered as satellite reflections, whereas even weaker reflections, which do not follow these rules, can be either interpreted as higher-order satellite reflections or attributed to secondary diffraction. The positions of the latter reflections in reciprocal space indicate that the atoms possessing the strongest scattering properties are nonuniformly distributed over the unit cells (in direct space) of both varieties, and the distribution follows the laws of replacement and displacement modulations of cations in the ideal fluorite structure. Thus, the 222 and 333 reflections are strong in the X-ray pattern from the phase with the 5*a* unit cell. In direct space, these reflections correspond to the planes intercepting 5/2 and 5/3 portions on the diagonal of the large *M*5 unit cell perpendicular to the [111] direction, i.e., the former plane intersects 2.5 small unit cells, and the latter plane intersects 1.66 unit cells, which corresponds to 1/3 of the diagonal. At the same time, the fact that the *M*5 unit cell is face-centered must lead to the appearance of planes dividing the spatial diagonal of the cube into three parts. If the first-order satellite is assigned to the 333 reflection in the coordinates of the large reciprocal unit cell, than the 222 reflection is a satellite of the 555 reflection with the opposite sign with respect to that of the first reflection (for the large unit cell, this is the 555 reflection). In this case, the (*nnn*) planes are separated by 1/3 of the spatial diagonal. The cations possessing strong scattering properties, among other atoms, are located on these planes. Since various cations of the synthetic muratite under consideration differ substantially in scattering ability, this arrangement must be manifested in high-resolution electron-microscope images. In the structures of all the varieties, the atoms possessing strong scattering properties must be located between the planes of the close packing of the oxygen atoms at distances of 1/3 of the spatial diagonal from each other. Actually, the six-membered clusters of the Y-polyhedra are located on these planes (more precisely, nearby these planes) in the crystal structure of natural muratite *M*3 (Fig. 4a).

For the satellite reflection with the indices 333 observed in the microdiffraction pattern from muratite *M*8, the respective distance from the origin of the coordinates in direct space is equal to 8/3 (the first-order satellite). The 555 reflection is a satellite of the 888 reflection. The corresponding planes are shown in the schematic representation of the idealized *M*8 structure projected along the $[\bar{1}10]$ axis (Fig. 4b), where the cations of the fluorite subcells are indicated by solid circles, and the projections of the planes containing the cations are shown by dashed lines.

Two possible alternatives for the projections of *M*5 along the $[\bar{1}10]$ axis with the origin of the coordinates

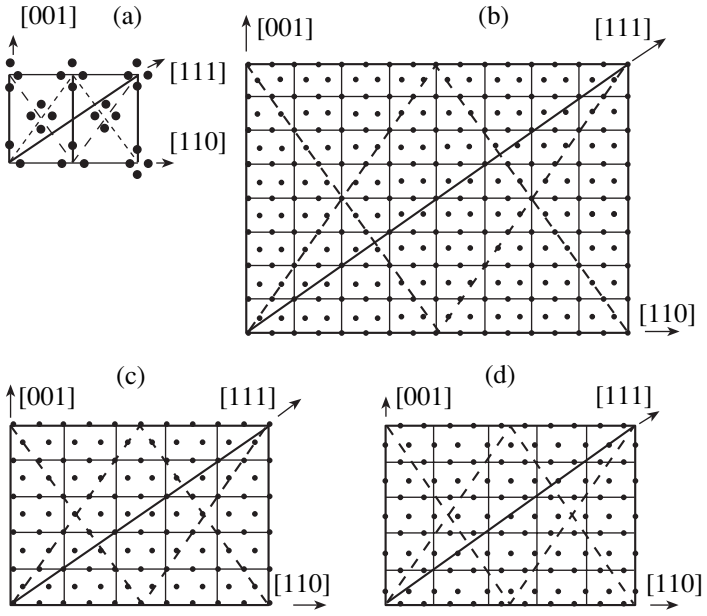

Fig. 4. Structures of murataites projected along the [$\bar{1}$10] axis: (a) *M*3, only yttrium atoms are shown; (b) schematic representation of the projections of *M*8 (the cations of the fluorite sublattice are indicated by solid circles, the projections of the planes containing the electron-rich atoms are shown by dashed lines); (c) and (d) schematic representations of the projections of *M*5 (two alternative origins of coordinates).

at the position occupied by the cation and at the position without the cation (the latter alternative is observed in the structure of *M*3, see Fig. 4a) are shown in Figs. 4c and 4d, respectively.

The high-resolution electron-microscope image of a microcrystal of murataite *M*8 is shown in Fig. 5. The image has pronounced lines, which form rhombi analogous to those shown by dashed lines in Fig. 4. This corresponds to the predominant arrangement of the heavy atoms on the (111) planes.

Other characteristic features of the distribution of superstructure reflections for other microcrystals are also of interest. Analysis of the geometric arrangement of these reflections led us to a conclusion about the incommensurate modulation in the corresponding crystals.

The results of our study provide evidence that all murataites, including synthetic specimens, can be considered as modulated structures with commensurate or incommensurate modulations. However, the proportion of microcrystals with incommensurate modulation in the material under study is at least an order of magnitude smaller than the proportion of microcrystals with commensurate modulation. The replacement and displacement modulation with a period of one-third of the spatial diagonal was revealed. This conclusion was reached taking into account the presence of satellites of the primary beam and the ratio of the intensities of the satellite reflections located on both sides of strong reflections at different distances relative to the primary electron beam. The reflections located closer to the primary beam appeared to be stronger, which indicates that the larger atom replaces the smaller atom, the scattering ability of the latter being smaller [9].

In the studies of the Bi_5O_3–Nb_2O_5 and Bi_5O_3–Ta_2O_5 double oxides [3, 10, 11], the authors described commensurate or incommensurate structures characterized by microdiffraction patterns analogous to those of murataites. The projection along the [110] direction showed periodic planar components, which are bounded by the (111) planes and inserted into a matrix.

The study [11] deserves special consideration. In the cited study, the one-dimensional modulation wave was revealed for oxide $(Bi_2O_3)_{0.8}(Nb_2O_5)_{0.2}$ in the projection

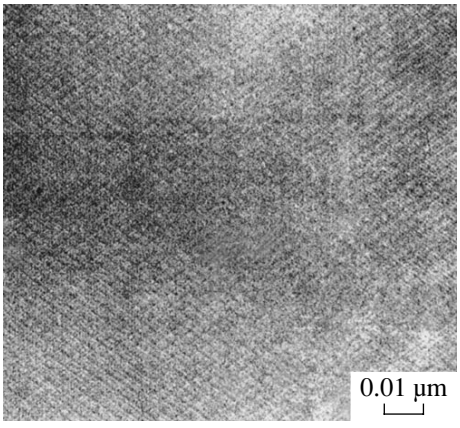

Fig. 5. Fragment of the high-resolution electron-microscope image of murataite *M*8 along the [$\bar{1}$10] direction; the magnifying power is 1.08×10^6.

along the [111] direction. The modulation wave was calculated taking into account the intensities of the (*nnn*)-type reflections, which were distributed analogously to those in *M*8. If it is assumed that the Nb atom ($Z = 41$, the atomic radius is 0.69 Å) replaces the Bi atom ($Z = 83$, the atomic radius is 0.74 Å), then the above-mentioned rule consistent with the experimental data is obeyed. Four modulation waves (replacement and displacement waves), including two waves for cations and two waves for anions, were constructed [11]. These waves differ in phases and amplitudes.

A similar one-dimensional representation of modulations (apparently, in a complicated form) would be expected for *M*8, because the number of components in the specimen is no less than that in *M*3.

The results of investigation of the phase diagram of two-component oxide Bi_2O_3–Nb_2O_5 were described in detail [12]. Niobium atoms were introduced into a bismuth matrix. The microdiffraction patterns, which were obtained for samples containing different amounts of niobium, evidenced commensurate fluorite-like 5*a* and 8*a* microcrystals along with incommensurate varieties. The niobium content was demonstrated to be linearly dependent on the modulation vector in the composition range from $x = 0.1$ to $x = 0.3$ (x is the fraction of niobium atoms), which corresponds to a change in the modulation vector q from 0.36 to 0.38. Hence, it follows that the changes in the modulation vector observed in the above-described murataites are, apparently, associated primarily with the changes in the composition of these specimens.

ACKNOWLEDGMENTS

We are grateful to N.R. Khisina and A.A. Katsnel'son for helpful discussions.

This study was supported by the Russian Foundation for Basic Research, project no. 00-05-64588.

REFERENCES

1. T. S. Ecrit and F. C. Hawthorn, Can. Mineral. **33**, 1223 (1995).
2. P. E. D. Morgan and F. J. Ryerson, J. Mater. Sci. Lett. **1**, 351 (1982).
3. P. E. D. Morgan, A. B. Harker, and J. F. Flintoff, Adv. Ceram. **8**, 234 (1984).
4. F. J. Ryerson, J. Am. Ceram. Soc. **66**, 629 (1983).
5. N. P. Laverov, B. I. Omel'yanenko, S. V. Yudintsev, and B. S. Nikonov, Geol. Rudn. Mestorozhd. **39**, 211 (1997).
6. H. T. Evans, Perspect. Struct. Chem. **4**, 1 (1971).
7. A. E. Portnov, L. S. Dubakina, and G. K. Krivokoneva, Dokl. Akad. Nauk SSSR **261**, 741 (1981).
8. N. P. Laverov, A. N. Gorshkov, S. V. Yudintsev, *et al.*, Dokl. Akad. Nauk **363**, 540 (1998).
9. V. I. Iveronova and G. P. Revkevich, *Theory of X-ray Scattering* (Mosk. Gos. Univ., Moscow, 1978).
10. Sh. D. Ling, R. L. Wither, S. Schmid, and J. G. Thompson, J. Solid State Chem. **137**, 46 (1998).
11. R. Miida and M. Tanaka, Jpn. J. Appl. Phys. **29**, 1132 (1990).
12. F. J. Ryerson, J. Am. Ceram. Soc. **66** (9), 629 (1983).

Translated by T. Safonova

Crystallography Reports, Vol. 47, No. 6, 2002, pp. 961–965. Translated from Kristallografiya, Vol. 47, No. 6, 2002, pp. 1031–1034.

STRUCTURE OF INORGANIC COMPOUNDS

Bimetallic Hydrogen Sulfates $K_4M^{II}[H(SO_4)_2]_2(H_2O)_2$ (M^{II} = Mn or Zn)

S. I. Troyanov*, I. V. Morozov*, and E. Kemnitz**

** Faculty of Chemistry, Moscow State University, Vorob'evy gory, Moscow, 119899 Russia*
e-mail: troyanov@thermo.chem.msu.ru
*** Institute für Chemie, Humboldt Universität, Berlin, Germany*

Received February 21, 2002

Abstract—Hydrogen sulfate hydrates $K_4\{M^{II}[H(SO_4)_2]_2(H_2O)_2\}$, where M^{II} = Mn or Zn, are synthesized, and their single-crystal structures are determined by X-ray diffraction. The structural units of the orthorhombic crystals (space group *Pccn*) are potassium and M^{II} cations, SO_4^{2-} and HSO_4^- anions, and water molecules. Strong (2.52 Å) and moderate-in-strength (2.71–2.75 Å) hydrogen bonds link the anions and water molecules into hexamers. The M^{II} cations, which have the octahedral environment (Mn–O, 2.14–2.19 Å and Zn–O, 2.07–2.11 Å), link the hexamers into flat layers. The structures of bimetallic hydrogen chalcogenate hydrates with different compositions are compared. © *2002 MAIK "Nauka/Interperiodica"*.

INTRODUCTION

The crystal structures of alkali metal hydrogen sulfates and selenates M^IHXO_4 and $M^I_3H(XO_4)_2$ (M^I = Rb or Cs and X = S or Se) have been studied in detail, because some of them exhibit high protonic conductivity at elevated temperatures [1–4]. Acid and superacid sulfates and selenates of bivalent metals $M^{II}(HXO_4)_2$ and $M^{II}(HXO_4)_2(H_2XO_4)_2$ [5, 6], as well as $M^{II}(HXO_4)_2 \cdot H_2O$ hydrates [6, 7], have been studied systematically. Acid salts that contain metal cations in different valence states have been studied to a significantly lesser degree. Only one structural type, $M^IM^{II}[H(XO_4)_2](H_2O)_2$ (M^I = K or Cs, M^{II} = Mg, Mn, Zn, or Fe and X = S or Se) [8–10], is known for the combination of monovalent and bivalent metals. In the literature, there are data on the preparation, spectral characteristics, and magnetic properties of a compound with a different ratio $M^I : M^{II}$, namely, $K_4MnH_2(SO_4)_4 \cdot 2H_2O$ [11, 12]. We managed to obtain this heterobimetallic hydrogen sulfate and an analogous compound of potassium and zinc. In this paper, the crystal structures of both compounds are reported.

EXPERIMENTAL

Synthesis. Compounds of the composition $K_4M^{II}[H(SO_4)_2]_2(H_2O)_2$ (M^{II} = Mn or Zn) were prepared by crystallization from aqueous solutions of K_2SO_4 and $M^{II}SO_4$ sulfates that were acidified with sulfuric acid. The molar ratio of the reactants was varied in order to optimize the synthesis conditions. It was found that the $K_4M^{II}[H(SO_4)_2]_2(H_2O)_2$ phases with M^{II} = Mn (**I**) and Zn (**II**) crystallize at the molar ratio 4 : 1 and a slight excess of acid. In some syntheses, $KHSO_4$ was used instead of potassium sulfate and the amount of sulfuric acid was correspondingly reduced. Less acid solutions afforded crystals of the $M^{II}SO_4$ sulfates, and at lesser ratios between K_2SO_4 and $M^{II}SO_4$, other heterobimetallic hydrogen sulfates, $KM^{II}[H(SO_4)_2](H_2O)_2$ [9], precipitated. The phase purity of the samples prepared was checked using X-ray powder diffraction. In order to grow large (up to 5 mm) single crystals, the solutions were concentrated and crystallization was performed at 50–60°C. The crystals obtained are not hygroscopic, but in air, they lose water over several months.

In the systems with magnesium or cadmium sulfates, similar crystallization experiments did not result in the formation of bimetallic hydrogen sulfates. The X-ray powder diffraction analysis of the crystallization products revealed the initial sulfates $M^{II}SO_4$ or their mixtures with $KHSO_4$.

X-ray diffraction study. The X-ray diffraction study of single crystals of **I** and **II** was performed at 180 K on a STADI-4 (Stoe) four-circle automated diffractometer (MoK_α radiation, graphite monochromator, λ = 0.71073 Å, ω-2θ scan mode). The crystallographic parameters and details of structure refinement are summarized in Table 1. The correction for absorption was performed by the empirical method on the basis of ψ scans of four reflections (**I**) or by the numerical method with allowance made for the real crystal shape (**II**).

The structures were solved by the direct method [13]. The non-hydrogen atoms were refined by the full-matrix least-squares procedure in the anisotropic

1063-7745/02/4706-0961$22.00 © 2002 MAIK "Nauka/Interperiodica"

Table 1. Crystal data and details of data collection and structure refinement for $K_4M^{II}[H(SO_4)_2]_2(H_2O)_2$

Compound	$K_4Mn[H(SO_4)_2]_2(H_2O)_2$	$K_4Zn[H(SO_4)_2]_2(H_2O)_2$
Molecular weight	633.63	644.06
Crystal system	Orthorhombic	Orthorhombic
Space group	*Pccn*	*Pccn*
a, Å	7.482(2)	7.442(3)
b, Å	20.908(5)	20.981(7)
c, Å	10.755(3)	10.585(4)
V, Å^3	1682.4(8)	1653(1)
Z	4	4
ρ_{calcd}, g/cm^3	2.502	2.588
$\mu(MoK_\alpha)$, mm^{-1}	2.362	3.092
Crystal size, mm	$0.50 \times 0.30 \times 0.20$	$0.68 \times 0.40 \times 0.36$
T, K	180(2)	180(2)
θ_{max}, deg	29.0	29.0
No. of reflections measured/unique	2849/2237	2125/2125
No. of reflections with $[I > 2\sigma(I)]$	1686	1692
No. of reflections/parameters in the least-squares refinement	1813/136	1784/136
R_1 $[I > 2\sigma(I)]/wR_2$ (all reflections)	0.0233/0.0668	0.0243/0.0861
$\Delta\rho_{max}/\Delta\rho_{min}$, *e*/Å^3	0.426/–0.418	0.441/–0.634

approximation [14]. The hydrogen atoms were located from difference electron-density syntheses and refined by the least-squares procedure in the isotropic approximation. The atomic coordinates and equivalent (isotropic for H atoms) thermal parameters for structures **I** and **II** are listed in Table 2. Since the two compounds are isostructural, the same system of atomic numbering is used for both structures. The interatomic distances in the coordination environment of the S, K, and M^{II} atoms and lengths of the hydrogen bonds are listed in Table 3.

RESULTS AND DISCUSSION

The crystal structure determination of the $K_4M^{II}[H(SO_4)_2]_2(H_2O)_2$ acid salts of manganese (**I**) and zinc (**II**) revealed that they are isostructural to each other and differ essentially from compounds of the structural type of bimetallic acid salts with a different composition that were studied earlier, $M^IM^{II}[H(XO_4)_2](H_2O)_2$ (M^I = K or Cs, M^{II} = Mg, Mn, or Zn, and *X* = S or Se) [8–10]. The asymmetric unit contains two K^+ cations, a medium-size M^{2+} cation (Mn or Zn), which occupies a special position on the twofold axis, two types of sulfate anions, and a water molecule (Fig. 1a). If the size of the coordination polyhedron of potassium is limited by the longest K–O distance of 3.30 Å, the coordination number of K(1) in structure **I** is equal to eight (the mean K–O distance is 2.875 Å), whereas in structure **II**, the coordination number is nine (2.910 Å) (Table 3). The coordination number of the K(2) atom in both structures is nine; the mean K–O distances (2.916 and 2.925 Å) correlate with the slightly increased radius upon changeover of the coordination number from eight to nine [15].

The almost regular octahedral coordination of the M^{II} cations includes four O atoms of the $S(2)O_4$ groups [O(5) and O(6)] and two O atoms of water molecules [$O(9)_w$] at close M^{II}–O distances. The mean Mn–O distance is 0.08 Å longer than the mean Zn–O distance, which agrees with the ionic radii of the metals [15].

In the SO_4 tetrahedra, the S–O bond lengths depend on the additional structural functions of the oxygen atoms (Table 3). In the $S(1)O_4$ tetrahedra, the distances to the O(1) and O(2) atoms, which contact only with K atoms, are the shortest (1.43–1.44 Å). The distances to the O(3) atom, which acts as a hydrogen acceptor in the O(9)–H(2)···O(3') bond, are slightly longer (1.45–1.46 Å). The S–O(4) bond is significantly longer (1.57 Å), because the O(4) atom acts as a donor in the O(4)–H(1)···O(7) hydrogen bond. In the $S(2)O_4$ tetrahedra, the S(2)–O(7) and S(2)–O(8) bond lengths (1.47 Å) are

Table 2. Atomic coordinates and equivalent (isotropic for H atoms) thermal parameters in the crystal structures of $K_4M^{II}[H(SO_4)_2]_2(H_2O)_2$

Atom	*x*	*y*	*z*	U_{eq}, Å^2
I, M^{II} = Mn				
Mn	0.25	0.25	0.15500(3)	0.0090(1)
K(1)	0.59815(6)	0.33368(2)	0.86031(4)	0.0172(1)
K(2)	0.22442(6)	0.05519(2)	0.16098(4)	0.0158(1)
S(1)	0.75882(6)	0.42815(2)	0.61155(4)	0.0122(1)
S(2)	0.36781(6)	0.33828(2)	0.40644(4)	0.0084(1)
O(1)	0.5922(2)	0.42381(8)	0.6781(1)	0.0250(3)
O(2)	0.8722(2)	0.47946(8)	0.6514(1)	0.0242(3)
O(3)	0.8535(2)	0.36741(7)	0.6082(1)	0.0262(3)
O(4)	0.7134(2)	0.44365(7)	0.4726(1)	0.0159(3)
O(5)	0.2663(2)	0.32411(6)	0.2917(1)	0.0129(3)
O(6)	0.2517(2)	0.32394(6)	0.5139(1)	0.0147(3)
O(7)	0.4075(2)	0.40702(6)	0.4063(1)	0.0158(3)
O(8)	0.5328(2)	0.30048(6)	0.4126(1)	0.0131(3)
O(9)	0.5420(2)	0.25517(7)	0.6523(1)	0.0130(3)
H(1)	0.623(4)	0.430(2)	0.453(3)	0.039(9)
H(2)	0.587(4)	0.220(2)	0.645(2)	0.027(7)
H(3)	0.560(5)	0.272(2)	0.591(3)	0.049(10)
II, M^{II} = Zn				
Zn	0.25	0.25	0.15525(3)	0.0114(1)
K(1)	0.60163(7)	0.33289(3)	0.85751(5)	0.0188(1)
K(2)	0.22348(7)	0.05561(2)	0.15920(5)	0.0179(1)
S(1)	0.75645(8)	0.42833(3)	0.61062(5)	0.0144(1)
S(2)	0.36269(7)	0.33619(3)	0.40569(5)	0.0105(1)
O(1)	0.5892(2)	0.4252(1)	0.6784(2)	0.0266(4)
O(2)	0.8719(2)	0.47987(9)	0.6483(2)	0.0258(4)
O(3)	0.8502(3)	0.36730(9)	0.6104(2)	0.0279(4)
O(4)	0.7103(3)	0.44219(9)	0.4690(2)	0.0186(4)
O(5)	0.2616(2)	0.32220(8)	0.2884(2)	0.0151(3)
O(6)	0.2461(2)	0.32142(8)	0.5150(2)	0.0164(3)
O(7)	0.4003(2)	0.40504(8)	0.4059(2)	0.0167(4)
O(8)	0.5303(2)	0.29931(8)	0.4117(1)	0.0148(3)
O(9)	0.5295(2)	0.25370(8)	0.6516(2)	0.0144(3)
H(1)	0.627(6)	0.430(2)	0.456(5)	0.065(11)
H(2)	0.551(5)	0.272(2)	0.581(3)	0.035(9)
H(3)	0.569(5)	0.217(2)	0.644(3)	0.034(9)

determined by the function of the O(7) and O(8) atoms as acceptors in hydrogen bonds. The S(2)–O(5) and S(2)–O(6) bonds involving the O atoms that coordinate the M^{II} atom are slightly longer (1.48 Å). The metal coordination produces a more pronounced effect on the S–O bond lengths as compared to the acceptor function of the oxygen atoms, because the radii of the Mn^{2+} and Zn^{2+} dications are relatively small. In the structures of

Table 3. Interatomic distances (Å) in the crystal structures of $K_4M^{II}[H(SO_4)_2]_2(H_2O)_2$

$M^{II}(r$, Å)*, distance	I, Mn(0.820)	II, Zn(0.745)
S(1)–O(1)	1.440(2)	1.438(2)
S(1)–O(2)	1.433(2)	1.438(2)
S(1)–O(3)	1.455(2)	1.458(2)
S(1)–O(4)	1.566(1)	1.565(2)
S(2)–O(5)	1.479(2)	1.481(2)
S(2)–O(6)	1.477(2)	1.479(2)
S(2)–O(7)	1.467(2)	1.472(2)
S(2)–O(8)	1.467(2)	1.469(2)
M^{II}–O(5)	2.140(1)	2.071(2)
M^{II}–O(6)	2.166(1)	2.110(2)
M^{II}–$O(9)_w$	2.188(1)	2.082(2)
M^{II}–O (mean)	2.165	2.088
K(1)–O (range)	2.72-3.10	2.71-3.28
K(1)–O (mean); c.n.	2.875; 8	2.910; 9
K(2)–O (range)	2.74-3.26	2.72-3.26
K(2)–O (mean); c.n.	2.925; 9	2.916; 9
O(4)–H(1)···O(7)**	2.517(2)	2.525(3)
$O(9)_w$–H(2)···O(3')**	2.721(2)	2.727(2)
$O(9)_w$–H(3)···O(8)**	2.747(2)	2.713(3)

* The cationic radii for M_{II} with C.N. = 6 and K^+ with C.N. = 8 and 9 are taken from [15].

** The O···O distances in the hydrogen bonds. The symmetry code for O(3') is 1.5 – *x*, 0.5 – *y*, *z*.

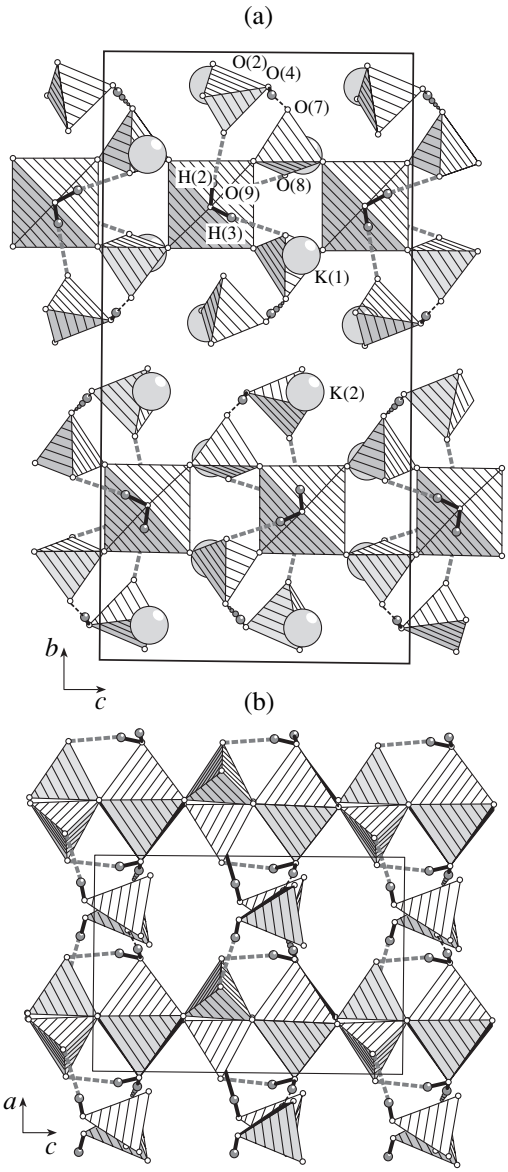

Fig. 1. Crystal structure of $K_4Mn[H(SO_4)_2]_2(H_2O)_2$ (**I**): (a) Projection along the *a* axis and (b) a layer of the structure in the projection along the *b* axis (K atoms are omitted). The coordination environments of the Mn and S atoms are shown as octahedra and tetrahedra, respectively.

hydrogen sulfates that contain only the singly charged cations (K, Rb, or Cs), the ratio of these effects is inverse [2–4].

One of the three independent hydrogen bonds, O(4)–H(1)···O(7), is strong (2.52–2.53 Å), whereas the bonds in which hydrogen donors are water molecules are weaker (2.71–2.75 Å). The hydrogen-bond system links the SO_4 anions and water molecules into hexameric units (Fig. 1b). Due to the coordination of the M^{II} atoms through the water molecules and the O(5) and O(6) atoms, the hexamers are linked into layers parallel to the *x*0*z* plane. In structures **I** and **II**, in distinction to those in the $M^IM^{II}[H(XO_4)_2](H_2O)_2$ structural type, all the H atoms are involved in hydrogen bonding. This is explained by the larger number of anions per M^{II} atom in the former structures as compared to the latter structures (four and two, respectively).

In the structural type of bivalent metal hydrogen chalcogenate monohydrates $M^{II}(HXO_4)_2 \cdot H_2O$ (M^{II} = Mg, Mn, or Cd [6, 7, 16]), hydrogen bonds between the anions are absent and water molecules act as both donors and acceptors of the H atoms in hydrogen bonds. In the absence of water molecules in structures $M^{II}(HXO_4)_2$, hydrogen bonds link the HXO_4^- anions to form infinite zigzag chains, which are connected by the $M^{II}O_6$ octahedra into a three-dimensional framework [6, 17].

Thus, two structural types are known for bimetallic acid chalcogenate hydrates, namely,

$M^{I}M^{II}[H(XO_4)_2](H_2O)_2$ and $K_4M^{II}[H(SO_4)_2]_2(H_2O)_2$. Compounds of these types have essentially different systems of hydrogen bonds and show different modes of connection of tetrahedra and octahedra into a two-dimensional or three-dimensional structure, respectively. We hope to obtain hydrogen selenates of the second type and heterobimetallic compounds with other metal combinations.

REFERENCES

1. A. I. Baranov, L. A. Shuvalov, and N. M. Shchagina, Pis'ma Zh. Éksp. Teor. Fiz. **36**, 381 (1982) [JETP Lett. **36**, 459 (1982)].
2. E. Kemnitz, C. Werner, and S. I. Troyanov, Eur. J. Solid State Inorg. Chem. **33**, 563 (1996).
3. E. Kemnitz, C. Werner, and S. I. Troyanov, Eur. J. Solid State Inorg. Chem. **33**, 581 (1996).
4. E. Kemnitz and S. I. Troyanov, Adv. Mol. Struct. Res. **4**, 79 (1998).
5. I. V. Morozov, S. I. Troyanov, A. Stiewe, and E. Kemnitz, Z. Anorg. Allg. Chem. **624**, 135 (1998).
6. E. Kemnitz, S. I. Troyanov, and H. Worzala, Eur. J. Solid State Inorg. Chem. **30**, 629 (1993).
7. H. Worzala, M. Schneider, E. Kemnitz, and S. I. Troyanov, Z. Anorg. Allg. Chem. **596**, 167 (1991).
8. J. Maciček, S. Gradinarov, R. Bonchev, and C. Balarew, Acta Crystallogr., Sect. C: Cryst. Struct. Commun. **50**, 1185 (1994).
9. S. I. Troyanov, I. V. Morozov, and E. Kemnitz, Kristallografiya **47** (5), 834 (2002) [Crystallogr. Rep. **47**, 768 (2002)].
10. M. Fleck, U. Kolitsch, B. Hertweck, *et al.*, Z. Kristallogr. **217**, 242 (2002).
11. A. Le Paullier-Malecot and L. Couture, J. Phys. Chem. **62**, 359 (1965).
12. A. Le Paullier-Malecot, J. Quant. Spectrosc. Radiat. Transf. **13**, 543 (1973).
13. G. M. Sheldrick, *SHELXS86: Program for the Solution of Crystal Structures* (University of Göttingen, Göttingen, 1990).
14. G. M. Sheldrick, *SHELXL93: Program for the Refinement of Crystal Structures* (University of Göttingen, Göttingen, 1993).
15. R. Shannon and C. T. Prewitt, Acta Crystallogr., Sect. B: Struct. Crystallogr. Cryst. Chem. **35**, 745 (1969).
16. A. Stiewe, E. Kemnitz, and S. Troyanov, Z. Kristallogr. **213**, 654 (1998).
17. M. A. Simonov, S. I. Troyanov, E. Kemnitz, *et al.*, Kristallografiya **31**, 1220 (1986) [Sov. Phys. Crystallogr. **31**, 721 (1986)].

Translated by I. Polyakova

Crystallography Reports, Vol. 47, No. 6, 2002, pp. 966–969. Translated from Kristallografiya, Vol. 47, No. 6, 2002, pp. 1035–1038.

STRUCTURE OF ORGANIC COMPOUNDS

In memory of V.L. Broude

Four Solid-Crystal Forms of Paraazoxyanisole and the Thermodynamic Relationships between Them

K. Z. Ogorodnik

Russian University of Peoples' Friendship, ul. Miklukho-Maklaya 6, Moscow, 117198 Russia
e-mail: ogorod@softel.ru

Received November 29, 2001

Abstract—It is shown that paraazoxyanisole has four solid-crystal forms. The heats and temperatures of melting and transition are related by the following five equations: Q_m(**IV**) = Q_m(**II**); Q_m(**IV**) = Q_m(**I**) + Q_m(**III**); T_m(**IV**) = T_m(**III**); T_{tr}(**II**–**III**) = T_m(**I**); and Q_{tr}(**II**–**III**) = Q_m(**I**), Q_m(SC**IV**) = 52.0 ± 0.3 kJ/mol. Earlier, similar relationships were established for the third homologue of paraazoxyanisole, Q_m[SC**IV**(C_3)] = 48.2 kJ/mol. It is found that for paraazoxyphenetole, Q_m[SC**IV**(C_2)] = 46.0 kJ/mol. © *2002 MAIK "Nauka/Interperiodica".*

INTRODUCTION

Investigations into the molecular structures and packings of solid-crystalline mesogenes furnish insights into the self-arrangement of molecules in the mesophase. Paraazoxyanisole (PAA, 4,4'-dimethoxyazoxybenzene; found in Chemical Abstracts as diazene or bis(4-methoxyphenyl)-1-oxide) was the first and most often used object of these studies. It is agreed that PAA is a model nematogene. The crystal structure of PAA was studied by X-ray [1–3] and neutron [4] diffraction techniques. A large number of studies have been concerned with the solid-crystal polymorphism of PAA [4–6]. Even the first comparison between the structures of the solid and liquid crystals required a decision to be made between two solid-crystal forms (forms that are stable and metastable at room temperature). Based on optical observations, the metastable form was preferred over the stable from [1]. Later, three solid-crystal forms of PAA were found in [4, 5] and the fourth form was found in [6]. What form should be used for comparison?

In many papers devoted to mesogenes that have three or four solid-crystal forms, some of which are characterized by X-ray diffraction, the question is posed as to whether the solid-crystal structure can serve as a prototype for the liquid-crystal structure [7]. We find a positive answer for the molecules that contain highly polar groups, for example, the CN group. On the other hand, we find the following opinion: "The solid-crystal state was obtained from the mesophase, but it is on no account its prototype" [8]. Later, a more logical conclusion was drawn, namely, "Characterization of different solid phases (including the homologues) can help us understand more precisely the short-range order in the liquid-crystal state" [9]. The evolution of the views on the comparison of the solid-crystal and liquid-crystal states to date led to the following statement: "Crystal polymorphism is the result of a very fine equilibrium between various intermolecular interactions" [10–12]. To date, information on the arrangement of molecules in the mesophase gained from a complete knowledge of the structure of three solid-crystal forms of the simplest molecule (belonging to the series of alkyl- or alkoxycyanobiphenyls) and a knowledge of the structure of one or two solid-crystal forms for all the homologues of the same and the related series is no larger than the information gained from a complete knowledge of the structure of a separate molecule and its conformers.

At present, we have the following data on the solid-crystal forms of PAA. The usual stable solid-crystal (SC) form SC**III**, which was prepared by crystallization from a solution or obtained upon long storage of a sample that solidified from a melt, melts at T_m(**III**) = 117–119°C [13] with the heat absorption ΔH_m(**III**) = 29.6–30.5 kJ/mol [13]. The metastable SC**I** form, which was obtained by rapid cooling of the nematic or isotropic phase, melts at 103–105°C [4, 5, 13]. Another metastable form, SC**II**, was found in a solidified melt against the melting temperature T_m(**II**) = 113°C [4, 6] with a thermal microscope [4, 5] and by the anomalous behavior of heat capacity just above 112.5°C [14]. The melting heat of SC**II** is unknown. The indications of one more PAA form are reported in [6]. Its melting heat is estimated as $\Delta H_m(\mathbf{IV}) \geq 1.4 \times \Delta H_m(\mathbf{III})$, and the melting point T_m(**IV**) lies near T_m(**III**). In this study, we obtained additional characteristics of solid-crystal forms of PAA based on the notion of binary mixtures of these molecules [15], which follows from the discrete-statistical model of the mesophase [16, 17], and using

1063-7745/02/4706-0966$22.00 © 2002 MAIK "Nauka/Interperiodica"

the thermomicroscopic observations of phase transformations in pure PAA and its binary mixtures with other compounds of the PAA homologous series.

EXPERIMENTAL

The studies were performed with commercial substances. If necessary, they were additionally purified by recrystallization from ethanol or hexane or by separation with a chromatographic column (silica gel as a filler and benzene as an eluent). Additional application of zone melting did not give noticeable results. The degree of purity was evaluated by comparison of the melting and clearing points with those reported in the literature with regard for the widths of these transitions. The phase state and the transitions were observed visually using a microscope equipped with a Mettler Toledo FP82 heating stage. The thermostatic control and the adjustment of a rate of heating (cooling) over a wide range (0.2–30 K/min) was performed with an FP90 processor of the same company. The accuracy and reproducibility of the temperature measurements using an instrument was ±0.1°C. The experimental error was determined by the reproducibility of the thermal past history of a sample. When specifying the temperature of an event, we should mention at what rate of temperature change it was observed; it was also desirable to mention the temperature at which this change began and the duration of staying at this temperature.

The observations of phase transformations in pure PAA revealed the following features. The substance was placed between the slide and the cover glass without any spacer. During the initial heatings at a rate of 5 K/min, noticeable melting began at 117.5–117.7°C and was completed at 118.3–118.4°C. Upon one more application to a column and threefold recrystallization from hexane (within three or four days), the PAA samples were first heated at a rate of 3 K/min, which resulted in a transformation into the nematic state at 117.5°C. Upon melting, small dark grains were observed (remained after the melting or appeared in the course of melting) against the light yellow background of the nematic. These grains were easily distinguished, since they moved in the liquid. On further heating, the grains melted (disappeared) at 118.3°C. If at this stage we reduced the heating rate to 1 K/min, the process repeated, but the melting of the crystals was completed somewhat earlier at 118.2°C. If the temperature of 117.5°C was maintained for 5–7 min, the new crystals did not disappear and melted as before at 118.2°C. These observations indicate that the melting of the stable SC**III** form of PAA is possibly a composite process that includes two events, namely, the melting of the crystals of one type and, simultaneously (or immediately after that), the formation and disappearance of the crystals of the other type. This fact agrees with the earlier measurements in [6]. The former melting point of PAA was reported by many authors [13], whereas the latter point was reported only in [18] as the melting point of the absolutely pure substance.

If we begin to cool the PAA sample at a rate of 9 K/min immediately after melting (for example, at 118.8°C), abrupt crystallization can occur near 80°C. On heating at a rate of 5–9 K/min, this polycrystalline mass melts at 104–106°C; at a rate of 3 K/min, the melting begins at 103.6°C and is completed at 104.5°C. On heating at a rate of 1.0–0.5 K/min, the melting begins at 103.3–103.1°C and is completed at 104.2–104.1°C. The clearing point T_{cl} of this sample can serve as a characteristic of its purity. On heating or cooling at a rate of 1.0–1.5 K/min, the points of the beginning of transitions coincide, $T_{cl}(\mathrm{N} \longrightarrow \mathbf{I}) = T_{cl}(\mathbf{I} \longrightarrow \mathrm{N}) =$ 133.5°C. The sample whose purity corresponds to $T_{cl}(\mathrm{N} \longrightarrow \mathbf{I}) = T_{cl}(\mathbf{I} \longrightarrow \mathrm{N}) = 134.5$°C behaves near 103–104°C at the same rates of heating and cooling in a different way. On heating at a rate of 3 K/min starting from 100°C (previously heated from 80° to 100°C at a rate of 9 K/min), it undergoes an abrupt (jumpwise) SC–SC transition at 102.9°C (on further heating, the sample melts at T_m(**III**) without noticeable beginning of melting). On heating from 101–102°C at a rate of 1 K/min, we observe melting at 103.9°C and abrupt crystallization at 104.3°C. At a rate of 0.5 K/min, we observe abrupt recrystallization at 103.9°C, which is preceded by the noticeable evolution of the solid-crystal texture and not visible melting.

Now, we pass on to the measurements of T_m(PAA) in the binary mixtures with the homologues and other related compounds. Under certain conditions for the components of the mixture, the dependence of T_m on the concentration of the substance in the mixture is described by the formula

$$T_m(X) = T_m(1)/(1 - 8.314(T_m(1)/Q_m^0)\ln X), \quad (1)$$

where X is the mole part of the excess component, and $T_m(1)$ and Q_m^0 are the absolute temperature and heat of melting (J/mol) of the pure substance [19]. It was shown that the mixtures of such molecules can exhibit a simple eutectic, whereas the relative stability of the solid-crystal forms of one or both components of the mixture can change noticeably [15]. Experimental evidence was obtained for the third and fifth homologues of PAA [15]. The measured T–X diagrams of the binary mixtures of PAA and its homologues, from the second to the seventh one, agree with those calculated according to formula (1) for Q_m^0 = 29.6–30.2 kJ/mol and $T_m(1)$ = 118.2–119.5°C [20, 21]; that is, in these mixtures, PAA exists as the stable SC**III** form. In [13], the eutectic line and the branch of the liquidus curve corresponding to the metastable SC**I** form of PAA were measured for a mixture of PAA with paraazoxyphenetole (PAPh). It follows from the aforesaid that, in order to reveal other solid-crystal forms of PAA, we should look

for similar molecules outside the homologous series and use other similarity criteria.

On heating at a rate of 5 K/min, a layer of the PAA + PAPh mixture with X(PAA) = 0.80 noticeably and abruptly clears up at 96.8°C, which corresponds to partial melting and wetting of the remaining polycrystalline mass. The temperature of the eutectic line for this mixture is 97.0°C (with the following values substituted in (1): for PAPh, $T_m(1)$ = 409.75 K and Q_m^0 = 28 890 J/mol [22]; and for PAA, $T_m(1)$ = 391.35 K and Q_m^0 = 29 570 J/mol [18]). Further heating (5 K/min) revives the melting at 109.3°C, and the last crystal disappears at 109.8°C. According to formula (1), T_m(PAA, SC**III**, X = 0.80) = 108.9°C. For the same concentration X(PAA) = 0.808 when paraazoanisole (PaA) is used as the admixture, the changes on passing the eutectic temperature T_{eu}(PAA, SC**III** + PaA) = 109.1°C are invisible to the human eye (the following parameters for PaA were borrowed from [22]: $T_m(1)$ = 437.15 K and Q_m^0 = 41 500 J/mol). The transition into the nematic state is completed at 113.0 ± 0.2°C for a heating rate of 1–2 K/min. This point in the T–X plane lies in curve (1) with $T_m(1)$ = 118.2°C and $Q_m^0 = Q_m^0$(SC**III**) + Q_m^0(SC**I**). Similar tests for the PAA + PaA mixture with X(PAA) = 0.820, 0.840, and 0.875 led to the same result. The values of T_m(PAA) in the PAA + PaA mixture that were reported in the well-known paper [22] also fall on the above curve. Thus, in the mixture with PaA, PAA behaves as a crystal form, and it is reasonable to identify it with SC**IV** and to characterize it with the specific value of melting heat, Q_m(PAA, SC**IV**) = 52.0 ± 0.3 kJ/mol.

RESULTS AND DISCUSSION

The existence of the PAA form under the conditions corresponding to a liquid solution suggests the virtual existence of the SC$\mathbf{IV}_{Vir}$ form of the pure substance. The elevated melting heat [6] at T_m(SC**III**) indicates that it is possible to obtain a stable enough solid polycrystalline SC$\mathbf{IV}_{Real}$ sample, if not a single crystal, of pure PAA corresponding to SC$\mathbf{IV}_{Vir}$. The formation energy of SC**IV** is equal to the sum of the two other heats of phase transitions, which suggests the existence of the SC(Z) form that undergoes the SC(Z) ⟶ SC(**III**) transition with the heat absorption $Q_{tr}(Z \longrightarrow \mathbf{III}) = Q_m(\mathbf{I})$ at $T_m(\mathbf{I})$. Hence, the formation heat of this SC(Z) form of PAA is the same as that of SC**IV**. Should we consider that these forms are identical with a solid-crystal form that can be rearranged and decompose at different temperatures, or are they different solid-crystal forms that have identical melting heats but different structures and, as a consequence, different stabilities and T_m values? We find the answer for PAA in additional experimental facts; a precedent is already known: the "stepping" isoenthalpic solid-crystal states were found for the third homologue of PAA (parapropoxyazoxybenzene).

Based on the above assumptions on SC(Z), we find from the relationships $Q_m(Z) = Q_{tr}(Z \longrightarrow \mathbf{III}) + Q_m(\mathbf{III})$ and $\Delta S_m(Z) = \Delta S_{tr}(Z \longrightarrow \mathbf{III}) + \Delta S_m(\mathbf{III})$ that

$$\begin{aligned} T_m(Z) &= Q_m(Z)/(Q_{tr}/T_{tr} + Q_m(\mathrm{III})/T_m(\mathrm{III})) \\ &= (Q_m(\mathrm{I}) + Q_m(\mathrm{III}))/(Q_m(\mathrm{I})/T_m(\mathrm{I}) \\ &\quad + Q_m(\mathrm{III})/T_m(\mathrm{III})). \end{aligned} \qquad (2)$$

Substituting the measured values of T_m(**III**) = 391.35 K and Q_m(**III**) = 29 570 J/mol from [20], T_m(**I**) = 377.25 K (own measurements), and Q_m(**I**) = 22 733 J/mol (the average of the values reported in [13, 23]) in (2), we obtain $T_m(Z)$ = 385.32 K (112.17°C). This value is close to 113°C reported in [5] and 112.5°C reported in [14], which refer to T_m(**II**). In addition to our arguments, the possibility of the SC**II** ⟶ SC**III** transition occurring near T_m(**I**) is supported by the observations in [4]: on slow heating, the metastable SC**I** form transforms near T_m(**I**) into another metastable form, which, in turn, under different conditions (rapid heating upon cooling) with equal probability either transforms into SC**III** or melts into the nematic. It is asserted in [4] that there is competition between these two processes of phase transformation. It is pertinent to note the observation that was not mentioned in the experimental section. On heating of the PAA + PAPh mixture with X(PAA) = 0.950 at a rate of 9 K/min, the excess PAA begins to melt at 111.9°C. The pronounced effect of minor admixtures (0.1–0.2%) on the relative stability of states and, hence, the probability of observing transformations between them is discussed in [13, 24]. The coincidence (within the accuracy and reproducibility of the measurements) of the $T_m(Z)$ value calculated with formula (2) and the observed T_m(**II**) value supports our suggestions embedded in formula (2). Thus, the data obtained are sufficient to assert that PAA exists in four solid-crystal forms, which are related thermodynamically as follows: Q_m(**IV**) = Q_m(**II**) = Q_m(**I**) + Q_m(**III**)—relationships (1) and (2); T_m(**IV**) = T_m(**III**)—relationship (3); and T_{tr}(**II**–**III**) = T_m(**I**), Q_{tr}(**II**–**III**) = Q_m(**I**)—relationships (4) and (5).

CONCLUSIONS

The relationships between the solid-crystal forms of PAA can be considered as general properties of mesogenes even for the reason that they were observed for different compounds. Relationship (3) is exhibited by many of the mesogenes belonging to the binary series of *p*-*n*-alkoxybenzylidene–*p*'-*n*-alkoxyaniline homologues [25–27], and relationships (1) and (2) are exhibited by alkyl- and alkoxycyanobiphenyls [28]. Three of the four solid-crystal forms of *trans*-4-*n*-heptyl-(4'-cyanophenyl)cyclohexane (PhCH-7) and two of the

three forms of PhCH-3 have identical melting heats (relationship 1) [29]. All five relationships are observed for the C(3) and C(5) homologues of PAA. The importance of the relationships that determine the mesogenic nature of the solid-crystalline forms lies in the fact that the studies of the molecular behavior in the mesophase are extended to the solid-crystal states. For example, relationship 3 requires that the lowest temperature solid-crystal forms should be used for comparison between the short-range orders in the solid and liquid crystals. The physical meaning of the relationships should be considered elsewhere. Some of them can appear to be equivalent, and relationship 5 looks the most "improbable."

Polymorphism is a necessary indication of the mesogenic behavior, despite the fact that many of the evident enantiotropic mesogenes, such as PAPh, do not exhibit solid-crystal polymorphism. The solid-crystal polymorphism can be hidden (virtual) under ambient conditions of observation and real in the melt, that is, according to the discrete-statistical model [16, 17], under the conditions of coexistence of crystal structures. Thus, the solid-crystal form of PAPh with Q_m(**IV**) = 46.0 kJ/mol, which is not known up to now, manifests itself under specific conditions, whereas for the known stable form, Q_m(**III**) = 26.87 kJ/mol [18]. The T_m values of both forms are the same, and therefore, they can exist in the melt with equal probability.

REFERENCES

1. J. P. Bernal and D. Crowfoot, Trans. Faraday Soc. **29**, 4760 (1933).
2. F. Wurstlin, Z. Kristallogr. **88**, 185 (1934).
3. W. R. Krigbaum, Y. Chatani, and P. G. Barber, Acta Crystallogr., Sect. B: Struct. Crystallogr. Cryst. Chem. **26**, 97 (1970).
4. L. Bata, V. L. Browde, *et al.*, Mol. Cryst. Liq. Cryst. **44**, 71 (1978).
5. R. C. Robinder and J. C. Poirier, J. Am. Chem. Soc. **90**, 4760 (1968).
6. K. Z. Ogorodnik and V. D. Karazhaev, Kristallografiya **26** (4), 859 (1981) [Sov. Phys. Crystallogr. **26**, 486 (1981)].
7. L. Walz and W. Haase, Mol. Cryst. Liq. Cryst. **4** (2), 53 (1968).
8. L. Walz, H. Paulus, and W. Haase, Z. Kristallogr. **180**, 97 (1987).
9. W. Haase, J. Loub, and H. Paulus, Z. Kristallogr. **202**, 7 (1992).
10. K. Hori, Y. Koma, *et al.*, Bull. Chem. Soc. Jpn. **69**, 891 (1996).
11. K. Hori and H. Wu, Liq. Cryst. **26**, 37 (1999).
12. A. Jákli, I. Jánossy, and A. Vajda, Liq. Cryst. **27**, 1035 (2000).
13. G. W. Smith, Mol. Cryst. Liq. Cryst. **30**, 101 (1975).
14. E. M. Barral, R. S. Porter, *et al.*, J. Phys. Chem. **71**, 895 (1967).
15. K. Z. Ogorodnik, Fiz. Mysl' Rossii, No. 3, 27 (2000).
16. K. Z. Ogorodnik, Fiz. Tverd. Tela (Leningrad) **17**, 2781 (1975) [Sov. Phys. Solid State **17**, 1851 (1975)].
17. K. Z. Ogorodnik, Kristallografiya **23** (5), 987 (1978) [Sov. Phys. Crystallogr. **23**, 557 (1978)].
18. H. Arnold, Z. Phys. Chem. **226**, 146 (1964).
19. I. Shreder, Gorn. Zh. **4**, 272 (1890).
20. D. Demus, Ch. Fietkau, *et al.*, Mol. Cryst. Liq. Cryst. **25**, 215 (1974).
21. E. C.-H. Hsu and J. F. Jonson, Mol. Cryst. Liq. Cryst. **20**, 177 (1973).
22. A. Bogojawlensky and N. Winogradov, Z. Phys. Chem. **4**, 433 (1907).
23. A. Gruger, F. Romain, *et al.*, Mol. Cryst. Liq. Cryst. **116**, 157 (1984).
24. A. K. Jaiswal, Natl. Acad. Sci. Lett. (India) **5**, 146 (1982).
25. D. Grasso, L. Abate, C. Gandolfo, and S. Fasone, Thermochim. Acta **61**, 227 (1983).
26. D. Grasso, C. Gandolfo, and S. Fasone, Thermochim. Acta **71**, 365 (1983).
27. D. Grasso, C. Gandolfo, and S. Fasone, Thermochim. Acta **77**, 413 (1984).
28. Yu. N. Morozov, Candidate's Dissertation in Chemistry (Moscow State Univ., Moscow, 1991).
29. W. Haase and R. Pendzialek, Mol. Cryst. Liq. Cryst. **97**, 209 (1983).

Translated by I. Polyakova

Crystallography Reports, Vol. 47, No. 6, 2002, pp. 970–972. Translated from Kristallografiya, Vol. 47, No. 6, 2002, pp. 1039–1041.

STRUCTURE OF ORGANIC COMPOUNDS

Crystal Structure of the Lanthanum(III) Complex $[La(DMSO)_6(H_2O)PW_{12}O_{40}] \cdot C_2H_5OH$ (*DMSO* is Dimethyl Sulfoxide)

M. S. Grigoriev*, I. B. Shirokova*, A. M. Fedoseev*, and C. Den Auwer**

** Institute of Physical Chemistry, Russian Academy of Sciences, Leninskiĭ pr. 31, Moscow, 119991 Russia*

*** Commissariat of Atomic Energy of France*

e-mail: grigoriev@ipc.rssi.ru

Received October 30, 2001

Abstract—The crystal structure of the $[La(DMSO)_6(H_2O)PW_{12}O_{40}] \cdot C_2H_5OH$ complex (**I**) (where *DMSO* is dimethyl sulfoxide) is determined by X-ray diffraction analysis. The coordination polyhedron of the La atom is a distorted tricapped trigonal prism in which two cap sites are occupied by oxygen atoms of the heteropolyanions. For these atoms, the La–O distances [2.760(9) and 2.801(9) Å] are considerably longer than the other distances [ranging from 2.441(10) to 2.569(10) Å] in the environment of the La atom. © *2002 MAIK "Nauka/Interperiodica".*

INTRODUCTION

Although the complex formation of trivalent and tetravalent *f* elements with unsaturated heteropolyanions (*HPA*) has been investigated in sufficient detail [1], the interaction between rare-earth elements and unsaturated heteropolyanions with a Keggin structure, i.e., homologs of unsaturated heteropolyanions, is less well understood. There is some evidence for low coordination capacities of heteropolyanions with a Keggin structure, in particular, $SiW_{12}O_{40}^{4-}$ [2]. However, recent X-ray structure investigations have revealed that the $PW_{12}O_{40}^{3-}$ anions can be coordinated to the trivalent rare-earth ions [3, 4]. The present paper reports on the results of X-ray structure analysis of one more complex between a rare-earth element with a phosphorus heteropolyanion and a molecular organic ligand, namely, the $[La(DMSO)_6(H_2O)PW_{12}O_{40}] \cdot C_2H_5OH$ complex (**I**) (where *DMSO* is dimethyl sulfoxide).

EXPERIMENTAL

Synthesis. Complex **I** was synthesized according to the following procedure. A solution of the heteropolyanion and then a solution of *DMSO* in specified amounts were added to an acidified solution of lanthanum nitrate. The initial water solutions were as follows: 1.0 mol/l $La(NO_3)_3$, 0.1 mol/l $Na_2HPW_{12}O_{40}$, and 1.0 mol/l *DMSO*. A mixing of the solutions of the aforementioned reactants in the molar ratio La : *HPA* : *DMSO* in the range from 1 : 1 : 1 to 1 : 1 : 8 led to the precipitation of curds. Then, these curds were dissolved by the addition of ethanol (up to ~50% by volume). The resultant solutions were allowed to stand at room temperature until colorless crystalline products precipitated. The crystalline products were washed with water in small amounts and dried in air. The most stable crystals, which were suitable for X-ray diffraction analysis, precipitated from a solution containing no more than 1 mol/l HNO_3 at the molar ratio La : *HPA* : *DMSO* = 1 : 1 : 6.

X-ray diffraction analysis. The composition of the $[La(DMSO)_6(H_2O)PW_{12}O_{40}] \cdot C_2H_5OH$ complex was determined using X-ray diffraction analysis. The X-ray diffraction experiment was performed with a single crystal $0.16 \times 0.14 \times 0.12$ mm in size. A set of experimental data was collected on an Enraf–Nonius KappaCCD area-detector diffractometer (MoK_α radiation, graphite monochromator). The unit cell parameters were determined using ten images with $\Delta\varphi = 1°$ and were then refined over the entire set of experimental data. Crystals of **I** are monoclinic; at 20°C, the unit cell parameters are as follows: a = 14.0656(1) Å, b = 17.0617(2) Å, c = 25.2247(3) Å, β = 99.861(1)°, Z = 4, d_{calcd} = 3.952 g cm^{-3}, and space group $P2_1/c$. The intensities of reflections were measured for a hemisphere of the reciprocal space with the maximum angle $\theta = 27.5°$. A total of 50 856 reflections were measured, of which 13 632 were unique reflections, including 11 769 reflections with $I > 2\sigma(I)$. The large number of equivalent reflections made it possible to introduce absorption corrections according to the MULABS procedure included in the PLATON software package [5]. The structure was solved by the direct method (SHELXS86 [6]) and refined in the anisotropic approximation for the non-hydrogen atoms with the use of the full-matrix least-square procedure on F^2 (SHELXL93 [7]) for all the reflections involved. All the non-hydrogen atoms of the

heteropolyanions and molecular ligands were located from the electron-density difference Fourier synthesis. Three peaks remaining in the electron-density difference Fourier map were assigned to the ethanol molecule. The position of the O atom in the ethanol molecule was determined using the shortened contact with the O atom of coordinationally bound water. Among the six *DMSO* molecules, two molecules were disordered and involved two S sites with occupancies of 0.61 and 0.39. The hydrogen atoms (except for those involved in the disordered molecules of *DMSO*, the water molecule, and the ethanol OH group) were placed in the geometrically calculated positions. In this case, the thermal parameters of the hydrogen atoms were assumed to be 1.5 times larger than the equivalent thermal parameters of the C atoms to which the hydrogen atoms were attached (for the central C atom of the ethanol molecule, the coefficient was equal to 1.2). The final refinement (758 parameters) converged to $R_1 = 0.0503$ and $wR_2 = 0.1158$ [for reflections with $I > 2\sigma(I)$].

Interatomic distances (Å) in the environment of the La atom

La–O(1)	2.533 (10)
La–O(2)	2.459 (10)
La–O(3)	2.462 (10)
La–O(4)	2.500 (10)
La–O(5)	2.514 (11)
La–O(6)	2.441 (10)
La–O_w	2.569 (10)
La–O(45)	2.760 (9)
La–O(39*A*)	2.801 (9)

Note: The O(1), O(2), O(3), O(4), O(5), and O(6) atoms belong to the *DMSO* molecules, and the O(45) and O(39*A*) atoms are involved in the heteropolyanions.

RESULTS AND DISCUSSION

In structure **I**, the coordination number of the La atom is nine. The environment of the La atom involves six O atoms of the *DMSO* molecules, the molecule of coordinationally bound water, and two terminal O atoms of two $PW_{12}O_{40}^{3-}$ heteropolyanions. It can be seen from the table that, for the O atoms of the $PW_{12}O_{40}^{3-}$ heteropolyanions, the La–O distances are significantly longer than the other distances in the environment of the La atom. The coordination of the heteropolyanions to the La atoms leads to the formation of electroneutral zigzag chains (Fig. 1).

The coordination polyhedron of the La atom can be represented as a distorted tricapped trigonal prism (Fig. 2). Both oxygen atoms of the heteropolyanions occupy two cap sites. In the $[Nd(DMAA)_6PW_{12}O_{40}]$ complex (where *DMAA* is dimethylacetamide) studied in our earlier works [3, 4], two O atoms of the heteropolyanions are also involved in the coordination polyhedron of the Nd atom and the relevant Nd–O distances also substantially exceed (by ~0.2 Å) the Nd–O distances for the O atoms of the molecular ligands. The coordination polyhedron of the Nd atom in the

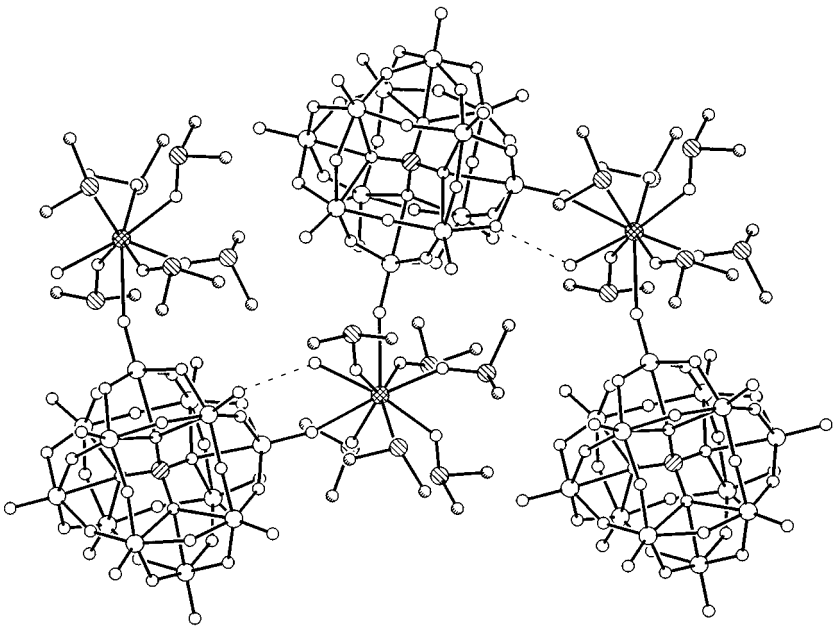

Fig. 1. An $[La(DMSO)_6(H_2O)PW_{12}O_{40}]_n$ electroneutral chain in structure **I**. The hydrogen atoms are not shown. For disordered molecules of *DMSO*, only one position of the S atom is depicted. Dashed lines indicate the presumed hydrogen bonds. Designations: (⊗) La, (○) W, (▨) P, (▨) S, (○) O, and (○) C.

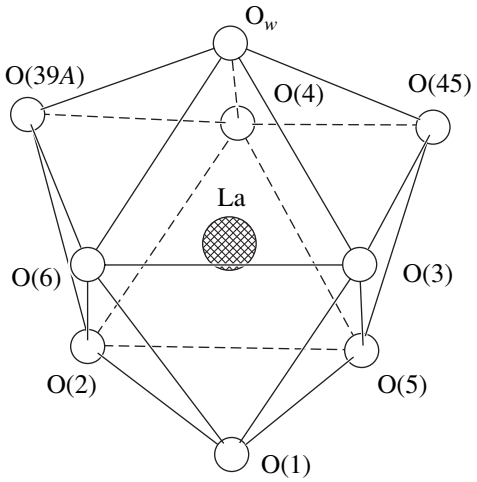

Fig. 2. A coordination polyhedron of the La atom.

[Nd(*DMAA*)$_6$PW$_{12}$O$_{40}$] complex was described as a bicapped trigonal prism in which both oxygen atoms of the heteropolyanions occupy cap sites. It should be noted that, in the complexes of lanthanides with iodo- and telluromolybdates [8, 9], all the Ln–O distances are nearly identical and the O atoms of these anions do not occupy specific sites in the coordination polyhedra of the Ln atoms.

The molecule of coordinationally bound water is involved in hydrogen bonds with one of the bridging (with respect to the W atoms) oxygen atoms of the heteropolyanions [O$_w$⋯O(34), 2.864(14) Å] and the O(47) atom of the ethanol molecule [O$_w$⋯O(47), 2.65(2) Å]. It seems likely that the ethanol molecule participates as a proton donor in the weak hydrogen bond with the bridging oxygen atom of the heteropolyanion [O(47)⋯O(17), 2.95 Å].

CONCLUSION

Our investigation confirmed that the $PW_{12}O_{40}^{3-}$ anions can be coordinated to the trivalent rare-earth ions. It was demonstrated that the difference in the bond strengths for the oxygen atoms involved in the heteropolyanions and organic molecular ligands is responsible for the existence of the specific sites occupied by the oxygen atoms of the heteropolyanions in the coordination polyhedra of the rare-earth atoms.

REFERENCES

1. A. B. Yusov and V. P. Shilov, Radiokhimiya **44**, 3 (1999).
2. M. A. Petrukhina, M. A. Fedotov, I. V. Tat'yanina, and E. A. Torchenkova, Zh. Neorg. Khim. **35**, 2110 (1990).
3. I. B. Shirokova, A. M. Fedoseev, M. S. Grigoriev, *et al.*, in *Proceedings of the 3rd All-Russia Conference on Radiochemistry "Radiochemistry-2000," St. Petersburg, 2000*, p. 20.
4. I. B. Shirokova, M. S. Grigoriev, V. I. Makarenkov, *et al.*, Koord. Khim. **27**, 772 (2001).
5. A. L. Spek, *PLATON: Multipurpose Crystallographic Tool* (Univ. of Utrecht, Utrecht, The Netherlands, 1998).
6. G. M. Sheldrick, Acta Crystallogr., Sect. A: Found. Crystallogr. **46**, 467 (1990).
7. G. M. Sheldrick, *SHELXL93: Program for the Refinement of Crystal Structures* (Univ. of Göpttingen, Göttingen, 1993).
8. M. S. Grigoriev, Yu. T. Struchkov, A. M. Fedoseev, *et al.*, Zh. Neorg. Khim. **37**, 2507 (1992).
9. A. M. Fedoseev, M. S. Grigoriev, N. A. Budantseva, *et al.*, J. Lumin. **87–89**, 1065 (2000).

Translated by O. Borovik-Romanova

Crystallography Reports, Vol. 47, No. 6, 2002, pp. 973–978. Translated from Kristallografiya, Vol. 47, No. 6, 2002, pp. 1042–1047.

STRUCTURE OF ORGANIC COMPOUNDS

X-ray Mapping in Heterocyclic Design: IX. X-ray Structure Investigation of Conjugated Aminodienes

V. B. Rybakov*, E. V. Babaev*, A. A. Tsisevich*, A. V. Arakcheeva, and A. Schoenleber*****

** Faculty of Chemistry, Moscow State University, Vorob'evy gory, Moscow, 119899 Russia*

e-mail: rybakov@biocryst.phys.msu.su

*** Baĭkov Institute of Metallurgy and Materials, Russian Academy of Sciences, Leninskiĭ pr. 49, Moscow, 119991 Russia*

**** Institute of Crystallography, University of Lausanne, BSP, 1015 Lausanne, Switzerland*

Received March 12, 2002

Abstract—The single-crystal structures of two aminodienes containing an oxazole fragment, namely, 1-piperidyl-4-[5-(4-nitrophenyl)-oxazol-2-yl]-buta-1,3-diene $C_{18}H_{19}N_3O_3$ (**IIa**) and 1-hexamethyleneimine-4-[5-(4-nitrophenyl)-oxazol-2-yl]-buta-1,3-diene $C_{19}H_{21}N_3O_3$ (**IIb**), are studied by X-ray diffraction. Structures **IIa** [a = 16.181(6) Å, b = 5.939(3) Å, c = 17.337(9) Å, β = 96.13(2)°, Z = 4, and space group $P2_1$] and **IIb** [a = 7.4704(11) Å, b = 10.9904(19) Å, c = 43.434(6) Å, β = 91.24(1)°, Z = 8, and space group $P2_1/c$] are solved by the direct method and refined to R = 0.060 and 0.238, respectively. Although the ring sizes of the cyclic amines in compounds **IIa** and **IIb** are different, the designs of two structures are identical. Each structure contains two topologically identical but crystallographically independent molecules. In structure **IIa**, the intramolecular hydrogen bonds between the N atoms of the oxazole fragments and the H atoms of the diene fragments are formed. In structure **IIb**, similar bonds are absent. © *2002 MAIK "Nauka/Interperiodica".*

INTRODUCTION

This study continues the series of our structural investigations of heterocyclic compounds that are able to enter readily into different rearrangements and ring-transformation reactions [1–20]. By analogy with our previous studies, we determined step-by-step the structures of all the intermediates and final products of the multistage cyclization and recyclization reactions. The data on the molecular structures of 1-piperidyl-4-[5-(4-nitrophenyl)-oxazol-2-yl]-buta-1,3-diene $C_{18}H_{19}N_3O_3$ (**IIa**) and 1-hexamethyleneimine-4-[5-(4-nitrophenyl)-oxazol-2-yl]-buta-1,3-diene $C_{19}H_{21}N_3O_3$ (**IIb**), which are considered in this paper, are not available in the Cambridge Structural Database (version 11.01) [21].

Compound **IIa** was synthesized by scheme *1*[1]

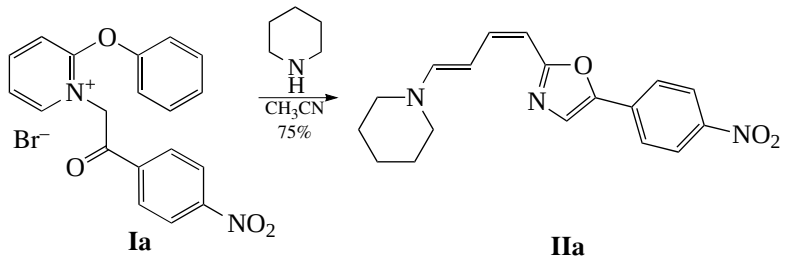

Ia **IIa**

according to the following procedure: 1-(4-Nitrophenacyl)-2-phenoxypyridinium bromide (0.1 g, 0.24 mmol) was dissolved in acetonitrile. Piperidine (0.04 g, 0.48 mmol) was added on stirring at room temperature to the yellow solution obtained. The solution became dark red. The mixture was allowed to stand at room temperature for two days. Violet needle crystals that precipitated were filtered off and washed with an ether. An additional amount of pure product could be isolated by the dilution of the filtrate with water followed by filtration of the precipitate. The yield was 0.06 g (75%) of 1-piperidyl-4-[5-(4-nitrophenyl)-oxazol-2-yl]}-buta-

[1] With the participation of T.A. Smirnova.

1,3-diene (**IIa**). The synthesis and other transformations of the initial pyridinium salt will be reported elsewhere.

The synthesis of compound **IIb** by scheme *2* was described earlier in [22]:

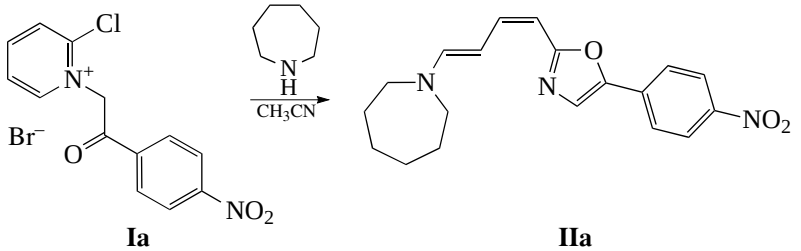

Ia **IIa**

According to [23], compounds **IIa** and **IIb** exhibit an antimicrobal activity. For this reason, their crystal structures have been studied in detail. The structural characteristics of these compounds are also of particular interest from the standpoint of X-ray mapping of the structures, because we studied earlier the structures of a series of 2-substituted *N*-phenacylpyridinium salts and the products of their transformations, which belong to various classes of heterocycles, for example, pyridone derivatives such as oxazolopyridine [1, 2, 6], cationic thiazolopyridine [24], and indolizine [4, 11].

EXPERIMENTAL

The intensities of diffraction reflections for **IIa** were measured at room temperature on a CAD4 four-circle diffractometer [25] (MoK_α radiation, graphite monochromator, ω scan mode). The experimental data for **IIb** were collected at room temperature in the dynamic mode on a KM4-CCD four-circle diffractometer [26] (MoK_α radiation, graphite monochromator, CCD

Table 1. Crystallographic characteristics and details of the X-ray diffraction experiment and structure-refinement parameters for **IIa** and **IIb**

Compound	$C_{18}H_{19}N_3O_3$ (**IIa**)	$C_{19}H_{21}N_3O_3$ (**IIb**)
Crystal system	Monoclinic	Monoclinic
Space group	$P2_1$	$P2_1/c$
a, Å	16.181(6)	7.470(1)
b, Å	5.939(3)	10.990(2)
c, Å	17.337(9)	43.434(6)
β, deg	96.13(2)	91.24(1)
V, Å^3	1656.5(13)	3565.2(10)
Z	4	8
ρ_{calcd}, g/cm^3	1.305	1.265
μ(MoK_α), cm^{-1}	0.091	0.087
Crystal size, mm	0.35 × 0.40 × 0.45	0.10 × 0.12 × 0.02
θ_{max}, deg	28	30
No. of reflections with $I \geq 2\sigma(I)$/No. of parameters	4218/290	2131/177
R_1/wR_2	0.062/0.130	0.238/0.462
$\Delta\rho_{max}/\Delta\rho_{min}$, e/Å^3	0.172/–0.130	0.322/–0.320

Table 2. Bond lengths *d* (Å) in structures **IIa** and **IIb** (molecules *A* and *B*)

Bond	*d*	
	IIa	**IIb**
N(1)–C(2)	1.486(8)	1.473(12)
N(1)–C(6)	1.403(8)	
N(1)–C(7)		1.473(12)
N(1)–C(8)	1.351(4)	1.43(2)
C(2)–C(3)	1.433(8)	1.436(10)
C(3)–C(4)	1.533(11)	1.436(10)
C(4)–C(5)	1.479(11)	1.436(10)
C(5)–C(6)	1.417(7)	1.436(10)
C(6)–C(7)		1.436(10)
C(8)–C(9)	1.335(4)	1.37(2)
C(9)–C(10)	1.409(4)	1.408(18)
C(10)–C(11)	1.345(4)	1.36(2)
C(11)–C(12)	1.421(4)	1.45(2)
C(12)–N(2)	1.309(3)	1.278(18)
C(12)–O(1)	1.372(3)	1.356(16)
C(13)–O(1)	1.380(3)	1.401(14)
C(13)–C(14)	1.350(4)	1.275(19)
C(13)–C(15)	1.441(4)	1.52(2)
C(14)–N(2)	1.360(4)	1.39(2)
C(15)–C(16)	1.407(7)	1.457(13)
C(15)–C(20)	1.380(7)	1.457(13)
C(16)–C(17)	1.359(10)	1.349(16)
C(17)–C(18)	1.344(7)	1.404(13)
C(18)–C(19)	1.400(7)	1.404(13)
C(18)–N(3)	1.458(4)	1.44(2)
C(19)–C(20)	1.356(11)	1.349(15)
N(3)–O(31)	1.214(2)	1.248(11)
N(3)–O(32)	1.214(2)	1.248(11)

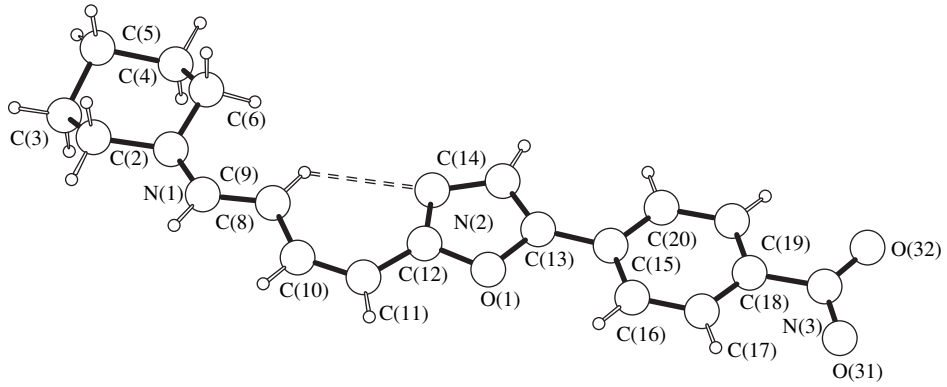

Fig. 1. Molecular structure of **IIa** and the atomic numbering.

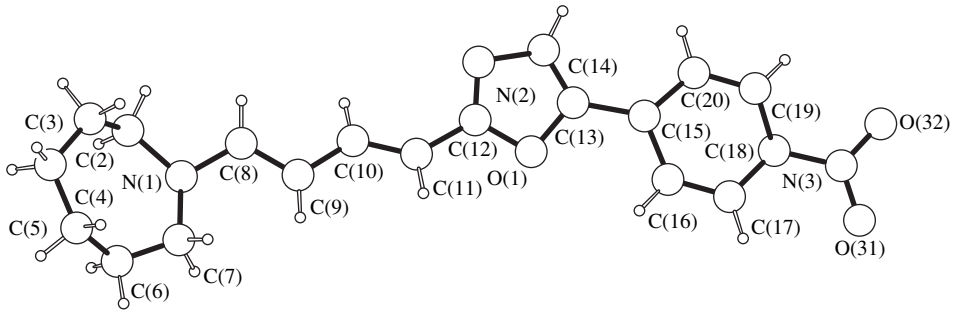

Fig. 2. Molecular structure of **IIb** and the atomic numbering.

detector, crystal-to-detector distance 51.7 mm). The unit cell parameters were determined and refined using 25 reflections in the θ range 14°–16° for **IIa** and 9640 reflections with $I > 6\sigma(I)$ from the whole data-collection range for **IIb**. The main experimental parameters and crystal data for compounds **IIa** and **IIb** are summarized in Table 1.

Since the crystals of the compounds studied were small and had small coefficients of linear absorption, the correction for absorption was not introduced. The primary processing of the experimental data for **IIa** was performed with the WinGX98 program package [27]. The integral intensities for **IIb** were obtained and primarily processed with the KM4 program package [28]. All the following calculations were performed with the SHELX97 program package [29]. The crystal structures were solved by the direct method. All the nonhydrogen atoms in structures **IIa** and **IIb** were refined in the anisotropic and isotropic approximations, respectively. The system of atomic numbering in the two compounds is the same. Since structures **IIa** and **IIb** contained two crystallographically independent molecules (*A* and *B*), the full-matrix least-squares refinement was performed under the restriction that the lengths of the analogous bonds in each structure were identical. The thermal parameters of the corresponding atoms were also kept equal. The hydrogen atoms in both structures were located from geometric considerations and refined within a rider model together with the corresponding carbon atoms. The thermal parameters of the hydrogen atoms were calculated from those of the corresponding carbon atoms [$U_{iso}(H) = 1.2U_{iso/eq}(C)$]. The structural data for crystals **IIa** and **IIb** (CIF files) were deposited in the Cambridge Structural Database [21], CCDC nos. 191971 and 191972. The interatomic distances in structures **IIa** and **IIb** are listed in Table 2. The drawings of the molecular structures **IIa** and **IIb** obtained with the PLUTON96 program [30] are shown in Figs. 1 and 2, respectively. The interatomic and intermolecular contacts involving hydrogen atoms for structures **IIa** and **IIb**, which were calculated using the PARST95 program [31], are listed in Tables 3 and 4, respectively.

RESULTS AND DISCUSSION

The compositions of the compounds studied differ only in the size of the cyclic amine, which is the six-membered piperidine ring in **IIa** and the seven-membered hexamethyleneimine ring in **IIb**. However, the three-dimensional structures of the compounds studied differ fundamentally. Compound **IIa** is the 1*E*,3*Z*-isomer, whereas compound **IIb** has the 1*E*,3*E*-configuration of the substituted diene fragment. The formation of the *E*,*Z*- and *E*,*E*-isomers was discussed earlier in [22].

Table 3. Parameters of interatomic contacts in **IIa**

D–H	*d*(*D*–H)	*d*(*D*···*A*)	*d*(H···*A*)	ω*DHA*	*A*	Symmetry operation
C(9*A*)–H(9*A*)	0.93	3.07(1)	2.490(8)	120.8(5)	N(2*A*)	[*x*; *y*; *z*]
C(16*A*)–H(16*A*)	0.93	2.88(1)	2.590(6)	98.7(5)	O(1*A*)	[*x*; *y*; *z*]
C(17*A*)–H(17*A*)	0.93	2.71(1)	2.408(8)	98.4(6)	O(31*A*)	[*x*; *y*; *z*]
C(19*A*)–H(19*A*)	0.93	2.71(1)	2.445(7)	96.5(5)	O(32*A*)	[*x*; *y*; *z*]
C(9*B*)–H(9*B*)	0.93	3.10(1)	2.501(8)	122.4(5)	N(2*B*)	[*x*; *y*; *z*]
C(17*B*)–H(17*B*)	0.93	2.72(1)	2.411(7)	99.1(5)	O(31*B*)	[*x*; *y*; *z*]
C*(19B)–H(19B)*	0.93	2.74(1)	2.484(8)	96.0(6)	O(32*B*)	[*x*; *y*; *z*]
C(20*B*)–H(20*B*)	0.93	2.84(1)	2.505(6)	101.1(6)	O(1*B*)	[*x*; *y*; *z*]
C(3*A*)–H(3*A*1)	0.97	3.76(1)	2.975(6)	139.2(6)	N(3*B*)	[1 – *x*; 1/2 + *y*; 2 – *z*]
C(3*A*)–H(3*A*1)	0.97	3.71(1)	2.781(7)	160.6(6)	O(32*B*)	[1 – *x*; 1/2 + *y*; 2 – *z*]
C(3*A*)–H(3*A*2)	0.97	3.73(1)	2.786(8)	164.1(6)	O(32*B*)	[1 – *x*; *y* – 1/2; 2 – *z*]
C(5*A*)–H(5*A*1)	0.97	3.61(1)	2.745(7)	148.6(6)	O(31*B*)	[1 – *x*; *y* – 1/2; 2 – *z*]
C(11*A*)–H(11*A*)	0.93	3.33(1)	2.675(7)	128.3(5)	O(31*A*)	[2 – *x*; *y* + 3/2; 2 – *z*]
C(10*A*)–H(10*A*)	0.93	3.38(1)	2.757(5)	125.4(5)	O(31*A*)	[2 – *x*; *y* + 3/2; 2 – *z*]
C(17*A*)–H(17*A*)	0.93	3.62(1)	2.848(5)	140.6(5)	O(1*A*)	[2 – *x*; *y* – 1/2; 2 – *z*]
C(19*A*)–H(19*A*)	0.93	3.36(1)	2.529(6)	148.8(5)	O(31*B*)	[*x*; *y* – 2; *z*]
C(3*B*)–H(3*B*1)	0.97	3.61(1)	2.763(6)	146.1(6)	O(32*A*)	[2 – *x*; *y* + 1/2; 1 – *z*]
C(5*B*)–H(5*B*2)	0.97	3.69(1)	2.959(8)	132.9(7)	O(31*A*)	[2 – *x*; *y* – 1/2; 1 – *z*]
C(11*B*)–H(11*B*)	0.93	3.32(1)	2.694(7)	125.1(5)	O(32*B*)	[1 – *x*; *y* – 3/2; 1 – *z*]
C(10*B*)–H(10*B*)	0.93	3.32(1)	2.704(5)	124.2(5)	O(32*B*)	[1 – *x*; *y* – 3/2; 1 – *z*]
C(14*B*)–H(14*B*)	0.93	3.66(1)	2.988(6)	130.4(5)	O(32*A*)	[*x*; 1 + *y*; *z*]
C(17*B*)–H(17*B*)	0.93	3.41(1)	2.561(6)	151.1(5)	O(32*A*)	[*x*; *y* + 2; *z*]
C(19*B*)–H(19*B*)	0.93	3.59(1)	2.780(5)	145.6(5)	O(1*B*)	[1 – *x*; *y* + 1/2; 1 – *z*]

Note: *D* is a donor, *A* is an acceptor, and H is a hydrogen atom; the *d* distances and ω angles are given in Å and degrees, respectively.

The structure of molecules **IIa** is convenient for the formation of the C(9)H(9)···N(2) intramolecular hydrogen bond (Table 3, Fig. 1), which cannot be formed in the molecules of compound **IIb** (Fig. 2). Moreover, molecule **IIb** is longer than molecule **IIa** (the difference in the lengths of the similar N(1)···N(3) fragments is 0.836 Å). As a consequence of these two factors, the molecular packings and the habits of the crystals are different. For example, compound **IIa** crystallizes as dark red well-edged prisms, whereas crystals **IIb** are very fine plates that are colored dark red, almost black, and exhibit metallic iridescence. Because of the very small size of crystals **IIb**, we managed to collect a relatively satisfactory set of intensities (suitable only for the determination of the model) using a highly sensitive CCD detector. It was assumed earlier [22] that the intense crystal color is due to the intramolecular charge transfer from the amino group to the nitro group via the azapolyene system according to scheme *3* (illustrated by the example of 1*E*,3*Z*-isomer).

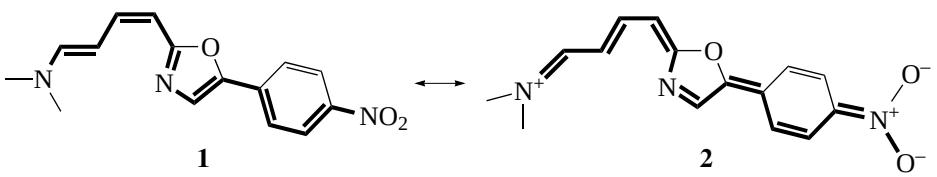

1 **2**

The data of the X-ray diffraction study reveal the degree of contribution of the charge-transfer structures to the structures of the dienes under consideration. Now, we compare the bond lengths in the conjugation chains between the amino and nitro groups obtained in this study with those in the hypothetical resonance structures **1** and **2**. First, let us consider the nitrophenyl group. The C–N distances between the phenyl radical and the NO_2 group and the N–O distances in crystals **IIa** and **IIb** are slightly different, but in both crys-

Table 4. Parameters of interatomic contacts in **IIb**

D–H	*d*(*D*–H)	*d*(*D*···*A*)	*d*(H···*A*)	ω*DHA*	*A*	Symmetry operation
C(7*A*)–H(7*A*2)	0.97	3.82(6)	2.89(1)	161(3)	O(31*B*)	[*x*; *y*; *z*]
C(10*A*)–H(10*A*)	0.93	3.13(3)	2.93(2)	94(1)	N(2*A*)	[*x*; *y*; *z*]
C(16*A*)–H(16*A*)	0.93	2.91(2)	2.59(1)	101(1)	O(1*A*)	[*x*; *y*; *z*]
C(17*A*)–H(17*A*)	0.93	2.75(2)	2.48(2)	97(1)	O(31*A*)	[*x*; *y*; *z*]
C(19*A*)–H(19*A*)	0.93	2.73(2)	2.43(2)	99(1)	O(32*A*)	[*x*; *y*; *z*]
C(3*B*)–H(3*B*1)	0.97	3.65(4)	2.75(3)	154(2)	O(32*A*)	[*x*; *y*; *z*]
C(7*B*)–H(7*B*2)	0.97	3.85(6)	2.93(3)	158(2)	O(31*A*)	[*x*; *y*; *z*]
C(10*B*)–H(10*B*)	0.93	3.09(2)	2.85(2)	96(1)	N(2*B*)	[*x*; *y*; *z*]
C(16*B*)–H(16*B*)	0.93	2.97(2)	2.65(1)	101(1)	O(1*B*)	[*x*; *y*; *z*]
C(17*B*)–H(17*B*)	0.93	2.70(2)	2.40(2)	98(1)	O(31*B*)	[*x*; *y*; *z*]
C(19*B*)–H(19*B*)	0.93	2.78(3)	2.51(2)	97(1)	O(32*B*)	[*x*; *y*; *z*]
C(2*A*)–H(2*A*1)	0.97	3.54(2)	2.63(1)	157(1)	O(31*A*)	[1 – *x*; *y* – 1/2; 1/2 – *z*]
C(8*A*)–H(8*A*)	0.93	3.52(3)	2.72(2)	145(1)	O(31*A*)	[1 – *x*; *y* – 1/2; 1/2 – *z*]
C(2*A*)–H(2*A*2)	0.97	3.71(4)	2.94(3)	137(2)	O(32*B*)	[*x* – 1; *y*; *z*]
C(6*A*)–H(6*A*2)	0.97	3.51(2)	2.73(2)	138(1)	O(32*A*)	[*x* – 1; *y*; *z*]
C(16*A*)–H(16*A*)	0.93	3.64(3)	2.86(2)	142(1)	N(2*A*)	[*x* – 1; *y*; *z*]
C(2*B*)–H(2*B*1)	0.97	3.34(2)	2.51(2)	144(1)	O(31*B*)	[2 – *x*; *y* – 1/2; 1/2 – *z*]
C(8*B*)–H(8*B*)	0.93	3.50(3)	2.64(1)	155(1)	O(31*B*)	[2 – *x*; *y* – 1/2; 1/2 – *z*]
C(14*A*)–H(14*A*)	0.93	3.74(3)	2.93(2)	146(1)	O(1*B*)	[2 – *x*; *y* – 1/2; 1/2 – *z*]
C(16*B*)–H(16*B*)	0.93	3.57(2)	2.69(2)	159(1)	N(2*B*)	[2 – *x*; *y* + 1/2; 1/2 – *z*]
C(11*B*)–H(11*B*)	0.93	3.81(3)	2.98(2)	150(1)	N(2*A*)	[2 – *x*; *y* + 1/2; 1/2 – *z*]
C(6*B*)–H(6*B*2)	0.97	3.54(3)	2.73(1)	142(1)	O(32*B*)	[2 – *x*; *y* + 1/2; 1/2 – *z*]

Note: *D* is a donor, *A* is an acceptor, and H is a hydrogen atom; the *d* distances and ω angles are given in Å and degrees, respectively.

tals, their values correspond better to structure **1**. The phenyl ring is slightly distorted, and its geometric parameters correspond better to structure **2**, because the C(16)–C(17) and C(19)–C20) bonds [1.35(2) Å] are significantly shorter than all the other bonds in the ring [1.40(2)–1.46(2) Å]. Second, we consider the oxazole fragment. The five-membered rings in molecules **IIa** and **IIb** have different geometries. Actually, in molecule **IIa**, the double bonds in the C(12)N(2)C(14)C(13) azadiene fragment are evidently delocalized, since the C(12)–N(2), N(2)–C(14), and C(13)–C(14) distances are smoothened [1.31(1), 1.36(1), and 1.35(2) Å, respectively]. In the similar azadiene structural fragment of molecule **IIb**, the corresponding bond lengths alternate to a larger degree [1.28(2), 1.39(2), and 1.28(2) Å, respectively], which counts in favor of the contribution of structure **1** to the structure of the five-membered ring. Third, consider the diene fragment. The lengths of the formally single and double bonds in the butadiene fragments of both molecules agree more closely with structure **1**, but the bond-length alternation in this fragment of compound **IIa** is more pronounced than that in **IIb**. It is difficult to draw a more definite conclusion regarding the contribution of structures **1** and **2** to the geometry of the molecules because of the poor quality of the experimental data for crystal **IIb**.

It follows from the totality of data obtained that structure **2**, in which charge transfer is observed, contributes to the structures of both the compounds considered; however, the real molecular structures are intermediate between the resonance structures **1** and **2**.

Conformational analysis of the cyclic amines was not the object of this study; however, the parameters of ring puckering can be calculated from the atomic coordinates.

ACKNOWLEDGMENTS

We are grateful to Prof. G. Chapuis, Institute of Crystallography, University of Lausanne, who kindly allowed us to perform the diffraction experiment. We also acknowledge the support of the Russian Foundation for Basic Research in the payment of the license for using the Cambridge Structural Database, project no. 99-07-90133.

REFERENCES

1. E. V. Babaev, S. V. Bozhenko, D. A. Maiboroda, *et al.*, Bull. Soc. Chim. Belg. **106** (9–10), 631 (1997).
2. S. G. Zhukov, V. B. Rybakov, E. V. Babaev, *et al.*, Acta Crystallogr., Sect. C: Cryst. Struct. Commun. **53**, 1909 (1997).
3. E. V. Babaev, S. V. Bozhenko, S. G. Zhukov, and V. B. Rybakov, Khim. Geterotsikl. Soedin., No. 8, 1105 (1997).
4. E. V. Babaev, A. V. Efimov, S. G. Zhukov, and V. B. Rybakov, Khim. Geterotsikl. Soedin., No. 7, 983 (1998).
5. V. B. Rybakov, S. G. Zhukov, E. V. Babaev, *et al.*, Kristallografiya **44** (6), 1067 (1999) [Crystallogr. Rep. **44**, 997 (1999)].
6. E. V. Babaev, V. B. Rybakov, S. G. Zhukov, and I. A. Orlova, Khim. Geterotsikl. Soedin., No. 4, 542 (1999).
7. V. B. Rybakov, S. G. Zhukov, E. V. Babaev, *et al.*, Kristallografiya **45** (1), 108 (2000) [Crystallogr. Rep. **45**, 103 (2000)].
8. V. B. Rybakov, S. G. Zhukov, E. V. Babaev, *et al.*, Kristallografiya **45** (2), 292 (2000) [Crystallogr. Rep. **45**, 261 (2000)].
9. S. G. Zhukov, E. V. Babaev, V. V. Chernyshev, *et al.*, Z. Kristallogr. **215**, 306 (2000).
10. V. B. Rybakov, S. G. Zhukov, K. Yu. Pasichnichenko, and E. V. Babaev, Koord. Khim. **26** (9), 714 (2000).
11. E. V. Babaev, A. V. Efimov, V. B. Rybakov, and S. G. Zhukov, Khim. Geterotsikl. Soedin., No. 3, 401 (2000).
12. E. V. Babaev, K. Yu. Pasichnichenko, V. B. Rybakov, *et al.*, Khim. Geterotsikl. Soedin., No. 9, 1245 (2000).
13. E. V. Babaev, K. Yu. Pasichnichenko, V. B. Rybakov, and S. G. Zhukov, Khim. Geterotsikl. Soedin., No. 10, 1378 (2000).
14. V. B. Rybakov, E. V. Babaev, and Y. V. Dlinnykh, Acta Crystallogr., Sect. E: Struct. Rep. **57**, 814 (2001).
15. V. B. Rybakov, S. G. Zhukov, E. V. Babaev, and E. J. Sonneveld, Kristallografiya **46** (3), 435 (2001) [Crystallogr. Rep. **46**, 385 (2001)].
16. V. B. Rybakov, S. I. Troyanov, E. V. Babaev, *et al.*, Kristallografiya **46** (6), 1069 (2001) [Crystallogr. Rep. **46**, 986 (2001)].
17. V. B. Rybakov, E. V. Babaev, K. Yu. Pasichnichenko, and E. J. Sonneveld, Kristallografiya **47** (1), 76 (2002) [Crystallogr. Rep. **47**, 69 (2002)].
18. V. B. Rybakov, E. V. Babaev, and V. V. Chernyshev, Kristallografiya **47** (3), 473 (2002) [Crystallogr. Rep. **47**, 428 (2002)].
19. V. B. Rybakov, E. V. Babaev, and K. Yu. Pasichnichenko, Kristallografiya **47** (4), 678 (2002) [Crystallogr. Rep. **47**, 622 (2002)].
20. V. B. Rybakov, E. V. Babaev, and E. N. Belykh, Acta Crystallogr., Sect. E: Struct. Rep. **58**, 126 (2002).
21. F. H. Allen and O. Kennard, Chem. Des. Automat. News **8** (1), 31 (1993).
22. E. V. Babaev and A. A. Tsisevich, J. Chem. Soc., Perkin Trans. 1, No. 4, 399 (1999).
23. D. A. Maĭboroda, E. V. Babaev, and L. V. Goncharenko, Khim.-Farm. Zh., No. 6, 24 (1998).
24. E. V. Babaev, A. A. Bush, I. A. Orlova, *et al.*, Tetrahedron Lett. **40** (42), 7553 (1999).
25. *Enraf–Nonius CAD4 Software. Version 5.0.* (Enraf–Nonius, Delft, The Netherlands, 1989).
26. *CrysAlis Software System. Version 1.166.* (Oxford Diffraction Ltd, Oxford, 2001).
27. L. J. Farrugia, *WinGX98: X-ray Crystallographic Programs for Windows* (University of Glasgow, Glasgow, 1998).
28. *KM4 Software. Version 1.164.* (Oxford Diffraction Ltd, Oxford, 2000).
29. G. M. Sheldrick, *SHELX97: Program for the Solution and Refinement of Crystal Structures* (Univ. of Göttingen, Göttingen, 1997).
30. A. L. Spek, *PLUTON96: Molecular Graphics Program* (Univ. of Utrecht, Utrecht, The Netherlands, 1996).
31. M. Nardelli, J. Appl. Crystallogr. **28**, 659 (1995).

Translated by I. Polyakova

Crystallography Reports, Vol. 47, No. 6, 2002, pp. 979–990. Translated from Kristallografiya, Vol. 47, No. 6, 2002, pp. 1048–1059.

LATTICE DYNAMICS AND PHASE TRANSITIONS

Domain Structure of $Na_{1-x}Li_xNbO_3$ Crystals[1]

E. S. Gagarina, E. I. Éknadiosyants, L. A. Reznichenko, L. A. Shilkina, I. P. Raevskiĭ, V. P. Sakhnenko, V. G. Smotrakov, and V. V. Eremkin

Research Institute of Physics, Rostov State University, pr. Stachki 194, Rostov-on-Don, 344104 Russia

e-mail: egag@ip.rsu.ru

Received August 27, 2001

Abstract—The domain structure of single-crystal and ceramic samples of $Na_{1-x}Li_xNbO_3$ solid solutions (at $x \le 0.14$) in the orthorhombic ferroelectric and antiferroelectric phases at room temperature is investigated by optical and electron microscopies and X-ray diffraction. The characteristic feature of the domain structure is the formation of 90° complexes consisting of laminar domains with a specific orientation relative to the lattice of the initial cubic phase. Consideration is given to the specific features in packing of these complexes and typical configurations of domains in the crystals. Observations revealed that the domain structure can involve 90°, 60°, 120°, and 180° boundaries, as well as (*hhl*) boundaries of the *S* type whose orientation depends on the cell distortion and changes with a variation in *x*. The indices of these boundaries are determined. The density of 180° boundaries in the ferroelectric phase is very low compared to that of non-90° boundaries.

INTRODUCTION

This paper reports on the results of investigations into the domain structure of single-crystal and hot-pressed ceramic samples of $Na_{1-x}Li_xNbO_3$ (NLN) solid solutions at $x \le 0.14$. Among the perovskite oxides, crystals of $NaNbO_3$ (NN) and $NaNbO_3$-based solid solutions stand out as materials undergoing a large number of phase transitions [1, 2] and exhibiting high sensitivity of their properties to preparation conditions and different-type defects. In the above concentration range, NLN crystals at room temperature have a monoclinically distorted perovskite cell with the parameters $a = c > b$ and $\alpha = \gamma = 90° < \beta$. The true symmetry is orthorhombic. The vectors **A** and **C** of the orthorhombic cell are as follows: $\mathbf{A} = \mathbf{a} - \mathbf{c}$ and $\mathbf{C} = \mathbf{a} + \mathbf{c}$. The vector **B** is parallel to the **b** axis of the perovskite cell. An increase in the lithium concentration results in a transition from the antiferroelectric state (**B** = 4**b**, *mmm*, *M*4 phase) to the ferroelectric state (**B** = 2**b**, 2*mm*, *M*2 phase) [3–7]. In NLN and NN crystals, unlike the majority of perovskite antiferroelectrics [1], the direction of the spontaneous antipolarization $\pm\mathbf{P}_s$ is parallel to the long diagonal of the *ac* face of the perovskite cell (the **A** axis). Note that the spontaneous polarization vector $\mathbf{P}_s$ in the ferroelectric phase *M*2 is also aligned with the long diagonal of the *ac* face. The phases *M*4 and *M*2 are similar to the phases *P* [8] and *Q* [9] in the NN crystal. In this crystal, the *Q* phase either exists in the metastable state or is induced by an electric field and the *P* and *Q* phases can coexist [10–12]. In a narrow concentration range in the vicinity of $x = 0.12$, the phase is rhombohedral (the concentration $x = 0.145$ corresponds to the solubility limit of lithium in the NN crystal) [13, 14].

According to the X-ray structure investigations performed in our earlier works [5–7], the ferroelectric *M*2 and antiferroelectric *M*4 phases in NLN solid solutions coexist in the concentration ranges $0.01 \le x \le 0.05$ for crystals and $0.032 \le x \le 0.0375$ for ceramic samples. The results of electrical measurements carried out with ceramic materials indicate the presence of ferroelectric clusters whose size and amount can increase upon polarization of NN ceramic samples and introduction of the second component into them [13–16]. Pozdnyakova *et al.* [17] showed that the antiferroelectric and ferroelectric phases coexist in the concentration range $0.015 < x < 0.0225$. Moreover, Sadel *et al.* [18, 19] and Zhong *et al.* [20] studied NLN single crystals with $x = 0.02$–0.03 and revealed that the spontaneous polarization $\mathbf{P}_s$ is directed parallel to the **b** axis. All these findings, including the data on the ferroelastic properties of NN compounds, have given impetus to the investigation into the domain structure of NLN solid solutions, especially as only the crystal optical data on the domain structure of crystals at $x = 0.02$ [18] are available in the literature.

SAMPLE PREPARATION AND EXPERIMENTAL TECHNIQUE

The NLN crystals studied in this work were grown using the flux (crystals **I** with concentrations $x \le 0.04$) and Czochralski methods (crystals **II** with

[1] This paper was presented at the Symposium "Order, Disorder, and Properties of Oxides," Sochi, Russia, 2001.

Parameters of the perovskite unit cell of the NLN crystals under investigation and the values of $R_x = (I_{211} + I_{230}/I_{102})/R_0$

x, %	a, nm	b, nm	β, deg	R_x	x, %	a, nm	b, nm	β, deg	R_x
Crystals **I**					3.5	0.39200	0.38782	90.62	0.24
1.2	0.39142	0.38799	90.67	1.00	3.7	0.39200	0.38781	90.63	0.17
2.0	0.39153	0.38760	90.66	0.85	4.0	0.39197	0.38784	90.63	0.12
2.5	0.39154	0.38766	90.66	0.80	Crystals **II**				
3.0	0.39163	0.38758	90.63	0.70	7.5	0.39184	0.38764	90.69	0.00
3.2	0.39180	0.38780	90.62	0.30					

$x \approx 0.075$).[2] Moreover, we examined NLN ceramic samples ($x \leq 0.14$) prepared through the solid-phase two-stage synthesis from Nb_2O_5 pentoxide and Na_2CO_3 and Li_2CO_3 carbonates (at a temperature of 800°C for 5 h and at 850°C for 5 h), followed by sintering under hot pressing at 200 kg/cm^2 for 40 min in the temperature range 1050–1200°C depending on the composition. The previously studied system Na_2CO_3–Nb_2O_5–B_2O_3 served as an initial system for preparing crystals **I** [21]. This system was also used to grow NN crystals. The NLN crystals were synthesized through partial replacement of Na_2CO_3 by Li_2CO_3 in the initial batch. Crystals **I** were transparent plates ($1.5 \times 1.5 \times 0.3$ mm^3 in mean size) or elongated parallelepipeds ($0.3 \times 0.3 \times 1.5$ mm^3 in mean size) with the {100} faces.[3] Crystals **II** were semitransparent colorless boules $7 \times 7 \times 20$ mm^3 in mean size. The crystal compositions were evaluated from the concentration dependence of the temperature of the phase transition between the orthorhombic (*M*4 or *M*2) phase and the lower temperature rhombohedral ferroelectric phase *N* observed in the NN compound [2]. This concentration dependence was constructed according to the data taken from [20, 22, 23]. X-ray structure investigations were performed on a DRON-3 diffractometer [FeK_α radiation, θ/2 (2θ) scan and ω scan (at a fixed counter) modes] and a Weissenberg goniometer (CuK_α radiation). The domain structures were examined with an Nu-2E optical polarizing microscope (crystals **I**)[4] and an ÉMV-100B transmission electron microscope with the use of direct platinum–carbon replicas (crystals **II** and ceramic samples). The samples under investigation were preliminarily etched. The optimum results were obtained by etching in a mixture of concentrated nitric and hydrofluoric acids in the ratio 3 : 2 at temperatures of 80–100°C for 2–4 h. The deposit of etching products was removed using additional treatment in nitric acid at 80°C for 30 min. However, the crystal surface in places was covered with a thin film that could be formed upon pouring of the melt and was not completely removed during etching.

X-RAY DIFFRACTION INVESTIGATIONS OF CRYSTALS

The table presents the parameters of the perovskite cells of the single crystals studied and the quantities $R_x = (I_{211} + I_{230}/I_{102})/R_0$, which give rough estimates of the volume ratio of the phases *M*4 and *M*2 in the crystal. Here, I_{211} and I_{230} are the experimental intensities of the (211) and (230) superstructure reflections observed only in the *M*4 phase, I_{102} is the experimental intensity of the (102) reflection observed in both phases (the reflection indices correspond to an orthorhombic cell, and the reflection intensities were determined from the X-ray diffraction patterns of single crystals in powdered form), and $R_0 \approx 2.2$ is the aforementioned intensity ratio for the NN crystal. Note that the quantity R_x is a characteristic averaged over the crystals prepared from a particular batch with a certain value of x and can change from crystal to crystal.

Instead of single reflections, the X-ray diffraction patterns of the studied crystals exhibit groups of reflections, each associated with diffraction by different twin components (domains). Figures 1a–1d display the characteristic splitting patterns of reflections (reciprocal lattice points) of the (*h*00) type. Two characteristic angular splittings Δω of the reflections are observed in the experiment. Their magnitudes depend on the unit cell parameters of a particular crystal and amount, on average, to 0.3° and 0.6°.

Let us now introduce a coordinate system (x, y, z) whose axes coincide with the axes of the cubic cell. Figure 1e shows the schematic diagram of splitting of the *h*00 reciprocal lattice points, which is repeated (wholly or in part) from crystal to crystal. The observed splitting can be explained by the fact that twins (90° ferroelectric or antiferroelectric domains) with the $(100)_m$ or $(001)_m$ twinning planes aligned parallel to the (100) planes of the cubic phase are formed by displacing the lattice of the prototype phase through the angle $\mu = \beta - 90°$. As a result, six complexes of orientational domains of the S_1 and S_2 type are formed in the crystal (Fig. 1f). For definiteness, we choose the axes of the

[2] Crystals **II** were grown by L.M. Kazaryan, a researcher from the Institute of Physical Research, Academy of Sciences of Armenia, Armenia.

[3] The indices *hkl* and hkl_m refer to the pseudocubic and monoclinically distorted perovskite cells, respectively.

[4] All the micrographs presented below were obtained in crossed nicols in the transmitted light. The orientation of the nicols is shown with respect to the {100} facet of the crystal.

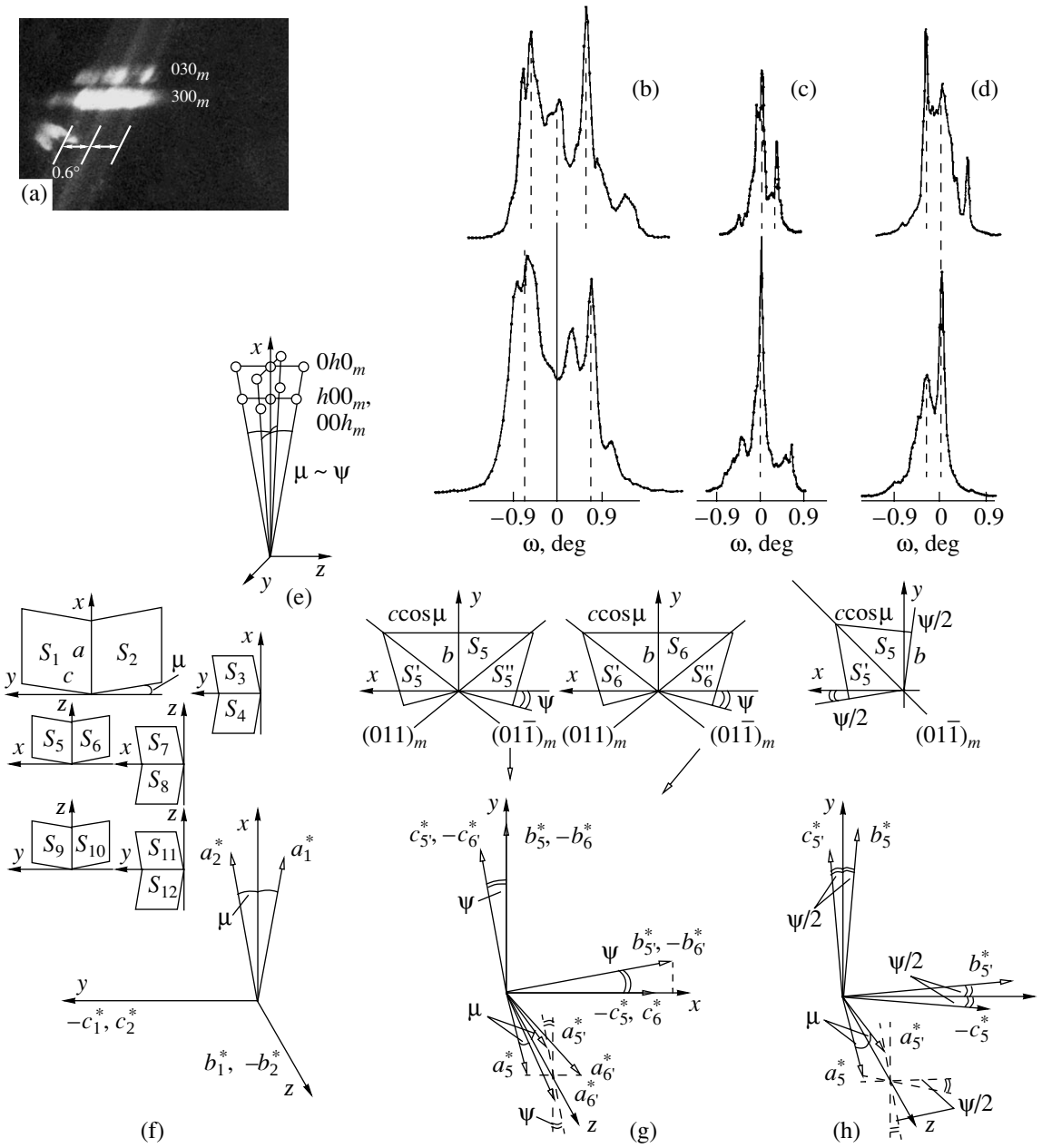

Fig. 1. (a–d) Experimental splittings of the *h*00 reflections and (e–h) splitting schemes of the reciprocal lattice points for $Na_{1-x}Li_xNbO_3$ crystals. (a) The 300 reflection in the Weissenberg photograph of a zero layer line upon rotation of the crystal around the [010] axis ($x \approx 0.012$). (b–d) Fragments of the X-ray diffraction patterns (ω scan mode) for the 020_m (at the top) and 200_m (at the bottom) reflections of crystals (b) **II** and **I** at $x \approx$ (c) 0.02 and (d) 0.04. Dashed lines indicate the origin of the coordinates and the peaks corresponding to the twin components. (e) Typical splitting diagram of the *h*00 points. (f–h) Twin complexes (at the top) with the twining planes (f) (100) and (g, h) $(011)_m$ and $(01\bar{1})_m$ for the components S_5 and S_6 at (g) $(001)_m \parallel (100)$ and (h) $(01\bar{1})_m \parallel (1\bar{1}0)$ and the corresponding orientations of the reciprocal vectors (at the bottom) for (f) the components S_1 and S_2 and (g, h) upon twinning along the $(01\bar{1})_m$ plane.

monoclinically distorted cells in such a way that the **a** axes in the contiguous domains lie in the twinning plane. Each complex brings about the splitting of the $h00_m$ point lying along the direction perpendicular to the twinning plane into two points. In this case, the **a*** axes of the components make the angle 2μ, and the other points $00h_m$ and $0h0_m$ located on the perpendicular coordinate axes remain nonsplit. Additional splitting of the *h*00 points occurs through the components *S*' and *S*'' arising upon twinning along the $(011)_m$ planes

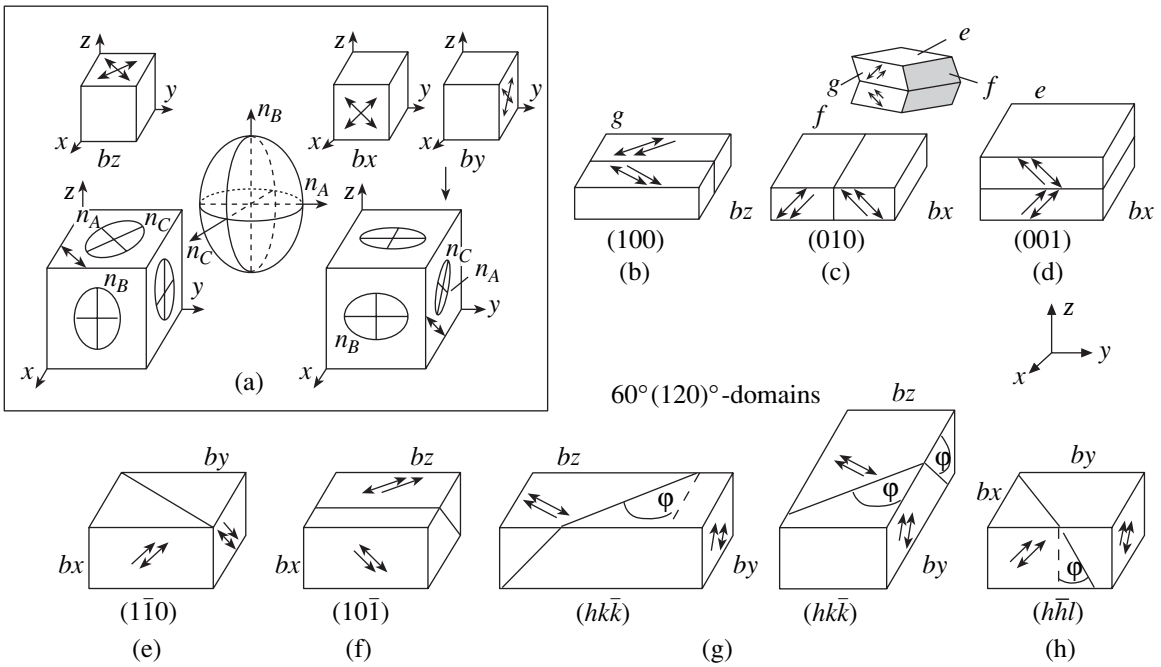

Fig. 2. (a) Optical indicatrix and types of domains at different extinction positions for the parallel polarized light (arrows indicate the possible orientations of the vectors $\mathbf{P}_s$ or $\pm\mathbf{P}_s$). (b–h) Main types of boundaries for 90° and 60° (120°) domains in the orthorhombic phase with a monoclinically distorted perovskite subcell (three different types of surfaces denoted as *g*, *e*, and *f* according to the notation proposed by Wood *et al.* [11] are represented for 90° domains).

(60° and 120° ferroelectric or antiferroelectric domains), as can be seen, for example, for the complexes S_5 and S_6 in Fig. 1g. These planes in the contiguous 90° domains are parallel to each other and belong to the same $[100]_m$ zone with the twining plane $(001)_m$ but do not coincide with the corresponding planes of the cubic phase. The angle ψ can be calculated from the formula $\psi = 2\arctan(c\cos\mu/b) - 90°$. Since we can write the approximate equality $\psi \approx \mu \approx 0.6°$ for NLN crystals in the concentration range studied (see table) and an insignificant deviation of the vectors **a*** of the components *S*' and *S*" from the coordinate planes can be ignored, the splitting of the *h*00 point for the above six complexes each in the case of twinning along the $(011)_m$ planes can be represented by the schematic diagram depicted in Fig. 1e. The experimental patterns of diffraction reflection splitting (Figs. 1a–1c) contain reflections from part of the components shown in Fig. 1e. Similar patterns of the reflection splitting were also observed earlier for a number of crystals of the perovskite type, KDP, etc. [24–27]. The other possible $(110)_m$ planes that can be involved in the formation of 60° domains are not parallel for components of the complex with the $(001)_m$ twinning plane and bring about the formation of incoherent strained boundaries.

The experimental angular splittings $\Delta\omega \approx 0.3°$ are explained by the twinning along the $(011)_m$ planes, which coincide with the (110) planes of the cubic cell of the prototype phase (Figs. 1d, 1h). In this case, the angle of the deviation of the vectors **b*** and **c*** from the coordinate axes is equal to $\psi/2$ and, correspondingly, the splitting shown in Fig. 1e should increase by $\Delta\omega \approx 0.3$. The twinning planes $(011)_m \parallel (110)$ are characteristic of distortions at which the cubic lattice transforms into the tetragonal lattice [27]. However, the tetragonal phase in NLN and NN crystals is observed at higher temperatures [2, 7]. The existence of the aforementioned planes can be due to a specific structural "memory" fixed by the defects. Note that, unlike the idealized schemes depicted in Figs. 1e–1h, the real crystals are characterized by more complex patterns associated with different-type defects (Figs. 1a–1d).

MICROSCOPIC INVESTIGATIONS OF THE DOMAIN STRUCTURE

Now, we assume that the *z* axis of the chosen coordinate system is perpendicular to the observation plane, i.e., to the developed face of the plate. According to the optical indicatrix whose axes coincide with the axes of the orthorhombic cell ($n_B > n_C > n_A$ for the NN crystal [28, 29]) and the extinction positions in the polarized light with crossed nicols, the domains observed can be classified into two types (Fig. 2a): the *bz* ($b \parallel z$) domains with the vectors $\mathbf{P}_s(\pm\mathbf{P}_s)$ parallel to the observation plane and the *bx* ($b \parallel x$) and *by* ($b \parallel y$) domains with the vectors $\mathbf{P}_s(\pm\mathbf{P}_s)$ parallel to the *xz* and *yz* plane, respectively. The *bz* domains are characterized by an extinction that is symmetric with respect to the crystal face-

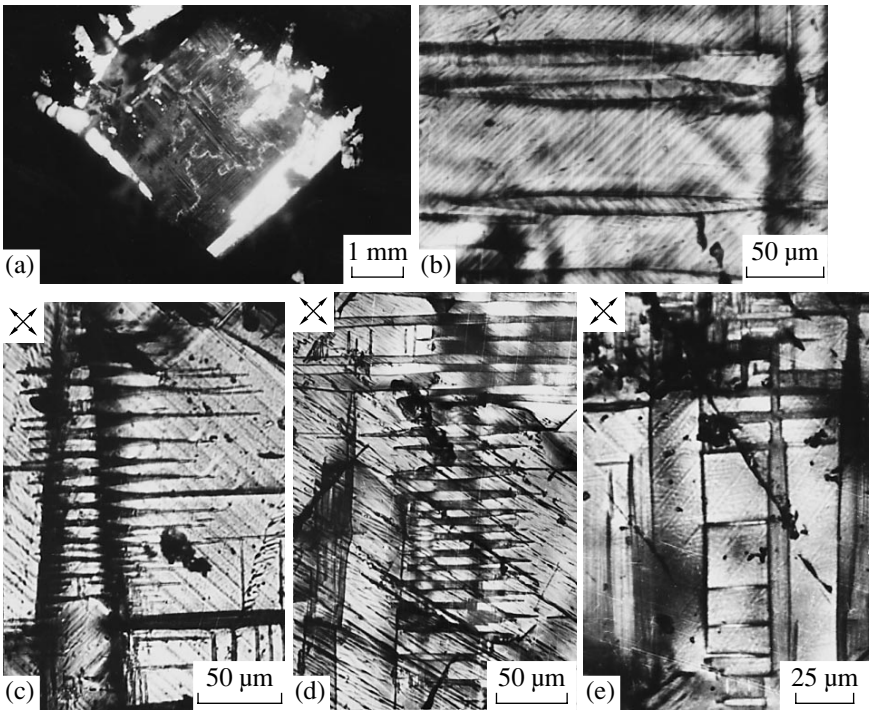

Fig. 3. (a) Micrograph of the crystal ($x \approx 0.012$) with strained bright boundaries. Typical configurations of the tapered lenslike 60° (120°) *bx* and *by* domains formed in crystals with $x \approx$ (b) 0.02 (*M*4 phase), (c) 0.037 (*M*2 phase), (d) 0.012 (*M*4 phase), and (e) 0.04 (*M*2 phase).

ting {100}, and the *bx* and *by* domains give the parallel extinction. The possible boundaries between the contiguous domains are determined by symmetry and the conditions of mechanical matching [30–32]. With the use of the data obtained in earlier investigations of the domain structure of the NN crystals and the observations of the present work, the main types of the 90°, 60°, and 120° domain boundaries that differ in orientation with respect to the observation plane are schematically represented in Figs. 2b–2h. The (*hhl*) and (110) boundaries are noncharged for the 60° and 120° ferroelectric domains, respectively.[5] The former boundaries are *S*-type boundaries with temperature-dependent Miller indices [31].

Optical observations of the domain structure revealed that the complexes of 90° laminar domains are predominant in crystals **I**, as is the case with NN crystals [11, 28, 33]. It is evident that the presence of complexes with different orientations of boundaries leads to the appearance of considerable mechanical stresses. The crystals are composed of separate blocks of domains whose sizes vary, on average, from 20 to 150 μm. The blocks often have strained boundaries that are sometimes bright when observed with a polarizing microscope at the extinction position (Fig. 3a). The width of the domains in 90° complexes is equal to 20 μm or less. A high density of boundaries and the development of tapered forms and intersections are characteristic of the domain structure. This complex domain structure is formed during the preparation of the crystals due to the phase transitions that occur under extremely nonequilibrium conditions arising at the instant of melt pouring: the occurrence of large temperature gradients, the formation of complex phase fronts, and their propagation over the crystal. Below, we will consider the domain configurations most frequently observed in the crystals under investigation.

Figures 3b–3e show the typical regions of interaction between the *bx* and *by* domains observed in the *M*4 and *M*2 phases. The wedge-shaped, relatively wide (10–70 μm) regions of polysynthetically twinned 90° domains 15 μm in size can be seen in Fig. 3b. The region of the 90° *bx* domains alternates with the region of the 90° *by* domains, which are the 60° domains with respect to the former domains and form curved distorted boundaries along the (110) planes. These domains correspond to the 90° complexes separated by the $(011)_m$ boundaries shown in Fig. 1g. The 60° and 120° domains are often formed at the grain boundary junctions (Figs. 3c, 3d). As is known, this is one of the factors that favor a decrease in the elastic energy with the formation of small-sized tapered domains and zigzag boundaries. There are lenslike domains extended along the [110] directions, which most likely have no

[5] In this work, we are dealing with regular domain structures and typical domain configurations; however, the experimental data have defied unambiguous interpretation. For this reason, hereafter, the domain structure in the ferroelectric *M*2 phase will be described in terms of 60° or 120° domains for noncharged boundaries.

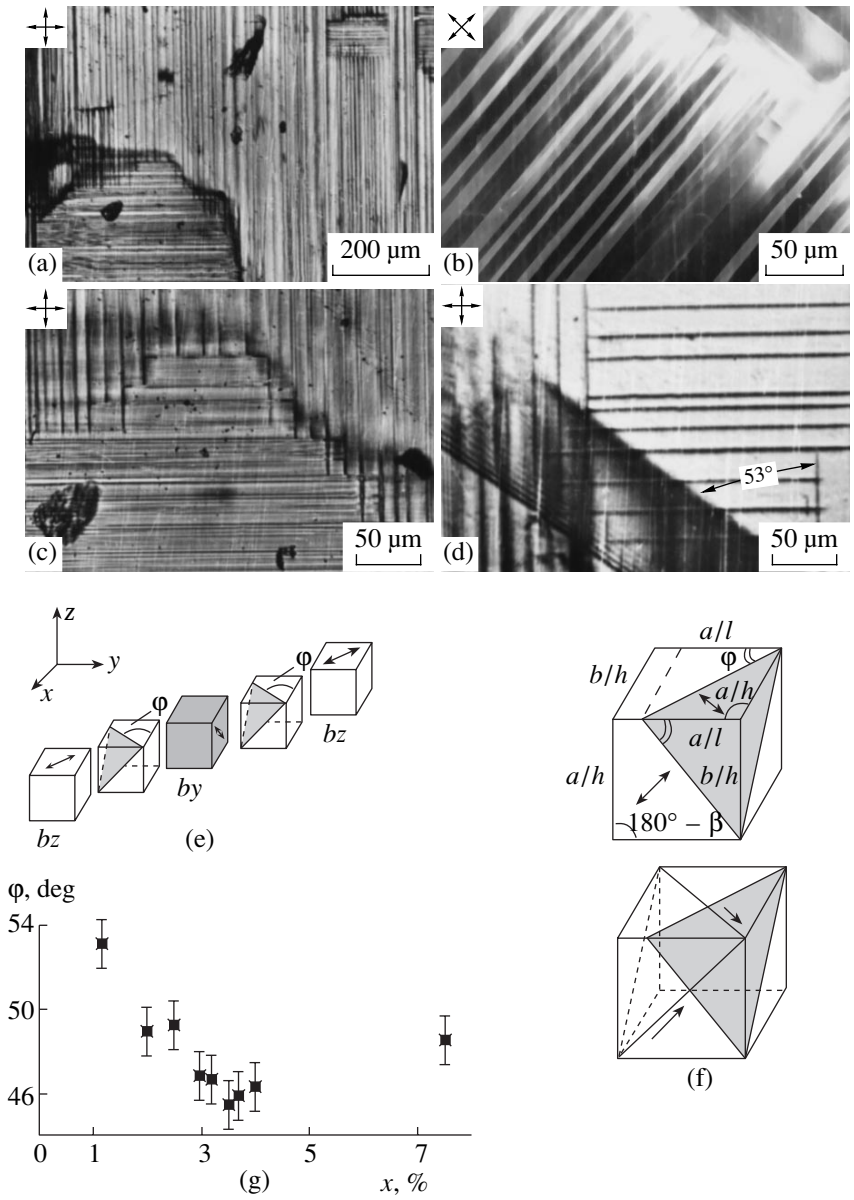

Fig. 4. (a–c) Micrographs of 90° *bz* domains: (a) large-sized regions with mutually perpendicular (100) boundaries, (b) the region of 90° *bz* domains at the extinction position, and (c) the boundaries between the regions of 90° domains. (d) Micrograph of the *hhl* tilt boundaries between the *bz* and *by* domains and (e) scheme of their orientation ($x \approx 0.012$, *M*4 phase). (f) Scheme of the orientation of the *hhl* boundary for the antiferroelectric (at the top) and ferroelectric (at the bottom) phases. (g) Calculated dependence of the angle φ on the concentration *x* for $Na_{1-x}Li_xNbO_3$ crystals.

time to collapse upon sharp cooling of the crystals. An increase in the concentration *x*, i.e., in the volume of the ferroelectric phase is attended by an increase in the volume fraction of 120° tapered domains in the crystals (Fig. 3e).

Figure 4a shows large-sized regions of polysynthetic laminar 90° *bz* domains with mutually perpendicular boundaries (100) and (010), which correspond to the complexes depicted in Fig. 1f. At the extinction position, the contiguous 90° domains are not extinct at once due to the low monoclinic distortion of the cell (Fig. 4b). The blocks form boundaries along the (100) planes or stepped boundaries that have an arbitrary orientation and involve mutually intersected regions with wedging-out of individual domains and planar regions of the (100) type (Fig. 4c). The resulting boundaries are incoherent and should contain strongly distorted structural regions in boundary layers. These boundaries are sometimes bright at the extinction position. It can be believed [26] that the relaxation of stresses along these boundaries is provided by transition regions with an intermediate orientation of lattices.

The bright region of *bz* domains with wedged narrow regions of 90° *bz* domains in the form of mutually

perpendicular dark stripes can be seen in the micrograph represented in Fig. 4d. At the bottom of this figure, we can see the wide dark region (with bright *bz* domains against its background) characterized by the *hhl* boundaries. This can be judged from the angle (equal to 53°) formed by the boundary trace on the surface with the [100] direction and also from the interference fringes arising from a boundary tilt. The value of *h*/*l* can be calculated using the formula derived from the coherence condition for domains that are in contact at a planar boundary [34]; that is,

$$h/l = (\eta_a^2 - \eta_b^2 + \eta^2)/4\eta\eta_a, \quad (1)$$

where $\eta_a - 1$, $\eta_b - 1$, and η are the components of the strain matrix describing the distortion of the cubic lattice. Substitution of $\eta_a = a\cos(\mu/2)/a_0$, $\eta_b = b/a_0$, and $\eta = a\sin(\mu/2)/a_0$ (where $\mu = (\beta - 90°)$), $a_0 = V^{1/3}$, and V is the perovskite cell volume) gives

$$h/l = (a^2 - b^2)/(2a^2\sin\mu). \quad (2)$$

As can be seen from Fig. 4f, formula (2) has a simple geometric meaning and can be reduced to an equality between the magnitudes of the lattice vectors (for the contiguous domains) parallel to the boundary trace on the faces with a mixed extinction; that is,

$$(a/l)^2 + (b/h)^2 = (a/h)^2 + (a/l)^2 - 2a^2\cos(180° - \beta)/(hl). \quad (3)$$

The dependence of the angle φ of the boundary orientation on x [where $\varphi = \arctan(bl/(ah))$] according to the data presented in the table is plotted in Fig. 4g. The angles φ calculated by formula (2) are very close to those calculated from the relationship $\varphi = \arctan(2d'/3b')$, where $b' = (a\cos(\mu/2) - a_0)/a_0$ and $d' = \tan(\mu/2)$ [32], in which the first orders of the distortions are taken into account. A similar boundary with $\varphi = 54°44'$ was observed in the NN crystals [29, 35, 36].[6] Zhelnova and Fesenko [35] were the first to observe a change in the orientation of this boundary with a variation in the temperature. The indices of the boundary were not determined. In [29], the authors assigned irrational indices to this boundary at room temperature. However, the calculation of the ratio *h*/*l* according to the aforementioned formula for φ leads to the indices (7.7.10).

On this basis, we constructed the scheme (Fig. 4e) illustrating the orientation of the *hhl* boundary observed in the crystal (Fig. 4d) and the directions of the vector $\pm\mathbf{P}_s$. The ratio *h*/*l* calculated for this boundary is equal to 0.746, which, taking into account the error, corresponds to the (334) plane.

[6] The direction of the vector $\pm\mathbf{P}_s$ is not always correctly given in the twin structure schemes reported in [29, 36] (the angle $\varphi \approx 54°$ on the *ab* face should be subtended by the *b* axis), whereas the experimental conoscopic patterns obtained in [29] correspond to the scheme depicted in Fig. 4f.

The crystal region with a mixed extinction can be seen at the center in Figs. 5a and 5b. The observed domain structure, as a whole, is explained by the scheme displayed in Fig. 5c. The large-sized prismatic *bz* domains of the order of 50 μm wide are contiguous with the *bx* and *by* domains, which are the 60° domains with respect to the *bz* domains. The (011) and (111) inclined planes bound the connected region of the *bz* domains and are responsible for the interference fringes at the boundaries. The surface is smooth in the region that is contiguous with the *bz* domains. Note that this region is slightly bright at the extinction position. As was noted by Wood *et al.* [11] for the NN crystals, a similar effect is characteristic of the *e* surfaces (Fig. 2e) and can be associated with lattice deformations in the vicinity of 90° boundaries parallel to the observation plane. Microcracks are observed at the *SS*" boundary between the 90° complexes of the *bx* and *by* domains. This boundary corresponds to the aforementioned incoherent 60° $(110)_m$ boundary between the complexes of 90° domains. The (111) boundary is the (*hhl*) boundary with the angle $\varphi \approx 45°$ (see Fig. 4g, $x \approx 0.03$). Zigzag boundaries formed by these planes between the 90° *bz* and *by* (*bx*) complexes frequently occur in the *M*2 and *M*4 phases in boundary regions between large-sized domain complexes. For example, the small-sized laminar *bz* domains, which, together with 90° *bx* domains, form the 60° boundaries whose trace on the crystal surface makes an angle of approximately 45° with the boundaries of the 90° domains, can be seen in the micrograph of the crystal (Fig. 5d) in the region with a mixed extinction. At the parallel position, numerous interference fringes indicating the boundary tilt are observed in the region of the *bz* domains. The scheme for the formation of these domain configurations for noncharged boundaries is represented in Fig. 5e. Similar boundaries were observed by Chen and Feng [12] in the *Q* phase of the NN crystals.

Figure 6 shows the electron micrographs of the etched surfaces of the (100) cleavages of crystals **II**. As could be expected, the domain structure of these crystals is less complex and more regular than that of crystals **I**. We examined three mutually perpendicular (100) cleavages parallel and perpendicular to the boule axis. It should be noted that the domain structures observed on these surfaces are characterized by different main structural motifs. The layered structures (with a layer thickness of 0.1 μm or less) oriented, for the most part, normally to the boule axis can be seen in the cleavages parallel to the boule axis. As follows from the etch relief, these cleavages correspond to the *f* (Fig. 6a) and *g* (Fig. 6b) surfaces of the 90° domains. The region of intersection between the orthogonal complexes of the 90° domains can be seen at the top left of Fig. 6b. This region is similar to those observed in Fig. 4c. The cleavage perpendicular to the boule axis (Fig. 6c) predominantly corresponds to the *e* surface. The cleavage fragment in which the *f* surface is dominant is displayed in Fig. 6d. We can see the layers of 90° domains with the

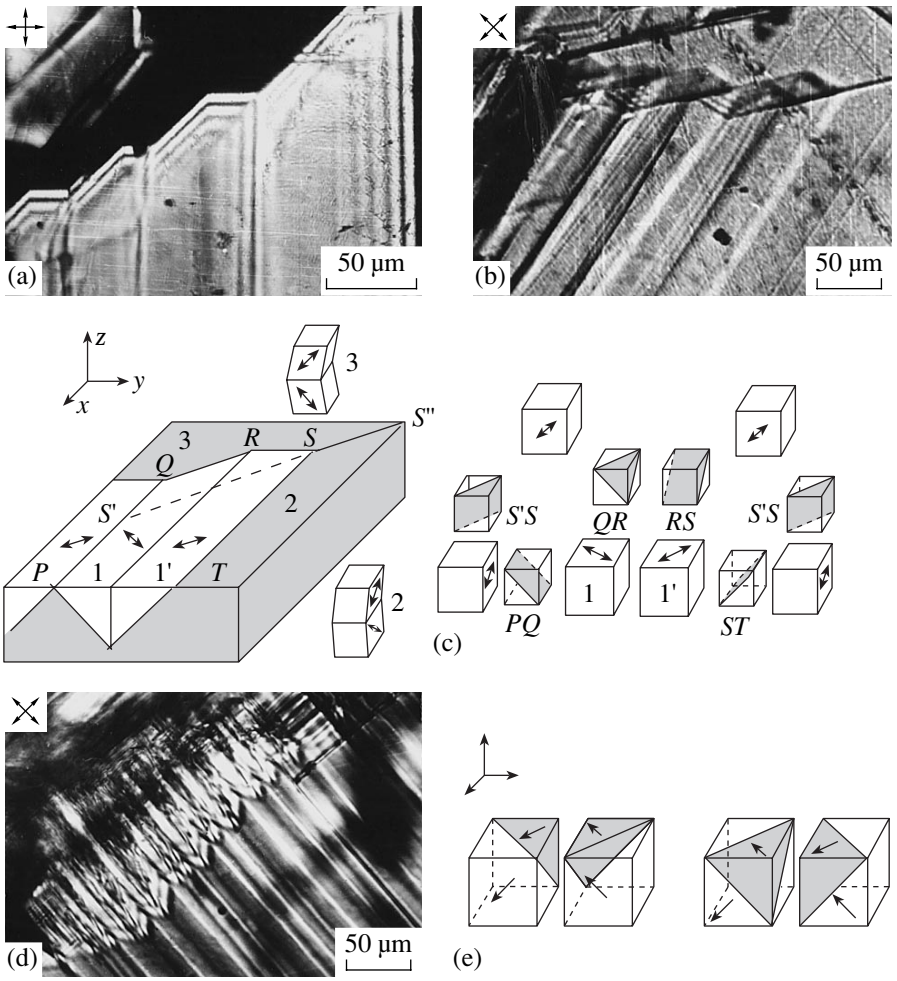

Fig. 5. (a, b) Micrographs of prismatic *bz* domains with the (110) and (111) tilt boundaries in the region with a mixed extinction ($x \approx 0.03$, *M*4 phase) and (c) scheme for the formation of the domain structure observed. (d) Micrograph of the zigzag boundaries between the 90° complexes of the *bz* and *bx* domains ($x \approx 0.04$, *M*2 phase) and (e) scheme for the formation of these configurations.

$(001)_m$ boundaries, which are transversely crossed by the 180° $(010)_m$ walls or 180° wedges. In the last case, the boundaries should involve charged regions, because only the $(010)_m$ plane is parallel to the vectors $\mathbf{P}_s$ in the contiguous 90° domains. The alternation of 180° $(010)_m$ walls results in the formation of specific staggered structures (Figs. 6e, 6f). The boundaries between the smooth surface and the region of the 90° domains whose traces are parallel to their 90° boundaries can be seen in Fig. 6d. Most likely, these are the traces of the (100) boundary that connects the orthogonal complexes of the 90° domains (Fig. 4c).

The micrographs of the ceramic samples cleaved parallel to the direction of the pressure applied in the course of hot pressing are represented in Fig. 7. The cleavage surface is rough and, as a rule, has a stepped structure. There are 60°, 120°, 90°, and 180° domains. As in the case of single crystals, the domain structure is predominantly built up of blocks consisting of laminar 90° domains with (100) boundaries (Figs. 7a–7c). The mean width of the laminar domains varies from 0.05 to 0.5 μm, and the domains form boundaries along the (110) planes. These boundaries can be seen at the center of Fig. 7a and at the left of Fig. 7b in the oblique section close to the (111) plane. The tendency of the twinning planes (100) of the laminar arrays of 90° domains to be arranged along the same direction is observed in certain cleavages (Fig. 7c). This correlates with the X-ray diffraction data obtained, according to which the X-ray diffraction patterns of the cleavages parallel and perpendicular to the direction of the applied pressure are often characterized by the textures along the $[010]_m$ and $[100]_m$ directions, respectively (Fig. 1g). This is consistent with the fact that a number of crystal grains, in accord with the Le Chatelier principle, tend to have such an orientation that the axis corresponding to the smallest parameter of the perovskite cell is parallel to the direction of the pressure applied in the course of hot pressing. Possibly, this was the reason for the anisotropy previously revealed in the properties of NN-based ceramic materials in the directions per-

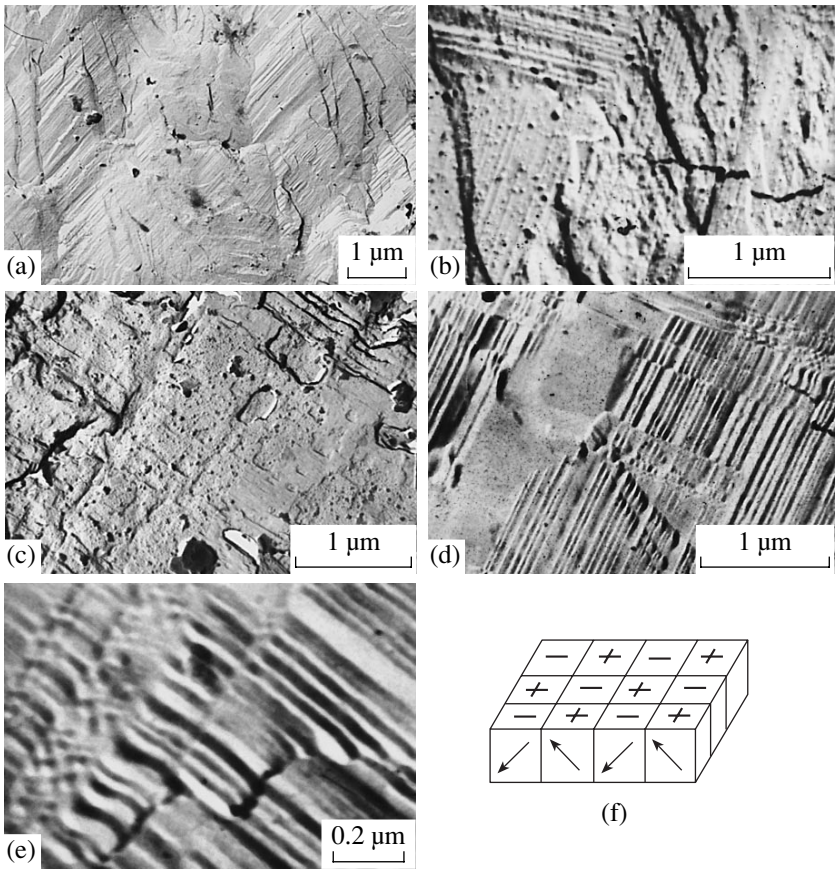

Fig. 6. Micrographs of the domain structure on the cleavages of crystals **II**: (a) the *f* surface and (b) the *g* surface of the (100) cleavages parallel to the boule axis, (c) the *e* surface of the cleavage perpendicular to the boule axis, and (d, e) fragments of the 90° and 180° domain structures on the cleavage parallel to the boule axis. (f) Scheme of staggered configurations formed upon intersection of 90° domains by 180° domain walls.

pendicular and parallel to the direction of the pressure applied [37, 38].

The 180° domain structure (Fig. 7d) manifests itself beginning with $x = 0.02$ and is similar to the domain structures observed for crystals **II** (Figs. 6d, 6e). On the whole, the 180° domain structure is characterized by a small scale and can only sometimes be seen on the cleavage surfaces. The very small-scale regular structure can also be seen in Fig. 7e. This structure can correspond either to a staggered 180° domain structure or to the alternation of 120° domains with the (110) boundaries.

As the concentration x increases, there appears a tendency toward an increase in the size of crystal grains and, as in the case with crystals **I**, toward a decrease in the volume occupied by the complexes of 90° domains. In the concentration range under investigation, the grain size varies up to 18 μm and, on average, is of the order of 4 μm. Starting with $x = 0.10$, the rough surfaces are observed in large-sized grains. These surfaces are formed upon cracking in the grain bulk, appear as fan-shaped divergent stripes, and are associated with a high density of dislocations in these regions (Figs. 7b, 7f, on the right). Edge splitting is frequently observed at the boundaries of these regions, which suggests high stresses arising at the boundaries. On the whole, the degree of structure imperfection increases in this concentration range close to the solubility limit of lithium and to the narrow range of the existence of the rhombohedral phase [13, 14]. An increase in the grain size often leads to the spontaneous destruction of the ceramic samples, as was noted by Reznichenko *et al.* [39, 40], who studied the influence of this factor and the decrease in the volume concentration of 90° domains in samples on the strength characteristics of ceramic materials.

The interlayers forming double boundaries between grains are observed in certain cases. For example, such an interlayer (indicated by the arrow) in the form of a dark stripe can be seen at the boundary of a cuboctahedral grain in Fig. 7h. These interlayers correspond to the phase that is in the liquid state during the sintering of the ceramic sample. As was previously found in [41], the formation of this phase is characteristic of ceramic materials based on alkali metal niobates in distinction to PZT-based ceramic materials.

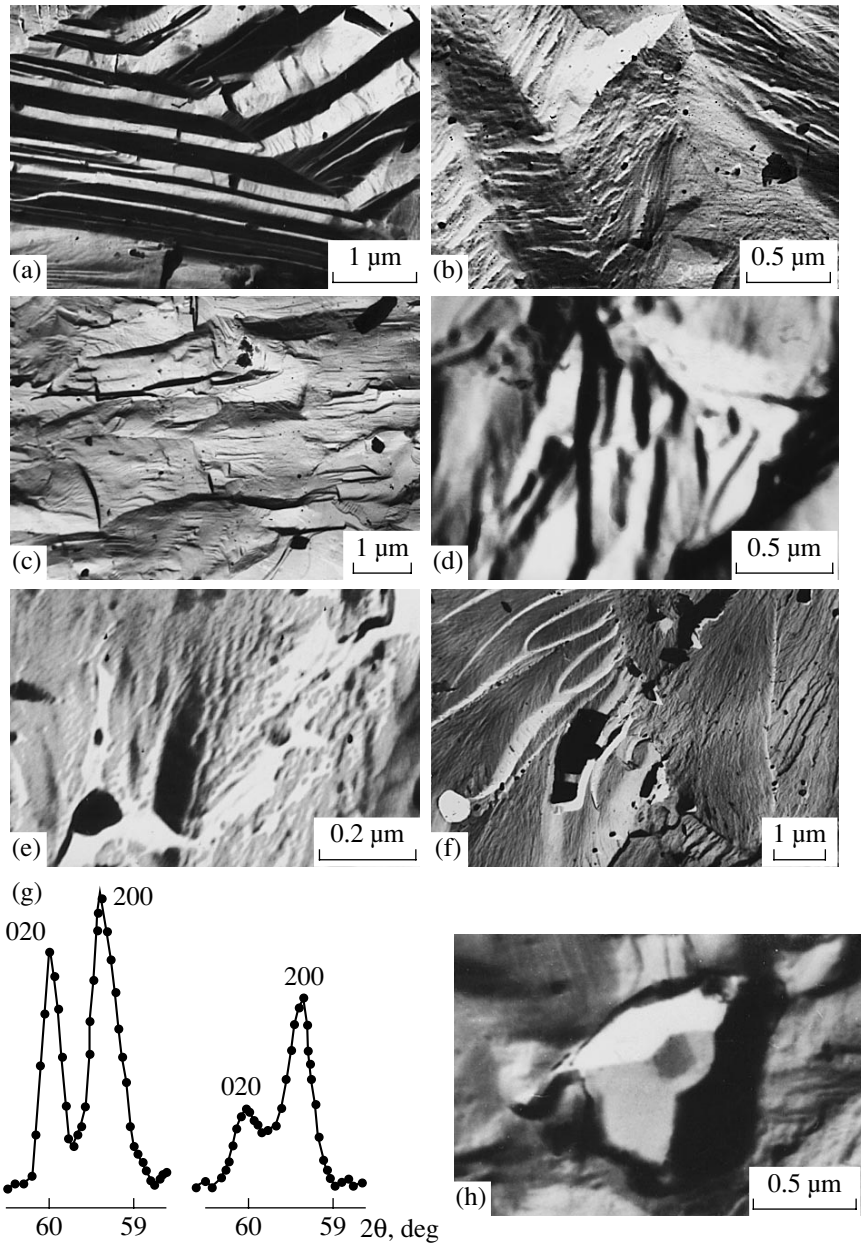

Fig. 7. (a–f, h) Micrographs of the cleavages of $Na_{1-x}Li_xNbO_3$ hot-pressed ceramic samples at concentrations x = (a) 0.0225, (b) 0.1025, (c) 0.04, (d) 0.02, (e) 0.03, and (f, h) 0.014. (g) X-ray diffraction profiles for the cleavages perpendicular (on the left) and parallel (on the right) to the direction of the pressure applied in the course of hot pressing for the sample with x = 0.04.

CONCLUSIONS

Thus, in this work, we investigated the domain structures of hot-pressed ceramic materials and crystals grown using the flux and Czochralski methods. The preparation conditions and the solid state of these objects differ significantly. However, their domain structures have a common feature, namely, the predominance of the regions composed of polysynthetic lamellar twins (90° domains) with the specific orientation $[(001)_m \parallel (001)]$ relative to the lattice of the initial cubic phase, which is characteristic of materials undergoing martensitic phase transitions [42]. With an increase in x and the relative concentration of the $M2$ phase, there is a tendency for the volume occupied by the tapered 120° domains with (110) boundaries to increase.

It was found that the matching of the complexes of the 90° domains is characterized by the following specific features. The (100) and (011) boundaries between these domains occur most frequently. The $(011)_m$ and $(110)_m$ planes [at the 90° $(001)_m$ boundary] are not equivalent with respect to the formation of the 60° and 120° boundaries between the complexes in contrast with single domains. The former plane is coherent, whereas the latter plane is incoherent. Boundaries of

the former type (planar or strained, curved in the elastic strain field of contiguous regions) are universal in occurrence. Boundaries of the latter type are very rarely observed, and microcracks are formed along these boundaries. Instead of these boundaries, the 90° complexes are often characterized by *hhl* boundaries (in combination with $(011)_m$ boundaries) or zigzag *hhl* boundaries. The above features are responsible for the particular splittings of the reflections in the X-ray diffraction patterns of the crystals under investigation. These splittings correspond to a set of orientational states that restore the *m*3*m* symmetry of the prototype phase.

The *hhl* boundaries in NLN crystals were observed in our work for the first time. The concentration dependence of the orientation of these boundaries was calculated from the parameters of the perovskite cell. This dependence is in good agreement with the experimental data. Note that, when the angle of the spontaneous displacement obeys the relationship $2\sin\mu \geq 1 - (b/a)^2$ [see formula (2)], we have $h/l \leq 1$, which holds for the studied crystals. If the above relationship is not satisfied, we obtain $h/l > 1$. The latter case is true for $KNbO_3$ crystals, in which the (772) and (331) boundaries were observed by Chen *et al.* [43].

The 180° domain boundaries corresponding to the ferroelectric *M*2 phase were observed in the crystals grown by the Czochralski method and the ceramic samples. As was noted above, the X-ray diffraction data obtained for the ceramic samples indicate the presence of the *M*2 phase beginning with $x = 0.032$. At the same time, the results of electrical measurements demonstrate the existence of ferroelectric clusters even at $x \geq 0$ [15]; moreover, the macroscopic ferroelectric properties manifest themselves at $x > 0.015$ [13, 14]. An examination of the cleavages of the ceramic samples revealed that the 180° domain structure is observed beginning with $x = 0.02$. Note that, in the *P* (*M*4) phase of the NN (NLN) compounds, the atomic structure along the **b** axis is characterized by the alternation of pairs of octahedra rotated about this axis in different directions. This alternation of the octahedron pairs coincides with the alternation in the directions of displacements of Nb ions along the **A** axis. The breaking of the strict order in the alternation can lead to the structure of the ferroelectric *Q* (*M*2) phase, in which the octahedra are rotated in the same direction and Nb ions are displaced unidirectionally [7–9]. Chen and Feng [12] observed satellite reflections along the **b*** direction of the reciprocal lattice due to the translational domain walls in the *P* and *Q* phases. These structural distortions can be responsible for the formation of ferroelectric phase microregions at low concentrations *x* whose existence is indicated by the results of electrical measurements. As the concentration *x* increases, the *M*2 phase becomes stable and these microregions grow and transform into macroregions. At concentrations below $x = 0.032$, the volume of the ferroelectric phase is too small to be recorded by the X-ray methods. However, this phase already manifests itself in the form of the 180° domain structure on the cleavages of the ceramic samples. It should be noted that the density of the 180° domain walls increases with an increase in the concentration *x* but remains very low compared to the density of non-180° boundaries. This confirms the data obtained by Fesenko *et al.* [44], who, judging from a decrease in ε upon polarization, made the inference that domain orientations differing from the 180° orientation are predominant in NN-based solid solutions. In our single crystals grown by the flux method, the 180° domain structure was not observed even in the concentration range in which the *M*2 phase is predominant according to the X-ray diffraction data. This can be explained by the fact that the 180° domain structure is of very small scale and cannot be seen with the use of optical methods. Possibly, this situation is associated with the high electrical conductivity (up to 10^{-4}–$10^{-2}\ \Omega^{-1}\ cm^{-1}$) of the crystals under investigation as compared to the conductivity of the crystals grown by the Czochralski method and the ceramic samples (10^{-10}–$10^{-13}\ \Omega^{-1}\ cm^{-1}$) and also with the influence of screening. Such an electrical conductivity is characteristic of the NN crystals prepared using a $NaBO_2$ solvent [21].

The data for NLN crystals (with $x = 0.02$–0.03) grown using the flux [18, 19] and Czochralski [20] methods are available in the literature. As was noted above, the experimental data on the pyroelectric current along the **b** axis [19, 20] and the hysteresis loops [20], as well as the observations of the domain structure in electric fields [18] allowed these authors to draw the conclusion that spontaneous polarization $\boldsymbol{P}_s$ is present, i.e., that the *M*4 phase in the NLN compounds is ferroelectric. Note that the spontaneous polarizations $\boldsymbol{P}_s$ determined in [19] and [20] differ by one order of magnitude (25 and 2.5 $\mu C/cm^2$, respectively). The polarization $\boldsymbol{P}_s$ obtained in [19] exceeds the polarization $\boldsymbol{P}_s$ in the *Q* phase of the NN compound ($\approx$10 $\mu C/cm^2$ [45]). It should be noted that the anomalies in the temperature dependences of the permittivity $\varepsilon(T)$ for our crystals upon phase transitions agree with the data reported by Zhong *et al.* [20]. In particular, unlike the results obtained in [19], the maximum in the dependence $\varepsilon(T)$ in the vicinity of 350°C upon phase transition between the orthorhombic phases is well defined and is not smeared. This suggests a high concentration of defects in the crystals studied in [18, 19]. Since the crystals investigated in the present work were similar in their properties to the crystals obtained in [20], we quite possibly did not observe etch patterns associated with $\mathbf{P}_s \parallel \mathbf{b}$ due to the low spontaneous polarization P_s. However, it cannot be ruled out that the effects indicating this polarization are associated with the heterophase structure of the crystals under consideration and their inhomogeneity, as was repeatedly noted earlier for NN crystals [10, 12, 46].

ACKNOWLEDGMENTS

This work was supported by the Russian Foundation for Basic Research, project nos. 99-02-17575 and 02-02-17781.

REFERENCES

1. G. A. Smolenskiĭ, V. A. Bokov, V. A. Isupov, N. N. Kraĭnik, R. E. Pasynkov, A. I. Sokolov, and N. K. Yushin, *The Physics of Ferroelectric Phenomena* (Nauka, Leningrad, 1985).
2. H. D. Megaw, Ferroelectrics **7**, 87 (1974).
3. N. N. Kraĭnik, Izv. Akad. Nauk SSSR, Ser. Fiz. **22**, 1492 (1958).
4. T. Nitta, J. Am. Ceram. Soc. **51** (11), 626 (1968).
5. L. A. Shilkina, L. A. Reznichenko, M. F. Kupriyanov, and E. G. Fesenko, Zh. Tekh. Fiz. **47** (10), 2173 (1977) [Sov. Phys. Tech. Phys. **22**, 1262 (1977)].
6. L. A. Shilkina, I. V. Pozdnyakova, L. A. Reznichenko, *et al.*, in *Proceedings of the 8th International Meeting on Physics of Ferroelectrics–Semiconductors (IMFS-8), Rostov-on-Don, 1998*, p. 190.
7. E. S. Gagarina, L. A. Shilkina, L. A. Reznichenko, *et al.*, Izv. Akad. Nauk, Ser. Fiz. **65** (6), 780 (2001).
8. A. C. Sakowski-Cowley, K. Lukaszewicz, and H. D. Megaw, Acta Crystallogr., Sect. B: Struct. Crystallogr. Cryst. Chem. **25**, 851 (1969).
9. V. A. Shuvaeva, M. Yu. Antipin, S. V. Lindeman, *et al.*, Ferroelectrics **141**, 307 (1993).
10. I. Lefkowitz, K. Lukaszewicz, and H. D. Megaw, Acta Crystallogr. **20**, 670 (1966).
11. E. A. Wood, R. C. Miller, and J. P. Remeica, Acta Crystallogr. **15**, 1273 (1962).
12. J. Chen and D. Feng, Phys. Status Solidi A **109**, 171 (1988).
13. L. A. Reznichenko and L. A. Shilkina, Izv. Akad. Nauk SSSR, Ser. Fiz. **39** (5), 1118 (1975).
14. L. A. Reznichenko and L. A. Shilkina, Zh. Tekh. Fiz. **47** (2), 453 (1977) [Sov. Phys. Tech. Phys. **22**, 272 (1977)].
15. L. A. Reznitchenko, A. V. Turik, E. M. Kuznetsova, and V. P. Sakhnenko, J. Phys.: Condens. Matter **13** (17), 3875 (2001).
16. R. H. Dungan and R. D. Golding, J. Am. Ceram. Soc. **47**, 73 (1964).
17. I. N. Pozdnyakova, L. A. Reznichenko, and V. G. Gavrilyachenko, Pis'ma Zh. Tekh. Fiz. **25** (18), 81 (1999) [Tech. Phys. Lett. **25**, 752 (1999)].
18. A. Sadel, R. von der Muhll, and J. Ravez, Mater. Res. Bull. **18**, 45 (1983).
19. A. Sadel, R. von der Muhll, J. Ravez, and P. Hagenmuller, Ferroelectrics **47**, 169 (1983).
20. W. L. Zhong, P. L. Zhang, H. S. Zhao, *et al.*, Phys. Rev. B **46**, 10 583 (1992).
21. O. A. Zhelnova, V. G. Smotrakov, I. P. Raevskiĭ, and E. G. Fesenko, Kristallografiya **28** (5), 1052 (1983) [Sov. Phys. Crystallogr. **28**, 623 (1983)].
22. R. R. Zeyfang, R. M. Henson, and W. J. Maier, J. Appl. Phys. **48** (7), 3014 (1977).
23. M. N. Palatnikov, K. J. Borman, and V. Samulyonis, Acta Univ. Latviensis **559**, 34 (1991).
24. V. Yu. Topolov, E. S. Gagarina, and E. S. Tsikhotskiĭ, Kristallografiya **37** (2), 439 (1992) [Sov. Phys. Crystallogr. **37**, 227 (1992)].
25. E. S. Gagarina, S. M. Zaĭtsev, V. Yu. Topolov, *et al.*, Kristallografiya **43** (3), 453 (1998) [Crystallogr. Rep. **43**, 415 (1998)].
26. S. Kh. Aknazarov, L. G. Shabel'nikov, and V. Sh. Shekhtman, Fiz. Tverd. Tela (Leningrad) **17** (1), 30 (1975) [Sov. Phys. Solid State **17**, 16 (1975)].
27. L. G. Shabel'nikov, V. Sh. Shekhtman, and O. M. Tsarev, Fiz. Tverd. Tela (Leningrad) **18** (6), 1529 (1976) [Sov. Phys. Solid State **18**, 889 (1976)].
28. F. Jona, G. Shirane, and R. Pepinsky, Phys. Rev. **97** (6), 1584 (1955).
29. O. A. Zhelnova, O. E. Fesenko, V. G. Smotrakov, and S. M. Zaĭtsev, Kristallografiya **28** (5), 932 (1983) [Sov. Phys. Crystallogr. **28**, 552 (1983)].
30. L. A. Shuvalov, Izv. Akad. Nauk SSSR, Ser. Fiz. **43** (8), 1554 (1979).
31. J. Fousek and V. Janovec, J. Appl. Phys. **40**, 135 (1969).
32. J. Sapriel, Phys. Rev. B **12** (11), 5128 (1975).
33. J. Dec, Cryst. Res. Technol. **18** (2), 195 (1983).
34. V. Yu. Topolov, L. E. Balyunis, A. V. Turik, and O. E. Fesenko, Kristallografiya **35** (3), 755 (1990) [Sov. Phys. Crystallogr. **35**, 441 (1990)].
35. O. A. Zhelnova and O. E. Fesenko, Fiz. Tverd. Tela (Leningrad) **27** (1), 8 (1985) [Sov. Phys. Solid State **27**, 4 (1985)].
36. J. Dec, Ferroelectrics **81**, 123 (1988).
37. I. P. Raevskiĭ and L. A. Reznichenko, Available from VINITI, No. 3251-78 (1978).
38. I. P. Raevskiĭ, L. A. Reznichenko, and A. N. Kalitvanskiĭ, Zh. Tekh. Fiz. **50** (9), 1983 (1980) [Sov. Phys. Tech. Phys. **25**, 1154 (1980)].
39. L. A. Reznichenko, V. A. Aleshin, V. A. Chernyshkov, *et al.*, in *Semiconductors–Ferroelectrics* (RGPU, Rostov-on-Don, 1994), Vol. 5, p. 123.
40. E. I. Bondarenko, V. A. Chernyshkov, and L. A. Reznichenko, in *"Piezoelectric Materials and Transducers:" Proceedings of the 1st Interdepartmental Workshop "Physics of Strength of Ferroelectrics and Related Materials," Rostov-on-Don, 1991*, p. 56.
41. L. A. Reznichenko, L. A. Shilkina, O. N. Razumovskaya, and V. A. Aleshin, in *"Semiconductors–Ferroelectrics": Proceedings of the 7th International Workshop on Physics of Ferroelectrics–Semiconductors* (Kniga, Rostov-on-Don, 1996), Vol. 6, p. 149.
42. A. L. Roĭtburd, Usp. Fiz. Nauk **113** (1), 69 (1974) [Sov. Phys. Usp. **17**, 326 (1974)].
43. J. Chen, W. Wang, Q. Li, and D. Feng, Cryst. Res. Technol. **23** (6), 747 (1988).
44. E. G. Fesenko, A. Ya. Dantsiger, L. A. Reznichenko, *et al.*, Zh. Tekh. Fiz. **52** (11), 2262 (1982) [Sov. Phys. Tech. Phys. **27**, 1389 (1982)].
45. L. E. Cross and B. J. Nicholson, Philos. Mag. **46**, 453 (1955).
46. R. C. Miller, E. A. Wood, J. P. Remeica, and A. Savage, J. Appl. Phys. **33** (5), 1623 (1962).

Translated by O. Borovik-Romanova

Crystallography Reports, Vol. 47, No. 6, 2002, pp. 991–995. Translated from Kristallografiya, Vol. 47, No. 6, 2002, pp. 1060–1064.

LATTICE DYNAMICS AND PHASE TRANSITIONS

Phase Transitions in Nonstoichiometric Strontium Tantalates with the Cryolite Structure[1]

I. E. Animitsa*, S. G. Titova, A. Ya. Neĭman*, N. A. Kochetova*, D. I. Bronin***, and E. V. Isaeva***

** Ural State University, pr. Lenina 51, Yekaterinburg, 620083 Russia*

*** Institute of Metallurgy, Ural Division, Russian Academy of Sciences, Yekaterinburg, Russia*

**** Institute of High-Temperature Electrochemistry, Ural Division, Russian Academy of Sciences, ul. S. Kovalevskoĭ 20, Yekaterinburg, 620219 Russia*

e-mail: irina.animitsa@usu.ru

Received January 10, 2002

Abstract—The structural transformations of $Sr_6Ta_2O_{11}$ and $Sr_{5.92}Ta_{2.08}O_{11.12}$ oxygen-deficient cryolites with variations in the partial pressures of oxygen $p(O_2)$ and water vapor $p(H_2O)$ are investigated using X-ray diffraction, thermogravimetry, and electrical conductivity measurements. It is found that a change in the oxygen partial pressure leads to a phase transition accompanied by the transformation of the cubic cell into the tetragonal cell, most probably, due to ordering of oxygen vacancies. The intercalation of water into the matrix of the complex oxides under investigation results in a structural–chemical transformation during which the solid solution undergoes a transition to an oxyhydrate phase of variable composition and the cubic cell transforms into the orthorhombic cell. © *2002 MAIK "Nauka/Interperiodica".*

INTRODUCTION

In recent years, oxygen-deficient complex oxides of the general formula $ABO_{3-\delta}$ with a perovskite-like structure have been investigated extensively, because these materials can possess a considerable oxygen ion conductivity at high temperatures and a protonic conductivity at low temperatures [1, 2]. The nature of the predominant charge carriers depends on the ambient conditions [*T*, $p(O_2)$, and $p(H_2O)$]. Within the quasi-chemical formalism, the formation of these carriers can be described by the following reactions of dissolution of oxygen or water vapors in the oxide, provided the matrix structure is retained:

$$1/2O_{2(g)} + V_O^{\bullet\bullet} \Leftrightarrow O_O^x + 2h^\bullet, \quad (1)$$

$$H_2O_{(g)} + V_O^{\bullet\bullet} + O_O^x \Leftrightarrow 2OH_O^\bullet, \quad (2)$$

where $V_O^{\bullet\bullet}$ is the oxygen vacancy, O_O^x is the oxygen atom at a regular lattice site, $OH_O^\bullet$ is the hydroxy group with an effective positive charge in the oxygen sublattice, and $h^\bullet$ is the hole. Consequently, the oxides can either absorb or release O_2 (or H_2O), depending on the partial pressure of oxygen (or water vapors) in the atmosphere.

In the general case, apart from the ambient conditions responsible for the charge carrier concentration, the degree of disordering δ of the oxide (concentration of oxygen vacancies) also directly correlates with the particular (oxygen ion or protonic) type of conduction. From this viewpoint, it is of interest to consider oxides with a large oxygen deficit for the purpose of attaining an appreciable degree of unipolar ionic conduction.

However, since the structure is capable of accumulating high concentrations of defects, the interaction of the oxide with components of the gaseous medium (O_2 and H_2O) can be accompanied by different phase transformations. In turn, these transformations can manifest themselves in an anomalous (i.e., nonlinear) behavior of the phase-sensitive properties.

Among the materials with a perovskite-like structure, there are oxygen-deficient cryolites (double perovskites) of the general formula $Me_6M_2O_{11}$, where *Me* is an alkaline-earth metal and *M* is Nb or Ta. The unit cell of these compounds contains four formula units ABO_3; hence, one in every twelve sites in the oxygen sublattice is unoccupied [3, 4]. It is these specific structural features that provide unipolar oxygen ion transfer at high temperatures in dry atmospheres and proton transfer at temperatures below 600°C in moist atmospheres [5, 6]. Therefore, by varying the thermodynamic parameters over a wide range, it is possible to determine the stability range of a particular structure, on the one hand, and to reveal the factors responsible for the formation of new structures, on the other.

In the present work, we elucidated how the changes in the temperature *T* and the partial pressures of oxygen $p(O_2)$ and water vapor $p(H_2O)$ affect the electrical and

[1] This paper was presented at the Symposium "Phase Transformations in Solid Solutions and Alloys," Sochi, Russia, 2001.

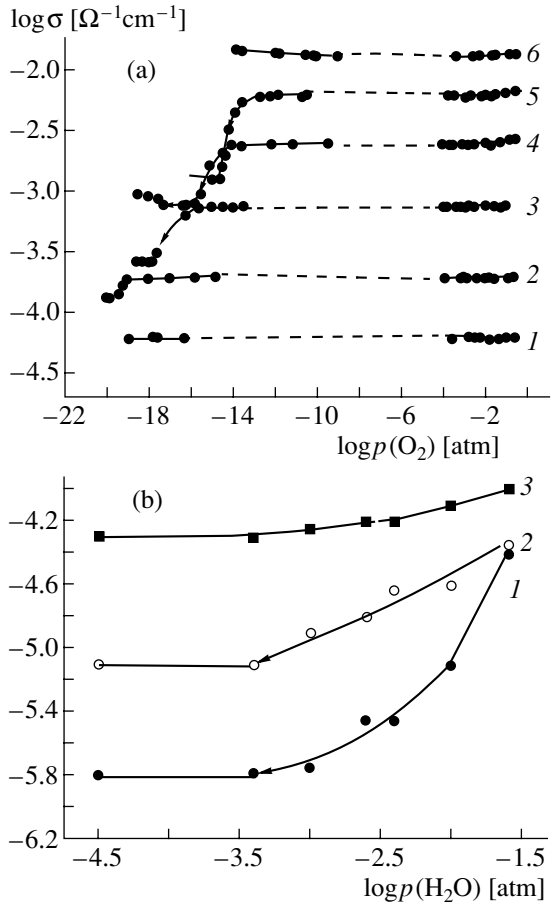

Fig. 1. Dependences of the conductivity isotherm of $Sr_6Ta_2O_{11}$ on the partial pressures (a) $p(O_2)$ and (b) $p(H_2O)$. Temperature, °C: (a) (*1*) 500, (*2*) 600, (*3*) 700, (*4*) 800, (*5*) 885, and (*6*) 1200 and (b) (*1*) 475, (*2*) 500, and (*3*) 600.

thermogravimetric characteristics and the structure of the compound $Sr_6Ta_2O_{11}$ and its solid solution $Sr_{5.92}Ta_{2.08}O_{11.12}$.

EXPERIMENTAL

Samples of $Sr_6Ta_2O_{11}$ and $Sr_{5.92}Ta_{2.08}O_{11.12}$ were prepared by solid-phase synthesis from the initial reactants $SrCO_3$ (special-purity grade) and Ta_2O_5 (special-purity grade). The temperature increased stepwise in 100-K intervals in the range 800–1300°C, followed by isothermal treatment for 10–20 h and intermediate grinding after each stage of the synthesis.

X-ray structure investigation was performed on a DRON UM1 diffractometer (CuK_α radiation, Ni filter). The structure was refined by the Rietveld full-profile method according to the GSAS software package [7]. The data collection was carried out in the 2θ range 10°–80° with a step of 0.02° and an exposure time of 10 s per point.

The electrical measurements were carried out by the two-point probe method with the use of samples prepared in the form of pellets with fired Pt electrodes under variations in the temperature and the partial pressures of oxygen and water vapors. The resistance of the studied samples was measured using impedance spectroscopy on a Zahner Electric IM6 impedance spectrometer in the frequency range from 0.5 Hz to 1 MHz with ac voltage amplitudes ranging from 10 to 50 mV. The bulk resistance was calculated according to the Bouckamp program.

The thermogravimetric measurements were performed by continuous weighing in an atmosphere with a specified moisture content on a setup consisting of an ADV-200 analytical balance, a furnace, and a temperature controller.

In order to produce the dry atmosphere, atmospheric air was passed sequentially through a concentrated sulfuric acid and a P_2O_5 powder [$p(H_2O) \approx 10^{-5}$ atm]. The moist atmosphere was obtained by bubbling atmospheric air through a saturated KBr solution [$p(H_2O)$ = 0.023 atm]. Atmospheres with intermediate moisture contents were prepared by bubbling atmospheric air through a temperature-controlled vessel with water at a specified temperature.

The partial pressure of oxygen was varied and controlled with the use of a pump and a detector prepared from stabilized ZrO_2.

RESULTS AND DISCUSSION

The electrical conductivity of $Sr_6Ta_2O_{11}$ and $Sr_{5.92}Ta_{2.08}O_{11.12}$ samples was investigated in a dry air atmosphere [$p(H_2O) \approx 10^{-5}$ atm] at temperatures of 500–1300°C over a wide range of oxygen partial pressures. It was found that the electrical conductivity does not depend on the oxygen partial pressure $p(O_2)$. This confirms the assumption that the electrical conduction predominantly occurs through the oxygen ion mechanism without a noticeable contribution of electron transfer (Fig. 1a). However, in the limited temperature range 700–1100°C at low pressures $p(O_2) < 10^{-12}$ atm, the conductivity undergoes a reversible jumpwise decrease to a constant value and then remains unchanged; i.e., no noticeable increase in the electronic component of the conductivity occurs in the low-conduction state. This allows us to assume that the observed effect is unrelated to changes in the oxidation states of elements that are in the highest stable oxidation states in the compounds. The temperature of the transition under investigation regularly increases with an increase in the oxygen partial pressure $p(O_2)$. X-ray diffraction analysis of the $Sr_{5.92}Ta_{2.08}O_{11.12}$ sample quenched at a temperature of 800°C and an oxygen partial pressure $p(O_2) < 10^{-12}$ atm revealed insignificant tetragonal distortions ($a = b = 8.2602 \pm 0.0003$ Å and $c = 8.3017 \pm 0.0003$ Å) as compared to the initial cubic

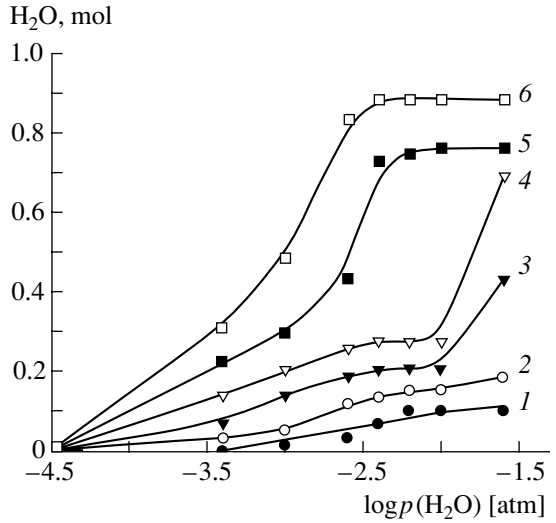

Fig. 2. Dependences of the content of water intercalated into the $Sr_6Ta_2O_{11}$ sample on the partial pressure of water vapors. Temperature, °C: (*1*) 550, (*2*) 500, (*3*) 450, (*4*) 430, (*5*) 400, and (*6*) 300.

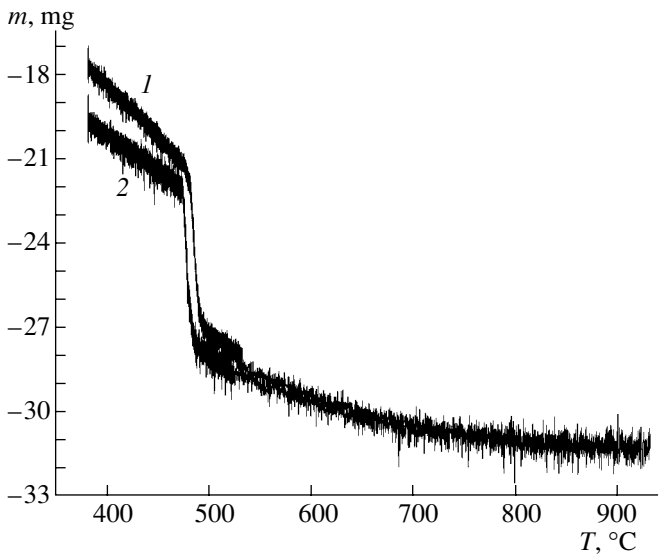

Fig. 3. Thermogravimetric curves for the $Sr_6Ta_2O_{11}$ sample upon cooling in moist atmospheres of (*1*) oxygen and (*2*) argon. $p(H_2O) = 0.02$ atm.

lattice (a = 8.3237 ± 0.0003 Å). Most likely, this is caused by the ordering of oxygen vacancies. Since this ordering is certain to be due to a transformation occurring in the *B* sublattice containing atoms of different sorts (Sr and Ta) with low mobilities, the above effect cannot be observed at relatively low temperatures (below 700°C) and, naturally, at high temperatures (above 1200°C) at which defects are arranged predominantly in a random manner. It is assumed that the effect under consideration is caused by an increase in the concentration of minority carriers with a decrease in the oxygen partial pressure $p(O_2)$ (thermally activated oxygen vacancies and electrons).

In a moist air atmosphere [$p(H_2O) \approx 10^{-2}$ atm], the studied compounds at $T < 600$°C exhibit a predominantly protonic conductivity [5]. In this respect, the intercalation of water was examined at temperatures below 600°C under variations in the partial pressure of water vapors. The conductivity isotherms and the dependences of the content of water intercalated into the $Sr_6Ta_2O_{11}$ sample on the partial pressure of water vapors are depicted in Figs. 1b and 2, respectively. It can be seen that the intercalation of water in small amounts (up to 0.3–0.4 mol) is attended by a monotonic change in the properties, but the matrix structure of the complex oxide remains unchanged. As the partial pressure of water vapors increases, the conductivity and the sample weight jumpwise increase in the vicinity of $p(H_2O) \approx 10^{-2}$ atm at temperatures of 450–475°C. The total water content at 300°C is equal to 0.9 mol H_2O per formula unit. This is close to a theoretical value of 1 mol, which corresponds to the complete filling of oxygen vacancies with water molecules in accordance with reaction (2). Similar dependences were obtained for the $Sr_{5.92}Ta_{2.08}O_{11.12}$ sample; however, the total water content amounted to 60% of the theoretically predicted value.

The thermogravimetric investigations performed in moist atmospheres of oxygen and argon upon slow cooling at a rate of 1 K/h also demonstrated that the sample weight monotonically increases beginning with 1000°C and then jumpwise increases at 475°C. A further decrease in the temperature results in an insignificant absorption of water. The results obtained for a sample weighing ~1 g are presented in Fig. 3. It can be

Table 1. Results of the structure refinement of $Sr_{5.92}Ta_{2.08}O_{11.12}$ prepared in dry air

Atoms	Positions	Coordinates			Filling factors	Thermal parameters, Å^2
		x	y	z		
Ta	4*a*	0	0	0	1.00	0.002(3)
Sr(1)	4*b*	0	0	0.50	1.00	0.077(5)
Sr(2)	8*c*	0.25	0.25	0.25	1.00	0.067(5)
O	24*e*	0.222(6)	0	0	0.849(6)	0.185(5)

seen that the composition of the atmosphere used does not substantially affect the thermograms.

According to X-ray diffraction analysis, the $Sr_{5.92}Ta_{2.08}O_{11.12}$ sample prepared in a dry air atmosphere has a cubic symmetry with space group *Fm*3*m* (Fig. 4a, Table 1). The unit cell parameters are as follows: $a = b = c = 8.3237 \pm 0.0003$ Å and $\alpha = \beta = \gamma = 90°$. The thermal parameters were calculated in the isotropic approximation according to the formula $\exp(-8\pi^2 B \sin^2\theta/\lambda^2)$. The results obtained are in good agreement with the description of the cryolite structure as a perovskite superstructure, i.e., as the double perovskite $A_2(B'B'')X_6$ with an ordered arrangement of large-sized octahedra [SrO_6] and small-sized octahedra [TaO_6] [8]. The high symmetry of this compound allows us to draw the conclusion that oxygen vacancies are arranged in a random manner. It should be noted that the filling factor for the oxygen sublattice is less than unity. This confirms the inference that the compounds under investigation have an oxygen deficit and that their structures are adequately described as structurally disordered phases.

X-ray structure analysis of the samples containing the maximum amount of water (according to the thermogravimetric data) demonstrated that the (200), (220), and (311) diffraction reflections of the initial cubic cell are split into three lines, whereas the (222) reflection is not split. This suggests that the samples studied have a single-phase composition and that their structures undergo orthorhombic distortions. The Rietveld full-profile refinement of the structure of the hydrated $Sr_{5.92}Ta_{2.08}O_{11.12}$ sample revealed that this compound crystallizes in the orthorhombic crystal system with space group *Fmmm* (Fig. 4b, Table 2). The unit cell parameters are as follows: $a = 8.2236 \pm 0.0003$ Å, $b = 8.3172 \pm 0.0003$ Å, $c = 8.3659 \pm 0.0003$ Å, and $\alpha = \beta = \gamma = 90°$. It should be noted that X-ray diffraction analysis is characterized by a low sensitivity to scattering by light atoms. As a consequence, the oxygen atoms were located with a large error (up to 0.006 Å) and the positions of hydrogen atoms in the sample prepared in the moist air atmosphere were not determined. A comparison of the data presented in Tables 1 and 2 shows that the second sample has a higher total oxygen content, which agrees with the thermogravimetric data. Moreover, the filling of oxygen vacancies with water molecules occurs in a preferential direction. This results in the lowering of the symmetry of the structure. The large discrepancy factors can be explained in terms of the strongly defective structure of the samples. Note that the intercalation of water molecules leads to an increase both in the half-width at half-maximum

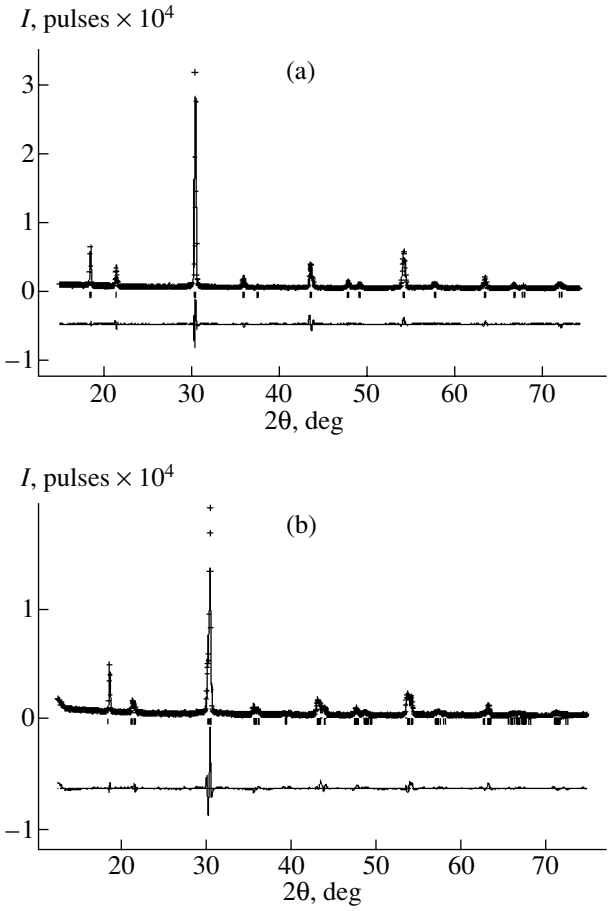

Fig. 4. Observed, calculated, and difference X-ray diffraction profiles for the anhydrous $Sr_{5.92}Ta_{2.08}O_{11.12}$ sample (a) prior to and (b) after treatment in moist oxygen at $p(H_2O) = 0.02$ atm.

Table 2. Results of the structure refinement of $Sr_{5.92}Ta_{2.08}O_{11.12} \cdot 0.6H_2O$ prepared in moist oxygen

Atoms	Positions	Coordinates			Filling factors	Thermal parameters, Å^2
		x	*y*	*z*		
Ta	4*a*	0	0	0	1.00	0.003(3)
Sr(1)	4*b*	0	0	0.5	1.00	0.104(5)
Sr(2)	8*c*	0.25	0.25	0.25	1.00	0.054(5)
O(100)	8*e*	0.232(6)	0	0	0.83(6)	0.275(5)
O(010)	8*g*	0	0.258(6)	0	1.00	0.275(5)
O(001)	8*h*	0	0	0.156	0.83(6)	0.275(5)

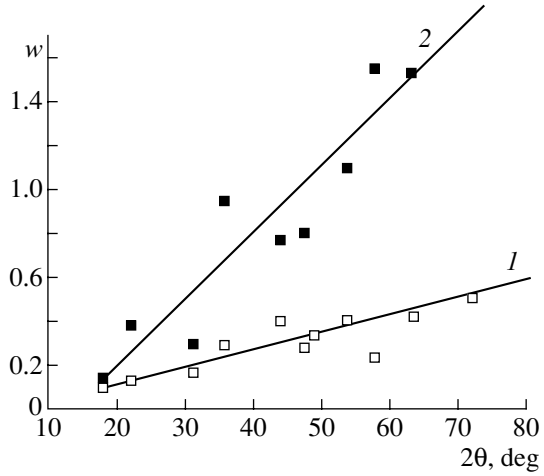

Fig. 5. Experimental dependences of the half-width at half-maximum for X-ray reflections on their angular position for the anhydrous $Sr_{5.92}Ta_{2.08}O_{11.12}$ sample (a) prior to and (b) after treatment in moist oxygen at $p(H_2O) = 0.02$ atm.

(HWHM) for X-ray reflections over the entire 2θ range (Fig. 5) and in the discrepancy factors (Tables 1, 2).

Therefore, the change in the thermodynamic conditions results in variations in the chemical composition of the system, which, in turn, leads to a structural transformation. Since the solid–solid structural transition is accompanied by a jumpwise change in the chemical composition, it can be conventionally described as a morphotropic transition. On the other hand, the hydration is attended by a chemical transformation. On this basis, we can propose the following scheme of the chemical reaction:

$$Sr_6Ta_2O_{11}(xH_2O) + (y - x)H_2O \Leftrightarrow Sr_6Ta_2O_{11} \cdot yH_2O. \quad (3)$$

According to scheme (3), this process can be treated as a transformation of the solid solution, most probably, into an oxyhydrate phase of variable composition. Note that scheme (3) involves conventional chemical formulas, because the discussion of the nature of hydrogen-containing particles does not enter into the scope of this paper. The transformation of the crystal structure can be governed by a number of factors. Actually, the intercalation of water into the matrix of the complex oxide and the filling of oxygen vacancies result in (i) a change in the ratio between octahedra and tetrahedra, (ii) the formation of energetically nonequivalent oxygen atoms (and, consequently, OH groups), and (iii) a change in the acid–base properties of the oxide. The problem of revealing these subtle effects calls for further investigation. This problem is of particular importance, because its solution can provide a way of elucidating the mechanism of proton transfer in complex oxide systems.

CONCLUSIONS

Thus, it was found that oxygen-deficient cryolites can undergo structural and chemical transformations due to variations in the partial pressures of oxygen and water vapors.

In a dry atmosphere and at low oxygen partial pressures $p(O_2) < 10^{-12}$ atm, the $Sr_6Ta_2O_{11}$ and $Sr_{5.92}Ta_{2.08}O_{11.12}$ compounds containing oxygen vacancies undergo a phase transition in the limited temperature range 700–1100°C. In this case, the oxygen ion transfer remains predominant and the symmetry of the unit cell is lowered from cubic to tetragonal. It was assumed that this transition is caused by an ordering of the oxygen sublattice.

It was demonstrated that the intercalation of water into the compounds studied (at low temperatures and a high moisture content) results in structural transformation. This is accompanied by a lowering of the symmetry from cubic to orthorhombic and a chemical reaction with the formation of a new oxyhydrate phase of variable composition.

ACKNOWLEDGMENTS

This work was supported by the Russian Foundation for Basic Research (project no. 99-03-32502), the Ministry of Education of the Russian Federation (project no. E00-5.0-170), the International Association of Assistance for the promotion of co-operation with scientists from the New Independent States of the former Soviet Union (project no. 99-00636), and the American Foundation for Civilian Research and Development (CRDF).

REFERENCES

1. S. F. Pal'guev, *High-Temperature Protogenic Solid Electrolytes* (Ural. Otd. Ross. Akad. Nauk, Yekaterinburg, 1998).
2. T. Norby, Solid State Ionics **125**, 1 (1999).
3. A. Neiman, A. Podkorytov, and V. Zhukovskii, Phys. Status Solidi A **101**, 371 (1987).
4. P. P. Leshchenko, L. N. Lykova, L. M. Kovba, and E. A. Ippolitova, Zh. Neorg. Khim. **27**, 1285 (1982).
5. I. E. Animitsa, A. Ya. Neĭman, A. R. Sharafutdinov, and M. G. Kazakova, Élektrokhimiya **37**, 305 (2001).
6. I. Animitsa, A. Neiman, A. Sharafutdinov, and S. Nochrin, Solid State Ionics **136–137**, 265 (2000).
7. A. C. Larson and R. B. von Dreele, LANSCE, MS-H805 (Los Alamos National Laboratory, 1986).
8. A. Wells, *Structural Inorganic Chemistry* (Clarendon, Oxford, 1984; Mir, Moscow, 1987).

Translated by O. Borovik-Romanova

Crystallography Reports, Vol. 47, No. 6, 2002, pp. 996–1002. Translated from Kristallografiya, Vol. 47, No. 6, 2002, pp. 1065–1071.

LATTICE DYNAMICS AND PHASE TRANSITIONS

Phase States in Rotationally Distorted Perovskites[1]

M. P. Ivliev

Research Institute of Physics, Rostov State University, pr. Stachki 194, Rostov-on-Don, 344090 Russia

e-mail: ivlmp@km.ru

Received January 10, 2002

Abstract—The thermodynamic and crystallochemical conditions determining the types of the rotational phase transitions and their sequence in cubic perovskites are established. It is shown that a decrease in the tolerance factor and a change of the *A*-cation and its charge stimulates the softening of the rotational-vibrational mode M_3. As an example, the compounds $A_xNa_{1-x}NbO_3$ (A = K, Li) are considered. © *2002 MAIK "Nauka/Interperiodica".*

INTRODUCTION

Perovskites described by the general formula ABX_3 have a simple cubic lattice of symmetry $Pm\bar{3}m$–O_h^1. Their structure consists of a three-dimensional framework formed by BX_6 octahedra that share vertices and whose voids are occupied by *A*-cations. The anions are either the halide ions $X^- = F^-, Cl^-, Br^-$, …, then $A^+ = K^+, Rb^+, Cd^+, Tl^+$, … and $B^{2+} = Pb^{2+}, Cd^{2+}, Ca^{2+}, Mn^{2+}$, …, or oxygen ions $X^{2-} = O^{2-}$, then the following combinations of cations are possible: A^+B^{5+}, $A^{2+}B^{4+}$, and $A^{3+}B^{3+}$, where $A^+ = Na^+$ and K^+; $B^{5+} = Nb^{5+}$ and Ta^{5+}; $A^{2+} = Sr^{2+}, Pb^{2+}, Ba^{2+}, Ca^{2+}$, …; $B^{4+} = Ti^{4+}, Zr^{4+}, Gf^{4+}$, …; $A^{3+} = La^{3+}, Pr^{3+}, Sm^{3+}$, …; and $B^{3+} = Al^{3+}$, … [1, 2].

The crystals of this family undergo numerous phase transitions caused by the rotation of octahedra (crumpling or rotational phase transitions) and are characterized by the formation of various types of order [2–4]. The rotational phase transitions in a number of compounds were theoretically studied elsewhere [2, 5–8]. However, the analysis and systematization of the experimental data accumulated by now require a more general approach that would allow one to study the whole variety of the types of order. Below, the rotational phase transitions are considered within the framework of the phenomenological theory. We studied the effect of various crystallochemical characteristics of compounds, such as the tolerance factor t [2] and the charge of *A*-cations, on the formation of various phase states.

The whole set of rotational distortions in perovskites is described by two three-component order parameters [2, 6], of which one, ψ, belongs to the three-ray star of the vector $\mathbf{k} = \frac{1}{2}(\mathbf{b}_1 + \mathbf{b}_2)$, where $\mathbf{b}_i$ are the reciprocal-lattice vectors, whereas the other, φ, belongs to the one-ray star of the vector $\mathbf{k} = \frac{1}{2}(\mathbf{b}_1 + \mathbf{b}_2 + \mathbf{b}_3)$. These order parameters are transformed according to irreducible transformations 3 and 7, respectively [9]. To each of these order parameters there correspond its own lattice-vibration mode—M_3 to ψ and R_{25} to φ.

The table lists the types of order observed in crystals and provided by the condensation of the order parameters ψ and φ borrowed from [2–4, 10–12]. According to [2], these types of order have the following symmetries:

$$000 - O_h^1\ Pm\bar{3}m \quad Z = 1,$$

$$00\varphi - D_{4h}^{18}\ I4/mcm \quad Z = 4,$$

$$\varphi\varphi\varphi - D_{3d}^{6}\ R\bar{3}c \quad Z = 2,$$

$$00\psi - D_{4h}^{5}\ P4/mbm \quad Z = 2,$$

$$0\psi\varphi - D_{2h}^{17}\ Cmcm \quad Z = 8,$$

$$\varphi\varphi\psi - D_{2h}^{16}\ Pncm \quad Z = 4,$$

$$\psi_1\psi_2\varphi - D_{2h}^{13}\ Pmmn \quad Z = 8,$$

$$\varphi_1\varphi_2\psi - C_{2h}^{2}\ P2_1/m \quad Z = 8,$$

where Z is the number of formula units per unit cell, Z_A is the charge of the *A*-cation, t is the tolerance factor equal to $t = R_{AX}/\sqrt{2R_{BX}}$, where R_{NL} is the distance between the N and L ions equal to the sum of their ionic radii with due regard for the coordination number (the values of the ionic radii were taken from [13]), T_j is the temperature of the jth rotational phase transition, and G_i is a set of order parameters characterizing the ith dissymmetric phase.

[1] This study was presented to the Symposium "Order, Disorder and Properties of Oxides" (ODPO), Sochi, Russia, 2001.

1063-7745/02/4706-0996$22.00 © 2002 MAIK "Nauka/Interperiodica"

Successive phase transitions from the cubic phase (000) in some crystals caused by the condensation of the order parameter ψ (mode M_3) and φ (mode R_{25})

Compound	T_1, K	G_1	T_2, K	G_2	T_3, K	G_3	Z_A	t
AlF_3		φφφ					0	
ReO_3		φφφ					0	
$LaAlO_3$	700	φφφ					3	0.93
$PrAlO_3$	1320	φφφ	205	φ0φ	151	$\varphi_1 0 \varphi_2$	3	0.91
$SmAlO_3$	2100	φφφ	1100	φφψ			3	0.90
$SrTiO_3$	110	00φ					2	0.96
$SrZrO_3$	1440	00φ	1130	ψ0φ	1000	ψφφ	2	0.88
$CaTiO_3$	1533	φφψ					2	0.85
$RbCdF_3$	124	00φ					1	0.95
$TlCdF_3$	191	00φ					1	0.94
$RbCaF_3$	198	00φ	50	0ψφ			1	0.93
$KCdF_3$	487.5	00ψ	472.7	φφψ			1	0.92
$KCaF_3$	560	0φψ	551	φφψ			1	0.90
$RbCdCl_3$	387	00ψ	383	0φψ	340	φφψ	1	0.90
$CsPbCl_3$	320	00ψ	314	φ0ψ	310	φφψ	1	0.87
$CsPbBr_3$	403	00ψ	361	φφψ			1	0.84
$CsSrCl_3$	386	00ψ	381	φ0ψ	362	$\varphi_1\varphi_2\psi$	1	0.86
$NaNbO_3$	914	00ψ	848	φ0ψ	793	$\varphi\psi_1\psi_2$	1	0.87
$NaTaO_3$	903	00ψ	838	φ0ψ	758	φφψ	1	0.86

If $t < 1$, the dimensions of the *A*-cations are less than the dimensions of the cavity formed by the octahedra. In most occasions, the rotational phase transitions are observed in precisely such crystals, which signifies that this discrepancy in the crystallochemical parameters of the compound components in the perovskite structure is the necessary condition for the formation of an instability resulting in structure "crumpling."

Analyzing the data indicated in the table, we see that inside the group of compounds with similar chemical bonds such as $ACdF_3$ (*A* = K, Tl, Rb), $CsPbX_3$ (*X* = Cl, Br), $ATiO_3$ (*A* = Sr, Ca), and $AAlO_3$ (*A* = La, Pr, Sm), the type of the phase states depends on the sequence of phase formation and the tolerance factor *t*. Comparing the order observed in various groups, we see that an important role is also played by the charge of the *A*-cation. In order to establish in what way various crystallochemical factors influence the formation of phase states, one has first to determine the conditions providing the formation of various sequences of order and then to single out the major parameters determining their formation.

PHENOMENOLOGICAL THEORY OF ROTATIONAL PHASE TRANSITIONS

At the first stage of the study of phase transitions, we shall ignore the details of the thermodynamic behavior of compounds, i.e., where possible, we assume that the transformation is either a second-order phase transition or a first-order phase transition close to a second-order one. The model thermodynamic potential used to describe all the possible rotational phase transitions provided by the condensation of M_3 and R_{25} has the form

$$\Phi = \Phi_M + \Phi_R + \Phi_{MR}, \quad (1)$$

where

$$\Phi_M = \alpha_{1M}G_{1M} + \alpha_{2M}G_{1M}^2 + \beta_{1M}G_{2M} + \ldots,$$

$$\Phi_R = \alpha_{1R}G_{1R} + \alpha_{2R}G_{1R}^2 + \beta_{1R}G_{2R} + \sigma_R G_{1R}G_{2R} + \omega_R G_{3R} + \beta_{2R}G_{2R}^2\ldots,$$

$$\Phi_{MR} = \gamma_1 G_{1M}G_{1R} + (\gamma_2 - \gamma_1)\sum_{i=1}^{3}\varphi_i^2\psi_i^2 + k_1\Sigma\psi_i^2\varphi_j^2\varphi_k^2 + k_2 G_{1M}G_{2R} + k_3\Sigma\varphi_i^2\psi_j^2\psi_k^2 + k_4 G_{1R}G_{2M} + \ldots,$$

$$G_{1M} = \sum_{i=1}^{3}\psi_i^2,$$

$$G_{2M} = \sum_{i<j}\psi_i^2\psi_j^2, \quad G_{3M} = \psi_1^2\psi_2^2\psi_3^2, \quad \psi \in M_3,$$

$$G_{1R} = \sum_{i=1}^{3}\varphi_i^2, \quad G_{2R} = \sum_{i<j}\varphi_i^2\varphi_j^2,$$

$$G_{3R} = \varphi_1^2\varphi_2^2\varphi_3^2, \quad \varphi \in R_{25}$$

and, in all the cases, $i < j < k$.

This potential has the terms characterizing the contributions that come from each order parameter, $\Phi_M(\psi)$ and $\Phi_R(\varphi)$, and also the mixed invariants that describe the interaction between these order parameters $\Phi_{MR}(\varphi, \psi)$. The thermodynamic potential Φ_R is written with an accuracy which provides the analysis of the solutions of the type $\varphi_1\varphi_2\psi_3$. Using this thermodynamic potential, we have to determine the conditions for the formation of the following chains of ordering (in all cases, the initial symmetric phase is cubic $\varphi = \psi = 0$, sp. gr. O_h^1):

$$\begin{aligned}
&1.\ 000 \longrightarrow 00\psi \longrightarrow 0\varphi\psi \longrightarrow \varphi\varphi\psi,\\
&2.\ 000 \longrightarrow 00\psi \longrightarrow \varphi\varphi\psi,\\
&3.\ 000 \longrightarrow 00\psi \longrightarrow 0\varphi\psi \longrightarrow \psi_1\varphi\psi_3,\\
&4.\ 000 \longrightarrow 0\varphi\psi \longrightarrow \varphi\varphi\psi,\\
&5.\ 000 \longrightarrow 00\varphi \longrightarrow 0\psi\varphi \longrightarrow \varphi\varphi\psi,\\
&6.\ 000 \longrightarrow \varphi\varphi\varphi \longrightarrow \varphi\varphi\psi,\\
&7.\ 000 \longrightarrow \varphi\varphi\psi.
\end{aligned} \tag{2}$$

The analysis of this set of phases shows that both order parameters are critical, i.e., $\alpha_{1M} \longrightarrow 0$ and $\alpha_{1R} \longrightarrow 0$; then, in some instances, first, the order parameter ψ ($\alpha_{1M} < \alpha_{1R}$) appears, whereas in some other instances, φ ($\alpha_{1R} < \alpha_{1M}$) appears. Moreover, upon condensation, the order parameters become orthogonal to one another. This signifies that $\gamma_1 < 0$ and $\gamma_2 > 0$. It should also be indicated that in all cases, except for case 3, one can assume that β_{1M} has a high value because all the types of ordering are characterized by not more than one component of the order parameter ψ. Later, it will be shown that the assumption that $\alpha_{2R} > 0$, $\alpha_{2M} > 0$, $\sigma_R < 0$, $k = k_1 + k_2 < 0$, $\omega_R < 0$, and $\omega_M < 0$ can be used to describe the types of ordering considered here.

Figures 1 and 2 show the diagrams of the phase states for various relationships between the coefficients of thermodynamic potential (1).

The sequence of ordering is formed in the following way. If $\alpha_{1M} < \alpha_{1R}$, then first the M_3 mode is condensed and the $00\psi_3$ order appears. Since $\gamma_1 < 0$ and $\gamma_2 > 0$, the existence of the order parameter ψ_3 "softens" the system with respect to φ_1 and φ_2 and makes it more "rigid" with respect to φ_3. The order parameter φ ($\varphi^2 = \varphi_1^2 + \varphi_2^2$) arises at $\alpha_{1R} = -\gamma_1(-\alpha_{1M}/2\alpha_{2M})$. If $\Gamma > 0$, where $\Gamma = 4\alpha_{2M}\alpha_{2R} - \gamma_1^2$, the phase transition is of the second order; if $\Gamma < 0$, it is of the first order. The phase diagram (Fig. 1a) has a triple point, where the $00\psi_3$, $\varphi_1 0\psi_3$, and $\varphi\varphi\psi_3$ phases coexist. In this case, if $\Delta_R < 0$ and $\Delta_R = 4\alpha_{2R}\beta_{2R} - \sigma_R^2$, the phases $\varphi_1 0\psi_3$ and $\varphi\varphi\psi_3$ are separated by the line of fourth-order phase transitions; if $\Delta_R > 0$, then between these phases the phase $\varphi_1\varphi_2\psi_3$ is formed. This diagram was studied in [7], where, in particular, it was shown that this sequence of phases observed in $CsSrCl_3$ [4] could be described under the assumption that $\Delta_R > 0$.

If $\alpha_{1M} \sim \alpha_{1R}$ and $\Gamma < 0$, the appearance of one order parameter destabilizes the system with respect to the other order parameter, and therefore both order parameters, ψ and φ, appear simultaneously ($\varphi^2 = \varphi_1^2 + \varphi_2^2$). The diagram in Fig. 1b illustrates a possible direct transition from the symmetric phase into the phase with a complex condensate (ψ, φ) along the line of the first-order phase transitions. This diagram also has a triple point, but it is located at the boundary with the symmetric phase.

If $\alpha_{1R} < \alpha_{1M}$, then, first, the order parameter φ appears (Fig. 1c). If $\psi = 0$ ($\alpha_{1M} > 0$) under the condition that $\omega_R < 0$, the stable phases can be only $\varphi 00$ and $\varphi\varphi\varphi$ [14]. The phase $\varphi\varphi 0$ is unstable for all α_{1R} and β_{1R}, because the stability regions with respect to $\varphi_1 - \varphi_2 = 0$ and φ_3, which are determined by the relationships

$$\beta_{1R} \le \beta_{1R}^{(1)} = -\sigma_R\left(\frac{-\alpha_{1R}}{2\alpha_{2R}}\right) - \frac{\Delta_R}{8\alpha_{2R}}\left(\frac{-\alpha_{1R}}{2\alpha_{2R}}\right)^2,$$

$$\beta_{1R} \ge \beta_{1R}^{(2)} = -\left(\alpha_R + \frac{\omega_R}{2}\right)\left(\frac{-\alpha_{1R}}{2\alpha_{2R}}\right),$$

do not overlap at $\omega_R < 0$.

The appearance of ψ_3 ($\alpha_{1M} \gtrsim \alpha_{1R}$) is accompanied by the transformation of the phase $\varphi\varphi 0$ into $\varphi\varphi\psi_3$ and results in the formation of a slight kink at the stability boundary of the phase $\varphi\varphi\psi_3$ with respect to $\varphi_1 - \varphi_2 = 0$:

$$\beta_{1R}^{(3)} = \beta_{1R}^{(1)} - \frac{2\alpha_{2R}x - \sigma_R\gamma_1}{\Gamma}(-\alpha_{1M} + \alpha_{1M}^{(1)}),$$

$$\alpha_{1M}^{(1)} = -\gamma_1\left(\frac{-\alpha_{1R}}{2\alpha_{2R}}\right), \quad \sigma_{1M} < \alpha_{1M}^{(1)}.$$

On the contrary, the appearance of ψ_3 drastically changes the direction of the stability boundary with respect to φ_3:

$$\beta_{1R}^{(4)} = \beta_{1R}^{(2)} + \frac{2\alpha_{2R}(\gamma_2 - \gamma_1)}{4\alpha_{2M}\alpha_{2R} - \gamma_1(2\gamma_1 - \gamma_2)}\left(-\frac{\alpha_{1R}}{2\alpha_{2R}}\right)^{-1}(\alpha_{1M} - \alpha_{1M}^{(1)}).$$

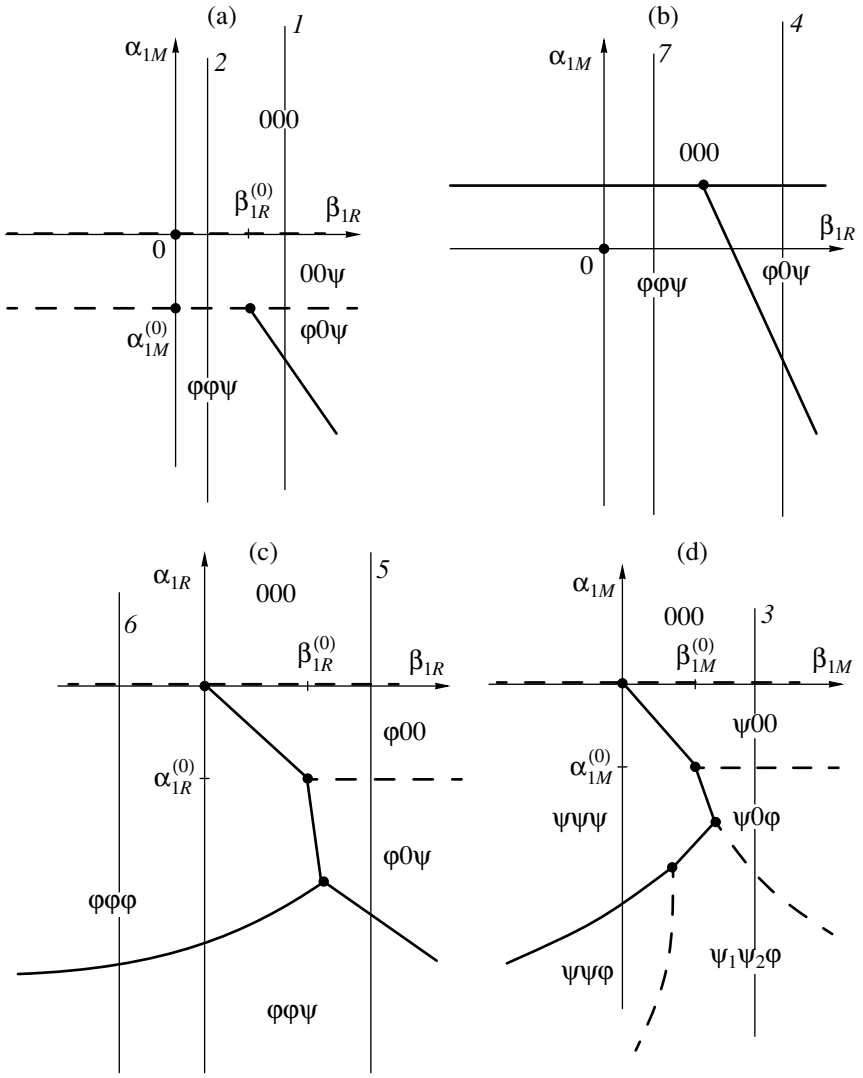

Fig. 1. Diagrams of the phase states of thermodynamic potential (1) in the $\alpha_1\beta_1$ plane. The solid and dashed lines indicate the lines of the first- and second-order phase transitions, respectively. Thin solid lines indicate the thermodynamic paths along which the sequences of phases from set (2) are formed (they are enumerated in the same way as in set (2)): (a) $\alpha_{1M} \lesssim \alpha_{1R}$, $\Gamma > 0$, $\Delta_R < 0$, $\beta_{1R}^{(0)} = -k\left(\frac{-\alpha_{1M}^{(0)}}{2\alpha_{2M}}\right)$; (b) $\alpha_{1M} \sim \alpha_{1R}$, $\Gamma < 0$; (c) $\alpha_{1R} \lesssim \alpha_{1M}$, $\Gamma > 0$, $\Delta_R < 0$, $\beta_{1R}^{(0)} = -\left(\sigma_R - \frac{\omega_R}{9}\right)\left(\frac{-\alpha_{1R}^{(0)}}{2\alpha_{2R}}\right)$; and (d) $\alpha_{1M} \lesssim \alpha_{1R}$, $\Gamma > 0$, $\beta_{1R} > 0$, $\Delta_M > 0$.

The line $\beta_{1R}^{(4)}$ becomes almost parallel to the β_{1R} axis even at a slight deviation of α_{1M} from $\alpha_{1M}^{(1)}$, because $(-\alpha_{1R}/2\alpha_{2R}) \ll 1$. This results in the intersection of the boundaries $\beta_{1R}^{(4)}$ and $\beta_{1R}^{(3)}$ and the formation of the region in which the phase $\varphi\varphi\psi$ is stable. If $\Delta_R < 0$, the phases $\varphi 0\psi_3$ and $\varphi\varphi\psi_3$ are adjacent along the line of first-order phase transitions; if $\Delta_R > 0$, then, the phase $\varphi_1\varphi_2\psi_3$ arises between these phases.

The phase diagram in Fig. 1d is similar to that in Fig. 1c under the condition that $\Delta_R > 0$ (i.e., in the presence of the phase $\varphi_1\varphi_2\psi_3$) with the replacement of φ_i by ψ_i and ψ_i by φ_i and the introduction of the corresponding new notation for the coefficients. Thus, instead of β_{1R} we have β_{1M}, instead of $\Delta_R > 0$, we have $4\alpha_{2M}\beta_{2M} - \sigma_M^2 > 0$. It should be indicated that this analogy is possible only because thermodynamic potential (1) is symmetric with respect to this replacement and the corresponding new notation.

Figure 2 shows the diagrams of the phase states in the plane α_{1M}, α_{1R}. To each sequence of ordering entering set (2) there corresponds its own thermodynamic path indicated by the same number on the phase plane (Figs. 1, 2). Thus, on the path *1* (Figs. 1a, 2a), the

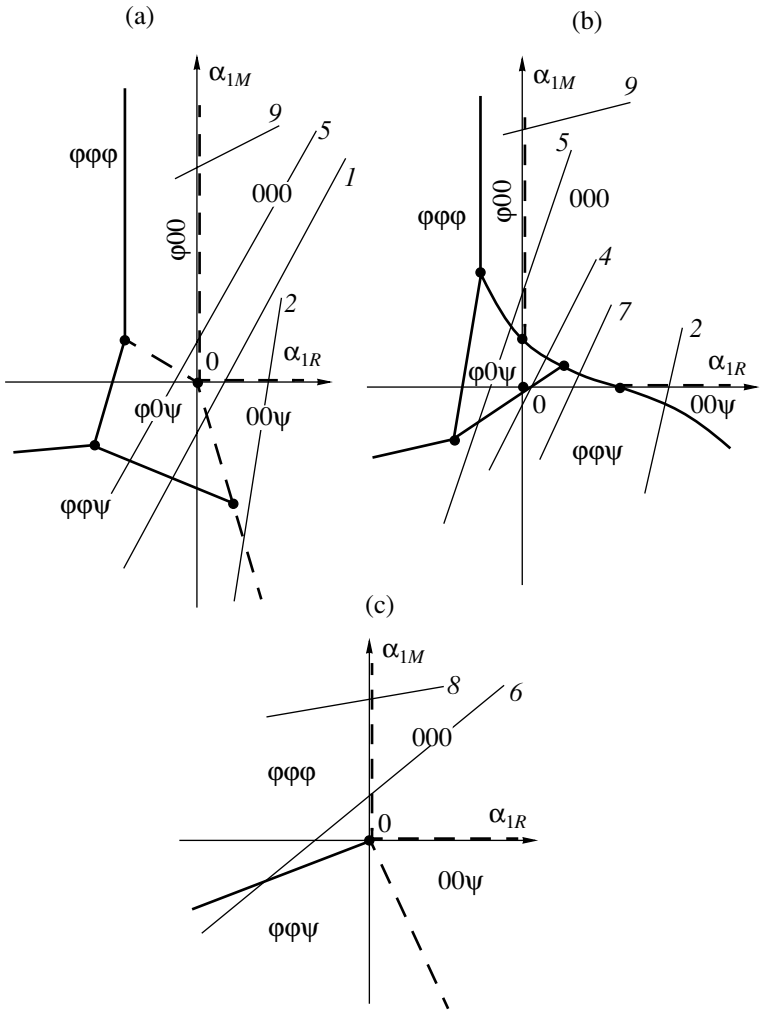

Fig. 2. Diagrams of phase states of thermodynamic potential (1) in the $\alpha_{1M}\alpha_{1R}$ plane: (a) $\beta_{1R} > 0$, $\Gamma > 0$; (b) $\beta_{1R} > 0$, $\Gamma < 0$; and (c) $\beta_{1R} < 0$.

sequence of phases is formed which was really observed in $RbCdCl_3$, $CsPbCl_3$, and $NaTaO_3$; on the path *2* (Figs. 1a, 2a, 2b), the sequence is formed that was observed in $KCdF_3$ and $CsPbBr_3$; on path *3* (Fig. 1d), the sequence that was observed in $NaNbO_3$; on path *4* (Figs. 1b, 2b), the sequence that was observed in $KCaF_3$; on path *5* (Figs. 1c, 2a, 2b), the sequence that was observed in $SrZrO_3$; on path *6* (Figs. 1c, 2c), the sequence that was observed in $SmAlO_3$; and, finally, on path *7* (Figs. 1b, 2b), the sequence that was observed in $CaTiO_3$.

DISCUSSION OF RESULTS

Analyzing the changes in the paths depending on the crystallochemical parameters, we can state the following:

—In compounds where the *A*-cation is absent, MF_3 (*M* = Al, Ti, …), ReO_3, etc., only one rotationally distorted phase is observed, which arises as a result of the condensation of three components of the mode R_{25} – φφφ [10, 12]. This type of ordering can be described with the aid of thermodynamic potential (1) under the condition that α_{1R} changes its sign, $\alpha_{1M} > 0$, and $\beta_{1R} < 0$ (path *8*, Fig. 2c);

—in the compounds with $Z_A = 3$ at $t > 0.91$, ordering of type φφφ is observed. A decrease in t ($t \lesssim 0.9$) results in the fact that, in addition to R_{25}, also the mode M_3 is condensed (sequence *6* in set (2)). In this case, α_{1R} and α_{1M} change their signs, but $\alpha_{1R} < \alpha_{1M}$ and $\beta_{1R} < 0$ (Figs. 1c, 2c);

—at $Z_A = 2$ and at $t \lesssim 1$, only one component of the mode R_{25}, 00φ, is condensed (α_{1R} changes its sign, $\alpha_{1M} > 0$ and $\beta_{1R} > 0$, path *9* (Figs. 2a, 2b)). At $t \lesssim 0.9$, first R_{25} is condensed and then M_3 (sequence *5* in set (2)) (Figs. 1c, 2a, 2b); in other words, both α_{1R} and α_{1M} change their signs, but $\alpha_{1R} \lesssim \alpha_{1M}$ and $\beta_{1R} > \beta_{1R}^{(0)}$. Finally, at $t \sim 0.85$, both modes M_3 and R_{25} are condensed simultaneously (sequence *7* from (2)); i.e., α_{1R}

and α_{1M} change their signs, $\alpha_{1M} \sim \alpha_{1R}$, $\beta_{1R} < \beta_{1R}^{(0)}$, $\Gamma < 0$ (Figs. 1b, 2b);

—in compounds with $Z_A = 1$ at $t \lesssim 1$, only one type of ordering is observed, 00φ, which is induced by the mode R_{25}; with a decrease in t ($t \lesssim 0.93$), first R_{25} is condensed and then M_3 (α_{1R} and α_{1M} change their signs, $\alpha_{1R} \lesssim \alpha_{1M}$, $\beta_{1R} > \beta_{1R}^{(0)}$). A further decrease in t ($t \sim 0.9$) results in the fact that the modes R_{25} and M_3 are condensed simultaneously (sequence *4* from (2) (Figs. 1b, 2b), α_{1R} and α_{1M} change their signs, $\alpha_{1M} \sim \alpha_{1R}$, $\beta_{1R} > \beta_{1R}^{(0)}$, and $\Gamma < 0$). Finally, if t decreases even more ($t \sim 0.87$), the mode M_3 becomes softer and first the order parameter ψ appears and then the parameter φ (mode R_{25}) (sequences *1* and *2* from (2)); i.e., α_{1R} and α_{1M} change their signs, $\alpha_{1M} \lesssim \alpha_{1R}$ and $\beta_{1R} \gtrsim \beta_{1R}^{(0)}$ for *1* from (2) or $\beta_{1R} \lesssim \beta_{1R}^{(0)}$ for *2* from (2) (Fig. 1a). It should be emphasized that the variant in which first the mode M_3 is condensed and only then the mode R_{25} was not observed in the compounds with $Z_A = 2.3$.

Thus, with a decrease in t, the sequences of the phase states and the corresponding thermodynamic paths are transformed in the following way:

at $Z_A = 1$ $\quad 9 \longrightarrow 5 \longrightarrow 4 \longrightarrow 1 \longrightarrow 2$ (Figs. 2a, 2b),

at $Z_A = 2$ $\quad 9 \longrightarrow 5 \longrightarrow 7$ (Figs. 2a, 2b),

at $Z_A = 3$ $\quad 8 \longrightarrow 6$ (Fig. 2c).

This signifies that with a decrease in t, the temperature of the condensation of the mode M_3 increases faster than the temperature of condensation of the mode R_{25}, although at $t \lesssim 1$ the latter was higher. At sufficiently low t ($t \sim 0.9$, $Z_A = 1$), both M_3 and R_{25} modes are condensed simultaneously. Then, at $t \sim 0.87$, first M_3 and only then R_{25} are condensed. A similar pattern is also observed in compounds with $Z_A = 2$. However, the latter variant of condensation—first of M_3 and only then of R_{25}—is not observed in these compounds because, hypothetically, this could happen only at $t < 0.85$, but at such t values even the existence of the cubic perovskite structure is dubious.

At the same time, with a change in the Z_A value, the coefficient β_{1R} noticeably changes. Thus, at $Z_A = 0$, we have $\beta_{1R} < 0$; at $Z_A = 1, 2$, we have $\beta_{1R} > 0$; and at $Z_A = 3$, the coefficient β_{1R} becomes negative again. In other words, the coefficient β_{1R} depends on Z_A in a complicated nonmonotonic way.

It follows from the above consideration that the key factor for the formation of the phase sequence is, first, the relationship between α_{1M} and α_{1R} and, second, the location of the thermodynamic path with respect to the multicritical N-tuple point $\alpha_1 = 0$, $\beta_{1R} = 0$. The effect of the crystallochemical parameters on these relationships is as follows: an increase in t at $Z_A = \text{const} \neq 0$, stimulates the system softness with respect to M_3 to a higher degree than with respect to R_{25}, and, in a similar way, a decrease in Z_A ($Z_A \neq 0$) at $t = \text{const}$ also stimulates the system softness with respect mainly to M_3.

Now, consider the factors that promote the formation of this dependence. A decrease in t ($t < 1$) signifies that the dimensions of the cavity formed by octahedra increase in comparison with the dimensions of an *A*-cation. This creates favorable conditions for the rotation of BX_6 octahedra and an increase in the root-mean square deviation of *A*-cations from the centers of the cavities, i.e., promotes an increase in the degree of its localization. At the rotations corresponding to the M_3 mode, the local field with the symmetry of a quadrupole moment arises in the cavity and interacts with the delocalized *A*-cations, thus decreasing the energy of this mode and providing its condensation. The R_{25} mode interacts with the delocalized *A*-cations to a much lesser degree, because it creates a field with the symmetry of the third-order multipole moment at the center of the cavity. Therefore, an increase in delocalization stimulates system softening with respect to M_3 to a larger degree than with respect to R_{25}. A decrease in Z_A in the presence of a "free space" for an *A*-cation inside the cavity reduces the attraction of *A*-cations to the cavity center, which also increases its delocalization and promotes system softening with respect to M_3.

The above considerations allow one to explain the character of the dependence of the temperature of the rotational phase transitions in the solid solutions $A_xNa_{1-x}NbO_3$ at $x \ll 1$ (where A = K, Li) on the concentration x. In the cubic lithium niobate phase, two soft modes are present, M_3 and R_{25} [12]. Since the factor t in $NaNbO_3$ is $t \approx 0.87$, $Z_A \approx 1$, then first the mode M_3 is condensed and only then the R_{25} mode (sequence *3* in set (2), Fig. 4). The replacement of Na^+ by a larger K^+ results in a considerable reduction of the free space for both *A*-cation and anions. Therefore, with an increase in x, the temperatures of all the rotational phase transitions drastically decrease ($\Delta T_c \sim 15$–20°C at $\Delta x \sim 0.01$) [15]. On the contrary, the replacement of Na^+ by a smaller Li^+ should be accompanied by an increase in the temperatures of all the rotational phase transitions. Indeed, according to the data obtained for $Na_{1-x}Li_xNbO_3$ single crystals [16], at $x \gtrsim 0.04$, the temperatures of the rotational phase transitions start noticeably increasing; however, in the $0 \lesssim x \lesssim 0.04$ region, they remain practically constant. The existence of a plateau at $x \lesssim 0.04$ seems to be associated with the interaction of Li with the structural defects in a $NaNbO_3$ crystal.

ACKNOWLEDGMENTS

This study was supported by the Russian Foundation for Basic research, project no. 99-02-17575.

REFERENCES

1. G. A. Smolenskiĭ, V. A. Bokov, V. A. Isupov, *et al.*, *The Physics of Ferroelectric Phenomena* (Nauka, Leningrad, 1985).
2. K. S. Aleksandrov, A. T. Anistratov, B. V. Beznosikov, *et al.*, *Phase Transitions in Crystals of Halide Compounds ABX_3* (Nauka, Novosibirsk, 1981).
3. S. Hirotsu, J. Harada, N. Iizumi, *et al.*, J. Phys. Soc. Jpn. **37** (5), 1393 (1974).
4. M. Midorikawa, Y. Ishibashi, and Y. Takagi, J. Phys. Soc. Jpn. **41** (6), 2001 (1976).
5. S. Hirotsu, T. Suzuki, and S. J. Sawada, J. Phys. Soc. Jpn. **43** (2), 575 (1977).
6. V. I. Zinenko, A. I. Krupnyĭ, and L. A. Pozdnyakova, Kristallografiya **22** (5), 1015 (1977) [Sov. Phys. Crystallogr. **22**, 578 (1977)].
7. E. S. Larin, Fiz. Tverd. Tela (Leningrad) **26** (10), 3019 (1984) [Sov. Phys. Solid State **26**, 1820 (1984)].
8. M. P. Ivliev, L. A. Reznichenko, and V. P. Sakhnenko, in *Proceedings of the International Scientific and Practical Conference "Fundamental Problems of Modern Piezoelectronics" (Piezotechnology-95)*, Rostov-on-Don, Azov, 1995, Vol. 1, p. 112.
9. O. V. Kovalev, *Irreducible and Induced Representations and Corepresentations of the Fedorov Groups* (Nauka, Moscow, 1986).
10. P. Daniel, A. Bulou, M. Rousseau, *et al.*, Phase Transit. **33**, 91 (1991).
11. C. Ridou, M. Rousseau, P. Daniel, *et al.*, Ferroelectrics **124**, 293 (1991).
12. C. N. R. Rao and J. Gopalakrishnan, *New Directions in Solid State Chemistry* (Cambridge Univ. Press, Cambridge, 1986; Nauka, Novosibirsk, 1990).
13. G. B. Bokiĭ, *Crystal Chemistry* (Nauka, Moscow, 1971).
14. Yu. M. Gufan and V. P. Sakhnenko, Zh. Éksp. Teor. Fiz. **69** (4), 1428 (1975) [Sov. Phys. JETP **42**, 728 (1975)].
15. M. Ahtee and A. W. Hewat, Acta Crystallogr., Sect. A: Cryst. Phys., Diffr., Theor. Gen. Crystallogr. **34**, 309 (1978).
16. E. S. Gagarina, L. A. Shilkina, L. A. Reznichenko, *et al.*, Izv. Akad. Nauk, Ser. Fiz. **65** (6), 778 (2001).

Translated by L. Man